STUDIA UNIVERSITATIS
BABEŞ-BOLYAI

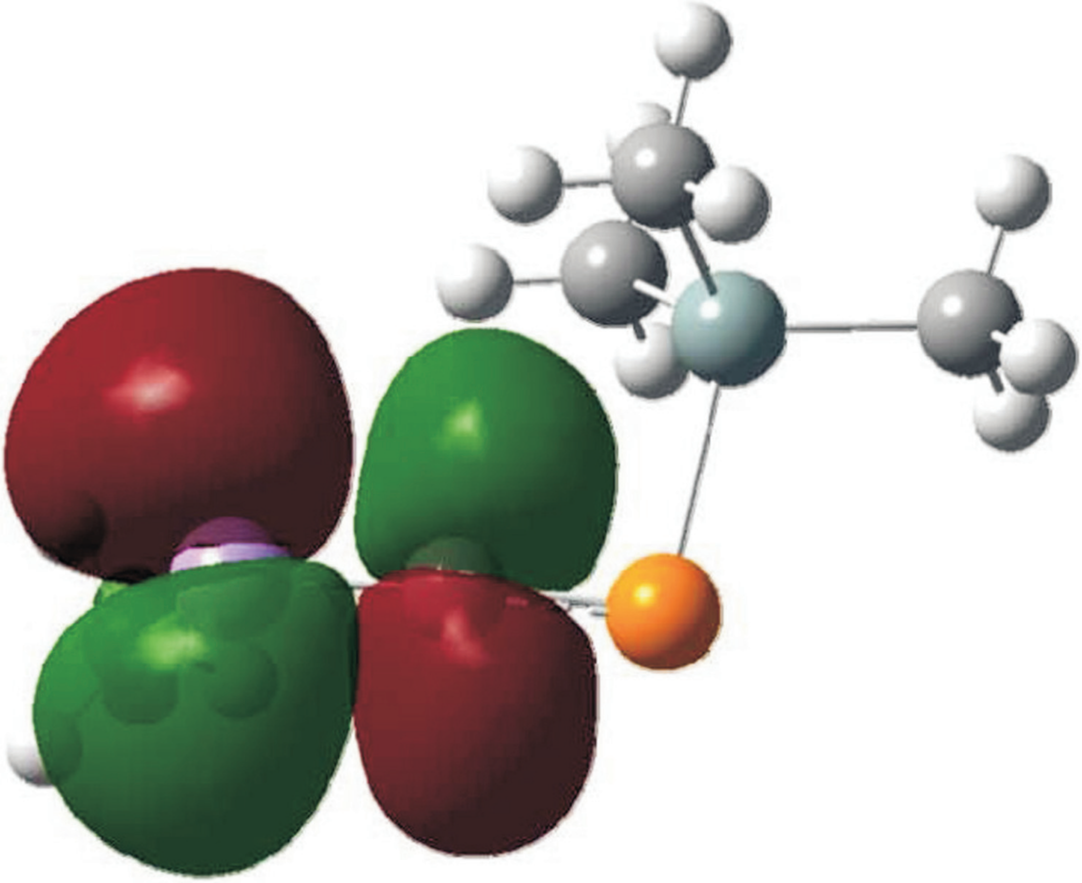

CHEMIA

2/2010
tom I

ANUL LV 2010

S T U D I A

UNIVERSITATIS BABEŞ-BOLYAI

CHEMIA

2

tom I

Desktop Editing Office: 51ST B.P. Hasdeu Street, Cluj-Napoca, Romania, Phone + 40 264-405352

CONTENT – SOMMAIRE – INHALT – CUPRINS

Studia Universitatis Babes-Bolyai Chemia has been selected for coverage in Thomson Reuters products and custom information services. Beginning with V. 53 (1) 2008, this publication is indexed and abstracted in the following:

- Science Citation Index Expanded (also known as SciSearch®)
- Chemistry Citation Index®
- Journal Citation Reports/Science Edition

IOAN SILAGHI-DUMITRESCU
1950-2009

Corresponding member of the Romanian Academy

Born in 1950, he attended primary school in his home village (Botiz, Satu Mare county) and followed on with highschool in Satu-Mare.

Graduated in 1974 from the Inorganic Chemistry of the Department of Chemistry of the Babes-Bolyai University at Cluj-Napoca, Romania, he obtained his PhD from the same university in 1981. After three years spent in the industry at the Sanex Enterprise for Fine Ceramics in Construction (1974-1977), he joined the faculty at the Department of Chemistry and Chemical Engineering of the Babes-Bolyai University, where he eventually became a full professor in 1994; here, he served as head of the Inorganic Chemistry Chair (1994-2007) and as Dean of the Department (2008-2009).

Professor Ioan Silaghi-Dumitrescu's research contributions were in the fields of inorganic and organometallic chemistry, with synthesis and structural characterization of transition metal compounds as well as of compounds involving elements from main groups 13, 14 and 15 (e.g., cumulene and heterocumulene systems with heavy elements, biologically-active compounds).

He was among the first researchers in Romania to approach chemistry with computational techniques, starting very early on from force constant calculations and spectrum simulations to offer general principles for assigning coordination modes with thiophosphoric ligands at a time when structural analysis with X-ray diffraction was not available in Romania. He then evolved towards quantum chemistry, where he provided notable contributions with molecular modeling studies. His results on the structure of clusters involving main group (post-transition) elements, organometallic clusters, cumulenic and heterocumulenic systems, nanotubes and calixarenes, were reported in journals among the most prestigious in the field of chemistry. Much of his research was aimed not solely at obtaining structural information, but also at understanding and guiding experiments performed in his own research group as well as by collaborators from various countries, thereby allowing for establishing strategies in synthesis and for explanation and prediction of properties for a wide range of inorganic, organometallic and organic compounds. His results have been reported in 182 scientific articles in relevant journals across the world (December 2009).

The Center for Molecular Modeling and Quantum Chemistry founded by him in 2007 (developed from the Laboratory for Structure and Molecular Modeling established in 1996), featuring an internationally-competitive computational infrastructure, has consolidated the school of theoretical chemistry in Cluj and has provided a sound basis for high-level collaborations with prominent researchers from the United States of America and from China.

He was a visiting professor at the National Autonomous University in Mexico (UNAM) in the Theoretical Chemistry Group at the Institute of Chemistry (1995-1996) and at the University of Georgia, Athens, Georgia (USA) (2000-2008, for 1-2 months each year). He also had research-related stays at the University of Nottingham (1992) and Heidelberg University (1993-1994), and was engaged in active collaborations with groups from the Universities in Toulouse, Rouen, Lille, Leipzig, Braunschweig, Köln, Budapest, Pecs, Beijing, Guanjou, Moskow (Idaho).

He received the *"Gheorghe Spacu*" prize from the Romanian Academy for his "Research in structure and molecular topology" in 1989 and the *"Gheorghe Spacu*" Medal and “Diploma de Onoare” from the Romanian Society of Chemistry (2009).

Editorial Board

Ioan Silaghi-Dumitrescu - List of Publications

Binuclear cyclopentadienylcobalt sulfur and phosphinidene complexes Cp2Co2E2 (E = S, PX): Comparison with their Iron carbonyl analogues, Li, Guoliang; Li, Qian-Shu; Silaghi-Dumitrescu, Ioan; King, Bruce R.; Schaefer, Henry F, Journal of Organometallic Chemistry (2010), 695(6), 804-808.

On the microwave-assisted synthesis of acylphenothiazine derivatives-Experiment versus theory synergism, Gaina, Luiza; Porumb, Dan; Silaghi-Dumitrescu, Ioan; Cristea, Castelia; Silaghi-Dumitrescu, Luminita, Canadian Journal of Chemistry (2010), 88(1), 42-49.

(Diethylenetriamine)bis(theophyllinato)zinc(II) dihydrate. Mihaly, Bela; Forizs, Edit; Kun, Attila-Zsolt; Silaghi-Dumitrescu, Ioan, Acta Crystallographica, Section E: Structure Reports Online (2009), E65(5), m579.

An insight into the structure of model germaphosphaallenes, Petrar, P. M.; Nemes, G.; Silaghi-Dumitrescu, I.; Escudie, J.; Ranaivonjatovo, Molecular Physics (2009), 107(8-12), 1161-1167

Butterfly and rhombus structures for binuclear cobalt carbonyl sulfur and phosphinidene complexes of the type Co2(CO)6E2 (E = S, PX), Li, Guoliang; Li, Qian-Shu; Silaghi-Dumitrescu, Ioan; King, R. Bruce; Schaefer, Henry F., III, Dalton Transactions (2009), (47), 10474-10480.

Endohedral Nickel, Palladium, and Platinum Atoms in 10-Vertex Germanium Clusters: Competition between Bicapped Square Antiprismatic and Pentagonal Prismatic Structures, King, R. B.; Silaghi-Dumitrescu, I.; Uta, M. M, Journal of Physical Chemistry A (2009), 113(3), 527-533.

From closo to isocloso structures and beyond in cobaltaboranes with 9 to 12 vertices, King R Bruce; Silaghi-Dumitrescu Ioan; Sovago Ioana, Inorganic chemistry (2009), 48(21), 10117-25.

Kinetic versus thermodynamic isomers of the deltahedral cobaltadicarbaboranes, King R Bruce; Silaghi-Dumitrescu Ioan; Sovago Ioana, Inorganic chemistry (2009), 48(12), 5088-95.

N,N' and N,O chelated phosphenium cations containing aminotroponiminate or aminotroponate units, Pop, Lucian-Cristian; Katir, Nadia; Castel, Annie; Silaghi-Dumitrescu, Luminita; Delpech, Fabien; Silaghi-Dumitrescu, Ioan; Gornitzka, Heinz; MacLeod-Carey, Desmond; Saffon, Nathalie, Journal of Organometallic Chemistry (2009), 694(9-10), 1562-1566.

Narrow-rim alkenyl calix[n]arene. Synthesis and spectral characterization, Saponar, Alina; Popovici, Elisabeth-Jeanne; Popovici, Nicolae; Bica, Ecaterina; Nemes, Gabriela; Petrar, Petronela; Silaghi-Dumitrescu, Ioan, Revista de Chimie (2009), 60(3), 278-282.

Stabilisation of an inorganic digallane by the phosphinobisthiolato P,S,S pincer ligand PPh(2-SC6H4)2, Valean, Ana-Maria; Gomez-Ruiz, Santiago; Loennecke, Peter; Silaghi-Dumitrescu, Ioan; Silaghi-Dumitrescu, Luminita; Hey-Hawkins, Evamarie, New Journal of Chemistry (2009), 33(8), 1771-1779.

The unique palladium-centered pentagonal antiprismatic cationic bismuth cluster: a comparison of related metal-centered 10-vertex pnictogen cluster structures by density functional theory, King R B; Silaghi-Dumitrescu I; Uta M M, Inorganic chemistry (2009), 48(17), 8508-14.

Lower Rim Silyl Substituted Calix[8]Arenes, Fleuret, Nathan; Paic, Sebastian; Nemes, Gabriela; Septelean, Raluca; Petrar, Petronela; Silaghi-Dumitrescu, Ioan, Studia Universitatis Babes-Bolyai, Chemia (2009), 54(3), 81-88.

Theoretical aspects of main group multiple bonded systems, Silaghi-Dumitrescu, Ioan; Petrar, Petronela; Nemes, Gabriela; King, R. Bruce, Computational Inorganic and Bioinorganic Chemistry (2009), 563-575.

vic-Dichlorodiphosphapropenes - synthesis and coordination ability, Septelean, Raluca; Nemes, Gabriela; Escudie, Jean; Silaghi-Dumitrescu, Ioan; Ranaivonjatovo, Henri; Petrar, Petronela; Gornitzka, Heinz; Silaghi-Dumitrescu, Luminita; Saffon, Nathalie, European Journal of Inorganic Chemistry (2009), (5), 628-634.

Beyond the icosahedron: a density functional theory study of 14-atom germanium clusters, King, R. Bruce; Silaghi-Dumitrescu, Ioan; Uta, Matei M, European Journal of Inorganic Chemistry (2008), (25), 3996-4003.

Beyond the Wade-Mingos Rules in Bare 10- and 12-Vertex Germanium Clusters: Transition States for Symmetry Breaking Processes, King, R. B.; Silaghi-Dumitrescu, I.; Uta, M. M, Journal of Chemical Theory and Computation (2008), 4(1), 209-215.

Bis(phosphanylamino)benzene ligands: a zinc(II) complex and an unusual nickel(I) complex with a Dewar-benzene-type Ni2P2N2 backbone, Majoumo-Mbe, F.; Kuehl, O.; Loennecke, P.; Silaghi-Dumitrescu, I.; Hey-Hawkins, E, Dalton Transactions (2008), (23), 3107-3114.

Germanium cluster polyhedral, Silaghi-Dumitrescu, Ioan; King, Bruce, Studia Universitatis Babes-Bolyai, Chemia (2008), 53(2), 83-88.

Interplay among Tetrahedrane, Butterfly Diradical, and Planar Rhombus Structures in the Chemistry of the Binuclear Iron Carbonyl Phosphinidene Complexes Fe2(CO)6(PX)2, Silaghi-Dumitrescu, Ioan; Bitterwolf, Thomas E.; King, R. Bruce, Journal of the American Chemical Society (2008), 130(3), 901-906.

Palladium(II) and Platinum(II) Complexes with Heteroditopic 10-(Aryl)phenoxarsine (Aryl = 2-C6H4OR, R = H, Me, Pri) Ligands: Solvent-Oriented Crystallization of cis Isomers, Moldovan, Natalia; Loennecke, Peter; Silaghi-Dumitrescu, Ioan; Silaghi-Dumitrescu, Luminita; Hey-Hawkins, Evamarie, Inorganic Chemistry (2008), 47(5), 1524-1531.

Polyhedral structures with three-, four-, and five fold symmetry in metal-centered ten-vertex germanium clusters, King R Bruce; Silaghi-Dumitrescu Ioan; Uta Matei-Maria (2008), 14(15), 4542-50.

Process for preparation of calixarene derivatives for the extraction of rare earth metal ions, Ursales, Traian; Popovici, Nicolae; Popovici, Elisabeth-Jeanne; Silaghi-Dumitrescu, Ioan; Palibroda, Nicolae. 121691 B1 20080228 Patent written in Romanian. Application: RO 2003-200300816 20031003. Priority: CAN 150:35528 AN 2008:361932.

Serinolic amino-s-triazines: iterative synthesis and rotational stereochemistry phenomena as N-substituted derivatives of 2-aminopropane-1,3-diols, Pintea, Monica; Fazekas, Marijana; Lameiras, Pedro; Cadis, Ionut; Berghian, Camelia; Silaghi-Dumitrescu, Ioan; Popa, Flavia; Bele, Constantin; Ple, Nelly; Darabantu, Mircea, Tetrahedron (2008), 64(37), 8851-8870.

Synthesis and characterisation of some copper oxide catalysts for ozone decomposition, Dan, C.; Popovici, E.-J.; Imre-Lucaci, F.; Popovici, N.; Marginean, P.; Silaghi-Dumitrescu, I, Journal of Optoelectronics and Advanced Materials (2008), 10(9), 2234-2236.

Temperature induced rotation in a [4.4]cyclophane, Bogdan, Niculina D.; Condamine, Eric; Toupet, Loic; Ramondenc, Yvan; Silaghi-Dumitrescu, Ioan; Grosu, Ion, Tetrahedron Letters (2008), 49(35), 5204-5207. **Abstract**

The role of "external" lone pairs in the chemical bonding of bare post-transition element clusters: the Wade-Mingos rules versus the jellium model, King, R. B.; Silaghi-Dumitrescu, I, Dalton Transactions (2008), (44), 6083-6088.

When Arsine Makes the Difference: Chelating Phosphino and Bridging Arsinoarylthiolato Gallium, Valean, Ana Maria; Gomez-Ruiz, Santiago; Lonnecke, Peter; Silaghi-Dumitrescu, Ioan; Silaghi-Dumitrescu, Luminita; Hey-Hawkins, Evamarie, Inorganic Chemistry (2008), 47(23), 11284-11293.

1,1,4,4-Tetrabenzyl-1,4-diphosphinane-1,4-diium dibromide deuterochloroform disolvate, Fild, Manfred; Krueger, Oana N.; Silaghi-Dumitrescu, Ioan; Thoene, Carsten, Acta Crystallographica, Section E: Structure Reports Online (2007), E63(12), o4525, o4525/1-o4525/8.

1,3-Digermacyclobutanes with exocyclic C:P and C:P:S double bonds. Petrar, Petronela Maria; Nemes, Gabriela; Silaghi-Dumitrescu, Ioan; Ranaivonjatovo, Henri; Gornitzka, Heinz; Escudie, Jean, Chemical Communications (2007), (40), 4149-4151

Calix[n]arene derivatives with binding properties toward Eu3+, Saponar, Alina; Silaghi-Dumitrescu, Ioan; Popovici, Elisabeth-Jeanne; Popovici, Nicolae, Studia Universitatis Babes-Bolyai, Chemia (2007), 52(4), 67-74.

Synthesis of Ester Derivatives of Calix[n]arene, Saponar, Alina; Popovici, Elisabeth-Jeanne; Grecu, Rodica; Silaghi-Dumitrescu, Ioan; Popovici, Nicolae, Studia Universitatis Babes-Bolyai, Chemia (2009), 54(4), 203-210.

cis- -1,4-Diphenyl-1,4-diphosphorinane- 2P:P'-bis[pentacarbonylchromium(0)] deuterochloroform solvate,, Fild, Manfred; Krueger, Oana N.; Silaghi-Dumitrescu, Ioan; Thoene, Carsten; Weinkauf, Andreas, Acta Crystallographica, Section E: Structure Reports Online (2007), E63(12), m3011, m3011/1-m3011/9.

Density functional theory study of twelve-atom germanium clusters: conflict between the Wade-Mingos rules and optimum vertex degrees, King, R. Bruce; Silaghi-Dumitrescu, Ioan; Uta, Matei M, Dalton Transactions (2007), (3), 364-372.

New [4.4]cyclophane diketals, monoketones, and diketones: design, synthesis, and structural analysis, Bogdan, Niculina; Grosu, Ion; Condamine, Eric; Toupet, Loiec; Ramondenc, Yvan; Silaghi-Dumitrescu, Ioan; Ple, Gerard; Bogdan, Elena, European Journal of Organic Chemistry (2007), (28), 4674-4687.

New Digermylalkenes and Digermylalkynes: [1,3]-Chlorine Shifts in Organogermanium Chemistry? Nemes, Gabriela; Escudie, Jean; Silaghi-Dumitrescu, Ioan; Ranaivonjatovo, Henri; Silaghi-Dumitrescu, Luminita; Gornitzka, Heinz, Organometallics (2007), 26(21), 5136-5139.

Secondary interactions in heteroallenic systems with P:C-E units, Nemes, G.; Silaghi-Dumitrescu, I.; Petrar, P. M.; Septelean, R.; Silaghi-Dumitrescu, L, Studia Universitatis Babes-Bolyai, Chemia (2007), 52(1), 3-9.

Silatropic migration in (1-trimethylsilylindenyl)(indenyl)dimethylsilane, bis(1-trimethylsilylindenyl)dimethylsilane and related compounds, Nemes, Gabriela; Silaghi-Dumitrescu, Luminita; Silaghi-Dumitrescu, Ioan; Escudie, Jean; Ranaivonjatovo, Henri; Zukerman-Schpector, Julio, Revue Roumaine de Chimie (2007), 52(8-9), 809-816.

Studies on some ozone decomposition catalysts based on nickel oxide, Dan, Crina; Popovici, Elisabeth-Jeanne; Imre, Florica; Indrea, Emil; Marginean, Petre; Silaghi-Dumitrescu, Ioan, Studia Universitatis Babes-Bolyai, Chemia (2007), 52(1), 91-95.

Synthesis and characterization of calix[4]arene with different donor groups at the "narrow" rim, Saponar, Alina; Silaghi-Dumitrescu, Ioan; Popovici, Elisabeth-Jeanne; Popovici, Nicolae, Revista de Chimie (2007), 58(5), 481-483.

Synthesis and characterization of some mixed ligand zinc(II) complexes of theophylline, Mihaly, Bela; Forizs, Edit; Silaghi-Dumitrescu, Ioan, Studia Universitatis Babes-Bolyai, Chemia (2007), 52(4), 111-116.

Synthesis and characterization of the first arsanylbis(methylene)phosphorane (Me3Si)2C:P(Mes*):C(Cl)As(F)Mes*, Petrar, Petronela Maria; Nemes, Gabriela; Silaghi-Dumitrescu, Luminita; Silaghi-Dumitrescu, Ioan; Escudie, Jean; Gornitzka, Heinz; Ranaivonjatovo, Henri, Revue Roumaine de Chimie (2007), 52(1-2), 45-49.

Synthesis and properties of organogermanium and organotin dithiophosphonate complexes; crystal structures of (C6H5)2Sn(Cl)[(p-MeOC6H4)(EtO)PS2-S, S'], Me2Sn[(p-MeOC6H4)(MeO)PS2-S]2, Me2Sn[(p-MeOC6H4)(iPrO)PS2-S]2, and Me2Ge{[(C6H5)3SiO](p-MeOC6H4)PS2-S}2, Fild, Manfred; Krueger, Oana; Silaghi-Dumitrescu, Ioan; Thoene, Carsten; Weinkauf, Andreas, Phosphorus, Sulfur and Silicon and the Related Elements (2007), 182(10), 2283-2310.

Synthesis and spectral characterization of some calix[4]pyrogallolarenes, Popovici, N.; Ursales, T. N.; Silaghi-Dumitrescu, I.; Saponar, Alina; Popovici, Elisabeth-Jeanne, Acta Universitatis Cibiniensis, Seria F: Chemia (2007), 10(2), 51-57.

The formylation of bis-(N-alkyl-phenothiazinyl)-methane; a theoretical approach, Porumb, Dan; Silaghi-Dumitrescu, Ioan; Gaina, Luiza; Silaghi-Dumitrescu, Luminita; Cristea, Castelia; Cormos, Gabriela, Studia Universitatis Babes-Bolyai, Chemia (2007), 52(4), 39-42.

Towards new double-bonded organophosphorus derivatives of C:P:C:P type, Nemes, Gabriela; Septelean, Raluca; Petrar, Petronela M.; Silaghi-Dumitrescu, Luminita; Silaghi-Dumitrescu, Ioan, Studia Universitatis Babes-Bolyai, Chemia (2007), 52(4), 89-94.

α -(3,7-Dioxa-r-1-azabicyclo[3.3.0]oct-c-5-ylmethoxy)-diazines. Part 2: Functionalization via directed ortho-metalation and cross-coupling reactions, Berghian, Camelia; Condamine, Eric; Ple, Nelly; Turck, Alain; Silaghi-Dumitrescu, Ioan; Maiereanu, Carmen; Darabantu, Mircea, Tetrahedron (2006), 62(31), 7339-7354.

A quantum chemical conformational analysis of p-tert-butyl/pentyl/octyl-calix[8]arenes, Lupan, Alexandru; Saponar, Alina; Silaghi-Dumitrescu, Ioan; Kun, Attila; Silaghi-Dumitrescu, Luminita; Popovici, Elisabeth Jeanne, Studia Universitatis Babes-Bolyai, Chemia (2006), 51(2), 27-34.

Butterfly Diradical Intermediates in Photochemical Reactions of Fe2(CO)6(mu -S2), Silaghi-Dumitrescu, Ioan; Bitterwolf, Thomas E.; King, R. Bruce, Journal of the American Chemical Society (2006), 128(16), 5342-5343.

Co-complexes of ortho-dilithiated thiophenol or 2-trimethylsilylthiophenol with lithiated TMEDA molecules: synthesis, crystal structures and theoretical studies (TMEDA = N,N,N',N'-tetramethylethylenediamine), Hildebrand, Alexandra; Loennecke, Peter; Silaghi-Dumitrescu, Luminita; Silaghi-Dumitrescu, Ioan; Hey-Hawkins, Evamarie, Dalton Transactions (2006), (7), 967-974.

Density Functional Theory Study of 10-Atom Germanium Clusters: Effect of Electron Count on Cluster Geometry. King, R. B.; Silaghi-Dumitrescu, I.; Uta, M. M, Inorganic Chemistry (2006), 45(13), 4974-4981.

DFT and the electromerism in complexes of iron with diatomic ligands, Silaghi-Dumitrescu, Radu; Silaghi-Dumitrescu, Ioan., Journal of Inorganic Biochemistry (2006), 100(1), 161-166.

First synthesis of a G-2 melamine dendrimer with serinolic peripheral groups, Darabantu, Mircea; Pintea, Monica; Fazekas, Marijana; Lameiras, Pedro; Berghian, Camelia; Delhom, Isabelle; Silaghi-Dumitrescu, Ioan; Ple, Nelly; Turck, Alain, Letters in Organic Chemistry (2006), 3(12), 905-910.

Molecular Rotors: Design, Synthesis, Structural Analysis, and Silver Complex of New [7.7]Cyclophanes, Bogdan, Niculina; Grosu, Ion; Benoit, Guillaume; Toupet, Loiec; Ramondenc, Yvan; Condamine, Eric; Silaghi-Dumitrescu, Ioan; Ple, Gerard, Organic Letters (2006), 8(12), 2619-2622.

New halo compounds of silicon and tin, potential precursors of >E=C=P-heteroallenic systems, Petrar, Petronela Maria; Nemes, Gabriela; Silaghi-Dumitrescu, Ioan; Silaghi-Dumitrescu, Luminita, Studia Universitatis Babes-Bolyai, Chemia (2006), 51(1), 77-82

New low symmetry low energy structures of 11-atom bare germanium clusters: A density functional theory study, King, R. B.; Silaghi-Dumitrescu, I.; Lupan, A, Chemical Physics (2006), 327(2-3), 344-350.

Phosphavinylidene(oxo)phosphorane Mes*P(O):C:PMes*: a diphosphaallene featuring λ 5σ 3- and λ 3σ 2-phosphorus atoms, Septelean, Raluca; Ranaivonjatovo, Henri; Nemes, Gabriela; Escudie, Jean; Silaghi-Dumitrescu, Ioan; Gornitzka, Heinz; Silaghi-Dumitrescu, Luminita; Massou, Stephane, European Journal of Inorganic Chemistry (2006), (21), 4237-4241.

Special issue: Computational inorganic chemistry - Part 3 of 3. [In: Chemtracts; 2006, 19(2)], Silaghi-Dumitrescu, Radu; Silaghi-Dumitrescu, Ioan. USA. (2006), 41 pp. Publisher: (Data Trace Publishing Co., Baltimore, Md.) Book written in English. CAN 146:175448 AN 2007:

Special theme issue inorganic computational chemistry, Part I. [In: Chemtracts, 2006; 18(11)], Silaghi-Dumitrescu, Radu; Silaghi-Dumitrescu, Ioan; Editors. USA. (2006), 41 pp. Publisher: (Data Trace Publishing Co., Baltimore, Md.) Book written in English. CAN 146:175447 AN 2006:1324965

Structural, energetic and electronic characterization of the chiral carbon-nitride nanotubes, Rada, Simona; Silaghi-Dumitrescu, Ioan, Revue Roumaine de Chimie (2006), 51(2), 141-145.

Synthesis of new bromo-stannanes: toward unsaturated tin derivatives, Petrar, Petronela Maria; Nemes, Gabriela; Silaghi-Dumitrescu, Ioan; Silaghi-Dumitrescu, Luminita, Studia Universitatis Babes-Bolyai, Chemia (2006), 51(2), 35-40.

A quantum chemical study on boron nitride and carbon nitride nanotubes., Rada, Simona; Dumitrescu, Ioan Silaghi, Studia Universitatis Babes-Bolyai, Chemia (2005), 50(2), 155-158.

A surprisingly stable 1-(chlorosilyl)-2-phosphaethenyllithium compound, RCl2SiC(Li):PMes*, Nemes, Gabriela Cretiu; Ranaivonjatovo, Henri; Escudie, Jean; Silaghi-Dumitrescu, Ioan; Silaghi-Dumitrescu, Luminita; Gornitzka, Heinz, European Journal of Inorganic Chemistry (2005), (6), 1109-1113.

Adsorption of 6-mercaptopurine and 6-mercaptopurine riboside on silver colloid: a pH dependent surface enhanced Raman spectroscopy and density functional theory study. Part I. 6-Mercaptopurine, Szeghalmi, A. V.; Leopold, L.; Pinzaru, S.; Chis, V.; Silaghi-Dumitrescu, I.; Schmitt, M.; Popp, J.; Kiefer, W, Journal of Molecular Structure (2005), 735-736 103-113.

Anodic oxidation of difluorenyls bridged through a dimethylsilyl group and of the 9-trimethylsilyl fluorene: Towards new three-dimensional polyfluorenes, Silaghi-Dumitrescu, Ioan; Escudie, Jean; Cretiu-Nemes, Gabriela; Raoult, Eugene; Rault-Berthelot, Joelle, Synthetic Metals (2005), 151(2), 114-119

Applications of carbon-nitride nanotubes to molecular engines photochemically engineered, Rada, Simona; Dumitrescu, Ioan Silaghi; Maties, Vistrian; Rada, Marius, Revista de Chimie (Bucharest, Romania) (2005), 56(5), 490-494.

Computational inorganic chemistry - a useful tool and more, Silaghi-Dumitrescu, Radu; Silaghi-Dumitrescu, Ioan, Chemtracts (2005), 18(11), 595-619.

Density Functional Study of 8- and 11-Vertex Polyhedral Borane Structures: Comparison with Bare Germanium Clusters, King, R. B.; Silaghi-Dumitrescu, I.; Lupan, A, Inorganic Chemistry (2005), 44(22), 7819-7824.

Density Functional Theory Study of 11-Atom Germanium Clusters: Effect of Electron Count on Cluster Geometry, King, R. B.; Silaghi-Dumitrescu, I.; Lupan, A, Inorganic Chemistry (2005), 44(10), 3579-3588.

Density functional theory study of eight-atom germanium clusters: effect of electron count on cluster geometry, King, R. B.; Silaghi-Dumitrescu, I.; Lupan, A, Dalton Transactions (2005), (10), 1858-1864

Difluorenylsilanes, -germanes, and -stannanes Exhibiting an Unprecedented Parallel Arrangement of the Fluorene Units, Nemes, Gabriela Cretiu; Silaghi-Dumitrescu, Luminita; Silaghi-Dumitrescu, Ioan; Escudie, Jean; Ranaivonjatovo, Henri; Molloy, Kieran C.; Mahon, Mary F.; Zukerman-Schpector, Julio, Organometallics (2005), 24(6), 1134-1144.

Discontinuum between ferrous-superoxo and ferric-peroxo in heme [FeO2]9 complexes? Silaghi-Dumitrescu, Radu; Silaghi-Dumitrescu, Ioan, Studia Universitatis Babes-Bolyai, Chemia (2005), 50(1), 11-15.

Electronic properties of C80-xNx tubes with chair geometry, Rada, Simona; Dumitrescu, Ioan Silaghi; Maties, Vistrian; Rada, Marius, Revista de Chimie (2005), 56(2), 144-147.

Germanium cluster polyhedra: a density functional theory study, Silaghi-Dumitrescu, Ioan; Kun, Attila; Lupan, Alex; King, R. Bruce, Lecture Series on Computer and Computational Sciences (2005), 4 A(Advances in Computational Methods in Sciences and Engineering), 804-806. Publisher: Brill Academic Publishers, ISSN: 1573-4196.

Periodic Cages, Diudea, Mircea V.; Nagy, Csaba L.; Silaghi-Dumitrescu, Ioan; Graovac, Ante; Janezic, Dusanka; Vikic-Topic, Drazen, Journal of Chemical Information and Modeling (2005), 45(2), 293-299

75. Structural, energetic and electronic properties of pure/doped BN nanotubes, Rada, Simona; Dumitrescu, Ioan Silaghi, Studia Universitatis Babes-Bolyai, Chemia (2005), 50(1), 297-306.

Synthesis and Stereochemistry of New Bis(1,3-Oxathian-2-yl) Derivatives: Epimerisation and Chair-Twist Equilibria, Cismas, C.; Grosu, I.; Ple, G.; Condamine, E.; Ramondenc, Y.; Toupet, L.; Silaghi-Dumitrescu, I.; Nemes, G.; Terec, A.; Muntean, L Structural Chemistry (2005), 16(4), 369-377.

The first evidence for a transient stibaallene ArSbCCR2, Baiget, Lise; Ranaivonjatovo, Henri; Escudie, Jean; Nemes, Gabriela Cretiu; Silaghi-Dumitrescu, Ioan; Silaghi-Dumitrescu, Luminita, Journal of Organometallic Chemistry (2005), 690(2), 307-312.

The shapes of hypoelectronic six-vertex anionic bare boron clusters: effects of the countercations, King, R. B.; Silaghi-Dumitrescu, I.; Lupan, A.; Kun, A, Main Group Chemistry (2005), 4(4), 291-302

3,7-dioxa-1-azabicyclo[3.3.0]octanes substituted at the C-5 position - >From local to global stereochemistry, Darabantu, Mircea; Maiereanu, Carmen; Silaghi-Dumitrescu, Ioan; Toupet, Loic; Condamine, Eric; Ramondenc, Yvan; Berghian, Camelia; Ple, Gerard; Ple, Nelly, European Journal of Organic Chemistry (2004), (12), 2644-2661.

A complex problem of diastereoisomerism: Synthesis and stereochemistry of 1,4-bis-{r-1-aza-c-5-ethyl-3,7-dioxabicyclo[3.3.0]octane-c-2-yl}-benzene, Maiereanu, Carmen; Toupet, Loic; Condamine, Eric; Silaghi-Dumitrescu, Ioan; Ple, Gerard; Ramondenc, Yvan; Darabantu, Mircea, Revue Roumaine de Chimie (2004), 49(7), 595-602.

A novel disiloxanediolato-derivative of tin(IV), Petrar, Petronela M.; Nemes, Gabriela Cretiu; Silaghi-Dumitrescu, Ioan. Studia Universitatis Babes-Bolyai, Chemia (2004), 49(2), 209-216.

Conformational and configurational analysis on some calix[4]resorcinarenes functionalized with organo-phosphorus groups, Ursales, Traian-Nicolae; Silaghi-Dumitrescu, Ioan, Revue Roumaine de Chimie (2004), 49(2), 143-147.

Electronic properties of the zigzag carbon-nitride nanotubes, Rada, Simona; Dumitrescu, Ioan Silaghi. Studia Universitatis Babes-Bolyai, Chemia (2004), 49(2), 217-222.

Hemes revisited by density functional approaches. 1: The axial ligand and the dioxygen-peroxo chemistry, Silaghi-Dumitrescu, Radu; Silaghi-Dumitrescu, Ioan Revue Roumaine de Chimie (2004), 49(3-4), 257-268.

New materials based on phosphorylated calix[n]arenes, Ursales, T. N.; Silaghi-Dumitrescu, I.; Popovici, E.-J.; Ursales, A.; Popovici, N Journal of Optoelectronics and Advanced Materials (2004), 6(1), 307-313.

Possible hybrids between polyoxometalates and calixarenes, Ursales, T. N.; Silaghi-Dumitrescu, I.; Grecu, R.; Silaghi-Dumitrescu, L.; Popovici, N.; Popovici, E.-J, Journal of Optoelectronics and Advanced Materials (2004), 6(2), 471-476.

Synthesis of calix[n]arenes with pendant diphenyl phosphate functionalities at the "narrow rim", Ursaels, T.-N.; Popovici, N.; Silaghi-Dumitrescu, I.; Popovici, E.-J, Acta Universitatis Cibiniensis, Seria F: Chemia (2004), 7(1), 71-75.

Synthesis of some new O-alkenyl calix[6]arene and calix[8]arene derivatives, Ursales, Traian-Nicolae; Silaghi-Dumitrescu, Ioan; Ciocan, Cristina; Palibroda, Nicolae; Popovici, Nicolae; Popovici, Elisabeth-Jeanne. Revue Roumaine de Chimie (2004), 49(9), 741-745.

The conformational analysis of some calix[4]arenes substituted at the "lower rim" with organo-phosphorus groups, Ursales, Traian-Nicolae; Silaghi-Dumitrescu, Ioan, Revue Roumaine de Chimie (2004), 49(5), 437-441.

Tin(IV) halide complexes of AsPh3) The structures of trans-SnCl4(AsPh3)2 and SnBr4(AsPh3).AsPh3, Mahon Mary F; Moldovan Natalia L; Molloy Kieran C; Muresan Alexandra; Silaghi-Dumitrescu Ioan; Silaghi-Dumitrescu Luminita, Dalton transactions (2004), (23), 4017-21.

1-Aza-5-hydroxymethyl-3,7-dioxabicyclo[3.3.0]octanes: Chelating properties related to their conformational chirality, Maiereanu, Carmen; Condamine, Eric; Silaghi-Dumitrescu, Ioan; Darabantu, Mircea, Studia Universitatis Babes-Bolyai, Chemia (2003), 48(2), 91-101.

Azocoupling products. Part IV. The structure of dyes obtained by azo-coupling reaction of 1-(4-hydroxy-6-methylpyrimidin-2-yl)-3-methylpyrazolin-5-one with aromatic diazonium salts, Panea, Ioan; Ghirisan, Adina; Baldea, Ioan; Silaghi-Dumitrescu, Ioan; Craciun, Liliana; Silberg, Ioan A, Studia Universitatis Babes-Bolyai, Chemia (2003), 48(2), 67-83.

Computational Study of the Non-Heme Iron Active Site in Superoxide Reductase and Its Reaction with Superoxide, Silaghi-Dumitrescu, Radu; Silaghi-Dumitrescu, Ioan; Coulter, Eric D.; Kurtz, Donald M., Jr. Inorganic Chemistry (2003), 42(2), 446-456

Computational study of the non-heme iron active site in superoxide reductase and its reaction with superoxide, Silaghi-Dumitrescu Radu; Silaghi-Dumitrescu Ioan; Coulter Eric D; Kurtz Donald M Jr, Inorganic chemistry (2003), 42(2), 446-56.

Density Functional Theory Study of Nine-Atom Germanium Clusters: Effect of Electron Count on Cluster Geometry, King, R. B.; Silaghi-Dumitrescu, I, Inorganic Chemistry (2003), 42(21), 6701-6708.

Density functional theory study of nine-atom germanium clusters: effect of electron count on cluster geometry, King R B; Silaghi-Dumitrescu I, Inorganic chemistry (2003), 42(21), 6701-8.

Influences of Changes in Multitopic Tris(pyrazolyl)methane Ligand Topology on Silver(I) Supramolecular Structures, Reger, Daniel L.; Semeniuc, Radu F.; Silaghi-Dumitrescu, Ioan; Smith, Mark D Inorganic Chemistry (2003), 42(12), 3751-3764.

Influences of changes in multitopic tris(pyrazolyl)methane ligand topology on silver(I) supramolecular structures, Reger Daniel L; Semeniuc Radu F; Silaghi-Dumitrescu Ioan; Smith Mark D, Inorganic chemistry (2003), 42(12), 3751-64

Molecular structure and infrared spectra of 2-bromopropane by ab initio HF and post HF calculations, Grecu, Rodica; Kun, Attila; Silaghi-Dumitrescu, Ioan, Revue Roumaine de Chimie (2003), Volume Date 2002, 47(10-11), 1055-1061.

New halo compounds of Si, P, As, and Sb bearing a bulky substituted fluorenyl group, Baiget, L.; Bouslikhane, M.; Escudie, J.; Nemes, G. Cretiu; Silaghi-Dumitrescu, I.; Silaghi-Dumitrescu, L, Phosphorus, Sulfur and Silicon and the Related Elements (2003), 178(9), 1949-1961.

One pot synthesis a new calix[n]arene derivatives, Ursales, T.-N.; Popovici, E.-J.; Silaghi-Dumitrescu, I.; Popovici, N, Acta Universitatis Cibiniensis, Seria F: Chemia (2003), 6(2), 9-13

Relative stability of conformers of some organophosphorus calix[4]arenes, Ursales, Traian-Nicolae; Silaghi-Dumitrescu, Ioan, Revista de Chimie, (2003), 54(9), 756-758

Small fulleroids, Diudea, Mircea V.; Silaghi-Dumitrescu, IoanStudia Universitatis Babes-Bolyai, Chemia (2003), 48(1), 21-30.

Stereocontrolled synthesis by anomeric effects of substituted 1-aza-3,7-dioxabicyclo[3.3.0]octanes, Maiereanu, Carmen; Silaghi-Dumitrescu, Ioan; Berghian, Camelia; Pintea, Monica; Fazekas, Marijana; Darabantu, Mircea, Studia Universitatis Babes-Bolyai, Chemia (2003), 48(2), 103-112.

Synthesis and characterization of some new phosphorylated cavitands from calix[4]resorcinarenes, Ursales, Traian-Nicolae; Silaghi-Dumitrescu, Ioan, Revista de Chimie, (2003), 54(11), 888-889.

Synthesis and reactivity of difluoromethylene bridged diphospha-derivatives, Toetoes, R.; Silaghi-Dumitrescu, I, Studia Universitatis Babes-Bolyai, Chemia (2003), 48(2), 149-163.

Synthesis, characterization and conformational analysis of methyl-, propyl-, and isopropylcalix[4]resorcinarenes, Ursales, Traian-Nicolae; Ursales, Adina; Silaghi-Dumitrescu, Ioan. Revista de Chimie) (2003), 54(3), 229-231.

A density functional theory study of five-, six- and seven-atom germanium clusters: distortions from ideal bipyramidal deltahedra in hypoelectronic structures, King, R. B.; Silaghi-Dumitrescu, I.; Kun, A, Journal of the Chemical Society, Dalton Transactions (2002), (21), 3999-4004.

Ring-chain tautomerism and other versatile behaviour of 1,4-diimino- and 1,2-phenylene derivatives of some C-substituted serinols. Maiereanu, Carmen; Darabantu, Mircea; Ple, Gerard; Berghian, Camelia; Condamine, Eric; Ramondenc, Yvan; Silaghi-Dumitrescu, Ion; Mager, Sorin. Tetrahedron (2002), 58(13), 2681-2693

Crystal, molecular, and electronic structure of 9,9'-bis(trimethylsilyl)fluorine, Silaghi-Dumitrescu, Ioan; Cretiu, Gabriela; Silaghi-Dumitrescu, Luminita; Haiduc, Ionel; Toscano, Alfredo; Cea-Olivares, Raymundo, Revue Roumaine de Chimie 2001, 46(4), 289-295.

Crystal, molecular, and electronic structure of 9,9'-bis(trimethylsilyl)fluorene, Silaghi-Dumitrescu, Ioan; Cretiu, Gabriela; Silaghi-Dumitrescu, Luminita; Haiduc, Ionel; Toscano, Alfredo; Cea-Olivares, Raymundo, Revue Roumaine de Chimie (2002), 46(4), 289-295.

Difluorenylsilane derivatives, a class of compounds exhibiting strong intra- and intermolecular C-H···π interactions. Crystal and molecular structures of bis(9-methylfluoren-9-yl)dimethylsilane and (9-methylfluoren-9-yl)(fluoren-9-yl) dimethylsilane, Cretiu, Gabriela; Silaghi-Dumitrescu, Luminita; Silaghi-Dumitrescu, Ioan; Escudie, Jean; Toscano, Alfredo; Hernandez, Simon; Cea-Olivares, Raymundo, Journal of Organometallic Chemistry (2002), 659(1-2), 95-101.

Electronic structure of hypervalent organoarsenic bromo derivatives. An ab initio RHF and DFT-B3LYP investigation of H5-XAsBrx systems, Silaghi-Dumitrescu, L.; Silaghi-Dumitrescu, I, Studia Universitatis Babes-Bolyai, Chemia (2002), 47(1-2), 203-211.

Toroidal fullerenes from squared tiled tori, Diudea, Mircea V.; Silaghi-Dumitrescu, Ioan; Parv, Bazil, Internet Electronic Journal of Molecular Design [online computer file] (2002), 1(1), 10-22.

Toroidal fullerenes from squared tiled tori, Diudea, Mircea V.; Silaghi-Dumitrescu, Ioan; Parv, Bazil. Internet Electronic Journal of Molecular Design [online computer file] (2002), 1(1), 10-22

Distortions from octahedral symmetry in hypoelectronic six-vertex polyhedral clusters of the group 13 elements boron, indium, and thallium as studied by density functional theory, King, R. Bruce; Silaghi-Dumitrescu, Ioan; Kun, Attila, Inorganic chemistry (2001), 40(10), 2450-2.

Electronic and magnetic properties of (tetrakis(2-pyridylmethyl)-ethylenediamine)iron(II) perchlorate. A comparison of different computational methods, Chen, Guangju; Liu, Ruozhuang; Silaghi-Dumitrescu, I.; Espinosa-Perez, G.; Zentella-Dehesa, A.; Lara-Ochoa, F, International Journal of Quantum Chemistry (2001), 83(2), 60-69.

Solvent effects in infrared spectra and ab initio calculations of 2-bromopropane, Grecu, R.; Kun, A.; Silaghi-Dumitrescu, I, Journal of Molecular Structure (2001), 565-566 39-42

Structural distortions in homoleptic (RE)4A (E = O, S, Se; A = C, Si, Ge, Sn): implications for the CVD of tin sulfides, Barone, Giampaolo; Hibbert, Thomas G.; Mahon, Mary F.; Molloy, Kieran C.; Parkin, Ivan P.; Price, Louise S.; Silaghi-Dumitrescu, Ioan, Journal of the Chemical Society, Dalton Transactions (2001), (23), 3435-3445.

Toranes versus torenes, Diudea, Mircea V.; Silaghi-Dumitrescu, Ioan; Parv, Bazil, MATCH (2001), 44 117-133.

Voltammetric behaviour of 1,4-benzothiazino[2,3-b]phenothiazine and some of its derivatives. II. The influence of N-substitution and S-oxidation, Cristea, Castelia; Filip, Cecilia; Silaghi-Dumitrescu, Ioan; Silberg, Ioan A, Revue Roumaine de Chimie (2001), 45(7-8), 639-642.

(Tetrakis(2-pyridylmethyl)ethylenediamine)iron(II) Perchlorate. Study of Density Functional Methods, Chen, Guangju; Espinosa-Perez, G.; Zentella-Dehesa, A.; Silaghi-Dumitrescu, I.; Lara-Ochoa, F, Inorganic Chemistry (2000), 39(16), 3440-3448.

(Tetrakis(2-pyridylmethyl)ethylenediamine)iron(II) perchlorate. Study of density functional methods, Chen G; Espinosa-Perez G; Zentella-Dehesa A; Silaghi-Dumitrescu I; Lara-Ochoa F, Inorganic chemistry (2000), 39(16), 3440-8.

A new tubular arrangement of a dimethylsilyl bridged calix[4]resorcinarene, Lara-Ochoa, F.; Garcia, M. Martinez; Teran, R.; Cruz-Almanza, R.; Espinosa-Perez, G.; Chen, G.; Silaghi-Dumitrescu, I, Supramolecular Chemistry (2000), 11(4), 263-273.

Bromination of (AsPh2)2O: the structure of tribromo-diphenylarsenic(V), Silaghi-Dumitrescu, Luminita; Silaghi-Dumitrescu, Ioan; Silaghi-Dumitrescu, Radu; Haiduc, Ionel; Blake, Alexander J.; Sowerby, D. Bryan. Revista de la Sociedad Quimica de Mexico (2000), 44(2), 134-138.

Synthesis and stereochemistry of some new spiro-1,3-perhydrooxazines, Muntean, Luminita; Grosu, Ion; Ple, Gerard; Mager, Sorin; Silaghi-Dumitrescu, Ioan, Monatshefte fuer Chemie (2000), 131(9), 975-983.

Synthesis and stereochemistry of some 1,3-oxazolidine systems based on TRIS (α ,α ,α -trimethylolaminomethane) and related aminopolyols skeleton. Part 2: 1-aza-3,7-dioxabicyclo[3.3.0]octanes. Darabantu, Mircea; Ple, Gerard; Maiereanu, Carmen; Silaghi-Dumitrescu, Ion; Ramondenc, Yvan; Mager, Sorin. Tetrahedron (2000), 56(23), 3799-3816

Synthesis and stereochemistry of some 1,3-oxazolidine systems based on TRIS (α ,α ,α -trimethylolaminomethane) and related aminopolyols skeleton. Part 1: (Di)spiro-1,3-oxazolidines. Darabantu, Mircea; Ple, Gerard; Silaghi-Dumitrescu, Ion; Maiereanu, Carmen; Turos, Istvan; Silberg, Ioan A.; Mager, Sorin. Tetrahedron (2000), 56(23), 3785-3798

Is the trigonal prismatic distortion the answer for the geometry of In(III) four members dithiochelate compounds? The crystal and molecular structure of In(S2AsR2)3 (R = Me, Ph). Silaghi-Dumitrescu, Luminita; Silaghi-Dumitrescu, Ion; Haiduc, Ionel; Toscano, Ruben-Alfredo; Garcia-Montalvo, Veronica; Cea-Olivares, Raymundo. Zeitschrift fuer Anorganische und Allgemeine Chemie (1999), 625(2), 347-351

The crystal and molecular structure of the 2,4,6,8-tetra-t-Bu-phenothiazine 0.5 benzene adduct, Silaghi-Dumitrescu, I.; Silberg, I. A.; Filip, S.; Vlassa, M.; Silaghi-Dumitrescu, L.; Hernandez-Ortega, S, Journal of Molecular Structure (2000), 526 279-286.

An interactive workstation for molecular-mechanics modeling of chemical structures. Horvat, Dragos; Silaghi-Dumitrescu, Ion. Revue Roumaine de Chimie (1992), 37(10), 1165-74

1-(Acridin-9'-yl)-pyrazolin-3- and -5-ones. A new class of heterocycles with potential biological activity, Cristea, Ioan; Popovici, Mariana M.; Mendel, Maria T.; Silaghi-Dumitrescu, Ioan; Kozma, Erika, Heterocyclic Communications (1999), 5(6), 543-548.

A new organodithiophosphoric derivative; synthesis and structural characterization of bis(diphenylborano)dithiophosphoric [(C6H5)2BO]2P(S)SH, Gabriela, Cretiu; Reka, Torok; Delia, Bugnariu; Oxana, Jeman; Silaghi-Dumitrescu, Ioan, Studia Universitatis Babes-Bolyai, Chemia (1999), 44(1-2), 177-182.

An AM1 investigation of the structures of C60:tBu-calix[8]arene 1:1 adducts, Lara-Ochoa, F.; Cogordan, J. A.; Cruz, R.; Martinez, M.; Silaghi-Dumitrescu, I, Fullerene Science and Technology (1999), 7(3), 411-419.

Molecular orbital calculations and physical properties of 1,4-benzothiazino[2,3-b]phenothiazine and its substituted derivatives, Silberg, I. A.; Silaghi-Dumitrescu, I.; Cristea, C.; Tordo, P.; Gigmes, D, Heterocyclic Communications (1999), 5(2), 147-150.

Stable isomers of sila- and germadodecahedrane. A semiempirical (AM1) investigation of the structure of 4/6 and 4/5/6 ring containing E20 (E=Si,Ge) systems, Silaghi-Dumitrescu, Ioan; Kun, Attila; Haiduc, Ionel, Fullerene Science and Technology (1999), 7(5), 841-854.

Why does the yellow isomer of [Sn{(PPh2Se)2-Se,Se'}2] present a square planar four-co-ordinated tin(II)? A molecular orbital approach, Silaghi-Dumitrescu, Ioan; Silaghi-Dumitrescu, Luminita; Cea-Olivares, Raymundo, Main Group Metal Chemistry (1999), 22(1), 5-8.

Synthesis and ring-ring tautomerism of some spirooxazolidines based on i-p-nitrophenylserinol skeleton. Darabantu, Mircea; Ple, Gerard; Gaina, Luiza; Maierean, Carmen; Silaghi-Dumitrescu, Ion. Studia Universitatis Babes-Bolyai, Chemia (1998), 43(1-2), 179-192

Cis and/or trans dioxaphosphetanes. A molecular orbital study of some model (RPO)2 systems, Silaghi-Dumitrescu, Ioan; Horea, Alin,Revue Roumaine de Chimie (1997), 42(7), 599-604.

Comparative PM3-MO study of the E2O2 and E2N2 (E = P, As) four-membered-ring systems, Silaghi-Dumitrescu, Ioan; Horea, Alin; Pascu, Sofia; Silaghi-Dumitrescu, Luminita; Haiduc, Ionel, Phosphorus, Sulfur and Silicon and the Related Elements (1997), 124 & 125 441-444.

Ion-molecule interactions in organic electrochemical systems. I. NMR investigations of electrolyte solutions used in lithium anode batteries, Silberg, Ioan Alexandru; Oniciu, Liviu; Bobos, Liviu-Dorel; Silaghi-Dumitrescu, Ioan; Avram, Silvia; Cuibus, Cristina. Revue Roumaine de Chimie (1997), 42(7), 535-542.

On the formation of cyclodisilazanes via the coordination of bis(dialkylamino)silanes to halosilanes: an ab initio and AM1 molecular orbital study of the 4644 R2Si(NR'2)2:SiX4 ring systems, Silaghi-Dumitrescu, Ioan; Lara-Ochoa, Francisco; Haiduc, Ionel, THEOCHEM (1997), 397 213-222.

On the structure of bis(9-fluorenyl)dimethylsilane: a sterically crowded molecule with relatively low barriers of rotations around the Si-C(fluorenyl) bonds X-ray diffraction analysis and AM1 molecular orbital calculations, Silaghi-Dumitrescu, Luminita; Haiduc, Ionel; Cea-Olivares, Raymundo; Silaghi-Dumitrescu, Ioan; Escudie, Jean; Couret, Claude, Journal of Organometallic Chemistry (1997), 545-546 1-7.

Structural studies of tetrazoles. Crystal and molecular structure and ab initio calculations of 1-phenyl-1H-tetrazole-5-thiolate, as its [diaqua(18-crown-6)sodium] salt: an anionic tetrazole free of direct metal interactions, Jimenez-Sandoval, Omar; Cea-Olivares, Raymundo; Hernandez-Ortega, Simon; Silaghi-Dumitrescu, Ioan, Heteroatom Chemistry (1997), 8(4), 351-359.

The first oxygen-bridged diorganoarsenic(V) compound: the crystal structure of AsMe2(S)OAs(S)Me2, Silaghi-Dumitrescu, Luminita; Pascu, Sofia; Silaghi-Dumitrescu, Ioan; Haiduc, Ionel; Gibbons, Martin N.; Sowerby, D. Bryan, Journal of Organometallic Chemistry (1997), 549(1-2), 187-192.

A12B12 (A = B,Al; B = N,P) 4/6 fullerene-like cages and their hydrogenated forms stabilized by exohedral bonds. An AM1 molecular orbital study, Silaghi-Dumitrescu, Ioan; Lara-Ochoa, Francisco; Haiduc, Ionel, THEOCHEM (1996), 370(1), 17-23.

Coordinative dimerization of aminosilanes. Model MNDO and ab initio molecular orbital calculations, Lara-Ochoa, Francisco; Silaghi-Dumitrescu, Ioan; Haiduc, Ionel. Main Group Chemistry (1996), 1(4), 387-398.

Interactions between calix[8]arenes and fullerenes. Molecular dynamics and molecular mechanics simulation of the 1:1 and 1:2 complexes, Lara-Ochoa, Francisco; Cogordan, Juan Antonio; Silaghi-Dumitrescu, IoanFullerene Science and Technology (1996), 4(5), 887-896

Ion molecule interaction in organic electrochemical systems III. Acrylonitrile-quaternary ammonium cations adducts and their possible implications in electrohydrodimerization processes, Silberg, I. A.; Ciomos, Forentina; Silaghi-Dumitrescu, I, Studia Universitatis Babes-Bolyai, Chemia (1996), 41(2), 167-172.

More about boron-nitrogen B12+3nN12+3n fullerene-like cages. An ab initio and AM1 investigation of some 4/6 isomers, Silaghi-Dumitrescu, Ioan; Lara-Ochoa, Francisco; Bishof, Peter; Haiduc, Ionel, THEOCHEM (1996), 367 47-54.

Oxidation of (AsPh2)2E (E = O or S); supramolecular hydrogen-bonded self-assembly of an unusual tetranuclear adduct and crystal structure of [AsPh2(O)OH· AsPh2(S)OH]2, Silaghi-Dumitrescu, Luminita; Gibbons, Martin N.; Silaghi-Dumitrescu, Ioan; Zukerman-Schpector, Julio; Haiduc, Ionel; Sowerby, D. Bryan, Journal of Organometallic Chemistry (1996), 517(1-2), 101-106.

On the geometries and electronic structures of XH2SiNH2 (X = F, Cl, Br) silanes. MNDO molecular orbital calculations, Silaghi-Dumitrescu, Ioan; Haiduc, Ionel, Studia Universitatis Babes-Bolyai, Chemia (1995), 40(1-2), 91-98.

An improved first-order optimization of molecular structure taking account of molecular topology, Horvath, Dragos; Silaghi-Dumitrescu, Ioan, Studia Universitatis Babes-Bolyai, Chemia (1994), 39(1-2), 15-27.

An old ligand in a new environment: triply bridged O,O'-dimethyldithiophosphate in the organosamarium complex [(C5Me5)Sm{S2P(OMe)2}2]2, Rieckhoff, Melanie; Noltemeyer, Mathias; Edelmann, Frank T.; Haiduc, Ionel; Silaghi-Dumitrescu, Ioan, Journal of Organometallic Chemistry (1994), 469(1), C22-C23.

Chelating versus bridging coordination of dithiophosphates in copper complexes. An EHMO study, Silaghi-Dumitrescu, Ioan; Serban, Liliana; Silaghi-Dumitrescu, Luminita; Haiduc, Ionel, Revue Roumaine de Chimie (1994), 39(12), 1397-405.

On the geometry of 1,3-diazadiphosphetidines. The cis-trans isomerism, Silaghi-Dumitrescu, Ioan; Haiduc, Ionel, Phosphorus, Sulfur and Silicon and the Related Elements (1994), 91(1-4), 21-36.

ansa-Metallocene derivatives of samarium and ytterbium with soft donor ligands, Edelmann, Frank T.; Rieckhoff, Melanie; Haiduc, Ionel; Silaghi-Dumitrescu, Ioan, Journal of Organometallic Chemistry (1993), 447(2), 203-8.

Fully inorganic (carbon-free) fullerenes? The boron-nitrogen case, Silaghi-Dumitrescu, Ioan; Haiduc, Ionel; Sowerby, D. Bryan, Inorganic Chemistry (1993), 32(17), 3755-8.

On the ring angles in the four-membered cyclodiphosphazanes, Silaghi-Dumitrescu, Ioan; Haiduc, Ionel, Studia Universitatis Babes-Bolyai, Chemia (1993), 38(1-2), 183-186.

Molecular topology. 2. A computer program for multiple bond, cycle and radical approximations of DS index, Diudea, Mircea V.; Silaghi-Dumitrescu, Ioan, Revue Roumaine de Chimie (1991), 36(1-3), 263-9.

Molecular topology. 2. A computer program for multiple bond, cycle and radical approximations of DS index, Diudea, Mircea V.; Silaghi-Dumitrescu, Ioan, Revue Roumaine de Chimie (1991), 36(8), 975-82.

The richness of structures available to P2N2 inorganic heterocycles. A topological and molecular orbital (EHMO) analysis, Haiduc, Ionel; Silaghi-Dumitrescu, Ioan, Revue Roumaine de Chimie (1991), 36(4-7), 527-44.

The electronic structure of silyl amide ([H3SiNSiH3]-) anion. A simple molecular orbital treatment, Silaghi-Dumitrescu, Ioan; Haiduc, Ionel, Revue Roumaine de Chimie (1990), 35(3), 475-84.

The infrared spectra of methyl(O-methyl)dithiophosphonic acid. Multiplicity of some bands due to different conformers, Grecu, Rodica; Constantinescu, Rodica; Silaghi-Dumitrescu, I.; Haiduc, IJournal of Molecular Structure (1990), 218 111-16.

Molecular structure modeling by using a basic line formula interpreter, Horvath, D.; Silaghi-Dumitrescu, I, Studia Universitatis Babes-Bolyai, Chemia (1989), 34(2), 41-5.

Molecular topology. I. Valence group electronegativity as a vertex discriminator, Diudea, Mircea V.; Silaghi-Dumitrescu, Ioan Revue Roumaine de Chimie (1989), 34(5), 1175-82.

The sulfotropic molecular rearrangement of tetraorganodiarsine disulfides, Silaghi-Dumitrescu, Luminita; Silaghi-Dumitrescu, Ioan; Haiduc, Ionel. Revue Roumaine de Chimie (1989), 34(1), 305-15.

Vibrational spectra and coordination behavior of organo-dithiophosphorus ligands, Silaghi-Dumitrescu, Ioan; Grecu, Rodica; Silaghi-Dumitrescu, Luminita; Haiduc, Ionel, Studia Universitatis Babes-Bolyai, Chemia (1989), 34(1), 97-101.

Electronic structure and bonding in diamidoboron cations. A molecular orbital study of diamidoboron(1+) [H2NBNH2]+, Silaghi-Dumitrescu, Ioan; Haiduc, Ionel, Revue Roumaine de Chimie (1988), 33(9-10), 851-6.

Linear versus bent bis(diphosphine)iminium cations. A molecular orbital discussion of the bonding in [H3PNPH3]+ and related species, Silaghi-Dumitrescu, I.; Haiduc, I, Revue Roumaine de Chimie (1988), 33(2), 133-42.

Inorganic (carbon-free) chelate rings, Haiduc, Ionel; Silaghi-Dumitrescu, Ioan Coordination Chemistry Reviews (1986), 74 127-270.

The bonding in dialkyldithiophosphinato metal complexes. A molecular orbital study of bis(dimethyldithiophosphinato)nickel(II), Silaghi-Dumitrescu, Ioan; Haiduc, Ionel, Revue Roumaine de Chimie (1986), 31(11-12), 955-62.

Why are cyclodisilazane rings more stable than cyclodisiloxanes? A qualitative molecular orbital approach to the bonding in cyclodisilazanes and cyclodisiloxanes, Silaghi-Dumitrescu, Ioan; Haiduc, Ionel, Inorganica Chimica Acta (1986), 112(2), 159-65.

The crystal and molecular structure of a versatile bidentate ligand: tetraphenyldithioimidodiphosphinate, Ph2(S)PNHP(S)Ph2, Hitchcock, Peter B.; Nixon, John F.; Silaghi-Dumitrescu, Ioan; Haiduc, Ionel, Inorganica Chimica Acta (1985), 96(1), 77-80.

The electronic structure and bonding in the thiophosphoryl cation PS+, Silaghi-Dumitrescu, I.; Haiduc, I, Phosphorus and Sulfur and the Related Elements (1985), 22(1), 85-91.

Electronic structure and force constants of the dithionitronium cation NS2-, Silaghi-Dumitrescu, I.; Haiduc, I, THEOCHEM (1984), 15(3-4), 217-23.

Vibrational spectra of phosphorodithioic metal complexes. Normal coordinate treatment of bis(O-isopropyl ethyldithiophosphonato)nickel(II), Haiduc, I.; Silaghi-Dumitrescu, I.; Grecu, Rodica; Constantinescu, Rodica; Silaghi-Dumitrescu, Luminita, Journal of Molecular Structure (1984), 114 467-70.

Bonding in organophosphorus dithio acids. A CNDO/2 calculation of electronic structure, Silaghi-Dumitrescu, Ioan; Haiduc, Ionel, Phosphorus and Sulfur and the Related Elements (1982), 12(2), 205-12.

Normal coordinate analysis of the vibrational spectrum of dimethyldithioarsinato anion, (CH3)2AsS2-, Silaghi-Dumitrescu, Ioan; Silaghi-Dumitrescu, Luminita; Haiduc, Ionel, Revue Roumaine de Chimie (1982), 27(8), 911-16.

A simple topology-based method for estimating stretching force constants of ABn molecules, Silaghi-Dumitrescu, I Revue Roumaine de Chimie (1981), 26(11-12), 1441-5.

The infrared spectrum of dimethyldithiophosphinato anion (CH3)2 PS2-. Normal coordinate analysis and Urey-Bradley force field calculation, Silaghi-Dumitrescu, Ioan; Haiduc, Ionel, Revue Roumaine de Chimie (1980), 25(6), 815-21.

Vibrational characteristics of nickel(II) dithiophosphinato chelates. Normal coordinate analysis and Urey-Bradley force field calculation of Ni[S2P(CH3)2]2, Silaghi-Dumitrescu, Ioan; Haiduc, Ionel Revue Roumaine de Chimie (1980), 25(6), 823-30.

STUDIA UNIVERSITATIS BABEŞ-BOLYAI, CHEMIA, XLV, 2, TOM I, 2010

Dedicated to the memory of Prof. dr. Ioan Silaghi-Dumitrescu marking 60 years from his birth

A THEORETICAL APPROACH ON THE STRUCTURE OF ARSAALLENES -As=C=C< AND ARSAPHOSPHAALLENES -As=C=P-

PETRONELA M. PETRAR[*], GABRIELA NEMES, LUMINITA SILAGHI-DUMITRESCU

ABSTRACT. Calculations at the B3LYP/6-311 level were performed on a series of arsaallenes and arsaphosphaallenes of the type RAs=C=CR2 and RAs=C=PR in order to evaluate the nature of the As=C bond. The influence of several substituents (F, Cl, OMe, $SiMe_3$) on the order of the bond was also investigated.

Keywords: *arsaallenes, arsaphosphaallenes, DFT calculations*

INTRODUCTION

Derivatives of the type E=C=E' (E, E' = group 14 and 15 elements) have become the focus of research only in the last decades [1]. So far, only a few heteroallenic derivatives of the type -As=C=E (E = CR_2 [2], PR [3], AsR [4]) have been isolated and structurally investigated. The arsenic – carbon distance has a small value of 1.758 Å as reported in Mes*As=C=AsMes* (Mes* = 2,4,6-tri-*tert* butylphenyl) [4] and Mes*As=C=CR_2 (CR_2 = fluorenyl) [2]. The As-C-C bond angle for this derivative is 169.7°, with the central carbon atom deviated from the expected linearity. The supermesityl group lies at a 102° angle from the As=C double bond. For the arsaphosphaallene Mes*As=C=PMes*, problems of symmetry in the X-ray diffraction did not allow to determine exactly the bond lengths and bond angles [3].

We have previously investigated the nature of the As-C bond in heteroallenic derivatives of the type As(V)=C=E (As(V) = $\lambda^5\sigma^4$ As), where E=C, P(III) (P(III) = $\lambda^3\sigma^2$ P), [5]. A model for the structure of $H_3As=C=CH_2$ according to NBO analysis at the B3LYP/6-311G(d, p) level was proposed, in which As has a lone pair in an *sp* type orbital.

---

[*] *Universitatea Babeş-Bolyai, Facultatea de Chimie şi Inginerie Chimică, Str. Kogălniceanu Nr. 1, RO-400084 Cluj-Napoca, Romania; ppetrar@chem.ubbcluj.ro*

A comparison with the analogues in which As has the formal oxidation state III can be very interesting, especially since there are more As(III) (As(III) = $\lambda^3\sigma^2$ As), derivatives of this type reported in the literature and the experimental data for doubly bonded As(V) is very scarce.

In order to asses the nature of the As-C bond in arsaallenes -As=C=C< and arsaphosphaallenes -As=C=P-, a theoretical investigation was carried out at the B3LYP/6-311G(d, p) level of the theory. Model compounds of the type $RAs=C=CR_2$ (R= H, Me, Ph), were studied as well as those in which one or two R groups have been replaced by one or two R' groups (R'= F, Cl, OMe, $SiMe_3$) on the As or the C atom. The same R' substituents were used for the arsaphosphaallenes. All geometries were optimized and a frequency calculation was run in order to verify if the obtained structures are indeed global minima. An NBO analysis was performed, in order to evaluate the nature of the orbitals involved in bonding and the Wiberg bond order for the As=C and C=C bonds was calculated for each case.

RESULTS AND DISCUSSION

For the model compound $HAs=C=CH_2$, the As=C bond has a length of 1.77 Å, in agreement with the experimental data obtained for the arsaallene $Mes^*As=C=CR_2$ (1.758 Å) [2], and a bond order of 1.85. (The calculated bond order in the case of $H_3As=C=CH_2$ at the same level of theory was found to be 1.07). The calculated C=C bond length is 1.30 Å (1.314 Å by X-ray [2]). The geometry around the arsenic in $HAs=C=CH_2$ is angular, with the H-As-C bond angle of 94°. This suggests that the bonding involves the valence $4s^2 4p^3$ arsenic orbitals rather than hybrid ones, as expected for heavier main group elements. An NBO analysis shows that the lone pair on the As atom lies in an orbital with strong *s* character, and that almost pure *p* orbitals are contributing to the formation of the σ and π bonding to the carbon atom. The same is expected for the other arsaallenes investigated.

As for the only arsaallene characterized experimentally, $Mes^*As=C=CR_2$, (As-C-C bond angle of 169.7°) the value of the angle As-C-C for $HAs=C=CH_2$ is not 180° but 173.8°. We can thus conclude that the deviation from the linearity of the allenic unit is not the result of steric hindrance or crystal-packing effects, but is inherent to the nature of the arsaallene. Moreover, the most significant second order interaction involves the As(III) lone pair as a donor and the antibonding *s* orbital of the C-C bond, which is also present for all the derivatives discussed below (figure 1). This interaction could account for the slight narrowing of the angle.

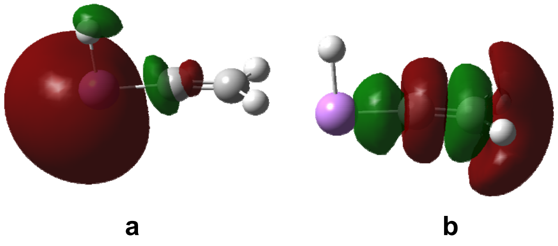

Figure 1. NB orbitals involved in second order perturbation interactions for $HAs=C=CH_2$. (a) lone pair electrons on As; (b) anti-bonding non-Lewis orbital on the C-C bond

I. Monosubstituted arsaallenes $R'As=C=CR_2$ and $RAs=C=CRR'$

In the case of substitution with one R' group (R' = F, Cl, OMe and $SiMe_3$), two types of derivatives were considered: with R' on the arsenic, and on the terminal carbon atom of the allenic unit. The group R was either H, Me or Ph. The results obtained from the geometry optimization and NBO analysis are given in table 1.

It can be noticed that in every case the isomer bearing the R' group on the arsenic atom is more stable. However, in the case of substitution with $SiMe_3$, the energy difference is significantly smaller. As in the case of As(V) derivatives, substitution of arsenic with an electron-withdrawing group or atom leads to a decrease in the bond order of the As=C bond.

For the H_2AsC_2R' isomers, there is a decrease of the bond order when going from $HAs=C=CR'H$ to $R'As=C=CH_2$, for R' = F, Cl, and OMe. This is explained by charge donation from the lone pairs of the R' to a vacant antibonding orbital of π symmetry on the As-C bond. The value of the second order perturbation energy is 7.31 for R' = F, 5.15 for Cl and 11.30 for R' = OMe, which also reflects the magnitude of the bond order decrease. The two natural bonding orbitals involved in the interaction are illustrated in figure 2 for the case R' = OMe.

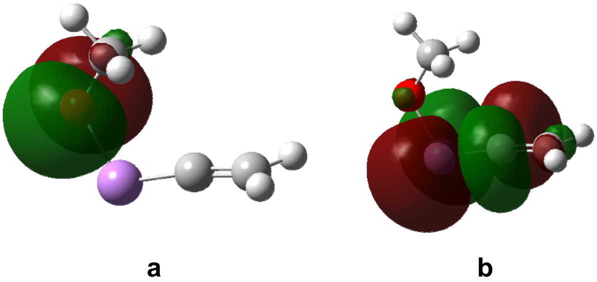

Figure 2. NB orbitals involved in second order perturbation interactions for $(MeO)As=C=CH_2$. (a) lone pair electrons on O; (b) anti-bonding non-Lewis orbital on the C-C bond

However, for R’ = $SiMe_3$, the bond order of the arsenic-carbon bond is higher in the case of $Me_3SiAs=C=CH_2$ (1.86, close to the bond order calculated for $HAs=C=CH_2$) than for the corresponding isomer, substituted at the terminal carbon atom, $HAs=C=CH(SiMe_3)$ (1.80). This is because in the case of the latter, there is a charge transfer from an orbital localized on C_2-Si and the antibonding orbital of π symmetry of the As-C_1 bond. The two orbitals are shown in figure 3. The same phenomenon is observed for all $SiMe_3$ substituted derivatives.

Table 1. Selective data for $R'As=C=CR_2$ and $RAs=C=CRR'$, calculated at the B3LYP/6-311G(d, p) level (bond lengths in Å, bond angles in degrees). The Wiberg bond orders for As=C and C=C are also given.

Molecule	**Energy (a.u.)**	**ΔE (kcal/mol)**	**As=C**	**C1=C2**	**As-C-C**	**W BO As=C**	**W BO C=C**
$HAs=C=CH_2$	-2313.843087	-	1.77	1.30	173.8	**1.85**	2.02
$MeAs=C=CMe_2$	-2431.831534	-	1.76	1.31	173.5	**1.84**	1.88
$PhAs=C=CPh_2$	-3007.169658	-	1.76	1.32	172.7	**1.81**	1.80
HAs=C=CHF	-2413.096739	20.5	1.76	1.31	172.6	**1.87**	1.92
$FAs=C=CH_2$	-2413.129358	0.0	1.76	1.31	174.8	**1.78**	2.03
HAs=C=CHCl	-2773.461680	24.7	1.76	1.30	173.1	**1.84**	1.95
$ClAs=C=CH_2$	-2773.501019	0.0	1.76	1.31	174.1	**1.81**	2.01
HAs=C=CH(OMe)	-2428.389328	11.8	1.76	1.31	170.5	**1.88**	1.87
$(MeO)As=C=CH_2$	-2428.408053	0.0	1.76	1.31	172.6	**1.74**	2.03
$HAs=C=CH(SiH_3)$	-2722.591752	3.1	1.78	1.30	173.8	**1.80**	2.03
$(Me_3Si)As=C=CH_2$	-2722.596750	0.0	1.76	1.31	176.1	**1.86**	1.98
MeAs=C=CMeF	-2491.763808	17.8	1.75	1.31	172.4	**1.83**	1.86
$FAs=C=CMe_2$	-2491.792168	0.0	1.75	1.32	175.4	**1.81**	1.87
MeAs=C=CMeCl	-2852.125134	24.3	1.76	1.30	173.2	**1.80**	1.90
$ClAs=C=CMe_2$	-2852.163852	0.0	1.75	1.31	175.1	**1.84**	1.85
MeAs=C=CMe(OMe)	-2507.048261	13.2	1.75	1.32	175.1	**1.86**	1.82
$MeOAs=C=CMe_2$	-2507.069265	0.0	1.76	1.32	171.9	**1.77**	1.87
$MeAs=C=CMe(SiMe_3)$	-2801.246316	4.9	1.77	1.31	174.1	**1.79**	1.96
$(Me_3Si)As=C=CMe_2$	-2801.254090	0.0	1.77	1.31	174.9	**1.86**	1.85
PhAs=C=CPhF	-2875.324550	17.4	1.75	1.32	170.4	**1.79**	1.80
$FAs=C=CPh_2$	-2875.352230	0.0	1.75	1.33	175.5	**1.82**	1.78
PhAs=C=CPhCl	-3235.682429	25.9	1.76	1.31	171.8	**1.75**	1.85
$ClAs=C=CPh_2$	-3235.723670	0.0	1.74	1.33	176.0	**1.86**	1.76
PhAs=C=CPh(OMe)	-2890.618419	4.3	1.75	1.33	170.1	**1.81**	1.73
$MeOAs=C=CPh_2$	-2890.625224	0.0	1.75	1.32	174.0	**1.81**	1.79
$PhAs=C=CPh(SiMe_3)$	-3184.803748	6.8	1.77	1.31	174.8	**1.75**	1.92
$Ph(SiMe_3)As=C=CPh_2$	-3184.814571	0.0	1.76	1.32	174.2	**1.89**	1.76

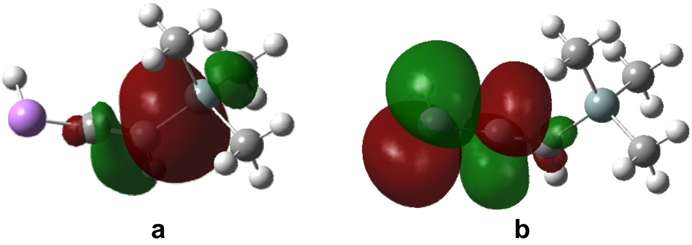

Figure 3. NB orbitals involved in second order perturbation interactions for HAs=C=CH(SiMe$_3$). (a) σ orbital on the C$_2$-Si bond; (b) π anti-bonding non-Lewis orbital on the As=C$_1$ bond

Going from the hydrogen to the methyl-substituted series, it can be noticed that the bond order for the fluorinated derivative decreases. The NBO analysis shows second order interactions between the π orbital situated on the As-C bond and a C$_2$-C$_3$ (from methyl) antibonding orbital, which lowers the bond order. The chlorinated species also display different values when R = Me. Thus, MeAs=C=CMeCl has a lower bond order for the As-C bond than ClAs=C=CMe$_2$, in contrast with the hydrogen-substituted analogues. When the chlorine is on the carbon atom, a charge transfer occurs from the π orbital situated on the As-C and a σ^* (C-Cl) orbital, which was not present for HAs=C=CHCl. Also, the donation from the lone pairs of the Cl to the vacant antibonding orbital of π symmetry on the As-C bond is not present for the isomer ClAs=C=CMe$_2$, contrary to the case when R = H. The OMe and SiMe$_3$– substituted derivatives behave like their analogues with hydrogen instead of methyl.

The only other notable exception is for the isomers PhAs=C=CPhF (with a bond order of the As=C bond of 1.79) and FAs=C=CPh$_2$ (1.82). In this case, an interaction of the kind described for ClAs=C=CMe$_2$ influences the difference between the two values.

II. Disubstituted arsaallenes R’As=C=CRR’ and RAs=C=CR’$_2$

The same groups were considered in the case of the disubstitution by two R’ groups. From the calculated energies presented in table 2, there can be noticed that the RAs=C=CR’$_2$ isomer is always energetically favored, but that in the case of R’ = OMe and SiMe$_3$, the difference between the two types of derivatives is smaller. The bond order of the As=C bond is generally higher for R’As=C=CRR’ compounds, except when R = H, Me and R’ = F, OMe and R = H, R’ = Cl. This is due to donations from the lone pairs of F, Cl and O respectively to bonding orbitals on the As=C bond (mainly the one of π symmetry), similar to those described for R’As=C=CR$_2$ (see figure 2 for the shape of the orbitals involved). The same considerations as before can be applied to explain the variation of the As=C bond order for the derivatives with R' = F, Cl and OMe. The silyl group is a special case, mainly because of the lack of lone pairs on the silicon, so it will be discussed in detail. From table 2, it can be seen that the As=C bond order in is always smaller than in the corresponding isomer $Me_3SiAs=C=C(SiMe_3)R$. The explanation is similar as for the monosubstituted derivative, with a charge transfer from the bonding C2-Si orbital (figure 4a, for R = Me) to both the σ (figure 4b) and the π anti-bonding orbitals localized on the As-C bond. Only two such interactions are possible for $(Me_3Si)As=C=CR(SiMe_3)$, as opposed to four in the case of $RAs=C=C(SiMe_3)_2$ derivatives (from both C-Si bonding orbitals), which thus display a lower bond order.

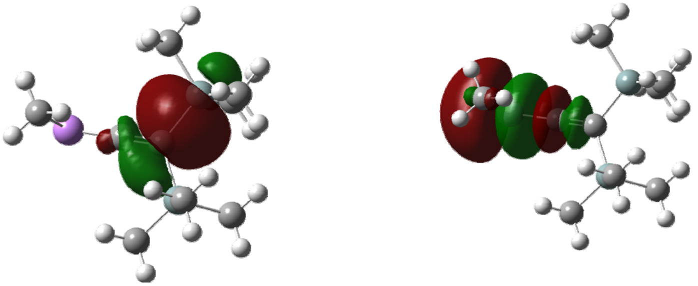
a b

Figure 4. NB orbitals involved in second order perturbation interactions for $MeAs=C=C(SiMe_3)_2$. (a) σ-orbital on the C_2-Si bond; (b) σ-anti-bonding non-Lewis orbital on the $As=C_1$ bond

This bond order is even lower for $PhAs=C=C(SiMe_3)_2$. The NBO analysis shows that in this case, a supplementary charge transfer occurs from the p-symmetry bonding orbital on the As-C bond to an antibonding orbital situated on a bond of the phenyl ring (see figure 5). This leads to a bond order of 1.67, the lowest for the entire series analyzed. However, As-C distance is not greatly influenced.

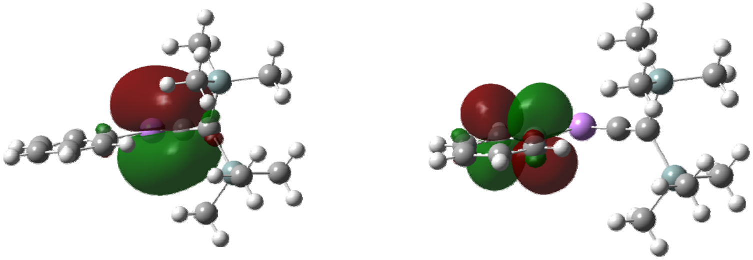
a b

Figure 5. NB orbitals involved in second order perturbation interactions for $PhAs=C=C(SiMe_3)_2$. (a) π-orbital on the C_2-Si bond; (b) π-anti-bonding non-Lewis orbital on a C=C bond of the phenyl ring

Table 2. Selective data for R'As=C=CRR' and RAs=C=CR'$_2$, calculated at the B3LYP/6-311G(d, p) level (bond lengths in Å, bond angles in degrees). The Wiberg bond orders for As=C and C=C are also given.

Molecule	Energy (a.u.)	ΔE (kcal/mol)	As=C	C1=C2	As-C-C	W BO As=C	W BO C=C
FAs=C=CHF	-2512.387693	0.0	1.74	1.31	173.6	**1.79**	1.91
HAs=C=CF$_2$	-2512.360844	16.8	1.75	1.30	170.9	**1.86**	1.84
ClAs=C=CHCl	-3233.120327	0.0	1.75	1.30	173.3	**1.79**	1.93
HAs=C=CCl$_2$	-3233.075782	28.0	1.76	1.30	172.6	**1.81**	1.87
(MeO)As=C=CH(OMe)	-2542.956023	0.0	1.74	1.32	171.4	**1.81**	1.85
HAs=C=C(OMe)$_2$	-2542.948974	4.4	1.75	1.33	162.8	**1.88**	1.73
(SiMe$_3$)As=C=CH(SiMe$_3$)	-3131.345021	0.0	1.77	1.31	175.1	**1.80**	1.98
HAs=C=C(SiMe$_3$)$_2$	-3131.339292	3.6	1.79	1.30	174.3	**1.72**	2.05
FAs=C=CMeF	-2551.724813	0.0	1.74	1.31	174.5	**1.80**	1.84
MeAs=C=CF$_2$	-2551.693708	19.5	1.75	1.30	171.0	**1.81**	1.85
ClAs=C=CMeCl	-3272.454314	0.0	1.75	1.31	174.0	**1.79**	1.86
MeAs=C=CCl$_2$	-3272.408031	29.0	1.75	1.30	172.9	**1.77**	1.89
(MeO)As=C=CMe(OMe)	-2582.284328	0.0	1.74	1.32	170.0	**1.82**	1.79
MeAs=C=C(OMe)$_2$	-2582.274268	6.3	1.75	1.32	171.9	**1.84**	1.81
(SiMe$_3$)As=C=CMe(SiMe$_3$)	-3170.670114	0.0	1.77	1.31	175.1	**1.80**	1.93
MeAs=C=C(SiMe$_3$)$_2$	-3170.666509	2.3	1.78	1.30	174.6	**1.72**	2.03
FAs=C=CPhF	-2743.507094	0.0	1.74	1.32	171.9	**1.81**	1.77
PhAs=C=CF$_2$	-2743.472533	21.7	1.75	1.30	168.9	**1.76**	1.85
ClAs=C=CPhCl	-3464.233759	0.0	1.74	1.31	173.6	**1.80**	1.80
PhAs=C=CCl$_2$	-3464.186502	29.7	1.76	1.30	172.5	**1.71**	1.90
(MeO)As=C=CPh(OMe)	-2774.066178	0.0	1.74	1.32	169.6	**1.81**	1.79
PhAs=C=C(OMe)$_2$	-2774.05281	8.4	1.75	1.32	170.8	**1.80**	1.81
(SiMe$_3$)As=C=CPh(SiMe$_3$)	-3362.450222	0.0	1.77	1.31	175.2	**1.82**	1.87
PhAs=C=C(SiMe$_3$)$_2$	-3362.444627	3.5	1.78	1.30	174.6	**1.67**	2.05

III. Arsaphosphaallenes R'As=C=PR and RAs=C=PR'

In the case of arsaphosphaallenes, the bond order of the As=C bond is lower than that of the corresponding arsaallenes (e.g., 1.82 for HAs=C=PH and 1.84 for HAs=C=CH$_2$; for complete data see table 3). This is readily explained by the NBO analysis: there is electron donation from the lone pair of the phosphorus atom in the σ-symmetry antibonding orbital localized on the As-C bond. The orbitals involved are shown in figure 6 for MeAs=C=PMe. In addition, charge transfer from the As lone pair to vacant orbitals on the P-C is present, similarly to the case of arsaallenes. The bond order of the P-C bond varies from 1.80 to 1.98.

The calculated energies for the model compounds show that for R' = Cl, SiMe$_3$, the RAs=C=PR' isomer is energetically favored, while in the case of F and OMe, R'As=C=PR have lower energies. In both cases though, the difference in energy is not significant, going up to only 7.1 kcal for R' = Cl and R = Ph. This relatively low value comparatively to that calculated for arsaallenes can be accounted by close values of bond energies of R-P and R-As, which are significantly different for R-As and C-R [6].

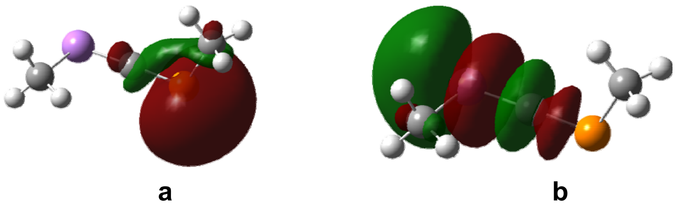

Figure 6. NB orbitals involved in second order perturbation interactions for MeAs=C=PMe. (a) lone pair on the P atom; (b) σ-anti-bonding non-Lewis orbital on the C=P bond

The value of the Wiberg bond order for the As=C is always much lower for the RAs=C=P($SiMe_3$) derivatives than for (Me_3Si)As=C=PR. This is explained by the NBO analysis in terms of a charge transfer from a P-Si bonding orbital to an antibonding orbital localized on the As=C bond (see figure 7 for the shape of the NB orbitals involved). The values of the second order interactions are 18.70 for R = H, 15.96 for R = Me and 14.72 for R = Ph. On the contrary, when Me_3Si group is on the arsenic atom, then the electron donation occurs from an As-Si orbital to an antibonding C-P orbital, which reduces the bond order of this bond for the (Me_3Si)As=C=PR compared to their isomers. The lack of this interaction explains the higher bond orders for (Me_3Si)As=C=PR: 1.98 for R=H, 1.96 for R=Me and 1.97 for R=Ph.

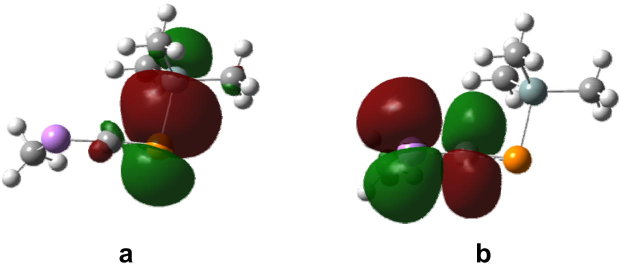

Figure 7. NB orbitals involved in second order perturbation interactions for MeAs=C=P$SiMe_3$. (a) σ-bonding orbital on the P-Si bond; (b) π-anti-bonding non-Lewis orbital on the As=C bond

As in the case of the arsaallenes, when R = H, R' = F, Cl, OMe, the lone pairs of the R' group play an important role in the value of the bond order of the As=C bond. Thus, when the groups are bonded to arsenic, the donation of electrons from lone pairs to an antibonding orbital of p symmetry on the As-C bond is present. For the HAs=C=PR' isomers, this charge transfer occurs to the more available P=C antibonding orbitals, leading to a decrease of the P=C bond order when compared to its isomer or the simplest model compound, HAs=C=PH.

Table 3. Selective data for RAs=C=PR' and R'As=C=PR, calculated at the B3LYP/6-311G(d, p) level (bond lengths in Å, bond angles in degrees). The Wiberg bond orders for As=C and C=C are also given.

Molecule	Energy (a.u.)	ΔE (kcal/mol)	As=C	C=P	As-C-P	W BO As=C	W BO C=P
HAs=C=PH	-2616.496293	-	1.77	1.64	170.1	**1.82**	1.94
MeAs=C=PMe	-2695.159405	-	1.76	1.64	170.5	**1.79**	1.89
PhAs=C=PPh	-3078.717049	-	1.76	1.64	168.6	**1.74**	1.84
HAs=C=PF	-2715.785965	0.0	1.76	1.64	168.0	**1.83**	1.83
FAs=C=PH	-2715.782567	2.1	1.76	1.64	170.2	**1.73**	1.94
HAs=C=PCl	-3076.145363	5.5	1.77	1.63	168.6	**1.79**	1.89
ClAs=C=PH	-3076.154206	0.0	1.76	1.64	169.6	**1.76**	1.92
HAs=C=P(OMe)	-2731.064527	0.0	1.76	1.64	166.8	**1.84**	1.81
(MeO)As=C=PH	-2731.058053	4.1	1.76	1.64	167.8	**1.72**	1.95
HAs=C=P(SiMe$_3$)	-3025.251322	1.1	1.78	1.63	172.2	**1.72**	1.98
(Me$_3$Si)As=C=PH	-3025.253113	0.0	1.76	1.65	171.7	**1.85**	1.86
MeAs=C=PF	-2755.119568	0.0	1.76	1.63	168.1	**1.77**	1.84
FAs=C=PMe	-2755.117374	1.4	1.76	1.64	170.3	**1.74**	1.88
MeAs=C=PCl	-3115.478872	6.2	1.76	1.63	169.0	**1.74**	1.89
ClAs=C=PMe	-3115.488827	0.0	1.76	1.64	169.7	**1.78**	1.86
MeAs=C=P(OMe)	-2770.397116	0.0	1.76	1.64	167.9	**1.80**	1.81
MeOAs=C=PMe	-2770.392069	3.2	1.76	1.64	168.4	**1.73**	1.89
MeAs=C=P(SiMe$_3$)	-3064.580612	2.0	1.78	1.64	172.3	**1.71**	1.96
(Me$_3$Si)As=C=PMe	-3064.583753	0.0	1.76	1.65	171.8	**1.83**	1.84
PhAs=C=PF	-2946.898555	0.0	1.76	1.63	156.3	**1.71**	1.85
FAs=C=PPh	-2946.897732	0.5	1.76	1.64	167.7	**1.75**	1.81
PhAs=C=PCl	-3307.257729	7.1	1.77	1.63	168.0	**1.68**	1.91
ClAs=C=PPh	-3307.269059	0.0	1.75	1.64	168.6	**1.79**	1.79
PhAs=C=P(OMe)	-2962.176075	0.0	1.76	1.64	165.5	**1.74**	1.81
MeOAs=C=PPh	-2962.172192	2.4	1.76	1.64	166.4	**1.73**	1.83
PhAs=C=P(SiMe$_3$)	-3256.35854	3.0	1.78	1.64	171.8	**1.67**	1.97
Ph(SiMe$_3$)As=C=PPh	-3256.363293	0.0	1.76	1.65	171.1	**1.84**	1.79

For MeAs=C=PCl, electron donation from the As=C bond to an orbital situated on the P-Cl bond occurs, which lowers the bond order. This interaction is present for R = Ph, but not for R = H, which explains the difference in the values of the As-C bond order when changing the R group.

CONCLUSIONS

The As-C bond in arsa- and arsaphosphaallenes has a calculated bond order between 1.67 and 1.90. The bonding of the arsenic in such derivatives involves the ‘pure’ atomic shell orbitals *4s* and *4p*, with the lone pair being situated in the *s* orbital. The strength of the bond is influenced by functionalization on both the arsenic and the terminal element of the As=C=E (E = C, P) unit. Substituents bearing lone pairs can influence it significantly, by charge transfer from the lone pairs to anti-bonding orbitals of the bond. The calculations indicate that increase of the bond order is favored by the presence of silyl groups on the arsenic atom, which can also afford the steric protection needed.

Whatever the group on As, C and P, the As=C, C=C and C=P bond lengths are about the same within 2 or 3 pm.

ACKNOWLEDGEMENT

The authors are grateful to Dr. Jean Escudié (Paul Sabatier University, Toulouse) for useful discussions on the manuscript. Through these, Dr. Escudie joins the authors in paying homage to the memory of Prof. Dr. Ioan Silaghi-Dumitrescu.

The computational resources acquired through the CMMCCC program (Capacitati, modul I, 130/14.09.2007) were employed.

COMPUTATIONAL DETAILS

The calculations were performed using the Gaussian 09 package [7], at the B3LYP [8]/6-311G (d, p) level of the theory. The results were visualized with GaussView 4.1. The input geometry was also built with GaussView; in every case the starting geometry included the As=C double bond. The structures were optimized and a vibrational analysis was performed in every case. Negative frequencies higher than -20 cm^{-1} were ignored. An NBO analysis was requested, together with a calculation of the Wiberg bond order, which was listed for the As=C and C=C/P bonds.

REFERENCES

1. For reviews on heteroallenes E=C=E' (E, E' = Si, Ge, Sn; $\lambda^3\sigma^2$ P and As) see: (a) J. Escudié, H. Ranaivonjatovo and L. Rigon, *Chem. Rev.* **2000**, *100,* 3639; (b) R. Appel, in *Multiple Bonds and Low Coordination in Phosphorus Chemistry*, Georg Thieme Verlag: Stuttgart, Germany, **1990**, 157; (c) B. Eichler and R. West, *Adv. Organomet. Chem*. **2001**, *46*, 1; (d) M. Yoshifuji and K. Toyota, in *The Chemistry of Organosilicon Compounds*; Rappoport, Z., Apeloig, Y., Eds.: John Wiley and Sons: Chichester, UK, **2001**, *3*, 491; (e) J. Escudié, H. Ranaivonjatovo, M. Bouslikhane, Y. El Harouch, L. Baiget and G. Cretiu Nemes, *Russ. Chem. Bull*. **2004**, *5*, 1020; (f) J. Escudié and H. Ranaivonjatovo, *Organometallics* **2007**, *26*, 1542.
2. M. Bouslikhane, H. Gornitzka, H. Ranaivonjatovo and J. Escudié, *Organometallics*, **2002**, *21*, 1531.
3. H. Ranaivonjatovo, H. Ramdane, H. Gornitzka, J. Escudié and J. Satgé, *Organometallics*, **1998**, *17*, 1631.
4. M. Bouslikhane, H. Gornitzka, J. Escudié, H. Ranaivonjatovo and H. Ramdane, *J. Am. Chem. Soc.*, **2000**, *122*, 12880.
5. P. M. Petrar, G. Nemes, R. Septelean, L. Silaghi-Dumitrescu and J. Escudié, *Rev. Roum. Chimie*, *submitted for publication*.
6. C. D. Schaeffer, C. A. Strausser, M. W. Thomsen and C. H. Yoder, *Data for General Organic and Physical Chemistry,* Franklin & Marshall College, **1989**, Table 6.
7. Gaussian 09, Revision A.02, M. J. Frisch, G. W. Trucks, H. B. Schlegel, G. E. Scuseria, M. A. Robb, J. R. Cheeseman, G. Scalmani, V. Barone, B. Mennucci, G. A. Petersson, H. Nakatsuji, M. Caricato, X. Li, H. P. Hratchian, A. F. Izmaylov, J. Bloino, G. Zheng, J. L. Sonnenberg, M. Hada, M. Ehara, K. Toyota, R. Fukuda, J. Hasegawa, M. Ishida, T. Nakajima, Y. Honda, O. Kitao, H. Nakai, T. Vreven, J. A. Montgomery, Jr., J. E. Peralta, F. Ogliaro, M. Bearpark, J. J. Heyd, E. Brothers, K. N. Kudin, V. N. Staroverov, R. Kobayashi, J. Normand, K. Raghavachari, A. Rendell, J. C. Burant, S. S. Iyengar, J. Tomasi, M. Cossi, N. Rega, J. M. Millam, M. Klene, J. E. Knox, J. B. Cross, V. Bakken, C. Adamo, J. Jaramillo, R. Gomperts, R. E. Stratmann, O. Yazyev, A. J. Austin, R. Cammi, C. Pomelli, J. W. Ochterski, R. L. Martin, K. Morokuma, V. G. Zakrzewski, G. A. Voth, P. Salvador, J. J. Dannenberg, S. Dapprich, A. D. Daniels, Ö. Farkas, J. B. Foresman, J. V. Ortiz, J. Cioslowski, and D. J. Fox, Gaussian, Inc., Wallingford CT, 2009.
8. a) A.D. Becke, *J.Chem.Phys.*, **1993**, *98*, 5648; b) C. Lee, W. Yang and R. G. Parr, *Phys. Rev. B*, **1988**, *37*, 785; c) S.H. Vosko, L. Wilk and M. Nusair, *Can. J. Phys.*, **1980**, *58*, 1200; d) P.J. Stephens, F.J. Devlin, C.F. Chabalowski and M.J. Frisch, *J. Phys. Chem.*, **1994**, *98*, 11623.

STUDIA UNIVERSITATIS BABEŞ-BOLYAI, CHEMIA, XLV, 2, TOM I, 2010

Dedicated to the memory of Prof. dr. Ioan Silaghi-Dumitrescu marking 60 years from his birth

ZINC-CONTAINING ACTIVE SITE IN A PARTIALLY MODIFIED 1GKM CRYSTAL STRUCTURE OF HISTIDINE AMMONIA-LYASE: A COMPUTATIONAL INVESTIGATION

AMALIA-LAURA SEFF[a], SAROLTA PILBÁK[b],
IOAN SILAGHI-DUMITRESCU[a], LÁSZLÓ POPPE[b]

ABSTRACT. The histidine ammonia-lyase (HAL) biocatalyst has an important role in the formation of (*E*)-urocanic acid from L-histidine eliminating ammonia. In order to investigate the active center of HAL, we have prepared "*in silico*" a HAL model with a compact active center on the basis of the recently appeared phenylalanine ammonia-lyase (PAL) structure (PDB code: 3CZO). Furthermore, to have a better view on the orientation of a key reaction intermediate within the active site, systematic conformational analysis has been performed. Furthermore, the possible positions of the L-histidine/(*E*)-urocanic acid were evaluated by optimization and docking.

Keywords: *histidine ammonia-lyase, homology modeling, conformational analysis, docking, Zn*$^{2+}$

INTRODUCTION

The degradation pathway of histidine in various organisms proceeds in a different way than for most of the other amino acids [1]. The histidine ammonia-lyase (HAL, EC 4.3.1.3) catalyzes the first step of the degradation with ammonia elimination from the L-histidine substrate forming the product (*E*)-urocanic acid (Scheme 1).

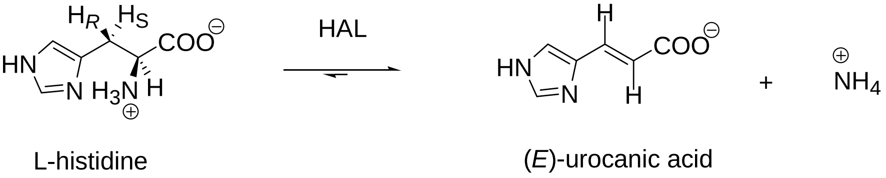

Scheme 1

---

[a] *Faculty of Chemistry and Chemical Engineering, Babeş-Bolyai University, Kogălniceanu Str. No. 1, RO-400084 Cluj-Napoca, Romania, samalia@chem.ubbcluj.ro*
[b] *Department of Organic Chemistry and Technology, Budapest University of Technology and Economics, H-1111 Budapest, Gellért tér 4, Hungary, poppe@mail.bme.hu*

The aforementioned product was identified as a component of human sweat [2] and a condition named histidinemia appears in case of the lack of HAL in humans [3]. Histidine ammonia-lyase together with the phenylalanine ammonia-lyase (PAL, EC 4.3.1.24) and tyrosine ammonia-lyase (TAL, EC 4.3.1.23) are a part of the family of ammonia-lyases. PAL and TAL as members of this family catalyze the elimination of ammonia from the corresponding L-amino acid forming unsaturated products as (*E*)-cinnamic acid and (*E*)-coumaric acid. These products have important biological roles from the amino acid catabolism to the formation of intermediates in different biosyntheses. HAL, PAL and TAL catalyze the ammonia elimination by the aid of the 5-methylene-3,5-dihydroimidazol-4-one (MIO) prosthetic group [4].

It was observed that cations, like Zn^{2+}, Cd^{2+} or Mn^{2+} can increase the activity of the HAL enzyme [5]. After elucidation of the X-ray structure of HAL [6], the importance of several amino acid residues at the active center (Tyr53, His83, Asn195, Gln277, Tyr280, Arg283, Phe329 and Glu414) for catalysis and substrate binding was evaluated by site-directed mutagenesis and it was supposed that Zn^{2+} may play a role in catalysis [7].

The present work describes the "*in silico*" preparation of the partially modified HAL structure (1GKM*mod*) from the crystal structure (1GKM) [8] of *Pseudomonas putida* HAL (*Pp*HAL), including modeling of a closed Tyr53-loop region which was necessary to obtain a closed active site. A systematic conformational analysis of the substrate covalently bound to the MIO prosthetic group (*N*-MIO intermediate) taking into account the presence of a Zn^{2+} cation and ligand docking results are also presented.

RESULTS AND DISCUSSION

Selection and modeling of the HAL crystal structure

According to the study with active site mutants of HAL [7], Tyr53, Glu414 and Tyr280 residues may have an important role in the abstraction of the pro-(S) β-proton from the L-histidine substrate. A comparison of the structure of *Pp*HAL to other ammonia-lyases showed that the loop with the essential Tyr53 adopts a partially open conformation (Figure 1).

The X-ray structure of plant PAL from *Petroselinum crispum* (PDB code: 1W27) determined at 1.7 Å resolution [9] has an opened, solvent accessible active site (Figure 1A). The bacterial *Pp*HAL (PDB code: 1GKM) structure reveals a partially opened, solvent accessible active site (Figure 1B). All the six crystal structures determined for HAL so far contain the catalytically essential Tyr53 in a partially open loop conformation. This may be the reason why these structures could not retain subtrate or product related ligands. Therefore, none of them could be used for theoretical investigation of the compact active center. Only the 1GKM crystal structure of HAL (inhibited with L-cysteine) was determined in the presence of an inhibitor in the active center.

The recently published ammonia-lyase crystal structure (PDB code: 3CZO) [10], determined for Anabaena variabilis PAL (AvPAL), contains the most compact active center in which the essential Tyr78 and the MIO prosthetic group are deeply buried and not solvent accessible (Figure 1C).

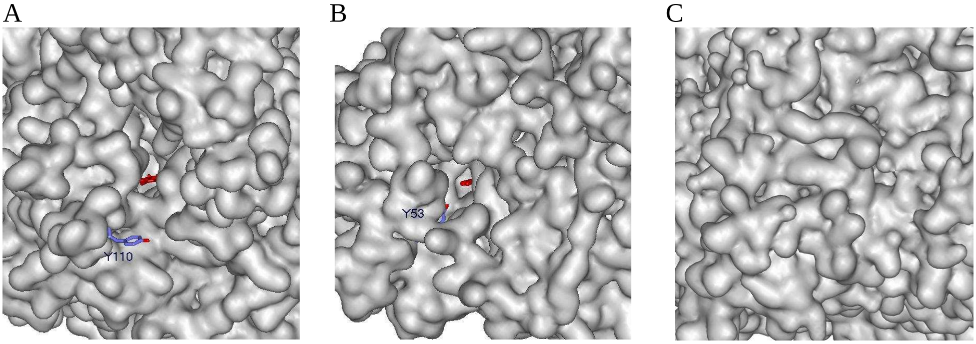

Figure 1. Comparison of the substrate entrance chanel towards MIO group (red) in several ammonia-lyase structures. Representation of molecular surface of (A) *Pc*PAL (PDB code 1W27), (B) *Pp*HAL (PDB code 1GKM) and (C) *Av*PAL (PDB code 3CZO) crystal structures. The analogous Tyr110 (A) and Tyr53 (B) residues are seen as stick models in the partially opened ammonia-lyase structures.

Our motivation to select the 1GKM HAL structure for further calculations was the presence of an inhibitor and the unique orientation of the side chain of Met382 amino acid within the active site.

Modification of the essential Tyr-containing loop region (39-80 amino acid sequence) of 1GKM HAL was based on the 3CZO PAL structure using homology modeling (Figure 2). The new (1GKM$_{mod}$) model contains a tightly closed active site and thus provides a well defined enzymic ambience for further theoretical investigation and calculations.

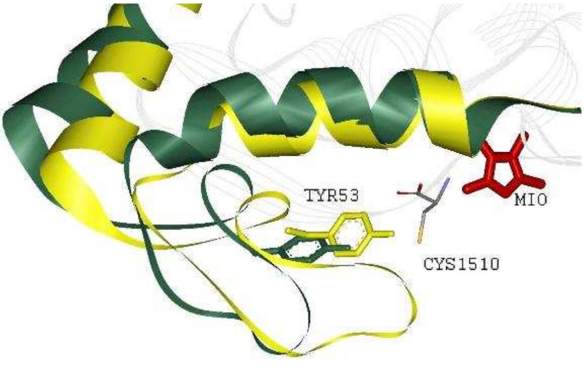

Figure 2. Overlay of the important Tyr53 loop regions of *Pp*HAL (1GKM, green chain; including the L-cysteine inhibitor in CPK color) and of the partially modified 1GKM$_{mod}$ (yellow chain) structures.

Conformational analysis of the N-MIO intermediate

The arrangement of L-cysteine inhibitor within the active center of 1GKM crystal structure provided the opportunity to replace the inhibitor with the natural substrate (L-histidine). In the *N*-MIO intermediate of the HAL reaction, the L-histidine is covalently bound to the MIO prosthetic group trough its amino group. The carboxyl group of the histidine substrate may point towards the Arg283 amino acid residue and the imidazole ring of the substrate may be in the hydrophobic part of the active site close to the His83 residue. In order to get the geometries of the possible orientation of the intermediate within the active site, the systematic conformational analysis search (CS) method has been used. The active center of the HAL structure was proposed to contain a Zn^{2+} ion [7]. Concerning on the Zn-binding site, the S atom of Met382 could be one of the coordinating ligand of the Zn^{2+} ion together with the imidazole group of His83 and substrate. The W544 water molecule was moved as the fourth ligand of Zn^{2+}.

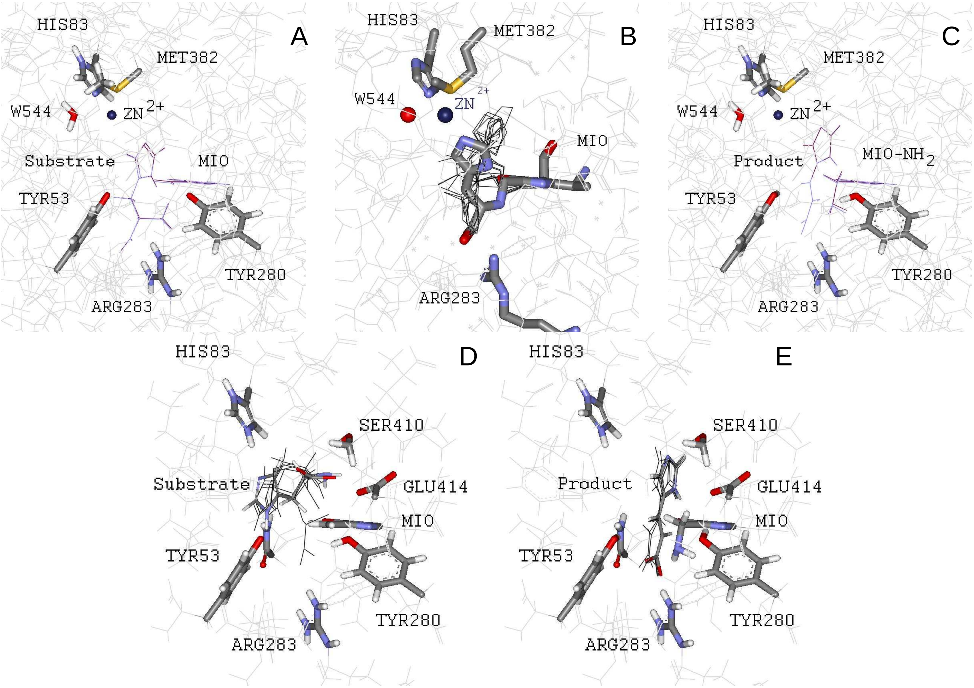

Figure 3. Optimized arrangements of substrate (A) and product (C), conformational analysis of the covalent intermediate (B), and docking results for the substrate (D) and product (E) in the modified HAL structure.

For the covalent intermediate model (Figure 3B), the best ligand energy conformation was selected and highlighted as stick model (imidazole group points towards His83 and carboxylate is in the close vicinity of Arg283) which was also in correspondence with the overall arrangement of the ligands found in the experimental structures of *Rhodobacter sphaeroides* TAL. The Zn^{2+} coordination set is formed by the imidazole group of His83 and of the substrate, the Met382 and a water molecule. The geometrical characterization of the optimized substrate, covalent intermediate and product structures is presented in the Table 1.

Table 1. Geometrical parameters resulted after optimization of the substrate/product structure and after conformational search of the covalent intermediate structure.

	Distances (Å)			
	d(Zn-N3$_{\mathrm{H83}}$)	d(Zn-N3$_{\mathrm{Lig}}$)	d(Zn-O$_{\mathrm{W544}}$)	d(Zn-S$_{\mathrm{M382}}$)
substrate	1.91	2.90	2.91	3.76
intermediate	1.91	2.67	2.91	3.76
product	1.91	3.05	2.91	3.76
	d(H$_{\mathrm{O\text{-}Y53}}$-Cβ$_{\mathrm{Lig}}$)	d(βH$_{\mathrm{Lig}}$-O$_{\mathrm{Y53}}$)	d(O$_{\mathrm{Lig}}$-H$_{\mathrm{R283}}$)	d(H$_{\mathrm{N1\text{-}Lig}}$-O$_{\mathrm{E414}}$)
subst./prod.	2.21	2.20	1.85/2.01	3.00/3.28
	Angles(º)			
	N3$_{\mathrm{H83}}$-Zn-N3$_{\mathrm{Lig}}$	N3$_{\mathrm{Lig}}$-Zn-O$_{\mathrm{W544}}$	O$_{\mathrm{W544}}$-Zn-S$_{\mathrm{M382}}$	S$_{\mathrm{M382}}$-Zn-N3$_{\mathrm{H83}}$
substrate	165.5	113.7	47.1	84.8
intermediate	164.0	86.8	47.1	66.6
product	147.2	117.6	47.1	70.4

Geometry optimization and ligand docking of the substrate/product

Geometry optimization of the substrate/product ligands within the active site of 1GKM$_{mod}$ was necessary because none of the crystal structures determined for HAL contain the natural L-histidine substrate or the (*E*)-urocanic acid product of the reaction.

For a good evaluation of the substrate/product position within the active site, molecular mechanics (MM+) optimization (Figure 3A and 3C) of the ligands derived from the best covalent *N*-MIO intermediate using HyperChem program [11] and ligand docking (Figure 3D and 3E) within the active center of 1GKM$_{mod}$ structure using AutoDock software [12, 13] were carried out.

CONCLUSIONS

Taking into account that partial modification of the 1W27 *Pc*PAL crystal structure by homology modeling [14, 15, 16] was already applied for computational investigation within the active site of the reaction mechanism, it can be considered that our novel HAL model (1GKM$_{mod}$) is eligible for further computational investigation of the possible geometry orientation of the L-histidine substrate/*N*-MIO intermediate/(*E*)-urocanic acid product.

Although the ligand docking is a computational tool which is dedicated to the evaluation of the possible positions of the ligand within the active site using different algorithms, the results obtained at the L-histidine and (*E*)-urocanate docking within the 1GKM$_{mod}$ active center revealed only for the (*E*)-urocanate product the following interactions: the carboxylate moiety establishes an interaction with the Arg283 and the imidazole ring points towards the His83 amino acid residue trough its N_3 atom.

EXPERIMENTAL SECTION

Selection of the HAL crystal structure for modification and modeling

There are six crystal structures determined for *Pseudomonas putida* histidine ammonia-lyase enzyme (Brookhaven Protein Data Bank codes: 1B8F, 1EB4, 1GK2, 1GK3, 1GKJ, 1GKM). Among the available structures the 1GKM structure was selected for computational investigation of HAL. This is the only structure which contains a ligand (L-cysteine) inside the active center and revealed a unique orientation of the side chain of Met382 amino acid within the active site compared to the other structures determined for HAL. The distance between the N atom of the amino moiety in L-cysteine and the C atom of the methylene group in MIO was 1.31 Å.

The 3CZO *Av*PAL crystal structure has the inner Tyr loop region (containing the essential Tyr53 amino acid) in a fully closed form. The 39-80 amino acid sequence of 1GKM HAL, which contains the important Tyr53 amino acid in a partially open loop conformation, was replaced by the corresponding homology model sequence of the 1GKM HAL based on 3CZO PAL. The resulted 1GKM$_{mod}$ model structure seemed to be eligible for calculations within the enzymic ambience taking into account the new position of the Tyr53 amino acid in comparison with the one from the crystal structure of *Pp*HAL within the active site (Figure 2).

Conformational analysis of the N-MIO intermediate

The initial ligand structures for the CS were built from the L-cysteine inhibitor (Cys1510) of the 1GKM crystal structure of *Pp*HAL. Therefore, the L-cysteine of the 1GKM was replaced by L-histidine in the 1GKM$_{mod}$ HAL structure. In the resulted starting conformation the carboxyl group of the MIO-bound L-histidine pointed towards the Arg283 residue and the imidazole ring of the substrate occupied a relative hydrophobic part of the active site close to the His83 residue. From the resulted 1GKM$_{mod}$ structure a region defined by a sphere of 15 Å radius around the C atom of the original L-cysteine (Cys1510) and a sphere of 12 Å radius around the O atom of a highly conserved water (W544 – close to the place where we propose the presence of the Zn^{2+} ion) was cut off for CS calculations as a closed active site model of HAL (including 146 amino acids and 43 water molecules). Next, by a HyperChem [11] standard procedure, hydrogen atoms were added to the amino acid moieties. In the starting structure, the *C*- and *N*-termini at cuttings were completed to neutral aldehyde and amino parts. The resulted overall structure and the hydrogen additions were verified and corrected [17]. From this verified raw *Pp*HAL active site model (partially modified 1GKM crystal structure including L-histidine), only one initial active site construct involving the substrate covalently bound to MIO trough the amino moiety (*N*-MIO model) was built. In this active site model a Zn^{2+} ion was included at a 1.9 Å distance from the N3 atom of His83 amino acid residue (as found in many Zn-containing protein structures). During CS on the covalently bound histidine and the imidazolone ring of the MIO in rigid enzymic environment (including 41 water molecules), 3 of the ligand torsion angles were varied for the *N*-MIO model. CS's were performed by HyperChem implemented CS module [11] using default settings (MM+ forcefield; gradient: 0.1 kcal/mol; Polak-Ribiere method; limits: 300 iterations, 150 optimizations, 15 conformations; test options: "skip if atoms are closer than 0.3 Å").

For the covalent intermediate model, the best ligand energy conformation was selected which was also in agreement with the overall arrangement (imidazole group points towards His83 and carboxylate is in the close vicinity of Arg283) found in the experimental inhibited structures of *Rhodobacter sphaeroides Rs*TAL.

Several *N*-MIO active site models were constructed by replacing the substrate-MIO part of the initial *Pp*HAL (1GKM$_{mod}$)/ L-histidine active site construct with the ligand arrangements resulted from the CS.

Geometry optimization and docking of L-histidine/(E)-urocanic acid in the active site model of PpHAL

In order to construct the L-histidine/(*E*)-urocanate ligand-containing starting structures, six different conformers resulted from the CS were used. The covalent bond (Figure 4) between the methylene group of the MIO and the amino moiety was cut in case of the substrate (indicated by the green line). The bond between the amino moiety and the carbon atom of the ligand was cut in case of the product (indicated by the blue line) and the structure was completed with the necessary olefinic bond to get (*E*)-urocanate.

Next, the 6 × 2 L-histidine/(*E*)-urocanate ligand structures were optimized within rigid enzymic environment, by the HyperChem implemented *Geometry optimization* using the default settings (MM+ forcefield; gradient: 0.1 kcal/mol; Polak-Ribiere method). From the resulted set of models, the two lowest energy substrate and product structures (ones obtained from the c12 and c14 optimizations) were used for further optimizations in which the essential parts of the active site (including the MIO-NH_2, the aromatic part of the His83, Tyr280, Tyr53, the –CH_2-CO-NH_2 part of Asn195, Asn313, Gln277, Gln413, the –CH_2-COO^- part of the Glu414, the -CH_2-OH part of Ser410 and the Zn^{2+} ion) were included.

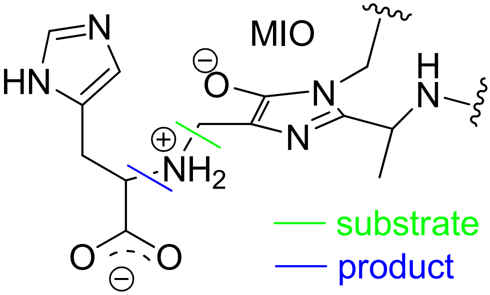

Figure 4. The bond cuts of the *N*-MIO intermediate to construct the L-histidine substrate (green) and (E)-urocanate product (blue) containing HAL models

The starting structures for the docking calculations were constructed from the active site model of *Pp*HAL 1GKM*mod* structure used for CS calculations. Only 29 amino acid residues (including the essential amino acid residues like His83, Arg283, Met382, Tyr53, Tyr280, Asn195 and Glu414, determined by mutagenesis) and the MIO prosthetic electrophilic group were used as environment for the substrate/product docking. We used separate initial active site models for the substrate (4 torsion angle were selected from the substrate using flexible-rigid docking) and for the product. For the docking process of L-histidine/(*E*)-urocanic acid in the 1GKM*mod* active site models, the AutoDock software [12, 13] was used. The Grid Parameter File was established with the default settings (Total Grid Pts per map: 77326; number of points 40 for x- and y-dimensions, 45 for z-dimension; spacing: 0.375 Å; center on ligand). The docking process of the L-histidine/(*E*)-urocanic acid in 1GKM*mod* active site model was performed by the AutoDockTools implemented Docking module using default settings (Lamarckian Genetic Algorithm also known as a Genetic Algorithm-Local Search: 10 runs; population size: 150; maximum number of energy evaluations: short setting).

For the product-containing 1GKM$_{mod}$ active site model, a set of the best docking energy poses were selected (Figure 3E), which were also in correspondence to the overall arrangement found for (*E*)-coumarate in wild-type *Rhodobacter sphaeroides bacterial* TAL (PDB code: 2O7B).

ACKNOWLEDGMENTS

ALS thanks the financial support of Romanian National University Research Council (CNCSIS, PNII-TD-400). *PL* thanks OTKA T048854 for financial support.

Supporting information available:

The coordinates of the 1GKM$_{mod}$ structure.

REFERENCES

1. L. Poppe, J. Rétey, *Angewandte Chemie, International Edition English*, **2005**, *44*, 3668.
2. H. Morrison, C. Bernasconi, G. Pandey, *Photochemistry and Photobiology*, **1984**, *40*, 549.
3. R.G. Taylor, H.L. Levy, R.R. McInnes, *Molecular Biology and Medicine*, **1991**, *8*, 101.
4. L. Poppe, *Current Opinion in Chemical Biology*, **2001**, *5*, 512.
5. C.B. Klee, *The Journal of Biological Chemistry*, **1972**, *247*, 1398.
6. T.F. Schwede, J. Rétey, G.E. Schulz, *Biochemistry*, **1999**, *38*, 5355.
7. D. Röther, L. Poppe, S. Viergutz, B. Langer, J. Rétey, *European Journal of Biochemistry*, **2001**, *268*, 6011.
8. M. Baedeker, G.E. Schulz, *European Journal of Biochemistry*, **2002**, *269*, 1790.
9. H. Ritter, G.E. Schulz, *Plant Cell*, **2004**, *16*, 3426.
10. L. Wang, A. Gamez, et al., *Journal of Molecular Biology*, **2008**, *380,* 623.
11. HyperChem version 7.0 (Hypercube, Inc. http://www.hyper.com/).
12. G.M. Morris, D.S. Goodsell, et al., *Journal of Computational Chemistry*, **1998**, *19*, 1639.
13. R. Huey, G.M. Morris, et al., *Journal of Computational Chemistry*, **2007**, *28*, 1145.
14. S. Pilbák, A. Tomin, J. Rétey, L. Poppe, *The FEBS Journal*, **2006**, *273*, 1004.
15. A.L. Seff, S. Pilbák, L. Poppe, *Studia Universitatis Babeş-Bolyai, Chemia* LIII, 2**008**, *2*, 67.
16. S. Bartsch, U.T. Bornscheuer, *Angewandte Chemie, International Edition English,* **2009**, *48*, 3362.
17. Molfunction, Institute of Molecular Function (http://www.molfunction.com/).

STUDIA UNIVERSITATIS BABEŞ-BOLYAI, CHEMIA, XLV, 2, TOM I, 2010

Dedicated to the memory of Prof. dr. Ioan Silaghi-Dumitrescu marking 60 years from his birth

CHEMICAL HARDNESS: QUANTUM OBSERVABLE?

MIHAI V. PUTZ[*]

ABSTRACT. The question whether chemical hardness may be regarded as ordinary quantum observable is responded in negative employing the second quantification within fermionic Fock space.

Keywords: *annihilation and creation particle operators, valence energy, electronic density, ionization and affinity energies*

INTRODUCTION

In modern quantum chemistry the chemical reactivity is conceptualized throughout specific indices, among which the chemical hardness stands a pre-eminent one, often seen as a companion of the electronegativity [1,2]. However, the phenomenological and analytical definitions of chemical hardness together with its principles, i.e. hard and soft-acids and bases HSAB and maximum hardness principles MHP, are systematically presented within the density functional theory framework and applied on paradigmatic atomic and molecular systems [3-6]. Despite this, the recent proof on the two decades question about the quantum nature of the electronegativity [7] opens the natural similar question about chemical hardness; this communication likes to offer an analytical answer in this regard.

INTRODUCING QUANTUM CHEMICAL HARDNESS

The fermionic Fock space is build by the aid of the creation and annihilation particle operators

$$\mathbf{a}^{+} = |1\rangle\langle 0| \, , \; \mathbf{a} = |0\rangle\langle 1| \, , \tag{1}$$

such that the vacuum and uni-particle sectors cover the entire particle projection space:

---

[*] *West University of Timişoara, Chemistry Department, Str. Pestalozzi No. 16, RO-300115 Timişoara, Romania, mvputz@cbg.uvt.ro*

$$\mathbf{1} = |0\rangle\langle 0| + |1\rangle\langle 1| = \mathbf{a}\mathbf{a}^{+} + \mathbf{a}^{+}\mathbf{a} = \{\mathbf{a},\mathbf{a}^{+}\}, \tag{2}$$

that allows for the equivalent density normalization relationships

$$\begin{aligned} 1 &= \langle\psi_0|\psi_0\rangle = \langle\psi_0|\mathbf{1}|\psi_0\rangle = \langle\psi_0|(\mathbf{a}\mathbf{a}^{+} + \mathbf{a}^{+}\mathbf{a})|\psi_0\rangle = \langle\psi_0|\mathbf{a}\mathbf{a}^{+}|\psi_0\rangle + \langle\psi_0|\mathbf{a}^{+}\mathbf{a}|\psi_0\rangle \\ &= |\langle 0|\psi_0\rangle|^2 + |\langle 1|\psi_0\rangle|^2 = (1-\rho_0) + \rho_0\,,\ \rho_0 \in [0,1]\,, \end{aligned} \tag{3}$$

for unperturbed state $|\psi_0\rangle$ with associated eigen-energy E_0 for a given atomic or molecular valence system.

In these conditions, the chemical processes of electronic exchange with environment (releasing by ionization or accepting through affinity) are modelled by the associate ionization and affinity second quantized wave-functions

$$|\psi_\lambda^I\rangle = (1 + \lambda\mathbf{a}\mathbf{a}^{+})|\psi_0\rangle = |\psi_0\rangle + \lambda|0\rangle\langle 1|1\rangle\langle 0|\psi_0\rangle = |\psi_0\rangle + \lambda\sqrt{1-\rho_0}\,|0\rangle\,, \tag{4a}$$

$$|\psi_\lambda^A\rangle = (1 + \lambda\mathbf{a}^{+}\mathbf{a})|\psi_0\rangle = |\psi_0\rangle + \lambda|1\rangle\langle 0|0\rangle\langle 1|\psi_0\rangle = |\psi_0\rangle + \lambda\sqrt{\rho_0}\,|1\rangle \tag{4b}$$

by means of the perturbation factor λ; they enter in calculation of the perturbed energy

$$\left\langle E_{\lambda\in\Re}^{I\leftrightarrow A}\right\rangle = \frac{\langle\psi_\lambda^I|H|\psi_\lambda^A\rangle}{\langle\psi_\lambda^I|\psi_\lambda^A\rangle} \tag{5}$$

and electronic density

$$\rho_{\lambda\in\Re}^{I\leftrightarrow A} = \frac{\langle\psi_\lambda^I|\mathbf{a}^{+}\mathbf{a}|\psi_\lambda^A\rangle}{\langle\psi_\lambda^I|\psi_\lambda^A\rangle} \tag{6}$$

that finally provide the chemical hardness realization as

$$\eta_\lambda = \frac{1}{2}\frac{\partial^2\langle E_\lambda\rangle}{\partial\rho_\lambda^2} \tag{7}$$

By considering the basic chain-derivation rule

$$\frac{\partial\bullet}{\partial\rho_\lambda} = \frac{\partial\bullet}{\partial\lambda}\cdot\frac{\partial\lambda}{\partial\rho_\lambda} \tag{8}$$

chemical hardness of Eq. (7) unfolds as

$$\eta_\lambda = \frac{1}{2}\left\{\left[\frac{\partial}{\partial\lambda}\left(\frac{\partial\langle E_\lambda\rangle}{\partial\lambda}\right)\right]\frac{\partial\lambda}{\partial\rho_\lambda}+\frac{\partial\langle E_\lambda\rangle}{\partial\lambda}\left[\frac{\partial}{\partial\lambda}\left(\frac{\partial\lambda}{\partial\rho_\lambda}\right)\right]\right\}\frac{\partial\lambda}{\partial\rho_\lambda} \tag{9}$$

to be in next evaluated.

QUANTUM VALUES OF CHEMICAL HARDNESS

Equation (9) may be further expressed by employing the inverse density and energy gradients respecting the chemical perturbation factor λ, see Ref. [7]:

$$\frac{\partial\lambda}{\partial\rho_\lambda} = \frac{(1+\lambda\rho_0)^2}{\rho_0(1-\rho_0)}, \tag{10a}$$

$$\frac{\partial\langle E_\lambda\rangle}{\partial\lambda} = E_0\frac{1-\rho_0}{(1+\lambda\rho_0)^2} \tag{10b}$$

toward the second order perturbation terms

$$\frac{\partial}{\partial\lambda}\left(\frac{\partial\lambda}{\partial\rho_\lambda}\right) = 2\frac{1+\lambda\rho_0}{1-\rho_0}, \tag{11a}$$

$$\frac{\partial}{\partial\lambda}\left(\frac{\partial\langle E_\lambda\rangle}{\partial\lambda}\right) = -2E_0\rho_0\frac{1-\rho_0}{(1+\lambda\rho_0)^3} \tag{11b}$$

leading with the chemical hardness limits

$$\eta_\lambda = 0\cdot E_0\frac{1+\lambda\rho_0}{\rho_0(1-\rho_0)} = \begin{cases} 0, & \rho_0 \in (0,1) \\ 0\cdot\infty = ?, & \rho_0 \to 0 \\ 0\cdot\infty = ?, & \rho_0 \to 1 \end{cases} \tag{12}$$

The results of Eq. (12) give the answer that the chemical hardness is *not* an observable, having neither a *non-zero* nor a *definite* value for any electronic density realization or limit, respectively. Such a behavior is somehow explained by the energetic nature of chemical hardness usually associated with the HOMO-LUMO gap for a molecular system, i.e. with an energy interval (or energy difference) rather than with an eigen-energy (or an energy level) of a spectrum.

However, the result (12) does not exclude the “real”, even as “hidden” or dispersed, values of chemical hardness: for the fractional occupied states – the first upper branch of Eq. (12) – are assessed to the open states of chemical bonding, while the empty or fully occupied valence states – the middle and lower branches of Eq. (12) – are described by the not definite (in eigen-value sense) of chemical hardness, since is uncertain it will allow fully engagement or inert chemical response in reactivity and bonding, respectively.

CONCLUSIONS

In modeling of chemical reactivity by means of electronegativity and chemical hardness, there was proofed that while electronegativity may be assumed as a quantum observable with an eigen-value equating the chemical potential [7], the chemical hardness, although as driving the chemical force in bonding through the electronegativity change with engaged charge change of a given (valence) system [2], cannot be associated with a non-zero or a definite energetic value for fractional or fully empty/filled electronic states in interacting states. However, the hidden quantum nature of chemical hardness may be appropriately fitted with the non-locality electronic measures of chemical bond accompanying any localized charge in bonding, being thus susceptible to be further considered in elucidation of aromaticity chemical concept, for instance. Yet, related studies in the second quantization framework are expected to be very fruitful in elucidating quantum aspects of chemical reactivity and bonding and will be addressed in the years to come and in subsequent communications.

REFERENCES

1. M. V. Putz, "Absolute and Chemical Electronegativity and Hardness", Nova Publishers Inc., New York, **2008**.
2. M. V. Putz, *International Journal of Molecular Sciences*, **2008**, *9*, 1050.
3. M. V. Putz, *MATCH Communication in Mathematical and in Computer Chemistry*, **2008**, *60*, 845.
4. M. V. Putz, N. Russo, E. Sicilia, *Journal of Computational Chemistry*, **2004**, *25*, 994.
5. M. V. Putz, *Journal of Theoretical and Computational Chemistry*, **2007**, *6*, 33.
6. M. V. Putz, *International Journal of Quantum Chemistry*, **2006**, *106*, 361.
7. M. V. Putz, *International Journal of Quantum Chemistry*, **2009**, *109*, 733.

STUDIA UNIVERSITATIS BABEŞ-BOLYAI, CHEMIA, XLV, 2, TOM I, 2010

Dedicated to the memory of Prof. dr. Ioan Silaghi-Dumitrescu marking 60 years from his birth

MATHEMATICAL MODELING AND SIMULATION OF COAL CO-GASIFICATION WITH WASTE/BIOMASS IN AN ENTRAINED-FLOW GASIFIER

VICTORIA MAXIM[a], CĂLIN-CRISTIAN CORMOŞ[a],
PAUL ŞERBAN AGACHI[a]

ABSTRACT. The aim of this paper is to evaluate the ways to use coal alone or in addition with biomass (sawdust, agricultural wastes etc.) or solid waste (animal residue, municipal solid wastes, waste paper etc.) trough co-gasification to supply syngas for energy vectors poly generation in an Integrated Gasification Combined Cycle (IGCC) with Carbon Capture and Storage (CCS).

This paper analyses various cases of blending coal with different renewable energy sources by means of mathematical modeling and simulation of the gasification process using the process flow modeling software ChemCAD.

The effect of varying the feedstock and the effect of varying the blending ratio coal vs. alternative fuel on the cold gas efficiency and hydrogen production potential is studied for the gasifier performance optimization.

Keywords: *Co-gasification, Coal, Renewable energy sources, Solid wastes, Mathematical modelling and simulation*

INTRODUCTION

The climate change and the reduction of greenhouse emissions are very important and actual in the context of modern society. There are many greenhouse gases sources: transport, agriculture, power generation plants, industry etc., but the larger contributor is the power generation field, with a percentage around 24% of all greenhouse gases emissions and is set to grow by 2030 around 40% [1]. Coal accounts for around one-third of the EU's electricity production and its utilization is regarded with concern because of the larger greenhouse emissions compared with other fossil fuels (e.g. natural gas and oil).

---

[a] *Universitatea Babeş-Bolyai, Facultatea de Chimie şi Inginerie Chimică, Str. Kogălniceanu Nr. 1, RO-400084 Cluj-Napoca,Romania,*
Emails: vgoia@chem.ubbcluj.ro, cormos@chem.ubbcluj.ro, sagachi@staff.ubbcluj.ro

The most powerful greenhouse gas is the carbon dioxide CO_2 which is produced by the transportation, industrial and energy generating sectors. In order to prevent the increasing trend of greenhouse gas emissions the carbon capture and storage technology was developed. The carbon capture and storage (CCS) is a way of mitigating the contribution of fossil fuel emission to global warming. This is based on capturing the carbon dioxide and storing it away either in deep geological formations, in deep ocean masses, or in the form of mineral carbonates [2, 3].

In close co-operation with industries and Member States, the EU government presently supports the development of CCS (Carbon Capture and Storage) technologies in coal-fired power plants [4]. The aim is to make zero emission power generation plants using CCS commercially feasible by 2020 [1,4].

Gasification of solid fuels is a process which converts the solid feedstock by partial oxidation with oxygen and steam into syngas. The syngas can be used in a large number of applications as: power generation, manufacture of various chemicals and fuels (e.g.. hydrogen, methanol, ammonia, fertilizers etc.). The gasifiers may be designed for wide variety of solid feedstock: fossil fuels (e.g. coal, lignite peat etc.), various biomass types (sawdust, agricultural wastes etc.) and solid waste (e.g. animal residue, municipal solid wastes, waste paper etc.). The chemical composition of syngas varies based on many factors: coal composition, size and rank, feeding system (dry or slurry), gasification agent used for oxidation (air or oxygen), temperature, pressure, residence time in the gasifier, heating rate, gasification island configuration, etc. [5,6].

The conventional Integrated Gasification Combined Cycle (IGCC) is a concept regarding the conversion of solid fuels into syngas, meaning that a mixture of carbon monoxide and hydrogen, which after ash removal and desulphurization is burned in a conventional Combined Cycle Gas Turbine (CCGT) to generate electrical power. A unit can be considered capture-ready if, at some point in the future, it can be retrofitted for CO_2 capture and sequestration and still be economical to operate [7]. IGCC is a carbon capture ready technology. The design for a modified IGCC scheme for poly-generation of electricity and hydrogen with CCS is presented in Figure1.

The core of the IGCC technology is the gasification process of a solid fuel either fossil fuels alone or in addition with various biomass types and solid waste having energetically value. The IGCC is one of the power generation technologies having the highest potential to capture CO_2 with the lowest penalties in energy efficiency and cost. The IGCC technology is very attractive for energy vectors poly-generation: electricity, hydrogen, heat and chemicals [8, 9].

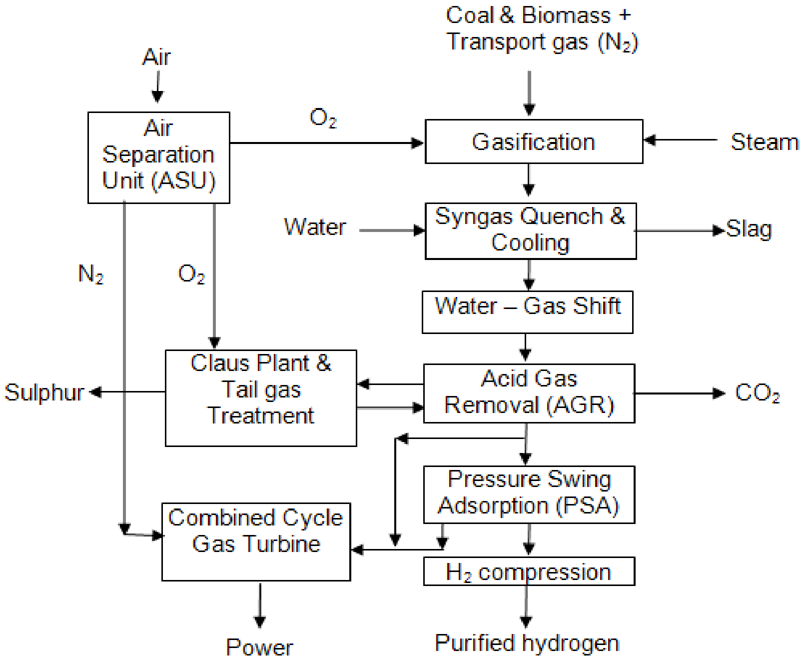

Figure 1. The IGCC scheme modified for poly-generation of electricity and hydrogen with carbon capture and storage (CCS)

The next section of this paper presents the gasifier concept, the feedstock caracteristics and the modeling and simulation of gasification process. The co-gasification of coal alone or in addition with biomass (sawdust, agricultural wastes) or solid waste (animal residue, municipal solid wastes, waste paper) will be analyzed by mathematical modeling and simulation using the process flow modeling software ChemCAD. The most appropriate mixture will be chosen by analyzing the syngas composition, Cold Gas Efficiency (CGE) and the hydrogen production potential. The behavior of co-gasification of coal with various sorts of biomass or solid wastes will be studied by varying the blending ratio.

RESULTS AND DISCUSSION

The main system component of the gasification process is the gasifier. It is a pressure vessel in which a fuel (coal or biomass/waste) togheter with air (or oxygen) and water are heated to high temperatures, above 900°C, to produce syngas (mainly a mixture of hydrogen and carbon monoxide). The syngas after cleaning is used to generate electricity in a gas turbine [10].

The gasification reactors can be grouped in one of the three main categories: moving-bed gasifiers, fluidised-bed gasifiers, and entrained-flow gasifiers. The caracteristics of these reactors can be found in the literature [6,11].

Based on several criteria such as: oxygen purity, gasifier throughputs, reliability and experience, cold gas efficiency (CGE), carbon conversion efficiency (CCE), syngas cooling options, influence of oxygen purity and gasifier feed system for hydrogen purification step, hydrogen production potential, capital cost etc., from the large range of gasifiers, as the most promising reactor for energy vectors poly-generation (mainly hydrogen and electricity) with Carbon Capture and Storage, a Shell gasifier has been chosen.

Table 1. Design assumptions for Shell gasifier

Parameters	Shell gasifier
Maximum pressure (bar)	40
Temperature (°C)	1400-1600
Carbon conversion (%)	>99

The Shell gasifier is a carbon steel vessel that contains a gasification chamber enclosed by a non-refractory membrane wall, which operates at 30-40 bar pressure, temperature range of 1500-1600°C, dry feed and one stage. The pulverized coal is stored under nitrogen, where it is pressurized and then pneumatically transported into the gasifier. The syngas is quenched with cooled recycled product gas and further cooled in a syngas cooler. Raw gas is cleaned in ceramic filters. A Shell gasifier configuration is shown in Figure 2. The image represents a dry-feed, pressurized, entrained-flow, slagging gasifier which can be operated on a wide variety of feedstocks [12].

The Shell gasifier used for the coal co-gasification with waste/biomass considered was the Gibbs Free Energy Reactor (GIBS). The Gibbs reactor model uses an equilibrium model based on equilibrium constants. Product rates, compositions, and thermal conditions are calculated by the minimization of Gibbs free energy This method has to define the specific chemical reactions used in the calculation [13].

The gasifier is operating at high temperatures with a high fuel conversion. Other gasifier design assumptions are: pressure drop 1 bar, operating pressure 40 bar and heat duty -22990 MJ/h.

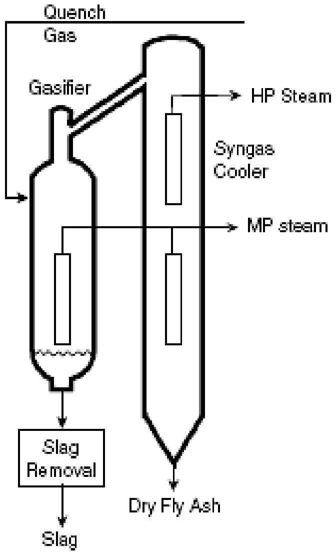

Figure 2. Schematic diagram of Shell gasifier

Figure 3 represents the flowsheet for a Shell gasification block mathematically modeled and simulated using ChemCAD software.

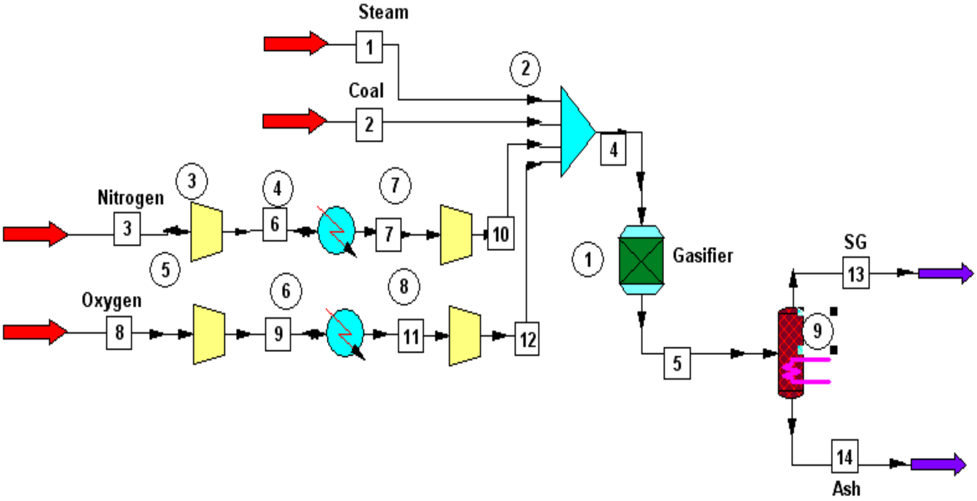

Figure 3. The Shell gasification diagram

Feedstocks

Coal is mainly the result of slow anaerobic transformation of biomass (wood, vegetation etc.) over millions of years. Coal is often classified in terms of its rank, which is determined by the degree of this anaerobic transformation from brown coal to anthracite [6, 14].

The most important biomass fuel is wood, but the trees are too valuable to be burned, instead residues from the woodworking industries as sawdust, could be a very valuable feedstock. Another biomass fuels are the agricultural residues such as: wheat straw, corn stalks, husks from rice, coconuts etc. Different solid wastes, such as: municipal solid wastes, waste paper, sewage, animal residues, can be used as feedstock to a gasification process as well.

For the gasification process the proximate analysis (fixed carbon, volatile matter, moisture, ash), the ultimate analysis (elemental, apart from ash) and ash composition must be known prior evaluation. These fuel characteristics mainly determine the key performance indicators of the gasification process (e.g. cold gas efficiency, oxygen and stream consumptions, hydrogen production potential etc.)

Case studies

This paper analyses eight different case studies of coal blending with different renewable energy sources, which use the same configuration for the gasification process, as follows:

- Case 1 - coal alone used as feedstock;
- Case 2 – coal in addition with sawdust (SWD) blending ratio 80/20% wt.;
- Case 3 – coal in addition with wheat straw (WS) blending ratio 80/20% wt.;
- Case 4 – coal in addition with corn stalks (CS) blending ratio 80/20% wt.;
- Case 5 – coal in addition with municipal solid wastes (MSW) blending ratio 80/20% wt.;
- Case 6 – coal in addition with waste paper (WP) blending ratio 80/20% wt.;
- Case 7 – coal in addition with sewage sludge (SWG) blending ratio 80/20% wt.;
- Case 8 – coal in addition with meat and bone meal (MBM) blending ratio 80/20% wt.

The fuel characteristics are presented in Table 2 [15].

Table 2. Fuel characteristics

Parameter	Coal	SWD	WS	CS	MSW	WP	SWG	MBM
Proximate analysis (% wt)								
Moisture (a.r.)	8.10	10.00	10.00	8.00	10.00	6.00	10.00	1.90
Volatile matter (dry)	28.51	80.05	69.94	73.40	72.70	82.50	54.50	73.40
Ash	14.19	0.98	14.48	7.00	13.90	8.21	37.56	18.80
Ultimate analysis (% wt dry)								
Carbon	72.04	49.20	41.11	44.80	41.20	49.25	36.19	46.20
Hydrogen	4.08	5.99	5.20	5.39	5.50	6.97	4.46	6.70
Nitrogen	1.67	0.82	1.01	0.85	0.50	0.34	5.63	9.70
Oxygen	7.36	42.98	37.36	41.75	38.70	35.00	15.00	17.07
Sulphur	0.65	0.03	0.24	0.21	0.20	0.20	1.06	0.65
Chlorine	0.01	0.00	0.60	0.00	0.00	0.03	0.10	0.88
Ash	14.19	0.98	14.48	7.00	13.90	8.21	37.56	18.80
Calorific value (MJ/kg dry)								
HHV – Gross	28.704	19.436	16.091	17.206	16.425	21.664	15.264	21.163
LHV – Net	27.803	18.113	14.943	16.016	15.211	20.125	14.279	19.683
Ash composition (%wt)								
SiO_2	52.20	9.44	54.64	63.30	52.45	19.44	39.80	0.00
Al_2O_3	27.30	1.56	5.73	0.00	16.21	63.97	11.70	0.00
Fe_2O_3	5.10	1.88	6.16	4.70	7.17	0.42	14.20	2.90
CaO	6.40	62.00	5.02	0.60	16.92	8.37	8.00	66.28
MgO	2.10	2.18	2.45	4.80	0.00	1.68	0.00	0.00
TiO_2	1.50	0.10	0.23	0.00	0.00	3.81	0.00	0.00
K_2O	1.00	15.00	14.09	8.40	0.00	0.23	0.80	13.00
Na_2O	0.30	0.61	2.16	0.50	7.25	0.83	0.60	17.82
SO_3	2.40	2.72	3.03	7.20	0.00	1.14	0.00	0.00
P_2O_5	1.30	1.23	2.43	2.10	0.00	0.10	0.00	0.00
SrO	0.00	0.15	0.00	0.00	0.00	0.00	0.00	0.00

The effects of coal blending with renewable energy sources (wood, agricultural wastes etc.) or alternative fuels (various wastes) are analyzed using the following key gasification process parameters[6,16]:

- *Cold gas efficiency (CGE):* is desirable that this indicator to be as high as possible on condition that hydrocarbons (mainly methane) present in syngas must be as low as possible (hydrocarbons negative influence the carbon capture plant capabilities). CGE represents the energy efficiency of the gasification process and it is defined as follow:

$$CGE = \frac{Syngas\ thermal\ energy\ [MW]}{Feedstock\ \ thermal\ energy\ [MW]} * 100 \qquad (1)$$

- *Hydrogen production potential:* similar to CGE, it is defined as the sum of carbon monoxide and hydrogen content in the syngas and it must be as high as possible. It gives a better idea of how much of the thermal energy of coal can be converted into hydrogen and it is calculated with the formula:

$$Hydrogen\ production\ potential = \frac{CO\ and\ H_2\ thermal\ energy\ [MW]}{Feedstock\ \ thermal\ energy\ [MW]} * 100 \qquad (2)$$

All the cases from 1 to 8 were simulated using the process flow modelling software ChemCAD. Table 3 presents the results of blending coal with renewable energy sources and solid wastes.

On the basis of the Cold Gas Efficiency (CGE) and the hydrogen production potential the following four cases have the highest efficiencies: Case 1 (coal alone), Case 2 (coal in addition with sawdust), Case 6 (coal in addition with waste paper) and Case 8 (coal in addition with meat and bone meal).

For Case 8 must be mentioned that the cold gas efficiency is higher on behalf of the good thermal properties of the alternative fuel used - MBM (high calorific value and carbon content, low moisture content), the relatively high methane content in the syngas compared with other cases. Figure 4 present the changes in the Cold Gas Efficiency for the considered case studies.

Table 3. The performance indicators

	UM	**Case 1**	**Case 2**	**Case 3**	**Case 4**	**Case 5**	**Case 6**	**Case 7**	**Case 8**
Solid fuel flowrate	t/h	165.4							
Solid fuel energy	MW_{th}	1164.7	1079.29	1053.08	1061.95	1055.29	1095.94	1047.59	1092.29
Steam/fuel		0.072	0.036	0.036	0.036	0.036	0.036	0.036	0.091
O2/fuel		0.848	0.788	0.788	0.788	0.776	0.788	0.788	0.727
N2/Fuel		0.09							
Syngas flowrate	t/h	310.94	299.02	294.61	292.5	288.15	291.83	283.08	285.04
Syngas composition									
CO	% vol	59.79	57.39	56.88	57.88	57.41	58.23	57.91	60.00
H_2	% vol	25.42	24.5	23.86	24.16	24.89	26.41	25.13	29.88
CH_4	% vol	0	0	0	0	0	0	0	0.06
H_2S	% vol	0.19	0.16	0.17	0.17	0.17	0.17	0.23	0.22
H_2O	% vol	5.2	6.29	8.11	7.90	7.65	6.54	6.73	4.28
Ar	% vol	0.9	0.81	0.90	0	0	0	0	0.62
Others	% vol	8.5	10.85	10.08	8.99	9.88	8.65	10.00	4.94
Syngas energ	MW_{th}	928.41	850.9	820.13	833.89	829.96	880.63	824.79	940.95
CGE	%	79.71	78.84	77.88	78.52	78.65	80.35	78.73	86.14
CO + H_2 energy	MW_{th}	924.46	847.73	816.84	830.59	826.68	877.25	820.43	935.45
H_2 prod. potential	%	79.37	78.54	77.57	78.21	78.34	80.05	78.32	85.64

As can be noticed in Figure 4, the Cold Gas Efficiency increases with the increase of the carbon percent in the feedstock.Case 2 (coal in addition with sawdust), Case 6 (coal in addition with waste paper) and Case 8 (coal in addition with meat and bone meal) have a higher carbon percent, hence a higher Cold Gas Efficiency.

Analyzing the syngas composition, the Cold Gas Efficiency (CGE) and the hydrogen production potential can be noticed that Case 8 is the most appropriate mixture, which could contribute to the reduction of fossil fuels dependency and CO_2 emissions. As a result, Case 8 was chosen for a further case study: the effect of varying the blending ratio of coal with MBM on the cold gas efficiency and syngas composition.

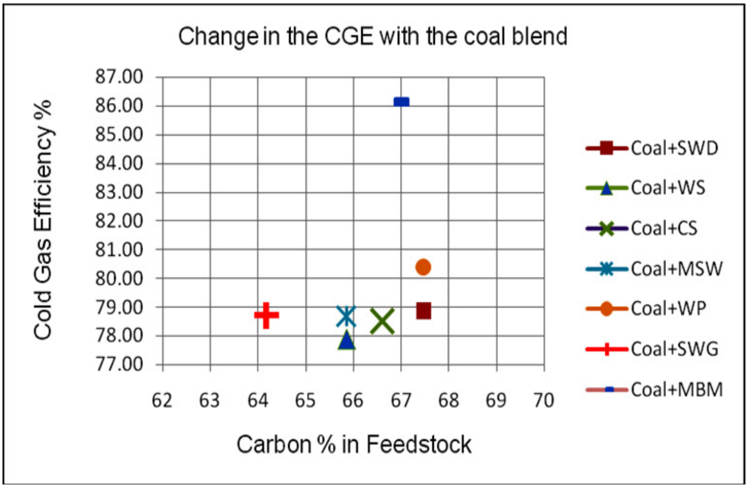

Figure 4. Changes in the CGE with the coal blend options

The blening ratio was varied from 0.1 to 0.5 (wt./wt. ratio on as received basis) and is defined by the following equation [17]:

$$\text{Blending}\ ratio = \frac{Biomass\ feed\ rate\ [Kg/h]}{Total\ feed\ rate\ [Kg/h]} \tag{3}$$

Figure 5 shows the change in the syngas composition with the blending ratio for Case 8 (coal in addition with meat and bone meal). With the increasing of blending ratio, the CO composition decreased from 59.79% to 52.51% and the H_2 composition increased from 25.42% to 34.84% (all syngas composition figures are expressed in molar percentages).

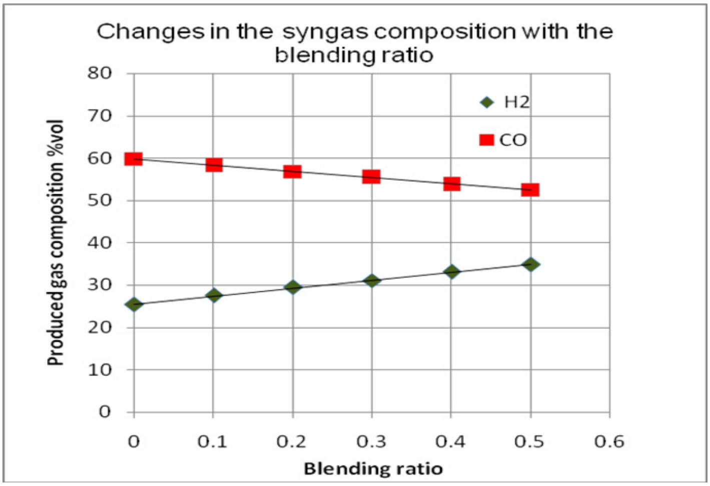

Figure 5. Change in the syngas composition with the blending ratio for Case 8

Figure 6 shows the change in the cold gas efficiency with the blending ratio for Case 8 (coal in addition with meat and bone meal), with the increasing of biomass ratio, cold gas efficiency increases from 79.71% to 90.35%.

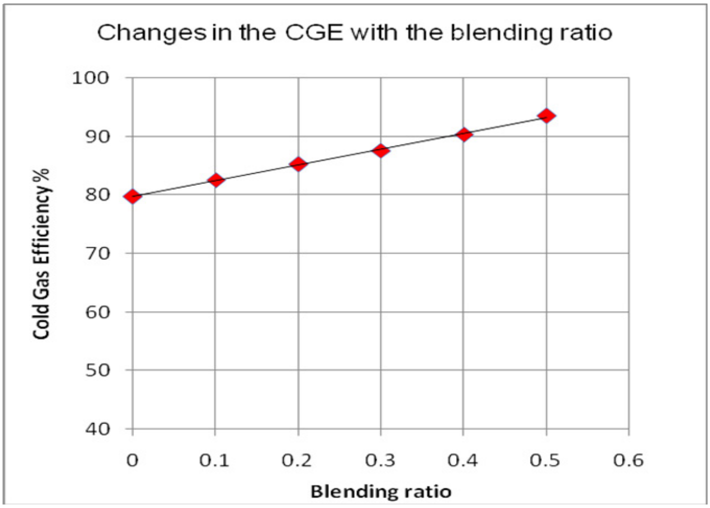

Figure 6. Change in the CGE with the blending ratio for Case 8

The results also indicate that blending coal with biomass or waste, besides the environmental benefits (conservation of fossil fuel resources and reduced CO_2 emissions with 3.58% to 17.93%, depending of the blending ratio) could provide a higher cold gas efficiency and hydrogen production potential.

CONCLUSIONS

The aim of this paper was to evaluate the coal co-gasification with various alternative and renewable solid fuels like wastes (animal residue, municipal solid wastes, waste paper etc.) or biomass (sawdust, agricultural wastes etc.) to supply syngas for energy vectors poly generation in an Integrated Gasification Combined Cycle (IGCC) with Carbon Capture and Storage (CCS).

In this paper was presented a study of the effect of varying different blends of feedstock (coal alone or in addition with biomass or solid waste) on the cold gas efficiency and hydrogen production potential in a entrained-flow gasifier (Shell technology was chosen based on best performances compared with other entrained-flow gasifiers). The best performances of the gasifier have been obtained for the following blends: coal in addition with meat and bone meal (MBM), coal in addition with waste paper and coal in addition with sawdust.

The technology of co-gasification of coal with renewable energy sources as waste and biomass can result in a very clean power plants using a wide range of feedstock. The use of renewable energy sources has real and tangible environmental benefits such as: the conservation of fossil fuel resources and the reduction of the CO_2 emissions with 3.58% to 17.93%, depending of the blending ratio used.

ACKNOWLEDGMENTS

The authors wish to thank for the financial support provided from the programs: (i) Investing in people! PhD scholarship, Project co-financed by the Sectoral Operational Programme Human Resources Development Contract POSDRU 6/1.5/S/3 – „Doctoral studies: through science towards society" and (ii) Romanian National University Research Council (CNCSIS) through grant no. 2455: “Innovative systems for poly-generation of energy vectors with carbon dioxide capture and storage based on co-gasification processes of coal and renewable energy sources (biomass) or solid waste”.

REFERENCES

1. European Commission, http://ec.europa.eu/energy
2. M. M. Maroto-Valer, C. Song, Y. Soong, “Environmental Challenges and Greenhouse Gas Control for Fossil Fuel Utilization in the 21st Century”, Kluwer Academic/Plenum, **2002**

3. S. Lombardi, L.K. Altunina, S.E. Beaubien, “Advances in the Geological Storage of Carbon Dioxide International Approaches to Reduce Anthropogenic Greenhouse Gas Emissions”, Springer, **2006**
4. Statistical Review of World Energy BP, www.bp.com
5. A.G. Collot, *International Journal of Coal Geology*, **2006**, *65*, 191
6. C. Higman, M. Van Der Burgt, **2008**, “Gasification”, Elsevier Science, Second edition
7. Massachusetts Institute of Technology, ”The future of coal an interdisciplinary study”, **2007**
8. E. Tzimas, A. Mercier, C.C. Cormos, S. Peteves, *Energy Policy*, **2007**, *35*, 3991
9. C C. Cormos, *Studia Universitatis Babes-Bolyai, Chemia*, **2009**, LIV, *1*, 81
10. National Energy Technology Laboratory , http://www.netl.doe.gov/
11. C.C. Cormos, “Decarbonizarea combustibililor fosili solizi prin gazeificare*”*, Cluj University Press, **2008**
12. B. G. Miller, “Coal Energy Systems”, Elsevier Academic Press, **2005**, chapter 5
13. Z.A. Zainal, R. Ali, C.H. Lean, K.N. Seetharamu*, EnergyConversManage* **2001**, *42*:1499
14. M. L. de Souza-Santos, ”Solid Fuels Combustion and Gasification Modeling, Simulation, and Equipment Operation”, Marcel Dekker Inc, New York, **2005**, chapter 2
15. Energy Research Centre of the Netherlands, **2010**, www.ecn.nl
16. J.C. Meerman, A.P.Faaij, W.C. Turkenburg, *Energy Procedia*, **2009***, 1*, 4241
17. K. Kumabe, T. Hanaoka, S. Fujimoto, T. Minowa, K. Sakanishi*, Fuel,* **2007**, *86*, 684

STUDIA UNIVERSITATIS BABEŞ-BOLYAI, CHEMIA, XLV, 2, TOM I, 2010

Dedicated to the memory of Prof. dr. Ioan Silaghi-Dumitrescu marking 60 years from his birth

COMPUTATIONAL ANALYSIS OF BONDING IN PhIO AND RELATED 'HYPERVALENT' IODINE COMPLEXES

RADU SILAGHI-DUMITRESCU[a]

ABSTRACT. Iodosylbenzene (iodosobenzene, PhIO) is a known oxygen atom transfer agent with interesting bioinorganic applications (e.g., formation of high-valent iron species), and is regarded as a representative member of a class of hypervalent iodine complexes. Iodine-oxygen bonding is analyzed in this and related complexes, based on molecular orbitals and Mulliken population analyses obtained from density functional theory (DFT) calculations. All data is seen to be straightforwardly interpretable in terms of a sigma dative bond between neutral iodine and oxygen units, as opposed to any alternative explanations involving iodine d-orbitals or hypervalence at the iodine.

Keywords: *hypervalence, iodosylbenzene, density functional, iodine*

INTRODUCTION

Iodosylbenzene (iodosobenzene, PhIO) is a known oxygen atom transfer agent with interesting bioinorganic applications, especially in formation of high-valent iron species with heme proteins/enzymes (e.g., peroxidases, cytochromes P450) and their models.[1-5] PhIO is regarded as a representative member of a class of hypervalent iodine complexes;[2] the term 'hypervalence' is rigorously defined as a situation where the number of valence electrons formally assignable to an atom exceeds the number of electrons that can be nominally accommodated within its valence shell. In particular, for iodine as well as for other main-group elements, 'hypervalence' would mean the presence of more than eight electrons within the valence shell. PhIO is often represented as Ph-I=O,[2] a formulation which clearly breaks the octet rule at the iodine. To avoid the apparent physical non-sense of breaking the octet rule, an alternative explanation has previously been proposed involving participation of the d-orbitals. In most cases however, it is advocated that X→O formulations be used instead of X=O. Nevertheless, the Ph-I=O notation is still widely used[2] and a clear formulation of the electronic structure of

---

[a] *Universitatea Babeş-Bolyai, Facultatea de Chimie şi Inginerie Chimică, Str. Kogălniceanu, Nr. 1, RO-400084 Cluj-Napoca,Romania, rsilaghi@chem.ubbcluj.ro*

this compound would be useful, among others, in establishing reaction mechanisms and electronic structures in bioinorganic problems of general applicability.

Here, the iodine-oxygen bonding is analyzed in PhIO and related complexes, based on molecular orbitals and Mulliken population analyses obtained from density functional theory (DFT) calculations. All data is seen to be straightforwardly interpretable in terms of a sigma dative bond between neutral iodine and oxygen units, as opposed to any alternative explanations involving iodine d-orbitals or hypervalence at the iodine.

RESULTS AND DISCUSSION

Figure 1 shows relevant frontier molecular orbitals computed for PhIO employing DFT procedures (full geometry optimization with BP86/6-31G**, a standard approach for bioinorganic centers for which these results shall be relevant, as detailed in Refs.[6-9]). The C-I-O angle is computed to be 106º, indicative of an sp^3-type spatial arrangement of the orbitals at the iodine. LUMO and HOMO-7 clearly illustrate a single σ bond between I and O. HOMO-4 and HOMO also clearly illustrate no net π interaction between the two elements. The 'pseudo-σ' (or, two-electron three-center) interaction (HOMO-5 and HOMO-1) also offers no net bonding. Thus, the I-O bond has a clean σ character, and the bond order is 1.

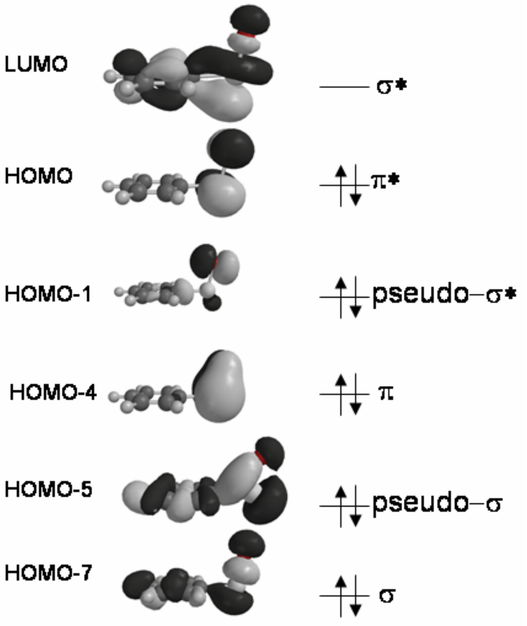

Figure 1. Bonding and anti-bonding orbitals for the I-O bond in PhIO.

The Mulliken population analysis shows that the oxygen atom in Figure 1 formally contains two electrons in each of its 2s, $2p_x$ and 2 p_y orbitals (assuming the z-axis to be along the I-O bond), with occupancies of 1.96, 1.61, and 1.87, respectively. In addition to these six electrons, the oxygen $2p_z$ orbital contains 1.17 electrons (equally distributed between the spin-up and spin-down orbitals). This data can be taken as indication of dative bonding between neutral PhI and an oxygen atom, PhI:→O; within this dative bond, the electrons are almost equally shared between the iodine and the oxygen, as illustrated in Figure 1 and by the -0.60 partial atomic charge on the oxygen atom. Gradual elongation of the I-O bond from the equilibrium length of 1.90 Å to 2.50 Å led to a gradual decrease in partial atomic charge on the oxygen, from -0.60 to -0.49; an *increase* would have been expected if the oxygen in PhIO was formally charged, O^{2-} or O^- - although one can also simply interpret these changes as evidence that heterolytic cleavage of the bond to generate on oxo moiety is not favoured. Such electronic structure description is completely consistent with the ability of PhIO to function as oxygen *atom* donor.

A similar situation is seen in the simpler aliphatic analogue, CH_3IO. The oxygen atom features a partial atomic charge of -0.61, and the orbital picture (not shown) is similar to that of Figure 1.

In the related $CH_3I(OH)_2$ species, the oxygen atoms feature partial atomic charges of -0.62 and -0.63, respectively, i.e. very similar to the oxygen atom in CH_3IO and in turn very similar to the water oxygen. $CH_3I(OH)_2$ formally results from CH_3I and two neutral hydroxyl radicals, HO, as opposed to CH_3IO resulting formally from CH_3I and a neutral oxygen atom. As the CH_3I iodine already has a formally closed-shell configuration, it can only engage in dative bonding. With a $2s^2$ $2p^4$ oxygen atom, such dative bonding is straightforward, as the oxygen can engage with an empty p orbital. On the other hand, with a hydroxyl radical-type oxygen ($2s^2$ $2p^5$), the I-O bond will contain one extra electron; in $CH_3I(OH)_2$, there will be a total of two extra electrons in the I-O σ systems, leading to a formal bond order of 0.5, and an expectedly longer I-O distance compared to CH_3IO. Indeed, the I-OH distances in $CH_3I(OH)_2$ are 2.16 Å and 2.17 Å, respectively, as opposed to 1.90 Å in CH_3IO. These two extra electrons in the σ system of $CH_3I(OH)_2$ also explain why although iodine engages in two dative bonds as opposed to only one in CH_3IO, the partial atomic charge on I is essentially the same in the two systems (0.47 vs 0.49, respectively).

In the related $CH_3I(O)(OH)_2$ species, the oxygen atoms feature partial atomic charges of -0.60 (on the OH oxygens) and -0.58 (on the non-protonated oxygen), respectively, suggesting that the three oxygen atoms have identical oxidation states. As expected (see above discussion on $CH_3I(OH)_2$), in $CH_3I(O)(OH)(OH)$ the I-OH bond lengths are distinctly longer than I-O, i.e.

2.10 Å, vs. 1.85 Å. The partial atomic charge on the iodine in $CH_3I(O)(OH)_2$ is 0.93, essentially double compared to CH_3IO or $CH_3I(OH)_2$ and reflecting a cumulative effect of the three dative bonds towards oxygenic ligands.

CONCLUSIONS

The partial atomic charges and bond lengths are consistent with an assignment of the I-O bond in PhIO as single dative, i.e. I→O. Within this bond, the electrons are distributed evenly between iodine and oxygen. An important point is that in none of the complexes examined is the octet rule *effectively* violated: there are indeed more than eight electrons in the non-participating and bonding orbitals around the iodine, but of all these electrons only 8 can be effectively assigned to iodine while the others effectively belong to oxygen. The I-O system holds 11 electrons (i.e., 10 electrons as shown in Figure 1, plus one electron of iodine involved in I-C bonding). We, therefore, see no need for the use of the term 'hypervalent' in connection to the complexes of this class (i.e., RIO, $RIO(OH)_2$, etc., where R is an organic substituent). The situation seen here appears in no way different from what is seen with other oxyanions (e.g. sulfate, nitrate), for all of which we advocate against the use of the term 'hypervalent' as well as against the use of a double-bond symbol, i.e., X→O with an oxygen atom accepting the dative bond, rather than X=O.

EXPERIMENTAL SECTION

The models were subjected to full geometry optimizations unless otherwise specified. Geometries were optimized for each spin state without any geometrical constraints, with the BP86 functional, which uses the gradient-corrected exchange functional proposed by Becke (1988),[10] the correlation functional by Perdew (1986),[11] and the DN** numerical basis set (comparable in size to 6-31G**), as implemented in Spartan.[12] For the SCF calculations, a fine grid was used, and the convergence criteria were set to 10^{-6} (for the root-mean square of electron density) and 10^{-8} (energy), respectively. For geometry optimization, convergence criteria were set to 0.001 au (maximum gradient criterion) and 0.0003 (maximum displacement criterion). Charges and spin densities were derived from Mulliken population analyses after DFT geometry optimization.

ACKNOWLEDGMENTS

This work was supported by CNCSIS –UEFISCSU, project PNII – IDEI code 565/2007.

REFERENCES

1. M. Sono; M.P. Roach; E.D. Coulter; J.H. Dawson. *Chem. Rev.*, **1996**, *96*, 2841.
2. L. Leman;L. Sanière; P. Dauban, R.H. Dodd. *ARKIVOC*, **2003**, 126.
3. T.L. Macdonald; W.G. Gutheim;R.B. Martin, F.P. Guengerich. *Biochemistry*, **1989**, *28*, 2071.
4. I.H. Hanna; J.A. Krauser; H. Cai; M.-S. Kim, F.P. Guengerich. *J. Biol. Chem.*, **2001**, *276*, 39553.
5. R.C. Blake, M.J. Coon. *J. Biol. Chem.*, **1989**, *264*, 3694.
6. R. Silaghi-Dumitrescu; B.J. Reeder; P. Nicholls; C.E. Cooper, M.T. Wilson. *Biochem. J.*, **2007**, *403*, 391.
7. R. Silaghi-Dumitrescu. *J. Biol. Inorg. Chem.*, **2004**, *9*, 471.
8. R. Silaghi-Dumitrescu,C.E. Cooper. *Dalton Trans.*, **2005**, 3477.
9. R. Silaghi-Dumitrescu, I. Silaghi-Dumitrescu. *Chemtracts - Inorganic Chemistry*, **2005**, 684.
10. A.D. Becke. *Phys. Rev.*, **1988**, 3098.
11. J.P. Perdew. *Phys. Rev.*, **1986**, *B33*, 8822.
12. *Spartan 5.0*, Wavefunction, Inc., 18401 Von Karman Avenue Suite 370, Irvine, CA 92612 U.S.A.

STUDIA UNIVERSITATIS BABEŞ-BOLYAI, CHEMIA, XLV, 2, TOM I, 2010

Dedicated to the memory of Prof. dr. Ioan Silaghi-Dumitrescu marking 60 years from his birth

ON THE MULTIPLE FACETS OF AROMATICITY: ORGANIC, INORGANIC, ORGANOMETALLIC, COORDINATION AND SUPRAMOLECULAR CASE STUDIES

MARILENA FERBINTEANU[a], FANICA CIMPOESU[b]

ABSTRACT. This work is an original synopsis over different structural patterns, from different areas of chemistry, unified under the broadened paradigm of the aromaticity. Cluster, coordination and supramolecular systems selected from our own work, as well as correlated literature examples are gathered together and revisited with state of the art electron structure methods and post-computational analyses. Methodological innovations, such as the vibronic approach and the simulation of resonance structures by enforced electron population of correspondingly prepared natural bond orbitals afforded the revealing of new keys for the old keyword of aromaticity.

Keywords: *aromaticity, ab initio calculations, vibronic models, resonance structures, natural bond orbitals, coordination chemistry, organometallic chemistry, supramolecular assembling.*

INTRODUCTION

The aromaticity [1,2] concept is a perennial asset in the heuristic panoply of chemistry, a valuable currency for exchanging ideas between experimental and theoretical sides of communities exploring structure-property correlations, in both fundamental and application respects. Aside the usefulness of the term for taxonomy and reactivity thumb rules in the organic chemistry, [3] its relevance goes up to the advanced material science issues. Thus, the delocalization effects that determine the molecular aromaticity share the same causal reasons with those driving the optical and electrical properties of polymeric conducting polyenes [4,5] and the special properties of nanoscale graphenes. [6]

---

[a] *University of Bucharest, Faculty of Chemistry, Inorganic Chemistry Department, Dumbrava Rosie 23, Bucharest 020462, Romania. marilena.cimpoesu@g.unibuc.ro*

[b] *Institute of Physical Chemistry, Splaiul Independentei 202, Bucharest 060021, Romania. cfanica@yahoo.com*

As offers-and-demands balance, there is a large variety of models devoted to the aromaticity, in answer to the general appeal of this topic, along the time-line of modern and contemporary chemistry. The models address, at various levels, electron structure parameters, going from semi-empirical conventions, such as the TREPE indexing (Topological Resonance Energy Per Electron) [7] to criteria worked by *ab initio* procedures, as the NICS case (Nucleus Independent Chemical Shifts) [8], keeping also correlations with instrumental checking *via* NMR shifts. [9] The above mentioned methods are usable also in the generalized purposes, for assessing the aromaticity in non-organic systems, going then beyond the classical early outline of the concept (namely, the Kekule-Erlenmeyer identification with the presence of benzene rings, [10] and the pioneering Hückel rules [11] of $(4n+2)\pi$ electron count in planar conjugated hydrocarbons).

Once the structural patterns of the extremely large variety of cluster systems started to be rationalized with the help of electron-count Wade-Mingos rules, [12] it became clear that aromaticity has rich manifestations in the realm inorganic and organometallic rings and clusters.[13,14] From its initial limitation to planar molecules, the aromaticity was generalized to three-dimensional and spherical patterns. [15]

In the key of such paradigms, the chemistry offers large open and uncharted areas, tempting audacious prospectors with promising new treasures. To answer this challenge, a good general culture in intricacies of cluster chemistry and structural methods is demanded. Fulfilling such commandments, a fine collection of correlations between cluster stereochemistry and electron counting concepts is offered by the works of Professor Ioan Silaghi-Dumitrescu. [16] At the same time, several aspects marked at the study of clusters with distorted polyhedral frames [17] can be presented as inquires open to the anti-aromaticity case studies. The puzzling case of electron Ge_{12}^{2-} cluster [18] showing high symmetry combined with antiaromatic-type NICS indices, i.e. putting in sheer contradiction the criteria of bond length distribution vs. ring-current determinations, proves the challenge of the running paradigms and the value of the heritage offered by professor's Silaghi-Dumitrescu works, his topics pointing the way to new exploratory paths. Honoring such achievements, we will present selected parts from our investigations on several systems proposed as prototypic examples, illustrating the variety of landscapes in the realm of aromaticity concepts.

RESULTS AND DISCUSSION

I. Revisiting the basic organic prototypes: aromaticity in C_6H_6 *and the antiaromaticity of* C_4H_4

We will set our starting point with the most celebrated representatives of the aromaticity-antiaromaticity dyad, namely the benzene and cyclobutadiene, respectively. In complex polyaromatic hydrocarbons,[3] the existence of aromatic type behaviour and properties is usually associated with the presence of blocks made of conjugated six-membered rings. For anti-aromaticity the situation is different, since there are no notorious cases of globally antiaromatic molecules assigned to the presence of smaller antiaromatic building blocks. The anti-aromatic behaviour is manifested in different ways, most generally characterized by the presence of a distortion (C=C and C-C bond length alternation and the eventual non-planarity of the rings). Conversely, the aromaticity can be generally presented as resistance to distortion, the system adopting the most symmetrical molecular geometry, with respect of the given topology. The anti-aromatic bond length distortion can be considered a pseudo-Jahn Teller effect [19] and the aromaticity itself can be outlined as balance of factors related to the π-distortivity effects.[2a] We revisited [20] the antiaromaticity of these two systems combining state of the art CASSCF (Complete Active Space Self Consistent Field) calculations and the vibronic modelling, a complex approach taking into account the coupling between vibration and electronic factors. [21] The methodological procedures are not trivial, since, even tough the computer codes for structural chemistry have become increasingly accessible, powerful and user-friendly, it is not a simple task to recover from the massive black box of an *ab initio* calculation the pieces needed to recover a picture in line with the chemical intuition perspectives. For instance, the general knowledge takes the π problem at benzene as a frontier MO picture, while using Hartree-Fock (HF) as starting procedure, and 6-311+G* basis set we must retrieve the set of six π-type molecular orbitals (belonging to the a_{1u}, e_{1g}, e_{2u}, b_{2g}, representations of the D_{6h} point group) from the positions 12, 15, 16, 22, 23, 48, respectively (the HOMO-LUMO couple being located at the 21-22 sequence).

Therefore, to set-up a CASSCF procedure one must construct the active space with carefully selected molecular orbitals, the use of chemical intuition being a key step in the art of this kind of multi-configuration calculations. The CASSCF(6,6) calculation (where the numbers in brackets specify the use of 6 electrons in 6 orbitals) produces 175 spin singlet states. We identifyied the series of 1,3,9,10, 22 levels as being relevant for interpreting the results in terms resonance concepts. Thus, the mentioned series of states can be presented as superposition of the celebrated resonance structures of Kekule and Dewar type. As suggested on Fig.1b chart also, the first two states (the $^1A_{1g}$ groundstate and the $^1B_{2u}$ excited one) can be presented, respectivelly, as the *in-phase* (sum) and *out-of-phase* (difference) of Kekule-type resonance structures. The upper three levels are combination of Dewar-type resonances (a degenerate couple $^1E_{2g}$ and a totaly symmetric combination with equal weights of all three components). We have selected 5 relevant states out of the many CASSCF levels, to span their making from 5 resonance structures, the identification of the adequation to this fenomenology being checked by rather complicate succesion of steps.

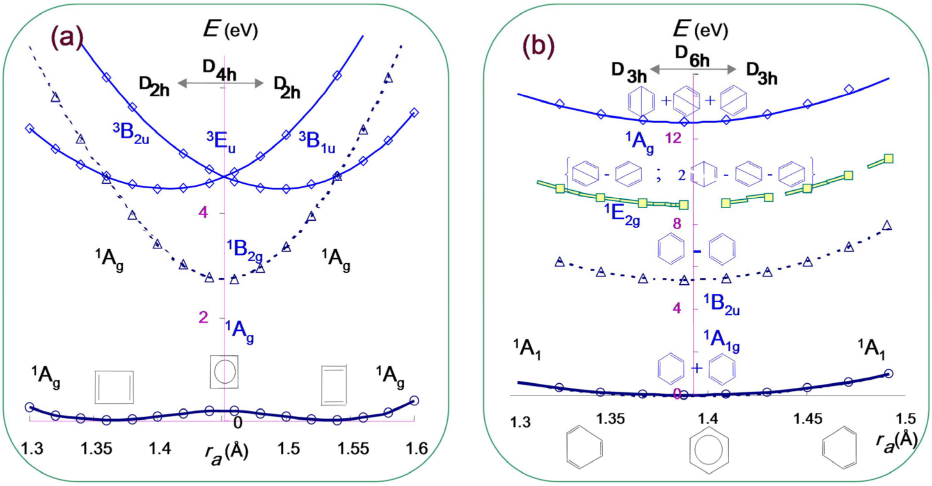

Figure 1. Energy profiles, as function of bond alternating distortion, for selected ground and excited states of: a) cyclobutadiene b) benzene. One observes the pseudo Jahn-Teller effect (double well potential energy of the ground state) that correspond to the anti-aromaticity. The aromaticity is interpreted as resistance against distortion trend (parabola profile). The states were selected from the set of CASSCF calculations to correspond to the interpretation in terms of resonance structures.

The resonance ideas are sometimes presented in as puzzling, suggesting the physical non-reality of separate resonance structures. In fact, the resonance structures are not so imaginary things, neither bogus nor counterfeit. These are the quite concretely writable wave-functions, serving to obtain a given set of states, by their linear combination. In both C_6H_6 and C_4H_4 cases, the ground state can be taken, at the point of high symmetry, as the $\Psi_{sym} \propto (K_1+K_2)$ superposition of the two Kekule resonances, while the first excited one is the $\Psi_{asym} \propto (K_1\text{-}K_2)$ combination. The aromaticity is then characterized by keeping the high molecular symmetry and the correspondingly symmetrical superposition of resonance components. The antiaromaticity can be considered as the trend toward a distorted state, by adopting a pattern adequate for a given single resonance component (i.e. having alternating bonds according to the single vs. double character), i.e. either K_1 or K_2, as shown in different extremes of the panel a of Figure 1.

Conversely, the individual resonance structures can be presented as a mixing between ground and excited states, as these were defined in the high symmetry point, e.g. $K_1 \propto (\Psi_{sym} + \Psi_{asym})$ or $K_2 \propto (\Psi_{sym} - \Psi_{asym})$. Then, the antiaromaticity can be formulated as this kind of interstate coupling, promoted by a distortion coordinate. It is, therefore, a case of vibronic coupling or, in other words, a pseudo Jahn-Teller effect. The pseudo Jahn-Teller effect,[19] i.e. the spontaneous distortion of a symmetrical system with non-degenerate groundstate, is a balance of two opposite terms: a so-called vibronic part, that cumulates all the effects due to the mixing between ground and excited states, and a non-vibronic element that contains all the remaining effects.

The vibronic modeling, comprising terms that account for the dynamic factors, has more general virtues even in cases when there is no distortion of Jahn-Teller or pseudo Jahn-Teller type. The force constant for any given nuclear coordinate can be put as a sum of non-vibronic and vibronic terms, $k=k_0+k_v$. The non-vibronic term can be intuitively interpreted as a sort of mechanical resistance of the molecular skeleton against the given distortion. The pseudo Jahn-Teller distortion becomes visible when the vibronic term ($k_v<0$, that gives negative contribution to the force constant with respect of a nuclear distortion coordinate) dominates the non-vibronic one ($k_o > 0$, a positive contribution). In the frame of vibronic modeling the aromaticity and antiaromaticity can be then presented as two cases of a common mechanism, based on the mixing of two states $\Psi_{sym} \propto (K_1+K_2)$ and $\Psi_{asym} \propto (K_1-K_2)$ which yields a $k>0$ parameter for aromaticity and $k < 0$ for antiaromaticity. Our analyses showed that the π subsystem contributes in both aromatic and antiaromatic cases to the vibronic component $k_v <0$, while the nonvibronic one can be mostly assigned as due to the σ skeleton. Or, in other words, if only the π system existed, even the benzene would have been distorted. The σ skeleton is stronger in the case of benzene, because of in-plane hybrids matching perfectly the 120° bond angles. Then, k_0 predominates, leading to the conservation of the symmetric frame. The 90° bond angles in cyclobutadiene can be obtained only with pure *p* orbitals, loosing then the cohesive supplement from the *s* shell. Having a smaller positive k_0, determined by the weaker skeleton, the cyclobutadiene becomes the subject of the pseudo Jahn-Teller distortion. The energy profile of the ground state along the bond-alternating distortion shows two minima, corresponding to molecular frame distorted in rectangular way, the symmetrical square configuration being metastable, as transition point between these rectangular optimal geometries. Conversely, the energy profile for the benzene ground state is a parabola with minimum in the hexagonal symmetry.

Since the CASSCF, as electron structure calculation method, implies certain intricacies, we will attempt to commute now in presenting the aromaticity issue in more affordable frames, such as the Density Functional Theory (DFT).[22] In this view, *a posteriori*, to a B3LYP/6-311G* calculation for benzene, which is a straightforward task, we employed several steps worked with the help of Natural Bond Orbital (NBO) method.[23] Namely, localized orbital functions were obtained by corresponding input specification of the desired atom pairs. Thus, in one case we specified the three double bonds located between C1-C2, C3-C4 and C5-C6 couples, in order to mimic one Kekule structure (See panel *a* in Figure 2).

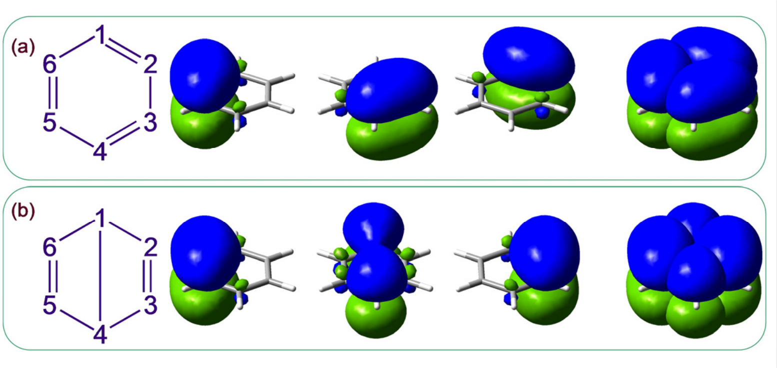

Figure 2. Computational experiments simulating the (a) Kekule and (b) Dewar resonance structures with the help of localized bond orbitals and enforced occupation of each state with a pair of electrons. In the right side, the superpositions of three individual orbitals from each set are presented.

Aiming for a Dewar structure, we succeeded in producing a distant C1-C4 weak bond, aside the regular C2-C3 and C5-C6 double bonds (See Figure 2b). This result is a non-standard approach, but at the same time can be worked in user-friendly manner, since the NBO code[24] can be easily controlled by specifying the desired connectivities and formal bond orders. If one imposes the double occupation of these localized bond orbitals, the total density breaks the hexagonal symmetry, showing the Kekule or Dewar π alternation patterns. One must point that this approach is different from the the so-called Natural Resonance Theory (NRT) [25] also related to the NBO frame. Another computational experiment consisted in taking these broken symmetry total densities and doing a non-iterative DFT calculation with the imposed frozen functions. The resulted energies are higher than those from regular DFT calculation, the gap measuring the stabilization gained by the molecular orbital delocalization. If one s the energy gap by 6, one obtains an equivalent of topological resonance energy per electron (TREPE). While the standard TREPE [7] is a semiempirical procedure based on Hückel-type approach, our computation experiment offers quantities resulted from state of the art DFT techniques. The corresponding amounts (per electron) are 0.10 a.u. (60.8 kcal) for the Kekule state and 0.42 a.u. (265.3 kcal) for the Dewar case. The above revisiting of the very classical prototypic systems of the aromaticity paradigm gave us the opportunity to present and assess methodological issues that can be applied on other examples of general aromaticity, as we will proceed in the following.

II. The spherical aromaticity in inorganic systems. The icosahedral borane

The $B_nH_n^{2-}$ dianions were assigned as aromatic[26] with the help of NICS indices,[8] having a new manifestation, i.e. the spherical aromaticity. This happens because the orbitals of the clusters having the atoms averagely distributed on the surface of a sphere, start to approximate, progressively with the increase of nuclearity, certain regularities similar to a giant atom virtually placed in the center of the cluster and carrying in its shells the valence (bonding and nonbonding) electrons of the constituents. The sign of the orbital components resemble the pattern known for atomic orbitals, or more precisely, the Spherical Harmonics angular functions. In Figure 3 a comparison of classical planar aromaticity with the 3D generalization is suggested. The aromaticity in rings is related to the circular symmetry, whose representations are driven by the $exp(\pm iM\varphi)$ functions, or equivalently, by the $\{cos(M\varphi)\ ,\ sin(M\varphi)\}$ couples. These form doubly degenerate shells, except the M=0 element, which is the trivial total symmetrical representation. Filling progressively the M=0,1,2, *etc* sub-shells drawn in the panel (*a*) of Figure 3, one obtains the 2,6,10,... electron count, spanning the $4n+2$ Hückel rule. In clusters, we go to higher spherical patterns. Here, the irreducible representations are Spherical Harmonics with L=0,1,2,... parameters, that are similar to the atomic shells, i.e. having a $2L+1$ multiplicity and L nodal planes in each subset. The lobes of the MOs constructing a pseudo-spherical cluster are "painted" in "colors" borrowed from the pattern of the Spherical Harmonics depicted in the panel (b) of Figure 3. More precisely, the LCAO components of an AO located at a given position on the sphere are proportional in sign and magnitude with the Spherical Harmonics at that coordinate. Then, the MOs are grouped in quasi-degenerate sets spanning the $2L+1$multiplicites of an appropriate L number. Then, progressively filling such sub-shells one obtains a 2, 8, 18, series, i.e. a $2(L+1)^2$ count. Such a regularity is called the Hirsch rule. [27] Since in many cases the effective symmetry is not so high, to completely match the spherical approximation, and also because the full complexity of electron structure is realized with the help of supplementary functions taken as derivatives of Spherical Harmonics, there are alternate regularities, such as Wade's electron count, which specifies the need of $2n+2$ polyhedral skeleton electron pairs [28] to achieve a good stability and therefore to claim the aromaticity case. Counting the valence electros in the $B_{12}H_{12}^{2-}$ as follows, 12×5 from boron atoms, 12 from hydrogens and 2 from dianion charge, one obtains a total of 50 electrons, apparently favorable to the Hirsh rule (with L=4). Counting the skeletal electron pairs (i.e. ignoring the 12×2 electrons comprised in the outer B-H bonds) one obtains a 26 count that satisfies Wade's rule for the electron pairs devoted to the cluster itself.

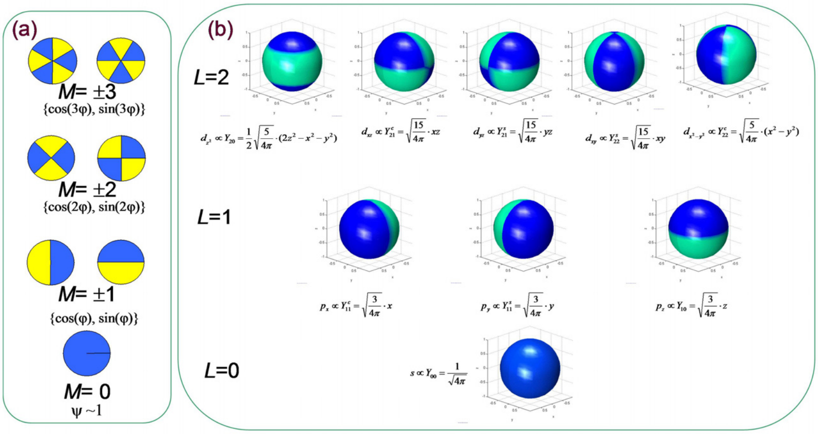

Figure 3. Symmetry regularities determining the aromaticity in (a) rings and (b) clusters, according to the patterns of cyclical and spherical symmetry, respectively. The different colors mark the different signs of the functions and nodal planes around a cycle and on the surface of a sphere.

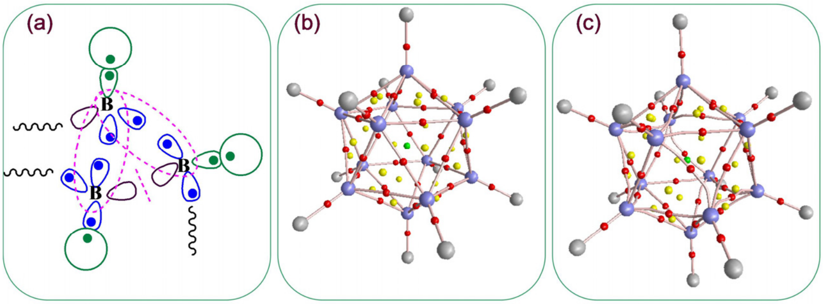

Figure 4. The bonding regime in boranes. a) the scheme of local electron deficiency, each B atom contributing with two electrons for the cluster; the possibility to assign formal localized bonds on and electron void areas is suggested. (b) The $B_{12}H_{12}^{2-}$ dianion with its critical points and bond paths. (c) The bond paths in the neutral $B_{12}H_{12}$ appear curved and distorted, as expression of the fact that the electron count of the neutral molecule is incompatible with a stable closed shell icosahedral configuration.

Besides, looking at point group symmetry reasons, one observes that the dianion realizes the completion of a four-degenerate HOMO level. This is why the dianion status is required, because otherwise the non-closed degenerate shell would lead to pseudo Jahn-Teller distortions. From this point of view, the neutral $B_{12}H_{12}$ could be called anti-aromatic. However, the things are a bit more complicated.

Another view on the aromaticity of boranes is the electron deficient nature of the boron. This implies a large delocalization, in order to spread the electron density over all the interatomic contacts. Employing the analysis of density distribution with the help of Bader's theory of Atoms in Molecules (AIM) [29, 30] one obtains the so called (3,-1) critical points, certifying the formation of a bond for each B-H unit and also for all the 30 B-B edges of the icosahedron, both in case of the dianion $B_{12}H_{12}^{2-}$ and for the neutral $B_{12}H_{12}$. The number of established bonds is larger than the available electron pairs (13 for dianion, 12 for the neutral molecule). It is interesting to compare the bond paths of the two related systems (depicted in Figures 4b and 4c). The bond paths are gradient lines joining points of maximal density located at nuclei, passing via the (3,-1) bond points. Regular bond paths are almost linear, while in certain cases these appear curved, as is visible for the neutral $B_{12}H_{12}$. Because of incomplete degenerate HOMO shell, the neutral $B_{12}H_{12}$ is unstable in the icosahedral symmetry, but we will discard for the moment the question of optimal geometry and the comparison of distortion isomers. In turn, the bond path bending resulted by taking the enforced icosahedral symmetry for $B_{12}H_{12}$ can be interpreted as a sign of the inner trends for distortion.

In the following we will try to transcribe the electron deficient boranes in terms of resonance structures. Because the number of electron pairs is larger than the number of interatomic bonds, the groundstate must be conceived as a superposition of many configurations. Each boron atom participates with two electrons to the cluster delocalization, while one electron per boron should be reserved for firm bonds with the outer hydrogen atoms. Each boron has 5 immediate neighbors, but is able to share Lewis-type electron pairs only with two of them. Each B atom has formally an empty valence orbital (See the the panel *a* of Figure 3).

Therefore, if draw a line for an electron pair shared by a B-B couple, each boron vertex of the B_{12} polyhedron has two emerging lines. The resonance structures can be then formulated as lines running over a total of 12 edges in the case of $B_{12}H_{12}$ and over 13 edges in the case of $B_{12}H_{12}^{2-}$ dianion. It is particularly more convenient to discuss the resonance structures of the neutral molecule. We will not detail now their complete count, which is a matter of specialized graph theory. We will confine ourselves in noticing that, marking by ticker lines the bonds, these can be grouped in a number of closed walks, ranging from 1 to 4 independent circuits (See Figures 5-7).

These circuits do not cross each-other and comprise, in ensemble, all the vertices of the icosahedron. In the case of the dianion $B_{12}H_{12}^{2-}$ one supplementary line can be drawn at any of the 18 remaining empty B-B lines (out ot the 30 B-B edges) to which no previous line was assigned (12 edges being occupied by the mentioned bond lines). Each possibility to design such walks can be considered as a resonance structure. The superposition of such resonance structures resolves the problem of electron deficiency and consequently offers a suggestion for the aromaticity of these systems, if accepting that aromaticity can be defined as the need for resonance superposition, in order to describe a stable structure. In this perspective, even the neutral $B_{12}H_{12}$ can be presented as aromatic while $B_{12}H_{12}^{2-}$ is the most aromatic, since it has more resonance structures, multiplied by a factor of 18 as compared to the $B_{12}H_{12}$ count as seen above.

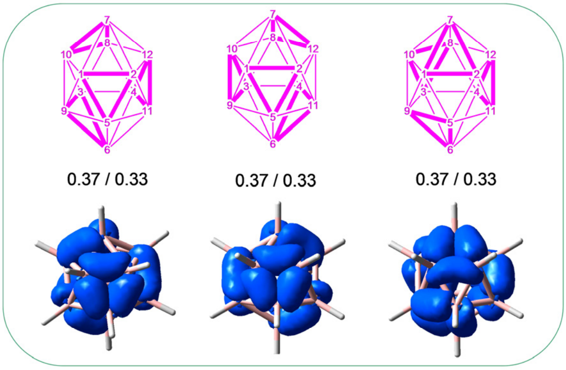

Figure 5. Selected equivalent resonance structures for $B_{12}H_{12}$, spanning 4 islands of 3-membered circuits, marked with bold lines in the graphs depicted in the upper part. The lower part contains the simulation of this resonance structure with the help of superposed correspondingly prepared and occupied localized bond orbitals. The numbers written in couples on the middle line are designed as a measure of resonance effect: the first number of each couple is estimated for dianion and the second for the neutral molecule. Each values represents the DFT energy gap (in a.u.) of between the localized resonance structure and the delocalized state, divided by 24, the number of cluster electrons, in order to have a resemblance with TREPE indices.

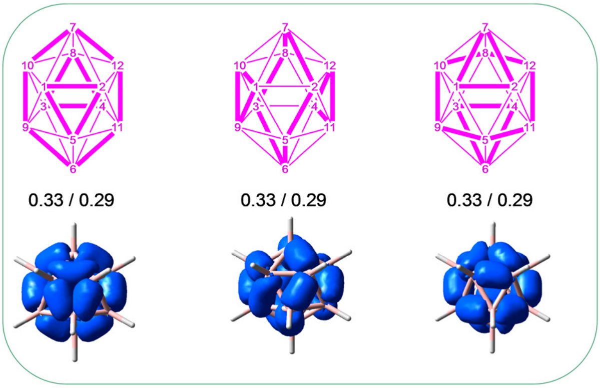

Figure 6. Selected equivalent resonance structures spanning 3 islands with 3,6,3 members. The interpretation is similar to the precedent figure.

The neutral system can be presented, at this stage, as intermediately aromatic, since, even letting it to relax at a lower symmetry the presence of resonance superposition will still be required to resolve its intrinsic electron deficiency. The complete picture will not be developed now. We will proceed, in turn, to an interesting computational experiment, mimicking the above mentioned types of resonance structures with the help of localized natural bond orbitals, using the same procedures as explained in the above section for benzene. This simulation of the resonance structures is a rather inedited deal, as well as, to the best of our knowledge, the whole explained picture of resonating bonds in boranes. The procedure offers also certain indices similar to the traditional TREPE, as explained above in the benzene case. We recall that, to be distinguished from TREPE, which are based on empirical methods, our approach is based on energy amounts primarily obtained at DFT level. Thus, the energy gap between the DFT energies of delocalized molecule and enforcedly localized resonance structure, divided by the number of electrons in the cluster, i.e. 24, stands for the values printed along with the resonance structures from figures 5-7. The values are presented in couples, the first one devoted to the dianion, the second to the neutral molecules. The resonance structures are, in fact drawn for the neutral molecule, the dianion presenting a supplementary number of resonances, due to the added electron pair. In our calculations the dianion was taken by a resonance structure obtained adding a lone pair, conventionally, on the first atom, B1. The definition as lone pair is convenient because in this way it appears delocalized towards the remaining boron neighbours and offers in this way a sort of simulated averaging over the three resonance structures obtainable by separate localization procedures. One observes that the defined indices show larger magnitudes for the dianion, as a measure of its larger aromaticity. At the same time, even though the resonance patterns differ very much in topological respects, their indices are comparable, suggesting that the resonance in borane may use such various patterns on almost equal footing. The pictures 5 and 6 offer, altogether with the formal resonance structures, the realistic electron density superposition realized with the localization approach. The figure 7 is confined to drawing only the formal graphs of several other selected resonances, altogether with their corresponding indices. In panel 7a is illustrated another topology with 3 rings of bond circuits, in 7b patterns with two 6-membered circuits, in 7c selected shapes with two unequal circuits (3 and 9 membered) and in 7d the case of single 12 member circuits. The classification of the resonance structures in the above suggested style is a challenging matter in itself, as graph theory issue, committing our interests in further developments in this sense.

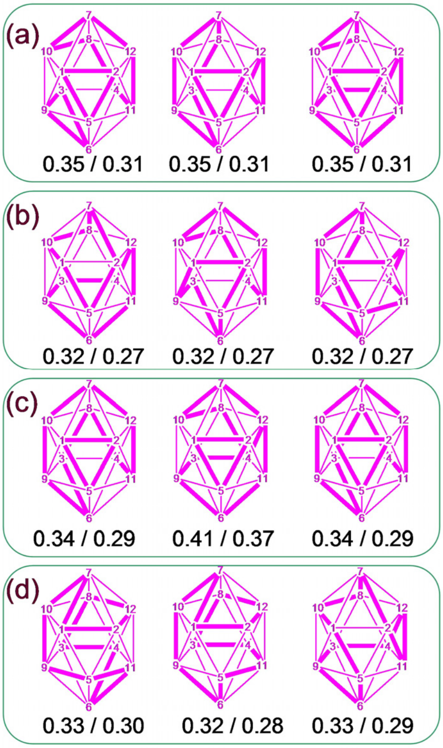

Figure 7. Selected equivalent resonance structures of $B_{12}H_{12}$, belonging different topological patterns : a) 3 circuits with 3,6,3 members; b) two circuits with 6,6 members; c) two circuits with 3,9 members; d) a single circuit with 12 members. The value couples below each graph are resonance indices for dianion and neutral cases, respectively.

III. The aromaticity in coordination systems. The diketonate ligands

The diketonate anions can be proposed as subject for inquires on aromaticity, since their structure with delocalized negative charge imply the use of resonance structures. We will address this issue in both the free anion and also coordination complexes with diketonates as ligand, using in this purpose the the so-called Natural Resonance Theory [25] which is a part of the NBO methods and computer codes.[23] The procedure is a bit different from our previously exposed methodology with localized orbitals and is distinct also from the genuine frame that imposed the concept of resonance, namely the Valence Bond theory (VB). [31] The NRT is not a multiconfigurational method. It offers a sort of surrogate for the effect of superposed resonance structures, fitting the total density from a regular DFT calculation (i.e. with delocalized MOs) in terms of contributions from occupation schemes with imposed localizations. This procedure offers a convenient user-friendly access to the resonance concepts.

We will take as study case a coordination system from our own synthetic results,[32] [Ni(*tmen*)(NO_2)(*dbm*)], where *tmen* is tetra-methylene-diamine and *dbm* is dibenzoyl-methanate, i.e. the diketonate taken in our focus. In Figure 8 we comparatively show the weights of main resonance structures for the free ligand and the coordinated one. The presented amounts do not complete a 100% total, since there are several other discarded small terms, assignable to hyperconjugation effects. The free ligand is less aromatic, since the contribution of the keto-enolate forms are smaller, being in competition with a carbanionic resonance. In the coordinated mode, the two keto-enolate resonance structures become the dominating contributors. In the presented case, the two twin diketonate resonances have slightly differing weights because of the asymmetry induced by the mixed ligand environment. The chelate can be interpreted as aromatic, since it can be presented as superposition of two equivalent resonance structures.

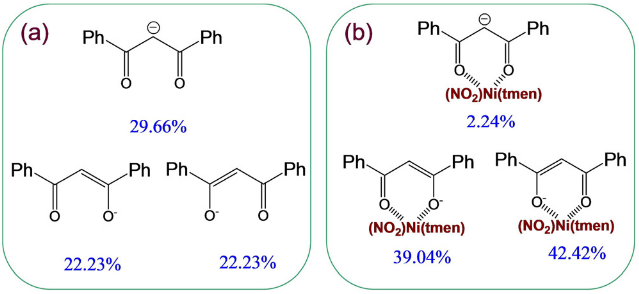

Figure 8. The resonance weights computed with the NRT (post DFT) method for the: (a) free and (b) coordinated, dibenzoyl-methanate ligand.

IV. Surface aromaticity in organometallic clusters

We will propose as example for this entry a system belonging to our previous work, a carbalane cluster with $\{Al_8C_6\}$ cubo-octahedral pattern.[33] Not only the theoretical analysis, but also the chemical tests suggested this system as aromatic, since the cluster core resisted well at several reactions that affected only its terminal groups, in a manner resembling the stability of benzene core against substitutions and additions. This cluster is electron deficient (like boranes), since the analysis of critical points of density identified implying the superposition of resonance structures, as suggested by panel more bonds than the available electron pairs, as seen in Figure 9a, the situation 9b.

There are $4^6 = 4096$ resonance structures, figure 9b presenting only a selected portion. Without entering the details, we point that there exist two different types of Al-C bonds, differing by certain overlap factors, one marked with full line, the others with dashed line. From each C site emerges one tick line and two dashed ones.

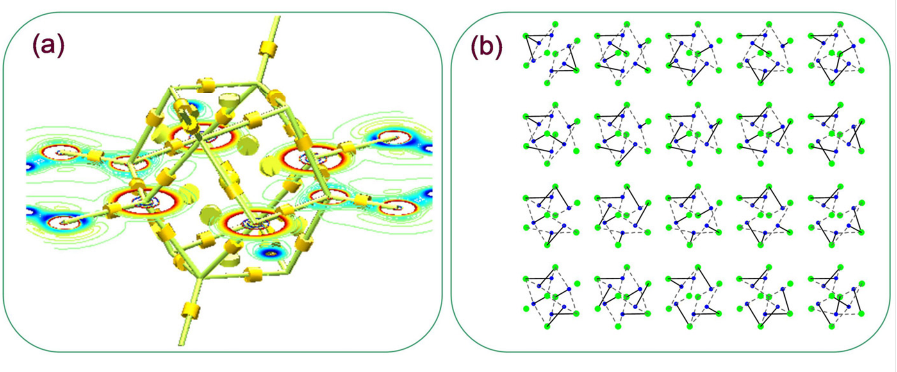

Figure 9. Synopsis of the delocalization and resonance effects in the carbalane with $\{Al_8C_6\}$ core, as images of surface aromaticity effects. The skeleton drawn in (a) corresponds to computed bond paths, with bond critical points marked with ticker cylinders. The C atoms are penta-conexe (with 4 bonds inside the cluster and one outer one, while the aluminum are represented as triconexe). The Laplacian of electron density is represented in a molecular section. In (b) one shows a selected part of the resonance structures with linkages between the the Al_8 and C_6 subsystems.

The resonance structures at one $\{Al_4C\}$ face of the cluster are obtained rotating the set of three bonds around the square frame, letting one Al site non-bonded. The rule for obtaining the resonance structures can be presented as decrypting the monomials resulted after expanding the following product:

$$(y1x2y3 + x1y2y4 + y1y3x4 + y2x3y4) \cdot (y5x6y7 + x5y6y8 + y5y7x8 + y6x7y8) \cdot$$

$$(x1y2y5 + y1x2y6 + y1x5y6 + y2y5x6) \cdot (x2y3y6 + y2x3y7 + y2x6y7 + y3y6x7) \cdot$$

$$(x3y4y7 + y3x4y8 + y3x7y8 + y4y7x8) \cdot (x1y4y5 + y1x4y8 + y1x5y8 + y4y5x8) .$$

The x_i (with i =1 to 8) stand for the aluminum the Al-C bonds conventionally marked by tick line, while the x_j represent the dashed ones. The subscript indices mark the Al atom touched by the bonds of the presented types.

V. An inedited case of supramolecular antiaromaticity

We present now a system with radicalic character that can be exploited as an unprecedented case of antiaromatic-type distortion in a supramolecular ordered network. The compound was synthesized[34] and explored by us for sake of magneto-structural correlations, the antiaromatic features remaining yet incompletely explored, presenting here an excerpt of the ongoing detailed analysis. The system is an octa-coordinated yttrium complex K[Y(QT)$_4$] with QT (Quinoline-Tempo) a diketonate chelatic ligand that has also a radical tail. The interaction between the NO radical groups of the ligand tails and the lattice potassium ions determines a supramolecular ordering with nodes made of K$^+$ ions surrounded by four radicals. The set of four interacting radicals resembles the configurational problem from the cyclobutadiene prototype (4 electrons in 4 orbitals). Even tough here there is not the case of similar genuine π system, the same factors that determine the rectangular shape of C_4H_4, are imposing the distortion in the actual {K(QT)$_4$} moieties of our system.

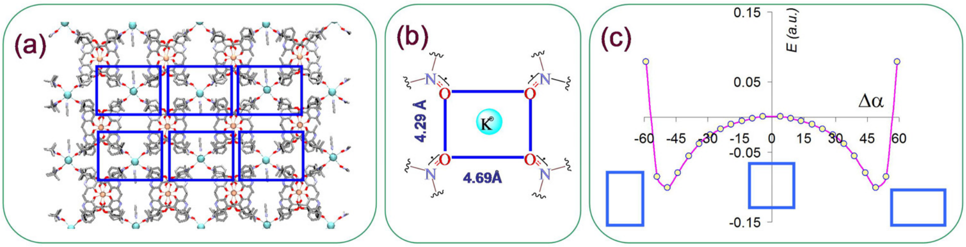

Figure 10. (a) The antiaromatic-type rectangular distortions in the supramolecular assemblies of the K[Y(QT)$_4$] complex with radicalic ligands. (b) The scheme of the {K(QT}$_4$} node with four-radical character and rectangular pattern. (c) A simplified simulation of the preference for distortion in the idealized model model [K(ONH$_2$)$_4$]$^+$ of the four radical complex node. The $\Delta\alpha$ coordinate measures the deviation of one O-K-O angle from the 90^o perfect square value. Namely, at the perfect square geometry $\Delta\alpha$=0, the energy profile shows a metastable transition point, the system spontaneously breaking its symmetry toward the minima corresponding to antiaromatic pattern.

The rectangular pattern of the whole supramolecular ordering is shown in Figure 10a, with the scheme of rectangular {K(QT)$_4$} nodes in 10b. In 11c we present a simulation of the preference for distortion, taken on a simplified model [K(ONH$_2$)$_4$]$^+$ with B3LYP/6-311G* DFT potential energy surface procedures. The double well potential proves the trend for the antiaromatic type of distortion in the four radical system, an effect which is cooperatively transmitted to the whole supramolecular network.

The system is interesting also from magneto-structural point of view, being a challenging detective story. Namely, the attempts to fit the experimental magnetic susceptibility with standard procedures lead systematically to results incompatible with the experimentally observed rectangular topology. The cause was a sort of accidental local minimum comprised in the standard phenomenological modeling. A clear cut of the question was done with the help of *ab initio* calculations, that helped us in choosing the right parametric balance, the situation being illustrative for the role of theoretical approaches, as valuable complements to experiments.

CONCLUSIONS

We presented a broad perspective on the aromaticity paradigm, analyzing prototypic molecules such as benzene and icosahedral boranes, as examples for organic and inorganic cases, and systems from our own results, to illustrate the coordination, [32] organometallic [33] and supramolecular [34] varieties. The aromaticity is a very generalizing and fruitful keyword, that catalyzes interdisciplinary results, establishing natural bonds between the experimental and theoretical sides. It is important to safeguard these links and the role of intuition, since with the advent of modern electron structure methods and codes, the thesaurus of heuristic ideas like hybridization, hypervalence, aromaticity, started to loose terrain in the front of accurate *ab initio* reproduction of structural parameters. The brute-force computational approach does not need, apparently, the *a priori* guidelines of these heuristic concepts originating from the experimental chemistry, but a real understanding is realized when we can find a simple meaning behind the output bulk information. It is a challenge to rebuild *a posteriori*, from the bare output of the electronic structure methods, the information matching the major keywords with *aprioric* virtues. The revisiting of the basic concepts is a steady temptation and a challenging task, with a rewarding outcome. In spite of its longstanding history, the aromaticity is still an active and appealing concept, that triggers theoretical debates and marks the way to new lands of experimental chemistry.

EXPERIMENTAL SECTION

The synthetic and structural details of the compounds belonging to our synthetic works were presented elsewhere. [33, 34]. The calculations were performed using the Gaussian 03,[35] Gamess [36] and NBO [24] software packages.

ACKNOWLEDGMENTS

Parts of this work were supported by the CNCSIS-UEFISCSU grant "Idei" 174/2007.

REFERENCES

1. (a) L. Salem, "The Molecular Orbital Theory of Conjugated Systems", Benjamin, New York, **1966**. (b) V. I. Minkin, M. N. Glukhovtsev, B. Y. Simkin, "Aromaticity and Antiaromaticity", Wiley, New York, **1994**.
2. (a) S. Shaik, A. Shurki, D. Danovich, P. C. Hiberty, *Chem. Rev.*, **2001**, *101*, 1501. (b) P. v. R. Schleyer, H. Jiao, *Pure Appl. Chem.*, **1996**, *68*, 209.
3. (a) E. Clar, "Polycyclic Hydrocarbons", Academic Press, London, **1964**. (b) T. M. Krygowski, M. K. Cyranski, Z. Czarnocki, G. Häfelinger, Alan R. Katritzky, *Tetrahedron*, **2000**, *56*, 1783.
4. (a) Z. Shuai, J. L. Bredas, *Physical Review*, **2000**, *B 62*, 15452. (b) W. Barford, R. J. Bursill, *Physical Review*, **2006**, *B 73*, 045106.
5. Y. Geerts, G. Klärner, K. Müllen, "In Electronic Materials: The Oligomer Approach", K. Müllen, G. Wagner, Eds.; Wiley-VCH:Weinheim, Germany, **1998**.
6. J.-N. Fuchs, P. Lederer, *Physical Review Letters*, **2007**, *98*, 016803. (b) B. Trauzettel, D. V. Bulaev, D. Loss, G. Burkard, *Nature Physics*, **2007**, *3*, 192.
7. (a) I. Gutman, M. Milun, N. Trinajstić, *J. Am. Chem. Soc.*, **1977**, *99*, 1692. (b) J. Aihara, *J. Am. Chem. Soc.*, **1976**, *98*, 2750; **1977**, *99*, 2048. (c) M. S. J. Dewar, C. de Llano, *J. Am. Chem. Soc.*, **1969**, *91*, 789. (d) A. Graovac, I. Gutman, M. Randić, N. Trinajstić, *J. Am. Chem. Soc.*, **1973**, *95*, 6267. (e) A. R. Katritzky, K. Jug, D. C. Oniciu, *Chem. Rev.*, **2001**, *101*, 1421.
8. P. v. R. Schleyer, C. Maerker, A. Dransfeld, H. Jiao, N. J. R. v. E. Hommes, *J. Am. Chem. Soc.*, **1996**, *118*, 6317.
9. (a) P. v. R. Schleyer, H. Jiao, *Pure Appl. Chem.* **1996**, *68*, 209. (b) T. M. Krygowski, M. K. Cyrański, Z. Czarnocki, G. Häfelinger, A. R. Katritzky, *Tetrahedron*, **2000**, *56*, 1783.
10. (a) A. Kekule´, *Bull. Soc. Chim. Fr.*, **1865**, *3*, 98. (b) E. Erlenmeyer, *Liebigs Ann. Chem.*, **1866**, *137*, 327.
11. E. Hückel, *Z. Physik*, **1931**, *70*, 204; *Z. Physik*, **1931**, *72*, 310; *Z. Physik*, **1932**, *76*, 628.
12. (a) K. Wade, *Chem. Commun.*, **1971**, 792. (b) D. M. P. Mingos, *Acc. Chem. Res.*, **1984**, *17*, 311.
13. (a) R. B. King, *Chem. Rev.*, **2001**, *101*, 1119, and references therein. (b) R.B. King, *Inorg. Chim. Acta*, **2003**, *350*, 126. (c) H. Tanaka, S. Neukermans, E. Janssens, R. E. Silverans, P. Lievens, *J. Am. Chem. Soc.*, **2003**, *125*, 2862.
14. (a) A. I. Boldyrev, J. Simons, *J. Am. Chem. Soc.*, **1998**, *120*, 7967. (b) X. Li, A. E. Kuznetsov, H. F. Zhang, A. I. Boldyrev, L.-S. Wang, *Science*, **2001**, *291*, 859. (c) A. Hirsch, Z. Chen, H. Jiao, *Angew. Chem.*, **2001**, *113*, 2916; *Angew. Chem., Int. Ed.*, **2001**, *40*, 2834.

15. (a) A. Hirsch, Z. Chen, H. Jiao, *Angew. Chem., Int. Ed.*, **2001**, *40*, 2834. (b) M. Bühl, A. Hirsch, *Chem. Rev.*, **2001**, *101*, 1153.
16. (a) R. B. King, I. Silaghi-Dumitrescu, *Inorg. Chem.*, **2003**, *42*, 6701. (b) R. B. King, I. Silaghi-Dumitrescu, A. Lupan, *Inorg. Chem.*, **2005**, *44*, 3579. (c) R. B. King, I. Silaghi-Dumitrescu, A. Lupan, *Inorg. Chem.,* **2005**, *44*, 7819. (d) R. B. King, I. Silaghi-Dumitrescu, M. M. Uta, *Inorg. Chem.,* **2006**, *45*, 4974.
17. (a) R. B. King, I. Silaghi-Dumitrescu, A. Kun, *Inorg. Chem.*, **2001**, *40*, 2450. (b) R. B. King, I. Silaghi-Dumitrescu, M. M. Uţă, *J. Chem. Theory Comput.,* **2008**, *4*, 209.
18. (a) R. B. King, I. Silaghi-Dumitrescu, M. M. Uţă, *Dalton Trans.*, **2007**, 364. (b) R. B. King, T. Heine, C. Corminboeuf, P. v. R. Schleyer, *J. Am. Chem. Soc.*, **2004**, *126*, 430.
19. I. B. Bersuker, *Chem. Rev.*, **2001**, *101*, 1067.
20. (a) F. Cimpoesu, K. Hirao, M. Ferbinteanu, Y. Fukuda, W. Linert, *Monatshefte fur Chemie*, **2005**, *136*, 1071. (b) F. Cimpoesu, V. Chihaia, N. Stanica, K. Hirao, *Advances In Quantum Chemistry*, **2003**, *44*, 273.
21. (a) I. B. Bersuker, "The Jahn-Teller Effect and Vibronic Interactions in Modern Chemistry", New-York, Plenum Press, 1984. (b) F. Cimpoesu, K. Hirao, "The Ab Initio Analytical Approach of Vibronic Quantities: Application to Inorganic Stereochemistry", *Advances In Quantum Chemistry*, **2003**, *44*, 370.
22. W. Koch, M. C. Holthausen, "A Chemist's Guide to Density Functional Theory", Wiley-VCH, Berlin, **2001**.
23. A. E. Reed, L. A. Curtiss, F. Weinhold, *Chem. Rev.*, **1988**, *88*, 899; the NBO3.0 program, E. D. Glendening, A. E. Reed, J. E. Carpenter, F. Weinhold.

24 NBO 5.0 Glendening E. D., Badenhoop J. K., Reed A. E., Carpenter J. E., Bohmann J. A., Morales C. M., Weinhold F., http://www.chem.wisc.edu/~nbo

25. (a) E. D. Glendening, F. Weinhold, *J. Comput. Chem.*, **1998**, *19*, 593; *19*, 610. (b) E. D. Glendening, J. K. Badenhoop, F. Weinhold, *J. Comput. Chem.*, **1998**, *19*, 628. (b) S. Feldgus, C. R. Landis, E. D. Glendening, F. Weinhold, *J. Comput. Chem.*, **2000**, *21*, 11.
26. (a) P. v. R. Schleyer, K. Najafian, "In The Borane, Carborane, Carbocation Continuum", J. Casanova, Ed., Wiley, New York, **1994**. (b) P. v. R.Schleyer, K. Najafian, *Inorg. Chem.*, **1998**, *37*, 3454. (c) M.L. McKee, Z.-X. Wang, P. v. R. Schleyer, *J. Am.Chem. Soc.*, **2000**, *122*, 4781.
27. A. Hirsch, Z. Chen, H. Jiao, *Angew. Chem., Int. Ed.*, **2001**, *40*, 2834.
28. (a) K. Wade, *Adv. Inorg. Chem. Radiochem.*, **1976**, *18*, 1. (b) E. D. Jemmis, M. M. Balakrishnarajan, D. Rabcharatna, *Chem. Rev.*, **2002**, *102*, 93.
29. (a) R. F. W. Bader "Atoms in Molecules - A Quantum Theory", University Press, Oxford , **1990**; (b) R. F. W. Bader, *Acc. Chem. Res.,* **1985**, *18***,** 9.
30. F. Biegler-König, "AIM2000" computer code, Bielefeld, **2000.**
31. (a) D. J. Klein, N. Trinajstić (Eds) "Valence Bond Theory and Chemical Structure", Elsevier, Amsterdam, **1990**; (b) D. L. Cooper, J. Gerratt, M. Raimondi, *Chem. Rev.,* **1991**, *91*, 929.

32. M. Ferbinteanu upublished results.
33. A. Stasch, M. Ferbinteanu, J. Prust, W. Zheng, F. Cimpoesu, H. W. Roesky, J. Magull, H.-G. Schmidt, M. Noltemeyer, *J. Am. Chem. Soc.,* **2002**, *124*, 5441.
34. L. Maretti, M. Ferbinteanu, F. Cimpoesu, S. M. Islam, Y. Ohba, T. Kajiwara, M. Yamashita, S. Yamauchi, *Inorg. Chem.,* **2007**, *46*, 660.
35. M. J. Frisch, G. W. Trucks, H. B. Schlegel, G. E. Scuseria, M. A. Robb, J. R. Cheeseman, J. A. Montgomery, Jr., T. Vreven, K. N. Kudin, J. C. Burant, J. M. Millam, S. S. Iyengar, J. Tomasi, V. Barone, B. Mennucci, M. Cossi, G. Scalmani, N. Rega, G. A. Petersson, H. Nakatsuji, M. Hada, M. Ehara, K. Toyota, R. Fukuda, J. Hasegawa, M. Ishida, T. Nakajima, Y. Honda, O. Kitao, H. Nakai, M. Klene, X. Li, J. E. Knox, H. P. Hratchian, J. B. Cross, V. Bakken, C. Adamo, J. Jaramillo, R. Gomperts, R. E. Stratmann, O. Yazyev, A. J. Austin, R. Cammi, C. Pomelli, J. W. Ochterski, P. Y. Ayala, K. Morokuma, G. A. Voth, P. Salvador, J. J. Dannenberg, V. G. Zakrzewski, S. Dapprich, A. D. Daniels, M. C. Strain, O. Farkas, D. K. Malick, A. D. Rabuck, K. Raghavachari, J. B. Foresman, J. V. Ortiz, Q. Cui, A. G. Baboul, S. Clifford, J. Cioslowski, B. B. Stefanov, G. Liu, A. Liashenko, P. Piskorz, I. Komaromi, R. L. Martin, D. J. Fox, T. Keith, M. A. Al-Laham, C. Y. Peng, A. Nanayakkara, M. Challacombe, P. M. W. Gill, B. Johnson, W. Chen, M. W. Wong, C. Gonzalez, and J. A. Pople, "*Gaussian* 03", Gaussian, Inc., Wallingford, **2004**.
36. M. W. Schmidt; K. K. Baldridge; J. A. Boatz, S. T. Elbert, M. S. Gordon, J. H. Jensen, S. Koseki, N. Matsunaga, K. A. Nguyen, S. J. Su, T. L.Windus, M. Dupuis, J. A. Montgomery, *J. Comput. Chem*., **1993**, *14*, 1347.

STUDIA UNIVERSITATIS BABEŞ-BOLYAI, CHEMIA, XLV, 2, TOM I, 2010

Dedicated to the memory of Prof. dr. Ioan Silaghi-Dumitrescu marking 60 years from his birth

SYNTHESIS AND THERMAL BEHAVIOR OF COPPER(II) COMPLEXES CONTAINING N,N'-TETRA(4-ANTIPYRILMETHYL)-1,2 DIAMINOETHANE AS LIGAND

**ELENA MARIA MOSOARCA[a], IMRE LABADI[b],
LUDOVIC SAJTI[a], RAMONA TUDOSE[a], VASILE SIMULESCU[a],
WOLFGANG LINERT[c] AND OTILIA COSTISOR[a,*]**

ABSTRACT. The synthesis of new complexes [Cu(TAMEN)][Zn(NCS)$_4$] and [Cu(TAMEN)ZnCl$_4$(H$_2$O)], where TAMEN stand for the Mannich base N,N'-tetra(4-antipirylmethyl)-1,2-diaminoethane are reported. The molecular formulas are proposed on the basis of elemental analysis, mass spectra, molar conductivity values, UV-VIS and IR spectra. The thermal behavior of the complexes was also investigated.

Keywords: *antipyrine, copper(II), zinc(II), Mannich base, thermal analysis.*

INTRODUCTION

Antipyrine and its derivatives are reported to exhibit analgesic and anti-inflammatory effects, antiviral, antibacterial and herbicidal activities [1-12]. Formation of complexes with some oligoelements may explain their pharmaceutical activity [13]. Antipyrine complexes with certain metal ions, including Pt(II) and Co(II) ions, have been shown to act as antitumor agents. In order to extend this class of pharmaceutics, Mannich bases containing two or four antipyrine fragments have been obtained [14]. Considering that more antipyrine active fragments would lead to a more efficient antipyretic and analgesic medicine, we synthesized and structurally characterized *3 d* metal complexes of antipyrine Mannich bases, namely, N,N'-bis(4-antipirylmethyl)-piperazine (BAMP) [15-16] and N,N'-tetra(4-antipyrylmethyl)-1,2 diaminoethane (TAMEN) [17]. Some of them have been biologically investigated as antimicrobial and antitumoral agents [18-21].

---

[a] *Institute of Chemistry Timisoara of Romanian Academy, 24 Mihai Viteazu Bd., 300223, Timisoara, Romania*

[b] *University of Szeged, Department of Inorganic and Analytical Chemistry, H-6701 Szeged, P.O. Box 440, Hungary*

[c] *Institute of Applied Synthetic Chemistry, Vienna University of Technology, Getreidemarkt,9/163-AC, A-1060 Vienna, Austria*

[*] Author for correspondence: ocostisor@acad-icht.tm.edu.ro

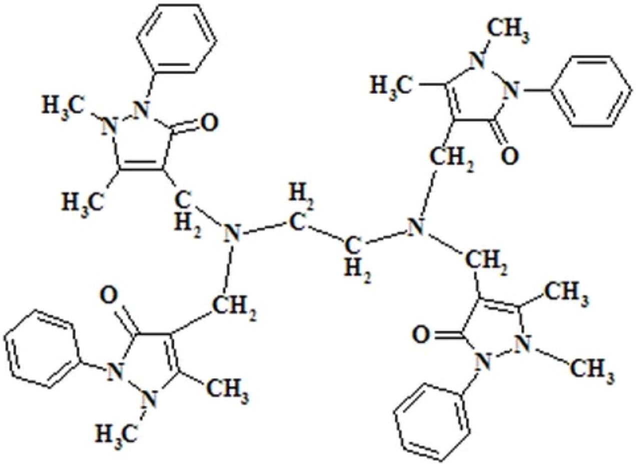

Figure 1. N,N'-tetra-(4-antipyrilmethyl)-1,2-ethanediamine (TAMEN)

The Mannich base, N,N'-tetra-(4-antipirylmethyl)1,2-ethanediamine (TAMEN) has a symmetric molecule with two groups of potential donor atoms separated by the ethylenediamine bridge (Figure 1). Tanks to the flexibility of the ethylenediamine bridge, TAMEN show a great versatility. Thus, when it acts as bis-tridentate ligand, binuclear complexes have been obtained [22]. Mononuclear complexes have been obtained when TAMEN acts as hexa- or tetradentate ligand [23-25]. The thermal behavior of some monometallic complexes containing TAMEN as ligands have been investigated and the decomposition mechanism for the studied complexes has been established [26-30]. As a continuous work in this field, the new bimetallic complexes [Cu(TAMEN)][Zn(NCS)$_4$] and [Cu(TAMEN)ZnCl$_4$(H$_2$O)] are reported along with their thermal behavior.

RESULTS AND DISCUSSION

The complexes [Cu(TAMEN)][Zn(NCS)$_4$] and [Cu(TAMEN)ZnCl$_4$(H$_2$O)] were obtained as microcrystalline powders, stable in air, insoluble in most common organic solvents like acetone, chloromethane or benzene, and soluble in DMSO, DMF, acetonitrile. Molar conductivity values of the two complexes in acetonitrile are quite different. Thus, [Cu(TAMEN)][Zn(NCS)$_4$] shows an 1:1 electrolyte type behaviour whereas [Cu(TAMEN)ZnCl$_4$(H$_2$O)] is a non-electrolyte [31].

The electronic spectrum of the free ligand shows bands at 244 and 280 nm assigned to the $\pi \rightarrow \pi^*$ and $n \rightarrow \pi^*$ transitions, respectively. In the spectra of the complexes, these are shifted to the higher values denoting the coordination of the ligand to the metal ion. An intense new band appears around 420 nm in the spectra of the complexes which is attributable to a charge transfer process. Further, the spectra show bands of low intensity in the quite similar region, around 700 nm denoting a similar geometry of the metal ion. According to the literature data, these bands can be assigned to the d-d transitions of copper(II) in a distorted octahedral ligand field [32-34].

The FT-IR spectra of the complexes were recorded and compared with that of the free ligand. Some important differences were noticed. First, the strong band at 1656 cm^{-1} due to the v(C=O) mode in the spectrum of the free ligand is shifted to 1630 and 1631 cm^{-1} for the complexes $[Cu(TAMEN)][Zn(NCS)_4]$ and $[Cu(TAMEN)ZnCl_4(H_2O)]$, respectively, proving coordination through antipyrine carbonyl oxygens, which further affect the pyrazolonic ring. Thus, in the spectrum of the free ligand bands assigned to the pyrazolone ring appear in the region 1347-1494 cm^{-1}. They are shifted to 1374-1493 cm^{-1} in the spectra of the complexes. New bands appear at 1573-1593 cm^{-1} in the IR spectra also and they are assigned to a combination of the ν(C=O) and ν(C=N) stretching modes. These changes can be explained by an important contribution of the mesomeric structures II and III of the antipyrine moiety [35].

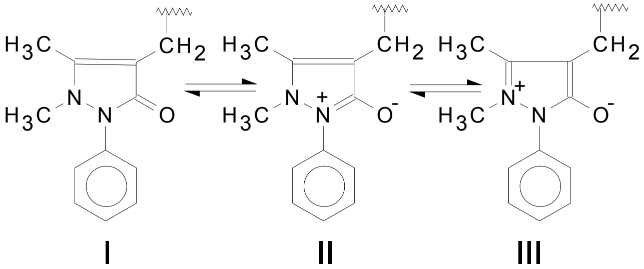

Figure 2. Mesomeric forms of the antipyrine fragment

Bands attributable to v(Cu-O) and v(Cu-N) can be identified in the spectra of both complexes. Thus, for $[Cu(TAMEN)][Zn(NCS)_4]$ the weak band at 526 cm^{-1} is assigned to v(Cu-O) and that at 412 cm^{-1} to v(Cu-N). For $[Cu(TAMEN)ZnCl_4(H_2O)]$ these modes appear at 439 cm^{-1} for v(Cu-O) and at 411 cm^{1} for v(Cu-N), respectively [36, 37]. In the spectrum of this compound a band attributable to v(Zn-O) at 521 cm^{-1} can be noticed. Infrared spectra demonstrate that TAMEN acts as a hexadentate ligand in the $[Cu(TAMEN)][Zn(NCS)_4]$ complex. The behaviour of TAMEN as a hexadentate ligand through N_2O_4 donor set in the cromophore $[Cu(TAMEN)]^{2+}$ has already been demonstrated [24] on the basis of crystallographic analyses. However, the differences between the positions and intensities of the stretching modes denote that TAMEN acts in a different mode in [Cu(TAMEN)$ZnCl_4(H_2O)$]. Based on our previous results, we assume that TAMEN acts here as a binucleating ligand with copper(II) coordinated by the NO_2 donor set and zinc(II) by O atoms of two antipyrine moieties. The six coordination number of copper(II) is achieved by coordination of two chloride ions and a water molecule. For Zn(II), the usual coordination number 4 is reached by two chloride ions. Crystallographic studies are in progress for this compound. The complex [Cu(TAMEN)][$Zn(NCS)_4$] exhibits a ν(CN) vibration at 2074 cm^{-1} and ν(CS) bands at 861 cm^{-1} and 446 cm^{-1} [δ(NCS)], characteristic to the M-NCS bond. Mass spectra showed the molecular peak for both compounds. For [Cu(TAMEN)][$Zn(NCS)_4$], the molecular peak was found at m/z 1222. Together with this signal, were observed as well other two isotopic signals at m/z 1223 and 1224 in the positive mode. In the same time in the negative mode the molecular peak appear at m/z 1222, together with several isotopic peaks from m/z 1215 to 1221. All of these data proved that the assumed structure of [Cu(TAMEN)][$Zn(NCS)_4$] is correct. The mass spectra obtained for the compound [Cu(TAMEN)$ZnCl_4(H_2O)$] showed the molecular peak (m/z 1149) both in the positive and in the negative mode, with a smaller intensity, probably due to the lower ionization process. As in the previous compound, the mass spectra confirmed the proposed structure for [Cu(TAMEN)$ZnCl_4(H_2O)$].

Thermoanalytical studies of complexes

The decomposition curves in the case of [Cu(TAMEN)][$Zn(NCS)_4$] shows that below 200ºC there is no definite peak on DTG and endothermic peak on DTA curve, so it could be concluded that there are no coordinated water molecules in the complex compound. In the temperature range 200-340ºC, a mass loss of 32.52% correspond to a partialy loss of ligand, accompanied by an exothermic process. In the temperature range 340-600ºC the mass loss of 45.45% corresponds to the loss of the rest of the ligand and a deposit of CuO+$Zn(SCN)_2$ is formed. On DTA curves the exothermic process is observed. Between 620-1000ºC from the $Zn(SCN)_2$, ZnO is formed. The mass loss is about 7.08 %.

The decomposition curves of complex [Cu(TAMEN)$ZnCl_4(H_2O)$] shows below the temperature of 150ºC a mass loss of about 1.70% that corresponds to the loss of one water molecule. This process is accompanied by an endothermic process on the DTA curve. The second stage of decomposition takes place between the temperature range 150-250ºC with a loss of two chlorine atoms (the mass loss about 6.25%) and a loss of 0.47 molecule of TAMEN. On DTA curve a large exothermic peak are started in this temperature range with two small maxima. Between 250-450ºC a part of ligand release the solid matter and an exothermic process appears on the DTA curve, corresponding to a 34.96% mass loss. The fourth stage of decomposition process occurs in the temperature range 450-1000ºC, corresponding to the mass loss of the rest of the ligand, about 45.84%, and to the formation of a deposit of CuO and ZnO. On the DTA curve a continuous exothermic process appears.

EXPERIMENTAL

All chemicals have been purchased from commercial sources and were used without further purification. Analytical data were obtained by a Perkin-Elmer model 240C elemental analyzer. Metal ions analysis was performed by atomic absorption spectroscopy with a GBC SENSAA spectrophotometer. IR spectra were recorded in KBr pellets with a JASCO 430 FT-IR spectrometer (4000–400 cm^{-1}). Electric conductivities were measured at room temperature in acetonitrile solutions with a WTW conductivity meter. Electronic absorption spectra of freshly prepared acetonitrile solutions (10^{-3} M) were measured on a Perkin Elmer Lambda 12 spectrophotometer. The mass spectra were obtained using a mass spectrometer Esquire 6000 ESI (electrospray ionization) from Bruker Daltonics. All the compounds analyzed were diluted before measurements at 10^{-5} M, in acetonitrile. A small syringe pump is included with the instrument system to provide the introduction of samples directly to either the electrospray. The solution was injected into the spray chamber by a Hamilton syringe, with a constant flow of 250 μl/h. The API-ESI (Atmospheric Pressure Interface-ElectroSpray Ionization) generates ions, focuses and transports them into the ion trap mass analyzer. The thermal analysis was performed with a computer-controlled MOM derivatograph. The mass of the investigated samples was 30-60 mg. The measurements were made between room temperature and 1000°C at a heating rate of 5°C/min, in ceramic crucibles under static atmosphere of air, with α-Al_2O_3 as reference substance.

Synthesis of the ligand and the complexes

The ligand TAMEN has been obtained following a Mannich type condensation between antipyrine, 1,2-ethandiamine and formaldehyde [14].

[Cu(TAMEN)][Zn(NCS)$_4$]

$CuCl_2 \cdot 2H_2O$ (0.17 g, 1 mmol) dissolved in 5 ml ethanol was mixed with TAMEN (0.86 g, 1 mmol) dissolved in 10 ml ethanol at 45°C and stirred for 30 min. Further, $Zn(CH_3COO)_2 \cdot 2H_2O$ (0.22 g, 1 mmol) and NH_4SCN (0.37g (4.75 mmol) dissolved in 5 ml EtOH was slowly added to the reaction mixture and stirred for 2 hours. The resulting green product was filtered, washed with ether and dried over $CaCl_2$ in air. Yield: (0.94 g) 77 %; UV-VIS (CH_3CN) spectrum**:** $\lambda_{max}(\varepsilon)$ = 269 (4 940), 295 (3110), 422 (480), 685 (50) nm. IR spectrum (KBr), ν /cm^{-1}: 2917 m, 2352 w, 2103 sh, 2074 s, 1630 m,1593 w, 1564 m, 1488 m, 1453 m, 1429 m, 1374 m, 1304 s, 1247 w, 1172 w, 1144 m, 1108 m, 1077 w, 1025 m, 901 m, 861 w, 808 w, 762 s, 695 s, 648 m, 607 m, 526 w, 505 w, 479 w. 446 w, 412 w. Molar conductivity in CH_3CN ($Ω^{-1}mol^{-1}cm^2$):120. *Anal.* Calcd. mass fractions of elements, *w*/%, for $CuZnC_{54}H_{56}O_4N_{14}S_4$ (MW 1222.30 g/mol) are: C 53.06, H 4.62, N 16.04, O 5.24, S 10.49, Cu 5.20, Zn 5.35; found: C 53.10, H 4.58, N 15.99, O 5.29, S 10.45, Cu 5.19, Zn 5.40. MS+: m/z 1222, 1223, 1224. MS-: m/z.1215, 1216, 1217, 1218, 1219, 1220, 1221, 1222

[Cu(TAMEN)ZnCl$_4$(H$_2$O)]

$CuCl_2 \cdot 2H_2O$ (0.17 g, 1 mmol) dissolved in 2 ml ethanol and $Zn(CH_3COO)_2$ (0.22 g, 1 mmol) was mixed with TAMEN (0.86 g, 1 mmol) dissolved in 20 ml ethanol under vigorous stirring. The green mixture was further stirred for 2 hours and the resulted blue product was filtered, washed with ether and dried over $CaCl_2$ in air. Yield: (0.88 g) 69%; UV-VIS spectrum (CH_3CN): λmax/nm 269, 299, 416 (240), 706, ε/l mol^{-1}cm^{-1} 4940, 3150) (30). IR spectrum (KBr) v/cm^{-1}: 3465m, 2921 m, 2352 w, 1631m, 1573 s, 1493 m, 1457 m, 1431 m, 1379 w, 1299 m, 1249 w, 1145 w,1107 m, 1078 m, 1026 m, 930w, 903 m, 864 w, 762 s, 696 s, 653 m, 607 m, 521w, 507 w, 461 w; 439 w, 411 w. Molar conductivity(CH_3CN) Λ/Ω-^{1}mol^{-1}cm^{2}: 20. *Anal.* Calcd. mass fractions of elements, *w*/%, for $CuZnC_{50}H_{58}O_5N_{10}Cl_4$ (MW 1149.81 g/mol) are: C 52.23, H 5.08, N 12.18, O 6.96, Cl 12.33, Cu 5.53, Zn 5.69; found: C 51,98, H 5.01, N 12.26, O 6.84, Cl 12.33, Cu 5.58, Zn 6.00. MS+: m/z 1148, 1149, 1150. MS-: m/z 1148, 1149.

CONCLUSION

New Cu(II) and Zn(II) complexes were synthetised and studied. Molar conductivity data shows that the complex $[Cu(TAMEN)][Zn(NCS)_4]$ presents a 1:1 electrolyte type in acetonitrile solution and $[Cu(TAMEN)ZnCl_4(H_2O)]$ a non-electrolyte type behavior. The visible absorption spectra of the complexes suggest that the copper(II) ions are in solution in a distorted octahedral ligand field. IR spectra have revealed that the ligand acts as a hexadentate donor in the case of $[Cu(TAMEN)][Zn(NCS)_4]$, through the four oxygen atoms belonging to the antipyrine fragments and two nitrogen atoms of ethylenediamine and as bis-tridentate in the case of $[Cu(TAMEN)ZnCl_4(H_2O)]$ through the O_2N donor set.

ACKNOWLEDGEMENTS

The authors would like to thank the Romanian and Hungarian Academies of Sciences for financial assistance. Thanks for financial support are also expressed to the "Fonds zur Förderung der Wissenschaftlichen Forschung in Österreich" (Project 19335-N17).

REFERENCES

1. C. H. Sayed, A. A. Hamed, G. A. Meligi, W. E. Boraie, M. Shafic, *Molecules,* **2003**, *8*, 322.
2. Y. Zhang, L. Yzhi, T. Hanbin, Z. Longgen, *Acta Crystallographica,* **2002**, *E58,* 24.
3. G. Turan-Zitouni, M. Sivaci, F. S. Kilic, K. Erol, *European Journal of Medicinal Chemistry,* **2001**, *36,* 685.
4. G. H. Sayed, A. Radwan, S. M. Mohamed, S. A. Shiba, M. Kalil, *Chinese Journal of Chemistry*, **1992**, *10*, 475.
5. M. Daoudi, N. B. Larbi, D. Benjelloun, A. Kerbal, J. P. Launaly, J. Bonvoisin, J. Jaud, M. Mimouni, J. Hadda, *Molecules,* **2003**, *8*, 269.
6. T. N. Sorrel, V. A. Vankai, M. L. Garrity, *Inorganic Chemistry,* **1991**, *30,* 207.
7. A. Togni, L. M. Venanzi, *Angewandte Chemie International Edition Eng.*, **1994**, *33,* 497.
8. A. Kandil, A. Hamid, *Journal of Drug Research,* **1980**, *12*, 27.
9. A. M. Farghlay, A. Hozza, *Pharmazie,* **1980**, *35*, 596.
10. H. Tronnier, *Acta Fac. Med. Univ. Brun*, **1972**, *40*, 211.
11. J. F. Cumming, *Clinical Pharmacology & Therapeutics,* **1976**, *19*, 486.
12. A. Doario, D. Craciunescu, C. Ghirvu, J. Nuno, *An. Quim,* **1977**, *73*, 1120.
13. N. T. Madhu, P. K. Radhakrishnan, M. Grunert, P. Weinberger, W.Linert, *Review in Inorganic Chemistry*, **2003**, *23,* 1 *and references therein*.
14. C. Mannich, W. Krösche*, Archiv der Pharmazie*, **1912**, *250*, 647. C. Mannich, B. Kather, *Archiv der Pharmazie,* **1919**, *18*, 257.
15. O. Costisor, A. Maurer, A. Tomescu, S. Policec, *Buletinul Stiintifico-Tehnic al Institutului Politehnic Timisoara, Seria Chimie,* **1981,** *26*, 93.
16. O. Costisor, A. Maurer, S. Policec, *Buletinul Stiintifico-Tehnic al Institutului Politehnic Timisoara, Seria Chimie,* **1981**, *26*, 87.
17. W. Linert, O. Costisor, R. Tudose, *Oriental Journal of Chemistry*, **1995**, *11*, 107.
18. Al. Stupariu, O. Costisor, E. Bedrosian, L. Radbea, E. Szabo, *Rev. Rom. Med. Veter.,* **1995**, *5*, 81.
19. R. Alexandrova, G. Rashkova, T. Popova, R. Tudose, E. M. Mosoarca, S. Slavov, O. Costisor, *Acta Morphologica and Anthropologica,* **2006**, *11,* 60.
20. R. Alexandrova, G. Rashkova, T. Popova, R. Tudose, E. M. Mosoarca, S. Slavov, O. Costisor, *Experimental Pathology and Parasiology,* **2005**, *8/2,* 93.
21. R. Alexandrova, A.Vacheva, M. Kirilova, G. Miloshev, E. M. Mosoarca, R. Tudose, O. Costisor, *Acta Morphologica and Anthropoogica,* **2007**, *12*, 72.
22. O. Costisor, W. Linert, S. Deusch, C. Stanescu, *Journal of Coordination Chemistry,* **1994**, *33,* 229.
23. R. Tudose, I. Pantenburg, E. M. Mosoarca, G. Meyer, O. Costisor, *Zeitschrift für anorganische und allgemeine Chemie,* **2005**, *632*, 1491.

24. R. Tudose, I. Pantenburg, E. M. Mosoarca, G. Meyer, O. Costisor, *Zeitschrift für anorganische und allgemeine Chemie,* **2005**, *631,* 2423.
25. E. M. Mosoarca, R. Tudose, R. Alexandrova, O. Costisor, *Chemical Bulletin of "Politehnica" University Timişoara,* **2004**, *63*, 49.
26. I. Labadi, R. Tudose, I. Fejer, Z. Jori, O. Costisor, *Journal of Thermal Analysis and Calorimetry,* **1999**, *56,* 553.
27. I. Labadi, Zs. Czibulya, R. Tudose, O. Costisor, *Journal of Thermal Analysis and Calorimetry,* **2004**, *77*, 553.
28. I. Labadi, E. Pal, R. Tudose, O. Costisor, *Journal of Thermal Analysis and Calorimetry,* **2006**, *83*, 681.
29. V. Sasca, E. M. Mosoarca, L. Avram, R. Tudose, O. Costisor, *Journal of Thermal Analysis and Calorimetry*, **2008,** *94(2),* 355.
30. E. M. Mosoarca, V. Sasca, L. Avram, R. Tudose, O. Costisor, *Journal of Thermal Analysis and Calorimetry,* **2008**, *94(2)*, 361.
31. W. Geary, *Journal of Coordination Chemistry Review,* **1971**, *7*, 81.
32. A.B.P. Lever, *Inorganic Electronic Spectroscopy,* Elsevier Publishing Company, Amsterdam, **1968**, 318.
33. N. T. Madhu, P. K. Radhakrishnan, *Transition Metal Chemistry, **2000**, 25, 287.*
34. N. Kalarani, S. Sangeetha, P. Kamalakannan and D. Venkappaya, *Russian Journal of Coordination Cheistry,* **2003**, *29 (12),* 845.
35. M. Hesse, H. Meier, B. Zeeh, *Spektroskopische Methoden in der Organischen Chemie,* G. Thieme Verlag, Stuttgart, **1987**, 255.
36. K. Nakamoto, *Infrared and Raman Spectra of Inorganic and Coordination Compounds,* John Wiley & Sons, New York, **1986**, 283.
37. J. R. Ferraro, *Low-frequency vibration of inorganic and coordination compounds,* Plenum Press, New York, **1971**, 65.

STUDIA UNIVERSITATIS BABEŞ-BOLYAI, CHEMIA, XLV, 2, TOM I, 2010

Dedicated to the memory of Prof. dr. Ioan Silaghi-Dumitrescu marking 60 years from his birth

MICROWAVES ASSSITED *N*-ALKYLATION OF PHENOTHIAZINE

LUIZA GĂINĂ, TIMEA DALLOS, CASTELIA CRISTEA[*],
TAMAS LOVASZ, IANI PERETEANU, MIHAI SURDUCAN
AND LUMINIȚA SILAGHI-DUMITRESCU

ABSTRACT. A *green chemistry* approach to the N-alkylation of phenothiazine is described. The chemical process was improved by applying the microwave assisted heating technique in closed vessel and by using safer solvents such as alcohol or PEG. Reaction conditions were optimized to give good yields in short reaction times.

Keywords: *Phenothiazine, N-alkylation, MAOS, green chemistry*

INTRODUCTION

N-alkyl-phenothiazine derivatives, proved to be extremely usefull substrates for the regioselective preparation of C-substituted phenothiazine derivatives *via* direct aromatic electrophilic substitution as well as by using organometallic intermediates [1-6]. N-methyl- and 10-ethylphenothiazines were prepared right at the begining of the phenothiazine chemistry by using the corresponding alcohols as alkylating agents [7] and the seeking for improved reaction conditions never stopped ever since. In alkaline conditions, alkyl halides proved to be excellent alkylating agents and large scale application were developed for the preparation of neuroleptic drugs containing this pharmacophore unit [8]. DMS [9] and oxalic acid esters [10] were also reported as alkylating agents.

The tremendous development of microwave assisted organic synthesis (MAOS) during the last decades is supported by certain advantages such as: reaction rate acceleration, milder reaction conditions, lower energy input, usually higher reaction yields and sometimes different selectivity, which were observed after microwave irradiation, as compared to conventional convective heating of the reaction mixtures [11,12]. These advantages successfully integrate *MAOS* into the *green chemistry* principles, seeking for the development of cleaner, environmentally benign and energy efficient processes [13].

---

[*] *Universitatea Babeş-Bolyai, Facultatea de Chimie şi Inginerie Chimică, Str. Kogălniceanu Nr. 1, RO-400084 Cluj-Napoca, Romania, castelia@chem.ubbcluj.ro*

The aim of this work is to describe our contribution to the improvment of the reaction conditions applied for the *N*-alkylation of phenothiazine with alkyl-halides, based on *green chemistry* principles and new technical possibilities offered by the use of modern *on-line* controlled microwave assisted reactors.

RESULTS AND DISCUSSION

A mixture of alkyl iodide and alcohol gave good yields of *N*-alkyl phenothiazine, when the reaction was performed at high temperatures (110-120 ^{0}C) in closed vessels (scheme 1). A volatile alcohol develops high internal pressures and may also participate to the *in situ* regeneration of alkyl iodide and for these reasons both the alkyl halide and the alcohol should contain the same alkyl chain. In these conditions, *N*-methyl-phenothiazine **1** was obtained more than 70% yield by using a mixture of methyl iodide and methanol, while a mixture of ethyl iodide and ethanol gave *N*-ethyl-phenothiazine **2** in lower yields (50-70%) [14,15]. 24 Hours of heating were required to complete these reactions and longer alkyl chains could not be attached to the heterocyclic nitrogen atom under these circumstances.

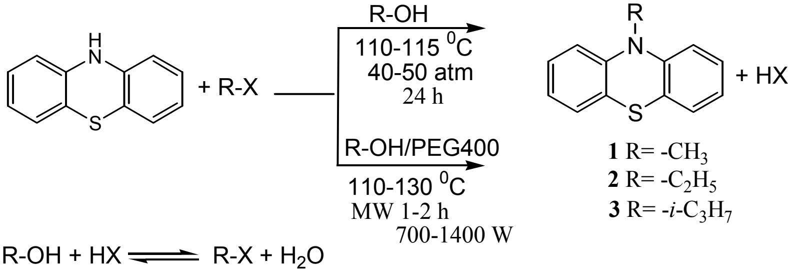

Scheme 1

Particularly efficient heating processes induced by the dielectric heating afforded shorter reaction times for the alkylation of phenothiazine with methyl iodide, ethyl iodide and *i*-propyl bromide respectively, in the presence of the proper alcohol, which is a solvent with medium absorbing properties of the microwave radiation (scheme 1). As it can be seen from table 1 which summarises the results obtained when different reaction conditions were applied, the best results were obtained when the corresponding alcohol was employed. Even though the recorded yields were decreasing with the increase of the alkyl chain, N-*i*-propyl-phenothiazine **3** could be obtained in 56% yields using an alkylating mixture of *i*-propyl bromide and isopropanol after 40 minutes of high power irradiation.

In our survey for safer solvents we selected PEG, a solvent capable to efficiently absorb microwave energy and thus to ensure a rapid heating of the reaction mixture by dipolar polarization mechanism.

However, as it can be seen in table 1, the yields in the methylation reaction were not improved neither when a mixture of alcohol and PEG (v/v 1:1), nor PEG was employed. Satisfactory yields were generated when catalytic amounts of were added Cs_2CO_3 to the PEG containing reaction mixture.

Table 1. Experimental conditions employed for the microwave assisted alkylation of phenothiazine with alkylhalides

Cpd	Solvent v/v	Temp$_{max}$ [^{0}C]	Power/time [W]/[min]	Yield %
1	MeOH	110	800W/20 min 1000W/90 min	79
	PEG400/CH_3OH 1/1	110	800W/20 min , 1000W/60 min	20
	PEG400	110	800W/20 min, 1000W/60 min	16
	n-BuOH, Cs_2CO_3	130	700W/1 min 800W/15 min	49
	PEG400 Cs_2CO_3	125	700W/2 min 800W/60 min	44
	BuOH, H_2O, Aliquat 336, KOH	130	700W/90 min, 800W/15 min	43
2	EtOH		800W/20 min 1000W90 min	65
	PEG400/EtOH, 1/1	140	500W/40 min 800W/30 min	54
	PEG400	130	800W/2 min 500W/60 min	17
3	*i*-PrOH	130	1400W/40 min	56
	PEG400, Cs_2CO_3	120	700W/2 min 800 W/60 min	10

Microwave irradiation was applied for the methylation of phenothiazine with methyl iodide under phase transfer catalysis conditions (using PTC catalyst Aliquat 336, butanol solvent and KOH base). Satisfactory yields were obtained in much shorter reaction time, as compared to classical PTC experiment which typically requires 48-72 hours of vigorous stirring.

CONCLUSIONS

MAOS can be successfully applied to the preparation of N-alkyl-phenothiazine with the advantage of a much shorter reaction time required in order to obtain comparable reaction yields with those resulted under conductive heating conditions. High power microwave irradiation of a mixture of phenothiazine, alkyl halide and alcohol may afford satisfactory yields of N-alkyl-phenothiazines containing more than 2 carbon atoms in the side chain.

EXPERIMENTAL SECTION

Microwave installation *Synthos 3000* equipped with temperature and pressure sensors, power control and software operation.

Merck reagents.

400 MHz NMR spectrometer Bruker Avance

Microwave assisted synthesis of N-alkyl-phenothiazine, general procedure:

The reaction mixture (phenothiazine, alkylhalide, as well as any starting materials required according to conditions listed in table 1) solved in the properly chosen solvent was introduced in the quartz reaction vessel, which was sealed and then subjected to microwave irradiation in the resonance cavity of the microwave power system. Samples temperatures were automatically monitored during the irradiation with the prescribed power level. Inside pressure was monitored during the experiment. After irradiation, the solvent was removed by filtration and the solid product was purified by recrystallization.

10-methyl-10*H*-phenothiazine 1

a) 5 mmol (1g) phenothiazine, 6.4 mmol (0.4 ml) methyl iodide, 10 ml MeOH were treated according to the general procedure and the parameters listed in table 1 were applied.

b) *Microwave assisted PTC methylation*

A mixture of 1.25 mmol (1g) phenothiazine, 1.6 mmol (0.1 ml) methyl iodide, 5 ml BuOH, 5 ml of 10% KOH aq. and catalytic ammounts of Aliquat 336 was vigorously stirred in the closed vessel, while microwave irradiation was applied according to conditions described in table 1. The resulted reaction mixture was pourred in water and the product was extracted in dichloromethane After solvent removal, the crude product was recrystallised from EtOH.

Recristallyzation from EtOH. White crystals m.p.= 99,5°C, (lit. 99°C, 101-103 °C [14])

^{1}H-RMN 400MHz, CDCl$_3$: δ(ppm): 3,38ppm (s, 3H, H$_a$); 6,82ppm (d, 2H, ^{3}J$_{orto}$= 8,4Hz, H$_1$); 6,93ppm (td, 2H, H$_3$); 7,14ppm (dd, 2H, ^{3}J$_{orto}$= 7,1Hz, ^{4}J$_{meta}$= 1,2Hz, H$_4$); 7,17ppm (td, 2H, ^{4}J$_{meta}$= 1,2Hz, H$_2$) **^{13}C-RMN,** CDCl$_3$:δ(ppm): 35,3ppm (CH$_3$, C$_a$); 114,0ppm (CH, C$_1$); 122,4ppm (CH, C$_3$); δ=123,4ppm (Cq, C$_{4a}$); 127,1ppm (CH, C$_2$); 127,4ppm (CH, C$_4$); 145,80ppm (Cq, C$_{9a}$).

10-ethyl-10*H*-phenothiazine 2

1.25 mmol (0.25g) phenothiazine, 1.6 mmol (0.2 ml) ethyl iodide, 10 ml EtOH were treated according to the general procedure and the parameters listed in table 1 were applied.

Recristallyzation from EtOH. White crystals m.p.= 104.5°C (lit. 101-103°C [14])

^{1}H-RMN 400MHz , CDCl$_3$: δ(ppm): 1,38ppm (t, 3H, ^{3}J= 6,8Hz, H$_b$); 3,88ppm (q, 2H, ^{3}J= 6,8Hz, H$_a$); 6,83ppm (d, 2H, ^{3}J$_{orto}$= 8,0Hz, H$_1$); 6,87ppm (t, 2H, H$_3$); 7,11ppm (m, 4H, ^{3}J$_{orto}$= 7,6Hz, H$_{2,4}$) **^{13}C-RMN,** CDCl$_3$: δ(ppm): 13,0ppm (CH$_3$, C$_b$); 41,7ppm (CH$_2$, C$_a$); 115,0ppm (CH, C$_1$); 122,2ppm (CH, C$_3$); 124,4ppm (Cq, C$_{4a}$); 127,2ppm (CH, C$_2$); 127,3ppm (CH, C$_4$); 144.9ppm (CH, C$_{9a}$)

10-isopropyl-10*H*-phenothiazine 3

1.25 mmol (0.25g) phenothiazine, 1.6 mmol (0.15 ml) *i*-propyl bromide, 10 ml *i*-PrOH were treated according to the general procedure and the parameters listed in table 1 were applied.

Recristallyzation from EtOH. m.p.= 60,5°C (lit 59-60 °C [14]

^{1}H-RMN 400MHz, CDCl$_3$: δ(ppm): 1,38ppm (d, 6H, ^{3}J= 7,2Hz, H$_b$); 3,46ppm (m, 2H, ^{3}J= 7,2Hz, H$_a$); 6,90ppm (t, 2H, H$_3$); 7,01ppm (d, 2H, ^{3}J$_{orto}$= 8,2Hz, H$_1$); 7,17ppm (m, 4H, ^{3}J$_{orto}$= 7,3Hz, H$_{2,4}$) **^{13}C-RMN, CDCl$_3$:** δ(ppm): 16,5ppm (CH$_3$, C$_b$); 33,7ppm (CH, C$_a$); 115,0pm (CH, C$_1$); 122,4ppm (CH, C$_3$); 123,4ppm (CH, C$_{4a}$); 127,2ppm (CH, C$_2$); 127,4ppm (CH, C$_4$); 145,1ppm (CH, C$_{9a}$)

ACKNOWLEDGMENTS

Financial support from Roumanian Ministery of Education Research, Youth and Sports, grant PN-II-ID-564 is greatly acknowledged.

REFERENCES

1. T. Kline, E. Sieber-McMaster, W.F.Lau, S. Natarajan, *Bioorg. & Med. Chem. Lett.*, **1997**, *7(8),* 1017.
2. S. Ebdrup, *Synthesis*, **1998**, *8*, 1107.
3. T. J. J. Müller, *Tetrahedron Letters*, **1999**, *40*, 6563.
4. Ng. Ph. Buu-Hoï, N. G. Hoán, *J. Chem. Soc.*, **1951**, 1834.

5. G. Cauquil, E. Casadevall, R. Greze, *Bull. Soc. Chim. Fr.*, **1964**, 590.
6. V. Fărcăşan, *Rev. Roum. Chim.*, **1970**, *15*, 178.
7. A. Bernthsen, *Ann.*, **1885**, *230*, 88.
8. R. R. Gupta, *Phenothiazines and 1,4-benzothiazines Chemical and Biomedical aspects* in Bioactive Molecules, Elsevier, **1988**, chapter 1.
9. Ng. Ph. Buu-Hoï, N. G. Hoán, *J. Chem. Soc.*, **1951**, 1834.
10. C. Lespagnol, *Bull. Soc. Chim. Fr.*, **1959**, 112.
11. A. Loupy (Ed), *Microwaves in Organic Chemistry*, Wiley-VCH Weinheim, **2002.**
12 P. Lidstrom, J. P. Tierney (Eds), *Microwave-Assisted Organic Synthesis*, Blackwell, Oxford, **2004**.
13. P. T. Anastas, J. C. Warner, "*Green Chemistry Theory and Practice*", Oxford Univ. Press, **1998**.
14. S. P. Massie, *Chem. Rev.*, **1954**, *54*, 797.
15. H. Bernstein, L. Rothstein, *J. Am. Chem. Soc.*, **1944**, *66*, 1886.

STUDIA UNIVERSITATIS BABEŞ-BOLYAI, CHEMIA, XLV, 2, TOM I, 2010

Dedicated to the memory of Prof. dr. Ioan Silaghi-Dumitrescu marking 60 years from his birth

PURINE METABOLISM DYSHOMEOSTASIS AND THE HETEROGENOUS NUCLEATION OF UROCONCREMENTS NOTE I. ALKALINE AND ALKALINE-EARTH METALS IN PURINE UROLITHIASIS

ZENO GARBAN[a], ADINA-ELENA AVACOVICI[b], GABRIELA GARBAN[c], FRANCISC PETER[b], GEORGE-DANIEL GHIBU[a], MIRCEA BOTOCA[d], ALIN CUMPĂNAŞ[d]

ABSTRACT. Biogenesis of lithiasic concrements constitutes a special domain when taking into account the location of lithiasis (currently named calculi or stones) in the organism, e.g.: sialolithiasis, rhinolithiasis, urolithiasis, flebolithiasis a.o. as well as the type of lithiasis.

In case of purine metabolites of endogenous (strictly metabolic) and exogenous (foods) origin the concrements formation in urine implies a heterogenous nucleation mechanism where metallic ions participate, too.

Problems concerning the purine uroconcrements (mainly with uric acid) and their content in alkaline and alkaline-earth metals were approached by investigations based on physico-chemical methods. Thus, by Fourier Transform - Infrared Spectroscopy the types of urolithiasis and by atomic absorption spectroscopy the metallogram (Na, K, Ca and Mg) of purine urolithiasis were established.

Keywords: *purine metabolism and uroconcrements; alkaline and alkaline-earth metals in purine uroconcrements*

INTRODUCTION

The problem of purine uroconcrements biogenesis is integrated in the modern approach of the complex aspects of proteomics and metallomics with application in the study of urolithiasis. Under the incidence of proteomics

---

[a] *Department of Biochemistry and Molecular Biology, Faculty of Food Products Technology, University of Agricultural Sciences and Veterinary Medicine of Banat Timisoara, Calea Aradului Nr. 119, RO-300 645 Timişoara, Romania, zeno.garban@yahoo.com*

[b] *Faculty of Industrial Chemistry and Environmental Engineering, University "Politehnica" of Timisoara*

[c] *Laboratory of Environment and Nutrition, Institute of Public Health Timisoara*

[d] *Clinic of Urology, Faculty of Medicine, University of Medicine and Pharmacy „Victor Babeş" Timişoara*

falls the nucleic acids (i.e. deoxyribonucleic acid - DNA and ribonucleic acid - RNA) biodegradation, resulting pyrimidine and purine derivatives Under the incidence of metallomics falls the metallic ions presence in blood and tissues as well as their capacity to generate in urine crystallization nuclei called „primers” or „starters” [1-4].

Commonly in the biogenesis of uroconcrements take part various metabolites like: purine derivatives (mostly uric acid), oxalic acid and oxalates, cystine, phosphates a.o. beside metallic ions ([5].

Nowadays the urolithiasis (kidney stones or urinary stones) represent about 1-2% of all diseases, about 12-40% among kidney diseases and affects about 3% of the acive people.

In the biochemical pathology of urolithiasis problems concerning the etiology, pathogenesis and composition of uroconcrements implies a complex inter- and multidisciplinary approach [6]. Efficient metaphylaxy and prophylaxy in case of urolithiasis can be achieved only by the exact knowledge of stone components [7].

The aim of the study was the determination of the qualitative composition of uroconcrements by Fourier Transform - Infrared Spectroscopy (abbreviated as FT-IR or FTIR) and thus the identification of the urolithiasis type as well as the determination, by atomic absorption spectroscopy (AAS), the concentration of alkaline and alkaline-earth metals in the purine urolithiasis.

RESULTS AND DISCUSSION

Free purines in the blood flow have the following sources: tissular purines - as a results of nucleic acid degradation; exogenous nucleoproteins - brought by food intake; newly synthetized purines in the organism - de novo biosynthesis [2, 8, 9].

Issues related to purine precursors of uroconcrements are integrated in the vast domain of proteomics. In this background there are discussed metabolic aspects, homeostasis and pathobiochemistry of purine metabolites.

In figure 1 there is presented the schematic degradation of nucleic acids with purine metabolites formation. Some of the resulted metabolites are prescursor of purine uroconcrements.

As metal ions play an important role in the biogenesis of uroconcrements [3,10] the discussed subject of this study can be integrated also in metallomics, a consequential domain for environment, medicine and biology [11, 12]

It is known that between some purine derivatives and metallic ions occur the process named „heterogenous nucleation” where the starters become precursors of uroconcrements with a continuous growth. The presence of purine metabolites, of metallic ions as well as a protein and glycoprotein or mucoprotein "matrix" in the urine allow the "starters" or "primers" formation [10, 13-15].

These urolithiasis appear as the consequence of disturbances in purine nucleotides metabolism, homeostasis and excretion of the biodegraded end products, i.e. purine derivatives (uric acid, xanthine, 2,8-dihydroxyadenine).

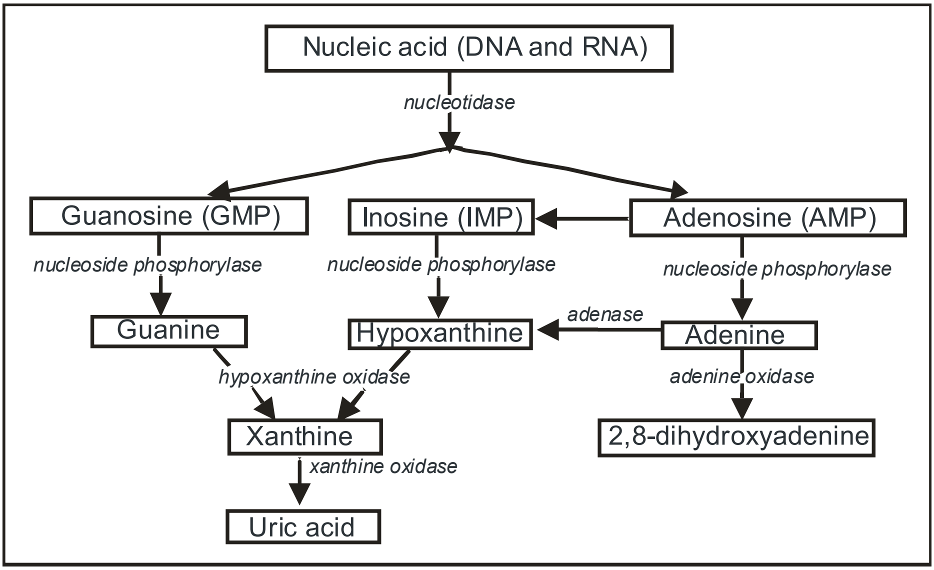

Figure 1. Main purine derivatives resulted from the biodegradation of nucleic acids

Uric acid is the end product of purine metabolism in man and is poorly soluble in biological fluids. It is excreted partly (2/3) by urinary tract and partly (1/3) eliminated by the gastrointestinal tract. Uric acid is filtered by the glomerulus and the filtered uric acid is almost completely reabsorbed in the proximal tubule. Further uric acid is secreted in to the lumen in the distal part of the proximal tubule and the daily urinary output of uric acid in a normal male on a purine-free diet is 1.6 - 3.6 mmoles (270 - 600 mg). The normal blood uric acid level is 40±70 mg/L in man and 35-60 mg/L in woman. Men tend to have higher values than women. Changes in the dietary intake of purines make relatively small differences to the blood plasma level of uric acid.

The in excess accumulation of uric acid in the urinary tract, alongside with other organic and inorganic substances (mainly metals) may lead - through coprecipitative processes - to starters formation in lithogenesis. This process is favorized by a lower urine pH and by the low urine flow rate.

Uric lithiasis has a relatively low frequency among urolithiasis but the most increased among purine lithiasis. Most uric acid stones result by the precipitation of uric acid from supersaturated urine. Uric acid urolithiasis is often accompanied by uric acid crystals in the urine sediment. Excessive urinary uric acid excretion may result from increased filtration of uric acid (from excessive dietary purine intake, metabolic errors, myeloproliferative disorders, or hemolysis), from tubular effects such as an isolated defect in renal tubular ureic reabsorption, or from generalized tubular disfunction. Uric acid excretion is increased in as many as 10% of pacients with hypercalciuria and urolithiasis. In endemic areas such as Southeast Asia and the Mediterranean region, uric acid stones are frequently not associated with hyperuricemia.

Xanthine lithiasis, rarely occured, is difficult to be found. Sometimes is necessary to make use of differential spectrophotometry, X ray diffraction or chromatography in order to diagnose it. It appears as a consequence of a metabolic disturbances in which xanthine oxidase is implicated. This enzyme catalyses the hypoxanthine oxidation to xanthine and then of the xanthine to uric acid [16,17]. Often this dysmetabolism could be observed in childhood and is the consequence of an inhereted xanthine oxidase deficiency.

The *2,8-dihydroxyadenine lithiasis* is very rare and in numerous cases may be confounded with uric lithiasis. At the origin is a defect in purine metabolism consisting in the deficiency of the adenine phosphoribosyl-transferase enzyme [18, 19]

Literature data concerning the purine derivatives concentration in urine, compiled by Altman and Dittmer [20] are presented in Table 1.

Table 1. Concentrations of purine nucleobases and other purine derivatives in urine

Nr.	Purine metabolites	Values (mg/kg body)	
		Mean	Range
1.	Adenine	0.020	0.016 – 0.240
2.	Guanine	0.006	0.003 – 0.009
	8-hydroxy-7-methyl-guanine	0.020	0.016 – 0.030
	7-methyl-guanine	0.090	0.080 – 0.110
	N^2-methyl-guanine	0.007	0.006 – 0.009
3.	Hypoxanthine	0.140	0.080 – 0.190
	1-methyl-hipoxanthine	0.006	0.003 – 0.010
4.	Xanthine	0.090	0.070 – 0.120
5.	Uric acid	2.000	0.800 – 3.000
	1,3-dimethyl-uric acid	traces	
6.	Purine bases - total		0.200 – 1.000

The presence of oxypurines, end products of purine catabolism, is conditioned by pH level. Data presented by Klinenberg et al., cited by Watts [21] reveal the solubility of the purinic metabolites: hypoxanthine, xanthine and uric acid (Table 2). It is noticed that solubility differs in serum and urine conditioned by the purine metabolites and the pH of the medium.

In order to identify the chemical substances present in urolithiasis "standard spectra" of the appropriate chemically pure compounds were recorded and the specific FT-IR absorption bands for every compound have been identified, confirmed by the available literature data [22-25].

Table 2. Data concerning pH-solubility relationship of purine metabolites

Medium	**pH**	**Solubility (mg/ 100 mL)**		
		Uric acid	**Xanthine**	**Hypoxanthine**
Serum	7.4	7	10	115
Urine	5.0	15	5	140
	7.0	200	13	150

Thus, there were recorded standard spectra for uric acid, xanthine, 2,8-dihydroxy-adenine, oxalates, phosphates, cystine, carbonates. Such a standard FT-IR spectrum for uric acid is given in figure 2.

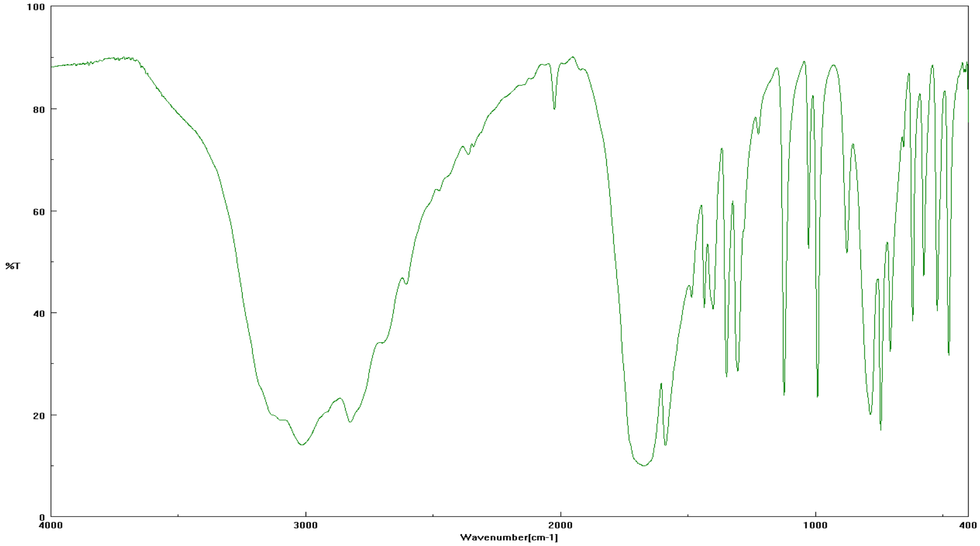

Figure 2. Standard spectrum of uric acid obtained by FT-IR

In the standard FT-IR spectrum of uric acid the significant bands were found: in the 2800-3300 cm^{-1} range for lactame and lactime O-H group streching vibrations (with peaks at 2825 cm^{-1} and 3014 cm^{-1}); in the 990-1150 cm^{-1} range for the purine skeleton ring vibrations (with peaks at 992 cm^{-1} and 1122 cm^{-1}); in the 700-800 cm^{-1} range for the purine skeleton ring vibrations (with peaks at 706 cm^{-1}, 743 cm^{-1} and 783 cm^{-1}). Also, regarding the uric acid spectrum, the characteristic vibrations for C-N, N-H and C=O peaks will be presented below.

Spectra for two uroconcrements, one with simple and other with mixed composition, are given in figure 3. In the case of the simple urolithiasis the recorded spectrum presents specific IR bands corres-ponding to certain wave numbers which are characteristic for urates (U) - fig.3a. The bands presented peaks at 1036 cm^{-1} - for the vibration type C-N stretching; 3014 cm^{-1} - for the vibration type N-H stretching and 1672 cm^{-1} - for the vibration type C=O stretching.

In the case of the mixed urolithiasis, containing uric acid and oxalates (U-O) - fig.3b, there were found not only the bands with characteristic peaks and vibrations types specific for uric acid (mentioned above) but also specific bands with characteristic peaks for oxalates. Specific bands and types of vibrations for oxalates are: 1620 cm^{-1} and 1319 cm^{-1} for the C=O asymmetric and symmetric streching, 781 cm^{-1} for the COO deformation and 518 cm^{-1} for the COO rocking (out-of-plane) vibrations.

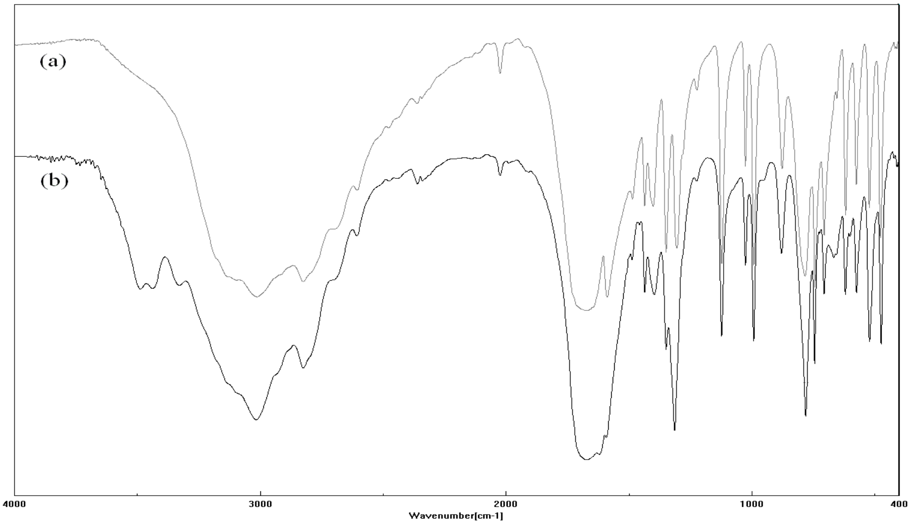

Figure 3. Spectra of some uroconcrements obtained by FT-IR : (a) simple calculus with uric acid – urates (U); (b) mixed calculus with urates and oxalates (O-U)

In case of calculi with mixed composition there are selected the expressive peaks of the IR spectra of the uroconcrements. For the identification of substances present in such a mixture, e.g. uroconcrements with urates and oxalates, Estepa and Daudon [26] proposed the building of „calibration curves" used in the evaluation of peaks and the estimation of the prevailing component. Appliance of this method will permit the evaluation of mixed uroconcrements. In the present paper three characteristic peaks were taken into consideration in the evaluation of uroconcrements with mixed composition.

In the FT-IR spectra of uroconcrements one can mark out various non-specific peaks for the type of urolithiasis. The presence of those peaks can be explained by the heterogenous nucleation process where the different characteristic lithogenetic compounds (e.g. urates, oxalates, phosphates etc.) and metallic ions precipitate on a „matrix" support. The existence of the preliminary matrix in the biogenesis of calculi is known and accepted long time ago [13]. Recent data revealed that renal stones are concretions containing 97.5% polycrystalline aggregate and 2.5% glycoprotein or mucoprotein matrix [27].

Based on the „standard spectra" and the recorded spectra for each uroconcrements there were possible to establish the qualitative chemical composition of the uroconcrements and to classify them into simple and mixed (binary and ternary) ones. In table 3 there are presented the distribution of urolithiasis types according to their chemical composition and gender of the patients.

Table 3. Synopsis on the composition of the uroconcrements investigated by FT-IR

Type of urolithiasis	**Composition**		**Number of cases**		
			Total	**Men**	**Women**
Simple	Purine derivatives	Urates (U)	34	14	20
		Xanthine (X)	--	--	--
		2,8-dihyroxyadenine (2,8-DHA)	--	--	--
	Oxalates (O)		38	23	15
	Phosphates (P)		19	6	13
	Cystine (C)		6	2	4
Simple uroconcrements - total			97	45	52
Mixed	Binary	Oxalates-urates (O-U)	11	3	8
		Urates-oxalates (U-O)	6	2	4
		Oxalates-phosphates (O-P)	31	13	18
		Oxalates-cholesterol (O-COL)	3	2	1
		Phosphates-oxalates (P-O)	15	3	12
		Phosphates-carbonates (P-CARB)	2	1	1
	Ternary	Oxalates-urates-phosphates (O-U-P)	5	2	3
		Phosphates-oxalates-carbonates (P-O-CARB)	2	2	--
Mixed uroconcrements – total			75	27	50
Total uroconcrements			172	72	102

Metals are important components of human organism but they are not produced or destroyed by the body. Being present in our environment, i.e. food, water, air, soil they are introduced in the organism mainly by food and water.

The occurrence of the metals in uroconcrements is an outcome of their presence in urine where they initiate the co-precipitative processes. It was observed in the urine of the patients with calculosis an increase of Ca and Mg concentration, while the concentrations of Na and K displayed minor variations.

By means of AAS, we determined the concentration of alkaline metals in the simple and mixed purine urolithiasis. The results are presented in Table 4.

Table 4. Quantity of alkaline metals in the purine urolithiasis

Type of urolithiasis		**Metals concentration (μg/g calculus)**			
		Sodium		**Potassium**	
		n	X ± SD	n	X ± SD
Simple	Urates (U)	34	586.12 ± 251.64	34	193.81 ± 125.18
Mixed	O-U	11	1722.31 ± 503.17	11	497.72 ± 184.16
	U-O	6	1364.05 ± 414.17	6	322.57 ± 156.74
	O-U-P	5	2249.33 ± 516.64	5	912.43 ± 206.17

n – number of cases; X- mean value; SD – standard deviation

Higher sodium concentration was found in case of mixed ternary and binary urolithiasis, more exactly in O-U-P and O-U lithiasis. Also, one can observe the indirect role of oxalates in the urolithiasis formation.

Regarding the alkaline-earth metals Ca and Mg their concentration was determined also by AAS. The results presented in table 5 revealed augmented quantities for Ca and Mg in the mixed purine urolithiasis O-U and O-U-P. Their quantity in the urolithiasis and especially that of Mg alkaline metals by the presence of phosphates, cases when result ammonio - magnesian phosphates.

Table 5. Quantity of alkaline-earth metals in the purine urolithiasis

Type of urolithiasis		**Metals concentration (μg/g calculus)**			
		Calcium		**Magnesium**	
		n	X ± SD	n	X ± SD
Simple	Urates (U)	34	611.43 ± 270.33	34	137.61 ± 91.27
Mixed	O-U	11	187 342.00 ± 52 814.00	11	412.93 ± 127.31
	U-O	6	121 416.00 ± 47 200.00	6	376.14 ± 102.19
	O-U-P	5	179 614.00 ± 50 139.00	5	969.56 ± 257.08

The analytical data of metallograms obtained by our investigations are similar with those in the literature [10, 28–31]. But, one must note that the composition of the uroconcrements and especially in metals is different from one patient to another and from one region to another. From these observations result that the difference is dependent not only on the purine metabolites (resulting from nucleoproteins) but also by the specific metallic composition of food nutrients and of the water. That is why metallomics - applied in the domain of uroconcrements biogenesis – integrate not only physiological and pathobiochemical aspects but also those related to the habitual environment (conditioned by geochemical peculiarities).

In the etiopathogeny of urolithiasis metals play an important role. They may intervene either indirectly as effectors (inhibitors-activators) of metabolic processes, or directly as substituents engaged in competing interactions owing to the difference in the solubility.

Urolithogenesis is a process which begins with the appearance of the so-called “primers” resulted by the heterogenous nucleation mechanism, involving the presence of specific lithogenic organic (urates, oxalates, cystine) or inorganic (phosphates, carbonates) components and metallic ions.

In the uroconcrement biogenesis can compete compounds with ion and/or non-ion structure. Beside these usually anionic structures there are ionic structures generated by some conditions: the pH , ionic strenght, osmolality a.o. – situations in which such forms may generate hydroxylated derivatives of purines (uric acid, xanthine, 2,8 –DHA).

To organic or inorganic compounds of uroconcrements may bond metallic ions, such as Na^+, K^+, $Ca^{2+,}$ Mg^{2+}, Zn^{2+}, Cu^{2+}, Fe^{2+}, Mn^{2+}, Pb^{2+} a.o. and non-metallic ions (NH_4^+). Though the metallic trace elements are in very small quantities they compete (obviously in a lesser degree) to the heterogenous nucleation mechanism of calculi. In the next paper (Note II) analytical data on the trace metals found in the uroconcrements studied by us will be presented.

Establishment of urolithiasis types and quantity of their metallic components are of interest not only for an accurate clinical guideline but also for the prophylaxy and metaphylaxy of urolithiasis.

CONCLUSIONS

By means of infrared spectroscopy there were established the following types of purine urolithiasis: simple - with urates (U); mixed - with oxalates-urates (O-U); urates-oxalates (U-O); oxalates-urates-phosphates (O-U-P).

The alkaline and alkaline-earth metals concentration in the simple and mixed purine urolithiasis, determined by atomic absorption spectroscopy, revealed a decrease as follows :

Ca > Na > K > Mg in case of U and O-U lithiasis
Ca > Na > Mg > K in case of U-O and O-U-P lithiasis

In mixed urolithiasis the concentration of Ca, Na, K and Mg was higher than in simple urolithiasis due to the presence of oxalates and phosphates which determine ionic bonds with the metals in uroconcrements.

EXPERIMENTAL SECTION

Samples obtainment. The study have been performed on the surgically removed or spontaneously eliminated urinary stones obtained from 172 patients admitted and treated in the Clinic of Urology Timişoara. The samples were collected during a period of 6 years.

Analytical determinations. First, in order to study the qualitative and quantitative composition of the kidney stones they were submitted to repeated washing with distilled water (to remove blood, mucous etc.), air-dried and finally powdered.

Next, the qualitative chemical composition of each urinary stone was determined by the Fourier Transform - Infrared Spectroscopy (FT-IR). For the spectra recording a JASCO FT-IR/410 spectrophotometer (Jasco, Japan), in the 400-4000 cm^{-1} wavenumber range at 4 cm^{-1} resolution, was used. The samples have been homogenized with KBr and converted in pellets using a manual 15 Ton Specac Pellet Press (Specac Ltd, U.K.). Initially there were recorded the FT-IR spectra of the chemically pure substances (presumed to be also in the composition of kidney stones) in order to create a database of „standard spectra” and afterwards the spectra of the powered kidney stones (with unknown composition). Subsequently to the obtainment of FT-IR spectra of uroconcrements the types of urolithiasis were established.

Further on by means of atomic absorption spectroscopy (AAS) the quantity of the alkaline (Na, K) and alkaline-earth (Ca, Mg) metals in the simple and mixed (binary and ternary) purine urolithiasis was determined. The concentrations of Na, K, Ca and Mg were expressed in μg/g calculus. For this investigation a PYE UNICAM apparatus Series SP 1900 was used.

Statistic evaluation. The analytical data were statistically processed by a computerized method. Mean values (X) and standard deviation (SD) of the metals concentration in the simple and mixed purine urolithiasis were determined.

REFERENCES

1. I.S. Williams, D.G. Chisholm,"Scientific Foundations of Urology", Vol. I, W. Heineman Medical Books Ltd., London, **1976**.
2. C. Borundel, A. Condacse, C.I. Rădulescu, "Hiperuricemiile", Ed. Medicală, Bucureşti, **1976**.
3. L.A. Kaplan, A.J. Pesce, S.A. Kazmierczak, „Clinical Chemistry: Theory, Analysis and correlation", 3th edition, Mosby Company, St. Louis-Baltimore-Boston-New York-London-Madrid-Toronto, **1996**.
4. F.L. Coe, A. Evan, E. Worcester, *Journal of Clinical Investigation*, **2005**, *115*, 2598.
5. F.L. Coe, J.H. Parks, "Nephrolithiasis. Pathogenesis and treatment", 2nd edition, Year Book Medical Publishers, Inc., Chicago-London-Boca Raton, **1988**.
6. P. Drăgan, Z. Garban, Gabriela Daranyi, F. Peter, Delia Popescu, *Timişoara Medicală*, **1993**, *37*, 43.
7. Z. Garban, Lucia Cristescu, Victoria Mihalca, P. Drăgan, *Timişoara Medicală*, **1981**, *26*, 54.
8. Z. Garban, Gabriela Garban, „Biochimie: Tratat Comprehensiv, Vol. III. Metabolisme", ediţia 3-a, Ed. Orizonturi Universitare, Timişoara, **2005**.
9. Y. Zhang, M. Morar, S.E. Ealick, *Cell. Mol. Life. Sci.*, **2008**, *65*, 3699.
10. W. Vahlensieck, G. Gasser (Eds.), „Pathogenese und Klinik der Harnsteine", Vol. XIII, Steinkopff Verlag, Darmstadt, **1988**.
11. O.M. Rannert, W.Y. Chan (Eds.),"Metabolism of trace metals in man", Vol.I, CRC Press Inc., Boca Raton, **1981**.
12. I. Silaghi-Dumitrescu, Z. Garban, P. Drăgan (Eds.), "Metal Elements in Environment, Medicine and Biology", Tome VIII, Publishing House Eurobit, Timişoara, **2008**.
13. W.H. Boyce, J.S. King, Jr. – *Ann. Rev. NY Acad.Sc*i., **1963**, 104, 563.
14. Z. Garban, P. Drăgan, Gisela Nemes, Gabriela Daranyi, Doina Popeţi, Livia Martoni - in "Meeting of the Federation of European Biochemical Societies: Metal ions, Proteins and Membranes", p.81, Algarve-Portugal, April 21-26, **1985**.
15. Adina Avacovici, Z. Garban, *Journal of Agroalimentary Processes and Technologies*, **2008**, *14*, 367.
16. J.E. Seegmiller, *Am. J. Med.*, **1968**, *45*, 780.
17. T. Gargah, A. Essid, A. Labassi, M. Hamzaoui, M.R. Lakhoua, *Saudi J. Kidney. Dis. Transpl.*, **2010**, *21*, 328.
18. H.A. Simmonds, *Clin. Nephrol.*, **1979**, *12*, 195.
19. P. Sreejith, K.L. Narasimhan, V. Sakhuja, *Indian. J. Nephrol.*, **2009**, *19*, 34.
20. P.L. Altman, S.D. Dittmer (Eds.), „Blood and other Body Fluids", Publ. by Federation of American Societies for Experimental Biology, Washington, **1968**.
21. R.V.E. Watts, "Chemical Diagnosis of Disease" (Brown S.S., Mitchel F.L., Young D.S., Eds.), Elsevier Amsterdam, **1979**, pp.1059-1119.

22. A. Hesse, G. Sanders, „Atlas of infrared spectra for the analysis of urinary concrements”, George Thieme Verlag, Stuttgart, **1988**.
23. J. Bellanato, “Renal Tract Stone: Metabolic Basis and Clinical practice” (Wickham J.E.A., Colibuck A., Eds.), Churchill Livingstone, New York, **1990**.
24. Gabriela Daranyi, P. Drăgan, Z. Garban, Gr. Sigartău, Adina Avacovici, S. Sarafolean, "Metal Elements in Environment, Medicine and Biology", Tome II (Garban Z., Drăgan P., Eds.), Publishing House Eurobit, Timişoara, **1997**.
25. Y. Ning, “Structural Identification of Organic Compounds with Spectroscopic Techniques”, John Wiley and Sons, New York, **2005**.
26. L. Estepa, M. Daudon, *Biospectroscopy*, **1997**, *3*, 347.
27. G.C.G. Koo – Renal colic-calculi, http://sunzi.lib.hku.hk/hkjo/view/23/2300054.pdf, **2010**.
28. A. Halabe, O. Sperling, *Miner.Electrolyte Metab*., **1994**, *20*, 424.
29. G. Capasso, P. Jaeger, W.G. Robertson, R.J. Unwin, *Curr. Pharm. Des*., **2005**, *11*, 4153.
30. D. Bazin, P. Chevallier, G. Matzen, P. Jungers, M. Daudon, *Urol. Res*., **2007**, *35*, 179.
31. I.A. Abboud, *Environ. Geochem Health*, **2008**, *30*, 11.

STUDIA UNIVERSITATIS BABEŞ-BOLYAI, CHEMIA, XLV, 2, TOM I, 2010

Dedicated to the memory of Prof. dr. Ioan Silaghi-Dumitrescu marking 60 years from his birth

PHENOL CONTAMINATED WATER REMEDIATION USING COMMERCIAL IMMOBILIZED BENTONITES AS ADSORBENTS

**MAJDIK CORNELIA, ANDRADA MĂICĂNEANU[*],
CERASELLA INDOLEAN, SILVIA BURCĂ, MARIA STANCA**

ABSTRACT. This work presents experimental results obtained in the process of phenol removal from model solutions using batch technique (magnetic stirring, 100 ml solution). As adsorbent we used five commercial bentonites immobilized in calcium alginate beads. Influences of bentonite provenience and quantity (2-10 grams), and phenol concentration (31-160 mg/L) over the process efficiency were studied. The adsorption capacity decreases in order B5 (Fort Benton) > B2 $\cong$ B3 $\geq$ B4 > B1 (BW200). Also, adsorption capacity increased with a decrease in the bentonite quantity and an increase of the initial phenol concentration. Maximum adsorption capacity was calculated to be 2.2013 mg phenol/g.

Keywords: *immobilized bentonite, alginate beads, phenol removal, adsorption*

INTRODUCTION

Water pollution is indeed of great concern since it is a major carrier of both organic and inorganic contaminants [1].

Aromatic compounds are a class of compounds regarded as ubiquitous pollutant. Many aromatic compounds exhibit carcinogenic, teratogenic or mutagenic properties [2].

Phenol is an aromatic compound that is one of common contaminants in wastewaters, being generated from petroleum and petrochemical, coal conversion, and phenol-producing industries [3].

Phenol are extensively used for the commercial production of a wide variety of resins including phenolic resins, which are used as construction materials for automobiles and appliances, epoxy resins and adhesives, and polyamides for various applications [4].

---

[*] *Universitatea Babeş-Bolyai, Facultatea de Chimie şi Inginerie Chimică, Str. Kogălniceanu Nr. 1, RO-400028 Cluj-Napoca, România, andrada@chem.ubbcluj.ro*

According to Romanian legislation the maximum allowable concentration of phenol in surface waters and municipal sewer system is 0.3 and 30 mg/L, respectively [5], therefore elimination of phenol becomes a necessity in order to preserve water quality.

The most common methods used for removal of phenol from industrial effluents include stripping, solvent extraction, chemical oxidation (using O_3, H_2O_2 and ClO_2), incineration, reverse osmosis and irradiation, ion exchange, biodegradation and adsorption methods [6-8]. Out of all these methods, adsorption has been known to be one of the most commonly used treatment methods for removal of phenol from industrial effluents, by virtue of its cost-effectiveness as well as efficiency [9].

Many of water contaminants can be removed by adsorption using natural and synthetic adsorbents. Due to their excellent adsorption properties, clay minerals are widely used in environmental applications. The removal of phenol is a good example for these applications [10].

There are a number of papers in the literature which deals with the removal of phenol by unmodified and modified (acid treated, organobentonites) clays [11-14]. All studies concluded that these types of materials can successfully remove phenol from aqueous solutions, due to their high specific surface area, and their chemical and mechanical stability.

Bentonite consists essentially of clay minerals of the smectite (montmorillonite) group and has a wide range of industrial applications including clarification of edible liquids (wine, for example) and mineral oils, paints, cosmetics and pharmaceuticals.

The abundance of bentonite in most continents of the world and its low cost make it a strong candidate as an adsorbent for the removal of many pollutants and wastewater remediation [3].

The aim of this work was to investigate, experimentally, the potential of five commercial bentonites used as beads (immobilized in calcium alginate) to adsorb phenol from aqueous solutions, in batch conditions.

RESULTS AND DISCUSSION

Bentonite provenience

In the first stage of the experiment, phenol adsorption was realised in a batch reactor with immobile phases using all five bentonites immobilized in calcium alginate beads. This experiment was performed in order to choose between the available bentonites the most effective one to continue the phenol adsorption study. The obtained results are presented in terms of phenol concentration evolution, figure 1, adsorption efficiency, figure 2, and adsorption capacity, figures 3 and 4, for the same quantity of bentonite present in the beads (8g) and the same phenol initial concentration (103.77 mg/L).

From figure 1 it can be observed that in the first 24 hours from the beginning of the experiment the highest quantity of phenol is removed. The highest drop in the concentration was observed for B5 sample, to 44 mg phenol/L from the initial 103.77 mg/L. The adsorption equilibrium was reached in 48 hours for all bentonite samples.

Figure 2 presents the evolution in time of adsorption efficiencies for all bentonite samples. Adsorption efficiency increases progressively until equilibrium is reached. Maximum values for adsorption efficiency are increasing from 12.12% obtained in case of B1 sample to 66.67% obtained in case of B5 sample. The adsorption efficiency decreases in order B5 > B2 $\cong$ B3 $\geq$ B4 > B1.

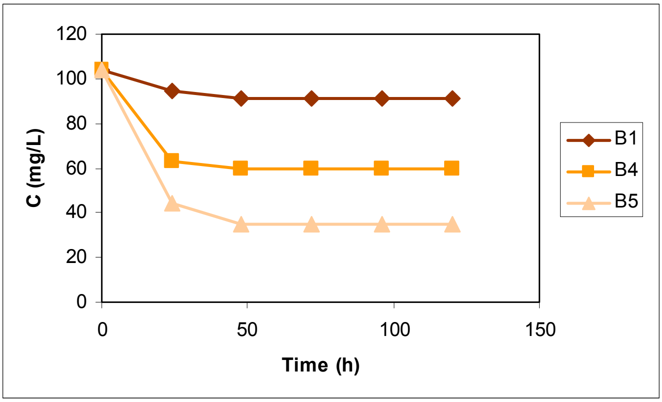

Figure 1. Time evolution of phenol concentration for three of the considered bentonites (8g bentonite, C_i = 103.77 mg phenol/L).

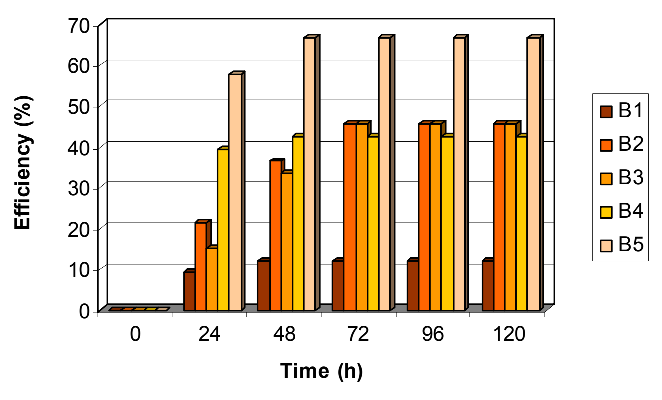

Figure 2. Influence of the bentonite type over the time evolution of adsorption efficiency for all considered bentonites (8g bentonite, C_i = 103.77 mg phenol/L).

Evolution of the adsorption process was also followed in terms of adsorption capacity, figure 3. Evolution of phenol adsorption capacity in time (not shown), follows a trend inverse proportional with concentration evolution. Therefore the adsorption capacity increases in time until equilibrium is reached, with a maximum increase after first 24 hours. Equilibrium adsorption capacities are presented in figure 3. Values between 0.1572 to 0.8648 mg phenol/g bentonite were calculated for B1 and B5 samples, respectively. The adsorption capacity decreases in the same order B5 > B2 ≅ B3 ≥ B4 > B1.

B5 bentonite sample, activated bentonite with an elevated montmorillonite content (up to 90%) and high specific surface area (around 750 m^2/g), was the most efficient sample by comparison with fibrous, powder and protein containing bentonite [15]. The activation procedure was not specified by the producer.

Taking into account the fact that B5 bentonite sample proved to be the most efficient one in the phenol adsorption process, this sample was next considered for the rest of adsorption experiments.

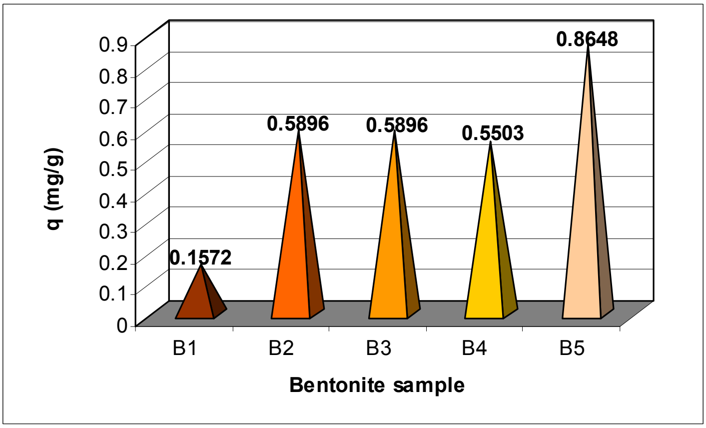

Figure 3. Adsorption capacity values for phenol removal in batch conditions (immobile phases) for all considered bentonites (8g bentonite, C_i = 103.77 mg phenol/L).

For B5 bentonite sample were also performed experiments in batch conditions under magnetic stirring (mobile phases) using the same conditions (8g and 103.77 mg phenol/L). The adsorption capacity determined in this case was calculated to be the same, but in this case equilibrium was reached in 90 minutes by comparison with 48 hours for the previous experiment. All the experiments realised from now on are realised using a batch reactor and magnetic stirring.

Bentonite quantity

For a better use of the adsorbent (optimisation of the adsorbent quantity) the next stage of the experiment was to study the evolution of the adsorption process for different quantities of B5 bentonite immobilized in calcium alginate beads (2-10g) at different initial concentrations of phenol in solution (31-160 mg/L). In figures 5 and 6 are presented the results obtained for C_i = 31.45 mg phenol/L and all considered bentonite quantities – 2, 4, 8 and 10g.

To have a more complete image of the adsorption process on the chosen bentonite sample, adsorption capacities were calculated in order to include in the numerical results also the bentonite quantities we used, figure 4. From the values in figure 4, it is easy to observe that as the bentonite quantity increases, the adsorption capacity decreases. Therefore if an adsorption process of this type is considered for practical uses, it will be necessary to take into consideration the initial phenol concentration and water quantity that need to be treated, in order to establish the appropriate bentonite quantity. Also adsorption efficiency should be calculated and evaluated along with bentonite quantity from the economic point of view. As our results show, an increase of the bentonite quantity will lead to an increase of adsorption efficiency, which will lead to an increase of the operating cost.

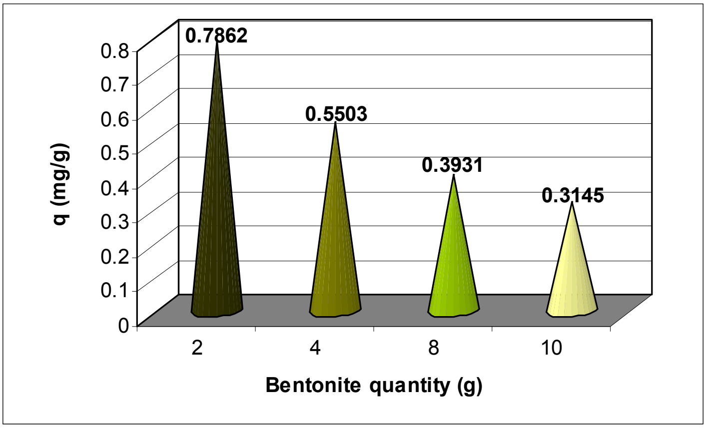

Figure 4. Adsorption capacity values for phenol removal in batch conditions (mobile phases) for different bentonite quantities (825 rpm, B5 bentonite, C_i = 31.45 mg phenol/L).

Phenol concentration in aqueous solution

In the final part of the study, the influence of the initial phenol concentration over the adsorption process was studied. Were used solutions containing between 31 and 160 mg phenol/L and as adsorbent 8g of B5 bentonite immobilized in calcium alginate beads.

Influence of phenol initial concentration over the evolution of phenol concentration in time is presented in figure 5. As the initial concentration decreases, the quantity of phenol retained in the first 15 minutes decreases also due to the smaller difference that exist between the concentration of phenol on the adsorbent surface and in the solution. Therefore the adsorption capacity of the immobilized B5, increases with an increase of the phenol initial concentration, from 0.5503 to 2.2013 mg phenol/L, figure 6. Equilibrium was reached after maximum 120 minutes for all five studied concentrations.

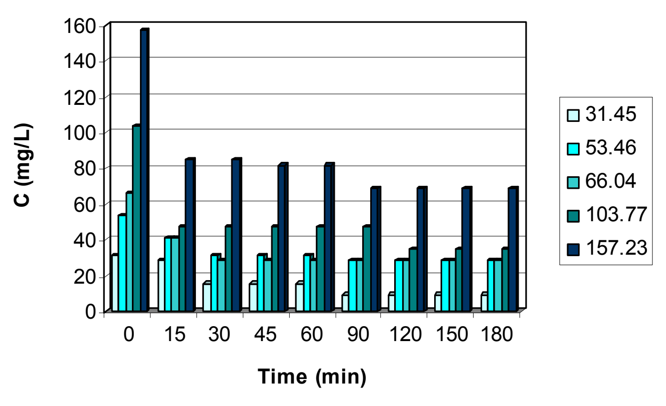

Figure 5. Influence of phenol initial concentration over the time evolution of the concentration (825 rpm, B5 bentonite, 8g).

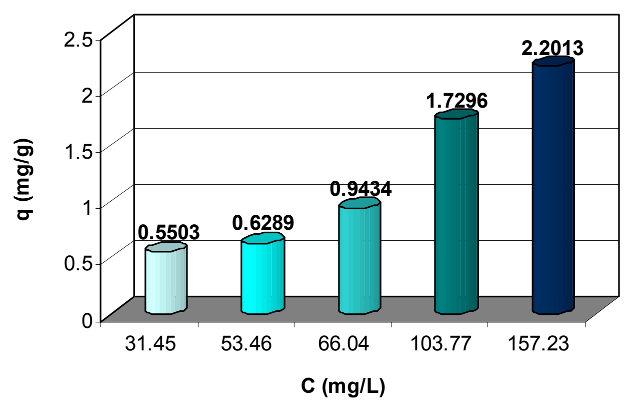

Figure 6. Adsorption capacity values for phenol removal in batch conditions (mobile phases) for different initial concentrations of phenol (825 rpm, B5 bentonite, 8g).

CONCLUSIONS

This work presents experimental results obtained in the process of phenol removal from model solutions using batch technique (magnetic stirring, 100 ml solution).

As adsorbent we used five commercial bentonites immobilized in calcium alginate beads. Influences of bentonite provenience and quantity (2-10 grams), and phenol concentration (31-160 mg/L) over the process efficiency were studied.

The adsorption capacity decreases in order B5 (Fort Benton) > B2 ≅ B3 ≥ B4 > B1 (BW200). Also, adsorption capacity increased with a decrease in the bentonite quantity and an increase of the initial phenol concentration. Maximum adsorption capacity was calculated to be 2.2013 mg phenol/g.

EXPERIMENTAL SECTION

We used five commercial sodium bentonites: BW 200 – powder sodium bentonite (B1), Gelbenton – purified fibrous bentonite (B2), Evergel – bentonite containing caseine, gelatine and egg albumine (B3), Nucleobent – powder sodium bentonite (B4) and Fort Benton Wyoming – activated bentonite (B5) purchased from Interker-wein Kft. (Hungary). The bentonite samples were used as powder, (d < 0.2 mm), without any chemical treatment. All chemicals used in this study were analytical reagent grade (phenol, alginic acid sodium salt, ethanol and $CaCl_2$).

In order to obtain the bentonite immobilized in alginate beads we used the cross-linking procedure with calcium alginate [16-19]. Thus, various quantities of bentonite (2, 4, 6, 8, 10 g) were suspended in 50-200 ml distilled water (water quantity increases with the bentonite quantity). This suspension was next blended with a mixture formed from 1 g Na-alginate and 2 ml ethanol. The mixture was then dropped with a peristaltic pump into a 0.2 M $CaCl_2$ solution. During this process, alginate-bentonite drops were gelled into beads with a diameter of 4.0 ± 0.2 mm. The Ca-alginate immobilized adsorbent beads were stored in 0.2 M $CaCl_2$ solution at 4°C for 1 hour to cure and to form the cross-linking bonds. The beads were rinsed with distilled water for remove excess of calcium ions and stored at 4°C prior to use.

For phenol adsorption study we used model solutions containing between 31 and 160 mg phenol/L. Concentration of phenol in solution was determined using a Jenway 6305 UV/VIS spectrophotometer (UV, 270 nm) after a preliminary centrifugation (14000 rpm, Mikro 200R Hettich centrifuge).

Phenol adsorption process was realized in a batch reactor with immobile and mobile phases (phenol aqueous solution – immobilized bentonite) using 100 ml phenol solution of different concentrations, in which Ca-alginate bentonite beads obtained from the desired quantity of adsorbent were suspended. For the batch experiments realized with mobile phases, we used a magnetic stirrer operated at 825 rpm.

In order to determine the exact concentration of phenol and establish the evolution of the removal process, in batch conditions, samples of 0.5 mL (dilution in each case was 50) from the supernatant were collected at different time intervals, every 24 hours when we used immobile phases, and every 15 minutes for the first hour and next every 30 minutes when we used mobile phases, until equilibrium was reached.

We studied the influence of the bentonite type and quantity, and phenol concentration in solution over the process efficiency in batch conditions. The experiments were carried out at room temperature (20°C) and without any modification of the pH value of the phenol aqueous solution.

The amount of phenol adsorbed under different conditions was calculated as adsorption capacities Q, (mg/g), while the effectiveness of the adsorption process was expressed as adsorption efficiencies E,(%); the calculated values of adsorption efficiencies and adsorption capacities should be regarded according to the precision of the determination methods we used [20].

REFERENCES

1. S. Froehner, R. Fernandez Martins, W. Furukawa, M.R. Errera, *Water Air and Soil Pollution*, **2009**, *199*, 107.
2. G. Zhao, L. Zhou, Y. Li, X. Liu, X. Ren, X. G. Liu, *Journal of Hazardous Materials,* **2009**, *169*, 402.
3. F.A. Banat, B. Al-Bashir, S. Al-Asheh, O. Hayajneh, *Environmental Pollution*, **2000**, *107*, 391.
4. H.H. Fang, O. Chen, *Water Research*, **1997**, *31*, 2229.
5. *** Romanian Government decisions, HG 188/2002 modified with HG 352/2005.
6. K.H. Lanouette, *Chemical Engineering,* **1977**, *84*, 99.
7. J.K. Spiker, D.L. Crawford, E.J. Thiel, *Applied Microbiology and Biotechnology*, **1992**, *37*, 518.
8. V. Srihari, S. Madhan Babu, A. Das, *Journal of Applied Science*, **2006**, *6*, 47.
9. B. Subramanyam, A. Das, *Desalination*, **2009**, *249*, 914.
10. S. Yapar, V. Özbudak, A. Dias, A. Lopes, *Journal of Hazardous Materials*, **2005**, *B121*, 135.
11. J.-Q. Jiang, C. Cooper, S. Ouki, *Chemosphere*, **2002**, *47*, 711.

12. S. Al-Ashed, F. Banat, L. Abu-Aitah, *Separation and Purification Technology*, **2003**, *33*, 1.
13. Y.-H. Shen, *Colloids and Surface A: Physicochemical and Engineering Aspects*, **2004**, *232*, 143.
14. N. Yilmaz, S. Yapar, *Applied Clay Science*, **2004**, *27*, 223.
15. http://www.aquatechnologies.com/info_bentonite_clay.htm
16. T.S. Pathak, J.-Ho Yun, J. Lee, K.-J. Paeng, *Carbohydrate Polymers*, **2010**, *article in press*, DOI:10.1016/j.carbpol.2010.03.025.
17. S. Peretz, O. Cinteză, *Colloids and Surfaces A: Physicochemical and Engineering Aspects*, **2008**, *319*, 165.
18. S.K. Papageorgiou, F.K. Katsaros, E.P. Kouvelos, J.W. Nolan, H. Le, *Journal of Hazardous Materials*, **2006**, *137*, 1765.
19. P. Ferreira Almeida, A. J. Almeida, *Journal of Controlled Release*, **2004**, *97*, 31.
20. H. Bedelean, A. Măicăneanu, S. Burcă, M. Stanca, *Studia Universitatis Babeş-Bolyai, Geologia*, **2010**, *55*, 9.

STUDIA UNIVERSITATIS BABEŞ-BOLYAI, CHEMIA, XLV, 2, TOM I, 2010

Dedicated to the memory of Prof. dr. Ioan Silaghi-Dumitrescu marking 60 years from his birth

GEOMETRY OPTIMIZATION AND COMPARATIVE DFT STUDY OF (DIETHYLENETRIAMINE)BIS(THEOPHYLLINATO)ZINC(II) DIHYDRATE

BÉLA MIHÁLY[*], ATTILA-ZSOLT KUN, EDIT FORIZS,
ADRIAN PATRUT, IOAN SILAGHI-DUMITRESCU

ABSTRACT. The paper reports on the molecular modelling of $[Zn(th)_2(dien)] \cdot 2H_2O$, which serves as the model compound for assessing metal–nucleobase interactions. The X-ray crystallographic data was completed by *ab initio* density functional theory. Structural parameters of the complex were investigated by using different methods: the unrestricted Becke three-parameter hybrid exchange functional, combined with the Lee–Yang–Parr correlation functional (B3LYP), the 6-311G(d,p), LANL2DZ, CRENBL, and DZVP basis sets applied for geometry optimizations.

***Keywords**: DFT, diethylenetriamine, theophylline, mixed ligand complexes, molecular modelling*

INTRODUCTION

The chemistry of metal complexes of theophylline (Scheme 1) has been extensively studied, mainly because of the capacity of these complexes to serve as model compounds for assessing the interaction between metal ions and oxopurine bases of nucleic acids. Previous research revealed that theophylline, *i.e.,* 1,3-dimethyl-2,6-dioxo-purine, is able to coordinate metal ions acting as a monodentate ligand *via* N7 in alkaline conditions [1–3] and *via* N9 in neutral conditions [4]; it can also form organometallic compounds *via* the C8 atom [5].

Several compounds in which theophylline acts as a bidentate ligand, forming N7/O6 chelates well also reported [6].

---

[*] *Babeş-Bolyai University, Faculty of Chemistry and Chemical Engineering, RO-400028 Cluj-Napoca, Romania, E-mail: mb15@chem.ubbcluj.ro*

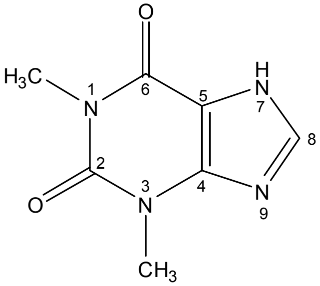

Scheme 1

In our research on coordination compounds with theophylline and various amines we reported the synthesis and characterization of several new mixed ligand complexes of Cu(II), Co(II) and Ni(II), containing the theophyllinato anion and 2-aminoethanol or benzylamine as co-ligands [7–10]. The synthesis of $[Zn(th)_2(dien)]\cdot 2H_2O$ and the corresponding X-Ray structure was also presented [11].

The aim of this work was the calculation of $[Zn(th)_2(dien)]\cdot 2H_2O$, at different levels of theory, in order to evaluate their accuracy by comparing them to experimental data. Results of geometry optimizations were in good agreement with the experimental values.

RESULTS AND DISCUSSION

Computational details

Geometry optimizations were performed by using the density functional theory (DFT) using the unrestricted Becke three-parameter hybrid exchange functional, combined with the Lee–Yang–Parr correlation functional (B3LYP). The 6-311G(d,p) [12] full electron and LANL2DZ (Los Alamos National Laboratory 2 Double Zeta) [13, 14] effective core potential (ECP) basis sets are internal, while the CRENBL ECP (Christiansen's effective core potential) [15, 16] and DZVP (Double Zeta Valence with Polarization) [17] full electron basis sets were obtained from the Basis Set Exchange webpage [18]. The *Gaussian09* electronic structure program package was used for calculations [19]. Optimizations were performed with the standard convergency criteria of *Gaussian09*, followed by vibrational analysis to make certain that the obtained geometries are true minima.

Optimized geometries

In the complex under study, the geometry around the pentacoordinated Zn(II) is a distorted trigonal bipyramide, consisting of three N atoms of the diethylenetriamine ligand and the N7 atom of each of the two theophyllinate moieties. The Zn–N_a distance found in the complex is longer than the Zn–N_e bond, corresponding to the typical appropriate distances found in trigonal bypiramidal structures. One of the two water molecules is positioned on the coordination axis, but relatively far from the central Zn(II) atom; consequently, it can be considered as being located outside the proper coordination sphere of Zn(II).

The molecular structure of [Zn(th)$_2$(dien)] with the water molecule, closer to the metal ion, was optimized in the gaseous phase. The final geometries and the structure determined by X-Ray diffraction are displayed in Figure 1. In all cases there are two hydrogen bonds present in the optimized structures; one between the C6=O of the equatorial theophylline and the N_2–H of dien moiety and the other formed between the C6=O of the axial theophylline and the water molecule.

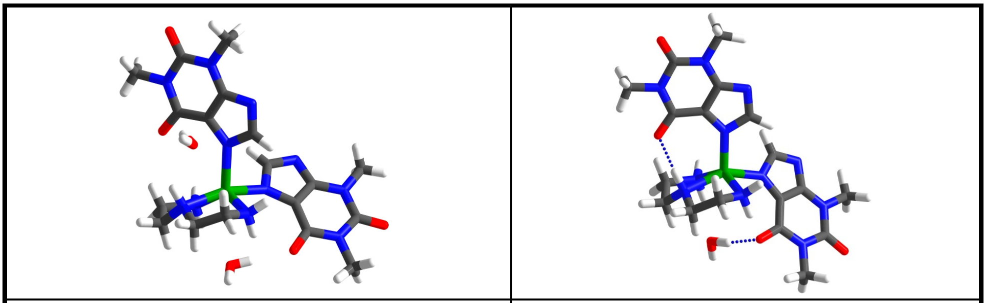

X-Ray molecular structure | **Calculated (B3LYP/6-311G**)**

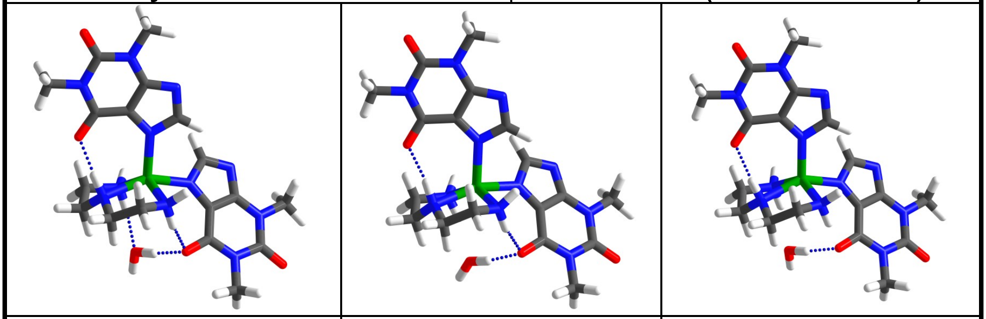

Calculated (B3LYP/LANL2DZ) | **Calculated (B3LYP/CRENBL ECP)** | **Calculated (B3LYP/DZVP)**

Figure 1. X-Ray molecular structure of [Zn(th)$_2$(dien)]·2H_2O, and the corresponding optimized structures.
(Color code: C – grey, N – blue, O – red, H – white, Zn – green)

The main geometrical parameters, optimized at different levels of theory, are listed in Table 1. Theoretical calculations revealed that the majority of optimized bond lengths are slightly longer than the experimental values.

This can be also considered as a consequence of having performed the theoretical calculations for an isolated molecule in gaseous phase, while the experimental results were recorded for the compound in solid state. Hydrogen bonds formation also contributes to the changes in geometry.

Our results suggest that the differences of bond lengths and bond angles between the experimental data and the predicted values are greater when using the DZVP basis set. According to the calculated values, the water molecule considered for optimization is located outside the coordination sphere. This statement is valid for all calculation techniques employed. Therefore, the Zn(II) atom is pentacoordinated, having distorted trigonal bipyramide geometry; hence, it cannot be considered as being hexacoordinated.

The mean error for angle values is greater, when using the DZVP basis set (see Table 1).

Table 1. Experimental and calculated geometry parameters.

	X-Ray	6-311G(d,p)	LANL2DZ	CRENBL ECP	DZVP
Distances (Å)					
Zn–N_a	2.120	2.087	2.159	2.127	2.110
Zn–N_e	2.074	2.031	2.097	2.142	2.049
Zn–N_1	2.084	2.161	2.183	2.204	2.199
Zn–N_2	2.220	2.215	2.242	2.246	2.244
Zn–N_3	2.092	2.175	2.201	2.231	2.207
Zn–O_w	3.190	3.735	3.639	3.592	3.819
Angles (°)					
N_a–Zn–N_e	95.5	104.2	102.0	96.1	105.3
N_a–Zn–N_1	93.3	91.2	90.8	92.1	90.8
N_a–Zn–N_2	165.1	151.9	154.1	161.7	149.6
N_a–Zn–N_3	97.2	94.0	92.9	95.2	93.9
N_e–Zn–N_1	119.6	114.9	118.5	116.9	115.5
N_e–Zn–N_3	101.9	101.2	101.8	96.8	101.8
N_1–Zn–N_3	135.9	140.9	137.8	144.6	139.5
N_e–Zn–O_w	171.6	166.7	170.0	171.8	167.0

N_a and N_e represent the N7 donor atom of theophylline ligands. The terminal N_1 and N_3 atoms of the dien ligand are in the equatorial plane, while the middle N_2 atom is located in an axial position. O_w designates the O atom of the nearer water molecule, opposite to the N_e position.

Reported data are in good agreement with the experimental ones, revealing that the CRENBL ECP and the B3LYP/LANL2DZ level of theory are suitable for the theoretical study of the system described above.

Vibrational analysis

Vibrational frequencies, calculated at the B3LYP/6-311G(d,p) level, were scaled by the typical factor 0.96. Several selected primary calculated harmonic frequencies are listed in Table 2, in comparison with the experimental data. The Gabedit program [20] was used for assigning the calculated harmonic frequencies.

The calculated values of the predicted harmonic vibrational frequencies are relatively close to the frequencies found in the experimental FTIR spectrum of the complex. The largest deviations occur for the B3LYP/CRENBL level of the theory.

It can be stated that the scaled frequencies of the DFT calculation are close to the corresponding FTIR vibration values, and that the DFT B3LYP method can predict accurately the vibrational frequencies for the system reported here.

Table 2. Comparison of the observed and calculated vibrational spectra.

Assignment	Exp. IR (KBr)	Calcd. (B3LYP/ 6-311G(d,p))	Calcd. (B3LYP/ LANL2DZ)	Calcd. (B3LYP/ CRENBL ECP)	Calcd. (B3LYP/ DZVP)
O−H str.	3496.31	3879.32 3528.82	3807.36	4216.31 3595.80	3828.73 3507.71
N−H str.	3353.6 3318.89 3272.61	3398.88 3391.68	3563.28 3559.56 3364.38 3298.10 3275.40	3739.65 3737.18 3492.71 3492.71–3451.96	3548.90 3548.64 3405.40 3393.47 3359.62
C−H str.	2940.91	3232.66–3005.89	3306.03 3296.73 3216.05–3022.41	3207.59–3058.50	3254.30–3027.60
C=O str.	1685.48 1664.27 1635.34	1758.63 1755.57	1668.08 1663.69	1864.99 1861.81 1787.50	1747.37 1744.49

CONCLUSIONS

Our calculations revealed that the utilized techniques were efficient in optimizing structural geometries of systems based on organic molecules and transition metal ions, such as Zn(II). The best calculation precision of the geometry parameters was obtained for the B3LYP/CRENBL ECP and B3LYP/LANL2DZ level of the theory.

ACKNOWLEDGMENTS

Calculations were performed at the Centre for Molecular Modelling and Quantum Computational Chemistry (CMMCCC) facilities in the framework of the CAPACITATI, 130/14.09.07 Category I, P1 Programme.

REFERENCES

1. N. S. Begum, H. Manohar, *Polyhedron*, **1994**, *13*, 307.
2. W. J. Birdsall, M. S. Zitzman, *J. Inorg. Nucl. Chem.*, **1979**, *41*, 116.
3. W. J. Birdsall, *Inorg. Chim. Acta*, **1985**, *99*, 59.
4. E. M. Griffith, E. L. Amma, *J. Chem. Soc., Chem. Commun.,* **1979***, 322.*
5. A. Romerosa, J. Suarez-Varela, M. A. Hidalgo, J. C. Avila-Roson, E. Colacio, *Inorg. Chem.*, **1997**, *36*, 3784.
6. D. J. Szalda, T. J. Kistenmacher, L. *G.* Marzilli, *J. Am. Chem. Soc.*, **1976**, *98 (26)*, 8371.
7. P. Bombicz, J. Madarász, E. Forizs, I. Foch, *Polyhedron*, **1997**, *16*, 3601.
8. S. Gál, J. Madarász, E. Forizs, I. Labádi, V. Izvekov, G. Pokol, *J. Therm. Anal. Cal.*, **1998**, *53*, 343.
9. E. Forizs, L. David, O. Cozar, V. Chiş, G. Damian, J. Csibi, *J. Mol. Struct.*, **1999**, *482*, 143.
10. B. Mihály, E. Forizs, I. Silaghi-Dumitrescu, *Studia Univ. Babes-Bolyai, Chemia,* **2007**, *LII*, *4*, 111.
11. B. Mihály, E. Forizs, A.-Z. Kun, I. Silaghi-Dumitrescu, *Acta Cryst.*, **2009**, *E65*, m579.
12. L. A. Curtiss, M. P. McGrath, J-P. Blandeau, N. E. Davis, R. C. Binning, Jr. L. Radom, *J. Chem. Phys.,* **1995**, *103*, 6104.
13. T. H. Dunning Jr., P. J. Hay, “Methods of Electronic Structure Theory”, Ed. H. F. Schaefer III., Plenum, New York, **1977**.
14. P. J. Hay, W. R. Wadt, *J. Chem. Phys.*, **1985**, *82*, 284.
15. M. M. Hurley, L. F. Pacios, P. A. Christiansen, R. B. Ross, W. C. J. Ermler, *Chem. Phys.*, **1986**, *84*, 6840.
16. L. A. LaJohn, P. A. Christiansen, R. B. Ross, T. Atashroo, W. C. J. Ermler, *Chem. Phys.*, **1987**, *87*, 2812.
17. N. Godbout, D. R. Salahub, J. Andzelm, E. Wimmer, *Can. J. Chem.*, **1992**, *70*, 560.
18. K. L. Schuchardt, B. T. Didier, T. Elsethagen, L. Sun, V. Gurumoorthi, J. Chase, J. Li, T. L. Windus, *J. Chem. Inf. Model.*, **2007**, *47(3)*, 1045. https://bse.pnl.gov/bse/portal

19. M. J. Frisch, G. W. Trucks, H. B. Schlegel, G. E. Scuseria, M. A. Robb, J. R. Cheeseman, G. Scalmani, V. Barone, B. Mennucci, G. A. Petersson, H. Nakatsuji, M. Caricato, X. Li, H. P. Hratchian, A. F. Izmaylov, J. Bloino, G. Zheng, J. L. Sonnenberg, M. Hada, M. Ehara, K. Toyota, R. Fukuda, J. Hasegawa, M. Ishida, T. Nakajima, Y. Honda, O. Kitao, H. Nakai, T. Vreven, J. A. Montgomery, Jr., J. E. Peralta, F. Ogliaro, M. Bearpark, J. J. Heyd, E. Brothers, K. N. Kudin, V. N. Staroverov, R. Kobayashi, J. Normand, K. Raghavachari, A. Rendell, J. C. Burant, S. S. Iyengar, J. Tomasi, M. Cossi, N. Rega, J. M. Millam, M. Klene, J. E. Knox, J. B. Cross, V. Bakken, C. Adamo, J. Jaramillo, R. Gomperts, R. E. Stratmann, O. Yazyev, A. J. Austin, R. Cammi, C. Pomelli, J. W. Ochterski, R. L. Martin, K. Morokuma, V. G. Zakrzewski, G. A. Voth, P. Salvador, J. J. Dannenberg, S. Dapprich, A. D. Daniels, O. Farkas, J. B. Foresman, J. V. Ortiz, J. Cioslowski, D. J. Fox, Gaussian 09, Revision A.02, Gaussian, Inc., Wallingford CT, **2009**.
20. A. R. Allouche, Gabedit 2.2.11., http://gabedit.sourceforge.net

STUDIA UNIVERSITATIS BABEŞ-BOLYAI, CHEMIA, XLV, 2, TOM I, 2010

Dedicated to the memory of Prof. dr. Ioan Silaghi-Dumitrescu marking 60 years from his birth

STUDIES ON THE EUROPIUM AND PALLADIUM EXTRACTION WITH SOME CALIX[6]ARENE DERIVATIVES

ALINA SAPONAR[a, *], ELISABETH-JEANNE POPOVICI[a],
IOANA PERHAIŢA[a], NICOLAE POPOVICI[a] AND
IOAN SILAGHI-DUMITRESCU[b]

ABSTRACT. The capability of *p-tert*-butyl calix[6]arene functionalized at the lower rim with 2-butenyl, ethyl acetate and/or N,N-diethylacetamide groups to extract Pd^{2+} and Eu^{3+} ions from aqueous medium have been investigated. Good extraction yield was obtained for calix[6]arene derivatives functionalized with *tri-* and *hexa-* ethylacetate and *tri-* and *hexa-* N,N-diethylacetamide groups. It vas revealed that the half or total substituted *p-tert*-butyl calix[6]arene ester derivatives present interest as liquid-liquid extraction reagents for precious metal and rare earth ions.

***Keywords**: Calixarene, liquid-liquid extraction, metal ions.*

INTRODUCTION

The development of efficient extraction agents to remove metal ions from both organic and aqueous effluents for either safe disposal or recycling has motivated research into the coordination properties of calixarene-based ligands.

Calixarenes are macrocycles made up of phenolic units linked by methylene bridges with host-guest properties. They are known as inexpensive, chemically stable molecular networks/systems utilizable as selective complexing agents for neutral molecules and ions [1-10]. Functionalised calix[n]arene (n = 4, 6, 8) have received much attention because of their increased molecular and ion binding capability revealed also by their ability to transport metal cations across organic membranes and to behave as metal carriers.

---

[a] *Raluca Ripan Institute for Research in Chemistry, Babes Bolyai University, 400294, Cluj-Napoca, Romania,* salina@chem.ubbcluj.ro*

[b] *Faculty of Chemistry and Chemical Engineering, Babes-Bolyai University, 400084, Cluj-Napoca, Romania.*

Selective and efficient cation receptors can be prepared by functionalization of the parent calixarene with metal coordinating groups. Usually, this is performed at the “narrow rim”, because of the easy synthesis of a great number of derivatives, which allows comparing the impact of some factors on the extraction behavior (i.e. cavity size, conformation, functional groups) and the flexibility to design a proper ligand to selectively recognize metal ions [11-23]. Liquid-liquid extraction experiments were carried out to recover metals from aqueous solution using as extractants calix[6]arene derivatives dissolved in organic solvents (i.e. chloroform, dichloromethane, toluene, acetonitrile), allowing the exploitation of the calixarene’s cone-shape and the chelating ring of oxygen, nitrogen and phosphorus donor atoms that encircle the guests.

Herein we present our studies referring to the extraction of some rare earth and precious metals, using the parent calix[6]arene and some new calix[6]arene derivatives obtained by functionalization at the narrow rim with ester and/or amido and/or alkenyl donor groups.

In this respect, ten calixarene- based compounds were used as extracting agents i.e. *p-tert*-butyl calix[6]arene and *p-tert*-butyl calix[6]arene grafted with two, three and four E-2-butenyl groups, three and six ethylacetate groups, three and six N,N-diethylacetamide groups, three 2-butenyl and three ethylacetate groups and three 2-butenyl and three N,N-diethylacetamide groups, respectively. Their capability to act as extraction reagents for Pd^{2+} and Eu^{3+} ions was investigated.

RESULTS AND DISCUSSION

A series of nine ester, amido and/or alkenyl calix[n]arene derivatives were tested as extracting reagent for precious metal and rare earth ions, in comparison with the parent calixarene (Figure 1).

The following calixarene-based compounds were used as extracting reagents: *p-tert*-butyl-calix[6]arene (**C6**), *bis*-2-butenyl-calix[6]arene (**C6Cr2**), *tris*-2-butenyl-calix[6]arene (**C6Cr3**), *tetra*-2-butenyl-calix[6]arene (**C6Cr4**), *tris*-ethylacetate-calix[6]arene (**C6Es3**), *tris*-N,N-diethylacetamide- calix[6]arene (**C6Am3**), *hexa*-ethylacetate-calix[6]arene (**C6Es6**), *hexa*-N,N-diethylacetamide-calix[6]arene (**C6Am6**), *tris*-N,N-diethylacetamide-*tris*-2-butenyl-calix[6]arene (**C6Am3Cr3**) and *tris*-ethylacetate-*tris*-2-butenyl-calix[6]arene (**C6Es3Cr3**).

Extraction was performed using 5-10 $x10^{-4}$ M aqueous solution of $PdCl_2$ or $Eu(NO_3)_3$ and $1x10^{-3}$ M solution of calixarene (Cx) in $CHCl_3$. Extraction yield was determined by monitoring the concentration of palladium or europium from the aqueous solutions, using Inductively Coupled Plasma Optical Emission Spectrometry.

Extraction of Pd^{2+} ions

The capability of *p-tert*-butyl calix[6]arene derivatives to extract Pd^{2+} ions was determined by liquid-liquid extraction experiments that were performed using equal volumes and equal concentrations of metal ions and calixarenes (Pd^{2+}:Cx = 1 :1), and a variable pH of the aqueous medium (Figure 2).

The extraction capability of the different calixarene-based compounds, at pH=2.5, varies between ~54 % for **C6Am6** and ~73% for **C6Es6.** *p-tert*-butyl calix[6]arene **C6** shows an extraction yield of 65%.

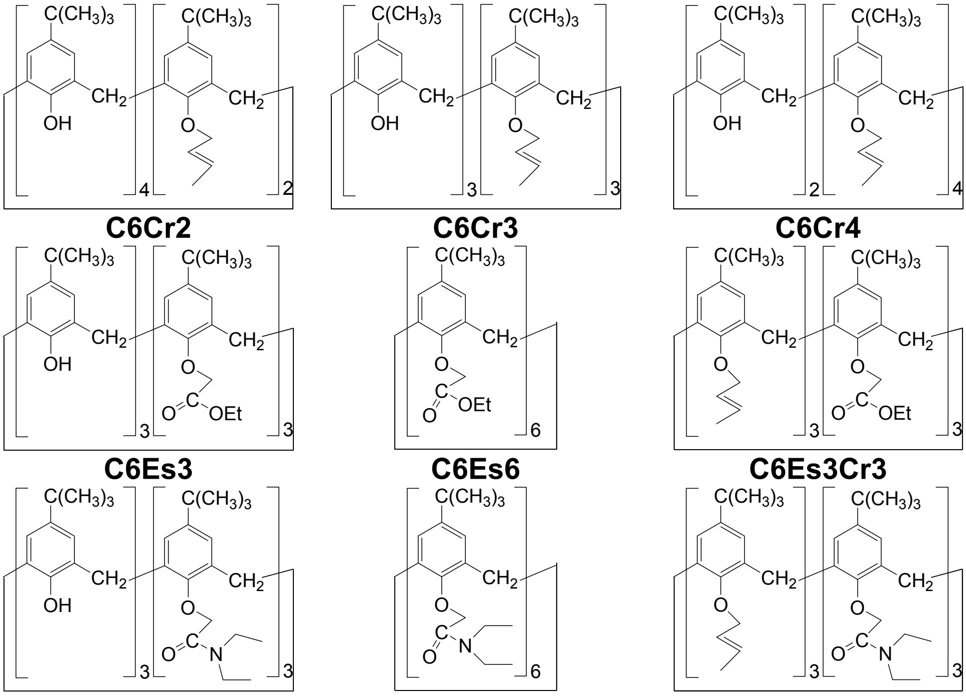

C6Cr2 **C6Cr3** **C6Cr4**

C6Es3 **C6Es6** **C6Es3Cr3**

C6Am3 **C6Am6** **C6Am3Cr3**

Figure 1. The calixarene derivatives used as extracting agents

The grafting of two or three alkenyl- as well as four or six amido-groups decreases the yield as compared with the parent calixarene. Favourable effect is shown by the functionalisation with ester groups. The highest extraction yield i.e. over 70 % is shown by calixarene-derivatives with the highest level of functionalisation i.e. compounds **C6Am3Cr3**, **C6Cr4** and **C6Es6**.

The extraction yield of the Pd^{2+} ions with calixarene-based compounds depends on the acidity of the aqueous medium. Excepting the *hexa*-ester calix[6]arene derivative, extraction yield from aqueous solutions with pH=4.1 is relatively low (under 60%). The highest extraction yield was obtained for **C6Es6** derivatives, namely 72.6% at pH=2.5 and 75.8% at pH = 4.1, respectively.

By comparing the total functionalized calixarene with the half substituted compounds, it can be concluded that, at pH=2.5, the *hexa* functionalized ester derivative (**C6Es6**) is more efficient as extractant than the *tri* functionalized one (**C6Es3**).

The capability of calixarene-based compounds to extract palladium ions in well defined extraction conditions can be estimated by the ratio ***r*** representing the ratio between the mol number of metal ion and calixarene.

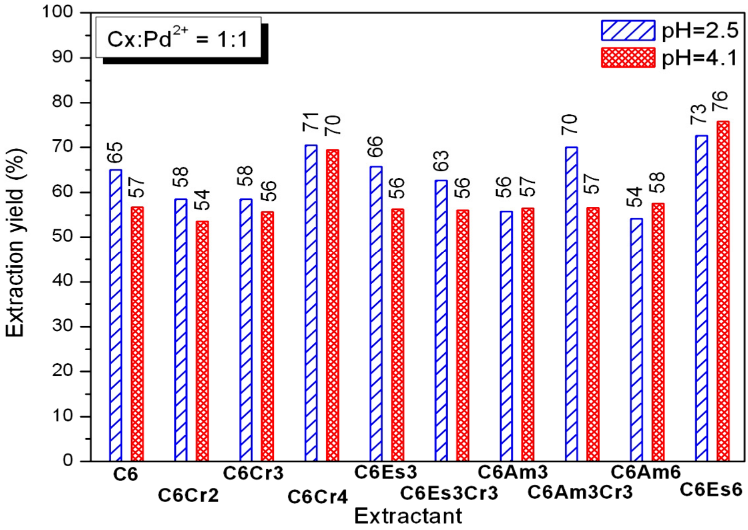

Figure 2. Variation of the extraction yield of Pd^{2+} from solutions with variable pH, using different calixarene-based compounds (c_{Cx}=1x 10^{-3}mol/l; c_{PdCl2}= 1x10^{-3} mol/l)

In our extraction conditions, for the ester calix[6]arene derivatives, the maximum r value was obtained at pH =2.5 for **C6Es3** (0.657) and at pH=4.1 for **C6Es6** (0.758) whereas for amido calix[6]arene derivatives, at pH =4.1 for both **C6Am3** (0.565) and **C6Am6** (0.575) compounds.

Extraction of Eu^{3+} *ions*

The capability of *p-tert*-butyl calix[6]arene derivatives to extract Eu^{3+} ions was determined by liquid-liquid extraction experiments that were performed using variable volumes with equal concentrations of metal ions and calixarenes so that Cx :Eu ratio be varied between 2:1 and 1:2, and variable pH of the aqueous medium.

The extraction yield (η) and the ratio (***r***) representing the mol number of Eu^{3+} extracted by 1 mol of calixarene-based compounds, at pH=2.8 are shown in Table 1. Extraction experiments were performed for 1:1, 2:1 and 1:2 ratio between the extractant (Cx) and the extracted species (Eu).

The *p-tert*-butyl calix[6]arene **C6** shows an extraction yield of only 23.9%, when working with calixarene: metal ratio equal to 1:1. The grafting of two alkenyl-groups slowly increases the yield as compared with the parent calixarene whereas the attaching of three or four alkenyl-groups decreases it. Opposite results were obtained in the case of experiments with calixarene: metal ratio equal to 2:1. The grafting of three or six ester groups increase the yield as compared with the parent calixarene or the other calixarene derivatives. Favorable effect is shown by the functionalization with ester groups, whatever the calixarene: metal ratio.

Table 1. The extraction data for europium ions, using different calixarene-based compounds (pH=2.8;c_{Cx}=$1x10^{-3}$mol/l; $c_{Eu(NO3)3}$= $1x10^{-3}$ mol/l)

Calixarene-based compounds	Ratio Cx:Eu=1:1		Ratio Cx:Eu = 2:1		Ratio Cx:Eu = 1:2	
	η (%)	***r***	η (%)	***r***	η (%)	***r***
C6	23.9	0.238	26.1	0.130	13.2	0.263
C6Cr2	31.9	0.319	21.3	0.106	20.4	0.408
C6Cr3	18.7	0.187	42.6	0.213	23.8	0.475
C6Cr4	12.5	0.124	38.6	0.193	29.6	0.592
C6Es3	57.1	0.570	58.3	0.291	44.6	0.891
C6Es3Cr3	34.2	0.342	55.2	0.276	61.1	1.222
C6Am3	38. 7	0.386	13.4	0.067	25.0	0.500
C6Am3Cr3	29. 9	0.298	16.8	0.083	20.3	0.405
C6Am6	50.1	0.500	18.3	0.091	27.9	0.557
C6Es6	51.9	0.519	48.5	0.242	26.2	0.523

The extraction yield of Eu(III) ions from aqueous solution (pH=2.8) varies between 12.5% for **C6Cr4** and 57.1% for **C6Es3**, in experiments with calixarene: metal ratio Cx:Eu= 1:1, between 13.4% for **C6Am3** and 58.3% for **C6Es3** for Cx:Eu= 2:1 and 13.2% for **C6** and 61.1% for **C6Es3Cr3** for Cx:Eu= 1:2.

Unexpectedly, the highest extraction yield for europium ions (61.1%) was obtained for **C6Es3Cr3** derivatives, when calixarene: metal ratio was 1:2. The grafting of alkenyl-groups alone or together with ester ones improve the calixarene capability to extract Eu(III) ions.

The extraction yield of the Eu^{3+} ions with calixarene-based compounds depends on the calixarene: metal ratio (Figure 3). In this case, the total functionalised ester calix[6]arene derivative is less efficient than the half substituted compound, contrary to the palladium situation. The maximum efficiency appears at **C6Es3** derivatives, for Cx:Eu= 2:1.

The capability of calixarene-based compounds to extract europium ions in well defined extraction conditions was estimated by the ratio ***r*** representing the mol number of metal ion extracted by 1 mol of calixarene. In our extraction conditions, for the ester substituted calix[6]arene, the maximum ***r*** value was obtained for Cx:Eu = 1:2, namely 0.891 for **C6Es3** and 0.523 for **C6Es6**. The additional grafting of three butenyl-groups to the **C6Es3** compound increases the ***r*** value to 1.222 thus suggesting that for **C6Es3Cr3** compound, a more complicated Eu^{3+} sequestration process is involved.

The capability of *p*-*tert*-butyl calix[6]arene derivatives to extract Eu^{3+} ions was also determined at pH=4.6, using europium nitrate solutions with different concentrations.

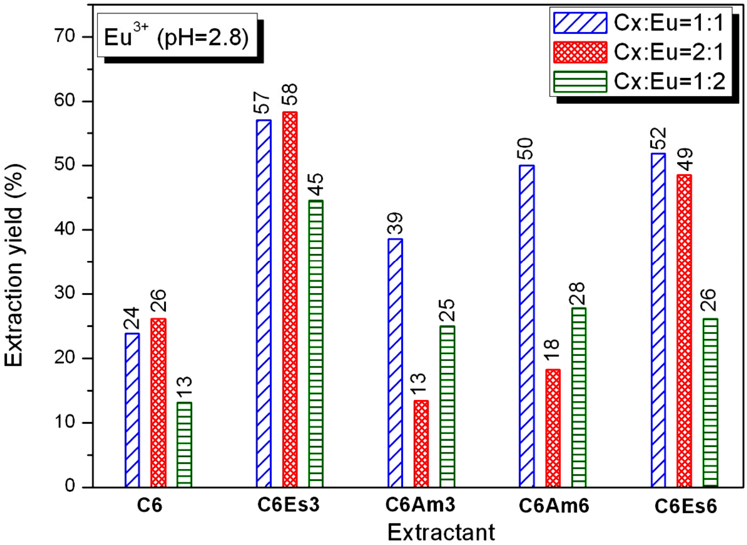

Figure 3. Variation of the extraction yield of Eu^{3+} using variable calixarene-to-europium ratios and different calixarene-based compounds (c_{Cx}=1x10^{-3}mol/l; $c_{Eu(NO3)3}$= 1x10^{-3} mol/l)

The extraction yield (η) and the ratio (***r***) representing the mol number of Eu^{3+} extracted by 1 mol of calixarene for different calixarene-based compounds, at pH=4.6 are shown in Table 2. Extraction experiments were performed for 1:1 ratio between the extractant (Cx) and the extracted species (Eu).

Table 2. The extraction data for europium ions, using different calixarene-based compounds and Eu^{3+} solutions with variable concentration (pH=4.6; Cx:Eu=1:1; $c_{Cx}=1x10^{-3}$mol/l)

Calixarene-based compounds	$1x10^{-3}$ mol Eu^{3+} /L		$5x10^{-4}$ mol Eu^{3+} /L	
	η (%)	***r***	η (%)	***r***
C6	32.4	0.324	23.2	0.231
C6Cr2	26.8	0.268	26.0	0.260
C6Cr3	30.3	0.303	25.3	0.253
C6Cr4	30.2	0.301	22.1	0.220
C6Es3	32.2	0.321	20.8	0.208
C6Es3Cr3	29.0	0.290	21.1	0.210
C6Am3	30.5	0.304	24.8	0.247
C6Am3Cr3	25.0	0.250	25.9	0.258
C6Am6	34.8	0.347	19.9	0.198
C6Es6	37.4	0.374	41.9	0.419

The extraction capability of the different calixarene-based compounds to extract Eu^{3+} ions in solutions with pH=4.6 is low. *p-tert*-butyl calix[6]arene **C6** shows an extraction yield of only 32.4% and 23.2% when working with $1x10^{-3}$ mol Eu^{3+} /L and $5x10^{-4}$ mol Eu^{3+} /L, respectively. In the first case, almost all calixarene-derivatives show a lower extraction capability than the parent calixarene. The only exceptions are the total substituted calix[6]arene with ester- and amido- groups (**C6Es6**; **C6Am6**).

With the exception of **C6Es3** and **C6Am3Cr3** derivatives, the best extraction results were obtained when working with $1x10^{-3}$M solutions.

In order to investigate whether the concentration of europium solutions influences also the extraction yield in more acidic medium, liquid-liquid extraction experiments were performed for some of the *hexa* substituted calix[6]arene, using diluted europium solutions ($5x10^{-4}$ mol Eu^{3+}/L) and variable Cx:Eu ratio (Figure 4)

The extraction of europium from diluted solution with pH=2.7 take place with a yield that varies between ~41% (**C6Am6**) and ~77 (**C6Es6**) for Cx:Eu=2:1 and ~26% (**C6Am3Cr3**) and 31% (**C6Am6**) for Cx:Eu=2:1. Although the extraction yield obtained with *hexa* ester calix[6]arene derivative is high (77%), in our experimental conditions, the ratio *r* representing the mol number of Eu^{3+} extracted by 1 mol of calixarene is only 0.191.

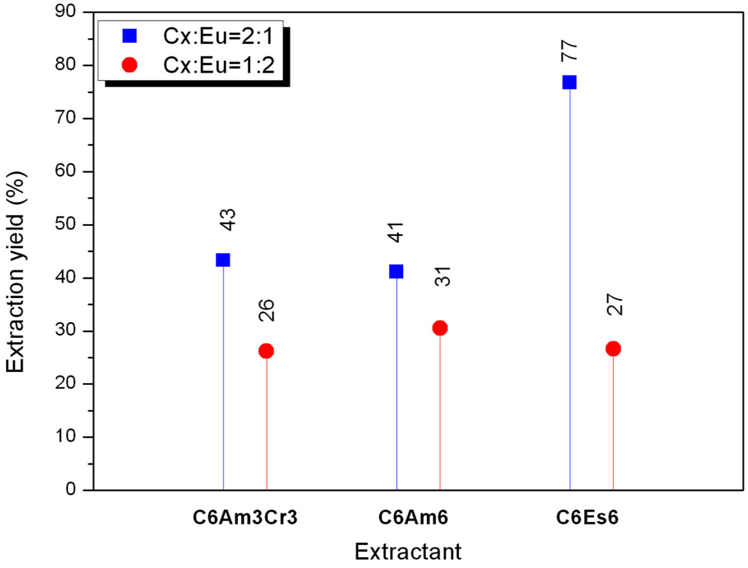

Figure 4. Variation of the extraction yield of Eu^{3+} using different calixarene-to-europium ratios and different calixarene-based compounds
(pH=2.7; $c_{Cx}=1\times10^{-3}$mol/L; $c_{Eu(NO3)3}= 5\times10^{-4}$)

CONCLUSIONS

The capability of *p-tert*-butyl calix[6]arene functionalised at the lower rim with 2-butenyl, ethyl acetate and/or N,N-diethylacetamide groups to extract precious or rare earth metallic ions have been investigated by liquid-liquid extraction experiments. Partial or total substituted calix[6]arenes with alkenyl and/or ester and/or amido donor groups were used to extract Pd^{2+} and Eu^{3+} ions from aqueous medium, in different experimental conditions i.e. pH, cation concentration, calixarene/metal ratio.

The best extraction capability was shown by calix[6]arene derivatives functionalized with *tri*- and *hexa*- ethylacetate groups. For palladium ions, the total functionalized calixarene derivative is more efficient as extractant than the half substituted compound; opposite results were obtained for europium extraction. The highest extraction yield is achieved at pH=2...3 for europium and 4...5 for palladium. In general, the capability of *p-tert*-butyl calix[6]arene derivatives to extract Eu^{3+} ions is smaller than for Pd^{2+}, whatever the pH value.

The extraction yield can be considerably improved by modifying the extraction conditions: ratio between calixarene derivatives and metallic ions, solutions concentration, the number of the extraction cycles, etc. The extraction yield of europium could be increased with 20-30% when the calixarene: metal ratio is modified from 1:1 to 2:1.

The *p-tert*-butyl calix[6]arene derivatives functionalized with *tri-* and *hexa-* ethyl acetate groups present great interest as liquid-liquid extraction reagents for precious metal and rare earth ions.

EXPERIMENTAL SECTION

Chemical reagents

All the calixarene-base compounds were synthesized according to the described methods [25-27]: *hexa-t*-butylcalix[6]arene (abbreviated **C6**), *hexa*–tbutyl–bis[(but-2-enyloxy]- *tetra*hydroxy calix[6]arene (**C6Cr2**), *hexa*-tbutyl-*tris*[(but-2-enyloxy]-*tri*hydroxy-calix[6] arene (**C6Cr3**), *hexa*–tbutyl–*tetra*kis-[(but-2-enyloxy]- dihydroxy calix[6] arene (**C6Cr4**),*hexa*-tbutyl-*tris*-[(ethoxycarbonyl)metoxy]-*tri*hydroxy-calix[6]arene(**C6Es3**), *hexa*-tbutyl-*tris* [(N,N-diethylamino carbonyl) methoxy]- *tri*hydroxy-calix[6] arene (**C6Am3**), *hexa-t*-butyl-*hexakis*-[(ethoxycarbonyl)metoxy]-calix[6]arene(**C6Es6**), *hexa*-tbutyl-*hexakis* [(N,N-diethylamino-carbonyl)methoxy] calix[6]arene (**C6Am6**), *hexa*-tbutyl-*tris*[(N,N-diethylamino-carbonyl)methoxy]- *tris*-(but-2-enyloxy)-calix[6]arene (**C6Am3Cr3**) and *hexa*- tbutyl-*tris* [(ethoxycarbonyl)methoxy]-*tris*-(but-2-enyloxy)-calix[6]arene (**C6Es3Cr3**).

Analytical-grade chloroform and deionized water were employed as solvents in the liquid-liquid extraction experiments. All others inorganic and organic reagents were standard grade and used without further purification.

Instrumentation and analysis

The metal concentration in aqueous medium was determined before and after extraction with ICP-OES - Spectroflame D Spectrophotometer (λ=340,458 nm and detection limit=0,01919 mg/l for palladium; λ=381,966 nm and detection limit=0,0081 mg/l for europium).

Liquid-liquid extraction of metal ions

The organic solutions were prepared by dissolving the required amount of calixarene derivative, in chloroform, to obtain a solution with $1x10^{-3}$ M concentration.

The aqueous solutions of metals were prepared by dissolving the required amount of $PdCl_2$ or $Eu(NO_3)_3.5H_2O$ in acidulated water to obtain $5...10x10^{-4}$ mol/L solutions. The acidity of the aqueous medium was monitored with a pH-instrument. The pH was adjusted to pH 2.5 and 4.1 with HCl, for Pd^{2+} solution and to pH 2.7-2.8 or 4.6 with HNO_3, for Eu^{3+} solutions.

Liquid-liquid extraction experiments were carried out by introducing the organic and aqueous solutions (1:1, 2:1 and 1:2 volumetric ratios) into extraction funnels and vigorously shaking them, for 30 minutes, using a mechanical shaker. The aqueous phase was left to settle, washed with $CHCl_3$, separated and analysed.

The measurements were carried out with an ICP-OES instrument, using standard conditions calibration. The extraction yield (η%) was calculated from the equation [28]:

$$\eta = (A_0 - A) / A_0 \times 100 \ \%$$

where A_0 and A are the initial and the final concentration (mg/L) of the metal salt before and after extraction, respectively.

ACKNOWLEDGEMENTS

The financial support of the Romanian Ministry of Education and Innovation under the project PNII 71-062 is gratefully appreciated.

REFERENCES

1. S. Erdemir, M. Bahadir, M. Yilmaz, *Journal of Hazardous Materials*, **2009**, *168*, 1170.
2. M.C. Semedo, A. Karmali, P.D. Barata, J.V. Prata, *Journal of Molecular Catalysis B: Enzymatic*, **2010**, *62*, 97.
3. M. Bayrakci, S. Ertul, M. Yilmaz, *Tetrahedron*, **2009**, *65*, 7963.
4. M. Atanassova, V. Lachkova, N. Vassilev, S. Varbanov, I. Dukov, *Polyhedron*, **2010**, *29*, 655.
5. M. A. Kamboh, I. B. Solangi, S. T. H. Sherazi, S. Memon, *Journal of Hazardous Materials*, **2009**, *172*, 234.
6. L Elsellami, V. Chartron, F. Vocanson, P. Conchon, C. Felix, C. Guillard, L. Retailleau, A. Houas, *Journal of Hazardous Materials*, **2009**, *166*, 1195.
7. K. Ohto, H. Ishibashi, H. Kawakita, K. Inoue, T. Oshima, *Journal of Inclusion Phenomena and Macrocyclic Chemistry*, **2009**, *65*, 111.
8. F. Yang, Y. Wang, B. Hong, X. Chai, *Journal of Inclusion Phenomena and Macrocyclic Chemistry*, **2009**, *64*, 67.
9. E. A. Shokova, V. V. Kovalev, *Russian Journal of Organic Chemistry*, **2009**, *45(9)*, 1275.
10. A. Hamdi, R. Souane, L. Kim, R. Abidi, L. Mutihac, J. Vicens, *Journal of Inclusion Phenomena and Macrocyclic Chemistry*, **2009**, *64*, 95.

11. G. Daneshvar, A. Jabbari, Y. Yamini, D. Paki, *Journal of Analytical Chemistry*, **2009**, *64(6)*, 602.
12. M. S. Gidwani, H. Kaur, U. Pal, S. K. Menon, *Journal of Analytical Chemistry,* **2009**, *64(2)*, 104.
13. M. Surowiec, R. Custelcean, K. Surowiec, R. A. Bartsch, *Tetrahedron*, **2009**, *65*, 7777.
14. N. Iki, *Journal of Inclusion Phenomena and Macrocyclic Chemistry*, **2009**, *64*, 1.
15. O. H. Altshuler, N. V. Malyshenko, G. J. Shkurenko, H. N. Altshuler, *Theoretical Foundations of Chemical Engineering*, **2009**, *43(1)*, 43.
16. R. Nie, X. Chang, Q. He, Z. Hu, Z. Li, *Journal of Hazardous Materials*, **2009**, *169*, 203.
17. U. Ocak, M. Ocak, K. Surowiec, R. A. Bartsch, M. G. Gorbunova, C. Tu, M. A. Surowiec, *Journal of Inclusion Phenomena and Macrocyclic Chemistry*, **2009**, *63*, 131.
18. X. Liu, K. Surowiec, R. A. Bartsch, *Tetrahedron*, **2009**, *65*, 5893.
19. Y.de Gaetano, I. Clarot, J.-B. Regnouf-de-Vains, *Tetrahedron Letters*, **2009**, *50*, 5793.
20. M. Surowiec, R. Custelcean, K. Surowiec, R. A. Bartsch, *Tetrahedron*, **2009**, *65*, 7777.
21. X. Liu, K. Surowiec, R. A. Bartsch, *Tetrahedron*, **2009**, *65*, 5893.
22. O. O. Karakus, H. Deligoz, *Analytical Letters*, **2010**, *43(5)*, 768.
23. N. Singh, D. Jang, *Supramolecular Chemistry*, **2009**, *21(5)*, 351.
24. T. A. Halgren, *J. Comput. Chem.*, **1999**, *20*, 720.
25. A. Saponar, E.-J. Popovici, N. Popovici, E. Bica, G. Nemes, P. Petronela, I. Silaghi-Dumitrescu*, Rev.Chim*., **2009**, *60(3)*, 278.
26. A. Saponar, I. Silaghi-Dumitrescu, E.-J. Popovici, N. Popovici, *Studia Universitatis Babes-Bolyai, Chemia*, **2007**, *LII (4)*, 67.
27. A. Saponar, E.-J. Popovici, R.Grecu, I. Silaghi-Dumitrescu, N. Popovici, *Studia Universitatis Babes-Bolyai, Chemia,* **2009***, LIV (4),* 203.
28. N. Toumi, F. Kajo, D. Fournier, F. Vocanson, R. Lamartine, I. Dumazet-Bonnamour, *Materials Science and Engineering* C, **2008**, *28*, 645.

STUDIA UNIVERSITATIS BABEŞ-BOLYAI, CHEMIA, XLV, 2, TOM I, 2010

Dedicated to the memory of Prof. dr. Ioan Silaghi-Dumitrescu marking 60 years from his birth

THE INFLUENCE OF COAGULANTS IN COLLOIDAL PARTICLES REMOVAL FROM DISPERSIONS

ADINA GHIRIŞAN[*], SIMION DRĂGAN

ABSTRACT. This study describes the physicochemical treatment applied to colloidal dispersion of carboxymethylcellulose (CMC) in order to improve the removal of colloidal particles from aqueous solution by sedimentation and pressure filtration. The physicohemical treatment consists in coagulation/ flocculation with different coagulants/flocculants at different concentrations. By coagulation-sedimentation combination the optimal parameters were established to be 5.9 for pH and 200 mg/g ($FeCl_3$/CMC) for coagulant concentration. By coagulation-filtration the best result were obtained with the coagulant concentration of 200 mg/g ($FeCl_3$/CMC) and pressure difference of 4 bar.

Keywords: *physicochemical treatment, coagulation, flocculation, sedimentation, pressure filtration, carboxymethylcellulose.*

INTRODUCTION

The application of physicochemical treatment in removing micron-size or colloidal particles is widespread in wastewater treatment, before sedimentation and membrane (micro-, ultra- and nano-) filtration when the fouling of filtering surface occurs [1].

Coagulation by chemical additives and flocculation by natural or synthetic materials are the most important physicochemical pretreatment steps in industrial wastewater used to reduce the suspended and colloidal materials responsible for color and turbidity of the wastewater. A well-chosen pretreatment process can change the structure of the system improving the sedimentation and membrane filtration processes.

Removal of colloidal and micro-size particles by coagulation/ flocculation, precipitation and neutralization involves particle destabilization and particle transport [2, 3]. Coagulants destabilize colloidal suspensions allowing particles to agglomerate into microflocs, while flocculants bring the microflocs into contact with each other forming large flocs.

---

[*] *Universitatea Babeş-Bolyai, Facultatea de Chimie şi Inginerie Chimică, Str. Kogălniceanu Nr. 1, RO-400084 Cluj-Napoca, Romania, ghirisan@chem.ubbcluj.ro*

Experimental determination have shown that destabilization in filtration is similar to destabilization in coagulation; effective coagulants/ flocculants are observed to be effective “filter aids”. In the same time, particles transport in filtration is analogous to transport in coagulation/ flocculation processes [4].

A great variety of destabilizing chemicals is currently available for this purpose, including metal salts (e.g., salts of Al(III), Fe(III)) and natural and synthetic polymers, which may be organic or inorganic.

The effect of a coagulation/flocculation treatment depends on the pH, the type and concentration of the used additives, and the characteristics of the feed suspension [5].

The objectives of the present work are: a). evaluation of the physicochemical pretreatment procedure in removal of colloidal particles of carboxymethylcellulose by filtration; b). optimization of pH and coagulant concentration by jar test apparatus; and c). determination of filtration kinetics by pressure filtration tests.

RESULTS AND DISCUSSION

a). Carboxymethylcellulose (CMC) solution contains colloidal particles that not settle if no coagulant is added, causing turbidity. In order to destabilize the system and to remove the colloidal particles of CMC from solution, preliminary tests are conducted in this work using different coagulants as ferric chloride $FeCl_3$, calcium chloride $CaCl_2$, and polyacrilamide (PAA) as flocculant, and a combination of these.

Considering the mean filtration rate of coagulated/flocculated 5 g/L CMC solutions as performance parameter, the best results obtained by vacuum filtration are shown in Table 1.

Table 1. Results of preliminary tests

Sample	**Coagulant concentration [mg/g]**	**V_f [m^3/m^2]**	**τ [s]**	**$w_f \cdot 10^6$ [m/s]**	**Observation**
Solution CMC 3%	0	-	-	-	Rapid fouling
Solution CMC 1%	0	0.00071	900	0.79	Rapid fouling
Solution CMC 0.5%	0	0.00116	900	1.29	Rapid fouling
Solution CMC 0.5% + $FeCl_3$	75	0.0174	900	16.4	Small flocs

Sample	**Coagulant concentration [mg/g]**	**V_f [m^3/m^2]**	**τ [s]**	**$w_f \cdot 10^6$ [m/s]**	**Observation**
Solution CMC 0.5% + $FeCl_3$	150	0.0358	900	39.4	Large flocs
Solution CMC 0.5% + $CaCl_2$	2980	0.0076	900	8.43	No structural modification
Solution CMC 0.5% + $CaCl_2$	5960	0.0063	900	7.03	No structural modification
Solution CMC 0.5% + PAA	120	0.0093	900	10.3	Small flocs
Solution CMC 0.5% + PAA	240	0.0109	900	12.18	Small flocs
Solution CMC 0.5% + $FeCl_3$ + PAA	75 120	0.0542	900	60.22	Large flocs
Solution CMC 0.5% + $FeCl_3$ + PAA	75 240	0.035	900	38.88	Gelling aggregates

As Table 1 shows, the filtration of initial samples (with CMC concentration 0.5 %, 1% or 3 %) leads to the rapid fouling of filter medium, without the possibility to measure the filtration rate for 3% CMC solution sample. The rapid fouling of filtering surface caused by blocking and internal clogging justifies the pretreatment of CMC solution using coagulants and/or flocculants.

Comparing the values of obtained filtration rate it was concluded that, in spite that addition of polyacrylamide (PAA) can accelerate the filtration process, for the next experiments only $FeCl_3$, which is friendlier with the environment than (PPA), will be used as coagulant.

b). In order to optimize the pH and the $FeCl_3$ dosage, considering coagulation procedure before a conventional sedimentation, the methods of A. Koohestanian [6] and S. W. Krasner [7] were applied. The variation of supernatant turbidity after sedimentation in jar test apparatus for different pH values and constant coagulant concentration of 200 mg/g plotted in Figure 1 shows the minimal values for pH of 5.9.

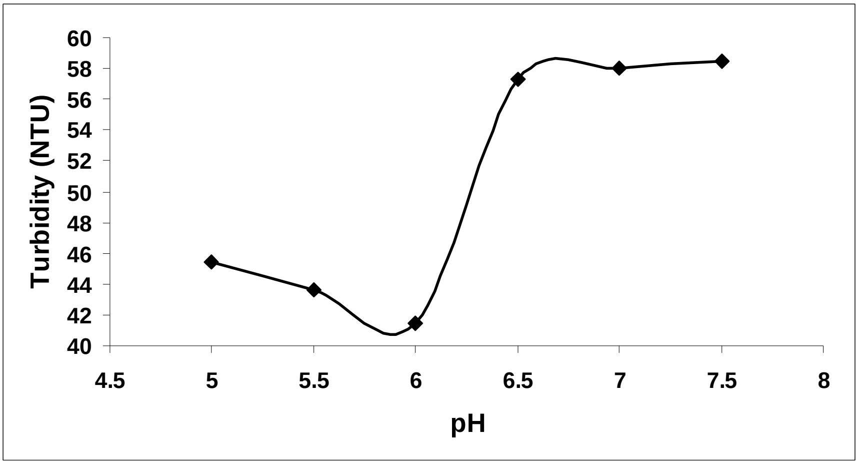

Figure 1. pH effect on the turbidity removal for 5 g/L CMC dispersion.

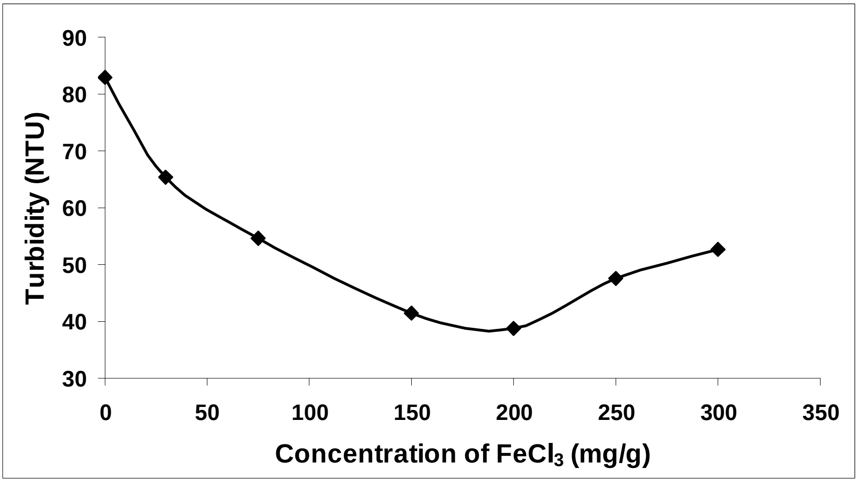

Figure 2. Coagulant concentration effect on the turbidity removal for 5 g/L CMC dispersion.

The influence of different concentrations of $FeCl_3$ added to CMC solution at constant pH = 5.9 is presented in Figure 2. As can be seen, by increasing the coagulant concentration, the supernatant turbidity decreases until the experimental concentration of coagulant is equal to 200 mg/g ($FeCl_3$/CMC). After this concentration the turbidity increases again. This means that for a concentration higher than 200 mg/g ($FeCl_3$/CMC) a re-dispersing of the flocs occurs, enhancing in this way the turbidity of solution.

Considering the combination coagulation-sedimentation at 200 mg/g ($FeCl_3$/CMC), the turbidity decreases from 83 NTU in initial solution to 38.76 NTU in supernatant, which means a turbidity removal with more than 53 %.

The progress of sedimentation, at optimal concentration of $FeCl_3$ equal to 200 mg/g ($FeCl_3$/CMC) and pH equal to 5.9 is shown in Figure 3. The mean settling rate of 0.63 mm/min was obtained by the typical curve.

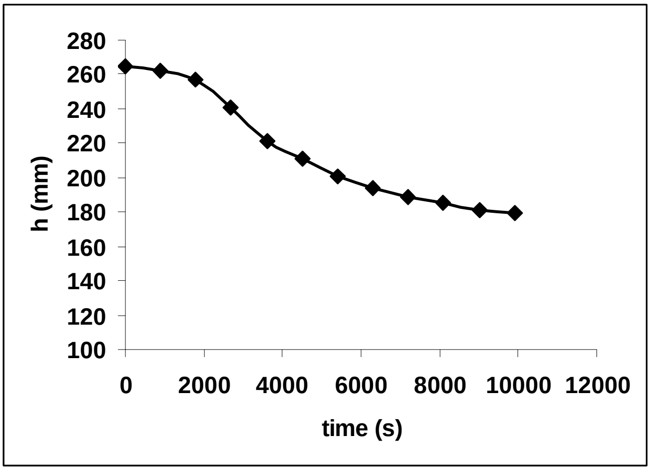

Figure 3. Sedimentation curve at optimal conditions.

c). To describe the pressure filtration, Darcy's law written as Equation 1, is proposed:

$$\frac{dV}{A \cdot dt} = \frac{\Delta p}{\eta\left(r_c \cdot c \cdot \frac{V}{A} + R_m\right)} \tag{1}$$

where V is the volume of filtrate (m^3), Δp – pressure difference (Pa), A - filtering surface (m^2), η - the liquid viscosity (Pa.s), r_c - specific resistance of the filter cake (m/kg), R_m - the resistance of the filter medium (m^{-1}), c – weight of solids/volume of filtrate (kg solid/m^3 filtrate).

Considering V/A = V_f (m^3/m^2) the specific filtrate volume, and integrating Equation (1) with the assumption of constant pressure, a linear dependence of t/V_f versus V_f is resulting (Equation 2):

$$\frac{t}{V_f} = \frac{\eta \cdot r_c \cdot c}{2 \cdot \Delta p} \cdot V_f + \frac{\eta \cdot R_m}{\Delta p} \tag{2}$$

The mean value of cake resistance r_c and the resistance of the filter membrane R_m determined from the slope *a* and the intercept *b* of linear plot t/V_f versus V_f are given by Equations (3) and (4):

$$r_c = \frac{a \cdot 2 \cdot \Delta p}{\eta \cdot c} \tag{3}$$

$$R_m = \frac{\Delta p \cdot b}{\eta} \tag{4}$$

Considering the results obtained by the combination coagulation-sedimentation procedure, pressure filtration tests were conducted after the coagulation with ferric chloride concentration between 150 mg/g and 200 mg/g ($FeCl_3$/CMC). Figures 4a and 4b show the influence of coagulant concentration on the filtration kinetics of 5 g/L CMC solution.

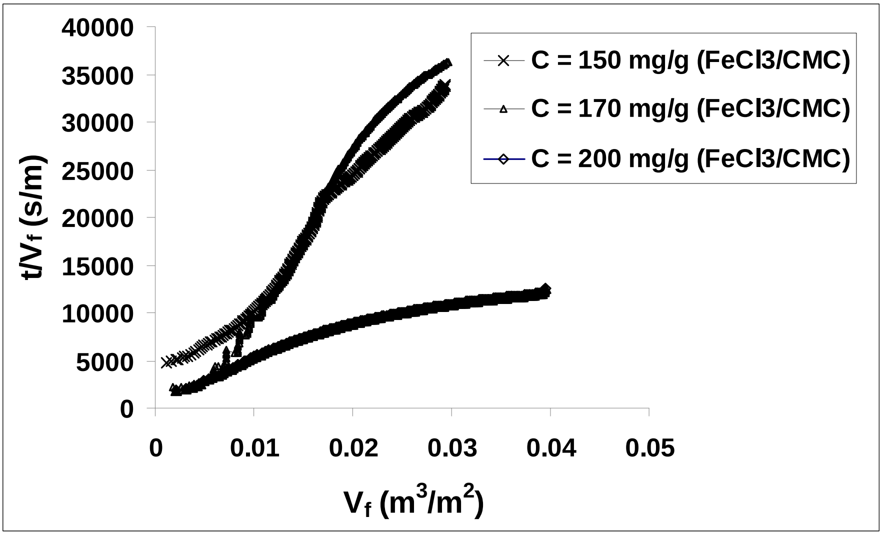

Figure 4a. Comparison of filtration behavior at 2 bar and different $FeCl_3$ dosage.

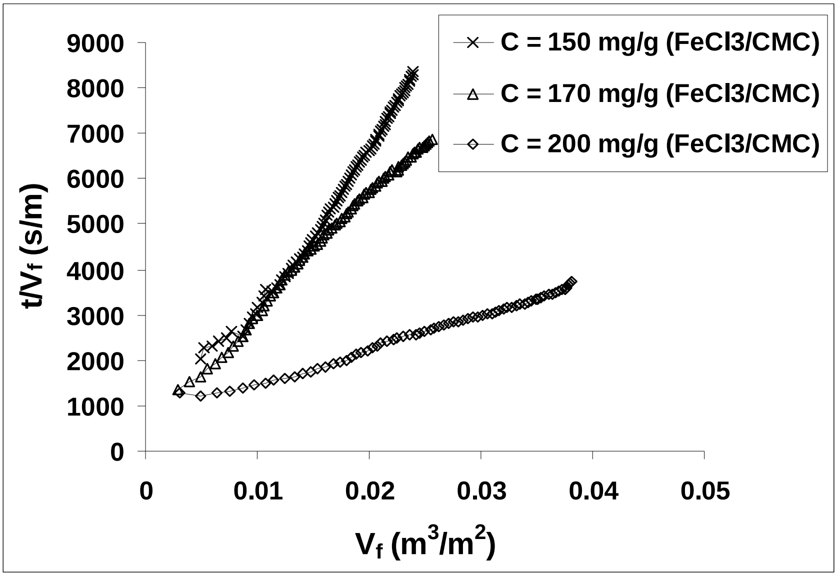

Figure 4b. Comparison of filtration behavior at 4 bar and different $FeCl_3$ dosage.

As it can be seen, an acceleration of the filtration process with the increase of the coagulant concentration is observed for experimental measurements at 2 bar and at 4 bar. In both cases a lower slope of the curves t/V_f vs. V_f was obtained when before pressure filtration a coagulant concentration of 200 mg/g ($FeCl_3$/CMC) was used.

Considering the effect of the coagulant concentration on the pressure filtration of 5 g/L CMC solutions, next results were determined from experimental data, using Equations (3) and (4): specific filter cake resistance of $r_c \approx 13.0\cdot10^{13}$ m/kg for coagulant concentration of 150 mg/g ($FeCl_3$/CMC), $r_c \approx 8.3\cdot10^{13}$ m/kg for 170 mg/g ($FeCl_3$/CMC), and $r_c \approx 2.0\cdot10^{13}$ m/kg for 200 mg/g ($FeCl_3$/CMC), and a mean medium resistance of $R_m \approx 3.0\cdot10^{11}$ m^{-1}, when the experiments were conducted at $\Delta p = 4$ bar.

Coagulant effect on turbidity removal by pressure filtration has shown a decrease from 83 NTU in initial samples to 6 - 8 NTU in filtrate, which means a turbidity removal with more than 90 %. This can be explained by adsorption phenomena and the retention of small particles on filter cake.

The influence of the pressure difference on the filtration test at coagulant concentration of 200 mg/g ($FeCl_3$/CMC) is shown in Figure 5. It can be seen an acceleration of filtration process with the increase of pressure difference from 1 bar to 4 bar.

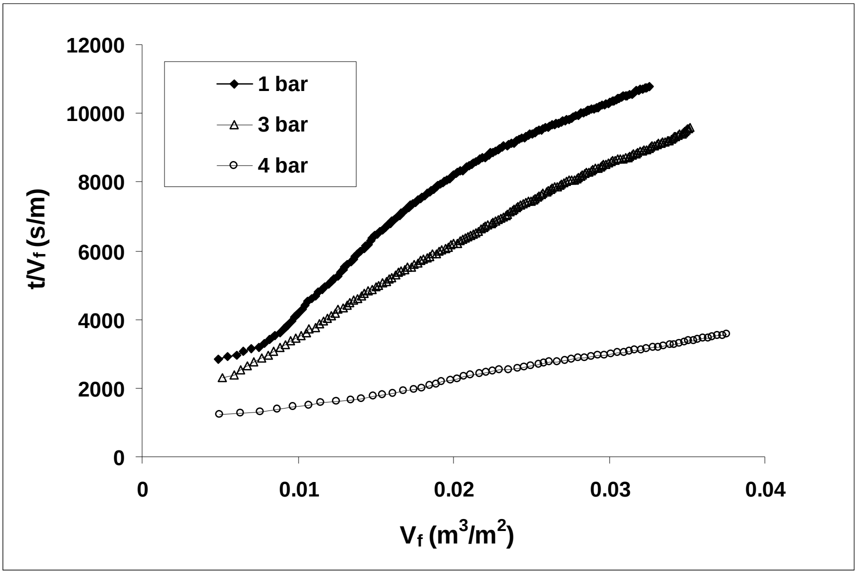

Figure 5. Comparison of filtration behavior at different pressure.

Specific filter cake resistances of $r_c \approx 6.0 \cdot 10^{13}$ m/kg for a difference pressure $\Delta p = 1$ bar, $r_c \approx 4.8 \cdot 10^{13}$ m/kg for $\Delta p = 3$ bar and $r_c = 2.0 \cdot 10^{13}$ m/kg for $\Delta p = 4$ bar were calculated considering experimental data at different pressures and constant coagulant concentration of 200 mg/g.

The results show that the specific filter cake resistance decreases with the increase of coagulant dosage and with the increase of pressure difference.

Considering the combination coagulation-filtration the best results were obtained for coagulant concentration of 200 mg/g ($FeCl_3$/CMC) and $\Delta p = 4$ bar. The mean filtration rate for these conditions, considering the calculated cake resistance, is $w_f = 20.5 \cdot 10^{-5}$ m/s, which is 3.5 times higher than filtration rate obtained for coagulant concentration of 150 mg/g ($FeCl_3$/CMC) and $\Delta p = 4$ bar ($w_f = 6.0 \cdot 10^{-5}$ m/s), and 10 times higher than filtration rate obtained for 200 mg/g ($FeCl_3$/CMC) and $\Delta p = 1$ bar ($w_f = 2.0 \cdot 10^{-5}$ m/s).

CONCLUSIONS

In this study coagulation with ferric chloride as physicochemical pretreatment before conventional sedimentation and before pressure filtration was applied to 5 g/L CMC solution samples in order to improve the removal of colloidal particles and to avoid membrane-fouling.

The optimal experimental parameters were obtained combining coagulation with settling in a jar test apparatus and coagulation with pressure filtration in Filtratest.

By coagulation-sedimentation combination the optimal parameters were established to be 5.9 for pH and 200 mg/g ($FeCl_3$/CMC) for coagulant concentration. The influence of coagulant concentration and pressure on filtration has shown an acceleration of filtration kinetics with the increase of the concentration of $FeCl_3$ from 150 mg/g to 200 mg/g and with the increase of pressure from 1 bar to 4 bar, by the reduction of the specific cake resistance.

After coagulation the turbidity of carboxymethylcellulose solution was found to be reduced by more than 53 % considering the combination coagulation-sedimentation and by more than 90% for the combination coagulation-filtration. This means that the procedure coagulation-filtration is more efficient for the removal of CMC particles due to adsorption phenomena and better retention of small particles on filter cake.

EXPERIMENTAL SECTION

Colloidal synthetic solutions of carboxymethylcellulose 5 g/L were obtained dissolving sodium carboxymethylcellulose, a white powder, in cold distillated water (initial turbidity was equal to 83 NTU).

Preliminary tests have been made using the laboratory vacuum equipment (Δp = 400 mm Hg).

A jar test apparatus model JLT 6 was used for the optimization of pH and dosage of coagulants/flocculants. Samples of 500 mL of 5 g/L CMC solution were placed in six beakers. To optimize the pH, solutions of 1.0 N NaOH and 1.0 N H_2SO_4 were added in each beaker containing the CMC solution and 200 mg/mg ($FeCl_3$/CMC), determined by preliminary tests.

After pH adjustment different concentrations of ferric chloride (30, 75, 150, 200, 250, 300 mg/g) were tested by stirring at 100 rpm for 1 min, and then at 30 rpm for 15 min. Then, the stirrer was turned off in order to let the sample to settle for 30 min. Supernatant was sampled 10 mm below the water surfaces, and the turbidity and pH were measured. The procedures were repeated at fixed dosage to examine the optimum pH.

Turbidity was measured by an Analytic turbidimeter Hanna type C-102 with a range of 0 – 100 FTU.

The pH was measured with a pH/mV meter type Orion 4 STAR from Thermo Electron Corporation.

Pressure filtration tests were performed with the laboratory filtration equipment FITRATEST from BOKELA GmbH having a pressure filter cell of steel with the capacity of 400 mL and the filtering surface of 20 cm^2. For each experiment sample of 100 mL 5g/L CMC solution was tested. FILTRATEST apparatus was operated at constant pressure; pressure difference Δp was chosen between 1 bar and 4 bar. The cumulative filtrate weight was recorded online by the computer and analyzed using Excel software. Three replicate experiments were carried out for each set of experimental conditions. The reproducibility of experiments was higher than 95 %. A SEFAR filter medium with pore size of 1.0 microns was tested during the pressure filtration.

REFERENCES

1. J. Bratby, “Coagulation and Flocculation in Water and Wastewater Treatment”, IWA Publishing, London, 2nd Edition, **2007**, chapters 3-5.
2. A. Ghirişan, „Separarea fizico-mecanică a sistemelor eterogene solid-lichid”, Ed. Casa Cărții de Ştiință, Cluj-Napoca, **2005**, chapter 3.
3. A. Ghirişan, S. Drăgan, A. Pop, M. Simihăian, V. Miclăuş, *Canadian Journal of Chemical Engineering*, **2007**, *85*, 900.
4. H. Stechemesser, B. Dobias, *Coagulation and Flocculation, Surfactant Science Series, CRC Press*, **2006**, *126*, 969.
5. A. Ghirişan, Al. Pop, M. Moceanu, V. Miclăuş, *Studia Universitatis Babeş-Bolyai, Chemia*, **2005**, *50(1)*, 97.
6. A. Koohestanian, M. Hosseini, Z. Abbasian, *American-Eurasian Journal of Agriculture & Environment Science*, **2008**, *4(2)*, 226.
7. S.W. Krasner, G. Amy, *Journal of American Water Works Association*, **1995**, *87(10)*, 93.

STUDIA UNIVERSITATIS BABEŞ-BOLYAI, CHEMIA, XLV, 2, TOM I, 2010

Dedicated to the memory of Prof. dr. Ioan Silaghi-Dumitrescu marking 60 years from his birth

KINETICS OF THE PHENOL OXIDATION BY PERMANGANATE IN ACIDIC MEDIA. THE INTERMEDIATE OXIDIZED SPECIES 4,4'-BIPHENOQUINONE EVOLUTION

LUCIAN COPOLOVICI[a,*] AND IOAN BALDEA[b]

ABSTRACT. The kinetics of phenol oxidation by permanganate has been carried out in relative strong acidic media, in the presence and in absence of manganese (II) as catalyst. Formation of an intermediate colored species that absorbs light at 400 nm has been observed during the course of reaction. Its formation and decay has been followed spectrophotometrically. The intermediate has been assigned as 4,4'-biphenoquinone. Kinetic laws for the formation and consumption of this intermediate have been established. Complicate rate equations of the *one-plus* form were deduced either for building up or for decomposition of the intermediate. Rate constants, pre-equilibrium constants and experimental activation energies were determined. Some mechanistic considerations were made.

Keywords: *phenol, permanganate, kinetics, 4,4'-biphenoquinone.*

INTRODUCTION

The kinetic study of oxidation by permanganate has received a considerable attention because of its importance in analytical [1,2] and organic chemistry [3-5]. Nevertheless, there are still unsolved aspects of the mechanisms of many permanganate oxidation reactions [6]. The reaction mechanisms of oxidation of various substrates, including phenols [7-15], in alkaline solutions are better understood [16-19], but they are more complex in acidic solutions due to ability of manganese to exist in various oxidation states between VII and II, as well as to the auto-catalytic character of numerous permanganate oxidations [20-25]. Knowledge of the phenol oxidation has applications in water purification [26] and some organic syntheses [3,4]. In this paper we report information obtained from a kinetic study by monitoring

---

[a] *Estonian University of Life Sciences, Institute of Agricultural and Environmental Sciences, Kreutzwaldi 1, Tartu 51014, Estonia. * E-mail: lucian.copolovici@emu.ee*

[b] *Babes-Bolyai University of Cluj, Faculty of Chemistry and Chemical Engineering, 11 Arany Janos Str. Cluj-Napoca, 400028 Romania, e-mail: ibaldea@chem.ubbcluj.ro*

the evolution of 4,4’-biphenoquinone intermediate during the phenol oxidation in acidic solution, either in the absence or in the presence of manganese (II) at the start of reaction.

RESULTS AND DISCUSSION

Spectra and mechanistic considerations. Substantial evidence has been obtained for the formation of an intermediate species that absorbs light within the region 350-450 nm, with a peak located at 400 nm. The mixing of aqueous phenol and permanganate in acidic media leads to solution color changes within an interval of several minutes. It starts purple-violet, rapidly turns yellowish-brown and faded to colorless in a slower pace. When phenol and permanganate were mixed and spectra recorded at 1 second intervals by a diode –array spectrophotometer, an absorption band emerge and then falls to zero around 400 nm. The permanganate ion peak at 525 nm decreases steadily from the start of the process [27]. No isosbestic points have been noticed on time-dependent spectra, suggesting the involvement of some consecutive steps. The same peak position was obtained when the reaction was carried out in the presence of Mn(II) in the reaction mixture. The spectra were presented previously [27] where we performed the reduction of MnO_4^- by Mn^{2+} in large excess. Mn(III) is the single species formed [28]. After complete decay of permanganate ion, a phenol solution was injected into the mixture to achieve a large excess concentration. A yellowish-brown color suddenly appeared during the mixing that further faded to colorless, as time elapses. Successive spectra were recorded and position of the peak is the same as when permanganate was the oxidizing agent. Because Mn(III) is a strong oxidizing agent (redox potential for the Mn(III)/Mn(II) couple of 1.5 - 1.6 V [29]), one can assume it reacts more rapidly with phenol than Mn(VII) does. Such a reaction rate also explains the catalytic effect of Mn(II) in permanganate oxidations. On the other hand, this system involves the same intermediate species as in the case of phenol - permanganate system.

A comparison of the spectra obtained with those of Mn_{aq}^{3+}, and $Mn(OH)^{2+}$ ions [30], Mn(IV) with a peak at 418 nm [31-33], identified by Insausti and co-workers [22,23] reveals that the intermediate is an oxidation product of phenol rather than an intermediate valence state of manganese. The spectra of *ortho*- and *para*-quinone differ from the one in discussion. A supplementary argument for the formation of such an intermediate is brought by the oxidation of *ortho*-cresol, when a similar intermediate with an absorption peak at 408 nm is formed. In the case of *para*-cresol oxidation either by permanganate or Mn(III), no absorption peak was found in this range of wavelength.

We consider that the intermediate is 4,4'-biphenoquinone formed by oxidative coupling of phenoxy radicals that is the primary oxidation product of phenol by Mn(VII) or Mn(III). Such a relative long-lived intermediate has been found in the case of phenol oxidation by ferrate (VI) in phosphate buffered solutions [34]. Similar behavior has been found by hexacyanoferrate(III) [35a], *trans*-dioxoruthenium(VI*)* [35b], oxochromium(IV) ion [35c] in acidic media oxidation. Lee and Sebastian [14] showed that phenoxy radicals undergo further coupling and oxidation reactions, which eventually produce a mixture of *ortho* and *para*- diphenoquinone, the final products of alkaline oxidation. Hay and co-workers described oxidative coupling with 2,6- disubstituted phenols [36]. D.T Yiu and co-workers [35b] showed that either by a hydrogen abstraction or by an electron transfer, the phenoxy radical is produced with ruthenium complex. It undergoes two rapid concurrent reactions. The first is a further three-electron oxidation to give *p*-benzoquinone and other organic products. The second is a coupling and oxidation process to give 4,4'-biphenoquinone, followed by a decay step. Therefore, we consider that the formation of 4,4'-biphenoquinone requires the following sequence of steps:

$$C_6H_5OH + HMnO_4 \longrightarrow C_6H_5O^{\circ} + H_2MnO_4 \qquad \text{(a)}$$
$$C_6H_5O^{\circ} \longleftrightarrow {}^{\circ}C_6H_5 = O \qquad \text{(b)} \qquad (1)$$
$$2^{\circ}C_6H_5 = O + Mn(VII) \longrightarrow OC_6H_4 = C_6H_4O + Mn(V) \qquad \text{(c)}$$

In the step (b) phenoxy radical switches to a carbon radical. The formation of a covalent bond between one of the limiting structures of the phenoxy radical and the oxidation can take place successively. The involvement of free radicals during the permanganate oxidation of phenols or other organic substrates is supported by the induced polymerization of ethylacrylate [24]. It has been mentioned previously in the case of other phenol oxidation [4,37,38].

Kinetics. Under large hydrogen ion concentration the final reduction product is Mn(II). No MnO_2 precipitate is formed. Our kinetic measurements were carried out under experimental conditions where the induction period was either imperceptible short or it was missing. At least three replicate runs were carried out for each set of experimental conditions, which yield rate constants that do not differ to more than 3 %. Under the excess of phenol, all absorbance recordings could be described by linear kinetics, regardless the absorbance was monitored at 525 nm for Mn(VII), or at 400 nm for the intermediate.

At 400 nm the evolution of absorbance against time, a biphasic curve, obeys the following equation:

$$A = [Mn(VII)]_0\,\varepsilon_0 e^{-k_{obsd}t} + s[Mn(VII)]_0\,\varepsilon_1 \frac{k'_{obsd}}{k''_{obsd} - k'_{obsd}}(e^{-k'_{obsd}} - e^{-k''_{obsd}t}) + \varepsilon_2[C_6H_5OH] \tag{2}$$

where k'_{obsd} and k''_{obsd} are pseudo-first-order rate coefficients for the formation and decay of the intermediate. ε_0, ε_1 and ε_2 stand for molar absorptivities of all three absorbing species (permanganate, biphenoquinone intermediate and phenol, respectively), *s* is a stoichiometry factor. $A_\infty = \varepsilon_2[C_6H_5OH]_0$ is the final absorbance. Since phenol and permanganate absorb light very weakly in this region of electronic spectrum and ε_0, $\varepsilon_2 << \varepsilon_1$, the first and the last terms in eq. (2) have an insignificant contribution. Therefore,

$$A - A_\infty = C \cdot (e^{-k'_{obsd}t} + e^{-k''_{obsd}t}) \tag{3}$$

The constant *C* is the factor in front of the parenthesis of the second term in eq. (2).

A non-linear regression of equation (3) was used for the data recorded at 400 nm and has fitted well with R^2 between 0.990 and 0.999 and χ^2 of the order of magnitude smaller than 10^{-6}. At constant hydrogen ion concentration, the dependence of the observed first-order rate constants on phenol concentration is presented in Table 1. These data were obtained in the absence and the presence of Mn(II) as catalyst.

Table 1. Observed first-order rate constants (mean values) for the two-step sequence at $[MnO_4^-] = 1.30\cdot10^{-4}$, $[HClO_4] = 0.38$, μ=0.4 and T = 298K in absence and presence of $3.33\cdot10^{-4}$ mol.L^{-1} Mn(II)

$[C_6H_5OH]$ mmol.L^{-1}	k'_{obsd} s^{-1}	k'_{obsd} s^{-1} Mn(II)	k''_{obsd} s^{-1}	k''_{obsd} s^{-1} Mn(II)
0.33	0.0180	0.032	0.00203	0.0015
0.67	0.0383	0.055	0.00315	0.0024
1.00	0.0526	-	0.00511	-
1.33	-	0.091	-	0.0041
1.67	0.074	0.125	0.00663	0.0050
2.00	0.087	0.150	0.00702	0.0057
2.67	0.120	0.180	0.00782	-
3.33	0.133	0.200	0.00864	0.0075
4.00	0.155	0.224	-	-
5.00	0.179	0.231	0.0091	0.0081
6.67	0.196	0.244	0.0096	0.0087
8.33	0.217	-	0.0100	-

In this paper we focused the attention on the formation and decay of 4,4'-biphenoquinone intermediate that has been followed at 400 nm and exhibits a biphasic behavior concerning the absorbance evolution. Its formation involves a total loss of four electrons from two phenol molecules. On the behalf of permanganate ions it means that 1.25 moles of this condensed compound are formed for each mole of permanganate reduced to Mn(II). Therefore it can be formed at least 1.25 times faster than permanganate consumption. Because of the involvement of the intermediate valence state of Mn, more reactive than Mn(VII), the building of such a species in the early stages of reaction can outpace the rate of disappearance of Mn(VII) reported previously [27].

The rate coefficient for the intermediate formation $k^{'}_{obsd}$ (s^{-1}) exhibits a tendency of leveling off towards larger concentration of phenol as shown in Figure 1. The curve can be described by the following equation:

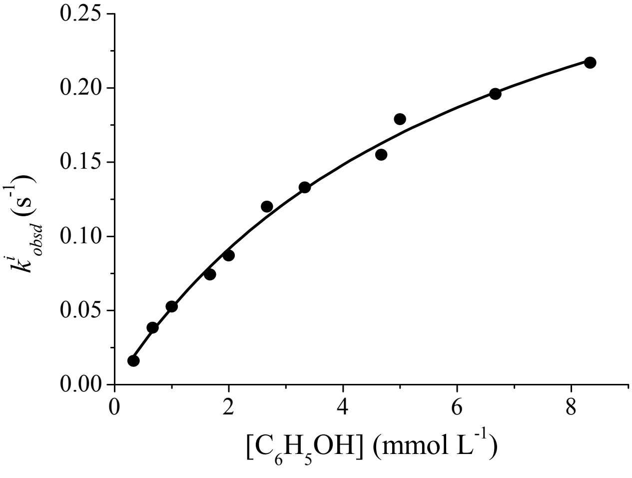

Figure 1. The first-order rate constant dependence on phenol concentration for the formation of intermediate.

$$k^{'}_{obsd} = \frac{a_1[C_6H_5OH]}{1+b_1[C_6H_5OH]} = \frac{(57.5\pm 2.5)[C_6H_5OH]}{1+(125\pm 11)[C_6H_5OH]} \tag{4}$$

with χ^2 = 0.000001 s^{-1} and R^2 =0.996. In the presence of Mn(II) ion, the same pattern has been observed and the equation is:

$$k^{'}_{obsd(Mn)} = \frac{a^{'}_1[C_6H_5OH]}{1+b^{'}_1[C_6H_5OH]} = \frac{(102\pm 5)[C_6H_5OH]}{1+(227\pm 20)[C_6H_5OH]} \tag{5}$$

The acceleration of reaction rate by Mn(II), which causes a supplementary decrease of Mn(VII) concentration, is due to the intermediate oxidation states of manganese that react faster with reducing organic species. For the case of Mn(II) initially added to the reaction mixture, data presented in columns 3 of Table 1 reveals also that k_{obsd}^{i} increases strongly at smaller concentration of phenol and not so pronounced at higher concentration. A similar tendency of leveling off also appears.

The linear form of this one-plus type equation as a double reciprocal of (4) and (5) also permits the determination of the coefficients.

$$\frac{1}{k_{obsd}^{'}} = \frac{1}{a[C_6H_5OH]} + \frac{b}{a} \tag{6}$$

The effect of the acidity on these rate coefficients was investigated within the range 0.07 – 0.7 mole·L^{-1} HClO$_4$. The mean rate coefficients obtained from at least three individual runs are given in Table 2. Data in the second and third columns fitted well with a linear dependence:

$$k_{obsd}^{'} = (3.0 \pm 8{,}5)\cdot 10^{-3} + (0.34 \pm 0.02)[H^{+}] \tag{7}$$

with R^2= 0.999 and SD = 0.004 in the absence of Mn(II), and

$$k_{obsd(Mn)}^{'} = (1.9 \pm 2.0)\cdot 10^{-2} + (0.52 \pm 0.05)[H^{+}] \tag{8}$$

in the case of the initial presence of Mn(II) species in the mixture.

Table 2. The effect of acid concentration on the rate. [C$_6$H$_5$OH]=3.33·10^{-3}, [MnO$_4^-$] = 1.30·10^{-4}, μ = 0.4 and T = 298K in absence and presence of 3.33·10^{-4} mol.L^{-1} Mn(II)

[HClO$_4$] mol.L^{-1}	$k_{obsd}^{'}$ s^{-1}	$k_{obsd}^{'}$ s^{-1} Mn(II)	$k_{obsd}^{''}$ s^{-1}	$k_{obsd}^{''}$ s^{-1} Mn(II)
0.0773	0.0249	0.065	0.00316	0.00319
0.155	0.0559	0.1046	0.0046	0.0049
-0.232	0.0884	0.139	0.00662	0.00572
0.387	0.133	0.200	0.00846	0.00746
0.541	0.189	0.288	0.0098	0.0089
0.619	0.207	0.340	0.0101	0.00908
0.773	0.267	0.428	0.0110	0.00928

The linear dependence of $k^{'}_{obsd}$ as described by eqs (6) and (7) indicates a first-order with respect to hydrogen ion, the intercept of the lines being not statistically different from zero.

By combining equations (4) and (7), the rate coefficient for the intermediate formation can be written as dependent of both phenol and acid concentrations as:

$$k^{'}_{obsd}=\frac{\alpha_1[C_6H_5OH][H^+]}{1+\beta_1[C_6H_5OH]} \quad \text{or} \quad \frac{[H^+]}{k^{'}_{obsd}}=\frac{1}{\alpha_1[C_6H_5OH]}+\frac{\beta_1}{\alpha_1} \tag{9}$$

The parameters are: α_1 = (144± 8) $L^2mol^{-2}s^{-1}$ β_1 =(125± 13) $L.mol^{-1}$ and R^2= 0.997. By using additionally the data in column 1 of Table 2 in the linear form of eq. (9), the parameters of the line are: slope = 0.0066, the intercept = 0.8696 and R^2= 0.9962 corresponding to α_1 = (144± 8) $L^2mol^{-2}s^{-1}$, β_1 = (132 ± 12) $L.mol^{-1}$.

It is obvious that the *p*-diphenoquinone intermediate is formed on the account of permanganate in the early stages of the reaction. Therefore, in the initial absence of Mn(II) ion, its formation is caused by the oxidation of phenol by permanganate, or when considering the first-order with respect to hydrogen ion, by permanganic acid. Indeed, when the process was followed at 400 nm and various initial concentrations of permanganate were used, always as limiting reactant, a linear dependence of k^{i}_{obsd} on permanganate has been found:

$$k^{'}_{obsd}=(9.2\pm 5.4)\cdot 10^{-3}+(9.1\pm 0.4)\cdot 10^{2}[MnO_4^-] \tag{10}$$

Note that in the early stages of reaction, under the larger concentration of oxidizing agent, the larger concentration of phenoxy free radicals is formed and the larger rate of biphenoquinone would be. The intercept is quite small and can be considered zero. It clearly justifies the use of equation (4), which is first order with respect to the colored oxidizing agent. Another possibility of the proton involvement could be its rapid bounding to phenol.

If one compares k_{obsd} at the permanganate consumption (λ = 525 nm), as obtained previously [27], with the apparent first-order rate coefficient $k^{'}_{obsd}$, the latter is greater than $1.25\cdot k_{obsd}$. The stoichiometric factor of 1.25 comes out from the need of 4-electron removal from reducing species to form a molecule of biphenoquinone. The involvement of intermediate valence-state of Mn, which react faster than Mn(VII) is apparent. The dependence in Table 1 proves the involvement of at least Mn(III) species revealing the autocatalysis/catalysis by Mn(II). On the other hand, the involvement of two terms in the denominator of rate equation (9) indicates also the presence of a fast reversible process.

The effect of temperature on the apparent first-order rate constant $k^{'}_{obsd}$ in the range of 15 – 40°C yielded an experimental activation energy of 67±2 kJ.mol^{-1}. A comparison with the smaller value of 12.5±1.9 kJ.mol^{-1} when permanganate consumption was monitored [27], indicates that the step of formation of phenoxy radical is not the rate-determining step for 4,4'-biphenoquinone formation, but its further oxidation or coupling. The switch from oxy free radical to a carbon free radical (eq. 1.b) seems also to take place rapidly within the π-conjugated electronic system. The coupling and further oxidation (or further oxidation of C-free radical and coupling) could also justify the linear dependence of k^{i}_{obsd} on permanganate.

Concerning the decay of the intermediate species, the same pattern of the one-plus type rate law has been found as dependent of the substrate concentration. The apparent first-order rate constant is:

$$k^{''}_{obsd} = \frac{a_2[C_6H_5OH]}{1+b_2[C_6H_5OH]} = \frac{(7.1\pm0.3)[C_6H_5OH]}{1+(547\pm33)[C_6H_5OH]} \tag{11}$$

with χ^2 = 1.5.10^{-7} s^{-1}and R^2 =0.997 for the consumption of the intermediate in the absence of Mn(II) ion. The linear form of eq.(10), as a double reciprocal, is presented in Figure 2.

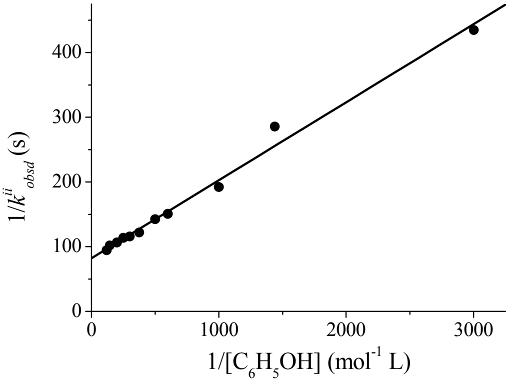

Figure 2. Double reciprocal plot of equation (5) with the data in Table 1

The parameters of the line are: slope = 1/a$_2$ = 0.141, intercept = b$_2$/a$_2$= 77.1, R^2 = 0.9877. The constants are a$_2$ =7.1±0.3 L.mol^{-1}s^{-1} and b$_2$ =547±33 L.mol^{-1}(errors statistically counted). On the other hand, as presented in the last two columns of table 1, a small decline of $k^{''}_{obsd}$, as compared to the values in the absence of Mn(II) in the mixture has been noticed for the disappearance of the biphenoquinone intermediate.

A more complex behavior has been found at the decay of the intermediate as dependent on the mineral acid in solution as compared to that of the intermediate formation. A one-plus type equation describes hydrogen ion effect on the observed rate. It infers the involvement of a rapid protonation pre-equilibrium. The apparent first-order rate constant is:

$$k''_{obsd} = \frac{a'_2[H^+]}{1+b'_2[H^+]} = \frac{(0.051 \pm 0.0023)[H^+]}{1+(3.47 \pm 0.25)[H^+]} \quad \frac{1}{k''_{obsd}} = \frac{1}{a'_2[H^+]} + \frac{b'_2}{a'_2} \quad (12)$$

It is characterized by $\chi^2 = 3.68.10^{-8}$, $R^2 = 0.998$ and $R^2 = 0.9968$ for the line. In the presence of Mn(II) the corresponding values are: $a'_2 = (5.6 \pm 0.3) \cdot 10^{-2}$ L.mol^{-1}s^{-1}, $b'_2 = 4.79 \pm 0.23$ L.mol^{-1} and $R^2 = 0.993$. These last values are not far from those in the absence of Mn(II), suggesting the interaction between phenol and 4,4'-biphenoquinone is not significantly influenced by the catalyst.

When combining equations (11) and (12), the decay rate of the intermediate is described by the following rate equation:

$$-\frac{d[OC_6H_4 = C_6H_4O]}{dt} = \frac{\alpha_2[C_6H_5OH][H^+]}{1+\beta_2[C_6H_5OH][H^+]}[OC_6H_4 = C_6H_4O] \quad (13)$$

and the first-order rate coefficient is:

$$k''_{obsd} = \frac{\alpha_2[C_6H_5OH][H^+]}{1+\beta_2[C_6H_5OH][H^+]} \quad (14)$$

with the parameters $\alpha_2 = (17.9 \pm 0.7)$ L^{2}mol^{-2}s^{-1} and $\beta_2 = (1.32 \pm 0.12) \cdot 10^3$ L^{2}mol^{-2}. It can be assigned to the reaction of the protonated *p*-diphenoquinone with the excess phenol molecule.

If this equation describes well the data, it should be applied to both series of measurements, when either phenol, or the acid has been maintained constant and the other was varied. Indeed, we obtained such a correlation in the linear form, as presented in Figure 3.

$$\frac{1}{k''_{obsd}} = \frac{1}{\alpha'''}\frac{1}{[C_6H_5OH][H^+]} + \frac{\beta'''}{\alpha'''} \quad (15)$$

with $R^2 = 0.993$, ($\beta_2/\alpha_2 = 74 \pm 4$) and ($1/\alpha_2 = 0.056 \pm 0.002$) mol^{2}s.L^{-2}.

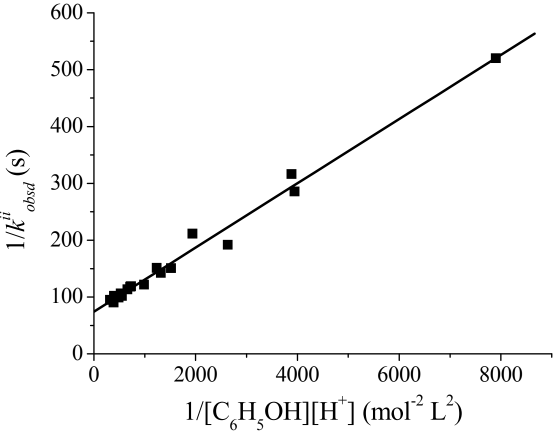

Figure 3. Linear presentation of all data (eq.14) of the two series of measurements (Tables 1 and 2) in the absence of Mn(II).

Accounting for the acid effects, interaction of protonated 4,4’-biphenoquinone is involved in the phenol oxidation to generate biphenols [39] with the stoichiometry:

$$HO-C_6H_4^+=C_6H_4=O+2C_6H_5-OH \rightarrow 2HO-C_6H_4-C_6H_4-OH+H^+ \quad (15)$$

It could proceed by two successive one-equivalent electron-transfer yielding free oxy radicals from phenol and biphenol. The apparent activation energy determined over the same range of temperature by the effects on $k^{''}_{obsd}$ is 50 ± 1 kJ.mol^{-1}, a value smaller than that of the intermediate formation, and could be attributed to the first one- equivalent electron-transfer step (or first hydrogen abstraction from phenol by protonated 4,4'-biphenoquinone). The second step involves a free oxy radical of biphenol, which would react faster with the second phenol molecule.

The overall stoichiometry of phenol – permanganate reaction found previously [27] implies that the partial oxidized products of phenol react further, and probably faster, up to the ring rupture, even in the presence of phenol excess with any oxidizing species in relative strong acid solution. A possible route could be by means of traces of benzoquinone formed by phenoxy radical oxidation. All intermediate oxidation states of manganese are able to bring about oxidative ring breakage of *o*-.or *p*-benzoquinone. The complexity of the system needs more data for a better elucidation of the elementary steps network.

CONCLUSIONS

The formation and decay of 4,4'-biphenoquinone, as an active intermediate, has been followed and the corresponding rate laws have been determined.

The presence of Mn(II) in the solution has a catalytic effect on the formation and practically no influence on the consumption of intermediate.

The one-plus rate laws revealed complex mechanisms with the involvement of some pre-equilibrium concerning the proton intervention. Third-order rate constants α and equilibrium constants β were estimated from the kinetics.

The apparent activation energies were also obtained, which argue the rate determining steps implied in the formation and redox consumption of 4,4'-biphenoquinone.

EXPERIMENTAL SECTION

Materials. Chemicals of analytical grade and ultra-pure water (deionised and tetra-distilled) were used throughout this study. A stock solution of $HClO_4$ was prepared from Merk's 70 % $HClO_4$ and standardized by titration. Stock solution of $NaClO_4$ was prepared from Merk's $NaClO_4.H_2O$ and standardized by titration after passing a measured volume over Vionit –100C (H-form) cationic resin. Working solution of $KMnO_4$ was prepared before each set of runs and standardized by titration with oxalic acid. The phenol solution was also prepared freshly from purified staff (distillation under low pressure; m.p. 40.5 – 41.5°C).

Kinetic measurements. Electronic absorption spectra were recorded either by using a M-40 Diode-Array Spectrophotometer or a Jasco UV-VIS V-530 spectrophotometer. A conventional spectrophotometrical method was used to monitor the progress of the reaction at constant temperature. Two wavelengths could be used: either at 525 nm, where permanganate ion exhibits an absorption peak and its disappearance was recorded, or 400 nm, where a biphasic plot has been obtained, the formation and the decay of a yellowish-brown colored intermediate species. The reaction was performed in a quartz 5-cm path length cuvette. It was started by injecting of 5 mL permanganate solution over the mixture of the other reactants. The mixing time does not exceed 1 second. Pseudo-first-order conditions were employed. Both the phenol and mineral acid were taken in excess as compared to permanganate oxidizing agent. Kinetic measurements were also carried out in the presence of Mn(II) ions, in a small excess as compared to permanganate.

ACKNOWLEDGMENT

Financial support of Romanian National University Research Council (CNCSIS) is gratefully acknowledged by the authors.

REFERENCES

1. P. Berka, Z. Zavesky, *Mikrochim. Acta*, **1974**, *3*, 493.
2. D. A. Skoog, D. M. West, *Fundamentals of Analytical Chemistry*, 1-st Ed. Holt, Reinhart and Winston, New-York, **1963**.
3. W. I. Taylor, A. R. Battersby, *Oxidative coupling of phenols*, Ed. Dekker, New York, **1967**.
4. L. K. Liu, C. S. Lin, *J. Chin. Chem. Soc.*, **1996**, *43*, 61.
5. S. Dash, S. Patel, B. K. Mishra, *Tetrahedron*, **2009**, *65,* 707.
6. F. Freeman, C. O. Fuselier, C. R. Armsted, C. E. Dalton, P. A. Davidson, E. M. Karchesfski, D. E. Krochman, M. N. Johnson, N. K. Jones, *J. Am. Chem. Soc.*, **1981**, *103*, 1154.
7. F. Freeman, *Rev. React. Species Chem. React.*, **1976**, *1*, 179.
8. R. Stewart, *Oxidation in Organic Chemistry*, Ed. K. B. Wiberg, Academic Press, New York, Part A, **1965**.
9. L. I. Simandi, M. Jaky, F. Freeman, C. O. Fuselier, E. M. Karchesfski, *Inorg. Chim. Acta*, **1978**, *31*, 457.
10. D. Benson, *Mechanisms of Oxidation by Metal Ions*, Elsevier, Amsterdam, **1976**.
11. L. I. Simandi, M. Jaky, N. T. Son, J. Hagedus-Vajda, *J. Chem. Soc. Perkin Trans 2*, **1977**, *10*, 1794.
12. R. H. Simoyi, P. de Kepper, I. R. Epstein, K. Kustin, *Inorg. Chem.*,**1986**, *25*, 538.
13. P. Bhatia, K. K. Banerji, *J. Chem. Soc. Perkin Trans 2*, **1983**, 1577.
14. D. G. Lee, C. F. Sebastian, *Can. J. Chem.*, **1981**, *59*, 2776.
15. D. G. Lee, C. F. Sebastian, *Can. J. Chem.*, **1981**, *59*, 2780.
16. R. G. Panari, R. B. Chougale, S. T. Nadibewoor, *J. Phys. Org. Chem.*,1998, *11*, 448.
17. R. G. Panari, R. B. Chougale, S. T. Nadibewoor, *Polish Journ. Chem.*, **1998**, 72, 99.
18. M. Jaky, J. Szammer, *J. Phys. Org. Chem.*, **1997**, *10*, 420.
19. B. K. Satsangi, S. Kothari, *J. Ind. Chem. Soc.*, 1980, *74*(1), 16.
20. J. W. Landbury, C. F. Cullis, *Chem. Rev.*, **1958**, *58,* 403.
21. M. J. Insausti, F. Mata-Perez, M. P. Alvarez-Macho, *An. Quim.*, **1991**, *87*, 877.
22. M. J. Insausti, F. Mata-Perez, M. P. Alvarez-Macho, *Collect. Czech. Chem. Commun.*, **1994**, *59*, 528.
23. M. J. Insausti, F. Mata-Perez, M. P. Alvarez-Macho, *Collect. Czech. Chem. Commun.*, **1996**, *61*, 232.
24. S. Vivekanandan, K. Venkatarao, M. Santappa, S. Shanmuganathan, *Indian J. Chem., Sect. A*, **1980**, *19*, 364; Alexandra Csavdari, I. Baldea, *Studia Univ. Babes-Bolyai, Chem.*, **2007**, *52(1)*, 35.

25. M.S. Manhas, F. Mohasmmed, Z. Khan, *Colloids and Surface. A. Physicochemical and Engineering Aspects,* **2007**, *253*, 165.
26. N. Kang, D. S. Lee, J. Yoon, *Chemosfere*, **2002**, *47*, 915.
27. L. Copolovici, I. Baldea, *Rev. Roum. Chim*., **2007,** *52,* 1045.
28. G. Davies, *Coordin. Chem. Rev.*, **1969**, *4*, 199.
29. A. McAuley, *Coordin. Chem. Rev.*, **1970**, *5,* 245.
30. F. Well, G. Davies, *Nature*, **1965**, *205*, 692; F. Well, G. Davies, *J. Chem. Soc.* A, **1967**, 1858; J. P. Fackler, I. D. Chawla, *Inorg. Chem.*, **1964**, *3*, 1130.
31. L. I. Simandi, M. Jaky, C. R. Savage, Z. A. Schelly, *J. Am. Chem. Soc.*, **1985**, *107,* 4220.
32. F. Mata, J. Perez-Bendito, A. Arranz, *Z. Phys. Chem. (Leipzig),* **1983**, *135,* 141.
33. M. I. Hussain, F. Ahmad, *Transition Met. Chem.*, **1990**, *15*, 185.
34. H. Huang, D. Sommerfeld, B. C. Dunn, E. M. Eyring, C. R. Lloyd, *J. Phys. Chem. A*, **2001**, *105*, 3536.
35. a) M. Bhattacharjee, M.K. Mahanti, *Int. J. Chem. Kinet.,* **1983**, *15,* 197; b) T.Y. Douglas Yiu, F.W.Mendy Lee, W.Y. William Lam,Tai-Chu Lau, *Inorg.Chem*., **2003**, *42*, 1225; c) A. Alajlouni, A. Bakac, J.H. Espenson, *Inorg. Chem.*, **1993**, *32*, 5792.
36. A. S. Hay*, J.Org.Chem*., **1969**, *34*, 1160; G.F.Endres, A.S.Hay, J. W. Eustance, *J. Org. Chem*., **1963**, *28*, 1300; A. S. Hay*, J.Polym Sci*., **1962**, *88,* 581; A. S. Hay, *Tetrahedron Lett*., **1965**, 4341.
37. J. D. Rush, J. E. Cyr, Z. Zhao, B. H. Bielski, *J. Free Radical Res.*, **1995**, 22, 349.
38. A. Al-Ajlouni, K. Shawakfeh, R. Rajal, *Kinetics and Catalysis*, **2009**, *50*, 88.
39. F. M. Menger, D. W. Carnahan, *J. Org. Chem.,* **1985**, *50*, 3927.

STUDIA UNIVERSITATIS BABEŞ-BOLYAI, CHEMIA, XLV, 2, TOM I, 2010

Dedicated to the memory of Prof. dr. Ioan Silaghi-Dumitrescu marking 60 years from his birth

SYNTHESIS OF TUNGSTEN TRIOXIDE MESOPOROUS POWDERS PREPARED BY INORGANIC SOL-GEL ROUTE

ECATERINA BICA[a, b], ELISABETH-JEANNE POPOVICI[a], MARIA ŞTEFAN[a], IOANA PERHAIȚA[a] AND IONEL CĂTĂLIN POPESCU[b]

ABSTRACT. Powders of mesoporous tungsten trioxide (WO_3) have been synthesized by an inorganic sol-gel route, in presence of polyethylene glycol PEG as porosity regulating agent. The influences of PEG addition and calcination regime on powder properties were investigated. Samples characterization was performed by thermal analysis, UV-Vis spectroscopy, as well as by surface area and porosity measurements.

Keywords: *Tungsten trioxide powders, sol-gel method, porosity, optical properties.*

INTRODUCTION

Tungsten trioxide (WO_3) is a semiconductor with special optical and electrical properties which explain its use as photoanode in electrochemical hydrogen production or as photocatalyst in pollutants photodegradation [1-4]. The energy band gap of 2.3 - 2.8 eV allows hole generation and quick formation of electron-hole pairs under UV light irradiation, which confer WO_3 a good photocatalytic activity [5, 6]. The morpho-structural properties of the powder, i.e. crystalline structure, porosity, surface morphology, particles size and optical characteristics are strongly influenced by the synthesis route and subsequent treatment conditions [7, 8].

Among the preparation methods, the sol-gel route offers many advantages such as molecular-scale homogeneity, high purity and reactivity, as well as controlled particles size and shape of the obtained product [9-12]. By this synthesis route, mesoporous WO_3 powders could be obtained in special preparation conditions. Their high photocatalytic activity in oxidation

---

[a] *Babeş-Bolyai University, “Raluca Ripan” Institute for Research in Chemistry, Fantanele 30, Cluj-Napoca, Romania, ebica@chem.ubbcluj.ro*

[b] *Babeş-Bolyai University, University, Faculty of Chemistry and Chemical Engineering, Arany Janos 11, Cluj-Napoca, Romania*

processes is correlated with a large surface area, with many active sites, which can adsorb water, molecular oxygen or hydroxyl group in order to produce active oxidizing species [13].

The present paper continues our studies concerning the preparation of WO_3 powders and thin films, with well defined properties [14-17]. In this context, tungsten trioxide powders were prepared by sol-gel method, in presence of polyethylene glycol (PEG), as porosity regulating agent. The influences of polymer additive and calcination regime on WO_3 powder properties were also investigated. Because the main goal of our studies is the preparation of WO_3-based materials with good photocatalytic properties, special attention was given to the powder porosity control.

RESULTS AND DISCUSSIONS

Tungsten trioxide powders were obtained from tungstic acid precursors ($WO_3.xH_2O$) prepared by sol-gel method, in the presence of polyethylene glycol with variable polymerization degree (PEG200, PEG400, PEG600). The thermal treatment was performed at 550^0C for 30 - 90 minutes (Table 1).

Table 1. Synthesis conditions of WO_3 samples

Precursor code	Polymer additive	Sample code	Thermal treatment
Pr_SG1	-	**SG1-30**	550^0C / 30 min
		SG1-90	550^0C / 90 min
Pr_SG2	PEG200	**SG2-30**	550^0C / 30 min
		SG2-90	550^0C / 90 min
Pr_SG3	PEG400	**SG3-30**	550^0C / 30 min
		SG3-90	550^0C / 90 min
Pr_SG4	PEG600	**SG4-30**	550^0C / 30 min
		SG4-90	550^0C / 90 min

In order to establish the optimal calcination regime, the tungstic acid precursors were investigated by thermal analysis. Thermogravimetric (TGA), differential thermogravimetric (DTG) and differential thermal analysis (DTA) results illustrate the difference between the thermal behavior of $WO_3.xH_2O$ precursors prepared with or without polymer additive (Fig.1).

The sample with no polymer additive (Pr-SG1) shows a total weight loss of ~12%. The two main decomposition steps are associated with the removal of physically (25-200^0C) and chemically bonded water (200-400^0C). The endothermic effect observed at 305^0C corresponds to the tungstic acid decomposition.

The thermal behavior of all PEG containing precursors was similar, the major difference being the total weight loss. Between 25-150^{o}C, there are two steps of weight loss, associated with the removal of physical adsorbed water and alcohol. The weight loss step noticed at 150-250^{0}C was related with PEG decomposition. DTG curves illustrate that the maximum weight loss is at ~215^{0}C (Pr_SG2), ~201^{o}C (Pr_SG3) and ~191^{o}C (Pr_SG4). On DTA curves, the corresponding endo-thermal peaks can be noticed at ~220^{o}C (Pr_SG2), ~207^{o}C (Pr_SG3) and ~201^{o}C (Pr_SG4). For PEG containing powders, one additional small exo-thermal effect can be observed at ~250^{0}C (Pr_SG2), ~246^{0}C (Pr_SG3) and 242^{0}C (Pr_SG4) that could be ascribed to the self-ignition of the residual polyalcohol.

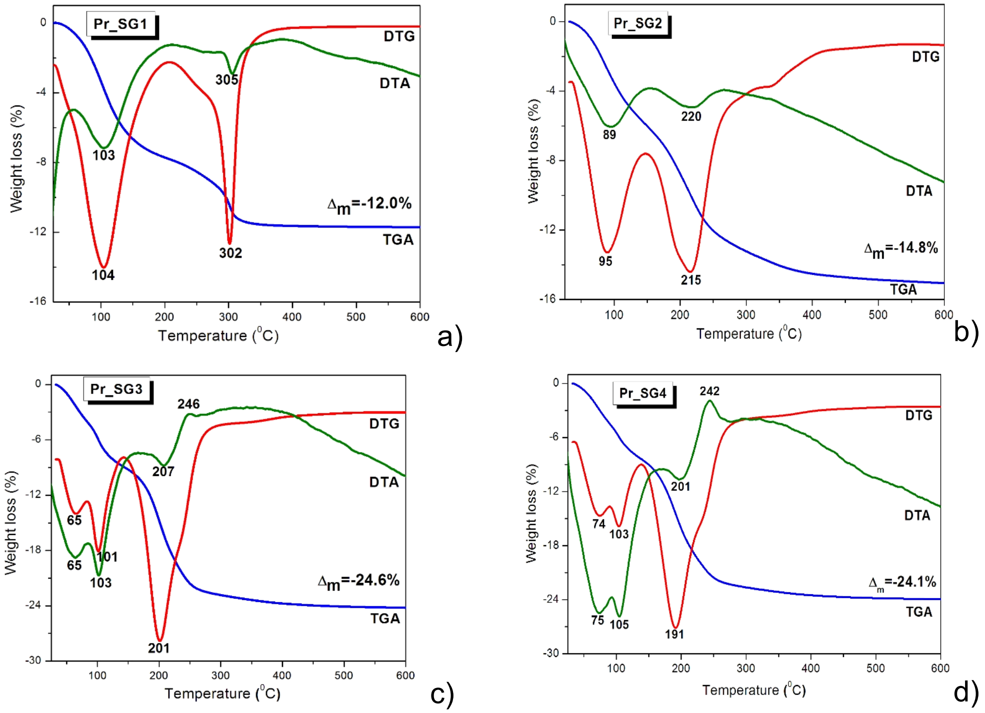

Figure 1. TGA/DTG/DTA curves of precursors with no polymer (a), PEG200 (b), PEG400 (c) and PEG600 (d) additive

According to the thermal analysis results, the conversion of precursors with or without polymer addition into tungstic oxide powders is finalized at 500^{0}C.

In order to obtain WO_3 powders with controlled porosity properties, the thermal treatment regime was investigated. For this reason, precursor samples were thermally treated for 30 min (short thermal treatment) and 90 min (long thermal treatment) at 550^0C. Subsequently, the specific surface area and porosity were determined using the nitrogen adsorption isotherms (Fig. 2).

The BET (Brunauer, Emmett & Teller) specific surface area was calculated by determining the monolayer volume of adsorbed gas (Table 2). The micro-pores (d<2nm) volume and area were calculated from the t-plot (thickness curve) using the Broekhoff-de Boer equation, involving the thickness evaluation of the monolayer of adsorbed gas. The mesopore (d = 2 - 50nm) and macropore (d > 50nm) volume and area distribution were determined using BJH (Barett, Joyner & Halenda) calculation, based on the variation of the thickness of both the adsorbate layer and the condensed liquid, with porosity [18].

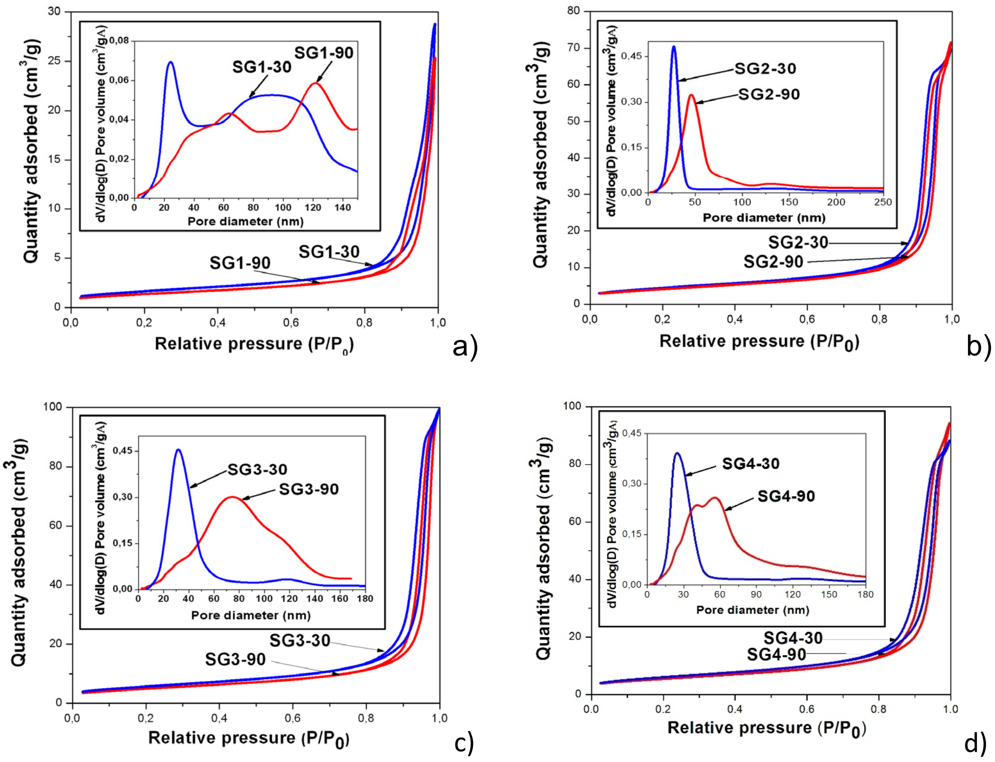

Figure 2. Adsorption-desorption isotherms of WO_3 samples and the volume pores distribution curve in function of pore diameter (inset): a) SG1 (WO_3); b) SG2 (WO_3/PEG200); c) SG3 (WO_3/PEG400); d) SG4(WO_3/PEG600)

Table 2. The surface area and porosity characteristics of WO_3 samples

Sample code	Specific surface area BET (m^2/g)	Micro-pores (t-plot)		Meso and Macro-pores (BJH-desorption)		
		Total volume (cm^3/g)	Total area (m^2/g)	Total volume (cm^3/g)	Total area (m^2/g)	Average diameter (nm)
SG1-30	5.9	0.0003	2.1	0.0453	5.7	103.7
SG1-90	4.9	0.0004	2.0	0.0400	4.8	33.7
SG2-30	16.2	0.0007	5.6	0.1121	18.5	123.1
SG2-90	15.0	0.0013	6.6	0.1132	16.5	27.5
SG3-30	20.3	0.0013	7.8	0.1577	22.7	108.8
SG3-90	17.6	0.0014	7.2	0.1545	18.6	33.2
SG4-30	21.7	0.0009	7.4	0.1409	24.9	116.5
SG4-90	19.6	0.0018	8.4	0.1498	22.4	26.7

The distribution curve of the no polymer containing WO_3 is multimodal which accounts for the heterogeneous porosity of the powder (Fig. 2a).

The increase of the calcination time decreases the surface area (from 5.9 to 4.9 m^2/g), at same time with the decrease of the meso- and macropore volume and area. Additionally, the average pore diameter decreases from ~103.7 nm to ~33.7 nm.

The addition of polyethylene glycol determines the regularization of pore dimensions, for both types of thermally treated samples. All distribution curves become unimodal (Fig. 2b-d). At the same time, the surface area of WO_3 powders increases in direct relation with the enlargement of the pore volume and area. The effect is stronger for polyalcohol with high polymerization degree. It can be concluded that PEG additive acts as porosity regulator.

The prolongation of the thermal treatment shifts the maximum of the distribution curve from mesopore to macropore domain. This suggests that the small size pores coalesced under the thermal treatment.

Tungsten trioxide powders prepared with PEG additive are mesoporous and show a relative homogeneous porosity as compared with no polymer containing WO_3 powder. The effect was stronger for sample prepared with PEG200.

The use of PEG with higher molecular weight increases the pore volume and area and consequently enlarges the BET specific surface area. The prolongation of the thermal treatment determines a slow displacement of pores size toward macropore domain, due to the complete removal of the organic material.

All tungsten trioxide powders absorb light in the visible domain and have a lime-fruit color. The influence of the polymer addition and thermal synthesis regime on the WO_3 powder color was put in evidence by the diffuse reflectance spectra depicted in Fig. 3. The no polymer containing WO_3 powder (SG1-30) presents a good reflection in the yellow-green spectral domain with a maximum at 519 nm. Moreover, the powder reflection is improved with about 15% by the thermal treatment (SG1-90).

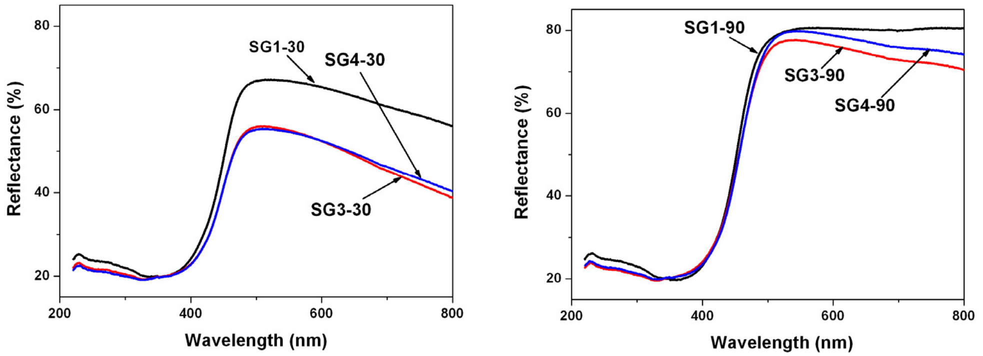

Figure 3. Diffuse reflectance spectra of WO_3 powders with no polymer containing (SG1), PEG400 (SG2) and PEG600(SG3) addition

The PEG addition seems to a blue-shift of the maximum reflectance and to decrease the reflectivity of WO_3 powders. The prolongation of the thermal treatment improves the powder reflectivity with about 20%.

Some of the optical characteristics of WO_3 powders, determined on the basis of the diffuse reflectance spectra, are summarized in Table 3. The optical band gap (Eg) was evaluated from the absorption spectra obtained by conversion of the diffuse reflectance spectra.

Table 3. Optical characteristics of WO_3 powders

Code probe	**Maximum reflectance (R_{max})**		**Wavelength cut-off $\lambda_{cut-off}$ (nm)**	**Eg (eV)**
	Wavelength λ (nm)	**Reflectance R (%)**		
SG1-30	519	67	481.5	2.58
SG1-90	563	81	488.9	2.54
SG3-30	512	56	490.8	2.53
SG3-90	543	78	496.1	2.50
SG4-30	510	55	482.9	2.57
SG4-90	545	80	494.1	2.51

According to the literature data, the band gap energy of semiconductors can be estimated from the wavelength cut-off ($\lambda_{cut-off}$) representing the intersection point between the tangent at the absorption curve and the x axe [19, 20]. The band gap energy is calculated using the relation Eg (eV) = 1240 / $\lambda_{cut-off}$ (nm).

The calculated values of the band gap energy are in 2.50 - 2.58 eV range, in good agreement with the literature data [21]. The band gap tends to decrease with both the polymer addition and the annealing duration.

The use of a relative longer thermal treatment is favorable for the obtaining of WO_3 powders with improved optical properties. The effect is stronger for samples prepared with PEG additive, probable in association with a more complete removal of organics.

Some of the tungsten trioxide powders were tested for photocatalytic activity in the dye degradation. For these preliminary tests, SG1-30 (WO_3) and SG3-30 (WO_3/PEG400) samples were used for the methylene blue photo-degradation. The efficiency values were 90% for SG1-30 and 40% for SG3-30, illustrating that WO_3 samples show significant photocatalytic activity. The incomplete removal of the organic material dramatically damages the photocatalytic activity for dye oxidative degradation.

CONCLUSIONS

Tungsten trioxide powders were prepared following an inorganic sol-gel route, in presence of polyethylene glycol i.e. PEG200, PEG400 and PEG600. The surface area and porosity as well as the optical properties of WO_3 powders are influenced by thermal treatment regime and PEG addition.

Tungsten trioxide powders prepared with PEG additive are mesoporous and show a relative homogeneous porosity as compared with the no polymer containing WO_3 powder. The effect is stronger for sample prepared with PEG200. The use of PEG with higher molecular weight increases the pore volume and area and consequently, enlarges the BET specific surface area. The increase of the thermal treatment time determines a slow displacement of pores dimensions toward the macropore domain, due to a better removal of the organic material.

As evidenced by the diffuse reflectance spectroscopy, the polymer addition and the thermal synthesis regime influence the color of WO_3 powder. The PEG addition exerts a blue-shift of the maximum reflectance and decreases the reflectivity of WO_3 powders. The use of a relative longer time for thermal treatment favors obtaining of WO_3 powders with improved optical properties. The calculated band gap energies are in good agreement with the literature data and decrease with both polymer addition and the annealing duration.

Some of the mesoporous tungsten trioxide powders were used as photocatalysts for a reference dye photodegradation. Thus, the tested WO_3 samples show a significant photocatalytic activity for the oxidative degradation of methylene blue. The incomplete removal of the organic material, associated with a short thermal treatment, damages the photocatalytic activity.

EXPERIMENTAL SECTION

Sample preparation

Tungsten trioxide (WO_3) powders were prepared from tungstic acid solution obtained by dissolving 8 g tungsten powder (Merck) into 60 ml 30% hydrogen peroxide (Merck). The dissolution process was conducted under magnetic stirring, at 0 -10^{0}C (exothermic reaction) and the H_2O_2 excess was removed by catalytic decomposition on Pt black [22]. In order to obtain powders with controlled porosity, polyethylene glycol (Carlo Erba) with variable molecular weight i.e. PEG200, PEG400 or PEG600 was used as additive. The yellow-translucent sol was dried at 70^{0}C, in air. The as obtained tungstic acid precursors were annealed at 550^{0}C, in air, for 30 or 90 minutes.

Sample characterization

The tungstic acid precursors were investigated by thermal analysis (Mettler Toledo TGA/SDTA851; heating rate 5^{0}C/min; N_2 atmosphere).

WO_3 powders were characterized by surface area measurements (Micromeritics Tristar II 3020 instrument, N_2 adsorption; BET method for surface area; the BJH method/desorption branch for pores size distribution) and UV-Vis spectroscopy/diffuse reflectance spectra (Jasco Spectrometer V650, with ILV 724 integrating sphere accessory, light source D2/WI). The photocatalytic activity was evaluated for methylene blue degradation (1g WO_3 powder was used for 100 ml aqueous 0.125 mM solution of methylene blue).

ACKNOWLEDGEMENTS

This work was supported by the Romanian Ministry of Education, Research and Innovation (Contract PNII 71-047).

REFERENCES

1. H. Wang, P. Xu, T. Wang, *Thin Solid Films*, **2001**, *388*, 68.
2. A. Watcharenwong, W. Chanmanee, N. R. Tacconi, C. R. Chenthamarakshan, P. Kajitvichyanukul, K. Rajeshwar, *Journal of Electroanalytical Chemistry,* **2008**, *612*, 112.
3. H. Liu, S. Huang, L. Zhang, S. Liu, W. Xin, L. Xu, *Catalysis Communications*, **2009**, *10*, 544.
4. A. Cremonesi, Y. Djaoued, D. Bersani, P.P. Lottici, *Thin Solid Films*, **2008**, *516*, 4128.

5. M. G. Hutchins, O. Abu-Alkhair, M.M. El-Nahass, K. Abd El-Hady, *Materials Chemistry and Physics*, **2006**, *98*, 401.
6. J. Sun, Y. Wang, R. Sun, S. Dong, *Materials Chemistry and Physics*, **2009**, *115*, 303.
7. M. Deepa, M. Kar, D.P. Singh, A.K. Srivastava, S. Ahmad, *Solar Energy Materials & Solar Cells*, **2008**, *92*, 170.
8. A. Cremonesi, Y. Djaoued, D. Bersani, P.P. Lottici, *Thin Solid Films*, **2008**, *516*, 4128.
9. J. Livage, M. Henry, C. Sanchez, *Progress in Solid State Chemistry*, **1988**, *18*, 259.
10. I. Jimenez, J. Arbiol, A. Cornet, J.R. Morante, *IEEE Sensors Journal*, **2002**, *2*, 329.
11. H. I.S. Nogueira, A.M.V. Cavaleiro, J. Rocha, T. Trindade, J.D. Pedrosa de Jesus, *Materials Research Bulletin*, **2004**, *39*, 683.
12. H. Liu, T. Peng, D. Ke, Z. Peng, C. Yan, *Materials Chemistry and Physics*, **2007**, *104*, 377.
13. Z. Lixia, Z. Qin, L. Qingcheng, *Journal Of Rare Earths*, **2006**, *24*, 60.
14. M. Stefan, E. Bica, L. Muresan, R. Grecu, E. Indrea, M. Trif, E. J. Popovici, *Journal of Optoelectronics and Advanced Materials – Symposia*, **2010**, *2,* 115.
15. E. Bica, M. Stefan, L. E. Muresan, E. Indrea, I. C. Popescu, E. J. Popovici, *Journal of Optoelectronics and Advanced Materials – Symposia*, **2009**, *1,* 1011.
16. E. Bica, M. Stefan, I. C. Popescu, L. Muresan, M. Trif, E. Indrea, E. J. Popovici, *Journal of Optoelectronics and Advanced Materials – Symposia*, **2010**, *2,* 107.
17. E. Bica, L. E. Muresan, L. Barbu-Tudoran, E. Indrea, I. C. Popescu, E. J. Popovici, *Studia Universitatis Babes-Bolyai, Chemia*, **2009**, *LIV,* 15.
18. P. A. Webb, C. Orr, “Analytical Methods in Fine Particle Technology”, Micromeritics Instrument Corporation, U.S.A., **1997**, chapter 3.
19. J. Portier, H.S. Hilal, I. Saadeddin, S.J. Hwang, M.A. Subramanian, G. Campet, *Progress in Solid State Chemistry*, **2004**, *32*, 207.
20. S. Gorai, P. Guha, D. Ganguli, S. Chaudhuri, *Materials Chemistry and Physics*, **2003**, *82*, 974–979.
21. G. R. Bamwenda, H. Arakawa, *Applied Catalysis A: General*, **2001**, *210*, 181.
22. M. Stefan, E. Bica, L.E. Muresan, E. Indrea, E.J. Popovici, *Journal of Optoelectronics and Advanced Materials – Symposia*, **2009**, *1,* 1004.

STUDIA UNIVERSITATIS BABEŞ-BOLYAI, CHEMIA, XLV, 2, TOM I, 2010

Dedicated to the memory of Prof. dr. Ioan Silaghi-Dumitrescu marking 60 years from his birth

GROWTH RATE OF HYDROXYAPATITE CRYSTALS OBTAINED BY PRECIPITATION

VALENTINA ROXANA DEJEU*, BARABÁS REKA, ANA-MARIA CORMOŞ, BOGYA ERZSÉBET SÁRA, PAUL-ŞERBAN AGACHI

ABSTRACT. Identification of a precipitation process consists in the formulation of a mathematical model which describes the real system characteristics. The model parameters have physical significance in terms like growth rate, nucleation rate or population density of particles. In the present work, the precipitation kinetics of hydroxyapatite (HAP) was studied at the laboratory scale using a 0.5 L batch reactor. The vessel was operated continuously at 25 ºC and 50 ºC at different feed concentrations. A methodology already known for other systems was applied to determine the kinetic parameters (growth rate) from the crystal size distribution (CSD) in the preparation of hydroxyapatite. Predicted particle size characteristics shown reasonable agreement with experimental data collected. The influence of feed concentration on particle size of hydroxyapatite was discussed too.

Keywords: *hydroxyapatite, growth rate, population balance, precipitation, particle formation, mathematical*

INTRODUCTION

The study of precipitation processes using chemical reaction engineering is based on a direct correlation between the processes kinetic (chemical reaction rates, nucleation and growth rates) and the final product quality (crystal shape and CSD). The way that this estimation is made is essential in the critical analysis of the accuracy and model validity. Several authors have presented methods for the simultaneous estimation of crystal growth and nucleation kinetics from batch crystallizations. In an early study, Bransom and Dunning (1949) derived a crystal population balance to analyse batch CSD for growth and nucleation kinetics. Misra and White (1971), Ness and White (1976) and McNeil et al. (1978) applied the population balance

---

* *Universitatea Babeş-Bolyai, Facultatea de Chimie şi Inginerie Chimică, Str. Kogălniceanu Nr. 1, RO-400084 Cluj-Napoca, Romania, vdejeu@chem.ubbcluj.ro*

to obtain both nucleation and crystal growth rates from the measurement of crystal size distributions during a batch experiment. In a refinement, Tavare and Garside (1986) applied the laplace transformation to the population balance. Qui and Rasmusson (1991) and Nvlt (1989), respectively, measured solution concentration during seeded batch cooling crystallizations and determined the crystal size distribution from which growth and nucleation rates were determined. Witkowski et al. (1990) used a non-linear parameter estimation technique to estimate nucleation and growth rates based on solution concentration and light obscuration measurements. Gutwald and Mersmann (1990) estimated growth and nucleation rates from constant supersaturation controlled batch crystallization. Qui and Rasmuson (1994) proposed a direct optimization method based on solution concentration and product CSD data from seeded batch experiments. Aoun etal. (1999) reviewed methods for determining precipitation kinetics and also presented a method for the simultaneous determination of growth and nucleation kinetics from batch experiments [1].

The precipitation of calcium phosphates has attracted the interest of many researches because of its importance in industrial water system scale formation (e.g. heat exchangers, cooling towers, boilers, etc.), in water treatment processes, in catalysis as supporting material, in agriculture as fertilizers, and basically in bio-mineralization processes [2, 3, 4]. Hydroxyapatite, thermodynamically the most stable calcium phosphate at pH > 5, is the main inorganic compound of hard tissues in vertebrates. Although the precipitation of HAP is of particular importance in the bio-mineralization processes, very little is known about the crystal growth mechanism [5].

In the present work, the precipitation kinetics and the influence of feed concentration on particle size of hydroxyapatite was studied at the laboratory scale. Kinetic parameters identification was realized using an optimization algorithm based on a least squares minimization.

Precipitation kinetics

For a global treatment of the growing phenomena is necessary to model the crystal size distribution using the population balance equation (PBE) [6, 7]. General form of PBE described by Randolph and Larson [8] is:

$$\frac{\partial n}{\partial t} + G\frac{\partial n}{\partial L} = B_{aggl} + B_{disr} - D_{aggl} - D_{disr} - \frac{nQ}{V} \qquad (1)$$

where the birth terms for agglomeration and disruption are:

$$B_{aggl} + B_{disr} = \frac{L^2}{2}\int \frac{K_{aggl}\, n(L_u)n(L_v)dL_u}{L_v^2} + \int K_{disr} S(L_u, L_v)n(L_u)n(L_v)dL_u \qquad (2)$$

and the death terms for agglomeration and disruption are:

$$D_{aggl} + D_{disr} = n(L)\int K_{aggl} n(L_u)dL_u + K_{disr} n(L) \tag{3}$$

The expression for the supersaturation was found to be:

$$S = \left(\frac{C_A^{\nu_A} C_B^{\nu_B}}{K_{sp}}\right)^{1/(\nu_A+\nu_B)} \tag{4}$$

Crystal growth rate data from industrial crystallizers are usually correlated empirically with environmental conditions, such as concentration and temperature using a power law model of the form:

$$G = k_g(\sigma+1)^g \tag{5}$$

The power coefficient g in the growth equation does not depend on the form of the equation used and is normally a number between 1 and 2. The constants g and k_g are temperature-dependent and are usually fit to the Arrhenius equation to obtain a general expression for growth rate as a function of temperature. The Arrhenius equation can be written as:

$$k_g = A\exp(-E_a / RT) \tag{6}$$

where A is a constant and E_a is the activation energy. The activation energy can be used to obtain information of whether the rate-controlling step is diffusion or surface integration. A complete crystal growth expression that includes both the effect of temperature and supersaturation on the growth rate would, therefore, be written as:

$$G = A\exp(-E_a / RT)(\sigma+1)^g \tag{7}$$

The agglomeration and disruption kernels are also assumed to depend on the supersaturation in power law form:

$$K_{aggl} = \beta_{aggl} f(\varepsilon)\sigma^g \tag{8}$$

$$K_{disr} = \beta_{disr} g(\varepsilon)\sigma^g \tag{9}$$

and the mean crystal residence time is:

$$\tau = \frac{Q}{V} \tag{10}$$

The method of moments, described by Hulburt and Katz [9], was used to solve PBE (a partial integro-differential equation). Using the method of moments, equation (1) becomes a set of ordinary differential equations in the moments. The j moment is:

$$\mu_j = \int_0^\infty L^j n(L) dL \tag{11}$$

The lower order moments (i.e., $j = 0,1,2,3$) are related to the physical description of the particle size distribution, i.e. μ_0 is related to the total number of particles, μ_1 is related to the total particle diameter, μ_2 is related to the total particle surface area and μ_3 is related to the total particle volume.

For a well-mixed batch reactor in which crystal breakage and agglomeration may be neglected, the population balance equation leads to the partial differential equation which describes the crystal size distribution n(L, t) as a function of both crystal size and time, where G is the overall linear growth rate (dL/dt); equation (1) becomes:

$$\frac{\partial n}{\partial t} + \frac{\partial (Gn)}{\partial t} = 0 \tag{12}$$

For example, if the crystal growth rate is invariant with size and in the absence of particle breakage and agglomeration, after the moment transformation equation (12) is represented by a set of ordinary differential equations (ODEs) in terms of the moments:

$$\begin{aligned} \frac{\partial \mu_0}{\partial t} &= 0 \\ \frac{\partial \mu_1}{\partial t} &= G\mu_0 \\ \frac{\partial \mu_2}{\partial t} &= 2G\mu_1 \\ \frac{\partial \mu_3}{\partial t} &= 3G\mu_2 \end{aligned} \tag{13}$$

$$c(t) = c(0) - \rho_c k_v \mu_3(t) \tag{14}$$

In order to model the time-dependent behavior of a continuous system, the mass balance (eq. 14) was solved together with eq. (5) over an interval of time. The values for g and k_g were obtained from a least – squares optimization.

RESULTS AND DISCUSSION

In Table 1 is presented the variation of the final particle mean diameter with concentration and temperature. When precipitation takes place at lower concentrations, the nucleation rate is slowly, the growth rate is faster (the diffusion phenomena become important in the process) and the particles grow. At higher concentrations the nucleation rate is faster, stabile nuclei are formed and no changes in the particle diameter are observed.

In a precipitation process, crystal size distribution depends on the $\frac{\textit{growth rate}}{\textit{nucleation rate}}$ ratio. At 20 ^{0}C the growth rate is slower, in the first stage many critical nuclei are formed, and then they simply redissolve because they are extremely unstable. At 50 ^{0}C the growth rate is faster, the number of the critical nuclei formed is insignificant so that the nuclei grow beyond a certain critical size and become stable.

The analysis of CSD (Figure 1 – (a) and (b)) using the population density data from the Counter Coulter exhibits almost oscillating behavior due to the agglomeration and particle disruption.

Table 1. Mean particle diameter at different work conditions

$C_{Ca_3(NO_3)_2}$ **[mol/l]**	$C_{(NH_4)_2HPO_4}$ **[mol/l]**	**Mean particle diameter [μm]**	
		20 ^{0}C	50 ^{0}C
1.25	0.46	0.02	0.02
1	0.4	0.02	0.02
0.67	0.3	4.61	0.02
0.5	0.24	5. 33	0.02
0.29	0.15	6. 13	0.02
0.15	0.09	6. 17	0.02

First it increases to a maximum and then decreases, eventually approaching steady state after 22 hours. This behavior could be observed for all concentrations and temperatures (only the representative concentrations were presented in this article).

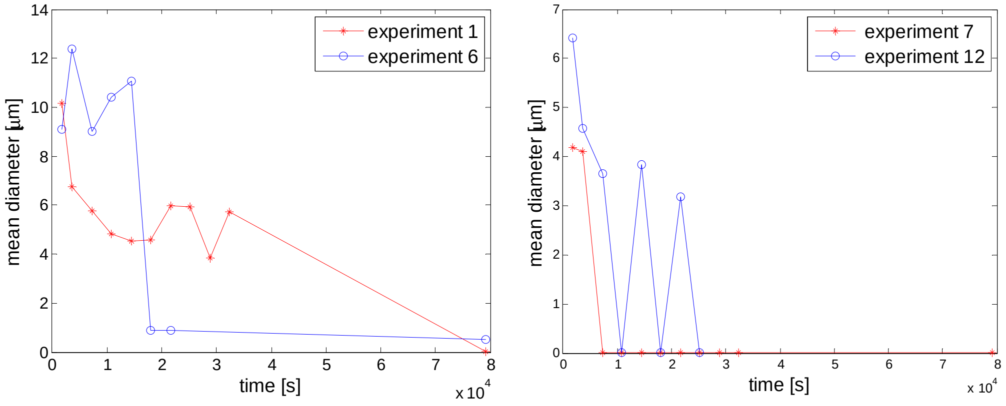

(a) **(b)**

Figure 1. Mean particle diameter vs time at 20 ^{0}C (a) and 50 ^{0}C (b)

According to the first law of precipitation, with progressively increasing concentration of the reacting solutions, the mean magnitude of the individual crystals of precipitates will pass through a maximum. As the time becomes greater, this maximum is displaced to the left side and upwards [10]. Figure 2 shows the initial particle size distribution and the distribution after 5 h of stirring (a semi-log graph, defined by a logarithmic scale on the x axis, and a linear scale on the y axis). The distribution gradually shifts to smaller sizes as large particles are reduced in size by breakage or attrition.

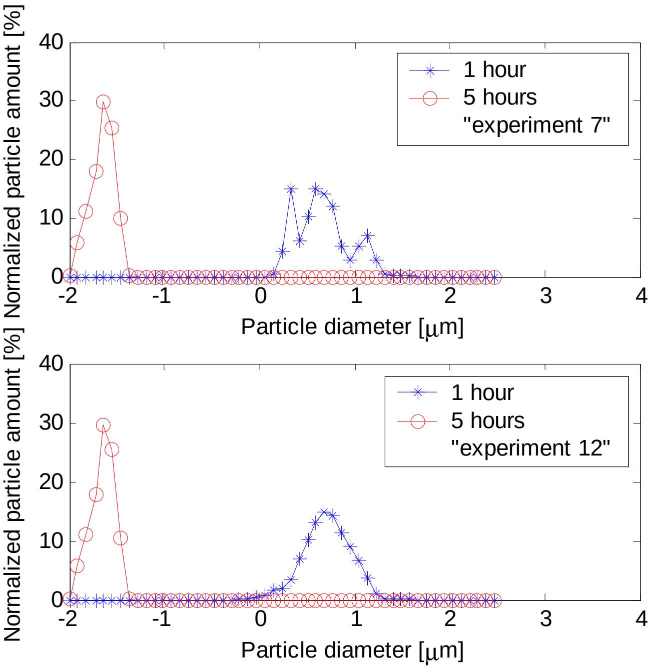

Figure 2. Number density

Furthermore, the measured total number of particles increases as each breakage event leads to a number of daughter particles (this behavior was observed at all range on concentration presented in Table 1).

The growth rate can be directly determined from the third moment, assuming that size-independent growth and the third moment (mass) is conserved in the agglomeration and disruption process. Knowing the moments of the distribution, growth rate G can be calculated from:

$$G = \frac{\mu_3}{3\mu_2\tau} \tag{15}$$

In Figure 3 – (a) and (b), the growth rate was plotted versus the time for 2 concentrations and 2 temperatures.

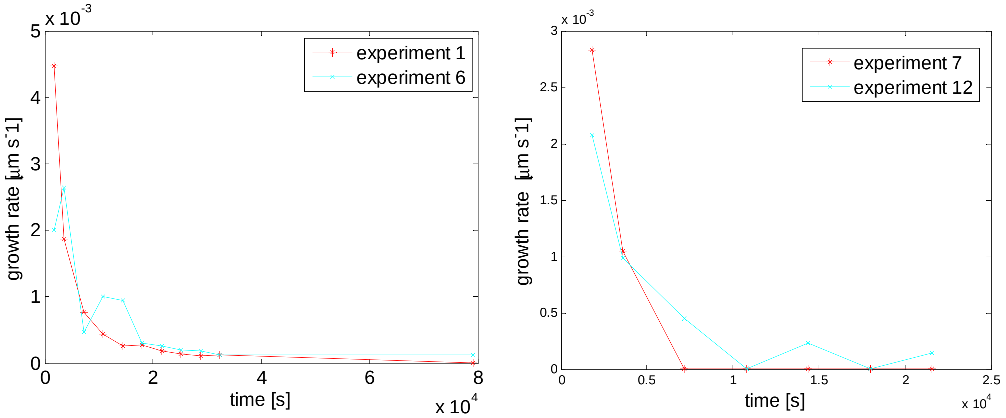

(a) (b)

Figure 3. Growth rate vs time at 20 ^{0}C (a) and 50 ^{0}C (b)

First an increase of the growth rate with time was observed for all conditions. The particles are agglomerating, as can be expected from the higher levels of supersaturation in the precipitation reactor. These aggregates continue to agglomerate by forming interparticle bonds. Then, due to breakage or attrition processes, a decrease was observed.

By combining the process model with an optimization algorithm the growth kinetics mechanism and parameters can be extracted from the experimental data. In Figure 4 –(a) and (b), the experimental growth rates were correlated with the growth rates obtained from the model predictions. It could be observed that the values obtained from the experiments were within the range of the simulation data. It should be considered that direct comparison of the kinetic data is not always possible.

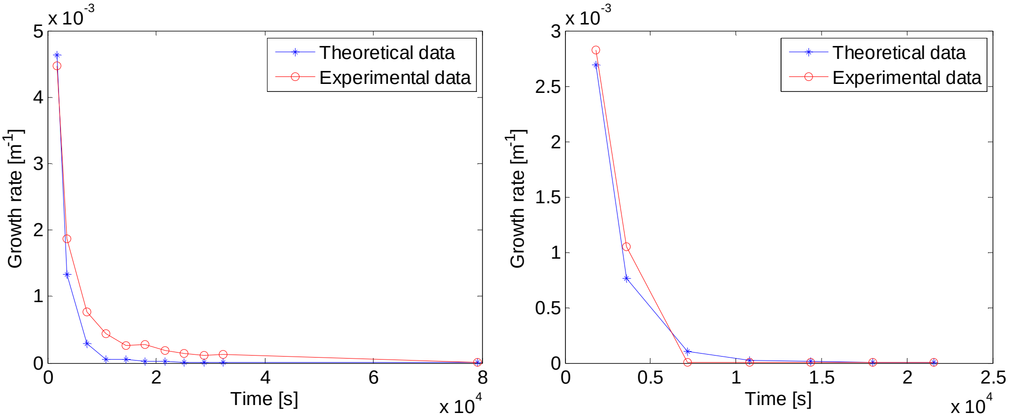

(a) (b)

Figure 4. Experimental and simulated growth rate vs time at (a) 20^{0}C and (b) 50^{0}C

Table 2. The values for the growth parameters

Experiment	g	k_g
1	1.79	$9.0\cdot10^{-13}$
2	1.68	$4.1\cdot10^{-12}$
3	1.92	$3.0\cdot10^{-13}$
4	1.95	$3.0\cdot10^{-13}$
5	1.95	$3.0\cdot10^{-13}$
6	1.98	$3.0\cdot10^{-13}$
7	1.74	$1.1\cdot10^{-12}$
8	2	$1.0\cdot10^{-13}$
9	1.90	$3.0\cdot10^{-13}$
10	1.54	$1.0\cdot10^{-13}$
11	1.83	$9.0\cdot10^{-13}$
12	1.98	$3.0\cdot10^{-13}$

Using an optimization algorithm based on a least squares minimization the growth parameters g and k_g from equation (5) were determined and the values are presented in Table 2. From the theoretical considerations, for diffusion controlled growth g = 1, for crystal growth originating from screw dislocations $g = 1 - 2$ and for polynuclear growth $g > 2$.

CONCLUSIONS

For the obtaining process of hydroxyapatite, a technique already known for other systems was used to determine the growth kinetics from experimental precipitation data (CSD). The model was able to predict reasonably well the growth rates for different work conditions (concentrations and temperatures) and can also be used to analyze experimental data from crystallization.

The results presented demonstrate that in the batch precipitation experiments is a strong dependence of the crystal size distributions on the feed concentrations and temperature. Due to this fact, small particles could be obtained at higher temperatures and supersaturations. Because the aggregation/growth rate increases with the supersaturation and the disruption rate increases with higher rotational speeds, further experiments are needed in order to show the dependence of the crystal size distribution on the mode of mixing.

EXPERIMENTAL SECTION

Hydroxyapatite was precipitated from reacting supersaturated solutions of calcium nitrate and bi-ammonia phosphate, at $pH = 11$ [11], according to the following equation:

$$\begin{aligned}&10Ca(NO_3)+6(HN_4)_2HPO_4+6NH_4OH+2NH_3\rightarrow\\&\qquad Ca_{10}(PO_4)_6(OH)_2+20NH_4NO_3+6H_2O\end{aligned} \tag{16}$$

To investigate the precipitation kinetics, the experiments were carried out under different feed concentrations and two temperatures (the values are presented in Table 3). At different preset times (see the plots), samples were taken and analyzed by laser light scattering technique using a Counter Coulter WING-SALD 7101.

Table 3. Experimental conditions (temperatures and feed concentrations)

Experiment		$C_{Ca_3(NO_3)_2}$ [mol/l]	$C_{(NH_4)_2HPO_4}$ [mol/l]
20 ^{0}C	50 ^{0}C		
1	7	1.25	0.46
2	8	1	0.4
3	9	0.67	0.3
4	10	0.5	0.24
5	11	0.29	0.15
6	12	0.15	0.09

NOTATIONS

B_{aggl}	birth rate due to agglomeration, m^{-4} s^{-1}
B_{disr}	birth rate due to disruption, m^{-4} s^{-1}
C	concentration of the reactant, g, mol m^{-3}
D_{aggl}	death rate due to agglomeration, m^{-4} s^{-1}
D_{disr}	death rate due to disruption, m^{-4} s^{-1}
g	kinetic order of growth, dimensionless
G	molecular growth rate, m s^{-1}
$\mathrm{k_v}$	volumetric shape factor
K_g	growth rate coefficient, m s^{-1}
K_{aggl}	agglomeration rate, m^3 s^{-1}
K_{disr}	disruption rate, s^{-1}
K_{sp}	solubility product, mol^2 m^{-6}
L	particle size, m
n	population density, # m^{-4}
Q	flow rate, m^3 s^{-1}
S	(relative) supersaturation, dimensionless
t	time, s
V	reactor volume, m^3

Greek letters

μ_j	j^{th} moment of distribution, m^{j-3}
β_{aggl}	agglomeration kernel
β_{disr}	disruption kernel
ε	power input per unit volume, W kg^{-1}
ρ	suspension density, g/l
σ	(absolute) supersaturation (*S*-1), dimensionless
τ	mean residence time, s

REFERENCES

1. R. Barabás, A. Pop, E. Fazakas, V. Dejeu, *Proc. 10th ECerS Conf.,* Göller Verlag, Baden-Baden, **2007**, 925.
2. N. Ellis, A. Margaritis, C.L. Briens, M.A. Bergougnou, *AIChE Journal*, **1996**, *42*, 87.
3. H.M. Hulburt, S. Katz, *Chem. Eng. Sci*., **1964**, *19*, 555.
4. A. Jones, “Crystallization Process Systems”, **2002**, chapter 5.
5. S. Koutsopoulos, *Langmuir*, **2001**, *17(26*), 8092.
6. C.L. Kibby, W.K. Hall, “The Chemistry of Biosurfaces Vol. 2”, M.L. Hair ed., Dekker, New York, **1972**, 663.
7. J.O. Leckie, W. Stumm, “In the changing chemistry of the oceans”, D. Dyrssen and D. Jagner, Eds. Almquist and Wiksell, Stockholm, **1972**.
8. P.P. von Weimarn*, Chem. Rev.,* **1926**, *2,* 217.
9. D. Ramkrishna, *Reviews in Chemical Engineering*, **1985**, *3(1),* 49.
10. A.D. Randolph, M.A. Larson, “Theory of Particulate Processes, 2nd ed.”; Academic Press: San Diego, CA, **1988**.
11. R. Zauner, A. Jones, *Chem. Eng. Sci*., **2000**, *55*, 4219.

STUDIA UNIVERSITATIS BABEŞ-BOLYAI, CHEMIA, XLV, 2, TOM I, 2010

Dedicated to the memory of Prof. dr. Ioan Silaghi-Dumitrescu marking 60 years from his birth

KINETIC INVESTIGATION IN TROLOX-DPPH· SYSTEM

LIDIA VARVARI, GABRIELLA SZABÓ, ADRIAN NICOARĂ*

ABSTRACT. A kinetic study using voltammetry and spectrophotometric measurements on the Trolox/DPPH•, in hydro-ethanolic and ethanolic medium is presented. The heterogenous electrochemical rates were obtained from the peak parameters in quasireversible and irreversible conditions and the homogenous rate constant and partial reaction orders were obtained using reaction half-life.

Keywords: *Antioxidants, Trolox, DPPH•, voltammetry, spectrophotometry, kinetics*

INTRODUCTION

A free radical is a chemical species able of independent existence, possessing one or more unpaired electrons. Biologically important free radicals are thus highly unstable molecules that have electrons available to react with various organic substrates, generated by oxidative stress that can lead to a series of biochemical alterations through chain radical reactions. The natural defence against the oxidative stress is based on the action of antioxidant compounds, also known as radical scavengers. They usually act by neutralising the unstable free radical molecules by supplying them with electrons, thus preventing or at least limiting the chain reactions that cause tissue damage [1-2]. There are several categories of substances acting as antioxidants, including vitamins, inorganic compounds, essential amino acids and polyphenols. Their capacity to scavenge free radicals is now universally recognised although the true mechanism by means of which they act is still not fully understood [3].

Several methods have been proposed for the detection of antioxidants, based on photometric, fluorimetric, chromatographic and electrochemical approaches. Inherent limitations of the analysis differ from method to method (low sensitivity, interferences, slow detection and cost of equipment) and have

---

* *Universitatea Babeş-Bolyai, Facultatea de Chimie şi Inginerie Chimică, Str. Kogălniceanu Nr. 1, RO-400084 Cluj-Napoca,Romania, anicoara@chem.ubbcluj.ro*

stimulated the study of simple, fast and sensitive methods for the characterization of antioxidants. In the past two decades the electrochemical methods, especially the amperometric ones, have been intensively used for antioxidant detection mostly because are fast and less expensive [4].

One of the most employed method of antioxidant activity determination uses a stable free radical 2,2-diphenyl-1-picrylhydrazyl (DPPH•). Having intense colour, which changes from violet to pale yellow during reaction with antioxidants, this free radical is suitable for spectrophotometric determination [5]. Because DPPH• free radical can exchange electrons at an electrode interface, its reaction with antioxidants is suitable also for electrochemical detection. In both mentioned cases, the antioxidants activity can be determined by following the consumption of DPPH• free radical. Correlating to free radical consumption when using a standard antioxidant, like 6-hydroxi-2,5,7,8,-tetramethyl-chroman-2-carboxylic acid (Trolox), it is possible to calculate the antioxidant activity of a complex natural matrix of antioxidants in terms of Trolox equivalent antioxidant activity [6].

The present study aims to investigate the elementary processes that occur during operation of an amperometric sensor for antioxidant activity determination. It is of interest to study the electrochemical behaviour of Trolox and DPPH• independently and in mixtures, employing spectrophotometric techniques for those processes that do not take place at electrode interface. After the obtaining of kinetic and thermodynamic information, it is possible to operate the amperometric detection in condition in which a judicious balance between desired performance descriptors can be more easily achieved.

RESULTS AND DISCUSSION

A detailed knowledge of the redox processes that occur in Trolox/ DPPH• system during amperometric detection of antioxidant activity requests a preliminary investigation of electrochemical behavior of isolated components of the system.

Cyclic voltamograms of Trolox (Figure 1a) show the presence of one pair of voltammetric peaks, indicating chemically reversible nature for Troloz reduction. The asymmetry of the peaks, with the anodic one smaller and broader, corroborated with the significant peak separation is the indication of a relative slow charge transfer. Figure 1b and 1c contain the influence of scan rate on the peak parameters. Presented data indicate transition between quasireversible and irreversible behavior when increasing the scan rate, as can be evidenced by deviation from linearity of the representations from Figure 1b and 1c.

Attempting to obtain physico-chemical information, one can use the peak parameters to calculate some thermodynamic and kinetic parameters.

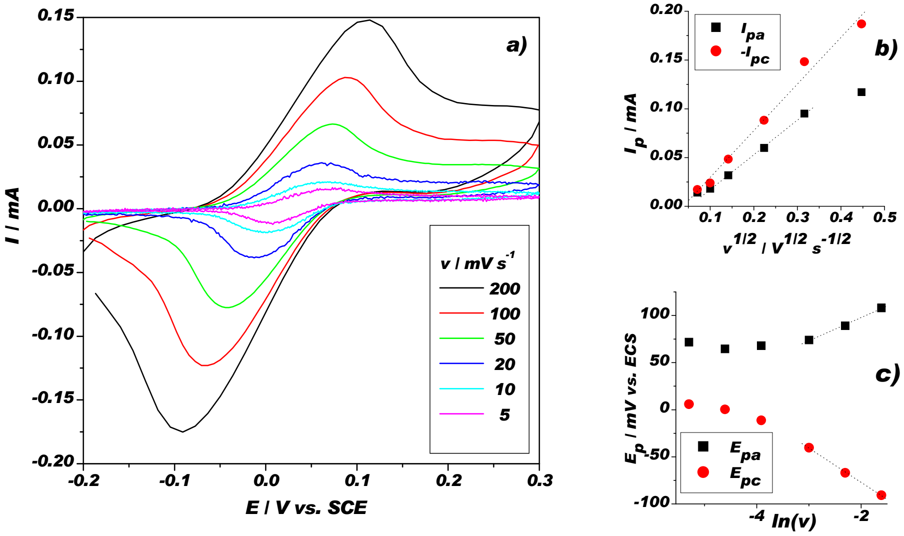

Figure 1. Voltammetric response of Trolox 4 mM hydro-ethanolic solution; the influence of the scan rate on cyclic votammograms, in a), on peaks current, in b), and on peaks potential, in c).

To simplify the requested analysis, in the present work the formal standard potential was calculated using the data from quasireversible domain, by simple mediation of the anodic and cathodic potentials, whereas calculation of the other parameters was performed using the data from irreversible domain. In these circumstances, the formal standard potential was found to be $E^{o\prime}=0.03$ V *vs.* SCE.

For an irreversible behavior, the peak parameters are given by:

$$
\begin{aligned}
I_{p,a} &= 2.99\,10^{5}\,n\left[(1-\alpha)n_a\right]^{1/2} A D^{1/2} C^{*} v^{1/2} \\
I_{p,c} &= -2.99\,10^{5}\,n\,(\alpha n_a)^{1/2} A D^{1/2} C^{*} v^{1/2} \\
E_{pa} &= E^{o'} - \frac{0.02569}{(1-\alpha)\,n_a}\left[0.78 - \ln\left(\frac{\sqrt{D_R}}{k^{o}}\right) - \ln\left(\sqrt{\frac{(1-\alpha)n_a}{0.02569}v}\right)\right] \\
E_{pc} &= E^{o'} - \frac{0.02569}{\alpha\,n_a}\left[0.78 + \ln\left(\frac{\sqrt{D_O}}{k^{o}}\right) + \ln\left(\sqrt{\frac{\alpha\,n_a}{0.02569}v}\right)\right]
\end{aligned}
\qquad (1)
$$

where n is the (total) number of exchanged electrons, n_a the number of electrons involved in the rate determining step, α the transfer coefficient, A the surface, v the scan rate, C* the concentration, D the diffusion coefficient of the reacting species (when mentioned, O denotes the oxidized and R, the reduced; otherwise denotes the reacting species) and k^o the standard rate constant [7].

In order to perform the parameter calculation, the peak parameters were plotted on convenient coordinates (I_p vs. $v^{1/2}$ and E_p vs. ln(v), as can be seen in Figure 1b and 1c, respectively) to ensure linearization. Using the slopes obtained by linear fitting of data presented in Figure 1c - 0.0246±0.0015 and 0.0364±0.0012 for anodic and, respectively, catodic peaks - one can first calculate $n_a \approx 1$ and $\alpha = 0.60 \pm 0.02$, values consistent to mentioned peak asymmetry. The next step employs the I_p vs. $v^{1/2}$ dependence, described by the slopes of linear correlation found to be $(3.56 \pm 0.07)10^{-4}$ and $(4.79 \pm 0.29)10^{-4}$, respectively. Assuming n=1, one can calculate D=1.2 10^{-6} cm^2 s^{-1}, value corresponding to the reduced form of Trolox. To calculate the standard rate constant, the intercepts of Figure 1c (0.147±0.004 and 0.150±0.003, respectively) lead to calculation of $k^o = (2.9 \pm 0.2)$ 10^{-4} cm s^{-1}.

Cyclic voltamograms of DPPH• (Figure 2a) show in the domain of potential employed of the Trolox study the presence of one pair of voltammetric peaks that reveal a chemically reversible nature of electron exchange of studied free radical. An additional chemical irreversible oxidation peak, not presented here, is not important for the present study, since it occurs at potentials well above the interest domain, where both Trolox and DPPH• exchange electrons [8]. As in Figure 1, the shape of the peaks and relative proportional influence of square root of scan rate on the peak currents suggest a redox process involving soluble species, without contribution of adsorbed species.

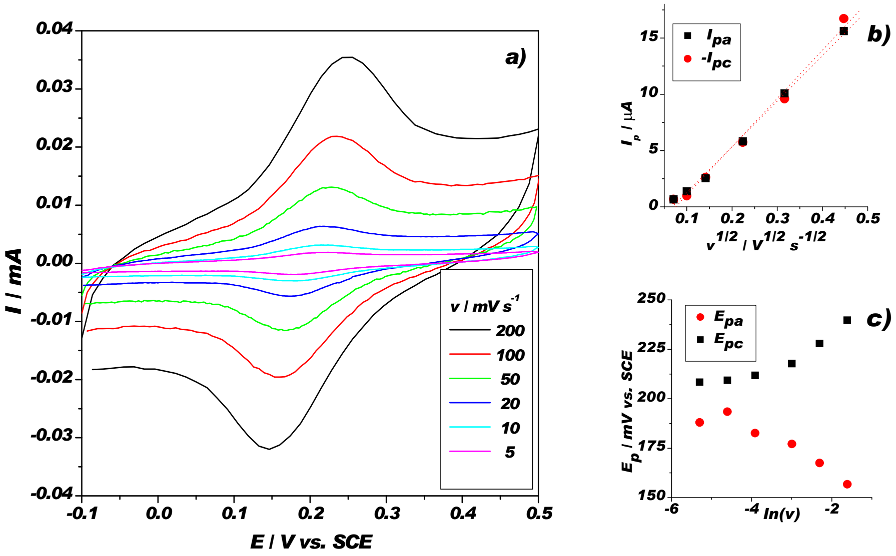

Figure 2. Voltammetric response of DPPH• 0.2 mM hydro-ethanolic solution; the influence of the scan rate on cyclic votammograms, in a), on peaks current, in b), and on peaks potential, in c).

As compared to Trolox, DPPH• presents more symmetric peaks, less separated, denoting a significant faster rate. Consequently, the linearization correlation between peak potential and ln(v) takes place on higher scan rates, as can be seen in Figure 2c. In these circumstances, the voltammetry was performed under quasireversible behavior, and mathematical analysis aiming calculation of physico-chemical information must be performed accordingly. The standard formal potential was calculated as above, being found $E^{o\prime}=0.19$ V *vs.* SCE. For a quasireversible system Matsuda and Ayabe proposed a diagram that correlates the peak separation with an *ad hoc* kinetic term

$$\Lambda = k^{o}\sqrt{\frac{0.02569}{D_{O}^{1-\alpha}D_{R}^{\alpha}v}} \qquad (2)$$

and links up the peak current to scan rate by using a second *ad hoc* kinetic term Ψ, both *ad hoc* kinetic terms being correlated through another diagram [9]. Under these assumptions, we found $n \approx 2$, $D_{DDPPH\bullet}=5.9\ 10^{-6}\ cm^{2}s^{-1}$, $k^{o}=1.3\ 10^{-2}$ cm s^{-1}.

For a full kinetic description of Trolox-DPPH• system a final voltammetric investigation was performed in order to describe the homogenous redox process. As can be seen in Figure 3, during addition of Trolox the peaks corresponding to DPPH• couple is marginable influenced, mostly due to modification of base line current. Moreover, the peak currents of Trolox couple are direct proportional to added Trolox concentration.

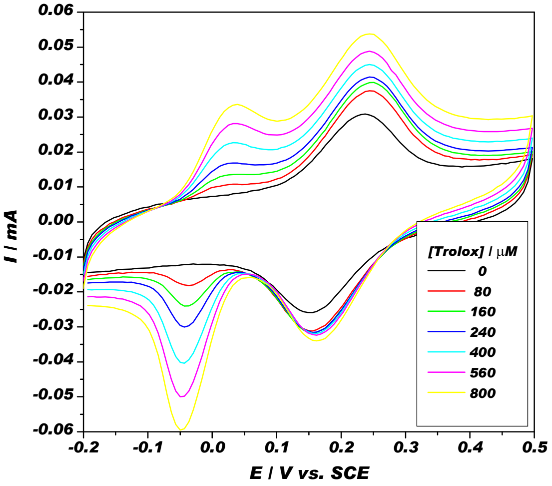

Figure 3. Voltammetric response of DPPH• 0.2 mM hydro-ethanolic solution with Trolox of concentration indicated in legend. Scan rate is 0.1 V s^{-1}.

All these suggest that, under studied experimental condition, the so-called homogenous coupled reaction cannot be evidenced. To obtain some kinetic information about this reaction, spectrophotometric measurements were further performed.

The reaction between DPPH• and Trolox in hydro-ethanolic mixtures was completed in few seconds, which prohibits kinetic measurement using employed instrumentation. For such fast systems, kinetic investigations can be made only in stopped-flow system. However, using ethanolic solution reaction is significant slower, allowing a preliminary insight into the kinetics in investigated system. Even if the values found in ethanolic solution could be related to previously found heterogeneous rate constants only with large precautions, the spectrophotometric measurements where further restricted to alcoholic solutions.

Ethanolic solutions of DPPH• obey Lambert-Beer law up to 2 10^{-4} M, absorption maximum was found at 516 nm with a molar extinction coefficient of 19 10^4 $M^{-1}cm^{-1}$. Reaction between ethanolic solutions of DPPH• and Trolox was reported as 1 mol of this antioxidant reduces 2 mol of free radical [6].

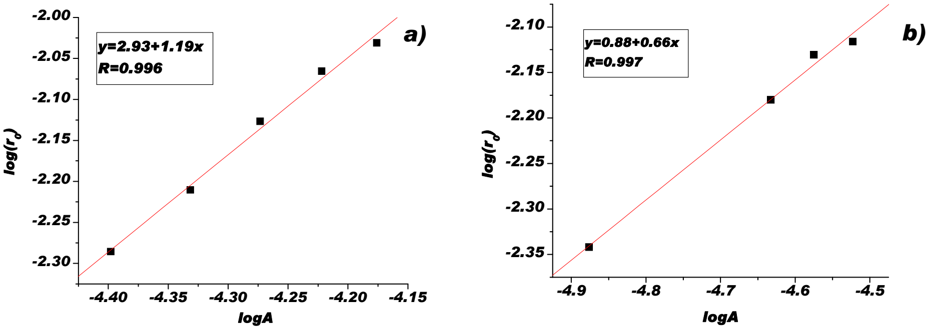

Figure 4. Dependence of initial rate on the DPPH• absorbance at constant DPPH• concentration, a), and at constant Trolox concentration, b).

Using different initial concentration of both species, on the basis of the rate law having the following expression, $r_0 = k\, c_{0DPPH}^{a}\, c_{0Trolox}^{b}$, partial reaction orders of 0.7 and 1.2 with respect to Trolox and DPPH•, respectively, were determined from the initial rates of the reaction, see Figure 4. As suggested by Brand-Williams and Bondet [5], the rate constant was determined from the half-life of the reaction:

$$t_{\frac{1}{2}} = \left(\left(2^{a+b-1} - 1\right)/k_e\right) \times c_{DPPH\bullet}^{1-a-b} \qquad (3)$$

where σ=2 represents the DPPH· number of mol reduced by the antioxidant and k_e is related to the rate constant by:

$$k_e = (a + b - 1)\frac{k}{\sigma^b} \tag{4}$$

The values of the rate constant determined at two different temperatures are presented in the table 1.

Table 1. The rate constant determined at different temperatures.

T (K)	$10^5 \cdot c_{0DPPH}$ (M)	$t_{1/2}$ (s)	k_e ($M^{-1} \cdot s^{-1}$)	k ($M^{-1} \cdot s^{-1}$)	$\bar{k}$ ($M^{-1} \cdot s^{-1}$)
298	6	48	113.8	206.0	203.3
	4	71	110.8	200.6	
293	6	55	99.3	180.6	184.7
	4	75	104.9	189.8	

CONCLUSIONS

The stable free radical DPPH•, which can be amperometrically detected, is consumed by the antioxidants from analysed sample allowing to evidence the antioxidants by quantifying the decrease of the DPPH• concentration. Trolox is further employed to quantify the activity of the natural antioxidants present in an analysed sample. We will further investigate the way in which the experimental finds endorse the utilisation of an amperometric sensor based on investigated system.

The results prove that the DPPH• free radical can be reduced during a reversible process, on a relative positive potential ($E^{o'}$=0.19 V *vs.* SCE). There are two positive consequences: the value of formal standard potential contributes to a good selectivity as analytes with more negative formal standard potential would not interfere, and de reversible nature of this process allows increasing of the sensibility as the oxidation product is available to re-reduction during a homogenous coupled chemical process. Another important original find is the kinetic constant of this heterogeneous reaction; the reasonable high value, of k^o=1.3 10^{-2} cm s^{-1}, is beneficial for the detection as the fast rates is a prerequisite for a low response time of detection.

The electrochemical investigation of Trolox revealed a reversible process at a more cathodic formal standard potential ($E^{o'}$=0.03 V *vs.* SCE). The difference of mentioned formal standard potentials constitute the driving force of reaction between Trolox and DPPH• in the investigated conditions. A smaller value would give a certain degree of reversibility, with detrimental reducing of linearity of the amperometric sensor. More important, the voltammetric peaks of Trolox are clearly separated from those of DPPH• free radical, allowing the use of analytical techniques that request the presence of Trolox in the investigated sample with antioxidants.

The last attempt was to investigate the homogenous redox reaction between Trolox - DPPH•. As the catalytic coupling was not evidenced by voltammetry, spectrophotometric techniques were employed. Yet again the kinetics was favourable, too fast to even evaluate the rate constant with utilized instrumentation when the reaction was investigated in hydro-ethanolic solution. Even in pure ethanolic solution the homogenous rate constant was reasonable large, of 203 M^{-1} s^{-1}, ensuring a small measuring time for the amperometric detection. The only draw-back is given by subunit value, of 0.7, for DPPH• free radical reaction order; poor linearity should be expected for the samples containing Trolox if the measurements are performed without reaching the equilibrium.

EXPERIMENTAL SECTION

Instrumentation

The voltammetric measurements were performed using a Computer controlled (via an AT-MIO-16F-5, National Instruments, USA, data acquisition board) analogical potentiostat (PS3, Meinsberg, Germany). A standard three-electrode electrochemical cell configuration was employed for the measurements. The working electrode was glassy carbon (A=0.0314 cm^2) reference electrode was a double-junction saturated calomel electrode (SCE) and the counter electrode was a spiralled Pt wire. Voltammetric measurements were performed at a temperature of 25±1 ^{o}C.

Spectrophotometric measurements were carried out on a Jasco V-530 UV/VIS spectrophotometer connected to a computer for data acquisition. Standard (1 cm x 1 cm x 4.5 cm) glass spectroscopic cuvette was used for visible absorbance measurement. Temperature was controlled by using an M 20 Lauda thermoregulating system. DPPH• spectrum was recorded in the range of 800 and 400 nm. Time course measurements were recorded at 516 nm wavelength at 25±0.5 ºC. Ultrasonication of stock solutions was performed with Transsonic T 420, Elma.

Reagents and solutions

Commercially available chemicals were obtained from Sigma-Aldrich. DPPH• stock solutions were prepared in absolute ethanol and ultra-sonicated for about 30 minutes. In order to avoid thermal decomposition and by light the solutions were kept in refrigerator. Trolox was dissolved in absolute ethanol and in hydro-alcoholic phosphate buffer. The hydro- ethanolic solutions (25% vv ethanol) were prepared by adding ethanol to the buffer solution with desired pH of 7.4. All the solutions contained 0.1 M KCl as supporting electrolyte.

ACKNOWLEDGMENTS

The authors acknowledge for the financial support granted by the National Research Council, project SENSALIM, PN II Nr. 71/098-2007.

REFERENCES

1. A. Somogyi, K. Rosta, P. Pusztai, Z. Tulassay, G. Nagy, *Physiological Measurements*, **2007**, *28*, R41.
2. L. Campanella, E. Martini, M. Tomassetti, *Talanta*, **2005**, *66*, 902.
3. L. Campanella, A. Bonanni, D. Bellantoni, G. Favero, M. Tomassetti, *Journal of Pharmaceutical and Biomedical Analysis*, **2004**, *36*, 91.
4. Ignatov, S. Ignatov, D. Shishniashvili, B. Ge, F.W. Scheller, F. Lisdat, *Biosensors and Bioelectronics*, **2002**, *17*, 191.
5. V. Bondet, W. Brand-Williams, C. Berset, *Lebensmittel-Wissenschaft und Technologie/ Food Science and Technology,* **1997**, *30*, 609.
6. S. Mildradovic, D. Ivekovic, B. Grabaric, *Bioelectrochemistry,* **2006**, *68,* 175.
7. R. Nicholson, I. Shain, *Analitical Chemistry*, **1964**, *36,* 706.
8. Mildradovic, D. Ivekovic, V. Rumenjak, B. Grabaric, *Electroanalysis*, **2005**, *17,* 1847.
9. A.J. Bard, L.R. Faulkner, *Electrochemical methods. Fundamentals and applications* 2nd ed., Wiley, **2001**, chapter 6.3.

STUDIA UNIVERSITATIS
BABEŞ-BOLYAI

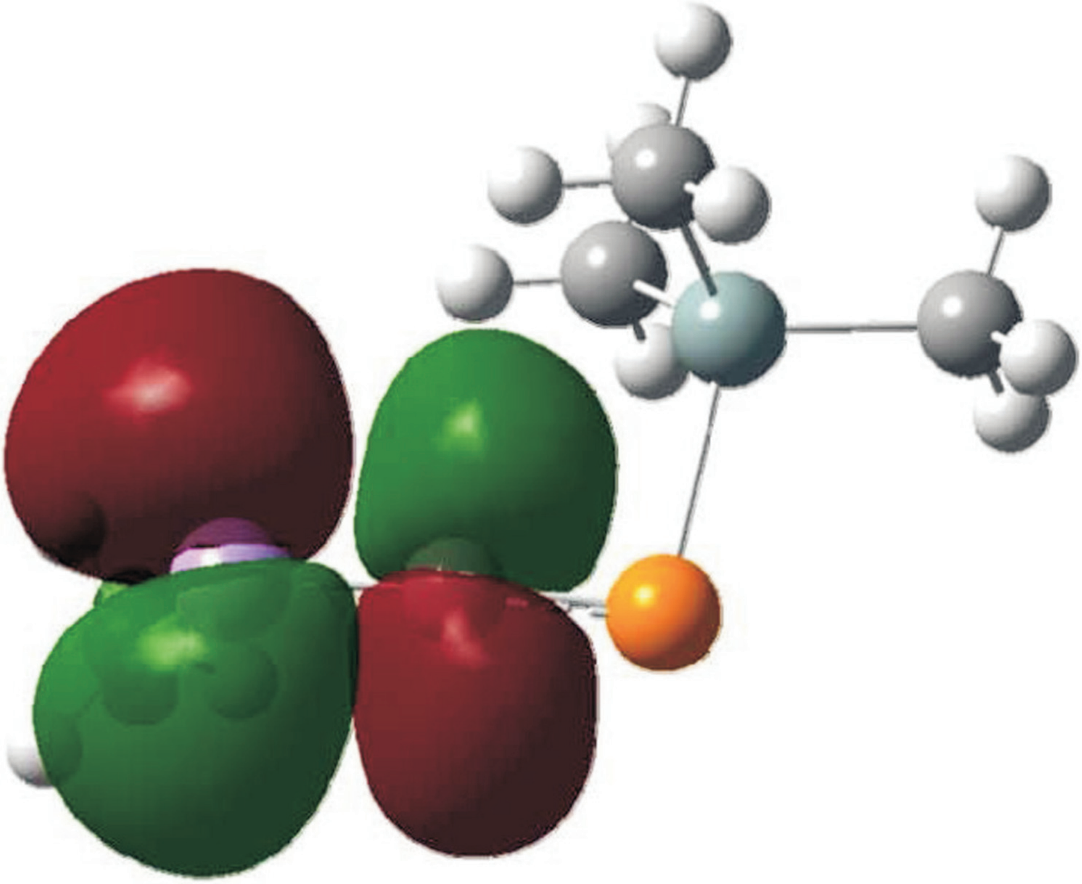

CHEMIA

2/2010
tom II

ANUL LV 2010

S T U D I A

UNIVERSITATIS BABEŞ-BOLYAI

CHEMIA

2

tom II

Desktop Editing Office: 51ST B.P. Hasdeu Street, Cluj-Napoca, Romania, Phone + 40 264-405352

CONTENT – SOMMAIRE – INHALT – CUPRINS

Studia Universitatis Babes-Bolyai Chemia has been selected for coverage in Thomson Reuters products and custom information services. Beginning with V. 53 (1) 2008, this publication is indexed and abstracted in the following:

- Science Citation Index Expanded (also known as SciSearch®)
- Chemistry Citation Index®
- Journal Citation Reports/Science Edition

STUDIA UNIVERSITATIS BABEŞ-BOLYAI, CHEMIA, XLV, 2, TOM II, 2010

Dedicated to the memory of Prof. dr. Ioan Silaghi-Dumitrescu marking 60 years from his birth

TOPOLOGY OF A NEW LATTICE CONTAINING PENTAGON TRIPLES

MONICA L. POP AND MIRCEA V. DIUDEA[a]

ABSTRACT. A new crystal-like network is designed by using some net operations. The topology of this hypothetical lattice is characterized by Omega polynomial and Cluj-Ilmenau CI index.

Keywords: *map operations, Omega polynomial, Cluj-Ilmenau index*

INTRODUCTION

In the nano-era, several new carbon structures: fullerenes (zero-dimensional), nanotubes (one dimensional), graphene (two dimensional), spongy carbon (three dimensional) and nano-diamond (three dimensional) [1,2] have been discovered. Inorganic clusters, like zeolites, also attracted the attention of scientists.

Zeolites are natural or synthetic aluminosilicates with an open three-dimensional crystal structure. Zeolites are members of the family of microporous solids known as "molecular sieves." This term refers to the property of these materials to selectively sort molecules based primarily on a size exclusion process. This is due to a regular structure of pores, of molecular dimensions, forming channels. The maximum size of the molecular or ionic species that can enter the pores of a zeolite is controlled by the dimensions of the channels [3-7].

Recent articles in crystallography promoted the idea of topological description and classification of crystal structures [8-13].

The present study presents a hypothetical crystal-like nano-carbon structure, with the topological description in terms of Omega counting polynomial.

OPERATIONS ON MAPS

Several operations on maps are known and used for various purposes.

Dualization *Du* of a map is achieved as follows: locate a point in the center of each face. Join two such points if their corresponding faces share

---

[a] *Faculty of Chemistry and Chemical Engineering, "Babes-Bolyai" University, Arany Janos Str. 11, 400084, Cluj, Romania*

a common edge. The transformed map is called the (Poincaré) *dual Du*(*M*). The vertices of *Du*(*M*) represent the faces of *M* and *vice*-*versa* [14]. Thus the following relations exist between the parent map parameters (denoted by subscript zero) and those of the transformed map:

$$Du(M)\text{: } v=f_0\text{ ; } e=e_0\text{ ; } f=v_0 \tag{1}$$

Dual of the dual recovers the original map: *Du*(*Du*(*M*)) = *M*. Tetrahedron is self dual while the other Platonic polyhedra form pairs: *Du*(Cube) = Octahedron; *Du*(Dodecahedron) = Icosahedron (see Figure 1 for symbols hereafter used). It is also known the Petrie dual.

Tetrahedron T Cube C Octahedron O

Dodecahedron D Icosahedron I

Figure 1. The five Platonic polyhedra.

Medial *Med* is another important operation on maps [15-17]. It is constructed as follows: put the new vertices as the midpoints of the original edges. Join two vertices if and only if the original edges span an angle (more exactly, the two edges must be incident and consecutive within a rotation path around their common vertex in the original map).

The medial graph is a subgraph of the line-graph [18]. In the line-graph each original vertex gives rise to a complete graph while in the medial graph only a cycle C_d (*i.e.*, a *d*-fold cycle, *d* being the vertex degree/ valence) is formed.

The medial of a map is a 4-valent graph and *Med*(*M*) = *Med*(*Du*(*M*)). The transformed parameters are:

$$Me(M)\text{: } v=e_0\,;\ e=2e_0\,;\ f=f_0+v_0 \tag{2}$$

The medial operation rotates parent *s*-gonal faces by *π/s*. Points in the medial represent original edges, thus this property can be used for topological analysis of edges in the parent polyhedron. Similarly, the points in dual give information on the topology of parent faces.

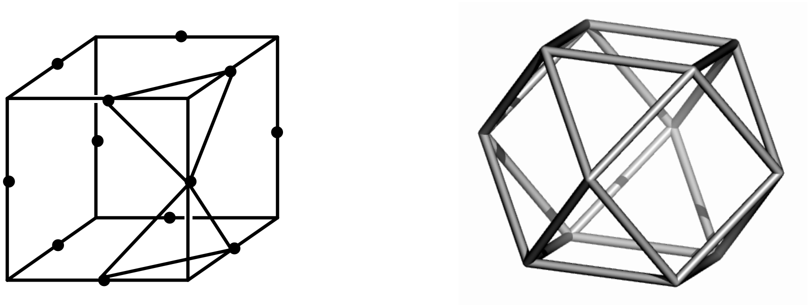

Figure 2. Medial operation; construction (left) and realization (right).

Truncation *Tr* is achieved by cutting of the neighborhood of each vertex by a plane close to the vertex, such that it intersects each edge incident to the vertex. Truncation is similar to the medial, with the main difference that each old edge will generate three new edges in the truncated map. The transformed parameters are:

$$Tr(M)\text{: } v=2e_0=d_0v_0\,;\ e=3e_0\,;\ f=f_0+v_0 \tag{3}$$

This was the main operation used by Archimedes in building his well-known 13 solids [3]. Note that truncation always provides a trivalent net. Figure 3 illustrates this operation.

Figure 3. Truncation; construction (left) and realization (right).

Leapfrog *Le* is a composite operation [16,17-24] that can be written as:

$$Le(M): Tr(Du(M))=Du \tag{4}$$

This operation rotates parent *s*-gonal faces by *π/s*. Note that the vertex degree in *Le*(*M*) is *always* 3. Leapfrog operation is illustrated, for a tetragonal face, in Figure 4.

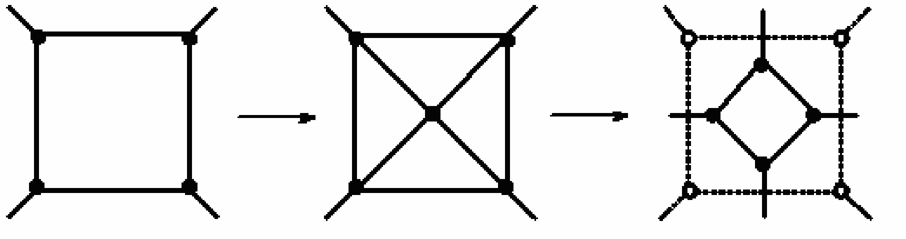

Figure 4. Leapfrogging a tetragonal face of a trivalent map; the white circles are the new vertices of *Le*(*M*).

A bounding polygon, of size $2d_0$, is formed around each original vertex. In the most frequent cases of 4- and 3-valent maps, the bounding polygon is an octagon and a hexagon, respectively (Figure 5).

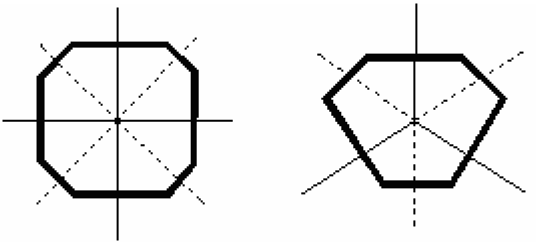

Figure 5. The bounding polygon around a 4-degree (left) and 3-degree (right) vertex.

In trivalent maps, *Le*(*M*) is the *tripling* operation. The complete transformed parameters are:

$$Le(M):\ v = s_0 f_0 = d_0 v_0\,;\ e = 3e_0\,; f = v_0 + f_0 \tag{5}$$

being the same as for *Tr*(*M*), eq 3.

A nice example of *Le* operation realization is: *Le*(D) = Fullerene C_{60} (Figure 6). The leapfrog operation can be used to insulate the parent faces by surrounding bounding polygons (see above).

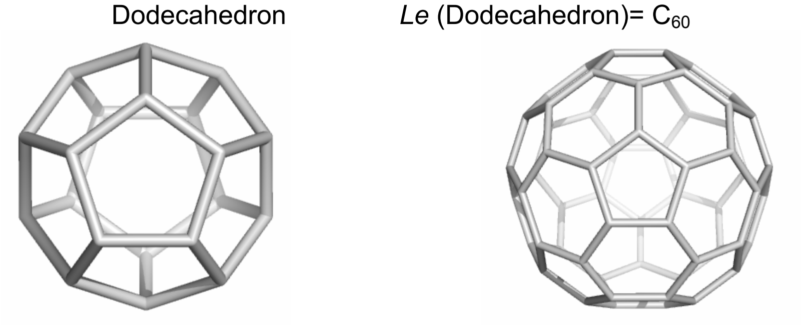
Dodecahedron

Le (Dodecahedron)= C_{60}

Figure 6. Leapfrog operation – molecular realization.

LATTICE BUILDING

The lattice under study (Figure 7), named S_2CL, was designed by the sequence: *Trs*(*Du*(*Med*(*Le*(Oct)))) and is a triple periodic network. In the above sequence, *Trs* means the truncation of some selected vertices. This sequence of operations introduces pentagon triples in a polygonal covering, which apparently violate the IPR (Isolated Pentagon Rule) condition in fullerene stability [25,26].

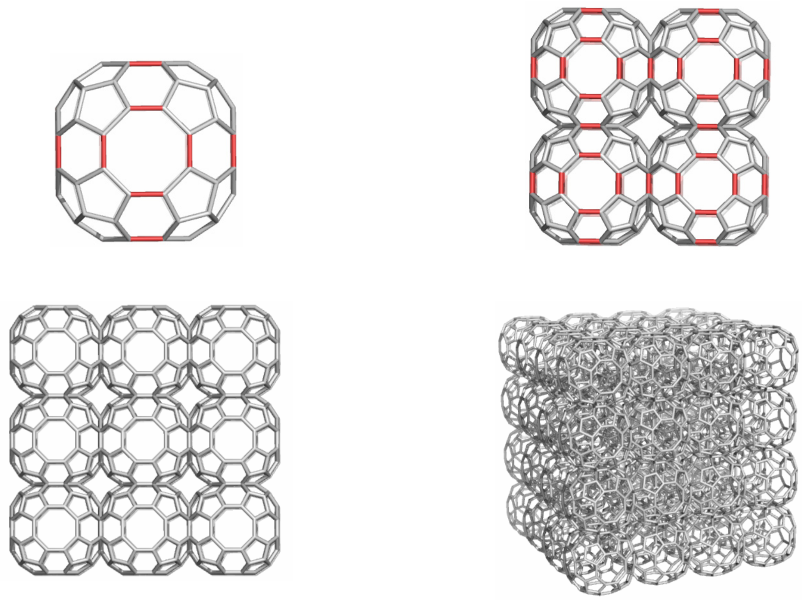

Figure 7. Lattice S_2CL; unit designed by *Trs*(*Du*(*Med*(*Le*(Oct)))); the red bonds mark the octagonal faces to be identified in construction of the network.

However, fullerenes which tessellation included pentagon triples have been obtained as real molecules. Calculation of stability of cages bearing pentagon triples [27] makes the subject of another article.

Network was performed by identifying the octagons in two neighbor units (Figure 7, left top corner). In this way, ordered channels appear, like those in zeolites.

For the topological characterization, cubic domains were constructed (Figure 7, right, bottom, corner). Formulas for Omega polynomial and examples are given in the next section.

OMEGA POLYNOMIAL IN CRYSTAL LATTCE

Two edges *e* and *f* of a plane graph *G* are in relation *opposite, e op f,* if they are opposite edges of an inner face of *G*. Then *e co f* holds by assuming the faces are isometric. Note that relation *co* involves distances in the whole graph while *op* is defined only locally (it relates face-opposite edges).

Using the relation *op* we can partition the edge set of *G* into *opposite* edge *strips, ops*: any two subsequent edges of an *ops* are in *op* relation and any three subsequent edges of such a strip belong to adjacent faces.

Note that John *et al*. [28,29] implicitly used the “*op*” relation in defining the Cluj-Ilmenau index *CI*.

Denote by *m*(*s*) or simply *m* the number of *ops* of length $s=|s_k|$ and define the Omega polynomial as [30-32]:

$$\Omega(x)=\sum_{s} m(s)\cdot x^{s} \qquad (6)$$

The exponent counts just the *ops* of length *s*; the coefficients *m* are easily counted from the symmetry of *G*. The first derivative (in *x*=1) provides the number of edges in *G*:

$$\Omega'(1)=\sum_{s} m\cdot s=e=\left|E(G)\right| \qquad (7)$$

On Omega polynomial, the Cluj-Ilmenau index [33], *CI*=*CI*(*G*), was defined:

$$CI(G)=\left\{[\Omega'(1)]^{2}-[\Omega'(1)+\Omega''(1)]\right\} \qquad (8)$$

We used here the topological description by Omega polynomial because this polynomial was created to describe the covering in polyhedral nanostructures and because it is the best in describing the constitutive parts of nanostructures, particularly for large structures, with a minimal computational cost [34].

Formulas for Omega polynomial in S_2CL network and examples are given in Table 1.

Table 1. Omega polynomial in S_2CL; R_{max}[8].

Formulas

$$\Omega(S2CL,x) = 24a^3 \cdot x^1 + 6a(a^2 + 9a - 4) \cdot x^2 + 12a(a-1)^2 \cdot x^4 + 3a \cdot x^{a(8+4(a-1))}$$

$$\Omega'(S2CL,1) = 24a^2(4a+1)$$

$$\Omega''(S2CL,1) = 48a(a^4 + 2a^3 + 4a^2 - 4a + 2)$$

$$CI(S2CL) = 24a(384a^5 + 190a^4 + 20a^3 - 12a^2 + 7a - 4)$$

Examples

Net	Omega	*CI*
111	$24x+36x^2+3x^8$	14040
222	$192x+216x^2+24x^4+6x^{24}$	741600
333	$648x+576x^2+144x^4+9x^{48}$	7858872
777	$8232x+4536x^2+3024x^4+21x^{224}$	1161954360
888	$12288+6336x^2+4704x^4+24x^{288}$	2567169792

Data were calculated by the original software Nano-Studio, developed at TOPO Group Cluj, Romania.

CONCLUSIONS

Design of S_2CL hypothetical crystal structure was performed by using some operations on maps. This network is aimed to simulate the ordered channels existing in some zeolites. The topology of the proposed network was described in terms of Omega polynomial.

ACKNOWLEDGMENTS

The authors wish to thank for the financial support provided from programs co-financed by The SECTORAL OPERATIONAL PROGRAMME HUMAN RESOURCES DEVELOPMENT, Contract **POSDRU 6/1.5/S/3 –** **„**Doctoral studies: through science towards society".

REFERENCES

1. M. V. Diudea, *Ed.*, *Nanostructures, novel architecture*, NOVA, **2005**.
2. M. V. Diudea and Cs. L. Nagy, *Periodic Nanostructures*, Springer, **2007**.
3. R. W. Thompson and A. Dyer, *Zeolites*, **1985**, *5*, 292.
4. Zh. Liu, T. Ohsuna, O. Terasaki, M. A. Camblor, M.-J. Diaz- Cabañas and K. Hiraga, *J. Am. Chem. Soc.*, **2001**, *123*, 5370.

5. Zh. Yang, Y. Xia and R. Mokaya, *J. Am. Chem. Soc.*, **2007**, *129*, 1673.
6. G. O. Brunner, *Zeolites*, **1993**, *13*, 88.
7. E. H. Ellison, *J. Phys. Chem.*, **2006**, *110*, 11406.
8. L. Carlucci, G. Ciani and D. Proserpio, *Coord. Chem. Rev.*, **2003**, *246*, 247.
9. L. Carlucci, G. Ciani and D. Proserpio, *Cryst. Eng. Comm.*, **2003**, *5*, 269.
10. V. A. Blatov, L. Carlucci, G. Ciani and D. Proserpio, *Cryst. Eng. Comm.*, **2004**, *6*, 377.
11. I. A. Baburin, V. A. Blatov, L. Carlucci, G. Ciani and D. Proserpio, *J. Solid State Chem.*, **2005**, *178*, 2452.
12. O. Delgado-Friedrichs and M. O'Keeffe, *J. Solid State Chem.*, **2005**, *178*, 2480.
13. V. A. Blatov, O. Delgado-Friedrichs, M. O'Keeffe and D. Proserpio, *Acta Cryst.*, **2007**, *A63*, 418.
14. T. Pisanski and M. Randić, in *Geometry at Work*, M. A. A. Notes, **2000**, *53*, 174.
15. P. W. Fowler and T. Pisanski, *J. Chem. Soc. Faraday Trans.* **1994**, *90*, 2865.
16. M. V. Diudea, and P. E. John, *Commun. Math. Comput. Chem.* (*MATCH*), **2001**, *44,* 103.
17. F. Harary, *Graph Theory*. Addison-Wesley, Reading, MA, **1969**.
18. M. V. Diudea, *Forma* (Tokyo), **2004**, *19* (3), 131.
19. P. W. Fowler, *Phys. Lett.*, **1986**, *131*, 444.
20. P. W. Fowler and J. I. Steer, *J. Chem. Soc.*, *Chem. Commun.*, **1987**, 1403.
21. P. W. Fowler and K.M.Rogers, *J. Chem. Soc.*, *Faraday Trans.*, **1998**, *94*, 1019.
22. P. W. Fowler and K.M.Rogers, *J. Chem. Soc.*, *Faraday Trans.*, **1998**, *94*, 2509.
23. M. V. Diudea, P. E. John, A. Graovac, M. Primorac, and T. Pisanski, *Croat. Chem. Acta*, **2003**, *76*, 153.
24. G. Brinkmann, P. W. Fowler, and M. Yoshida, *MATCH Commun. Math. Comput. Chem.*, **1998**, *38*, 7.
25. H. W. Kroto, *Nature*, **1987**, *329*, 529.
26. X. Han, S. J. Zhou, Y. Z. Tan, X. Wu, F. Gao, Z. J. Liao, R. B. Huang, Y. Q. Feng, X. Lu, S. Y. Xie, and L. S. Zheng*, Angew. Chem. Int. Ed.*, **2008**, *47*, 5340.
27. C. R. Wang, Z. Q. Shi, L. J. Wan, X. Lu, L. Dunsch, C. Y. Shu, Y. L. Tang, H. Shinohara, *J. Am. Chem. Soc.*, **2006**, *128*, 11352.
28. P. E John, A. E. Vizitiu, S. Cigher, and M. V. Diudea, *MATCH Commun. Math. Comput. Chem.*, **2007**, *57*, 479.
29. P. E. John, P. V. Khadikar, and J. Singh, *J. Math. Chem.*, **2007**, *42*, 37-45.
30. A. R. Ashrafi, M. Ghorbani, and M. Jalali, *Indian J. Chem.*, **2008**, *47A*, 535.
31. P. V. Khadikar, V. K. Agrawal, S. Karmarkar, *Bioorg. Med. Chem.,* **2002**, 10, 3499.
32. Cs. L. Nagy and M. V. Diudea, *Nano Studio*, "Babes-Bolyai" Univ., 2009.
33. A. R. Ashrafi, M. Jalali, M. Ghorbani, and M. V. Diudea, *MATCH Commun. Math. Comput. Chem.*, **2008**, *60*, 905.
34. M. V. Diudea, K. Nagy, M. L. Pop, F. Gholami-Nezhaad, and A.R. Ashrafi, *Int. J. Nanosci. Nanotechnol.*, **2010**, submitted.

STUDIA UNIVERSITATIS BABEŞ-BOLYAI, CHEMIA, XLV, 2, TOM II, 2010

Dedicated to the memory of Prof. dr. Ioan Silaghi-Dumitrescu marking 60 years from his birth

METHYLTIN(IV) TRICHLORIDE COMPLEXES OF *β*-KETIMINE, $MeSnCl_3[OC(Me)CHC(Me)NH(C_6H_3{}^iPr_2\text{-}2',6')\text{-}4]_n$ (n = 1,2). SOLUTION BEHAVIOR AND SOLID STATE STRUCTURE

CARMEN COMSA, RICHARD A. VARGA, CRISTIAN SILVESTRU[a,*]

ABSTRACT. Reaction of $MeSnCl_3$ with the *β*-ketimine $OC(Me)CHC(Me)NH(C_6H_3{}^iPr_2\text{-}2',6')\text{-}4$, in 1:1 and 1:2 molar ratio, gave the new methyltin(IV) trichloride adducts $MeSnCl_3[OC(Me)CHC(Me)NH(C_6H_3{}^iPr_2\text{-}2',6')\text{-}4]_n$ [n = 1 (**1**), n = 2 (**2**)]. The compounds were characterized by multinuclear NMR studies in solution. The crystal and molecular structure of **1** and **2** was established by single-crystal X-ray diffraction. The crystals contain discrete molecules in which the *β*-ketimine ligand is coordinated to a metal center through its oxygen atom. This results in trigonal bypyramidal $CSnCl_3O$ and octahedral $CSnCl_3O_2$ cores in **1** and **2**, respectively. In the crystals intermolecular Cl···H contacts result in supramolecular architectures.

Keywords: *methyltin(IV), trichloride complexes, β-ketimine, solution NMR studies, single-crystal X-ray diffraction.*

INTRODUCTION

The *β*-diketiminato ligands [Scheme 1 (a)] were widely used to stabilize unusual species and coordination numbers in metal complexes which can show interesting catalytic effects [1]. In contrast to the *β*-diketiminato ligands [1-6], the coordination potential of the *β*-ketiminato ligands [Scheme 1 (b)] in tin(II) and tin(IV) chemistry is much less investigated. Some three, four and six-coordinate, monomeric Sn(II) and Sn(IV) derivatives containing the chelated *β*-ketiminato $[OC(Me)CHC(Me)N(C_6H_3{}^iPr_2\text{-}2',6')\text{-}4]^-$ ligand, *i.e.* SnCl(L), $Sn(L)_2$ and $SnX_2(L)_2$, were reported only recently [7]. The *β*-diketimines and *β*-ketimines can also been used as neutral ligands. We have previously reported on some di- and triorganotin(IV) chloride adducts containing $OC(Me)CHC(Me)NH(C_6H_3{}^iPr_2\text{-}2',6')\text{-}4$ [8,9] and the molecular structures, established by single-crystal X-ray diffraction, were also described for some few other complexes of Ti [10], Zr [12], Mo [12], W [13], Al [14] and Sb [15].

---

[a] *Babeş-Bolyai University, Faculty of Chemistry and Chemical Engineering, Arany Janos 11, 400028 Cluj-Napoca, Romania; * cristi@chem.ubbcluj.ro*

In all these complexes the *β*-ketimine ligand is coordinated to the metal centre through its oxygen atom in a monometallic monoconnective fashion [Scheme 1 (c)].

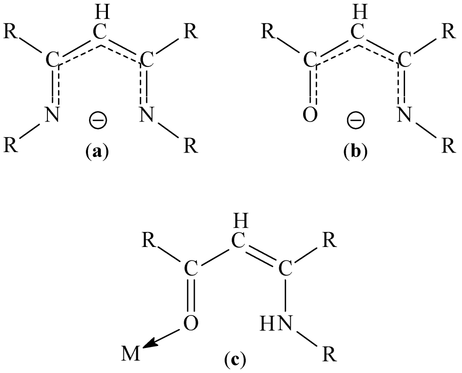

Scheme 1

We report here on the synthesis, solution behavior and solid state molecular structure of 1:1 and 1:2 adducts of methyltin(IV) trichloride, $MeSnCl_3[OC(Me)CHC(Me)NH(C_6H_3{}^iPr_2\text{-}2',6')\text{-}4]_n$ [n = 1 (**1**), n = 2 (**2**)].

RESULTS AND DISCUSSION

The new complexes **1** and **2** were obtained by reacting $MeSnCl_3$ with the *β*-ketimine in 1:1 and 1:2 molar ratio, respectively, in diethyl ether, at room temperature (Scheme 2).

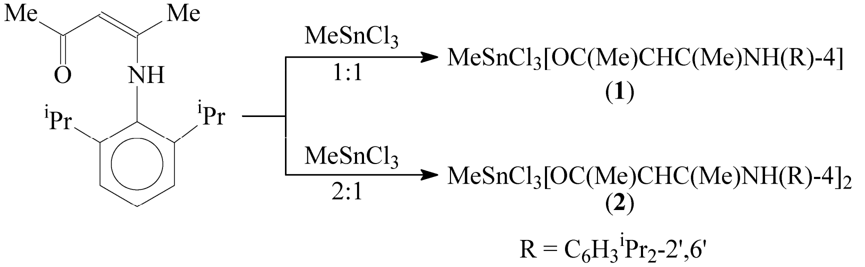

Scheme 2

The new adducts were isolated in very good yields (ca. 90%) as white-yellow powders. They are air-stable and soluble in common organic solvents. The compounds were investigated by multinuclear NMR spectroscopy (^1H, ^{13}C, ^{119}Sn) in solution and their molecular structures were established by single-crystal X-ray diffraction.

The NMR spectra were recorded in $CDCl_3$, at room temperature. The assignment of the ^1H and ^{13}C chemical shifts was made according to the numbering scheme shown in Scheme 3, based on 2D experiments.

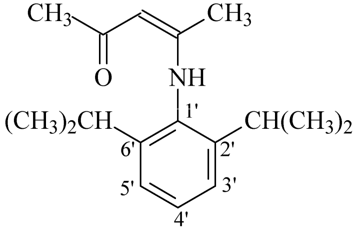

Scheme 3

The NMR (^1H, ^{13}C) spectra of compounds **1** and **2** are very similar. They exhibit in the alkyl and aryl regions the expected resonances for the *β*-ketimine ligand. In addition, a singlet resonance is observed for the protons of methyl group attached to tin. In the ^1H spectra for both compounds these resonances are surrounded by ^{117}Sn / ^{119}Sn satellites due to tin-proton couplings. The integral ratio between ^1H resonances for the protons in the *β*-ketimine ligand and CH_3Sn is consistent with the formation of 1:1 and 1:2 adducts, respectively. The presence of a resonance for the hydrogen attached to nitrogen of the *β*-ketimine ligand is indicative of its coordination to the metal centre in the protonated form.

For both compounds the ^{119}Sn NMR spectra exhibit only one resonance, indicative for the presence of only one tin-containing species in solution, with very likely a similar structure as found in solid state.

Single-crystals suitable for X-ray diffraction studies were obtained by slow diffusion of *n*-hexane into a solution of **1** or **2** in CH_2Cl_2. In both cases the crystals contain discrete monomers separated by distances between heavy atoms larger than the sum of the van der Waals radii for the corresponding atoms. The ORTEP diagrams of the molecular structures of **1** and **2**, with the atom numbering scheme, are shown in Figures 1 and 2. Selected interatomic distances and angles are listed in Tables 1 and 2.

A common structural feature for both adducts is the coordination of the *β*-ketimine ligand through its oxygen atom to tin. As in the free ligand, the acidic hydrogen of the *β*-ketimine is attached to the nitrogen atom and is involved in an intramolecular hydrogen bonding to the oxygen atom. A similar coordination pattern was observed in all the organotin(IV) complexes of the same *β*-ketimine described so far [8,9].

In the molecule of the 1:1 adduct **1** the oxygen atom is placed almost *trans* to a halogen atom [Cl(1)–Sn(1)–O(1) 169.12(12)°], thus resulting in a distorted trigonal bipyramidal $CSnCl_3O$ core.

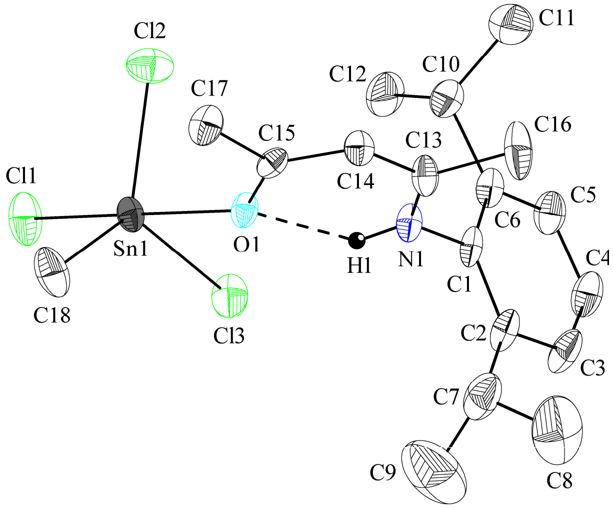

Figure 1. ORTEP representation at 20% probability and atom numbering scheme for **1**. Hydrogen atoms, except H(1) attached to nitrogen, are omitted for clarity.

Table 1. Interatomic bond distances (Å) and angles (°) for compound **1**.

Sn(1)–C(18)	2.099(7)	O(1)–C(15)	1.291(7)
Sn(1)–Cl(1)	2.408(2)	C(15)–C(17)	1.505(9)
Sn(1)–Cl(2)	2.312(2)	C(15)–C(14)	1.359(9)
Sn(1)–Cl(3)	2.335(2)	C(13)–C(16)	1.504(10)
Sn(1)–O(1)	2.191(4)	C(13)–C(14)	1.395(9)
		N(1)–C(13)	1.306(9)
Cl(1)–Sn(1)–O(1)	169.12(12)	N(1)–C(1)	1.448(8)
		N(1)–H(1)	0.856(19)
C(18)–Sn(1)–Cl(2)	123.9(3)	O(1)···H(1)	2.01(4)
C(18)–Sn(1)–Cl(3)	121.5(3)		
Cl(2)–Sn(1)–Cl(3)	113.36(10)	O(1)–C(15)–C(14)	121.5(6)
		O(1)–C(15)–C(17)	118.2(6)
Cl(1)–Sn(1)–C(18)	97.4(3)	C(14)–C(15)–C(17)	120.3(6)
Cl(1)–Sn(1)–Cl(2)	92.42(9)	C(13)–C(14)–C(15)	124.6(6)
Cl(1)–Sn(1)–Cl(3)	91.06(8)	N(1)–C(13)–C(14)	122.4(6)
		N(1)–C(13)–C(16)	118.8(7)
O(1)–Sn(1)–C(18)	92.5(3)	C(14)–C(13)–C(16)	118.9(7)
O(1)–Sn(1)–Cl(2)	85.74(14)	C(1)–N(1)–C(13)	126.5(6)
O(1)–Sn(1)–Cl(3)	79.89(12)	C(1)–N(1)–H(1)	113(4)
		C(13)–N(1)–H(1)	120(4)
Sn(1)–O(1)–C(15)	137.6(4)	C(15)–O(1)···H(1)	101(1)
		N(1)–H(1)···O(1)	129(3)

The length of the Sn(1)–O(1) bond [2.191(4) Å] suggests a stronger coordination [cf. the sums of the covalent and van der Waals radii are Σr_{cov}(Sn,O) ca. 2.06 Å and Σr_{vdW}(Sn,O) ca. 3.60 Å] [16]. As expected, the tin-oxygen distance in **1** is shorter than in the 1:1 adduct $Me_2SnCl_2[OC(Me)CHC(Me)N(C_6H_3{}^iPr_2\text{-}2',6')\text{-}4]$ [Sn–O 2.375(3) Å] [8], the presence of three chlorine atoms attached to tin increasing the acidity of the metal centre. The Sn(1) atom is displaced only 0.147 Å from the CCl_2 equatorial plane on the side of the axial Cl(1) atom and the Sn(1)–Cl(1) bond is slightly elongated [2.408(2) Å] in comparison with the equatorial Sn–Cl bonds [Sn(1)–Cl(2) 2.312(2), Sn(1)–Cl(3) 2.335(2) Å] due to the *trans* effect of the oxygen.

The molecule of **2** is centrosymmetric and features a distorted octahedral $CSnCl_3O_2$ core achieved due to almost *trans* coordination of two *β*-ketimine ligands [O(1)–Sn(1)–O(1') 170.9(2)º], which forces a square planar geometry of the covalent $CSnCl_3$ fragment. The strength of the tin-oxygen bonds in **2** is similar to that observed for **1**. In the equatorial plane, a difference in the length of the tin-chlorine bonds should be noted, *i.e.* those placed *trans* to each other are significantly elongated [Sn(1)–Cl(1) 2.462(2) Å] compared to Sn(1)–Cl(2) [2.386(3) Å], which is *trans* to the carbon atom attached to tin.

In both compounds, regardless the coordination geometry achieved around tin, the planar $OC_3N(H)$ core of the *β*-ketimine ligands is twisted to allow intramolecular interaction between an equatorial chlorine and the N*H* proton [Cl(3)···H(1) 2.70 Å in **1**, and Cl(1)···H(1) 2.73 Å in **2**].

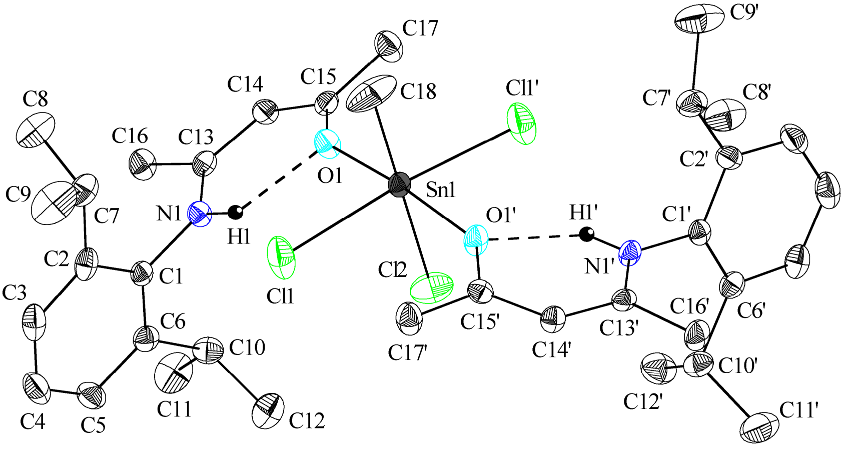

Figure 2. ORTEP representation at 20% probability and atom numbering scheme for **2**. Hydrogen atoms, except H(1) attached to nitrogen, are omitted for clarity [symmetry equivalent atoms (1 – *x*, *y*, 1.5 – *z*) are given by "prime"].

A closer check of the crystal structures of **1** and **2** revealed some supramolecular associations based on intermolecular Cl···H contacts between the molecular units [cf. Σr_{vdW}(Cl,H) ca. 3.0 Å] [16]. Thus, the molecules of **1** are associated into parallel polymeric chains through weak contacts which involve the axial chlorine atom [Cl(1)···H(17Ca)$_{ketimine\text{-}methyl}$ 2.93 Å] (Figure 3) and further weaker inter-chain contacts between the equatorial chlorine atoms from one chain and an aromatic proton from the neighbouring chain [Cl(3)···H(5’)$_{aryl}$ 2.93 Å] led to a 3D architecture.

Table 2. Interatomic bond distances (Å) and angles (°) for compound **2**.

Sn(1)–C(18)	2.094(9)	O(1)–C(15)	1.287(6)
Sn(1)–Cl(1)	2.4620(19)	C(15)–C(17)	1.476(8)
Sn(1)–Cl(2)	2.386(3)	C(15)–C(14)	1.389(7)
Sn(1)–O(1)	2.158(4)	C(13)–C(16)	1.501(7)
		C(13)–C(14)	1.384(7)
Cl(1)–Sn(1)–Cl(1’)	173.42(13)	N(1)–C(13)	1.321(7)
C(18)–Sn(1)–Cl(2)	180.000(1)	N(1)–C(1)	1.443(7)
O(1)–Sn(1)–O(1’)	170.9(2)	N(1)–H(1)	0.848(19)
		O(1)···H(1)	2.01(4)
O(1)–Sn(1)–C(18)	94.56(11)		
O(1)–Sn(1)–Cl(1)	82.73(11)	O(1)–C(15)–C(14)	119.6(5)
O(1)–Sn(1)–Cl(2)	85.44(11)	O(1)–C(15)–C(17)	120.2(5)
O(1)–Sn(1)–Cl(1’)	96.74(11)	C(14)–C(15)–C(17)	120.3(5)
		C(13)–C(14)–C(15)	126.1(5)
O(1’)–Sn(1)–C(18)	94.56(11)	N(1)–C(13)–C(14)	122.5(5)
O(1’)–Sn(1)–Cl(1)	96.74(11)	N(1)–C(13)–C(16)	118.3(5)
O(1’)–Sn(1)–Cl(2)	85.44(11)	C(14)–C(13)–C(16)	119.1(5)
O(1’)–Sn(1)–Cl(1’)	82.73(11)	C(1)–N(1)–C(13)	127.5(4)
		C(1)–N(1)–H(1)	117(3)
Cl(1)–Sn(1)–C(18)	93.29(6)	C(13)–N(1)–H(1)	116(3)
Cl(1)–Sn(1)–Cl(2)	86.71(6)	C(15)–O(1)···H(1)	101(1)
Cl(1’)–Sn(1)–C(18)	93.29(6)	N(1)–H(1)···O(1)	134(3)
Cl(1’)–Sn(1)–Cl(2)	86.71(6)		
Sn(1)–O(1)–C(15)	144.8(4)		

By contrast, in the crystal of **2** the molecular units are doubly connected (Figure 4) through intermolecular interactions based on the *trans* chlorine atoms [Cl(1)···H(16Ab)$_{ketimine\text{-}methyl}$ 2.81 Å], while the third halogen is not involved in any Cl···H contact. No further inter-chain contacts are established in the crystal of **2**.

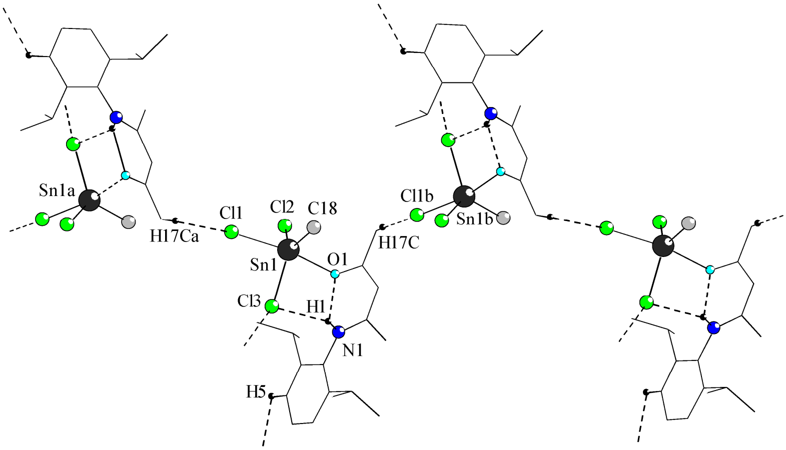

Figure 3. View of a chain polymer based on Cl···H contacts in the crystal of **1** (only H1 attached to nitrogen and hydrogens involved in intermolecular interactions are shown) [symmetry equivalent atoms: Sn1a (–*x*, 0.5+*y*, 1.5–*z*) and Sn1b (–*x*, –0.5+*y*, 1.5–*z*)].

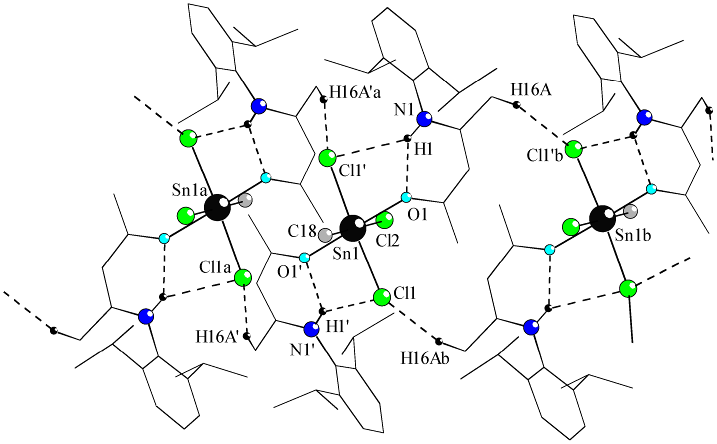

Figure 4. View of a polymeric ribbon-like association based on Cl···H contacts in the crystal of **2** (only H1 attached to nitrogen and hydrogens involved in intermolecular interactions are shown) [symmetry equivalent atoms: Sn1a (1–*x*, 1–*y*, 2–*z*); H16A'a (*x*, 1–*y*, 0.5+*z*); Sn1b (1–*x*, 1–*y*, 1–*z*) and Cl1b' (*x*, 1–*y*, –0.5+*z*)].

CONCLUSION

The first 1:1 and 1:2 adducts of an organotin(IV) trihalide with β-ketimine as neutral ligand, *i.e.* $\mathrm{MeSnCl_3[OC(Me)CHC(Me)NH(C_6H_3{}^{i}Pr_2\text{-}2',6')\text{-}4]_n}$ [n = 1 (**1**), n = 2 (**2**)], were isolated as stable, crystalline solids. They were characterized in solution using multinuclear and 2D NMR spectroscopy, the data being consistent with the proposed formulation. The solid-state molecular structure, as established by single-crystal X-ray diffraction, revealed the monometallic monoconnective nature of the β-ketimine, resulting in distorted trigonal bipyramidal $CSnCl_3O$ (oxygen and chlorine in axial positions) and octahedral $CSnCl_3O_2$ (*trans* O–Sn–O fragment) for **1** and **2**, respectively.

EXPERIMENTAL SECTION

Solvents were dried and distilled prior to use. $MeSnCl_3$ was commercially available. The β-ketimine, $OC(Me)CHC(Me)NH(C_6H_3{}^{i}Pr_2\text{-}2',6')\text{-}4$, was prepared according to a published procedure [9]. ^{1}H, ^{13}C and ^{119}Sn NMR spectra, including 2D experiments, were recorded on Bruker Avance 300 instrument using solutions in $CDCl_3$. The chemical shifts are reported in δ units (ppm) relative to the residual peak of the deuterated solvent (ref. $CHCl_3$: ^{1}H 7.26, ^{13}C 77.0 ppm) for ^{1}H and ^{13}C NMR spectra and neat $SnMe_4$ for and ^{119}Sn NMR spectra. The NMR spectra were processed using the *MestReC* and *MestReNova* software [17].

Preparation of $MeSnCl_3[OC(Me)CHC(Me)NH(C_6H_3{}^{i}Pr_2\text{-}2',6')\text{-}4]$ *(1)*

A solution of $MeSnCl_3$ in Et_2O (1.85 g, 7.70 mmol) was added to a stirred solution of $OC(Me)CHC(Me)NH(C_6H_3{}^{i}Pr_2\text{-}2',6')\text{-}4$ (2 g, 7.71 mmol) in 50 mL Et_2O, at room temperature, and the reaction mixture was stirred for 24 h. Then the solvent was removed in vacuum to give the title compound as a white-yellow powder. Yield: 3.5 g (91%), m.p. 124-125 ^{o}C. ^{1}H NMR (300 MHz, 20 ℃): δ 1.19d [6H_A, -CH(C*H*$_3$)$_2$, $^{3}J_{HH}$ 7.2 Hz], 1.21d [6H_B, -CH(C*H*$_3$)$_2$, $^{3}J_{HH}$ 7.4 Hz], 1.54s (3H, SnC*H*$_3$, $^{2}J_{117SnH}$ 106.0, $^{2}J_{119SnH}$ 110.8 Hz), 1.76s [3H, C*H*$_3$C(N)], 2.25s [3H, C*H*$_3$C(O)], 2.88hept [2H, -C*H*(CH$_3$)$_2$, $^{3}J_{HH}$ 6.8 Hz], 5.29s (1H, -C*H*=), 7.21d (2H, $H_{3',5'}$, $^{3}J_{HH}$ 7.7 Hz), 7.36t (1H, $H_{4'}$, $^{3}J_{HH}$ 7.7 Hz), 11.85s (1H, -N*H*-). ^{13}C NMR (75.4 MHz, 20 ℃): δ 16.47s (Sn*C*H$_3$), 20.03s [*C*H$_3$C(N)], 22.67s [-CH(*C*H$_3$)$_2$, (B)], 24.46s [-CH(*C*H$_3$)$_2$, (A)], 27.23s [*C*H$_3$C(O)], 28.62s [-*C*H(CH$_3$)$_2$], 97.76s (-*C*H=), 123.99s ($C_{3',5'}$), 129.44s ($C_{4'}$), 131.61s ($C_{1'}$), 145.15s ($C_{2',6'}$), 170.15s [CH$_3$*C*(N)], 191.61s [CH$_3$*C*(O)]. ^{119}Sn NMR (111.9 MHz): -210.4s.

Preparation of $MeSnCl_3[OC(Me)CHC(Me)NH(C_6H_3{}^{i}Pr_2\text{-}2',6')\text{-}4]_2$ *(2)*

A solution of $MeSnCl_3$ in Et_2O (0.46 g, 1.92 mmol) was added to a stirred solution of $OC(Me)CHC(Me)NH(C_6H_3{}^{i}Pr_2\text{-}2',6')\text{-}4$ (1 g, 3.85 mmol) in 50 mL Et_2O, at room temperature. The reaction mixture was stirred for 24 h and then the solvent was removed in vacuum to give the title compound as a white-yellow powder. Yield: 1.3 g (89%), m.p. 134-135 ^{o}C. ^{1}H NMR (300 MHz, 20 ℃): δ 1.17d [12H_A, -CH(C*H*$_3$)$_2$, $^{3}J_{HH}$ 6.8 Hz], 1.21d [12H_B, -CH(C*H*$_3$)$_2$, $^{3}J_{HH}$ 6.9 Hz], 1.53s (3H, SnC*H*$_3$, $^{2}J_{117SnH}$ 107.4, $^{2}J_{119SnH}$ 112.1 Hz), 1.70s [6H, C*H*$_3$C(N)], 2.19s [6H, C*H*$_3$C(O)], 2.95hept [4H, -C*H*(CH$_3$)$_2$, $^{3}J_{HH}$ 6.8 Hz], 5.25s (2H, -C*H*=), 7.20d (4H, $H_{3',5'}$, $^{3}J_{HH}$ 7.6 Hz), 7.33t (2H, $H_{4'}$, $^{3}J_{HH}$ 7.7 Hz), 11.94s (2H, -N*H*-). ^{13}C NMR (75.4 MHz, 20 ℃): δ 17.07s (Sn*C*H$_3$), 19.65s [*C*H$_3$C(N)], 22.69s [-CH(*C*H$_3$)$_2$, (B)], 24.52s [-CH(*C*H$_3$)$_2$, (A)], 28.10s [*C*H$_3$C(O)], 28.55s [-*C*H(CH$_3$)$_2$], 96.75s (-*C*H=), 123.78s ($C_{3',5'}$), 128.89s ($C_{4'}$), 132.46s ($C_{1'}$), 145.67s ($C_{2',6'}$), 166.99s [CH$_3$*C*(N)], 193.63s [CH$_3$*C*(O)]. ^{119}Sn NMR (111.9 MHz): -238.3s.

X-ray Crystallographic Study

Data were collected with a SMART APEX diffractometer (*National Center for X-Ray Diffractometry*, “Babes-Boyai” University, Cluj-Napoca, Romania) at 297 K, using a graphite monochromator to produce a wavelength (Mo-$K\alpha$) of 0.71073 Å. The crystal structure measurement and refinement data for compounds **1** and **2** are given in Table 3. Absorption correction was applied for both compounds (semi-empirical from equivalents). The structure was solved by direct methods (full-matrix least-squares on F^2). All non hydrogen atoms were refined with anisotropic thermal parameters. For structure solving and refinement a software package SHELX-97 was used [18]. The drawings were created with the Diamond program [19].

CCDC-770827 (**1**) and -770826 (**2**) contains the supplementary crystallographic data for this paper. These data can be obtained free of charge at www.ccdc.cam.ac.uk/conts/retrieving.html [or from the Cambridge Crystallographic Data Centre, 12, Union Road, Cambridge CB2 1EZ, UK; fax: (internat.) +44-1223/336-033; E-mail: deposit@ccdc.cam.ac.uk].

Table 3. Crystallographic data for compounds **1** and **2**.

	1	**2**
chemical formula	$C_{18}H_{28}Cl_3NOS$	$C_{35}H_{53}Cl_3N_2O_2S$
crystal habit	colorless block	colorless block
crystal size [mm]	0.40 x 0.28 x 0.23	0.31 x 0.28 x 0.2
crystal system	orthorhombic	monoclinic
space group	*Pbca*	*C2/c*
a [Å]	13.995(3)	15.575(5)
b [Å]	14.977(3)	18.136(6)
c [Å]	22.255(4)	14.000(5)
α [deg]	90	90
β [deg]	90	100.651(6)
γ [deg]	90	90
U [Å^3]	4664.9(15)	3886(2)
Z	8	4
D_c [g cm^{-3}]	1.422	1.297
M	499.45	758.83
F(000)	2016	1576
θ range [deg]	2.19 – 25.00	2.12 – 25.00
μ(Mo Kα) [mm^{-1}]	1.444	0.894
no. of reflections collected	32026	13862
no. of independent reflections	4102 (R_{int} = 0.0648)	3436 (R_{int} = 0.0548)
R_1 [$I > 2\sigma(I)$]	0.0745	0.0651
wR_2	0.1373	0.1412
no. of parameters	228	206
no. of restraints	1	1
GOF on F^2	1.327	1.139
largest difference electron density [e Å^{-3}]	0.617, –0.940	0.755, –1.465

ACKNOWLEDGEMENTS

This work was supported by the National University Research Council of Romania (CNCSIS, Research Project Nos. A-709/2006 and TD-340/2007). We also thank the NATIONAL CENTER FOR X-RAY DIFFRACTION ("Babes-Bolyai" University, Cluj-Napoca, Romania) for the support in the solid state structure determinations.

REFERENCES

1. L. Bourget-Merle, M. F. Lappert, J. R. Severn, *Chem. Rev.*, **2002**, *102*, 3031.
2. I. Saur, G. Rima, K. Miqueu, H. Gornitzka, J. Barrau, *J. Organomet. Chem.*, **2003**, *672*, 77.
3. L. W. Pineda, V. Jancik, K. Starke, R. B. Oswald, H. W. Roesky, *Angew. Chem., Int. Ed. Engl.*, **2006**, *45*, 2602.
4. A. P. Dove, V. C. Gibson, E. L. Marshall, H. S. Rzepa, A. J. P. White, D. J. Williams, *J. Am. Chem. Soc.*, **2006**, *128*, 9834.
5. A. Jana, H. W. Roesky, C. Schulzke, A. Doring, T. Beck, A. Pal, R. Herbst-Irmer, *Inorg. Chem.*, **2009**, *48*, 193.
6. A. Jana, H. W. Roesky, C. Schulzke, A. Doering, *Angew. Chem., Int. Ed. Engl.*, **2009**, *48*, 1106.
7. H.-M. Kao, S.-M. Ho, I-C. Chen, P.-C. Kuo, C.-Y. Lin, C.-Y Tu, C.-H. Hu, J.-H. Huang, G.-H. Lee, *Inorg. Chim. Acta*, **2008**, *361*, 2792.
8. C. I. Raţ, C. Comşa, C. Silvestru, *Acta Crystallogr.*, **2010**, *E66*, m130.
9. C. Comşa, A. Cristea, R. A. Varga, C. Silvestru, *Rev. Roum. Chim.*, **2010**, *in press*.
10. L. Kakaliou, W. J. Scanlon IV, B. Qian, S. W. Baek, M. R. Smith III, D. H. Motry, *Inorg. Chem.*, **1999**, *38*, 5964.
11. J. Kim, J.-W. Hwang, Y. Kim, M. H. Lee, Y. Han, Y. Do, *J. Organomet. Chem.*, **2001**, *620*, 1.
12. V. S. Sergienko, A. D. Garnovskii, M. A. Porai-Koshits, V. L. Abramenko, *Koord. Khim.*, **1985**, *11*, 1407.
13. V. S. Sergienko, V. L. Abramenko, A. B. Ilyukhin, *Zh. Neorg. Khim.*, **1997**, *42*, 945.
14. P. Shukla, J. C. Gordon, A. H. Cowley, J. N. Jones, *J. Organomet. Chem.*, **2005**, *690*, 1366.
15. L. A. Lesikar, A. F. Gushwa, A. F. Richards, *J. Organomet. Chem.*, **2008**, *693*, 3245.
16. J. Emsley, *Die Elemente*, Walter de Gruyter: Berlin, **1994**.
17. *MestReC* and *MestReNova*, Mestrelab Research S.L., A Coruña 15706, Santiago de Compostela.
18. G. M. Sheldrick, *Acta Crystallogr., Sect. A* **2008**, *64*, 112.
19. *DIAMOND – Visual Crystal Structure Information System*, Crystal Impact, Postfach 1251, 53002 Bonn, Germany, **2001**.

STUDIA UNIVERSITATIS BABEŞ-BOLYAI, CHEMIA, XLV, 2, TOM II, 2010

Dedicated to the memory of Prof. dr. Ioan Silaghi-Dumitrescu marking 60 years from his birth

SOLID STATE STRUCTURE OF A NEW NICKEL(II) (3*H*-2-THIOXO-1,3,4-THIADIAZOL-2-YL) THIOACETATO COMPLEX

MONICA M. VENTER[a, *], VASILE N. BERCEAN[b], RICHARD A. VARGA[a], VIOREL SASCA[c], TRAIAN PETRIŞOR JR.[d] AND LELIA CIONTEA[d]

ABSTRACT. Reaction of the monosodium salt of (3*H*-2-thioxo-1,3,4-thiadiazol-2-yl) thioacetic acid, $Na(C_2HN_2S_3CH_2COO)\cdot H_2O$ (**1**) with $NiSO_4\cdot 7H_2O$ produced the corresponding nickel(II) complex, $Ni(C_2HN_2S_3CH_2COO)_2\cdot nH_2O$ where n = 4 (**2**) and 6 (**3**). The product was characterized by means of microanalysis and thermal analysis. The crystal structure of **3** was determined by single-crystal X-ray diffraction. The molecular structure consists of discrete molecular units: one octahedral $[Ni(H_2O)_6]^{2+}$ cation and two organic anions, $(C_2HN_2S_3CH_2COO)^-$. The supramolecular structure of **3** is discussed by comparison with that of **1** in its decahydrate, dinuclear form, $[Na(C_2HN_2S_3CH_2COO)(H_2O)_4]_2\cdot 2H_2O$ (**1'**), and reveals the self-assembly of the ionic units into alternating columns through N-H···O, O-H···O/S and S···S interactions.

Keywords: *mercapto-1,3,4-thiadiazole derivatives; nickel(II) complex; thermal decomposition; crystal structure.*

INTRODUCTION

We have an on-going interest in the chemistry of mercapto-aza type heterocyclic compounds (i.e. trithiocyanuric acid, *Bismuthiol I* and *II)*, which have been proved valuable candidates for coordination and supramolecular chemistry.[1-3] 2,5-Dimercapto-1,3,4-thiadiazole (*Bismuthiol I*, Fig. 1a) displays a flat, rigid molecule with an extensive number of donor atoms which may generate a large variety of coordination and supramolecular patterns, leading in many cases to metallamacrocycles[4] and metal-organic frameworks (MOFs).[5,6] In order to improve the flexibility and to increase the coordination versatility

---

[a,*] *"Babeş-Bolyai" University, Faculty of Chemistry and Chemical Engineering, 400028 Cluj-Napoca, Romania; * monica@chem.ubbcluj.ro*

[b] *"Politehnica" University, Faculty of Industrial Chemistry and Environment Engineering, 300001 Timişoara, Romania*

[c] *Institute of Chemistry of the Romanian Academy, 300223 Timişoara, Romania*

[d] *Technical University, Materials Science Laboratory - Thin Films, 400020 Cluj-Napoca, Romania*

of the ligand, the *Bismuthiol I* skeleton was symmetrically extended with two carboxylic pedant arms. The resulting (1,3,4-thiadiazole-2,5-diyldithio)diacetic acid, $C_2N_2S_3(CH_2COOH)_2$ (Fig. 1b) was successfully used in its di-anionic form to build new coordination polymers with transition and rare earth metals.[7-15]

Concomitantly, we have initiated structural investigations on the asymmetric homologue, the (3*H*-2-thioxo-1,3,4-thiadiazol-2-yl)thioacetic acid, $C_2HN_2S_3CH_2COOH$ (Fig. 1c) and a large range of coordination and organic derivatives.[16-18]

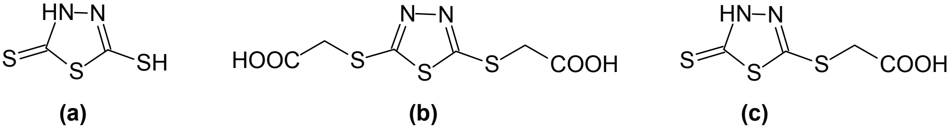

Figure 1. Schematic drawing of *Bismuthiol I* (a), (1,3,4-thiadiazole-2,5-diyldithio) diacetic acid (b) and (3*H*-2-thioxo-1,3,4-thiadiazole-2-yl)thioacetic acid (c).

Our choice for asymmetrically substituted *Bismuthiol I* skeleton targets the following objectives: (i) Selective deprotonation of the ligand due to the presence of different acidic groups in the molecule (Fig. 2); (ii) The use of mono-anionic molecule as coordination ligand and/or hydrogen bond donor, which might diversify the self-assembly pattern in solid state; (iii) The use of di-anionic molecule as selective ligand due to the different affinity of the thioamido and carboxylato groups towards metal cations.

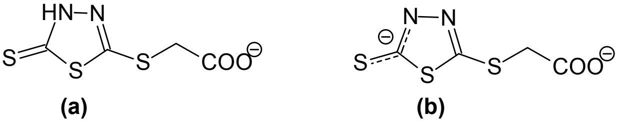

Figure 2. Schematic drawing of the mono- (a) and di-anionic (b) forms of (3*H*-2-thioxo-1,3,4-thiadiazol-2-yl)thioacetic acid.

In the view of the first two objectives, we have reported the general preparative procedure and the vibrational investigation of new metal complexes: $M(C_2HN_2S_3CH_2COO)_n$, n = 1, M = Na and K; n = 2, M = group 2 metals, Mn, Co, Ni, Cu and Zn, along with the structural characterization of $[Na(C_2HN_2S_3CH_2COO)(H_2O)_4]\cdot H_2O$.[16-18] The aim of this work is to complete the characterization of the nickel(II) homologue, $Ni(C_2HN_2S_3CH_2COO)_2\cdot nH_2O$ by means of microanalysis and thermal analysis, as well as single-crystal X-ray diffraction. The supramolecular structure of the title compound is discussed by comparison with that of the starting material in its decahydrate, dinuclear form, $[Na(C_2HN_2S_3CH_2COO)(H_2O)_4]_2\cdot 2H_2O$ (**1'**). It must be mentioned that the supramolecular structure of **1'** has not been reported previously, along with the molecular structure.[18]

RESULTS AND DISCUSSION

The reaction of the monosodium salt of (3*H*-2-thioxo-1,3,4-thiadiazol-2-yl)thioacetic acid, $Na(C_2HN_2S_3CH_2COO)\cdot H_2O$ (**1**) with $NiSO_4\cdot 7H_2O$ produced the corresponding nickel(II) complex described by the general empirical formula $Ni(C_2HN_2S_3CH_2COO)_2\cdot nH_2O$ where n = 4 (**2**) and 6 (**3**). The hexahydrate product (**3**) is stable only as freshly crystallized solid and turns into the tetrahydrate homologue (**2**) during drying at room temperature. The tetrahydrate product (**2**) shows a much higher stability under ambient conditions, preserving the crystal water.

Thermal analysis: The thermal stability of **2** was checked by thermogravimetric analysis. The simultaneous TG/DTA/DTG curves recorded in N_2 atmosphere are presented in Figure 3.

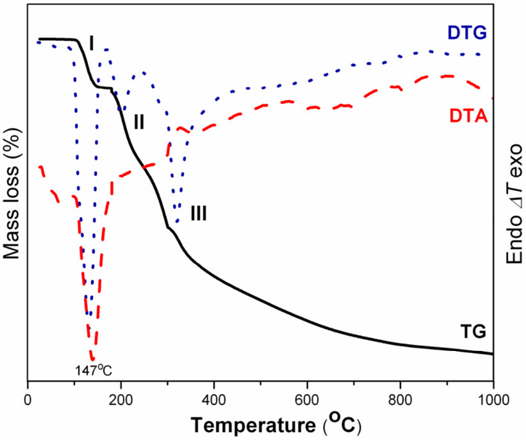

Figure 3. Simultaneous TG/DTA/DTG curves of **2** recorded in N_2 at 10°C/min.

The TG curve shows an initial weight loss (**I**) of -13.03% in the 100–160°C temperature range, which corresponds to the removal of four water molecules per formula unit (Calc. 13.21%). The DTA peak centred at 147°C reveals the most explicit endothermic process assigned to the dehydration step. Above 180°C the anhydrous complex undergoes a continuous mass loss caused by the decomposition of the organic part, and does not end before 1000°C. The major mass loss occurs in the 200–500°C temperature range revealed by the 205°C (**II**) and 318°C (**III**) peaks of the DTG curve. This thermal behaviour is in good agreement with the thermogravimetric analysis reported for Mn(II), Co(II) and rare earth complexes of (1,3,4-thiadiazole-2,5-diyldithio)diacetic acid.[9,10]

For a better elucidation of the decomposition process, the thermogravimetric measurements were repeated in air, coupled with QMS investigation of the evolved gas. The simultaneous TG/DTA and TG-QMS curves are presented in Figures 4 and 5. Due to the unexpected foaming produced by the energetic decomposition of the complex, the temperature rate was reduced twice, from 10ºC to 7.5ºC and 5ºC, respectively.

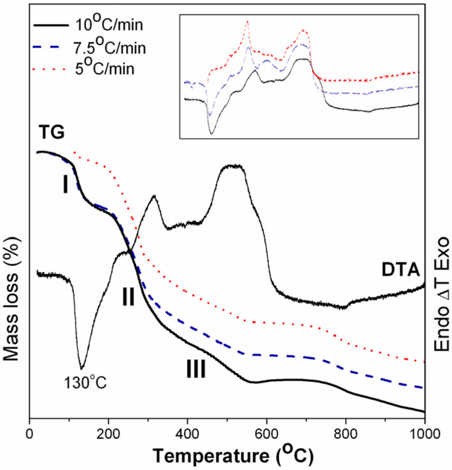

Figure 4. Simultaneous TG/DTA curves of **2** recorded in air at 10, 7.5 and 5ºC/min.

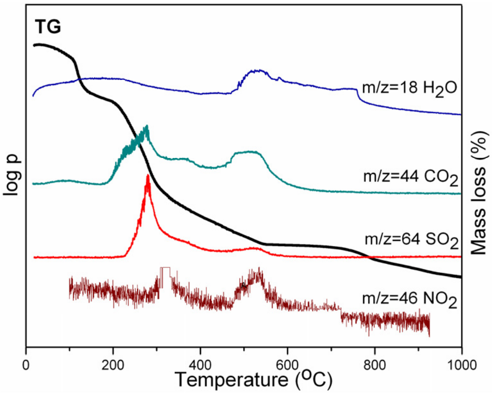

Figure 5. TG-QMS analysis of **2** recorded in air at 7.5ºC/min.

The TG/DTA curves recorded at different temperature rates are comparable. However, a slightly decrease in temperature of the DTA peaks can be observed as the temperature rate is reduced.

Similarly to the thermal behaviour in N_2 atmosphere, the first decomposition step in air (**I**) takes place in the 100–160ºC temperature range and corresponds to the complete dehydration of **2** ($4H_2O$, Exp. 13.1–13.3%, Calc. 13.21%) accompanied by an endothermic effect centred at 126–130ºC in the DTA plot. The water elimination is confirmed by the broad band of the QMS spectrum located in the mentioned thermal range.

Above 200ºC, the anhydrous complex undergoes a complex and continuous mass loss which reveals two major exothermic processes at 281–315 and 509–511ºC, respectively in the DTA plots and ends at 550–560ºC. The QMS plots reveal the evolution of NO_2, SO_2, CO_2 and H_2O, suggesting the combustion of the organic molecules in the 200–550ºC range. The overall mass loss of 55% recorded for this temperature range is consistent with the removal of the heterocyclic fragments $C_2HN_2S_2$ (Calc. 42.9%) and part of the pendant chain, C_2H_2 (Calc. 9.5%). The remaining 28.6% solid residue remains stable in the 560–750ºC temperature range and may be assigned to $NiSO_4$ (Calc. 28.4%) as a result of the rapid oxidation of the NiS intermediate. Such an oxidation process was proved by running TG/DTA/MS measurements on NiS in O_2 flow.[19]

Above 750ºC the decomposition continues and does not end before 1000ºC. The lack of SO_2 evolvement beyond 800ºC questions the previous formation of $NiSO_4$. As a consequence, FT-IR and XRD investigations on the solid residue are in progress and will be published elsewhere.

Structural analysis: The crystal structure of the hexahydrate complex, $[Ni(H_2O)_6](C_2HN_2S_3CH_2COO)_2$ (**3**) was determined by single-crystal X-ray diffraction. Suitable crystals were freshly crystallized from hot water. The molecular structure is presented in Figure 6 and selected metric data are given in Table 1.

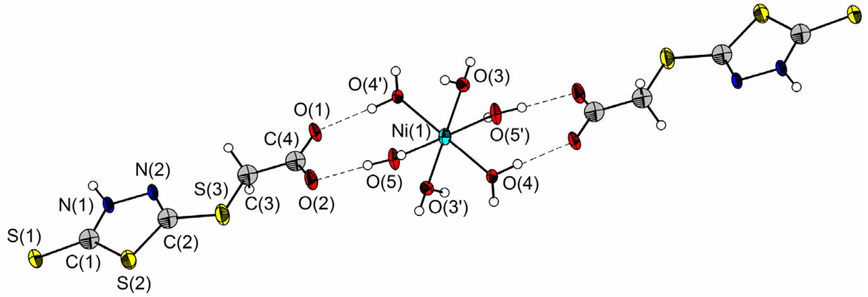

Figure 6. Ortep plot of **3**, showing the labeling used in the text.

Table 1. Selected metric data for **3**.

Bond lengths	**[Å]**	**Bond angles**	**[deg]**
Ni(1)-O(3)	2.054(3)	O(3)-Ni(1)-O(4)	86.37(13)
Ni(1)-O(4)	2.076(3)	O(3)-Ni(1)-O(5)	93.43(14)
Ni(1)-O(5)	2.021(3)	O(4)-Ni(1)-O(5)	90.36(14)
C(1)-N(1)	1.318(6)	C(1)-N(1)-N(2)	118.5(4)
C(2)-N(2)	1.274(6)	C(2)-N(2)-N(1)	109.5(4)
C(1)-S(2)	1.735(5)	C(1)-S(2)-C(2)	88.9(2)
C(2)-S(2)	1.743(4)	N(1)-C(1)-S(2)	108.2(3)
C(1)-S(1)	1.680(4)	N(2)-C(2)-S(2)	114.9(3)
C(2)-S(3)	1.745(4)	C(2)-S(3)-C(3)	98.1(2)
C(4)-O(1)	1.262(6)	O(1)-C(4)-O(2)	126.8(4)
C(4)-O(2)	1.230(6)		

The crystal structure of **3** will be discussed by comparison with that of $[Na(C_2HN_2S_3CH_2COO)(H_2O)_4]_2 \cdot 2H_2O$ (**1’**), the later being – to the best of our knowledge – the only crystallographic evidence for the (3*H*-2-thioxo-1,3,4-thiadiazol-2-yl)thioacetic moiety.[18] Moreover, the supramolecular structure of **1’** has not been reported previously.

The molecular structure of **3** reveals the presence of three ionic units, a $[Ni(H_2O)_6]^{2+}$ cation and two $(C_2HN_2S_3CH_2COO)^{-}$ anions, associated only through O-H···O hydrogen bonding (O···O 2.608 – 2.629 Å, O-H···O 177.29 – 177.39º) designated $R_2^2(7)$. The asymmetric unit of **3** consists of one half of the inorganic complex cation and one organic anion, the remainder being generated by an inversion center located at the metal atom. The structure of the $[Ni(H_2O)_6]^{2+}$ unit is largely unexceptional. The nickel(II) cation lays in an octahedral environment described by six water molecules. The very narrow range of the Ni-O bond lengths [2.021(3) – 2.076(3) Å], as well as the almost ideal O-Ni-O bond angles [86.37(13) – 93.43(14)º] support the proposed coordination geometry.

The structure of $(C_2HN_2S_3CH_2COO)^{-}$ is comparable with that of the corresponding ligand coordinated to sodium through the S(3) atom in **1'**. Thus, the structure of the heterocyclic unit is governed by the planarity of the dimercapto-thiadiazole skeleton, $C_2N_2S_3$ [Ex. C(1)-N(1)-N(2)-C(2) 1.5(6)º; N(1)-C(1)-S(2)-C(2) -0.2(3)º; S(1)-C(1)-N(1)-N(2) 179.1(3)º; S(3)-C(2)-N(2)-N(1) 179.9(3)º] and the thione tautomeric form of the thiocyanate fragment [C(1)-S(1) 1.680(4) Å]. The later structural feature is supported by comparison with similar CS thione groups in **1'** [1.667(3) Å] and related *Bismuthiol II* complexes [1.653(3) – 1.668(3) Å].[2] The pendant arm of the organic anion displays an uncoordinated and strongly delocalized carboxylato group [C-O 1.230(6) – 1.262(6) Å]. Despite the expected flexibility, the acetato chain is almost co-planar with the heterocycle [N(2)-C(2)-S(3)-C(3) -11.3(4)º; S(3)-C(3)-C(4)-O(2) 4.5(6)º].

The formation of the 3D supramolecular structure of **3** can be described by three association tendencies: the self-assembly of the organic anions, the self-assembly of the hydrated nickel cations, and the self assembly of the organic / inorganic parts.

The self-assembly of the $(C_2HN_2S_3CH_2COO)^{-}$ anions is driven by two distinctive interactions. First, the N(1)-H(1)···O(1) hydrogen bonding [N(1)···O(1) 2.721 Å; N(1)-H(1)···O(1) 170.07º] generates dimer aggregates describing ring patterns which contain a total of 16 atoms, two of them donors and two acceptors, and hence designated $R_2^2(16)$ (Fig. 7a).[20] The same motif can be identify in the crystal structure of **1'** [N(1)···O(1) 2.715 Å; N(1)-H(1)···O(1) 178.59º] (Fig. 7b). The dimer aggregates further associate through short S···S interactions, involving the thione S(1) atom in the case of **3** [S(1)···S(1) 3.458 Å] and the S(2)/S(3) atoms in the case of **1'** [S(2)···S(3) 3.420 Å]. Similar S···S interactions (3.45 – 3.71 Å) have been reported for related *Bismuthiol II* complexes.[2]

The self-assembly of the $[Ni(H_2O)_6]^{2+}$ cations in **3** is driven exclusively by water directed hydrogen bonding, leading to columns which run parallel to each other along the a axis (Fig. 8a). The inorganic and organic aggregates are alternatively linked through O-H···O and O-H···S interactions, producing a three dimensional supramolecular structure. Similarly, the 3D supramolecular structure of **1’** (Fig. 8b) shows hydrated, dinuclear sodium cation columns along the b axis, alternating with the organic aggregates.

Only in this case, the connection between the organic and inorganic parts consists of both O-H···O hydrogen bonding and S→Na coordination.

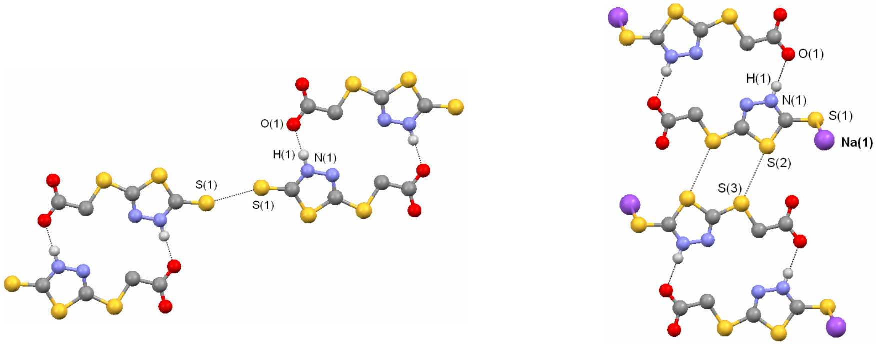

(a) **(b)**

Figure 7. Self-assembly pattern of organic anions in **3** (a) and **1’** (b). Some of the hydrogen atoms were omitted for clarity.

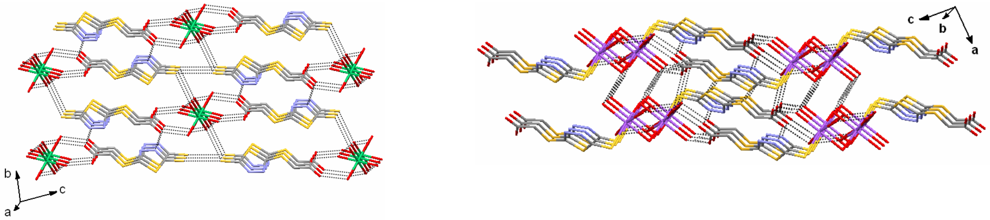

(a) **(b)**

Figure 8. The 3D supramolecular structure of **3** (a) and **1’** (b). Hydrogen atoms were omitted for clarity.

CONCLUSIONS

One new nickel complex of the mono-deprotonated (3H-2-thioxo-1,3,4-thiadiazol-2-yl)thioacetic acid was prepared and characterized in solid state by thermal analysis and single-crystal X-ray diffraction. The thermal decomposition of the tetrahydrate complex was carried out both in N_2 and air atmosphere and revealed the water content, as well as the organic unit combustion. However, none of these measurements were able to prove the formation of nickel chalcogenides bellow 1000ºC. The crystal structure of the hexahydrate complex shows uncoordinated anionic ligands and $[Ni(H_2O)_6]^{2+}$

cations which self-assemble through hydrogen bonding and S···S interactions, generating a 3D supramolecular structure. A similar structural behaviour was evidenced in the crystal structure of the starting material.

EXPERIMENTAL SECTION

Methods and materials

Elemental analyses were obtained on a VarioEL apparatus from Elementar Analysensysteme GmbH. Melting points (uncorrected) were measured in the 30-360°C range using a KRUSS KSPI digital apparatus. Thermal decompositions (TG/DTA/DTG) were carried out using a TGA/SDTA 851-LF 1100 Mettler apparatus. The samples with mass of about 30 mg were placed in alumina crucible of 150 μl and heated non-isothermally from 25ºC to 1000ºC with a heating rate of $10^oC\cdot min^{-1}$, under a nitrogen flow of $50\ ml\cdot min^{-1}$, with the exception of a short isothermal period of 5 min. at 180ºC necessary for a better delimitation of decomposition processes. Alternatively, TG/DTA analysis was carried out in air, in the temperature range 20-1000°C, at rates of 5, 7.5 and 10ºC/min, coupled with a quadrupole mass spectrometer (QMS) using an atmospheric sampling residual gas analyzer 200 QMS Stanford Research System. Drawings were created with the ORIGIN graphing and data analysis software package.[21]

The inorganic salts were purchased from commercial sources (Merck) as analytical pure substances and were used with no further purification. The preparation of (3*H*-2-thioxo-1,3,4-thiadiazol-5-yl)thioacetic acid was reported elsewhere.[22]

Synthesis

*Sodium (3H-2-thioxo-1,3,4-thiadiazol-2-yl)thioacetate monohydrate (**1**).* Solid (3H-2-thioxo-1,3,4-thiadiazol-2-yl)thioacetic acid (50 g, 0.24 mol) was added in small portions, under continuous stirring, to a clear solution of $NaHCO_3$ (20.2 g, 0.24 mol / 220 mL H_2O). After the fizzing stopped, the reaction mixture was heated slowly bellow boiling point to complete the reaction and dissolve the solid material. The resulting hot solution was filtered and cooled to deposit the product as colourless microcrystalline solid, which was further recrystallized from hot distilled water as colourless plates. The product is relatively stable in open atmosphere, at room temperature, as dry solid. In these conditions, it dehydrates continuously until the water content drops to monohydrate. It is soluble in hot water as well as alcohols and dmso. Yield: 47.8 g, 80%; mp: 234-6°C (dec). Microanalysis: found (calc. for $C_4H_5N_2S_3O_3Na$, MW 248.283) C 19.29 (19.35), H 1.76 (2.03), N 11.09 (11.28).

*Nickel(II) (3H-2-thioxo-1,3,4-thiadiazol-2-yl)thioacetate tetrahydrate (**2**).* Aqueous solutions of $NiSO_4\cdot 7H_2O$ (0.56 g, 2 mmol / 10 mL H_2O) and $Na(C_2N_2HS_3CH_2COO)\cdot H_2O$ (1 g, 4 mmol / 10 mL H_2O) were stirred at room temperature for 30 minutes. The green precipitate was filtered and further recrystallized from hot distilled water as green plates. Some of the crystals were suitable for X-ray diffraction analysis. The product is stable in open atmosphere, at room temperature, soluble in hot water and unsoluble in common organic solvents. Yield: 0.49 g, 49%; mp: 97-9°C (dec). Microanalysis: found (calc. for $C_8H_{14}N_4S_6O_8Ni$, MW 545,306) C 17.63 (17.62), H 2.23 (2.58), N 9.82 (10.27).

Crystallography

Cystallographic data for $[Ni(H_2O)_6](C_2HN_2S_3CH_2COO)_2$ (**3**) are summarized in Table 2. The single-crystal X-ray diffraction analysis was performed on a Bruker SMART APEX system (Babes-Bolyai University of Cluj-Napoca, Romania) using graphite monochromated Mo-Kα radiation (λ = 0.71073 Å). The software package SHELX-97 was used for structure solving and refinement.[23] Non-hydrogen atoms were refined anisotropically without exception. The hydrogen atoms were refined with a riding model and a mutual isotropic thermal parameter, except the hydrogen atom of the heterocycle which was found in a difference map and refined with a N–H distance of 0.95(6) Å. Drawings were created with the MERCURY and DIAMOND graphic visualization softwares.[24,25] **Supplementary material:** CCDC reference number 775075. Free information and copies: The Director, CCDC, 12 Union Road, Cambridge CB2 1EZ, UK (fax: +44-1223-336033; email: deposit@ccdc.cam.ac.uk or www: http:// www.ccdc.cam.ac.uk).

Table 2. Crystal data and structure refinement for **3**.

Empirical formula	$C_8H_{18}N_4O_{10}S_6Ni$
Formula weight	581.33
Temperature / K	297(2)
Crystal system; Space group	Triclinic; P-1
a / Å	4.8707(6)
b / Å	8.2334(10)
c / Å	14.1470(17)
α / °	98.622(2)
β / °	99.405(2)
γ / °	104.016(2)
Volume / $Å^3$	532.29(11)
Z	1
Absorption coefficient / mm^{-1}	1.553
Reflections collected / unique	5496 / 2159 [R(int) = 0.0308]
Refinement method	Full-matrix least-squares on F^2
Final R indices [I>2sigma(I)]	R1 = 0.0589, wR2 = 0.1165
R indices (all data)	R1 = 0.0671, wR2 = 0.1198
Goodness-of-fit on F^2	1.260

ACKNOWLEDGMENTS

The authors thank The National University Research Council Romania for financial support during the course of this work (Grant CNCSIS-A/2007-2008, 14-25/1449).

REFERENCES

1. I. Haiduc, M.F. Mahon, K.C. Molloy, M.M. Venter, *J. Organomet. Chem.*, **2001**, *627*, 6.
2. V. Bercean, C. Crainic, I. Haiduc, M.F. Mahon, K.C. Molloy, M.M. Venter, P.J. Wilson, *J. Chem. Soc., Dalton Trans.*, **2002**, 1036.
3. M.F. Mahon, K.C. Molloy, M.M. Venter, I. Haiduc, *Inorg. Chim. Acta*, **2003**, *348*, 75.
4. C. Ma, F. Li, D. Wang, H. Yin, J. Organomet. Chem., **2003**, *667*, 5.
5. J.D.E.T. Wilton-Ely, A. Schier, H. Schmidbauer, *Organomet*, **2001**, *20(10),* 1895.
6. J.D.E.T. Wilton-Ely, A. Schier, M.W. Mitzel, H. Schmidbauer, *Inorg. Chem*, **2001**, *40*, 6266.
7. Y.T. Wang, Y.T. Fan, Y.L. Wang, Y.H. Li, H.W. Hou, H.Y. Zhang, *Synth. React. Inorg. Met.-Org. Nano-Metal Chem.*, **2007**, *37(1),* 7.
8. Y.T. Wang, Y.L. Wang, Y.T. Fan, H.W. Hou, H.Y. Zhang, *Synth. React. Inorg. Met.-Org. Nano-Metal Chem.*, **2007**, *37(4),* 241.
9. Y.T. Wang, L.P Zhang, Y.T. Fan, H.W. Hou, X.Q. Shen, *Inorg. Chim. Acta*, **2007**, *360*, 2958.
10. D.X. Xue, W.X. Zhang, X.M. Chen, *J. Mol. Struct.*, **2008**, *877*, 36.
11. Y.T. Wang, X.Q. Shen, Y.T. Fan, H.C. Yao, H.W. Hou, *Supramol. Chem.*, **2008**, *20(5),* 501.
12. Y.T. Wang, M.C. YIN, Y.T. Fan, H.W. Hou, *J. Coord. Chem.*, **2008**, 61(6), 907.
13. Y.H. Yu, C. He, G.F. Hou, J.S. Gao, H.K. Zhang, *Acta Cryst.*, **2008**, *E64*, m794.
14. Y.T. Wang, Y. Xu, J. Solid State Chem., **2009**, *182*, 2707.
15. X.M. Yang, M.C. Yin, D.G. Ding, Y.T. Fan, *Synth. React. Inorg. Met.-Org. Nano-Metal Chem.*, **2009**, *39(1),* 36.
16. M.M. Venter, V. Chis, S. Cinta Pinzaru, V.N. Bercean, M. Ilici, I. Haiduc, *Studia Univ. Babes-Bolyai, Ser. Chem.*, **2006**, *LI(2),* 65.
17. M.M. Venter, A. Pascui, V.N. Bercean, S. Cinta Pinzaru, *Studia Univ. Babes-Bolyai, Ser. Chem.*, **2007**, *LII(1),* 55.
18. M.M. Venter, V.N. Bercean, M. Ilici, S. Cinta Pinzaru, *Rev. Roum. Chim.*, **2007**, *52(1-2)*, 75.
19. J.G. Dunn, C.E. Kelly, *J. Therm. Anal. Calorim.*, **1977**, *12(1),* 43.
20. J. Bernstein, R.E. Davis, L. Shimoni, N.L. Chang, *Angew. Chem. Int. Ed. Engl.*, **1995**, *34*, 1555.
21. *ORIGIN – Graphing and Data Analysis Software Package*, OriginLab Corporation, One Roundhouse Plaza, Northampton, MA 01060 USA, **2008**.
22. M.M. Venter, S. Cinta Pinzaru, I. Haiduc, V. Bercean, *Studia Univ. Babes-Bolyai, Physica*, **2004**, *XLIX(3),* 285.
23. G. M. Sheldrick, *Acta Crystallogr., Sect. A,* **2008**, *64*, 112.
24. C.F. Macrae, P.R. Edgington, P. McCabe, E. Pidcock, G.P. Shields, R. Taylor, M. Towler, J. van de Streek, *J. Appl. Cryst.*, **2006**, *39*, 453.
25. *DIAMOND – Visual Crystal Structure Information System*, Crystal Impact, Postfach 1251, 53002 Bonn, Germany, **2001**.

STUDIA UNIVERSITATIS BABEŞ-BOLYAI, CHEMIA, XLV, 2, TOM II, 2010

Dedicated to the memory of Prof. dr. Ioan Silaghi-Dumitrescu marking 60 years from his birth

AN IMPROVED SAMPLE PREPARATION OF STARCH-BASED FOODS FOR SYNTHETIC DYES ANALYSIS

SIMONA CODRUȚA COBZAC[*], DORINA CASONI, COSTEL SÂRBU

ABSTRACT. The purpose of this study is to develop a simple and fast sample preparation method for synthetic dyes determination from starch-based foods (puddings). Because at sample preparation stage the main problem is to extract quantitatively the dye unchanged, seven different extraction systems were tested. The extractions were carried out using two different techniques: magnetic stirring and sonication. Quantitative determinations were performed using molecular absorption spectrometry and standard calibration method. The efficiency of extraction of eight synthetic food dyes from spiked corn starch samples was evaluated in terms of recovery. The most efficient extraction solvent proved to be ammonia 25%, the recoveries for all dyes (exception for brilliant blue FCF dye) being higher than 92%. Ultrasounds assisted solvent extraction proved to be more efficient than magnetic stirring, leading to a recovery improvement up to 5% in most cases. Finally, commercial pudding samples were analyzed to assess applicability of this extraction procedure. The results obtained for determination of tartrazine in six identical samples showed no significant difference in terms of extracted amount of dye.

Keywords: *food dyes; starch-based foods; solvents extraction; extraction efficiency; ultrasounds assisted extraction; molecular absorption spectrophotometry*

INTRODUCTION

Foods additives have been used for centuries to enhance the quality of food products despite they are increasingly viewed as compounds with toxicological risk [1]. Synthetic dyes, a very important class of food additive, are commonly used in processed foodstuff to compensate the loss of natural colour which is destroyed during processing and storage or to provide the desired colored appearance. By comparing with natural dyes, synthetic dyes have several advantages such as high stability to oxygen, pH and light, great colors variety and color uniformity, low microbiological contamination

---

[*] *Universitatea Babeş-Bolyai, Facultatea de Chimie şi Inginerie Chimică, Str. Kogălniceanu, Nr. 1, RO-400084 Cluj-Napoca,Romania, codruta.cobzac@yahoo.com*

and relatively lower production costs. The use of food dyes is at least controversial because they are added only for esthetical role and some of these substances pose a potential risk to human health, especially to children that are considered a very vulnerable consumer group [2]. Specific directives in each country strictly regulate the use of synthetic food dyes, and safety data such as the acceptable daily intake have been repeatedly determined and evaluated by Food and Agricultural Organization (FAO) and World Health Organization (WHO) [3]. Consequently, accurate and reliable methods for the determination of synthetic dyes are required for assurance of food safety. While titrimetric and gravimetric methods are allowed for determining pure dyes content of color additives, spectrophotometric methods have been listed in the AOAC Official Methods of analysis since 1960 [4]. The speed, ease and efficacy of the spectrophotometric methods make them of particular value. Spectrophotometric methods often prove inadequate, in the analysis of real samples due to the overlapping of spectral absorption maxima. This drawback can be overpassed using complex spectrophotometric methods with chemometric data interpretation [5-7]. Another approach for food colorants determination can be solid-phase spectrometry when the dyes are adsorbed on Sephadex DEAE A-25 or Cl8 silica gel and the absorbance can be directly measured [8, 9]. Due to their properties, synthetic food colorants can be analyzed also by electrochemical techniques like absorbtive voltametry [10, 11] and polarography [12].

Chromatographic methods are playing an important role in dyes analysis [13]. The advantage of this technique consists in separation of colorant one from each other, followed by spectrophotometric VIS detection [14]. Generally RP [15, 16] ion-pair [17] and ion-chromatography [18] are used. Electrophoretic techniques are also used on large scale [19-21]

Due to the complexity of food matrices the isolation of dyes from sample is more problematic to the chemist than the determination step. Dyes isolation techniques have typically depended upon one of three general methodologies: leaching, liquid-liquid extraction, or active substrate absorption. As Marmion notes [22], there is no technique that can be used to all types of sample matrices, thus the chemist requires comprehensive knowledge to choose the technique and to optimize the extraction conditions. For example, the presence of high affinity binding agents such proteins, demand removal of the interfering matrix [23]. Various methods are used for the extraction of dyes from different foodstuff matrices [14, 24]. Given most analytical instruments handle liquid samples, attention is being paid to improving solids sample preparation. If the sample is water soluble, simple dissolution is carried out by manual or mechanical stirring, either with heating or at room temperature. Usually solid-phase extraction is used for purification [20, 25-27]. If the sample is insoluble (e.g., puddings, powder for ice-cream) quantitative extraction of dyes must be performed. Besides the simple liquid-solid extraction, also more complex extraction techniques are available [28]. In recent decades ultrasound has established an important place in different field (industrial, environmental, medical) and its applications has a growing trend in analytical chemistry [29].

Taking in account these considerations, the aim of this study was to find the optimum solvent system and the best technique that ensure the quantitative extraction of dyes from starch-based foods. A detailed study concerning synthetic food dyes extraction from starch was not yet performed.

RESULTS AND DISCUSSION

Absorption spectra of dyes

The analyzed food synthetic dyes are organic substances with high solubility in water conferred by the presence of at least one sulfonic group (salt forming moiety). They can be classified by the nature of chromophoric group in quinoline, azo, and triarylmethane. Depending on the pH values they can be more or less ionized. By careful visual examination of the VIS spectra it is apparent that they presenting isosbestic points, and changes of the wavelength (λ_{max}) and absorbance (A_{max}) induced by the some of pH value. In alkaline extreme environment it can be observed a decreasing of absorbance (A_{max}) for all colorants. There is although a pH range in which A_{max} and λ_{max} do not vary with pH value (Table 1). For good experimental results it is important that the absorbance measurements to be performed within this range. As was pointed out in the experimental part the residuum was dissolved in water, the pH of resulted solution being adjusted in this range.

Table 1. The stability range and specific wavelength λ_{max} for studied dyes.

No.	Compounds	Stability pH range	λ_{max} (nm)
1	Quinoline Yellow WS (E104)	1-9	415
2	Tartrazine (E102)	2-8	425
3	Sunset Yellow FCF (E110)	1-9	480
4	Azorubine (E122)	1-7	515
5	Ponceau 4R (E124)	1-9	507
6	Amaranth (Dye) (E123)	1-9	520
7	Brilliant Blue FCF (E133)	3-11	630
8	Patent Blue V (E131)	5-7	640

Recovery experiments and analysis of spiked samples

The extraction efficiency was evaluated in terms of recovery, calculated as ratio of the determined quantity to that used for preparing the spiked sample. The extracted quantity was calculated on the basis of the sample absorbance and calibration equation (Table 2) at the maximum wavelength that corresponds to each dye.

The efficiency of extraction solvents was tested on the synthetic spiked samples processed as mentioned above. There were used seven different extraction systems, chosen on the basis of dyes solubility, ionic force and pH value.

Table 2. The linear range and calibration equations for studied dyes.

No	Compounds	Linear range (ppm)	Calibration equations	R^2
1	Quinoline Yellow E104)	2-20	y= 0.0670x + 0.0304	0.9985
2	Tartrazine (E102)	2-40	y= 0.0349x + 0.0085	0.9999
3	Sunset Yellow (E110)	3-20	y= 0.0543x – 0.0077	0.9991
4	Azorubine (E122)	2-15	y= 0.0380x – 0.0473	0.9981
5	Ponceau 4R (E124)	4-15	y= 0.0374x – 0.0032	0.9985
6	Amaranth (Dye) (E123)	4-15	y= 0.0393x – 0.0119	0.9987
7	Brilliant Blue (E133)	1-8	y= 0.1359x + 0.0181	0.9997
8	Patent Blue V (E131)	1-10	y= 0.1679x + 0.0559	0.9985

The obtained results and expanded uncertainly U (±2s) for 95% are presented in Table 3. The profiles of recovery (Figure 1) illustrate that the high solubility of food dyes in water is not the most important parameter concerning the efficiency of extraction. This behaviour might be attributed to the specific interaction with starch. When pH was modified and ionic strength increased (extraction system 2 and 6) no improving of recovery was observed. Also, using methanol as extraction system, the extraction efficiency has not significantly increased. All these findings indicate that the interactions between starch and dyes are complex and extraction procedure is very difficult to be optimized. The best results obtained using ammonia 25% could be explained by a strong desorption effect generated by the resulted ammonium salts or by blocking the adsorption cites. Much more, the effect of ammonia is very similar in all cases and this fact is well illustrated in Fig. 1. In addition, as we can observe in Table 3, the best recoveries (higher than 92% for all studied dyes exception for brilliant blue) were obtained by using ammonia 25% as extraction solvent. For azorubine and ponceau 4R good recoveries (92.54% respectively 96.05%) were also obtained with methanol-ammonia 25% (9:1, v/v) mixture.

Table 3. Dyes recovery and expanded uncertainly U for 95% (n=6).

Compounds (Abbr.)	Recovery(%) ± U						
	Solvents extraction Systems						
	Water	Acetic buffer (pH=4)	MeOH	MeOH-HCl (9:1, v/v)	MeOH-NH_3 (9:1, v/v)	Ammonia buffer (pH=10)	Ammonia (25%)
Quinoline (E104)	3.3±0.6	2.5±0.3	5.3±0.7	4.0±0.8	2.6±0.6	54.8±5.0	95.5±9.2
Tartrazine (E102)	71.9±10.0	28.4±3.8	10.2±5.7	6.9±1.4	9.0±1.7	13.6±3.4	92.2±10.8
Sunset Yellow (E110)	31.5±5.3	12.9±2.2	12.9±1.7	14.5±2.5	14.8±1.7	20.± 3.3	93.5±12.1
Azorubine (E122)	23.9±4.1	2.6±0.5	5.6±0.6	6.1±1.2	92.5±9.6	10.1±1.4	96.1±6.2
Ponceau 4R (E124)	44.4±7.0	2.3±0.4	7.3±1.4	5.9±1.4	96.0±11.6	69.6±12.7	97.8±6.3
Amaranth (E123)	64.9±9.5	78.7±9.4	49.6±10.6	53.7±10.3	55.2±8.9	65.1±7.3	91.2±6.9
Brilliant Blue (E133)	36.9±6.3	46.3±4.6	30.6±6.0	35.9±6.4	36.0±8.4	37.40±9.9	84.9±4.3
Patent Blue V (E131)	78.7±12.0	81.2±0.5	55.1±9.5	46.5±10.0	54.3±10.0	68.5±15.2	92.2±3.2

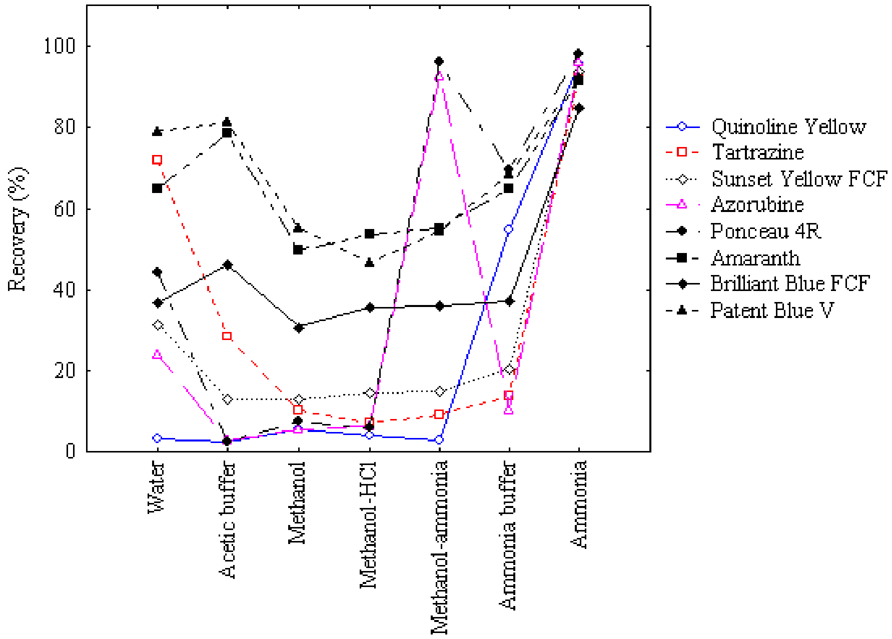

Figure 1. The influence of extraction system on the dyes recovery.

Dyes ultrasounds assisted extraction from spiked samples and puddings

The ultrasounds extraction efficiency of each colorant was tested using only ammonia 25% as extraction solvent. Absorption spectra of all extracts do not show degradation or displacement of maximum absorption wavelength. The obtained recovery data are presented in Table 4.

Table 4. Levels of dyes recovery obtained by ultrasounds assisted extraction using ammonia (25%) as solvent system.

No.	Name of compounds	Recovery(%) ± U
1	Quinoline Yellow WS	98.50±2.1
2	Tartrazine	99.25±2.0
3	Sunset Yellow FCF	98.63±3.2
4	Azorubine	99.62±1.7
5	Ponceau 4R	99.63±1.3
6	Amaranth Dye	98.12±2.0
7	Brilliant Blue FCF	85.23±3.6
8	Patent Blue V	93.39±2.2

By comparing the efficiency of assisted ultrasounds extraction (Table 3) with that obtained by mechanical stirring (Table 2), it can be observe that by applying ultrasounds assisted extraction, the recovery is significantly improved, more than 5% in most cases. The low “s” values illustrate a good precision of determinations.

In order to assess reliability of this extraction procedure to the food dyes analysis from real samples, determination of tartrazine from vanilla pudding was performed. Six identical samples (0.5000 g) were processed by the protocol described above using ammonia 25% as extraction solvent. Tartrazine was identified from the absorption spectra and its amount was calculated on the basis of the sample absorbance and calibration equation at the specific wavelength. The average concentration of tartrazine for six identical commercially vanilla pudding samples was 144.84 ± 0.05 mg/kg.

CONCLUSIONS

The results obtained in this study concerning the extraction of dyes from starch-based foods demonstrated that the most efficient system is ammonia 25%, in this case the recovery being higher than 92% for all studied food dyes (exception for brilliant blue FCF dye); for azorubine and ponceau 4R good recoveries (92.54% respectively 96.05%) were obtained also by using methanol-ammonia 25% (9:1,v/v) mixture as extraction system.

Ultrasounds assisted extraction proved to be a technique more efficient than simple mechanical stirring extraction, leading to a recovery improvement up to 5% in most cases. The technique developed in this paper was successfully applied for tartrazine determination from commercially pudding. The proposed method was found to be relative simple, precise, sensitive and accurate and might be efficiently applied for the determination of tartrazine and other food dyes in commercial available puddings.

EXPERIMENTAL SECTION

Chemicals

Methanol and Titrisol buffer solutions having pH from 1 to 12 and an error ΔpH = ±0.01 were acquired from Merck (Darmstad, Germany). Acetic acid (glacial), ammonia 25% and hydrochloric acid fuming (37%) were from Chemical Company (Iasi, Romania). Natrium acetate and ammonium chloride solid salts used for preparation of buffer solutions were purchased from Chimopar (Bucuresti, Romania). Solid dyes standards (Quinoline Yellow WS, Tartrazine, Sunset Yellow FCF, Ponceau 4R, Azorubine, Erythrosine, Amaranth, Brilliant Blue FCF, and Patent Blue V) were purchased from Merck or Fluka. Standard stock solutions of all dyes (100 mg/mL) were prepared by weighting appropriate amounts of solid colorant and dissolving them in deionized water. Working solutions of individual dyes were prepared by dilution of aliquots of stock solutions. Corn starch and vanilla pudding were purchased from local market.

Methods

VIS spectra and calibration curve determination

The absorbance spectra in VIS for each colorant was plotted for different pH values : 1 ; 2; 3; 4; 5; 6,86; 8; 9; 10; 11, and 12, at a concentration of $2x10^{-5}$M. The solution for calibration curves were prepared for each dye by successive dilution of stock aqua solution within the range 1-40 ppm. The absorbance was measured at specific λ_{max} of each compound.

Instrumentation

Ultrasound extractions were performed using a Transsonic T310 bath at 35 kHz. Spectrophotometric measurements were performed using a Jasco, V-550, UV/VIS spectrophotometer.

Extraction procedures

Eight different synthetic samples (0.1 mg/g), one for each of the studied dyes, were prepared by mixing of 30 g starch powder with 30 mL of aqueous dye solution (0.1mg/mL). After the evaporation of water at room temperature, the powders were homogenized and portions of 0.5000 g from each were precisely weighted. Each sample was mixed with 10 mL of extraction solvent and homogenized by magnetic stirring for 15 min. There were used seven extraction systems: 1-water; 2-acetic buffer (pH = 4); 3-methanol; 4-methanol-hydrochloric acid (6M) (9:1, v/v); 5-methanol-ammonia 25% (9:1, v/v), 6-ammonia buffer (pH = 10) and 7-ammonia 25%. In each case the slurry was passed through an inert filtering cartridge - like that used in solid phase extraction but filled with very fine particle of powder glass as stationary phase. The cartridge was previously washed with 3 mL of methanol and 5 mL of extraction solvent in each case. After filtration, the cartridge was washed with extraction solvent (5 mL). The effluent was evaporated to dryness at 40 ^{0}C in a stove and the residuum was dissolved in 5 mL water. The maximum absorbance was measured at specific wavelength for each dye, the extracted quantity being determined using standard calibration method. For all of the studied dyes, six identical synthetic samples were processed like described above.

The protocol for ultrasounds assisted extraction was similar as specified above. The extraction was performed in 25% ammonia in an ultrasonic bath for 15 minutes.

ACKNOWLEDGMENTS

The financial support of the Ministry of Education and Research of Romania (CNCSIS, IDEI 560/2007) is gratefully acknowledged.

REFERENCES

1. V. M. Ghorpade, S. S. Deshpande, D. K. Salunkhe, Maga JA, Tu AT, Food colours: Food additives and toxicology*,* Marcel Dekker, New York, **1995**.
2. F. M. Clydesdale, *Food Sci. Nutr.*, **1993**, *33*, 83.
3. A. Downham, P. Collins, *Int. J. Food Sci. Technol.*, **2000**, *35,* 5.
4. S. Bell, Official Methods of Analysis: Food Compositions, Additives, Natural Contaminants, Vol. 2, K. Helrich (Ed), Association of Official Analytical Chemists, Arlington, VA., **2002**.
5. K. Hofer, D. Jenewein, *Eur. Food Res.*, **1997**, *204*, 32.
6. J. J. Berzas Nevado, J. Rodríguez Flores, M.J. Villaseñor Llerena, N. Rodríguez Fariñas, *Fresenius J. Anal. Chem.*, **1999**, *365*, 383.
7. A. C. Moț, F. Saponar, D. Casoni, C. Cobzac, C. Sârbu, *Rev. Chim.,* **2009**, *60*, 647.
8. L. F. Capitán-Vallvey, M. D. Fernández, I. de Orbe, J. L. Vilchez, R. Avidad, *Analyst*, **1997**, *122*, 351.
9. F. Capitán, L. F. Capitán-Vallvey, M. D. Fernández, I. de Orbe, R. Avidad, *Anal. Chim. Acta*, **1996**, *331*, 141.

10. Y. Ni, J. Bai, L. Jin, *Ana.l Chim. Acta*, **1996**, *329*, 65.
11. J. J. Berzas Nevado, J. Rodríguez Flores, M. J. Villaseñor, L. Lerena, *Talanta*, **1997**, *44*, 467.
12. S. Chanlon, L. Joly-Pottuz, M. Chatelut, O. Vittori, J. L. Cretier, *J. Food Compos. Anal.*, **2005**, *18*, 503.
13. M. Kucharska, J. Grabka, *Talanta,* **2010**, *80*, 1045.
14. K. S. Minioti, C. F. Sakellariou, N. S. Thomaidis, *Anal. Chim. Acta*, **2007**, *583*, 103.
15. M. S. Garcia-Falcon, J. Simal Gandara, *Food Control,* **2005**, *16*, 293.
16. E. C. Vidotti, W. F. Costa, C. C. Oliveira, *Talanta*, **2006**, 68, 516.
17. M. G. Kiseleva, V. V. Pimenova, K. I. Eller, *J. Anal. Chem.*, **2003**, *58,* 685.
18. Q. Chen, S. Mou, X. Hou, J. M. Riviello, Z. Ni, *J. Chromatogr. A*, **1998**, *827*, 73.
19. A. De Villiers, F. Alberts, F. Lynen, A. Crouch, P. Sra, *Chromatographia*, **2003**, *58*, 393.
20. H.-Ya Huang, Y.-Chieh Shih, Y.-Chieh Chen, *J. Chromatogr. A,* **2002**, *959*, 317.
21. L. De Giovine, A. Piccioli Bocca, *Food Control*, **2003**, *14*, 131.
22. D. M. Marmion, Handbook of U. S. Colorants for Foods, Drugs, and Cosmetics. 2nd ed, John Wiley & Sons, New York, **1979**.
23. M. Tripathi, S. K. Khanna, M. Das, *J. AOAC Int.*, **2004**, 87, 657.
24. M. D. Luque de Castro, J. L. Luque-García, Acceleration and Automation of Solid Sample Treatment, Elsevier, Amsterdam, **2002**.
25. C. Van Peteghem, J. Bijl, *J. Chromatogr. A*, **1981**, *210*, 113.
26. J. F. Lawrenc, F. E. Lancaster, H. B. S. Conacher, *J. Chromatogr.*, **1981**, *210*, 168.
27. N. P. Boley, N. T. Crosby, P. Roper, L. Somers, *Analyst*, **1981**, *106*, 710.
28. E. Wisher, R. König, W. Feldheim*, Eur. Food Res. Technol.*, **1980**, *170*, 267.
29. F. Priego-Capote, M. D. Luque de Castro, *Trends Anal. Chem.*, **2004**, *23*, 644.

STUDIA UNIVERSITATIS BABEŞ-BOLYAI, CHEMIA, XLV, 2, TOM II, 2010

Dedicated to the memory of Prof. dr. Ioan Silaghi-Dumitrescu marking 60 years from his birth

AMMONIUM SALTS OF ORGANOPHOSPHORUS ACIDS. CRYSTAL AND MOLECULAR STRUCTURE OF $[Et_3NH]^+[(SPMe_2)(SPPh_2)N]^-$ AND $[2\text{-}\{O(CH_2CH_2)_2N(H)CH_2\}C_6H_4]^+[S_2P(OPr^i)_2]^-$

ANA MARIA PREDA[a], MONIKA KULCSAR[b], RICHARD A. VARGA[a], DRAGOS MARGINEANU[a], ANCA SILVESTRU[a,*]

ABSTRACT. The ammonium salts $[Et_3NH]^+L^-$ $\{L^- = [(SPMe_2)(SPPh_2)N]^-$ (**1**), $Ph_2PS_2^-$ (**2**)$\}$ were obtained in the reaction between triethylamine and the corresponding organophosphorus acid in a 1:1 molar ratio, while $[2\text{-}\{O(CH_2CH_2)_2N(H)CH_2\}C_6H_4]^+[S_2P(OPr^i)_2]^-$ (**3**) resulted as hydrolysis product in the process of growing crystals of $[2\text{-}\{O(CH_2CH_2)_2N(H)CH_2\}C_6H_4SeS_2P(OPr^i)_2$. Compounds **1** and **2** were characterized by ^1H and ^{31}P NMR spectroscopy. Single-crystal X-ray diffraction studies revealed the presence of short intermolecular S···H contacts which result in the formation of dimeric units in **1** and of a layered supramolecular structure in **3**.

Keywords*: onium salts, intermolecular interactions, supramolecular network, dimeric units*

INTRODUCTION

Organophosphorus acids of type **a** (diorganodichalcogeno-phosphinic acids, diorganodichalcogenophosphonic acids and diorgano-dichalcogeno-phosphoric acids) or of type **b** (tetraorganodichalcogeno-imidodiphosphinic acids) (Scheme 1) have attracted a considerable interest in last three decades. They proved a high capacity to build metal complexes both with main group or transition metals by displaying a large variety of coordination patterns and their metal complexes found applications in biology, catalysis or electronics.[1-12]

On the other hand, onium salts melting at low temperatures was observed to be suitable as ionic liquids.[13,14]

---

[a] *Babeş-Bolyai University, Faculty of Chemistry and Chemical Engineering, Arany Janos 11, 400028 Cluj-Napoca, Romania; * ancas@chem.ubbcluj.ro*

[b] *Departamento de Química Inorgánica, Instituto de Ciencia de Materiales de Aragón, Universidad de Zaragoza-C.S.I.C., E-50009 Zaragoza, Spain*

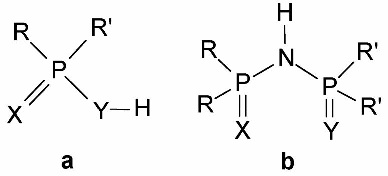

R = alkyl, aryl, alkoxy, aryloxy; X, Y = O, S.

Scheme 1

We report here about the new ammonium salts

$[Et_3NH]^+L^-$ $\{L^- = [(SPMe_2)(SPPh_2)N]^-$ (**1**), $[Ph_2PS_2]^-$ (**2**)$\}$ and

$[2\text{-}\{O(CH_2CH_2)_2N(H)CH_2\}C_6H_4]^+[S_2P(OPr^i)_2]^-$ (**3**).

RESULTS AND DISCUSSION

The ionic compounds $[Et_3NH]^+[(SPMe_2)(SPPh_2)N]^-$ (**1**) and $[Et_3NH]^+[S_2PPh_2]^-$ (**2**) were prepared according to eq. *(1)*, by reacting triethylamine either with the dimethyldiphenyldithioimidodiphosphinic acid or the diphenyldithiophosphinic acid, in a 1:1 molar ratio, in benzene, at room temperature.

$$Et_3N + LH \longrightarrow [Et_3NH]^+L^- \qquad (1)$$

$$L^- = (Me_2PS)(Ph_2PS)N^- \ (\mathbf{1}),\ \ Ph_2PS_2^- \ (\mathbf{2})$$

$[2\text{-}\{O(CH_2CH_2)_2N(H)CH_2\}C_6H_4]^+[S_2P(OPr^i)_2]^-$ (**3**) resulted as a hydrolysis product in the attempts to grow crystals of

$[2\text{-}\{O(CH_2CH_2)_2N(H)CH_2\}C_6H_4SeS_2P(OPr^i)_2$.

Compounds **1** and **2** were isolated in quantitative yields as microcrystalline solid species and were characterized by ^1H and ^{31}P NMR spectroscopy.

The ^1H NMR spectra display the expected resonances for the organic groups attached to phosphorus and nitrogen, respectively. The multiplicity of the ^1H resonances is determined by proton–proton and phosphorus–proton couplings. The N*H* protons in the triethylammonium cation give large singlet resonances at δ 10.02 and 10.22 ppm for **1** and **2**, respectively. The ^{31}P NMR spectra of the two compounds display two resonances in a 1:1 ratio for **1** and only one resonance for **2**, shifted in comparison with the corresponding free acids, due to the interaction with the cationic species.

Single-crystals suitable for X-ray diffraction studies were obtained for compounds **1** and **3** by slow diffusion from a mixture of CH_2Cl_2 and n-hexane (1:4, v/v). The ORTEP diagrams of the molecular structures of **1** and **3** with the atom numbering schemes are depicted in Figures 1 and 2, respectively, while selected interatomic distances and angles are listed in Table 1.

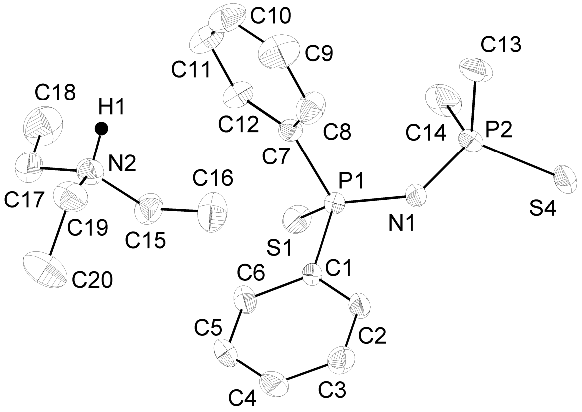

Figure 1. ORTEP plot of $[Et_3NH]^+$ $[(SPMe_2)(SPPh_2)N]^-$ (**1**). The atoms are drawn with 30% probability ellipsoids. Hydrogen atoms, except the one attached to nitrogen, are omitted for clarity.

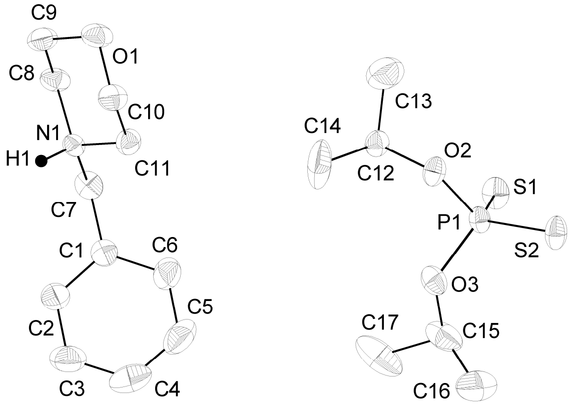

Figure 2. ORTEP plot of $[2\text{-}\{O(CH_2CH_2)_2N(H)CH_2\}C_6H_4]^+[S_2P(OPr^i)_2]^-$ (**3**). The atoms are drawn with 30% probability ellipsoids. Hydrogen atoms, except the one attached to nitrogen, are omitted for clarity.

Both compounds are ionic species in which the ammonium cations and the organophosphorus anions are held together by electrostatic interactions. The central atoms N2 and N1, respectively, in the ammonium cations in compounds **1** and **3** have a distorted tetrahedral coordination geometry, with angles ranging between 104(2) and 114.8(3)^{o} in **1** and 107.1(2) and 112.9(2)^{o} in **3**, respectively. The N–H distance is similar with those found in other ionic species containing $[Et_3NH]^+$ or $[Bu_3NH]^+$ cations.[15,16]

The organophosphorus ligands display almost equal P-S [1.971(1) and 1.985(1) Å in **1** and 1.968(1) and 1.980(2) Å in **3**] and P–N interatomic distances [1.594(3) and 1.596(3) Å in **1**], thus suggesting a symmetrical delocalization of the π electrons over the SPNPS system in **1** and the PS_2 system in **3**, respectively. However, these values are intermediate between those observed for single P–E and double P=E (E = S, N) bonds in the free acid $Ph_2P(S)SH$: P–S 2.077(1) and P=S 1.954(1) Å [17] and $Ph_2P(=S)–N=PPh_2(–SMe)$: P=S 1.954(1), P–S 2.071(1), P=N 1.562(2) and P–N 1.610(2) Å [18].

Table 1. Interatomic bond distances (Å) and angles (°) for compounds **1** and **3**

1		3	
N(1)–P(1)	1.594(3)	P(1)–S(1)	1.968(1)
N(1)–P(2)	1.596(3)	P(2)–S(2)	1.980(2)
P(1)–S(1)	1.971(1)	N(2)–H(1)	0.87(3)
P(2)–S(2)	1.985(1)	N(1)–C(7)	1.514(6)
N(2)–H(1)	0.87(2)	N(1)–C(8)	1.496(5)
N(2)–C(15)	1.488(4)	N(1)–C(5)	1.497(11)
N(2)–C(17)	1.501(5)		
N(2)–C(19)	1.489(5)		
P(1)–N(1)–P(2)	132.94(17)	S(1)–P(1)–S(2)	116.69(5)
C(15)–N(2)–C(19)	114.8(3)	C(7)–N(1)–C(8)	110.5(2)
C(15)–N(2)–C(17)	111.6(3)	C(7)–N(1)–C(11)	112.9(2)
C(19)–N(2)–C(17)	112.0(3)	C(8)–N(1)–C(11)	109.3(2)
C(15)–N(2)–H(1)	110(2)	C(7)–N(1)–H(1)	109.2(2)
C(17)–N(2)–H(1)	104(2)	C(8)–N(1)–H(1)	107.1(2)
C(19)–N(2)–H(1)	104(2)	C(11)–N(1)–H(1)	107.7(2)

A closer check of the crystal structures of **1** and **3** revealed intermolecular S···H contacts between cations and anions [cf. $\Sigma r_{vdW}(S,H)$ ca. 3.05 Å] [19]. In compound **1** dimeric associations are formed both by strong cation – anion hydrogen bonding [H1···S2’’’ 2.351(3) Å] and week inter-anions interactions [H13B”···S2’’’ 2.967(3) Å] (Figure 3).

By contrast, in the crystal of **3** a layered network is formed both by cation – anion hydrogen bonding [H1···S2’’ 2.53(3), H8A···S1’ 2.901(7) and S2’···H7B 2.981(2) Å] and inter–anions H···S interactions [H14B···S2’ 2.984(1) Å] (Figure 4). While in compound **1** only one sulfur atom is involved in hydrogen bonding, in compound **3** both sulfur atoms are involved, probably due to the small byte of the dithiophosphinato group in comparison with the highly flexible tetraorganoimidodiphosphinato moiety.

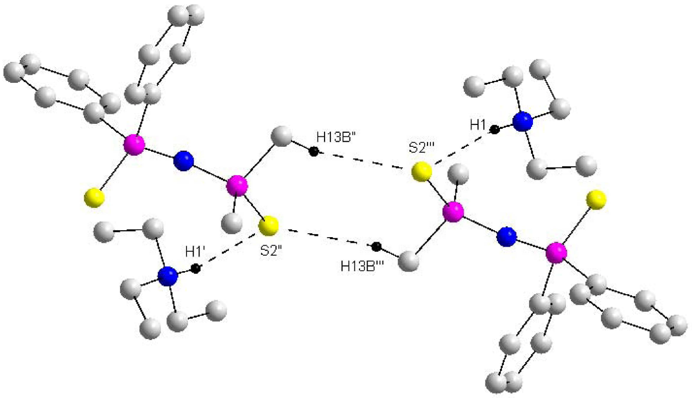

Figure 3. Dimeric association in the crystal of compound **1**.
[symmetry equivalent atoms (–*x*, 1 – *y*, 1 – *z*) are given by “prime”].

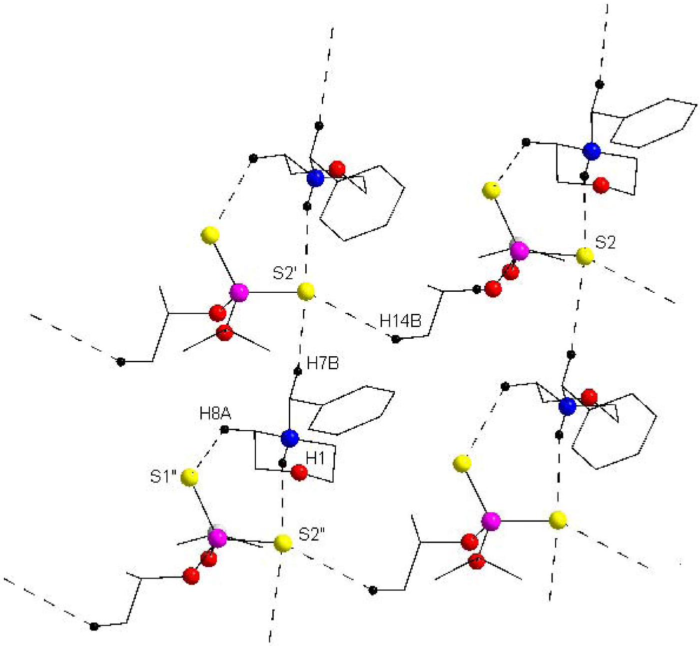

Figure 4. Polymeric association in the crystal of compound **3**.
[symmetry equivalent atoms (–0.5 + *x*, -0.5 + *y*, 0.5 + *z*) and (x, y, 1 + z) are given by “prime” and “second”, respectively].

The conformation of the S-P-N-P-S skeleton in compound **1** can be described as *syn* [S1-P1···P2-S2 torsion angle 89.2(8)°] [12], with both phosphorus-sulfur bonds oriented on the same side of the PNP plane at 1.54 and 0.85 Å, respectively.

CONCLUSIONS

New ammonium salts of organophosphorus ligands, *e.g.* $[Et_3NH]^+[(SPMe_2)(SPPh_2)N]^-$ and $[Et_3NH]^+[S_2PPh_2]^-$ were isolated as colorless, microcrystalline solids and were characterized in solution by ^1H and ^{31}P NMR. X-Ray diffraction studies on $[Et_3NH]^+[(SPMe_2)(SPPh_2)N]^-$ and the ammonium salt $[2\text{-}\{O(CH_2CH_2)_2N(H)CH_2\}C_6H_4]^+[S_2P(OPr^i)_2]^-$ revealed different association patterns in the crystals of the two compounds, *e.g.* dimeric units in the case of the tetraorganodithioimidodiphosphinato species and a polymeric layered structure in the case of the dithiophosphato derivative.

EXPERIMENTAL SECTION

Starting materials were commercially available (Fluka), or prepared following a published procedure: Ph_2PS_2H [17], $(Me_2PS)(Ph_2PS)NH$ [20]. ^1H and ^{31}P NMR spectra were recorded on a Bruker Avance 500 instrument using $CDCl_3$ solutions. The chemical shifts are reported in δ units (ppm) relative to the residual peak of the deuterated solvent (ref. $CHCl_3$: ^1H 7.26 ppm) for ^1H NMR and H_3PO_4 85% for ^{31}P NMR.

Preparation of $[Et_3NH]^+[(SPMe_2)(SPPh_2)N]^-$ (1)

A mixture of triethylamine (0.14 mL, 1 mmol) and $[(Me_2PS)(Ph_2PS)N]H$ (0.325 g, 0.1 mmol) in benzene (30 mL) was stirred for 12 h at room temperature. Then the solvent was removed in vacuum to give the title compound as a colorless powder. Yield: 0.4 g (94%), m.p. 172°C. ^1H NMR: δ 1.31t [9H, CH_2CH_3, $^3J_{HH}$ 7.4 Hz], 1,64d (6H, PCH_3, $^2J_{PH}$ 13,2 Hz), 3.29q (6H, CH_2CH_3, $^3J_{HH}$ 7.4 Hz), 7.24m (6H P-C_6H_5-*meta+para*), 8.02ddd (4H, P-C_6H_5-*ortho*, $^3J_{HH}$ 7.6, $^4J_{HH}$ 1.8, $^3J_{PH}$ 12.8 Hz), 10.02s (br., 1H, NH). ^{31}P NMR (121.4 MHz): 37.1s, br., Ph_2PS, 45.3s, br., Me_2PS.

$[Et_3NH]^+[S_2PPh_2]^-$ (**2**) was similarly obtained from triethylamine (0.14 mL, 1 mmol) and Ph_2PS_2H (0.375 g, 0.1 mmol). Yield: 0.44 g (92%), m.p. 81°C. ^1H NMR: δ 1.32t [9H, CH_2CH_3, $^3J_{HH}$ 7.3 Hz], 3.26q (6H, CH_2CH_3, $^3J_{HH}$ 7.3 Hz), 7.30 – 7.36m (6H P-C_6H_5-*meta+para*), 8.15ddd (4H, P-C_6H_5-*ortho*, $^3J_{HH}$ 7.9, $^4J_{HH}$ 1.6, $^3J_{PH}$ 13.9 Hz), 10.22s (br., 1H, NH). ^{31}P NMR (121.4 MHz): 61.4s.

X-ray Crystallographic Study

Block crystals of $[Et_3NH]^+[(SPMe_2)(SPPh_2)N]^-$ (**1**) and $[2\text{-}\{O(CH_2CH_2)_2N(H)CH_2\}C_6H_4]^+[S_2P(OPr^i)_2]^-$ (**3**) were attached with Paratone N oil on cryoloops. The data were collected at room temperature on a Bruker SMART APEX CCD diffractometer using graphite-monochromated Mo-Kα radiation (λ = 0.71073 Å). The details of the crystal structure determination and refinement are given in Table 2.

The structures were refined with anisotropic thermal parameters. The hydrogen atoms were refined with a riding model and a mutual isotropic thermal parameter. The hydrogen atoms bonded to the nitrogen in compounds **1** and **3** were found in a difference map and refined with a restrained N–H distance of 0.87(2) Å for **1** and 0.87(3) Å for **3**, respectively. For structure solving and refinement the software package SHELX-97 was used [21]. The drawings were created with the Diamond program [22].

Table 2. Crystallographic data for compounds **1** and **2**.

	1	**3**
chemical formula	$C_{20}H_{32}N_2P_2S_2$	$C_{17}H_{30}NO_3PS_2$
crystal habit	colorless block	colorless block
crystal size [mm]	0.25 x 0.22 x 0.2	0.38 x 0.33 x 0.18
crystal system	triclinic	monoclinic
space group	*P-1*	*P2(1)/n*
a [Å]	9.7823(11)	10.048(10)
b [Å]	10.7488(12)	17.246(17)
c [Å]	11.3737(13)	12.500(12)
α [deg]	91.951(2)	90
β [deg]	95.651(2)	92.469(17)
γ [deg]	93.647(2)	90
U [$Å^3$]	1186.7(2)	2164(4)
Z	2	4
D_c [g cm^{-3}]	1.194	1.202
M	426.54	391.53
F(000)	456	840
θ range [deg]	1.90 to 25.00	2.35 to 25.00
μ(Mo Kα) [mm^{-1}]	0.366	0.334
no. of reflections collected	11545	20438
no. of independent reflections	4177 (R_{int} = 0.0470)	3816 (R_{int} = 0.0491)
R_1 [$I > 2\sigma(I)$]	0.0616,	0.0611
wR_2	0.1270	0.1416
no. of parameters	244	225
no. of restraints	1	0
GOF on F^2	1.093	1.167
largest difference electron density [e $Å^{-3}$]	0.418 and -0.262	0.413 and -0.296

ACKNOWLEDGEMENTS

This work was supported by the National University Research Council of Romania (CNCSIS, Research Project No. ID-2404/2008). A. M. P. thanks the European Social Fund for a Scholarship (Education and Training Program 2008-2013, POSDRU/6/1.5/S/3).

SUPPLEMENTARY MATERIAL

CCDC 753670 and 753671 contain the supplementary crystallographic data for compounds **1** and **3**. These data can be obtained free of charge from The Cambridge Crystallographic Data Centre via www.ccdc.cam.ac.uk/data_request/cif.

REFERENCES

1. I. Haiduc, *Rev. Inorg. Chem*., **1981**, *3*, 353.
2. R.C. Mehrotra, G. Srivastava, B.P.S. Chauhan, *Coord. Chem. Rev*., **1984**, *55*, 207.
3. E.R.T. Tiekink, *Main Group Metal Chem*., **1992**, *15*, 161.
4. V.K. Jain, *Coord. Chem. Rev*., **1994**, *135/136*, 809.
5. I. Haiduc, *Phosphorus, Sulfur Silicon*, **1994**, *93–94*, 345.
6. I. Haiduc, D.B. Sowerby, S.-F. Lu,, *Polyhedron*, **1995**, *14*, 3389.
7. I. Haiduc, D.B. Sowerby, *Polyhedron*, **1996**, *15*, 2469.
8. C. Silvestru, I. Haiduc, *Coord. Chem. Rev*., **1996**, *147*, 117.
9. I. Haiduc, *Coord. Chem. Rev*., **1997**, *158*, 325.
10. T.Q. Ly, J.D. Woollins,, *Coord. Chem. Rev*., **1998**, *176*, 451.
11. R. Cea-Olivares, V. Garcia-Montalvo, J. Novosad, J.D. Woollins, R.A. Toscano, G. Espinosa-Perez, *Chem. Ber*., **1996**, *129*, 919.
13. C. Silvestru, J. E. Drake, *Coord. Chem. Rev*., **2001**, *223*, 117.
14. P. Wasserscheid, W. Keim, Angew. Chem., *Int. Ed*., **2000**, *39*, 3772.
15. H. J. Breunig, T. Koehne, O. Moldovan, A. M. Preda, A. Silvestru, C. Silvestru, 16. R. A. Varga, L. F. Piedra-Garza, U. Kortz, *J. Organomet. Chem*., **2010**, *695*, 1307.
17. R. Tacke, C. Burschka, I. Richter, B. Wagner, R. Willeke, *J. Am. Chem. Soc*., **2000**, *122*, 8480.
18. E. J. Brown, A. C. Whitwood, P. H. Walton, A.-K. Duhme-Klair, *J. Chem. Soc. Dalton Trans*., **2004**, 2458.
19. B. Krebs and G. Henkel, *Z. Anorg. Allg. Chem.* 1981, 475, 143.
20. I. Ghesner, A. Soran, C. Silvestru, J.E. Drake, *Polyhedron*, **2003**, *22*, 3395.
21. J. Emsley, *Die Elemente*, Walter de Gruyter: Berlin, **1994**.
22. R. Roesler, J.E. Drake, C. Silvestru, J. Yang, I. Haiduc, G. Espinosa-Perez, *J. Chem. Soc. Dalton Trans*., **1998**, 73.
23. G. M. Sheldrick, *Acta Crystallogr., Sect. A,* **2008**, *64*, 112.
24*. DIAMOND – Visual Crystal Structure Information System*, Crystal Impact, Postfach 1251, 53002 Bonn, Germany, **2001**.

STUDIA UNIVERSITATIS BABEŞ-BOLYAI, CHEMIA, XLV, 2, TOM II, 2010

Dedicated to the memory of Prof. dr. Ioan Silaghi-Dumitrescu marking 60 years from his birth

ARTIFICIAL NEURAL NETWORKS USED FOR INVESTIGATION OF FATTY ACID CONTENT OF ROMANIAN SUNFLOWER OILSEEDS GENOTYPES

DORINA BRĂTFĂLEAN, VASILE MIRCEA CRISTEA*, PAUL ŞERBAN AGACHI

ABSTRACT. The objective of this study was to investigate the efficiency of Artificial Neural Networks (ANNs) in classifying and predicting the fatty acid content from Romanian sunflower oilseeds genotypes, as solutions of computational engineering problems. The two-layer probabilistic ANN, using a radial basis layer and a competitive layer, has been used for classification. There were two criteria of classification, the degree of polyunsaturation and the linoleic/oleic acid ratio, which allowed the defining of two categories. The first ANN has been designed for classifying the first category into three groups defined by the polyunsaturated fatty acid content: group 1 of less than 40% polyunsaturated fatty acid, group 2 of 40%-50% polyunsaturated fatty acid, and group 3 of higher than 50% polyunsaturated fatty acid. The classification was based on the following acids in the samples: C14:00, C15:00, C16:00, C16:01, C17:00, C18:00, C18:01, C18:02, C18:03, C20:00, C20:01 and C22:00. The second designed ANN has been used for classifying the category of linoleic/oleic acid ratio into three groups: group 1 of linoleic/oleic acid ratio higher than 2, group 2 of linoleic/oleic acid ratio between 1 and 2 and group 3 of linoleic/oleic acid ratio less than 1. The results of both classifications revealed a good accuracy of the trained ANNs for classifying the sunflower oilseeds. The numerical tests demonstrated the computational advantages of the prediction methodology.

Keywords: *ANN, fatty acids, oilseeds, polyunsaturated fatty acid, sunflower genotypes.*

INTRODUCTION

Fats are a subclass of lipids, but the term “fat” is often used instead of the term denoting “lipid”. For nutrition labeling purposes, fat has been defined as triglycerides (substances extracted with organic solvent) or total lipids. Triglycerides are the building blocks of fats and oils, such as sunflower oil, which is extracted from sunflower seeds and is the most common vegetable fat.

---

[*] *Babeş-Bolyai University, Faculty of Chemistry and Chemical Engineering, 11. Arany Janos, RO-400028 Cluj-Napoca, Romania, mcristea@chem.ubbcluj.ro*

From the economical point of view sunflower oil is a very good source for valorisation due to the variety of fatty esters contained. Fatty acids are differentiated by their molecular composition [1]. One differentiating characteristic is the degree of saturation, according to which they are: saturated, monounsaturated or polyunsaturated. Other differentiating characteristics are the chain length and the number of carbon atoms in the fatty acid molecule. Fatty acids represent 95 of every 100 grams of fat or oil. Fatty acid variability and profile in the sunflower oil depend on the sunflower genotype. They found numerous applications as food (human and animal feeds), and non-food products (pharmaceutical field, cosmetics, bio-detergents, biodiesel, etc).

Due to their many applications, it is important to be able to assess the quality of different oilseeds. This may be performed on the basis of the fatty acids content. This is an important reason for searching and developing new methodologies that allow more flexible and better-controlled means for the classification of fatty acid content of fats.

The quality of food or other products is monitored based on their composition through laboratory analyses, while computational screening may be used for prediction and simulation, thus offering economic benefits [2]. Methodologies based on Artificial Neural Networks (ANNs) have become an efficient tool in many studies involving property classification and prediction.

Modelling and data mining methodologies based on ANNs are able to represent information on complex systems [3]. ANNs are adaptive systems that change their structure based on external or internal information that flows through the network. Neural networks are non-linear statistical data modelling tools [4]. They can be used to model complex relationships between inputs and outputs or to find patterns in data.

The aim of the present work has been the comparative investigation of fatty acid content for different Romanian sunflower genotypes, based on ANNs classification aptitude. Several genotypes of Romanian sunflower oilseeds have been considered in the investigation of the fatty acid content, using laboratory analytical techniques. The fatty acid methyl esters (FAMEs) were analyzed by gas-chromatography, and the results were used to test the ability of the specially trained ANNs for predicting the classis of genotypes, according to the type of their fatty acid contained.

Samples

The Romanian National Agricultural Research and Development Institute Fundulea provided the sunflower seeds used in this study. Before they were analyzed, the sunflower seeds were stored at a temperature of 5°C and low humidity [5]. First, the dry weight determination of each sample was performed in the laboratory. Around 10g of sunflower seeds at harvesting maturity were sampled for each sunflower genotype [6]. Ten inbred lines and five Romanian hybrids have been considered in this study. The genotypes are presented in Table 1.

Table1. Investigated inbred lines and Romanian sunflower hybrids

Genotype	LC-L1	LC-L2	LC-L3	LC-L4	LC-L5	LC-L6	LC-L7
Type of variety	Semi-precocious	Semi-precocious	Preco-cious	Tardif	Semi-precocious	Semi-Tardif	Semi-Tardif

enotype	LC-L8	LC-L9	LC-L10	R-H1	R-H2	R-H3	R-H4	R-H5
Type of variety	Semi-precocious	Precocious	Tardif	Alex	Favorit	Rapid	Top75	Turbo

The samples were collected for two types of laboratory analysis, qualitative and quantitative, and one computational method. The first method (quantitative) was the detection of the percent of fat from oilseeds by Accelerated Solvent Extractor (ASE) method, and the second method (qualitative) was gas the chromatograph analysis. The computational method was based on the ANNs classification capacity, using the Matlab software environment and its accompanying Neural Network Toolbox.

Procedure of total lipids extraction

Extraction of the total lipids from the sunflower seeds has been the initial step of this study. The ASE method was used according to Official Method of Analysis, 1999 [6]. This method has a similar operating principle as the Soxhlet Extraction method used for lipids extraction. ASE method involves the gravimetric determination of the oil using the light petroleum extract from sunflower seeds. The equipment consists in a metallic cell having six commune broiler based extractors. The petroleum extract is called “oil content”. Following the weighting step, the seed material was placed in a cellulose extraction cartridge and then introduced into the extractor. The parameters of the extraction process and the number of cycles were programmed by means of an electronic interface [7]. The advantage of the ASE method consists in the relatively high number of samples which can be investigated and the reduced time of extraction (6 samples and 30 min of extraction for one sample). The fat content has been computed by the direct expression:

$$Fat\ content[\%] = \frac{Mass\ of\ the\ extract}{Mass\ of\ the\ sample} \cdot 100 \tag{1}$$

The ASE method was used to determine quantitatively the fat from the sunflower oilseed.

Fatty acid methyl esters (FAMEs) preparation

FAMEs were produced in order to determine the content of total fatty acids in the extracted oils [6]. The first step for FAMEs preparation consists in the saponification procedure [2]. Two samples of 0.1g lipid extracted from each sunflower genotype were treated with 1 mL NaOH solution (1M) in methanol by refluxing for 1h at 100°C. After free fatty acid removal, the samples were esterified in the presence of H_2SO_4 as catalyst. The FAMEs were extracted with petroleum ether from the salt saturated mixture. After FAMEs drying, the Na_2SO_4 anhydride was added and the supernatant was poured in the specific cell.

Gas chromatography system

The fatty acids have been analyzed by gas chromatography (GC) according to the published methods [6]. The esters were separated by gas chromatograph (Carlo Erba model equipped with FID type FRATOVAP 300, and split/splitless injector and associated column (L=2m, d=3mm), containing 10% diethylene glycol succinat on Chromosorb W, AW). The temperature of the injection port was maintained at constant value of 190°C and the detector temperature at 225°C. The oven temperature was programmed to increase from 80°C to 200°C at a rate of 5°C /min using Argon as carrier gas, fed with a reference flow rate of 24mL/min. The peaks were identified based on their retention times using standard fatty acids methyl esters. All samples were run in duplicate.

Identification of FAMEs

The total amount of Miristic acid-C14:00, Pentadecanoic acid-C15:00, Palmitic acid-C16:00, Palmtoleic acid-C16:01, Heptadecanoic-C17:00, Stearic acid-C18:00, Oleic acid-C18:01, Linoleic acid-C18:02, Linolenic C18:03, Arachidic acid-C20.00, Behenic acid-C22:00, Gadoleic acid-C20:01 was computed from the GC peak area of each FAME. No correction factors or internal standards were used. The average values for the two replicates were accepted as the concentrations of the sunflower oil samples. The precision of the results is given in the description of ISO 5508/9 standard method.

ANN Classification

Probabilistic ANNs have been used for classification [8]. The designed ANN is a two-layer probabilistic neural network consisting in a radial basis layer and a competitive layer. The radial basis layer computes distances from the input vector to the training input vectors and produces a vector whose elements measure how close the particular input is to a training input. The competitive layer cumulates these contributions for each class of inputs to produce, as its net output, a vector of probabilities. The layer uses a compete transfer function for selecting the maximum of these probabilities and generates a vector having as elements a 1 (one) for the particular class and 0 (zero) for the other classes. The probabilistic ANN is guaranteed to converge to a Bayesian classifier. Artificial Neural Network Toolbox of Matlab software was used to build the present application [8, 9]. The input and hidden layer consist of fifteen neurons and the output layer includes three neurons. Output values of the network are rounded to the nearest integer to obtain the classes.

RESULTS AND DISCUSSION

Degree of fat extraction

First, the set of 15 sunflower seeds genotypes considered in the study (ten inbred lines and five hybrids) have been submitted to the investigations of fats and fatty acid content. The laboratory investigation determined the quantity of fat extracted by ASE method, as presented in Fig. 1.

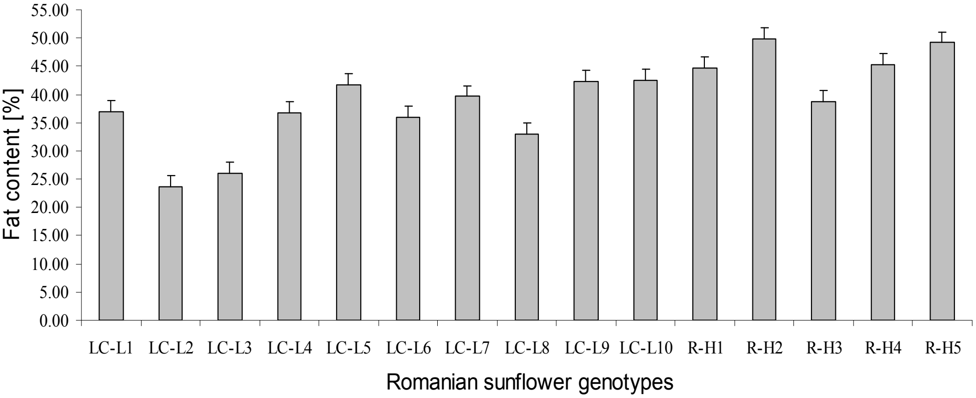

Figure 1. Fat content in the sunflower seeds of the investigated Romanian genotypes

For the case of the inbred lines the fat content ranges from 24.01% for the LC-L2 line to 42.49% for the LC-L10 line, while for the hybrids the fat content varies between 38.75% for the R-H3 line and 49.15% for the R-H2 line. Results confirm the large variability of fat content characterizing the Romanian sunflower seeds genotypes. The experimental results are show in Supporting Information.

Second, the profile of fatty acid analyzed thought GC-FID methods show that twelve types of fatty acids were determined [10]. The degree of saturation for the investigated inbred lines and Romanian sunflower hybrids are presented in Table 2.

Table 2. The degree of saturation results for the investigated inbred lines and Romanian sunflower hybrids.

Inbred lines and hybrids	Total Saturated fatty acids [%]	Total Monounsaturated fatty acids [%]	Total Polyunsaturated fatty acids [%]	Total Unsaturated fatty acids [%]	Saturated/ unsaturated acid ratio	Linoleic /oleic acid ratio
LC-L1	11.441	31.719	56.840	88.559	0.129	1.787
LC-L2	13.291	48.724	37.985	86.709	0.153	0.772
LC-L3	10.652	42.144	47.204	89.348	0.119	1.116
LC-L4	12.765	40.528	46.707	87.235	0.146	1.149
LC-L5	10.704	39.015	50.281	89.296	0.120	1.291
LC-L6	10.007	41.716	48.277	89.993	0.111	1.153
LC-L7	13.994	39.865	46.141	86.006	0.163	1.153
LC-L8	12.432	47.099	40.469	87.568	0.142	0.852
LC-L9	13.957	43.345	42.698	86.043	0.162	0.973
LC-L10	10.545	35.731	53.724	89.455	0.118	1.502
R-H1	12.081	29.138	58.781	87.919	0.137	2.014
R-H2	13.275	25.369	61.356	86.725	0.153	2.429
R-H3	14.060	27.330	58.610	85.940	0.164	2.149
R-H4	13.470	26.010	60.520	86.530	0.156	2.344
R-H5	13.836	26.548	59.616	86.164	0.161	2.256

ANN screening data

The classification of the samples according to the fatty acid content into three groups has been performed using ANNs. There were two criteria of classification, the degree of polyunsaturation and the linoleic/oleic acid ratio, which allowed the defining of two *categories*. As a result, the two considered categories are: the category of polyunsaturated fatty acids and the category of linoleic/oleic acid ratio. For each of the two considered categories, ANNs were used for classifying the samples into three *groups*.

The first classification, of polyunsaturated fatty acid category, was performed by the ANNs for dividing the samples into three groups according to the percentage of polyunsaturated fatty acid content. The ANN was trained using a set of input–output literature data [11-16]. Inputs of the ANN have been considered the contents of: Miristic acid-C14:00, Pentadecanoic acid-C15:00, Palmitic acid-C16:00, Palmitoleic acid-C16:01, Heptadecanoic-C17:00, Stearic acid-C18:00, Oleic acid-C18:01, Linoleic acid-C18:02, Linolenic C18:03, Arachidic acid-C20.00, Behenic acid-C22:00, Gadoleic acid-C20:01. The outputs of the ANN are: *group 1* of samples having the polyunsaturated fatty acid content less than 40%, *group 2* of samples having the polyunsaturated fatty acid content between 40%-50% and *group 3* of samples with the polyunsaturated fatty acid content higher than 50%. The ANN testing step followed the training procedure. A randomly selected testing set of 15 experimental samples obtained from the Romanian inbred line genotypes (not yet seen by the ANN) was given to the previously trained ANN in order to test its ability to properly perform the classification. The investigated sunflower genotypes have the polyunsaturated fatty acids content higher than 40%, except one inbred line having less than 40% polyunsaturated fatty acids (LC-L2 with 37.985%). The classification results for this testing set of samples are presented in Fig. 2, where the ANN predicted data are compared to the experimental results.

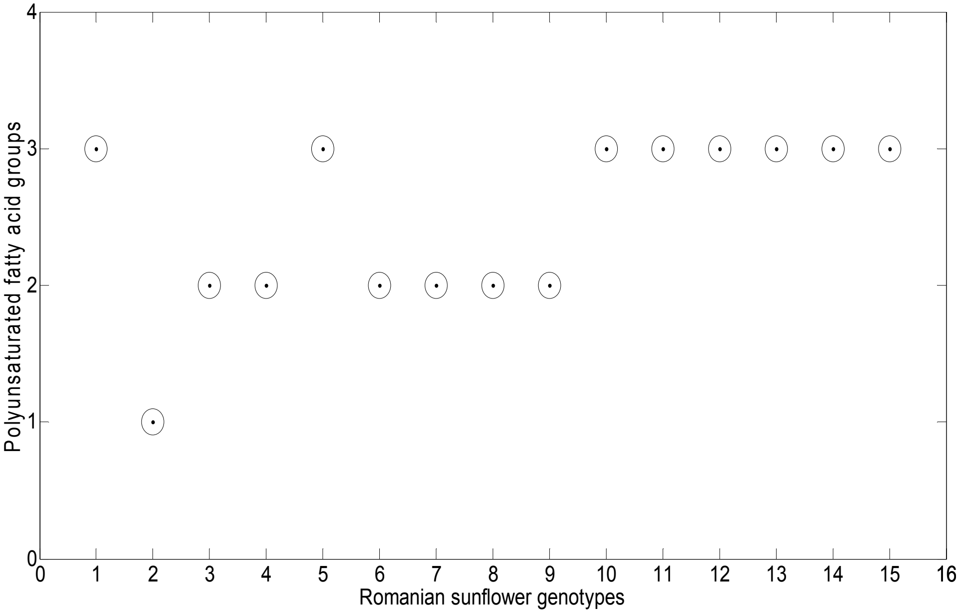

Figure 2. Classification results of polyunsaturated fatty acid groups, for the testing set of data; Group 1 of polyunsaturated fatty acid ≤40%, Group 2 of polyunsaturated fatty acid 40% - 50%, Group 3 of polyunsaturated fatty acid ≥ 50%; the ANN groups predictions, marked by "○", and the desired polyunsaturated fatty acid groups (experimental results), marked by "•".

The three groups predicted by ANN simulation for the classification of the polyunsaturated fatty acid reveal a very good fit between the classification groups performed by the ANN and the groups obtained by the ASE method.

The second ANN classification of the experimental data, according to the linolenic/oleic acid ratio criterion, was also based on a previous step of ANN training. Again, literature data was used to train the ANN [11-16]. Values of the linoleic/oleic acid ratio reveal which fatty acid is predominant in the oilseed, i.e. either the monounsaturated fatty acid (oleic acid) or the polyunsaturated fatty acid (linoleic acid). In order to test the ability of the trained ANN for classifying the data, the testing was performed on the set of 15 experimental samples obtained from the Romanian inbred lines genotypes. Classification results are presented in Fig. 3.

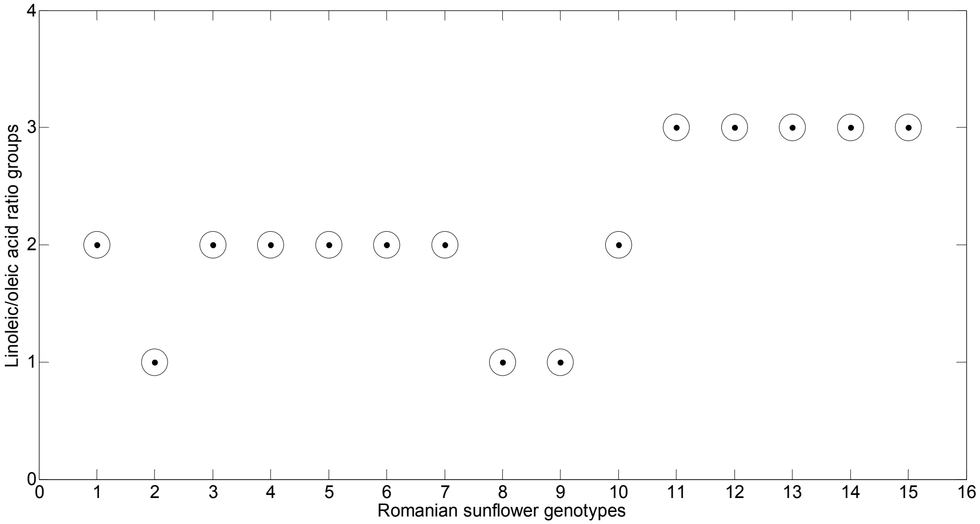

Figure 3. Classification results of linoleic/oleic acid ratio groups, for the testing set of data; Group 1 of linoleic/oleic acid ratio ≥ 2, Group 2 of linoleic/oleic acid ratio between 1-2, Group 3 of linoleic/oleic acid ratio ≤ 1;the ANN groups predictions, marked by "○", and the desired linoleic/oliec acid ratio groups (experimental results), marked by "•".

Again, the classification reveals a perfect fit between the groups obtained by the experimental investigations and the results predicted by the ANN.

The obtained results prove the capacity of the trained ANNs for making exact sunflower oil seed group classifications in the cases of samples of unknown group membership.

Prediction of determined classes

Furthermore, by merging the two categories presented in Fig. 2 and Fig. 3 the combined results presented in Fig. 4 have been obtained.

Results presented in Fig. 4 reveal the prediction of three *classes* of the Romanian sunflower seeds genotypes. The first class consists of ten investigated sunflower oilseed genotypes with a high content of polyunsaturated fatty acids and a linoleic/oleic acid ratio less than 1. The second class consists of two sunflower inbred lines (LC-L8 and LC-L9), where the linoleic acid is dominant and the polyunsaturated fatty acid content places it into group 2 of the first classification category. The third class is composed of three sunflower lines (LC-L1, LC-L5 and LC-L10) where the oleic acid is dominant and the polyunsaturated fatty acid content is higher than 50%, corresponding to group 3 of the first classification category. It may be also noticed that all five considered hybrid lines are oleic hybrids, as they predominantly contain the oleic acid.

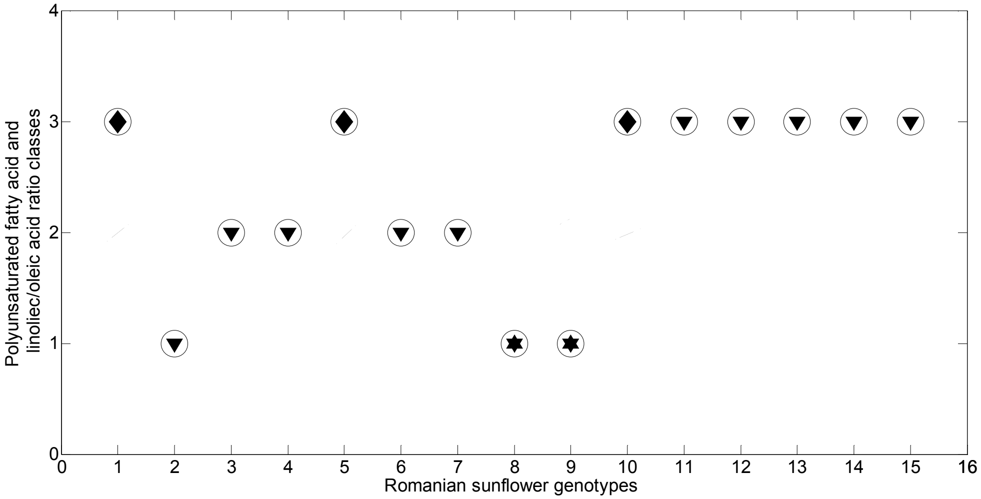

Figure 4. Classes of investigated Romanian sunflower genotypes; the ANN predicted classes are marked by “○” and the classes obtained from experimental data are: class 1 marked by “▼”, class 2 marked by “✸” and class 3 marked by “ ◆ ”.

It may be concluded that the investigated lines may be used in crossed hybridization in order to obtain new hybrids with high content of either oleic or linoleic acid. The investigated hybrid lines may be appreciated for their nutritional potential, due to their high polyunsaturated fatty acid content.

CONCLUSIONS

Several genotypes of Romanian sunflower oilseeds have been considered in the investigation of the fatty acid content, using laboratory analytical techniques. Methodologies based on the two layer probabilistic ANNs, consisting in a radial basis layer and a competitive layer, have been used for classification of sunflower oilseed genotypes according to fatty acid content. The ANNs were trained with experimental data from the literature. Two classifications (categories) were obtained, function of (1) the degree of polyunsaturation and (2) the linoleic/oleic acid ratio. Three groups have been considered for each investigated category. Three classes have been also predicted by the investigation of the Romanian sunflower oilseeds genotypes.

The classification aptitude of the designed ANNs proved to be very good, as the group classification has been performed with no error, for both categories. Moreover, the advantages of the classification based on ANNs are significant when taking into consideration the limited number of parameters required as ANN inputs and the number of samples needed for the training set. Further improvement may be obtained by extending the number of input parameters and by carefully filtering the training set of data.

Starting from the methodology of designing ANNs, aimed to predict and classify the sunflower seeds, further classification procedures may be developed for similar applications. ANNs incentives consist in the help they bring for characterizing the sunflower oils with economical implication as oil composition assessment is an essential feature to provide its potential use in different fields, such as: nutrition, pharmacy, health care or other nonfood applications.

ACKNOWLEDGMENTS

The authors would like to acknowledge the support for providing the sunflower seeds genotypes to the Agricultural Research and Development Institute Fundulea, and to the Romania-Slovenia bilateral cooperation project.

REFERENCES

1. L. D. Villamide, *British Poultry Science*, **2000**, *41*, 182.
2. D. Brodnjak-Voncina, Z. C. Kodbab, M. Novic, *Chemometrics and Intelligent Laboratory Systems*, **2005**, *75*, 31.
3. Y. Tsompanakis, N. D. Lagaros, G. E.Stavroulakis, *Advances in Engineering Software,* **2008**, *39*, 612.
4. L. Fengjun, X. Zongben, *Chaos, Solitons and Fractals*, **2008**, *36*, 572.
5. D. Bratfalean, V. M. Cristea, P. S. Agachi, D. F. Irimie, *Revue Roumanie de Chimie*, **2008**, *53*, 881.
6. AOAC, "Official Method of Analysis" Association of Official Analytical Cereal Chemists, Washington, DC, USA, **1999**.
7. B. Matthaüs, L. Brühl, *Journal of the American Oil Chemist's Society*, **2001**, *78*, 95.
8. D. Bratfalean, M. V. Cristea, P. S. Agachi, D. F. Irimie, A. Sarrafi, M. Petitprez, Proceedings of the *17th European Symposium on Computer Aided Process Engineering – ESCAPE17*, May, Bucharest, **2007**, 1.
9. M. V. Cristea, S. Varvara, L. Muresan, I. C. Popescu, *Indian Journal of Chemistry*, **2003**, *42A*, 764.
10. D. Bratfalean, D. F. Irimie, P. S. Agachi, *Studia Universitatis Babes-Bolyai, Chemia*, **2007**, *LII 2*, 47.
11. B. Perez-Vich, L. Velasco, J. M. Fernandez-Martinez, *Journal of the American Oil Chemist's Society*, **1998**, *75*, 547.
12. B. Perez-Vich, R. Garces, J. M. Fernandez-Martinez, *Heli,* **2000**, *23*, 77.
13. A. V. Vrânceanu, "*Floarea-soarelui Hibridă*", Ceres Press, Bucharest, **2000**, p.15-25, p. 650-720.
14. G. J. Seiler, "Potential Source of Reduced Palmitic and Stearic Fatty Acids in Sunflower Oil From a Population of Wild Helianthus Annuus*", ASHS Press, Alexandria* VA, **2002**, p.150-154.
15. N. Izquierdo, L. A. F. Andrade, V. Pereyra, *Field Crops Research*, **2002**, *77*, 115.
16. K. Warner, B. Vick, L.K. Leingrtner, R. Isaak, K. Doroff, Proceedings from the 18th session of the CCFO – Report of the eighteenth session of the codex committee on fats and oil, U.K., **2003**.

STUDIA UNIVERSITATIS BABEŞ-BOLYAI, CHEMIA, XLV, 2, TOM II, 2010

Dedicated to the memory of Prof. dr. Ioan Silaghi-Dumitrescu marking 60 years from his birth

SPECTROSCOPIC AND STRUCTURAL CHARACTERISATION OF SiO_2-Y_2O_3 BASED MATERIALS WITH LUMINESCENT PROPERTIES

LAURA ELENA MURESAN[a,*], ELISABETH-JEANNE POPOVICI[a],
ECATERINA BICA[a], ADRIAN-IONUŢ CADIŞ[a],
MARIUS MORAR[a] AND EMIL INDREA[b]

ABSTRACT. Cerium activated yttrium silicate phosphors show blue luminescence under UV excitation. Phosphor utilisation depends on powder characteristics and luminescence properties that are regulated during the synthesis stage. In this paper yttrium silicate based phosphors were prepared by solid state reaction using different molar ratio between SiO_2 and Y_2O_3. The effect of chemical composition and structure on luminescent properties of phosphors were investigated and discussed.

Keywords: *yttrium silicate, luminescence, solid state reaction*

INTRODUCTION

Yttrium silicate phosphors (Y_2SiO_5) doped with Eu^{3+}, Ce^{3+}, Pr^{3+}, Tb^{3+} or Yb^{3+} are well known luminescent materials due to their luminescent characteristics [1]. Under UV excitation Y_2SiO_5:Ce phosphor exhibits blue-white emission with the peak maximum situated at 414 nm.

Y_2SiO_5 phosphor is usually used as luminescent material in fluorescent lamps, field emission display (FED) and projection television (PTV) because of its brightness, acceptable atmospheric stability and quantum efficiency [2,3].

Many methods such as solid state reaction, sol gel techniques, spray pyrolysis and combustion synthesis have been used to prepare silicate phosphors [4-6]. The analysis of the Y_2O_3-SiO_2 phase diagram shows the presence of various compounds such as: Y_2O_3, SiO_2, Y_2SiO_5 and $Y_2Si_2O_7$, depending on the synthesis temperature [7,8].

In correspondence to the 1:1 molar ratio, we can find two type of monoclinic Y_2SiO_5 ($Y_2O_3.SiO_2$), known as X1-Y_2SiO_5 phase (crystallographic group P21/c) and X2- Y_2SiO_5 phase (crystallographic group B2/b) [9,10].The

---

[a] *Raluca Ripan Institute for Research in Chemistry, Babes Bolyai University, 400294, Cluj-Napoca, Romania, * laura_muresan2003@yahoo.com*

[b] *National Institute for R &D of Isotopic and Molecular Technologies, 400295 Cluj-Napoca, Romania*

second compound in the system is $Y_2Si_2O_7$ ($Y_2O_3.2SiO_2$), which shows an even more complex polymorphism, since six $Y_2Si_2O_7$ different structures are reported for it [11].

In practical applications the chemical reaction between rare earth oxides and silicon dioxide at elevated temperatures should be considered as a possible cause of drastic modification of both structure and luminescent properties of yttrium silicate-based powders.

In this paper yttrium silicate phosphor samples were prepared by solid state reaction using different molar ratios between SiO_2 and Y_2O_3. The effect of chemical composition and structure on optical properties of Ce^{3+} activated yttrium based silicates were investigated and discussed. Samples were characterised by infrared absorption spectroscopy (FT-IR), X-ray diffraction (XRD), and photoluminescence spectroscopy, i.e. emission (PL) and excitation (PLE) spectra.

RESULTS AND DISCUSSION

The Y_2O_3-SiO_2 phase diagram is currently explored with a variety of synthesis techniques especially in the 1:1 and 1:2 molar ratio domains because of the optical properties that can be induced by dispersion of rare-earth elements such as Eu^{3+}, Tb^{3+} and Ce^{3+} into the matrix. According to the diagram phase [8] several compounds can be detected depending on the Y_2O_3–SiO_2 molar ratio.

In order to study the influence of the powders composition on the structure and luminescent properties, yttrium silicate based materials were prepared by solid state reaction route at 1400^0C using different SiO_2:Y_2O_3 molar ratios ($MR_{Si:Y}$) namely: 1:4 (sample code YSO25); 1:1 (sample code YSO26); 1:0.5 (sample code YSO27) and 1:0.25 (sample code YSO28). The photoluminescence of the samples YSO29, YSO30, YSO31 and YSO32 was induced by adding 3% mol Ce /(Y+Ce) in the mixture of silicon dioxide and yttrium oxide.

The crystalline structure and structural homogeneity of the powders were put in evidence by XRD measurements (Figure 1).

The XRD patterns indicate that all the powders contain mainly crystalline phases. Also, the XRD patterns confirm the structural changes that occur due to the addition of various amounts of SiO_2 in the synthesis mixture. Different compounds such as: X1-Y_2SiO_5 (low temperature phase); X2-Y_2SiO_5 (high temperature phase) and monoclinic $Y_2Si_2O_7$ together with unreacted Y_2O_3 and SiO_2 can be identified. It can be also observed that the increase of SiO_2 amount in the synthesis mixture determines changes in both, the composition and structure.

Based on the XRD patterns, the unit cell parameters and the quantitative phase composition were determined through Rietveld refinement using the PowderCell software. The amount (volume percentage) of the various phases in the silicate based powders was calculated [12].

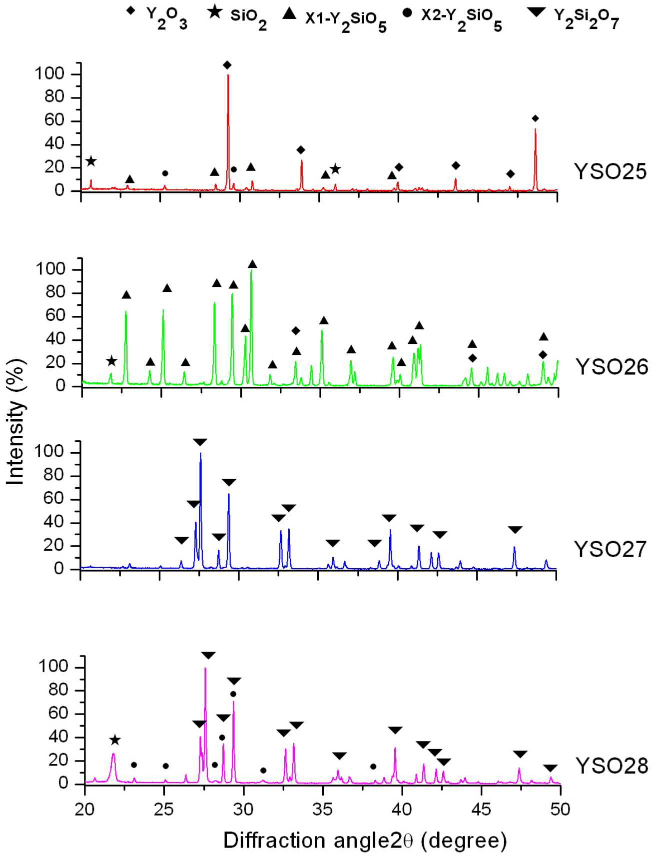

Figure 1. The X–ray diffraction patterns (λ_{Cu}=1.540598Å) of samples prepared with different $MR_{Si:Y}$

Composition of the starting synthesis mixtures together with some microstructural parameters are presented in Table 1.

When yttrium oxide is used in excess (the case of $MR_{Si:Y}$=1:4, sample YSO25), the synthesis mixture contains mainly un-reacted crystalline cubic yttrium oxide phase in proportion of 89.4 vol.% together with 2 vol.% of unreacted tetragonal silicon dioxide and 8.6 vol.% X1, X2 yttrium silicate. When stoichiometric amounts of yttrium oxide and silica oxide were used in sample YSO26, the phase X2-Y_2SiO_5 becomes the dominant (81.7 vol.%). Excess of silica dioxide ($MR_{Si:Y}$ = 1:0.5) in the synthesis mixture leads to the formation of one phase powder that consists only in monoclinic yttrium disilicate- $Y_2Si_2O_7$.

The results are in agreement with the literature data namely: Y_2O_3 -cubic phase (PDF 43-1036); SiO_2 tetragonal phase (PDF 39-1425); X1-Y_2SiO_5 monoclinic phase, (PDF 41-0004); X2-Y_2SiO_5 monoclinic phase (PDF 21-1458) and $Y_2Si_2O_7$ monoclinic phase (PDF 38-0440).

Table 1. Microstructural parameters for SiO_2 - Y_2O_3 based phosphors

Sample	$MR_{Si:Y}$	Microstructural parameters					
		Phase	*a[Å]*	*b[Å]*	*c[Å]*	*Beta*	V[$Å^3$]
YSO25	1:4	Y_2O_3-cubic(89.4%)	10.616	10.616	10.616	90.0	1189.0
		X1-Y_2SiO_5 (8.4%)	8.400	6.841	6.383	103.0	357.5
		X2-Y_2SiO_5 (0.2%)	10.317	6.623	12.583	103.7	835.1
		SiO_2tetragonal (2 %)	4.973	4.973	6.923	90.0	171.2
YSO26	1:1	Y_2O_3 -cubic (8.3%)	10.507	10.507	10.507	90.0	1159.9
		X2-Y_2SiO_5 (81.7 %)	10.420	6.726	12.499	102.6	854.9
		SiO_2tetragonal (10.0%)	4.973	4.973	6.923	90.0	171.2
YSO27	1:0.5	$Y_2Si_2O_7$monoclinic 100%	6.871	8.968	4.718	101.7	284.7
YSO28	1:0.25	$Y_2Si_2O_7$ (78.8%)	6.871	8.969	4.719	101.7	284.8
		X2-Y_2SiO_5 (6.2%)	10.453	6.732	12.444	103.0	854.0
		SiO_2 tetragonal (15.0%)	4.973	4.973	6.923	90.0	171.2

FT-IR spectra for yttrium silicate based samples are presented in Figure 2. Significant changes are observed as the amount of SiO_2 increases from 20 mol.% to 80 mol.%, in the synthesis mixture.

The vibrational bands in FT-IR spectra in 400-1400 cm^{-1} domain can be grouped in three main regions namely:

- 1070 -1200cm^{-1} domain for stretching vibrations of silicon atoms against oxygen atoms in Si-O-Si bonds in β-$Y_2Si_2O_7$ phase [13];
- 850 -1000cm^{-1} domain corresponds to Si-O stretching vibration involving non-bridging oxygen. The band situated at around 849 cm^{-1} is ascribed to multiple Si-O stretching in which all oxygen and silicon atoms of silicate groups participate in the vibration [13];
- 400- 600 cm^{-1} domain consist in lower vibrational bands more difficult to characterize, because single Y-O and Si-O vibrations coexist in similar spectral ranges. It can be stated that the vibrations situated in the range 600 to 500 cm^{-1} are mainly due to Y-O stretching, and those from 500 to 400 cm^{-1} are vibrations with a large component of Si-O bending [14,15].

It can be seen that as the SiO_2 amount decreases, the specific vibration for Si-O-Si bond in $Y_2Si_2O_7$ phase disappears (sample YSO27, YSO28) and bands from asymmetric stretching vibration in SiO_4^{2-} groups arise and become more structured (sample YSO25, YSO26).

Photoluminescence of Y_2SiO_5: Ce phosphor samples was evaluated on the basis of excitation (PLE) and emission (PL) spectra and compared with an internal standard where the $MR_{Si:Y}$ = 1:1. The internal standard was prepared by wet chemical synthesis route, using the SimAdd technique [16-18]. The intensity of the internal standard (YSO1.1) was considered to possess 100% photoluminescence [18].

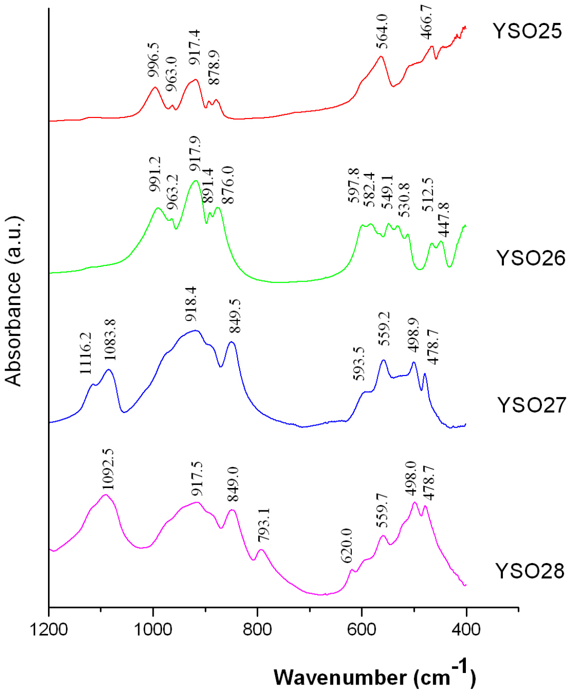

Figure 2. The FT-IR spectra of samples prepared with different $RM_{Si:Y}$

Figure 3 and Figure 4 show the PLE and PL spectra of Ce^{3+} activated Y_2SiO_5 samples synthesized by solid state reaction with different SiO_2:Y_2O_3 molar ratio.

The excitation spectra can give also information on the nature of the luminescent centres.

In this respect, the excitation spectra taken in the range of 220-400 nm present three wide bands (Figure 3). These bands (designated with I, II, III) are associated with the crystal field split of Ce^{3+} 5d electronic levels.

The excitation peaks of the internal standard (sample YSO 1.1) are situated at 265 nm, 300 nm and 356 nm, respectively.

The intensity and the position of excitation peaks of the yttrium silicate samples are variable and depend on the SiO_2:Y_2O_3 molar ratio. For samples YSO30 and YSO32, the peaks I and III present a shift from 265 nm to 246 nm and from 356 nm to 349 nm, respectively.

The excitation spectra for samples prepared with excess of SiO_2 namely YSO30 ($MR_{Si:Y}$=1:0.25) and YSO32 ($MR_{Si:Y}$=1:0.5) present a similar behaviour. Thus, the peak II with maximum situated at 301 nm for samples YSO30, YSO32 is more broad compared to the corresponding one situated at 299 nm for sample YSO29 and 300 nm for standard.

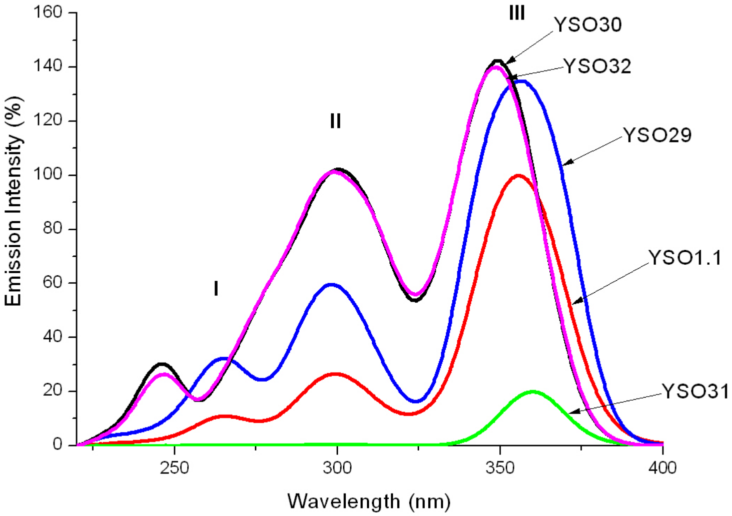

Figure 3. Excitation spectra of some YSO samples (λ_{em}=420nm)

The photoluminescent characteristics correlated with XRD and FT-IR data, lead to the conclusion that depending on the molar ratio, different luminescent centres are formed. In samples YSO30 and YSO32, the Ce^{3+} surrounding is given by the presence of the $Y_2Si_2O_7$ as host lattice, meanwhile in sample YSO 29 the luminescent centers are formed in an Y_2SiO_5 host lattice.

Excitation spectrum of the sample YSO31, prepared with SiO_2:Y_2O_3 molar ratio of 1:4, presents only one broad band with low intensity with a maximum situated at 361 nm. The reduced excitability of YSO31 sample can be also explained in correlation with XRD data. Due to the formation of a non-homogeneous powder that consists mainly in a mixture of unreacted Y_2O_3 and SiO_2 together with Y_2SiO_5 in relative small proportion, the incorporation degree of cerium is reduced.

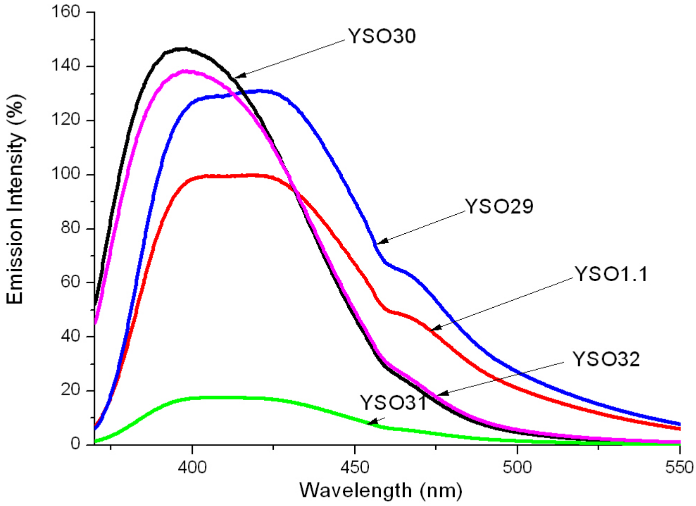

Figure 4. Emission spectra of some YSO samples (λ_{ex}=356nm)

Under UV light (365 nm) all YSO samples exhibit a luminescent emission situated in the blue domain of visible spectra. The emission spectra present a wide band with a maximum situated at around 400 nm as a result of the 4f energy levels splitting into $4f_{5/2}$ and $4f_{7/2}$ in cerium activator (Figure 4).

The Ce^{3+} activator (r_{Ce3+} = 0.106 nm) can easily substitute Y^{3+} from the oxide host lattice (r_{Y3+} = 0.104 nm) and populate two crystallographic sites in X1-Y_2SiO_5 and X2-Y_2SiO_5. If there is an excess of SiO_2, the chemical surrounding of the Ce^{3+} becomes more complicated due to the formation of $Y_2Si_2O_7$ with different structures [11].

A double broad emission band with peaks situated at around 402 nm and 423 nm respectively, due to the splitting of the $4f^1$ ground configuration of the cerium ions into $^2F_{5/2}$ and $^2F_{7/2}$ can be observed for both YSO1.1 (standard) and YSO29 sample.

Considering the XRD information for $MR_{Si:Y}$=1:1 we can assume that the luminescent centres in sample YSO29 are given mainly by the presence of Ce^{3+} activators in X2-Y_2SiO_5 host lattice.

The emission intensity and the peak positions are modified as the composition of the silicate based samples is changed. Sample prepared with excess of silicon dioxide posses similar emission curves as can be observed for samples YSO 30 and YSO32 in which the main component is $Y_2Si_2O_7$. This samples have high photoluminescence (I_{em} = 147% and I_{em} = 137%) with the maximum situated at 398 nm

Another tendency easily observed in the emission spectra is the large emission tail which extends toward the red region of the visible spectrum (from 450 to 550 nm) as well as the shoulder situated at 465 nm. This behaviour is associated with 5d-4f transitions and the formation of Y_2SiO_5 phase [19].

CONCLUSIONS

Yttrium silicate based materials were prepared by solid state reaction with different SiO_2:Y_2O_3 molar ratios in order to study the influence of the synthesis mixture composition on the structural and luminescent properties. It was revealed that $MR_{Si:Y}$ influences the structural and luminescent characteristics of samples.

The XRD patterns and FT-IR spectra put in evidence that the phosphor samples are formed from a mixture of unreacted Y_2O_3 and SiO_2 together with monoclinic X1-Y_2SiO_5, X2-Y_2SiO_5 and $Y_2Si_2O_7$ phases in various proportions depending on the molar ratio.

The photoluminescent investigations put in evidence that under UV light all yttrium silicate based samples exhibit more or less intense blue emission. The excitation spectra have three broad bands which present a shift toward shorter wavelengths as the content of the SiO_2 increase. The excess of Y_2O_3 leads to samples with small excitability and low emission intensity. This suggests that an insufficient amount of SiO_2 can not assure the formation of the proper host lattice surroundings for Ce^{3+}. An excess of SiO_2 in the synthesis mixture generates the formation of monoclinic yttrium disilicate phase with a high luminescent emission.

EXPERIMENTAL SECTION

Two samples series of yttrium based silicate powders were prepared by solid-state reaction method. In this respect, homogeneous synthesis mixtures containing Y_2O_3 (Sigma Aldrich) and SiO_2 (Sigma Aldrich) as generator of host-lattice and $Ce(NO_3)_3.5H_2O$ (Sigma Aldrich) as activator supplier were fired at high temperature (1400^0C) for 4 hours, in air, using alumina crucibles. The yttrium silicate based powders were carefully washed, dried and sieved.

The first sample series is formed from samples: YSO25, YSO26, YSO27 and YSO28 which are prepared using different SiO_2:Y_2O_3 molar ratios namely: 1:4, 1:1, 1:0.5 and 1:0.25 respectively.

Second set of samples consist of samples: YSO29, YSO30 YSO31,YSO32 which are prepared using different SiO_2:Y_2O_3 molar ratios namely: 1:1, 1:0.25, 1:4, 1:0.5 and are prepared using 3% mol Ce /(Y+Ce) in the synthesis mixture in order to generate photoluminescent properties. The internal standard (YSO1.1) was prepared by SimAdd method using ammonium oxalate (Merck 99.9%), yttrium oxide (Aldrich99.99%), cerium nitrate (Merck, extra pure) and silicagel powder (Alfa Aesar) as starting materials [16-18]. The synthesis consist in the thermal treatment at 1600^0C in nitrogen for 4 hrs of the precursor prepared by precipitation of yttrium-cerium nitrate solution, with ammonium oxalate solutions and silica suspension at pH=6 [18]. The post-precipitation stage consisted of 24 h aging, centrifuge separation, water wash and drying.

Samples were characterised by photoluminescence spectroscopy, X-ray diffraction (XRD), infrared absorption spectroscopy (FT-IR). The emission (PL) and excitation (PLE) spectra were registered with JASCO FP-6500 Spectrofluorimeter Wavel (Farbglasfilter WG 320/ Reichmann Feinoptik-Ger). X-ray diffraction patterns were obtained with BRUKER X8 ADVANCE X-Ray Diffractometer (CuKα λ=1.540598Å radiation). The infrared absorption spectra were measured with a NICOLET 6700 Spectrometer (KBr pellets technique).

ACKNOWLEDGMENTS

Financial support for this study was provided by the Romanian Ministry of Education, Research and Innovation (Project 71-122).

REFERENCES

1. W.M. Yen, S.Shionoya, H. Yamamoto, “Practical application of phosphors”, CRC press,Taylor& Francis Grup, Boca Roton-London-New York, **2007**.
2. R.Y. Lee, F.I. Zhang, *J.Vac. Sci. Technol*., **1998**, *B16*, 1013.
3. M. Leskelaa, *J. Alloys Compd.,* **1998**, *275-277*, 702.
4. H. Jiao, X. Wang, S. Ye, *J. Lumin*., **2007**, *122-123*, 113.
5. X.Qin, Y.Ju, S.Bernhard, Nan Yao, *Mater. Res. Bul*., **2007**, *42*, 1440.
6. H. Jiao, L. Wei, N. Zhang, M. Zhong, X. Jing, *J. Eur. Ceramic Soc.,* **2007**, *27*, 185.

7. E.M. Levin, C.R. Robbins, H.F. McMurdie, Phase Diagram for Ceramists, Fig. 2388, in M.K. Reser (Ed.), American Ceramic Society, Columbus, OH USA, **1969**.
8. Q.Y. Zhang, K. Pita, *J. Phys. D. Appl. Phys.*, **2002**, *35*, 3085.
9. C. Michel, G. Buisson, E.F. Bertaut, *C.R. Acad. Sci. B*,**1967**, *264*, 397.
10. N. I. Leonyuk, E. L. Belokoneva, G. Bocelli, L. Righi, E. V. Shvanskii, R. V. Henrykhson, N. V. Kulman, D. E. Kozhbakhteeva, *Cryst. Res. Technol.*, **1999**, *34*, 1175.
11. J. Felsche, *Struct. Bond.*, **1973**, *13*, 99.
12. W. Kraus, G. Nolze, *J. Appl. Crystallogr.,* **1996**, *29*, 301.
13. M. Dı´az, C. Pecharroma´n, *Chem. Mater.,* **2005**, *17,* 1774.
14. Y. Repelin, C. Proust, E. Husson, J. M. Beny, *J. Solid State Chem*., **1995**, *118*, 163.
15. A. M. Hofmeister, A. Chopelas, *Phys. Chem. Miner.,* **1991**, *17*, 503.
16. E.J. Popovici, L. Muresan, A. Hristea, E.Indrea, M. Vasilescu, *J. Alloys Compd.*, **2007**, *434-435*, 809.
17. L. Muresan, E.J. Popovici, R. Grecu and L. Barbu Tudoran, *J. Alloys Compd.*, **2009**, *471*, 421.
18. L Muresan, M. Stefan, E. Bica, M. Morar, E. Indrea, E.J. Popovici, *J. Optoelectron. Adv. M. - Symposia,* **2010**, *2*, 131.
19. J.A. Gonzalez-Ortega, E.M. Tejeda, N. Perea, *Opt. Mater.*, **2005**, *27*, 1221.

STUDIA UNIVERSITATIS BABEŞ-BOLYAI, CHEMIA, XLV, 2, TOM II, 2010

Dedicated to the memory of Prof. dr. Ioan Silaghi-Dumitrescu marking 60 years from his birth

STUDIES ON THE SYNTHESIS OF MANGANESE DOPED ZINC SULPHIDE NANOCRYSTALLINE POWDERS

ADRIAN-IONUȚ CADIŞ[a, b], ELISABETH-JEANNE POPOVICI[a], ECATERINA BICA[a, b], LUCIAN BARBU-TUDORAN[c]

ABSTRACT. New synthesis precipitation technique to prepare nanoparticles of Mn-doped zinc sulphide ZnS:Mn^{2+} have been attempted. Various capping agents have been used to control the morphostructural properties of ZnS:Mn^{2+} particles. Infrared absorption spectroscopy (FT-IR), photoluminescence spectroscopy (PL), scanning (SEM) and transmission electron microscopy (TEM) were used to characterise the powder samples. Strong luminescent ZnS:Mn^{2+} nanocrystalline powders could be precipitated at room temperature, from sodium sulphide and zinc-manganese acetate solutions, using the reagent simultaneous addition technique-SimAdd and methacrylic acid or sodium dodecyl sulphate as passivating agent.

Keywords: *ZnS nanoparticles, Mn-doped nanoparticles, photoluminescence.*

INTRODUCTION

In recent times, there have been extensive studies on luminescent semiconductor nanocrystals because of their potential applications in future optoelectronic devices. In undoped II–VI semiconductors (e.g., CdS, CdSe, and ZnS), the bandgap is engineered by control of the crystal size that leads to tunable band-edge emission [1–6]. Following the report of Bhargava and Gallagher [7], doped semiconductor nanocrystals have been regarded as a new class of luminescent material. Among them, ZnS nanoparticles doped with Mn^{2+} exhibit high luminescence quantum efficiency and short luminescence lifetime.

These materials, because they can be obtained in the form of thin films [8], powders and sols [9], have wide range of applications in sensors, displays, electronic devices, laser devices, and nonlinear optical devices, etc. [6-7].

---

[a] *"Raluca Ripan" Institute for Research in Chemistry, "Babes- Bolyai" University, Fântânele 30, 400294 Cluj-Napoca, Romania, * cadisadi@chem.ubbcluj.ro*

[b] *Faculty of Chemistry and Chemical Engineering, "Babes-Bolyai" University, 11, Arany Janos, 400028 Cluj-Napoca, Romania*

[c] *Electronic Microscopy Centre, "Babes-Bolyai" University, Clinicilor 5-7, 400006 Cluj-Napoca, Romania*

Having applications in various fields such as optoelectronics, photocatalysis, solar energy conversion, fluorescence microscopy, synthesis of un-doped or Mn-doped ZnS 1D nanostructure have also been reported recently by many researchers [10–13].

The increasing interest in un-doped or doped ZnS nanoparticles has lead to the development of a variety of chemical routes to prepare nanoparticles, including ultrasound [14] and microwave irradiation [15], sol–gel method [16], solid-state reaction [17] and chemical precipitation [18].

The morphostructural and luminescent properties of ZnS powders strongly depend on the specific preparation method and the experimental conditions.

The precipitation of zinc sulphide using the reagent sequential addition technique - *SeqAdd* is the most popular method due to some advantages such as the use of cheap raw materials, easy handling and large-scale-production potential [6].

The present paper reports our attempts to obtain ZnS:Mn nanoparticles by chemical precipitation, using a new wet-chemical synthesis route based on the reagent simultaneous addition technique - *SimAdd,* that was developed for the manufacture of microcrystalline phosphors [19]. In order to control the particle morphology and size, methacrylic acid and sodium dodecyl sulphate were used as passivating/capping agents. The influence of surfactants on the photoluminescence and morphostructural properties of ZnS:Mn^{2+} powders prepared by SimAdd was investigated, using scanning (SEM) and transmission (TEM) electron microscopy, infrared absorption (FTIR) and photoluminescence emission (PL) and excitation (PLE) spectroscopy.

RESULTS AND DISCUSSION

The preparation of ZnS:Mn^{2+} powder was based on the reaction, at room temperature, between zinc acetate and manganese acetate, as metal sources, and sodium sulphide, as chalcogen suplier. When using SimAdd technique, the reagents are simultaneously added into diluted zinc acetate solution containing no additives (C79 sample), sodium dodecyl sulphate – SDS (C80 sample) or methacrylic acid – MA (C81sample) as particle size regulating agent.

The main chemical process for the preparation of ZnS:Mn^{2+} powder i.e. for the formation of zinc-manganese double sulphide is described by the following equation:

$$(1\text{-}x)Zn(CH_3COO)_2 + xMn(CH_3COO)_2 + Na_2S \longrightarrow (1\text{-}x)ZnS \cdot xMnS + 2CH_3COONa$$

Under UV excitation, the as prepared ZnS:Mn^{2+} powders show the characteristic Mn^{2+} emission. Photoluminescence emission (PL) and excitation (PLE) spectra are depicted in Figure 1. Sample C79 prepared with no additive was used as internal standard (I_{600nm}=100%; I_{340nm}=100%).

Photoluminescence emission (PL) spectra consist of two broad emission bands namely, a strong orange one at about 600 nm and a very weak blue one at 400–480 nm.

The characteristic orange emission band can be attributed to the electronic transition between $^4T_1$ and $^6A_1$ energy levels of the Mn^{2+} 3d states. Mn^{2+} d-electron states act as efficient luminescent centres while interacting strongly with s–p electronic states of the ZnS host into which an external electronic excitation is normally directed. The blue emission is characteristic to zinc sulphide and it is usually influenced by many factors e.g. particles size, crystallinity, doping level, surface states of particles etc. Since a large portion of the atoms in nanocrystals is located on or near the surface, the surface properties should have significant effect on their optical properties.

Photoluminescence properties of ZnS:Mn^{2+} powders are influenced by the presence of the passivating agents into the precipitation medium. The use of the sodium dodecyl sulphate increases the orange emission intensity with 25% while the presence of methacrylic acid improves it with only 7%. On the other hand, the intensification of the blue emission is insignificant in the presence of sodium dodecyl sulphate (~0.5%) or methacrylic acid (~0.2%).

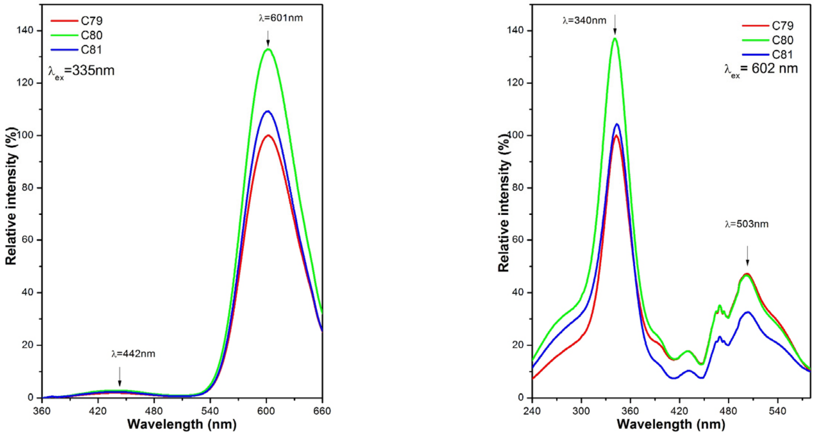

Figure 1. PL (left) and PLE (right) spectra of ZnS:Mn^{2+} powders prepared with no additive (C79), SDS (C80)and MA(C81)

Photoluminescence excitation spectra were registered by monitoring the characteristic orange emission (~ 600 nm) of Mn^{2+} under excitation with variable UV radiation. The highest PLE peak centred at about 340 nm can be attributed to the ZnS host lattice excitation whereas the multiple peaks in the 375-575 nm range can be related to Mn^{2+} presence.

In doped semiconductors, the possible paths for the luminescence excitation of the impurity ions include indirect excitation of the host lattice and direct excitation of impurity ions. This strong excitation absorption peak should arise from the direct excitation transitions of Mn^{2+}. According to the literature [20], the PLE peaks observed around 390, 430, 465, 500, and 535 nm can be attributed to the transitions between the $^6A_1(^6S)$ ground state and the excited states of $^4E(^4D)$, $^4T_2(^4D)$, $^4A_1(^4G)$ and $^4E(^4G)$, $^4T_2(^4G)$, $^4T_1(^4G)$ within the Mn^{2+} $3d^5$ configuration, respectively.

The influence of the passivating agents on photoluminescence properties is also evident in PLE spectra. The strong excitation peak related with the ZnS host (~ 340 nm) is increased with about 37 % in sample with SDS and only with 4 % in sample with MA. SDS seams to do not influence the excitation peaks associated with Mn^{2+} while MA addition decrease them with about 30%, comparative with ZnS:Mn^{2+} without surfactant.

Particle dimensions of ZnS:Mn^{2+} powders were evaluated by electron microscopy.

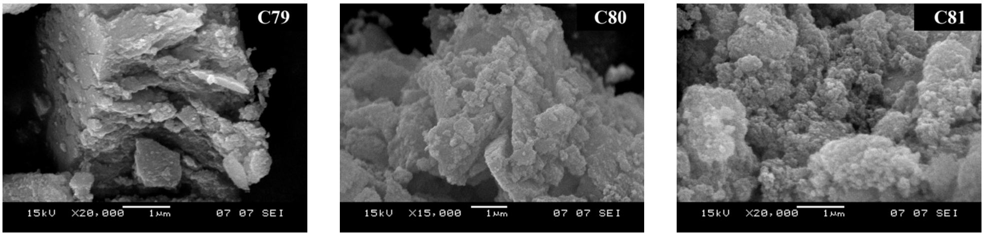

Figure 2. SEM images of different ZnS:Mn^{2+} samples obtained in various experimental conditions.

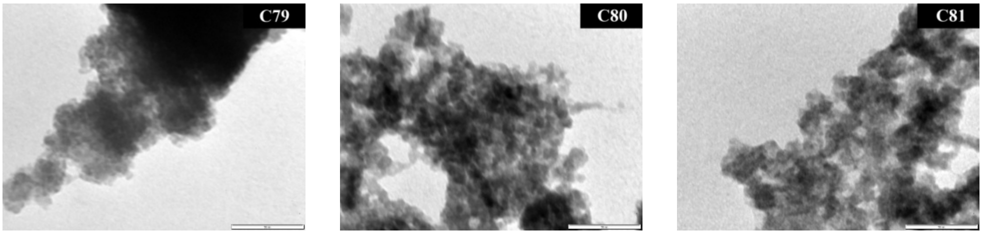

Figure 3. TEM images of different ZnS:Mn^{2+} samples obtained in various experimental conditions (scale bar=50 nm).

SEM investigation of samples prepared with and without surfactants i.e. C80-SDS, C81-MA and C79, shows that ZnS:Mn^{2+} powders consist in large conglomerates formed from tightly packed under-micron particles (Figure 2).

TEM images of samples C79-no surfactant, C80-SDS and C81-MA illustrate the nanocrystalline state of ZnS:Mn^{2+} all powders (Figure 3). The average diameter of nanoparticles is evaluated at 6-10 nm.

The nanopowders obtained by SimAdd technique have a high surface area and energy that account for the strong tendency of particles toward agglomeration. SDS and MA additives seem to increase the powder dispersability; no effect on the particles dimension could be noticed.

The as prepared ZnS nanopowders show a high capacity to absorb impurities and regulating agent from the precipitation medium, as illustrated by the infrared absorption spectra depicted in Figure 4. FTIR spectrum of C80-SDS contains the characteristic absorption bands of sodium dodecyl sulphate i.e. O–H stretching (3800–3200 cm^{-1}) and bending (1700–1600 cm^{-1}), C–H stretching of CH_3 and CH_2 groups (3000–2800 cm^{-1}), C=O asymmetric and symmetric stretching (1600 and 1400 cm^{-1}), C–O stretching (1025 cm^{-1}) and SO_2 stretching (1300–1100 cm^{-1}) vibrations [21].

FTIR spectroscopy illustrates that, in spite of the fact that the precipitate was thoroughly washed, ZnS:Mn^{2+} powders with large surface area contain residual CH_3COO^-, dodecyl sulphate and methacrylate ions.

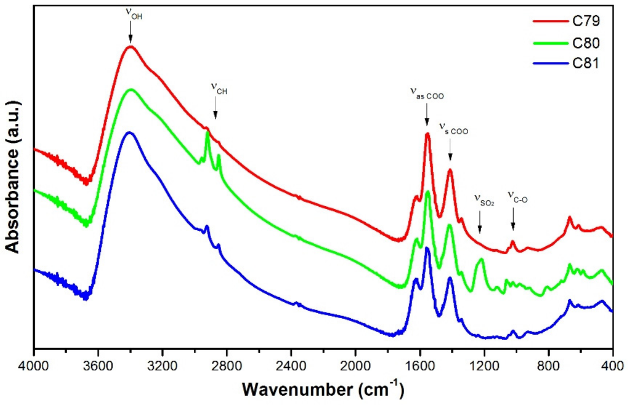

Figure 4. FT-IR spectra of ZnS:Mn^{2+} powders prepared with no additive (C79), SDS (C80) and MA (C81)

CONCLUSIONS

Luminescent manganese doped zinc sulphide (ZnS:Mn^{2+}) nanopowders could be obtained by precipitation, using the simultaneous reagent addition technique-*SimAdd,* with or without sodium dodecyl sulphate or methacrylic acid as particle size regulating agents.

The photoluminescence measurements show that ZnS:Mn^{2+} powders show strong orange luminescence (λ_{pk}~600 nm) characteristic to Mn^{2+}. The strong PL of the un-annealed ZnS:Mn^{2+} powders could be associated with the particle nano-dimension. The strongest photoluminescent powder was obtained in the presence of sodium dodecyl sulphate.

Although ZnS:Mn^{2+} powders are formed from nanosized crystallites (6-10 nm), they are tightly packed into larger and irregular shaped particles. The large surface area explains the high absorption capacity of the ZnS powder, as illustrated by FTIR investigations.

EXPERIMENTAL SECTION

Manganese doped zinc sulphide powders were prepared by precipitation, using the reagent simultaneous addition technique-*SimAdd*, from Zn-Mn acetate and sodium sulphide in aqueous medium, at room temperature. In this respect, equal volumes of 1M aqueous solution of zinc -manganese acetate (8 % mol Mn/(Zn+Mn) and 1M aqueous solution of sodium sulphide were added, under stirring, in water, with or without surfactant addition, sodium dodecyl sulphate and methacrylic acid. The white-pink ZnS powder was separated through centrifugation, washed with isopropyl alcohol and dried at 80ºC.

Infrared absorption spectra (FTIR) were registered on a NICOLET 6700 Spectrophotometer (KBr pellets technique). Photoluminescence emission (PL) and excitation (PLE) spectra were taken with JASCO FP-6500 Spectrofluorimeter (Farbglasfilter WG 320-ReichmannFeinoptik; Sample C79 prepared with no surfactant addition was used as internal standard I_{em}=100%). The transmission electron microscopy (TEM) was performed with JEM JEOL 1010 microscope and the scanning electron microscopy (SEM) images were obtained with a JEOL–JSM 5510LV instrument, using Au-coated samples.

ACKNOWLEDGMENTS

The Romanian Ministry of Education, Research and Innovation (Contract ID-2488/710) supported this research project.

REFERENCES

1. K. Sooklal, B. S. Cullum, S. M. Angel, C. J. Murphy, *Journal of Physical Chemistry,* **1996**, *100(11)*, 4551.
2. N. Murase, R. Jagannathar, Y. Kanematsu, M. Watanable, A. Kurita, K. Hirata, T. Yazawa, T. Kushida, *Journal of Physical Chemistry B,* **1999**, *103(5)*, 754.

3. W. Chen, V. F. Aguekian, N. Vassiliev, A. Y. Serov, N. G. Filosofov, *Journal of Chemical Physics*, **2005**, *123(12)*, 124707.
4. Z. Quan, Z. Wang, P. Yang, J. Lin, J. Fang, *Inorganic Chemistry*, **2007**, *46(4)*, 1354.
5. B. Y. Geng, L. D. Zhang, G. Z. Wang, T. Xie, Y. G. Zhang, G. W. Meng, *Applied Physics Letters*, **2004**, *84(12)*, 2157.
6. Z. L. Wang, Y. Liu, Z. Zhang, ”Handbook of Nanophase and Nanostructured Materials Synthesis”, Tsinghua University Press and Kluwer Academic Plenum Publishers, New York, **2002**.
7. R. N. Bhargava, D. Gallagher, X. Hong, A. Nurmikko, *Physical Review Letters,* **1994**, *72(3)*, 416.
8. M. Stefan, I. Baldea, R. Grecu, E. Indrea, E.J. Popovici, *Studia Universitatis Babes-Bolyai, Chemia*, **2009**, *54(3)*, 203.
9. A. I. Cadis, A. R. Tomsa, M. Stefan, R. Grecu, L. Barbu-Tudoran, L. Silaghi-Dumitrescu, E. J. Popovici, *Journal of Optoelectronics and Advanced Materials – Symposia*, **2010**, *2(1)*, 111.
10. F. Piret, C. Bouvy, W. Marine, B. L. Su, *Chemical Physics Letters*, **2007**, *441(1-3)*, 83.
11. X. J. Zheng, Y. Q. Chen, T. Zhang, C. B. Jiang, B. Yang, B. Yuan, S. X. Mao, W. Li, *Scripta Materialia*, **2010**, *62(7)*, 520.
12. C. Unni, D. Philip, K. G. Gopchandran, *Optical Materials*, **2009**, *32(1)*, 169.
13. J. S. Jang, C. J. Yu, S. H. Choi, S. M. Ji, E. S. Kim, J. S. Lee, *Journal of Catalysis*, **2008**, *254(1)*, 144.
14. A. R. Tomsa, E. J. Popovici, A. I. Cadis, M. Stefan, L. Barbu-Tudoran, S. Astilean, *Journal of Optoelectronics and Advanced Materials,* **2008**, *10(9)*, 2342.
15. J. Q. Sun, X. P. Shen, K. M. Chen, Q. Liu, W. Liu, *Solid State Communications*, **2008**, *147(11–12)*, 501.
16. M. M. Biggs, O. M. Ntwaeaborwa, J. J. Terblans, H. C. Swart, *Physica B: Condensed Matter*, **2009**, *404(22)*, 4470.
17. L. P. Wang, X. D. Xu, X. Yuan, *Journal of Luminescence*, **2010**, *130(1)*, 137.
18. A. I. Cadis, A. R. Tomsa, E. Bica, L. Barbu-Tudoran, L. Silaghi-Dumitrescu, E. J. Popovici, *Studia Universitatis Babes-Bolyai, Chemia,* **2009**, *54(3)*, 23.
19. E. J. Popovici, M. Stefan, F. I. Lucaci, L. Muresan, E. Bica, M. Morar, E. Indrea, L. Barbu-Tudoran, *Physics Procedia*, **2009**, *2(2)*, 603.
20. W. Q. Peng, S. C. Qu, G. W. Cong, X. Q. Zhang, Z. G. Wang, *Journal of Crystal Growth*, **2005**, *282(1-2)*, 179.
21. B.H. Stuart, ”Infrared Spectroscopy: Fundamentals and Applications”, John Wiley & Sons Ltd., Chichester, **2004**.

STUDIA UNIVERSITATIS BABEŞ-BOLYAI, CHEMIA, XLV, 2, TOM II, 2010

Dedicated to the memory of Prof. dr. Ioan Silaghi-Dumitrescu marking 60 years from his birth

RAMAN IMAGING OF IN VIVO DAMAGED SKIN TISSUES FROM MICE SPECIMENS

ALEXANDRA FALAMAS[a], SIMONA CINTA PINZARU[a,*],
CRISTINA A. DEHELEAN[b], MONICA M. VENTER[c]

ABSTRACT Autopsy skin tissues collected from mice specimens exposed to UVB irradiation and 7,12-dimethylbenz(a)anthracene were immersed in formalin solution mixed with colloidal silver nanoparticles and analyzed using Raman imaging. The aim of this study was probe the SERS technique applied to tissue analysis, to detect the main molecular components present in the investigated organs and to search for a new way of acquiring enhanced Raman signal from these tissues for early diagnostic. The analysis of the collected spectra indicated chemisorption of the nanoparticles into the tissue and the possibility to record high quality SERS signal.

Keywords: *Raman imaging, tissue SERS, skin cancer, mouse model, silver nanoparticles*

INTRODUCTION

Raman spectroscopy has currently become a powerful vibrational technique largely used to probe the molecular composition of biological tissues [1-5]. Raman spectra provide information on molecular vibrations leading thus to the possibility of highly specific fingerprinting of the molecular structure and biochemical composition of cells and tissues. In the past two decades there has been a renewed interest in Raman techniques due to the discovery of surface-enhanced Raman scattering (SERS) effect [6-9]. Briefly, the usually weak Raman signals can be greatly enhanced when Raman scattering takes place on molecules at the surface or in very close vicinity to gold or silver nanoparticles. The SERS effect is mainly employed for the investigation of the

---

[a] *Babes Bolyai University, Dept. of Physics, Kogalniceanu 1, RO 400084, Cluj-Napoca, România*
[b] *Victor Babeş University of Medicine and Pharmacy, Faculty of Pharmacy, Eftimie Murgu Square 2, RO- 300041, Timişoara, România*
[c] *Babes Bolyai University, Faculty of* Chemistry and Chemical Engineering Arany Janos *11, 400028 Cluj-Napoca, Romania*

molecular species adsorbed on noble metal nanoparticles. Recently, SERS was applied in the study of biological cells and tissue [10-12]. Two effects are responsible for this enhancement: the first mechanism is related to resonances between the surface plasmons of the metal nanostructures and the excitation and scattered fields during the Raman process giving rise to enhanced local excitation fields. The second enhancement mechanism is based on the adsorption of the molecules at certain surface sites, creating a charge-transfer state between the metal and the adsorbed scatterer.

SERS in conjunction with Raman imaging technique was applied in this study for the investigation of the damaged skin tissues from mice models exposed to UV-B radiation and chemical cancer promoters. The main attraction of the Raman imaging technique is the possibility to obtain a „complete picture" the chemical species distribution in the very complex sample. Each Raman spectrum at a particular x-y coordinate contains a wealth of information about the chemical composition and molecular structure. For thin, dried tissue sections this technique is a powerful molecular imaging tool for detailed pathological assessment of the tissue. These images contain information about the molecular components and different components can be visualized by post-processing of data, because of the possibility of plotting the concentration (i.e. fingerprint band intensity) of various biochemicals as a function of position.

The aim of the Raman imaging was also to investigate whether the SERS effect can be applied to study tissue samples and further to probe the technique as a very sensitive tool for early cancer diagnostic. Tissue SERS was expected due to the colloidal silver nanoparticles in which the autopsy samples were immersed. Analyzing the samples using Raman spectroscopy, by acquiring single Raman spectra, we obtained either typical Raman signal characteristic for skin tissue supported by the literature, or different spectra with sharp bands, characteristic for SERS effect. One possible explanation for this could be the fact that the spectra were collected from regions where no silver nanoparticles penetrated the tissues. This is likely since the nanoparticles could not have been homogenously distributed within the tissue sample. As a general characteristic in the field of tissue SERS, the amide I band is less representative but in the Raman spectra it has significant intensity. This is first confirmation weather the spectra collected are Raman or SERS, along with the presence or absence of the huge Ag-molecule mode observed around 22o cm^{-1}[10-12]. When medium intensity contribution is observed, that would be a suggestion that pure Raman signal is also collected nearby the SERS from the microscope objective collection cone. This could have been possible because of inhomogeneity distribution of the Ag nanoparticles inside the tissue. Due tot his, the spot of the laser may have encompassed the margins of a "hot spot", meaning that the SERS enhancement conditions varied more in the distance and location of the target molecule relative to the enhancing silver nanoparticles.

RESULTS AND DISCUSSION

The first results after two weeks of the skin exposure to the UVB radiation (295 nm) and the chemical carcinogen (7,12-dimethylbenz(a) anthracene, DMBA) application indicated by skin redness, lesions and after one month of exposure the visual aspects pointed towards important skin damages like photo aging and first steps to skin carcinoma. To get a better insight on the nature of the damage and to detect the main molecular components in the samples, the histopathology results of the thin tissue sections were correlated with the spectroscopic data.

A specific area of 180x180 µm was chosen from the skin sample collected from the NMRI specimen. In Fig.1 the Raman image collected from the sample can be observed among with the microscopic picture of the entire sample and the area used for investigation (left). This region was selected based on the density of the tissue. The Raman image shown in the middle displays the distribution of the amide I band in the investigated tissue. The last image in Fig.1 represents the HCA result and the distribution of the three clusters obtained after the analysis. The black pixels represent spectra with negative Quality Test results, which were removed from the analysis. The spectra shown in the figure are color coded averaged spectra each corresponding to one of the three clusters.

The selected area was divided after the HCA analysis into three clusters. The green one, corresponding to the main part of the tissue, the red one which could be assigned to the margins of the tissue and the blue one which is observed only in a few scattered points on the image. Each of the spectra presented in Fig.1 are shown with the same color as the corresponding cluster. The spectra look rather similar, presenting the same main features, such as the 1447 cm^{-1} band assigned to CH_2 bending in proteins and lipids, 1343 and 1315 cm^{-1} bands specific for DNA, as well as collagen, in the case of the later, 1131 cm^{-1} band attributed to C-C stretching vibrations of lipids and C-N stretching vibrations of proteins, 1003 cm^{-1} characteristic to phenylalanine and the 854 cm^{-1} assigned to ring breathing of tyrosine and C-C stretching of hydroxyproline ring specific to collagen [16-18].

Though, at a closer look, slight differences between them can be seen. For example the two bottom spectra present the amide I band of collagen around 1670 cm^{-1}, absent in the upper one. On the other hand, spectrum number 1 corresponding to the blue cluster presents an intense band at 1577 cm^{-1} assigned to tryptophan protein and guanine and adenine nucleic acids. In the 1180-1340 cm^{-1} spectral range, the spectra present the same bands, though differently amplified. The most contributions seen here are proteins, amide III bands (1252, 1225 cm^{-1}), phenylalanine and tryptophan (1209 cm^{-1}), nucleic acids (1181 cm^{-1}) and collagen (1316 cm^{-1}) [16-18]. Another difference lies in the band seen at 477 cm^{-1}, which has a very weak intensity in the green spectrum compared to the other two. Also, the 322 cm^{-1} seen more amplified in the bottom spectrum is assigned to the substrate of CaF_2 on which the thin tissue sections were placed.

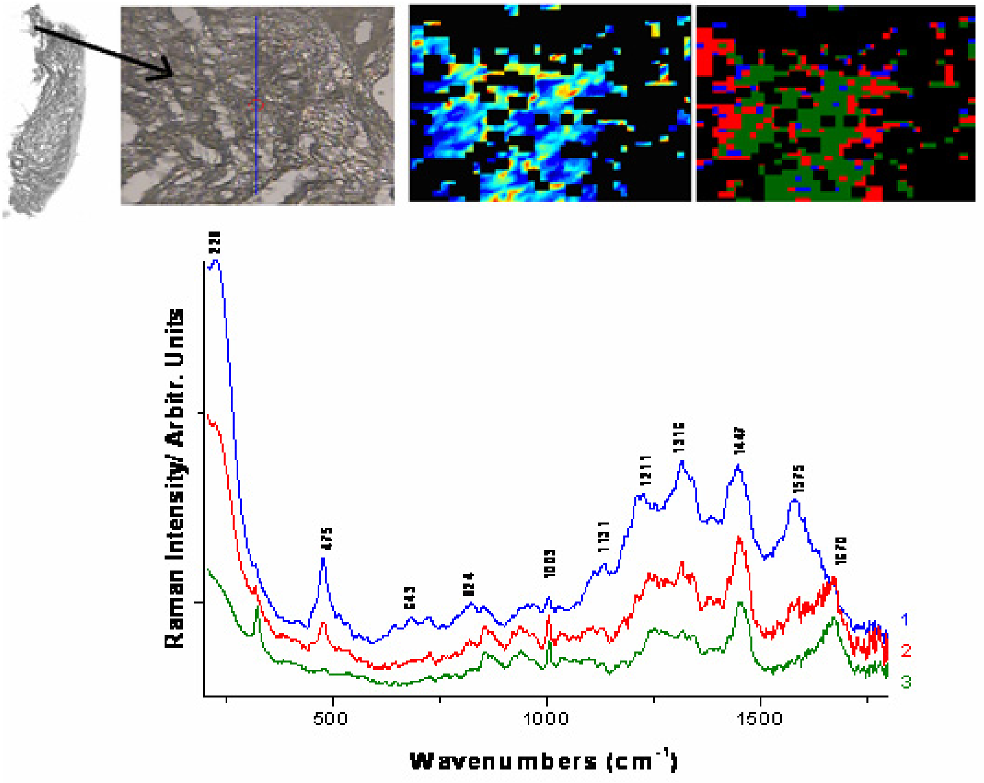

Figure 1. Microscopic image of the NMRI skin sample and the image of the area selected for investigation, the Raman map and the three clusters resulted after HCA analysis. In the below image the averaged-clustered spectra are presented, each corresponding to one cluster

One important observation is the appearance of the band at 228 cm^{-1} in the upper spectrum. This band can be seen in the middle one as well, though it seems as if it is not complete. The band could indicate the formation of Ag-O bond, meaning that the silver nanoparticles have penetrated the tissue and attached to the target molecules (SERS fingerprint). This could suggest that the upper spectrum is a SERS one, implying the method used in this study for acquiring SERS signal from biological tissues by inoculating them into colloidal nanoparticles, succeeded.

Keeping this in mind, an obvious conclusion would be that the only true SERS spectrum is the upper one assigned to the blue scattered cluster in the HCA image. The middle spectrum assigned to the red cluster has both Raman and SERS contributions and could be a result of the fact that the focus of the laser could have encompassed the margins of a "hot spot", meaning that the SERS enhancement conditions varied more in the distance and location of the target molecule relative to the enhancing silver nanoparticles. Another aspect that needs to be pointed out is the fact that the Ag nanoparticles are not distributed homogenously inside the tissue. The lower spectrum assigned to the main part of the tissue, the green cluster, is a Raman spectrum being very similar to the single Raman spectra acquired from the same sample (not shown here).

Analyzing the entire Raman image, SERS variability became evident in many ways. The intensity of the acquired signals varied from one point of acquisition to another and the resulted signals showed differences in peak locations. To understand what happened inside the tissue with the Ag colloidal nanoparticles, in Fig. 2 are presented three spectra found in the Raman image acquired from three consecutive points.

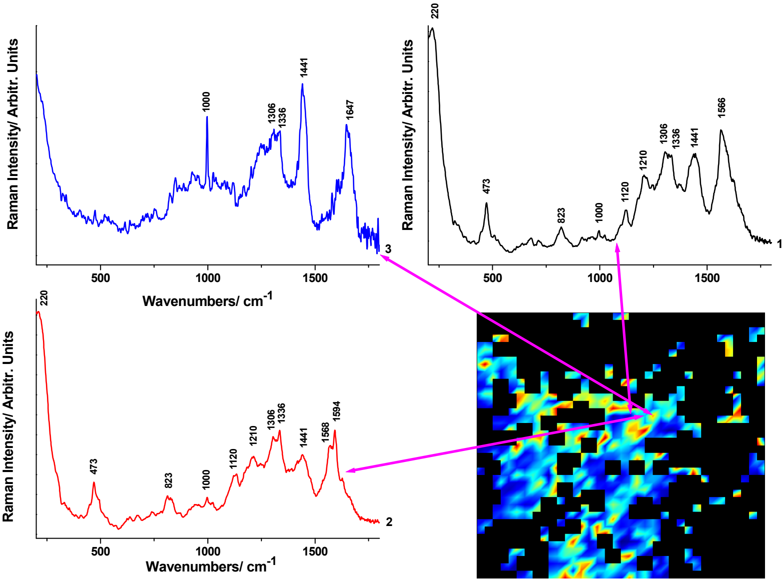

Figure 2. SERS spectra (1 and 2) in comparison to a Raman spectrum (3) acquired from three consecutive points from the Raman image.

Spectra 1 and 2 are SERS spectra, while the third is a Raman one. The differences between the Raman and the SERS spectra can easily be noticed, such as the absence of the amide I band at 1647 cm^{-1} from the SERS spectra, or the sharp intense phenylalanine band at 1000 cm^{-1} seen in the Raman spectrum.

On the other hand both SERS spectra present the 1568 cm^{-1} band assigned to tryptophan and nucleic acids [14], the 1210 cm^{-1} band assigned to phenylalanine and tryptophan [12], the 1120 cm^{-1} attributed to C-N stretching of proteins and C-C stretching of lipids and the 820 cm^{-1} band assigned to out of plane ring breathing of tyrosine and O-P-O stretching vibrations of DNA [12]. Although the main bands can be seen at the same wavenumbers, they are differently amplified and other weaker signals can be spotted as well. One possible explanation for the observed differences in the SERS spectra could be the fact that certain frequencies of scattering are more sensitive to the enhancement than others. Additionally, different portions of the tissue could have been subjected to the enhancement during the measurement. Depending on how many adsorbed molecules on the Ag nanoparticles, does the spot of the laser encompass, the spectra can present lots of fluctuations in signal intensities and frequencies. However, the epithelial layer would be more suitable for such SERS sensitive characterization and consequently, the method support further optimizations concerning the Ag nanoparticles incubation in order to perform routine applications in skin tissue monitoring.

For the present study we employed the damaged skin tissue only. Obviously, further SERS studies are required in order to investigate the molecular spectral response from normal tissue specimens for establishing an appropriate differentiation algorithm for early diagnostic.

CONCLUSIONS

In this study we have applied Raman imaging technique in conjunction with the SERS effect for the investigation of in vivo damaged biological skin tissues from mice specimens. The imaging display was obtained using the amide I band from proteins characteristic for tissue. SERS effect was evidenced for the studied skin sample. By inoculating Ag colloidal nanoparticles in biological tissues, we have proved here the possibility of recording SERS spectra which can be used to investigate the nature of the molecular components of carcinogenic skin tissue samples. To the best of our knowledge this is the first time when SERS effect was detected from skin tissues prepared in this manner.

EXPERIMENTAL SECTION

Sample Preparation and Animals Protocol: Female mice (NMRI specimens, 8 weeks old) were purchased from Charles River. The UMFT Bioethical Committee agrees the protocol and institutional guidelines were followed in the handling and care the animals. For the present study 2 animals from a group of 10 mice that were treated for skin carcinoma development were chose. The animals were accommodated to UMFT Biobase and they have been maintained in optimal conditions. The food was standard and was administrated as the water *ad libitum*. The day/night cycle was 12/12 hours and the humidity over 55%.

Tumor induction protocol has been largely described elsewhere [13,14]. For this study, NMRI mice specimens were exposed daily to UV radiation (295 nm) and orally in one dose completed by locally treated with 7,12-dimethylbenz(a)anthracene (DMBA) solution, a synthetic polycyclic aromatic hydrocarbon known to induce cancer in different organs. The skin carcinoma experimental model has been investigated after 10 weeks of photo-chemical damage evolution. Tissue samples were collected from the sacrificed mouse by CO_2 inhalation. For the skin biopsy only they were anesthesied with xylazine and ketamine. Samples from the skin were detached and immersed in 10% formalin solution mixed with colloidal silver nanoparticles prepared according to the Lee Meisel method. From these samples, thin tissue sections were prepared using a LEICA CM3050S cryostat and placed on CaF_2. The samples were not submitted to any preparation, like “freezing shock” in liquid nitrogen or washing.

Instrumentation: The Raman maps were collected using a Raman microscope coupled to a 785 nm diode laser (Kaiser Optical Systems). Each map had a dimension of 19 x 19 =361 spectra with a step size of 10 µm, exposure time 2 s per spectrum, number of acquisitions 2 and dwell time between 10-30 s. The laser power was set to 200 mW.

Data analysis: The resulting Raman images were processed using the CytoSpec [15] software package. The data sets were normalized resulting in a linear correction of the complete spectrum, removing all negative intensities, background subtraction, polynomial baseline correction and filtering. Low-intensity spectra were removed from the data sets because they corresponded to positions outside the tissue, near holes, near fissures or near margins. The intensity of the amide I band at 1656 cm^{-1} was used to determine whether some regions of the sample were too thin for the spectra to be included in the subsequent data analysis. In the end clustering analysis was performed on the data sets.

Cluster analysis identifies regions of the sample that have similar spectral response by clustering the spectra into groups or clusters such that differences in the intra-cluster spectral responses are minimized while simultaneously maximizing the inter-cluster differences between spectral responses. The hierarchical cluster analysis (HCA) algorithm calculates the symmetric distance matrix (size n×n) between all considered spectra (number n) as a measure of their pair wise similarity. The algorithm then searches for the minimum distance, collects the two most similar spectra into a first cluster and recalculates spectral distances between all remaining spectra and the first cluster. In the next step the algorithm performs a new search for the most similar objects, which now can be spectra or clusters. The two most similar objects are clustered again and the distance values of the newly formed cluster are recalculated. This iterative procedure is repeated n−1 times until all spectra have been merged into one cluster.

ACKNOWLEDGMENTS

This work was supported by CNCSIS-UEFISCSU grants (PNII-IDEI code 2284/2008 and 1257/2007). A. Falamas thanks to Dr. Christoph Krafft and Professor Jürgen Popp ("Friedrich Schiller" University of Jena, Germany) for useful discussions and access to laboratory facilities.

REFERENCES

1. C. Kendall, M. Isabelle, F. BayabtßHegemark, J. Hutchings, L. Orr, J. Babrah, R. Baker, N. Stone, *Analyst*, **2009**, *134*, 1029.
2. Ch. Krafft, B. Dietyek, J. Popp, *Analyst*, **2009**, *134*, 1046.
3. Ch. Krafft, M. Kirsch, C. Beleites, G. Schackert, R. Salzer, *Anal. Bioanal. Chem.*, **2007**, *389*, 1133.
4. M. Schmitt, J. Popp, *J. Raman Spectrosc.*, **2006**, *37*, 20.
5. K. Hering, D. Cialla, D. Ackermann, K. Doerfer, T. Meolleer, R.H. Scheidewind, R. Mattheis, W.R. Fritysche, P. Roesch, J. Popp, *Anal. Bioanal. Chem.*, **2008**, *390(1),* 113.
6. M. Fleischmann, P.J. Hendra, A.J. Mcquillian, *Chem. Phys. Lett.*, **1974**, *26*, 123.
7. D.L. Jeanmarie, R.P. Van Duyne, *J. Electroanal. Chem.*, **1977**, *84*, 1.
8. M.G. Albrecht, J.A. Creighton, *J. Electroanal. Chem.*, **1977**, *99(15),* 5215.
9. M. Moskovits, , *Rev. Mod. Phys.*, **1985**, *57(3),* 783.
10. S. Cinta Pinzaru, L.M. Andronie, I. Domsa, O. Cozar, S. Astilean, *J. Raman Spectrosc.*, **2008**, *39*, 331.

11. X. Qian, X.H. Peng, D.O. Ansari, Q. Yina-Goen, G.Z. Chen, D.M. Shin, L. Yang, A.N. Young, D. May, M.D. Wang, S. Nie, *Nat. Biotechnol.*, **2008**, *26*, 83.
12. S. Fendel, B. Schrader, *Fresenius J. Anal. Chem.,* **1998**, *360*, 609.
13. C. Dwivedi, E.R. Maydew, J.J. Hora, D.M. Ramaeker, X. Guan, *Eur. J. Cancer Prev.,* **2005**, *14(5),* 473.
14. L.H. Kligman, R. Elenitsas, *Melanoma Res.*, **2001**, *11*, 319.
15. *CytoSpec - Application for FT-IR spectroscopy imaging*, www.cytospec.com.
16. R.E. Kast, G.K. Serhatkulu, A. Cao, A.K. Pandya, H. Dai, J.S. Thakur, V.M. Naik, R. Naik, M.D. Klein, G.W. Aunner, R. Rabah, *Biopolym.* (*Biospectrosc.*)*,* **2008**, *89(3),* 235.
17. M.V.P. Chowdary, K.K. Kumar, S. Mathew, L. Rao, C.M. Krishna, J. Kurien, *Biopolym.* (*Biospectrosc.*)*,* **2009**, *91(7),* 539.
18. I. Nottingher, S. Verrier, S. Haque, J.M. Polak, L. Hench, *Biopolym.* (*Biospectrosc.*), **2003**, *72*, 230.

STUDIA UNIVERSITATIS BABEŞ-BOLYAI, CHEMIA, XLV, 2, TOM II, 2010

Dedicated to the memory of Prof. dr. Ioan Silaghi-Dumitrescu marking 60 years from his birth

KINETIC STUDY OF FLUE GAS DESULPHURIZATION WITH SODIUM CARBONATE AT LOW TEMPERATURE

SIMION DRĂGAN[a,*], ADINA GHIRIŞAN[a]

ABSTRACT. This paper presents the kinetic study of the dry desulphurization process at low temperature using solid adsorbents by thermogravimetric analysis technique. Experiments are performed in isothermal conditions, at three temperatures (373 K, 473 K and 573 K) with diameters of sodium carbonate granules of 31.5 µm and 900 µm and sulfur dioxide concentration of 0.5 % and 1.0 %. The particle size, temperature and gas flow rate show a dominant influence on the variation of carbonate conversion. The obtained activation energy values are in the range from 4.234 KJ/mol to 12.275 KJ/mol showing that the diffusion through the solid product layer is the determinate rate step of the process. The experimental results confirm that the shrinking Unreacted Core Model can be used to describe the sulfation of sodium carbonate at low temperature.

Keywords: *flue gas desulphurization, kinetic study, activation energy, sodium carbonate, unreacted core model, effective diffusion coefficient.*

INTRODUCTION

Problems concerning environmental protection are today very important, taking into consideration the big quantities of emissions (for example SO_2, SO_3, HF and HCl) evacuated in atmosphere [1, 2]. A particular case consists of the sulfur dioxide emissions. Sulfur dioxide is a harmful gas resulted in large quantities by fuel combustion with air excess, which in the atmosphere transforms itself into sulfuric acid – a major component of acidic rain, sulfuric acid being extremely soluble in water.

There are many processes used for the reduction of such emissions. The use of solid adsorbents to reduce SO_2 emissions from coal fired power plants has been investigated during the last twenty years [3-6].The adsorption phenomenon of sulfur dioxide on solid adsorbents can be: a physico-sorption process, characterized by weak bonds (on zeolites for example) or/and chemo-sorption characterized by strong bonds.

---

[a] *Babeş-Bolyai University, Faculty of Chemistry and Chemical Engineering, 11. Arany Janos, RO-400028 Cluj-Napoca, Romania; * sdragan@chem.ubbcluj.ro*

Adsorption of SO_2 on the sodium carbonate is a chemo-sorption process in accordance with reaction scheme (1):

$$Na_2CO_{3[s]} + SO_{2[g]} \rightarrow Na_2SO_{3[s]} + CO_{2[g]} \quad (1)$$

In the worldwide there are plants at pilot and industrial scale, which are using adsorption of sulfur dioxide on calcium oxide and soda ash or sodium carbonate with a smaller than 50 % adsorption degree [3, 4]. The investigations are oriented towards to the discovery of influence of some parameters such as: initial porosity of solid particles, their geometrical size, reaction temperature, concentration of sulfur dioxide in the gas mixture, as well as the contact time over the reaction [5].

The aim of the present study is the kinetic study of the desulphurization process at low temperature using sodium carbonate as solid adsorbent by thermogravimetric analysis.

RESULTS AND DISCUSSION

The primary thermogravimetric measurements have been converted into kinetic curves considering the transformation degree of sodium carbonate, as Equation 2 shows:

$$\eta_{Na2CO3} = \frac{53}{63} \cdot \frac{\Delta m_s}{\overline{x}^0_{Na2CO3} \cdot m^0_s} \quad (2)$$

and presented in Figure 1.

The experimental data presented in Figure 1 and Figure 2 show a significant influence of temperature and granule size on the conversion of sodium carbonate. Thus, it can be observed a positive effect on sodium carbonate conversion obtained by increasing the temperature and a negative effect by increasing the particle size.

As Figure 2 shows, for granule size of 900 μm, it can be achieve only a conversion lower than 30 % after a reaction times of 60 minutes, probably due to the strong influence of the SO_2 diffusion through the solid product layer.

The influence of the gas concentration and gas flow rate on the conversion of solid particles is less important, as it can be seen in Figure 3 and Figure 4.

The lower influence of the gas flow rate may be the qualitative confirmation for a kinetic mass transfer regime. A more accurate and quantitatively interpretation of the experimental results is not possible without kinetic modeling.

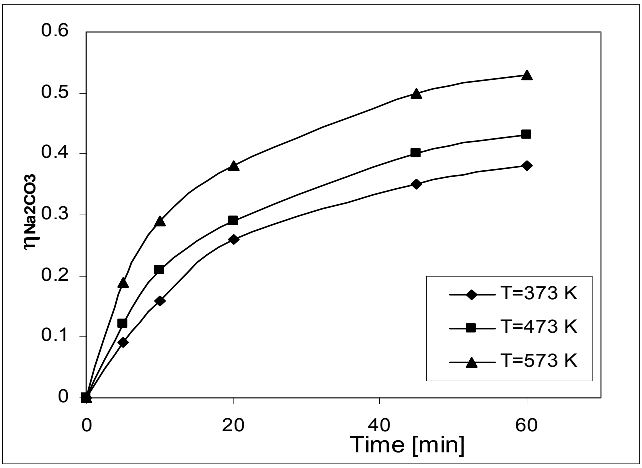

Figure 1. Kinetic curves conversion vs. time for d_{Na2CO3} = 31.5 μm, C_{SO2} = 0.5%, Gv = 1.55 x 10^{-4} m^3/s at different temperature.

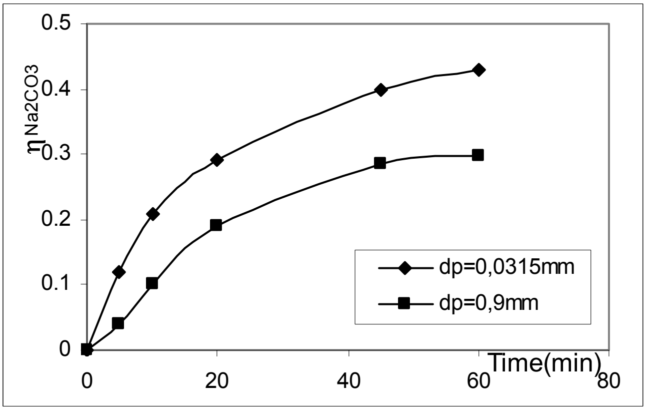

Figure 2. Kinetic curves conversion vs. time for different Na_2CO_3 diameters at C_{SO2}=0.5%, T=473 K and G_v=1.55 x 10^{-4} m^3/s.

To establish the mechanism of the desulphurization process the kinetic data presented in Figure 1 are processed using the *horizontal section method.* In accordance with this method for a constant conversion, the relative constant rate of the process k can be written as Equation (3) shows:

$$\bar{k} = \frac{1}{\tau} \qquad (3)$$

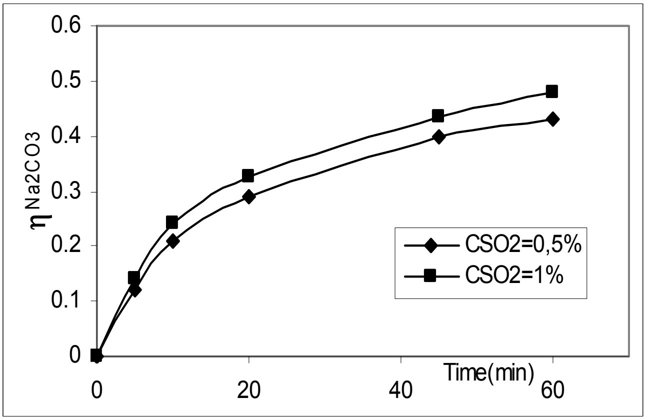

Figure 3. Kinetic curves conversion vs. time for d_{Na2CO3} = 31.5 μm at T=473 K, G_v=1.55 x 10^{-4} m^3/s and different SO_2 concentrations.

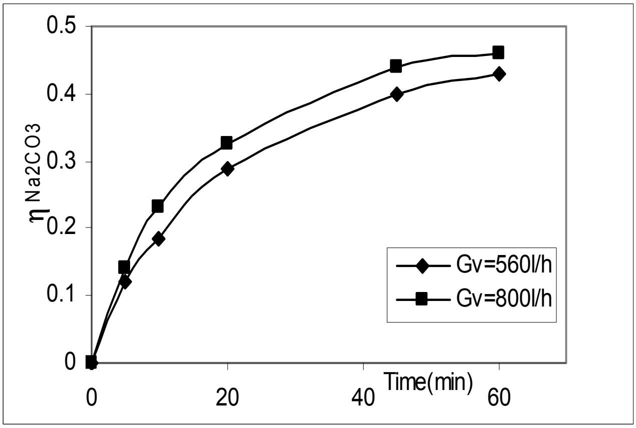

Figure 4. Kinetic curves conversion vs. time for d_{Na2CO3} = 31.5 μm at T=473 K, c_{SO2}=0,5% and different gas flow rates.

Considering the influence of the temperature on the constant rate k (Arrhenius Equation 4), and processing the kinetic curves in ln k – 1/T coordinates, a linear Arrhenius dependence at different sulfation degree can be obtained (Figure 5). From the slope (-Ea/R), the activation energy Ea can be determined:

$$k = k_0 \cdot e^{-\frac{Ea}{RT}} \tag{4}$$

$$\ln k = \ln k_0 - \frac{E_a}{R} \cdot \frac{1}{T} \tag{5}$$

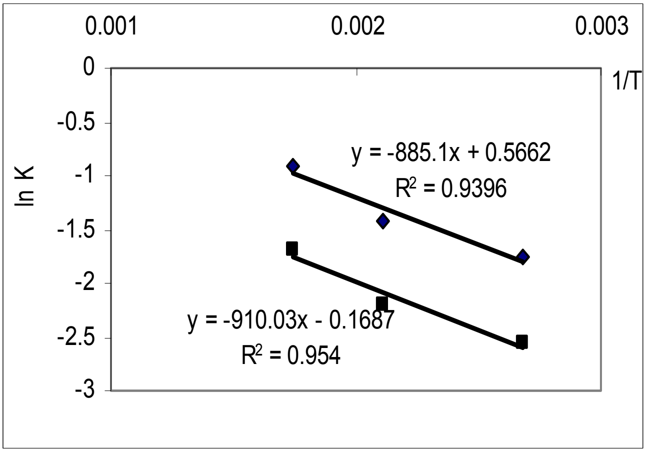

Figure 5. Determination of activation energy for particles of 31.5 µm at C_{SO2}=0.5 %, Gv=1.55 x 10^{-4} m^3/s at η_{Na2CO3}=0.1 and η_{Na2CO3}=0.2.

The activation energy values are in the range from 4.234 KJ/mol to 12.275 KJ/mol. These values indicate that mass transfer phenomena influenced the rate of the overall process, the diffusion through the solid product layer being the rate determining step [7].

Table 1. Activation energy values

d_p (mm)	w (m/s)	η_{Na2CO3}	E_a (KJ/mol)	$C_{SO2}*10^4$ (mol/l)
0.0315	0.5	0.1	7.325	
		0.2	7.531	2.23
	0.71	0.1	5.440	
		0.2	7.729	
0.0315	0.5	0.1	4.734	
		0.2	5.616	4.46
	0.71	0.1	6.565	
		0.2	12.275	
0.9	0.5	0.1	7.729	
		0.2	8.974	2.23
	0.71	0.1	5.082	
		0.2	7.169	
0.9	0.5	0.1	4.234	
		0.2	8.676	4.46
	0.71	0.1	4.346	
		0.2	5.178	

The kinetic equation which describes the sulfation process can be written as Equation 6 shows:

$$\frac{dn_{SO2}}{S \cdot d\tau} = -D_{ef_{SO2}} \cdot \frac{dc_{SO2}}{dr} \tag{6}$$

where S is the unreacted core surface of radius r:

$$S = 4\pi \cdot r^2 \tag{7}$$

The apparent activation energies are centralized in Table 1.

Considering sodium carbonate to be of spherical and homogeneous solid particles, the shrinking unreacted core model may be applied for the kinetic modeling of desulphurization process.

Combining Equation (6) and (7), as Equation (8) shows, and integrating in two steps, on the grain model theory:

$$\frac{-dn_{SO2}}{d\tau} = -4\pi r^2 \cdot D_{ef_{SO2}} \cdot \frac{dc_{SO2}}{dr} \tag{8}$$

$$\frac{-dn_{SO2}}{d\tau}\left(\frac{1}{r} - \frac{1}{R}\right) = 4\pi D_{ef_{SO2}} \cdot c_{SO2} \tag{9}$$

$$dn_{SO2} = \frac{\rho_{[]_s} \cdot \bar{X}_{Na2CO3}}{M_{Na2CO3}} \cdot 4\pi r^2 dr \tag{10}$$

$$dn_{SO2} = \rho^* \cdot 4\pi r^2 dr \tag{11}$$

Equation (9) becomes:

$$-\rho^*\left(\frac{1}{r} - \frac{1}{R}\right) \cdot r^2 \cdot \frac{dr}{d\tau} = D_{ef_{SO2}} \cdot c_{SO2} \tag{12}$$

or as function of Na_2CO_3-conversion (η_{Na2CO3}):

$$\left[\frac{1}{\left(1 - \eta_{Na2CO3}\right)^{1/3}} - 1\right]\frac{d\eta_{Na2CO3}}{d\tau} = 3 \cdot \frac{D_{ef_{SO2}}}{\rho^* \cdot R^2} \cdot c_{SO2} \tag{12'}$$

The integration of Equation (12) at constant concentration of SO_2, Equation (13) is obtained:

$$\tau = \frac{1}{6} \cdot \frac{\rho^* \cdot R^2}{D_{ef_{SO2}} \cdot c_{SO2}}\left[1 - 3\left(\frac{r}{R}\right)^2 + 2\left(\frac{r}{R}\right)^3\right] \tag{13}$$

or as function of Na_2CO_3-conversion (η_{Na2CO3}):

$$\tau = \frac{1}{6}\frac{\rho^* \cdot R^2}{D_{ef_{SO2}} \cdot c_{SO2}}\left[1 - 3\left(1-\eta_{Na2CO3}\right)^{2/3} + 2\left(1-\eta_{Na2CO3}\right)\right] = \frac{1}{6}\frac{\rho^* \cdot R^2}{D_{ef_{SO2}} \cdot c_{SO2}} F\left(\eta_{Na2CO3}\right) \tag{13'}$$

Equation (13') represents the mathematical model equation for sulfur dioxide diffusion through product layer.

For the validation of the proposed model the function $\tau = F(\eta)$ is shown for d_p=31.5 μm and C_{SO2}=0.5 % in Figure 6.

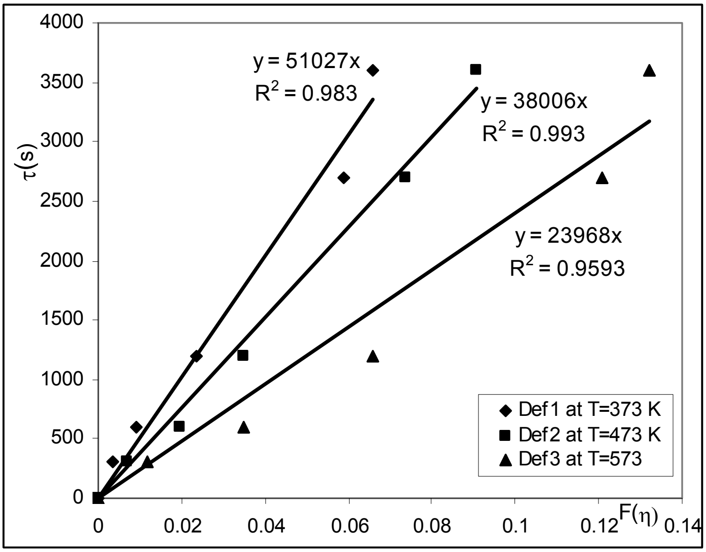

Figure 6. Dependence τ –F (η).

Table 2. D_{efSO2} through the product layer in our work conditions

T (K)	R (m)	Def (m²/s)	C_{SO2} *10⁴ (mol/l)	ρ^*_{Na2CO3} (mol/l)
373 473 573	15.75 x 10^{-6}	2.73 x 10^{-11} 3.67 x 10^{-11} 5.82 x 10^{-11}	2.23	7.53
373 473 573	45 x 10^{-5}	7.0 x 10^{-10} 11 x 10^{-10} 17 x 10^{-10}	2.23	7.53
373 473 573	15.75 x 10^{-6}	1.42 x 10^{-11} 1.98 x 10^{-11} 3.13 x 10^{-11}	4.46	7.53
373 473 573	45 x 10^{-5}	3.0 x 10^{-10} 6 x 10^{-10} 8 x 10^{-10}	4.46	7.53

The obtained values of D_{efSO2} in solid layer with the magnitude of 10^{-11}- 10^{-10} m^2/s are comparable with those founded in the literature [5, 6].

With the obtained slope's lines, the effective diffusion coefficient of SO_2 can be calculated with Equation (14):

$$D_{ef_{SO2}} = \frac{1}{6} \frac{\rho^* \cdot R^2}{6 \cdot c_{SO2} \cdot tg\alpha} \tag{14}$$

The values of the effective diffusion coefficients are centralized in Table 2.

CONCLUSIONS

The kinetic study of the gas desulphurization process with sodium carbonate at low temperature has shown a significant influence of temperature and granule size. A positive effect on sodium carbonate conversion was obtained by increasing the temperature and decreasing the particle size.

The apparent activation energy values evaluated from experimental data are in the range from 4.234 KJ/mol to 12.275 KJ/mol and have shown that the sulphur dioxide diffusion through the solid product layer is rate determining step of the overall process.

The kinetic data were quantitatively analyzed on the basis of the unreacted core model integrated in the general form. The macro kinetic SO_2 diffusion through the solid product layer model was validated and the obtained values of the SO_2 effective diffusion coefficients are comparable with those founded in the literature.

EXPERIMENTAL SECTION

In order to determine the effect of the temperature, grain size and gas flow rate on desulphurization process, the isothermal gravimetric method was used. The experiments were carried out on experimental equipment presented in Figure 7.

The installation contains a hand-made thermo balance, having a 20 mm diameter tubular reactor placed in a tubular electric furnace, with possibilities to operate in temperature range of 373 - 1473 K. The solid reactant, sodium carbonate placed in thin layer on a ceramic nacelle, was introduced in the tubular reactor and the experiments were carried out isothermally at three temperatures (373, 473, 573 K), with diameter of sodium carbonate granules of 31.5 µm and 900 µm and SO_2 concentration of 0.5 % and 1.0 %. The size distribution of solid particles was obtained by sieving of sodium carbonate on a Retzsch set of sieves, mesh between 0 - 1000 µm. Each sample was sulfated in a gas-air mixture containing 0.5 % and 1.0 % (vol.) SO_2, at constant flow rate of $G_v = 560$ l/h and $G_v = 800$ l/h.

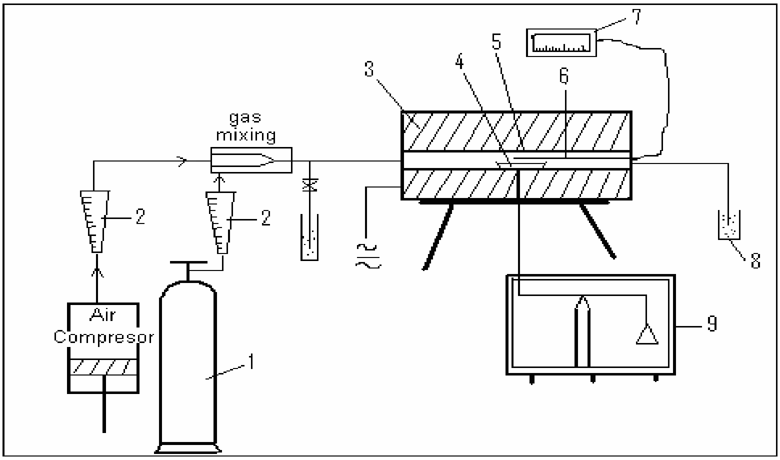

Figure 7. Experimental equipment.

1 - Gas cylinder with SO_2; 2 - Gas flow meter; 3 - Electric Furnace; 4 - Nacelle with solid sample; 5 - Tubular reactor; 6 - Thermocouple; 7 - Temperature controller; 8 - Absorbing vessel for gas; 9 - Thermo balance.

REFERENCES

1. H. Menig, „Emissionsminderung und Recycling – Grundlagen und Technologien", Ecomed Verlag, **1996**, chapter 5.
2. J.C. Mycock, McKenna and L. Theodore, "Handbook of Air Pollution Control Engineering and Technology", CRC Press, Inc, Boca Raton, **1995**.
3. S. Drăgan, *Rev. Chim. Buc.*, **1997**, *48(7),* 755.
4. S. Drăgan, I. Siminiceanu, *Rev. Chim. Buc*, **2004**, *55(11),* 857.
5. T.C. Keener, W.T. Davis, *JAPCA*, **1984**, *34(6)*, 123.
6. T. Kopac, G. Dogu, T. Dogu, *Chem. Eng. Sci.*, **1996**, *51(10)*, 2201.
7. L. Ifrim, C. Calistru, "Procesul tip adsorbtie-reactie-formare si crestere de germeni", Ed. IPI Iasi, **1987**, chapter 4.

STUDIA UNIVERSITATIS BABEŞ-BOLYAI, CHEMIA, XLV, 2, TOM II, 2010

Dedicated to the memory of Prof. dr. Ioan Silaghi-Dumitrescu marking 60 years from his birth

CARBON NANOTUBES-GRAPHITE PASTE ELECTRODE MODIFIED WITH Cu(II)-EXCHANGED ZEOLITE FOR H_2O_2 DETECTION

DELIA GLIGOR[a], CODRUȚA VARODI[b], ANDRADA MĂICĂNEANU[c], LIANA MARIA MUREŞAN[c, *]

ABSTRACT. Modification of a natural zeolite from Macicas (Cluj County, Romania) with copper(II) (Z-Cu), followed by its incorporation in carbon paste, made of carbon nanotubes and graphite powder as conductive matrix (Z-Cu-G-CNT-CPEs), lead to a stable modified electrode. The Z-Cu-G-CNT-CPEs electrodes show significant electrocatalytic activity toward H_2O_2 reduction. The rate constant for catalytic H_2O_2 reduction, estimated from rotating disk electrode measurements, extrapolated to zero H_2O_2 concentration was found to be 74.4 M^{-1} s^{-1} (pH 7). The amperometric detection of H_2O_2, at -400 mV *vs.* Ag/AgCl/KCl_{sat} is characterized by the following electroanalytical parameters: sensitivity of 15.33 mA M^{-1}, detection limit of 0.24 mM and linear domain up to 10 mM H_2O_2.

Keywords: *carbon paste electrodes, zeolite, hydrogen peroxide, carbon nanotubes*

INTRODUCTION

Hydrogen peroxide is an important analyte in food, pharmaceutical, clinical, industrial and environmental analyses [1]. H_2O_2 can be determined using different analytical methods such as: chemiluminometry [2], spectrophotometry [3], titrimetry [4], enzymatic [5], acoustic emission [6] and electrochemical methods [7].

Among the new materials used for H_2O_2 electrochemical detection, zeolite-modified electrodes are of high interest, due to the fact that zeolites offer the most complete range of interesting properties required at an electrochemical interface [8]. These properties can be greatly improved by metal ions incorporation, as zeolites are versatile cation-exchangers [9].

---

[a] *Facultatea de Ştiința Mediului, Universitatea Babeş-Bolyai, Str. M. Kogălniceanu Nr. 1, RO-400084 Cluj-Napoca, România*

[b] *Institutul Național de Cercetare Dezvoltare pentru Tehnologie Izotopică şi Moleculară, Str. Donath Nr. 65-103, RO-400293 Cluj-Napoca, România*

[c] *Facultatea de Chimie şi Inginerie Chimică, Universitatea Babeş-Bolyai, Str. Kogălniceanu Nr. 1, RO-400084 Cluj-Napoca, România, * limur@chem.ubbcluj.ro*

In last years, modified electrodes based on carbon nanotubes received considerable attention for determination of H_2O_2, due to the possibility to obtain a good detection limit and a wide linear range [10-13].

The aim of this work was to explore the possibility of using Cu(II)-exchanged zeolitic volcanic tuff (Z-Cu) from Macicas (Cluj County, Romania) containing 70-80% clinoptilolite [14], for preparation of an amperometric sensor for H_2O_2 detection. The electrochemical reduction of H_2O_2 was investigated using a carbon paste electrode based on Cu-modified natural zeolite, incorporated in carbon nanotube-graphite paste conductive matrix. The electrochemical behavior of the modified electrode has been characterized by using cyclic voltammetry at different scan rates and pH values. The electrocatalytic efficiency toward H_2O_2 reduction was estimated, using amperometry and rotating disk electrode measurements.

RESULTS AND DISCUSSION

Electrode material characterization

According to compositional investigations, performed previously, the zeolitic volcanic tuff sample, Macicas (Cluj County), contains 70-80% clinoptilolite, present as tabular crystals. The zeolitic volcanic tuff sample shows a remarkable homogeneity in its mineralogical and chemical composition and has specific surface area of 35 m^2/g [14-16].

Using ESEM technique we were able to analyze the surface morphology (figure 1A) and also to determine surface composition of the zeolitic volcanic tuff sample (figure 1B). Mass percent composition for the elements present is as follows: O-57.08%, Na-0.90%, Al-5.23%, Si-28.96%, K-1.91%, Ca-2.33%; Fe-3.60%. The elements distribution maps (results not shown) indicate a uniform distribution on the solid surface sample.

TEM images of the copper modified zeolite (figure 1C) show darker regions on the surface of the solid samples, which could be attributed to the presence of the metal on the surface. Due to the high concentration of the copper solution used during the modification treatment, part of the metal ions were deposited on the surface and probably transformed in copper oxide during the calcination process. On the TEM images of the electrode material Z-Cu-G-CNT (figure 1D), it is easy to observe the carbon nanotubes as fine lines and the graphite used as a conductive material as black dots on the investigated surface.

As can be observed from figure 2, the electrochemical behavior of Z-Cu-G-CNT-CPEs modified electrodes show a well shaped voltammetric response. In a first attempt, the redox peaks pair ($E^{0'}$ of -165 mV *vs.* Ag/AgCl/KCl_{sat}) for obtained modified electrodes was attributed to cooper ions, immobilized on the natural zeolite.

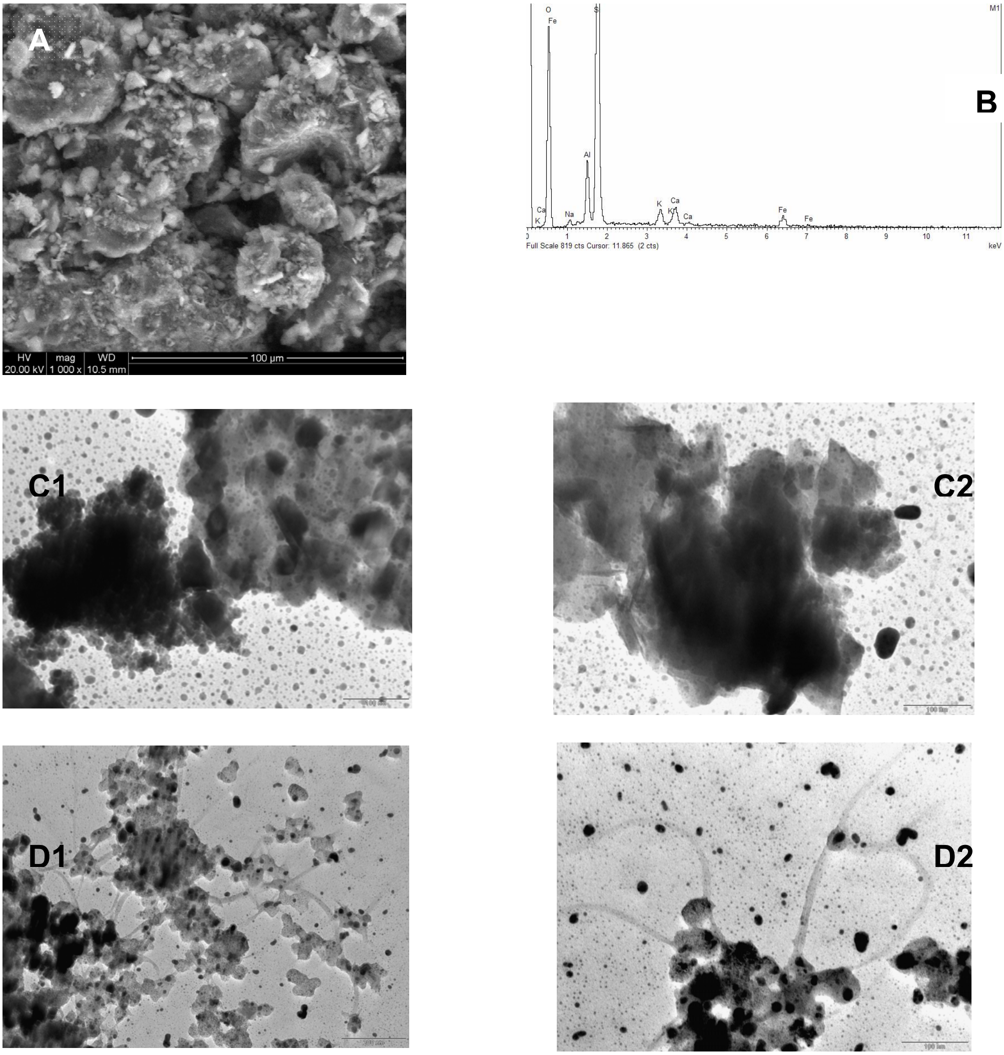

Figure 1. Electron microscopy images of zeolitic volcanic tuff (A), copper(II) modified zeolite (C1, C2) and electrode material (D1, D2). Note: (A) ESEM images; (B) ESEM spectra; (C) TEM images of different regions on copper(II) modified zeolite; (D) TEM images of the same region on Z-Cu-G-CNT material.

The redox response of the Z-Cu-G-CNT-CPEs was affected by pH (results not shown). Indeed, the formal standard potential, $E^{0'}$ (estimated as the average of the cathodic and the anodic peak potentials, recorded in the pH range from 3 to 9), changes with pH. This behavior suggests that the voltammetric response is a combined one, involving oxygen and Cu redox couples.

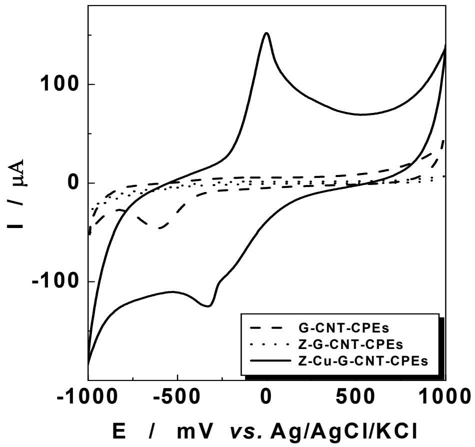

Figure 2. Cyclic voltammograms corresponding to obtained modified electrodes. Experimental conditions: starting potential, -1000 mV *vs.* Ag/AgCl/KCl$_{sat}$; potential scan rate, 10 mV s^{-1}; supporting electrolyte, 0.1 M phosphate buffer, pH 7.

Cyclic voltammetric measurements were performed in a wide range of potential scan rate (from 10 mV s^{-1} to 2 V s^{-1}), when the Z-Cu-G-CNT-CPEs electrodes were in contact with phosphate buffer solutions of different pH values (from 3 to 9). The slopes of the log–log peak current *vs*. potential scan rate dependence were close to 0.5 (Table 1), indicating the existence of a diffusion process of ions from zeolite to electrode surface, combined with the diffusion of counterions from solution, in order to maintain the electroneutrality.

Table 1. Parameters of the log-log linear regression corresponding to the peak current dependence on the potential scan rate for Z-Cu-G-CNT-CPEs. Experimental conditions: as in figure 2.

pH	**Slope**		**R/N**	
	oxidation	**reduction**	**oxidation**	**reduction**
3	0.61 ± 0.005	0.67 ± 0.02	0.999 / 12	0.993 / 12
5	0.75 ± 0.01	0.71 ± 0.01	0.999 / 7	0.999 / 7
7	0.44 ± 0.01	0.77 ± 0,03	0.997 / 11	0.994 / 9
9	0.67 ± 0.04	0.89 + 0.29	0.984 / 7	0.833 / 6

From the dependence of the peak potentials on the potential scan rate (results not shown), the heterogeneous electron-transfer rate constant (k$_S$, s^{-1}), for the redox process corresponding to Z-Cu-G-CNT-CPEs electrode was estimated to be 0.31 s^{-1} at pH 7 (figure 3A) using the Laviron treatment [17].

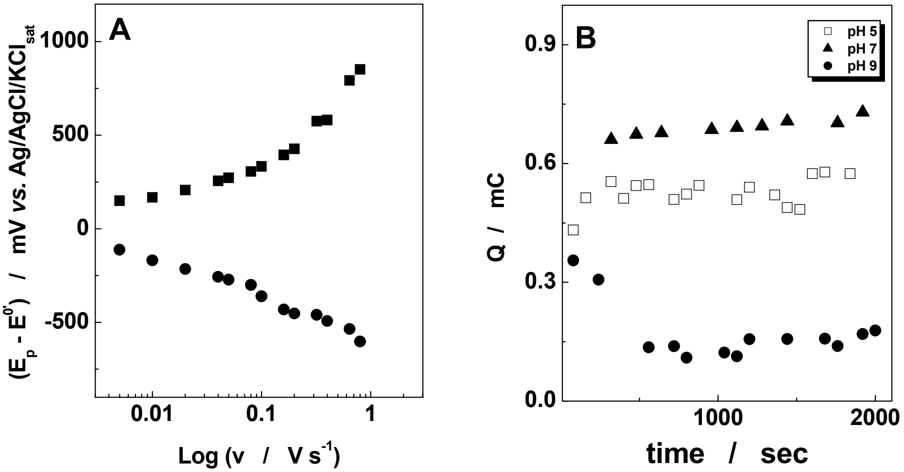

Figure 3. Experimental dependence of (Ep - $E^{o'}$) *vs.* logarithm of the scan rate (A) and time dependence of the charge amount (B) for Z-Cu-G-CNT-CPEs. Experimental conditions: scan rate, 50 mV s^{-1}; potential range, -1000 to 1000 mV *vs.* Ag/AgCl/KCl$_{sat}$.

The stability of the Z-Cu-G-CNT-CPEs electrodes was examined by continuous cycling of the electrode potential within the range covering the Z-Cu-G-CNT-CPEs redox activity, at different pH values of the surrounding solution, and the corresponding cyclic voltammograms were recorded. During such experiments, the charge amount (Q) involved in the redox process slightly decreases (figure 3B), while the shape of the voltammograms remained invariant (results not shown), except when the supporting electrolyte was pH 9. The best electrochemical stability was obtained at pH 7, which is the most used pH value for amperometric sensors for H_2O_2 detection. Considering that the decrease of the charge amount obeys zero order kinetics, the deactivation rate constant of the electrode response was estimated at pH 7 ($3.50\ 10^{-8}$ C s^{-1}). This very low value proves at the same time, that copper is strongly retained in the zeolite framework and it has high electrochemical stability.

Comparing the cyclic voltammograms recorded in phosphate buffer (pH 7) for a Z-Cu-G-CNT-CPEs electrode, in the absence and in the presence of 5 mM and 10 mM H_2O_2 (figure 4A), a good electrocatalytic activity for H_2O_2 reduction is shown. The Z-Cu-G-CNT-CPEs electrodes exhibit significant electrocatalytic efficiency, characterized by: (i) the decrease in overpotential for H_2O_2 reduction (~200 mV, estimated as the difference between the cathodic peak potentials observed on the Z-Cu-G-CNT-CPEs electrode and on Z-G-CNT-CPEs electrode); (ii) the electrocatalytic efficiency is improved when Cu-exchanged zeolite is used (63.2 for the Z-Cu-G-CNT-CPEs and 34.7 for

Z-G-CNT-CPEs, estimated as the ratio $((I_{peak})_{[H2O2]=5mM} - (I_{peak})_{[H2O2]=0})/(I_{peak})_{[H2O2]=0}$, at an applied potential of -400 mV *vs*. Ag/AgCl/KCl$_{sat}$). This good electrocatalytic activity is due to the presence of a high quantity of copper in the zeolite structure (1.9515 mg Cu^{2+}/g zeolite), knowing that copper is an efficient mediator for H_2O_2 reduction.

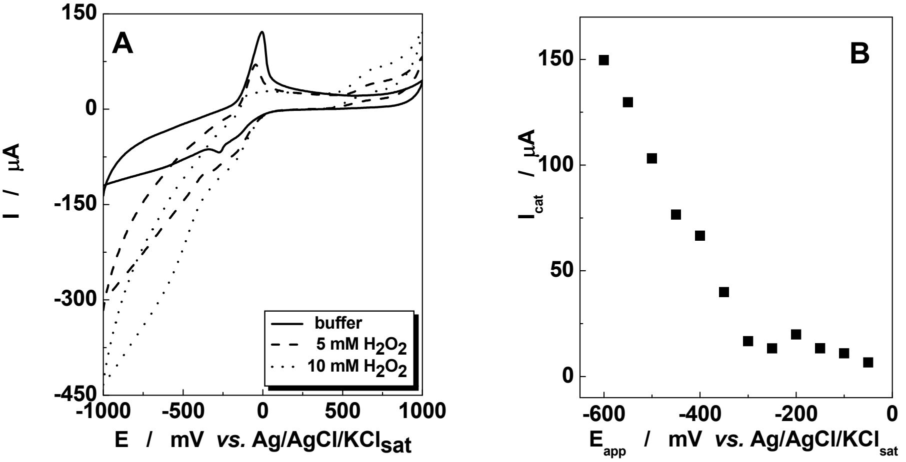

Figure 4. (A) Electrocatalytic activity of Z-Cu-G-CNT-CPEs electrode for H_2O_2 reduction, in absence and in presence of H_2O_2. Experimental conditions: starting potential, −1000 mV *vs*. Ag/AgCl/KCl$_{sat}$; scan rate, 10 mVs^{-1}; supporting electrolyte, 0.1 M phosphate buffer (pH 7.0).
(B) Effect of the applied potential on the electrocatalytic current recorded at Z-Cu-G-CNT-CPEs electrode, in presence of 5 mM H_2O_2. Experimental conditions: supporting electrolyte, 0.1 M phosphate buffer (pH 7.0); rotation speed, 800 rpm.

Rotating disk electrode measurements were employed to investigate the kinetics of the electrocatalytic reduction of H_2O_2 on the Z-Cu-G-CNT-CPEs electrodes. First, in order to find the optimal applied potential, its effect on the reduction electrocatalytic current was examined (figure 4B). Consequently, for all further measurements, the applied potential selected was -400mV *vs*. Ag/AgCl/KCl$_{sat}$.

Using the Koutecky–Levich treatment, applied for H_2O_2 reduction kinetics, the observed rate constants for H_2O_2 electrocatalytic reduction (k_{obs}) were evaluated at different H_2O_2 concentrations, at pH 7. The linear dependence between $1/I_{cat}$ and $1/\omega^{1/2}$ allowed calculation of k_{obs} values at different H_2O_2 concentrations. Supposing that the reduction reaction of H_2O_2 at the Z-Cu-G-CNT-CPEs obeys Michaelis–Menten kinetics, a plot of the reciprocal value of the observed rate constant *vs*. H_2O_2 concentration, results in a straight line (results not shown). From the slope and the intercept of this straight line, the extrapolated values of k_{obs} to zero H_2O_2 concentration ($k_{obs,\ [H2O2]\ =\ 0}$ = 74.4 M^{-1} s^{-1}, for Γ = $2.5\cdot10^{-7}$ mol cm^{-2}), the apparent Michaelis–Menten constant (K_M = 1.1 mM) and the turnover number for the electrocatalytic reaction (k_{+2} = 0.08 s^{-1}) were estimated.

Finally, using amperometric measurements, performed in the optimal experimental conditions mentioned above, the amperometric response of Z-Cu-G-CNT-CPEs to increasing concentrations of H_2O_2 was recorded. By plotting the steady-state current values *vs.* H_2O_2 concentration, two calibration curves were obtained at -400 and -150 mV *vs.* Ag/AgCl/KCl_{sat} (figure 5).

As can be seen from figure 5, the kinetic parameters are better when the applied potential was -400 mV *vs.* Ag/AgCl/KCl_{sat}. By fitting the amperometric calibration curve to Michaelis–Menten equation, the following kinetic parameters were found: K_M = 60.51 mM and I_{max} = 920 μA. At the same time, the electroanalytical parameters of Z-Cu-G-CNT-CPEs electrodes for H_2O_2 determination were estimated: the sensitivity (calculated as I_{max}/K_M ratio) was 15.33 mA M^{-1}; the linear range was up to 10 mM; the detection limit was 0.24 mM (signal to noise ratio of 3); the response time was less than 10 s. It can be observed that this detection limit is improved by using cooper in comparison with other modified electrodes that used carbon nanotubes [13].

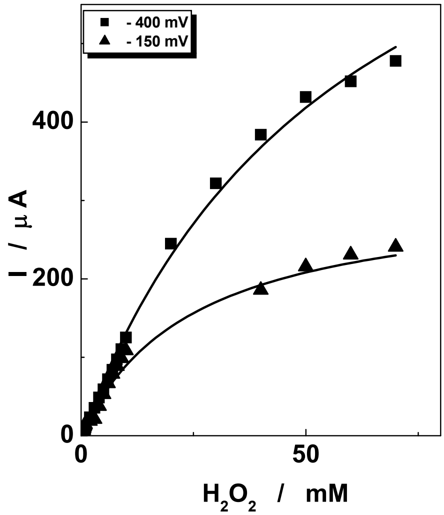

Figure 5. Calibration curves for H_2O_2 of Z-Cu-G-CNT-CPEs electrodes. Experimental conditions: applied potential, -400 mV and -150 mV *vs.* Ag/AgCl/KCl_{sat}; supporting electrolyte, 0.1 M phosphate buffer (pH 7.0); rotation speed, 800 rpm.

CONCLUSIONS

A new electrocatalytic system for mediated reduction of H_2O_2 based on carbon paste electrodes modified with a Cu-exchanged zeolite, using carbon nanotubes and graphite powder is proposed and investigated from physical-chemical, electrochemical and electrocatalytic point of view. Under operation in optimal conditions, the Z-Cu-G-CNT-CPEs electrodes exhibit a good electrochemical stability at pH 7 and electrocatalytic efficiency towards H_2O_2 reduction.

EXPERIMENTAL SECTION

Chemicals

Single-walled carbon nanotubes (CNT) were obtained from Sigma (St. Louis, MO, USA), graphite powder and paraffin oil from Fluka (Buchs, Switzerland) and hydrogen peroxide, $K_2HPO_4{\cdot}2H_2O$ and $KH_2PO_4{\cdot}H_2O$ from Merck (Darmstadt, Germany). NaCl, $Cu(SO_4)_2{\cdot}5H_2O$, ammonium solution 25% were purchased from Reactivul Bucharest.

All reagents were of analytical grade and used as received. The supporting electrolyte was 0.1 M phosphate buffer solution, obtained by mixing appropriate solutions of $K_2HPO_4{\cdot}2H_2O$ and $KH_2PO_4{\cdot}H_2O$.

Preparation of modified zeolite

A zeolitic volcanic tuff sample from Macicas (Cluj County), Z, granulation d < 0.2 mm, brought in –Na form was contacted with a solution containing copper in order to obtain the required modification.

Certain stages were involved in the zeolitic volcanic tuff preparation. First, solid samples were subjected to a mechanical treatment consisting of crushing, grinding and size separation. Next, samples were washed with distilled water and dried. A chemical treatment consisting of a contact with an alkaline solution, NaCl, pH 10, followed. After this last treatment, the zeolitic volcanic tuff sample was washed again with distilled water, until chlorine ions were no more detected in the washing water, and dried. [15] The zeolitic volcanic tuff sample is now prepared for the next stage, the ionic exchange with the desired metallic ion, in our case copper. The established quantity of zeolitic volcanic tuff prepared as described above, was brought in Z-Cu form using a $CuSO_4{\cdot}5H_2O$ 0.5N solution. The ionic exchange process (Na^+ ions from the zeolite structure were replaced with Cu^{2+} ions from aqueous solution) was realised in a batch reactor with solid and liquid phases as immobile phases, using a solid: liquid ratio of 1:10. Solid and solution were kept in contact for 24 hours. After this time interval, the copper modified zeolitic volcanic tuff sample was separated by filtration, dried for 6 hours at 105°C and then roasted at 400°C for 4 hours. In this way was obtained the M-Cu modified zeolitic volcanic tuff, containing 1.9515 mg Cu^{2+}/g zeolite. The initial and final concentrations of copper ions in solution, used to establish the quantity of copper retained in the zeolitic volcanic tuff sample, were determined using a JENWAY 6305 spectrophotometer, 25% ammonium solution at $\lambda = 440$ nm.

Electrode Preparation

The modified electrodes, Z-G-CNT-CPEs and Z-Cu-G-CNT-CPEs were prepared by hand mixing the unmodified or modified zeolites with CNTs, graphite powder (2:1:1, w/w) and paraffin oil. The resulting pastes were packed into a cavity at the end of a Teflon tube. Electrical contact was established *via* a copper wire connected to the paste. The electrode surface was smoothed by rubbing on a filter paper just prior to use.

Physical-chemical and electrochemical measurements

Zeolitic volcanic tuff samples morpholgy was investigated using environmental scanning electron microscopy (ESEM, INCAx-sight 6427 Oxford Instruments) and transmision electron microscopy (TEM, Jeol JEM1010 with a MegaViewIII CCD camera - SIS-Olympus). Using ESEM techniques we also could determine the superficial composition of the zeolitic volcanic tuff sample.

Electrochemical experiments were carried out using a typical three-electrode electrochemical cell. The modified carbon paste electrode was used as working electrode, a platinum ring as counter electrode and an $Ag/AgCl/KCl_{sat}$ as reference electrode. Cyclic voltammetry experiments were performed on a PC-controlled electrochemical analyzer (Autolab-PGSTAT 10, EcoChemie, Utrecht, The Netherlands).

Steady state amperometric measurements at different rotating speeds of the working electrode were performed using an EG&G rotator (Radiometer) and the same carbon paste as disk material. The current–time data were collected using the above-mentioned electrochemical analyzer.

Batch amperometric measurements at different H_2O_2 concentrations were carried out at an applied potential of -400 mV *vs.* $Ag/AgCl/KCl_{sat}$, under magnetic stirring, using 0.1 M phosphate buffer solution as supporting electrolyte. The current-time data were collected using the above-mentioned electrochemical analyzer.

The pH of the phosphate buffer solutions was adjusted using NaOH or H_3PO_4 and a pH-meter (HI255, Hanna Instruments, Romania), with a combined glass electrode.

The experimental results are the average of at least three identically prepared electrodes, if not otherwise mentioned.

ACKNOWLEDGMENTS

This work was supported by CNCSIS –UEFISCSU, project number PNII – IDEI 512/2007.

REFERENCES

1. C.-L. Wang, A. Mulchandani, *Analytical Chemistry*, **1995**, *67*, 1109.
2. S. Hanaoka, J.M. Lin, M. Yamada, *Analytica Chimica Acta*, **2001**, *426*, 57.
3. J.M. Fernandez-Romero, M.D. Luque de Castro, *Analytical Chem*istry, **1993**, *65*, 3048.
4. E.C Hurdis, J. Hendrik Romeyn, *Analytical Chemistry*, **1954**, *26*, 320.
5. C. Ruan, R. Yang, X. Chen, J. Deng, *Journal of Electroanalytical Chemistry*, **1998**, *455*, 121.
6. P.D. Wentzell, S.J. Vanslyke, K.P. Bateman, *Analytica Chimica Acta*, **1991**, *246*, 43.
7. Y. Yang, S. Mu, *Biosensors & Bioelectronics*, **2005**, *21*, 74.
8. A Walcarius, *Analytica Chimica Acta,* **1999**, *388*, 79.
9. A. Walcarius*, Analytica Chimica Acta,* **1999**, *384*, 1.
10. V. Vamvakaki, N. A. Chaniotakis, *Sensors and Actuators B*, **2007**, *126*, 193.
11 .Q. Zhao, Z. Gan, Q. Zhuang, *Electroanalysis*, **2002**, *14*, 1609.
12. J. Li, J.-D. Qiu, J.-J. Xu, H.-Y. Chen, X.-H. Xia, *Advanced Functional Materials*, **2007**, *17*, 1574.
13. J. Kruusma, V. Sammelselg, C. E. Banks, *Electrochemistry Communications*, **2008**, 10, 1872.
14. H. Bedelean, A. Măicăneanu, S. Burcă, M. Stanca, *Studia Universitatis Babeş-Bolyai, Geologia*, **2010**, *55*, 9.
15. H. Bedelean, M. Stanca, A. Măicăneanu, S. Burcă, *Studia Universitatis Babeş-Bolyai, Geologia*, **2006**, *51*, 43.
16. A. Măicăneanu, H. Bedelean, M. Stanca, “Zeoliţii naturali. Caracterizare şi aplicaţii în protecţia mediului”, Editura Presa Universitară Clujeană, Cluj-Napoca, **2008**, chapter 3.
17. E. Laviron, *Journal of Electroanalytical Chemistry*, **1979**, *101*, 19.

STUDIA UNIVERSITATIS BABEŞ-BOLYAI, CHEMIA, XLV, 2, TOM II, 2010

Dedicated to the memory of Prof. dr. Ioan Silaghi-Dumitrescu marking 60 years from his birth

BEHAVIOR OF MIXED DMPC-CHOLESTEROL MONOLAYERS AT THE AIR/WATER INTERFACE

AURORA MOCANU[*], ROXANA-DIANA PAŞCA, OSSI HOROVITZ,
MARIA TOMOAIA-COTISEL

ABSTRACT. The phase behaviour of cholesterol (CHO) and dimyristoyl phosphatidyl choline (DMPC) monolayers at the air/water interface was investigated by surface pressure measurements using Langmuir technique. Compression isotherms and isobars as functions of composition were represented, and the surface compressibility modulus was calculated, in order to characterize the physical states of the monolayers. At a constant lateral surface pressure, the monolayers were transferred by Langmuir-Blodgett technique (LBT) from air-water interface on solid supports and further studied by atomic force microscopy (AFM). This study shows that the strong interactions between DMPC and CHO lead to well defined two-dimensional nanostructures, which can have practical applications for biosensors fabrication. Also, this type of nanostructures seems plausible to occur in natural membranes and thus, can influence the protein distribution and protein function *in vivo*.

Keywords: *cholesterol, DMPC, monolayers, Langmuir-Blodgett technique, atomic force microscopy*

INTRODUCTION

Phospholipids and cholesterol are the primary constituents of vertebrate cell membranes [1, 2] and their interaction is important for the membrane organization and properties [3-5]. Possible interactions are hydrogen bonds between the cholesterol OH-group and carbonylic oxygen atoms of the phospholipid DMPC (Scheme 1) and van der Waals forces [6].

An approach to the understanding of these interactions is the investigation of the organization of such biomolecules at the air/aqueous solution interfaces in the two-dimensional monomolecular layers, at controlled lateral surface pressures. These monolayers are realized by spreading and compressing the biomolecules at the air/water interface [7-9]. Dimyristoyl

---

[*] *Babeş-Bolyai University, Faculty of Chemistry and Chemical Engineering, Arany Janos 11, 400028 Cluj-Napoca, Romania, mcotisel@chem.ubbcluj.ro*

phosphatidyl choline (DMPC) is a typical biomolecule forming highly ordered monolayers [10-12]. The DMPC molecules can be spread, compressed and oriented at the air/water interface at various lateral surface pressures to form DMPC monolayers of close-packed polar groups within the interfacial water having the hydrocarbon chains oriented into the air phase. The interaction of phospholipids with sterols was studied both in films at the air/water interface [5, 6, 13-16] and on solid support, by AFM techniques [17, 18].

In the present paper, we have chosen cholesterol (CHO) and DMPC (Scheme 1) to be investigated in monolayers, which are considered as membrane models, for a better understanding of their surface behavior in mixed films.

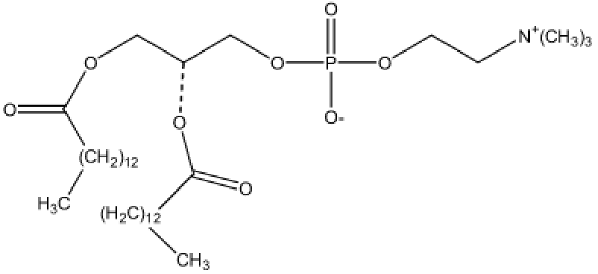

a.

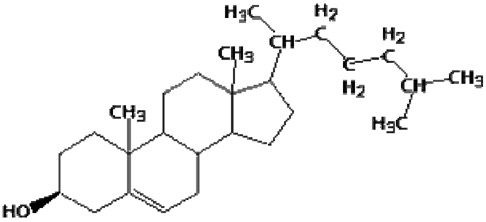

b.

Scheme 1. Chemical structures of DMPC (a) and cholesterol (b).

RESULTS AND DISCUSSION

The *compression isotherms* measured for DMPC, cholesterol and their mixtures at different ratios are represented as surface pressure, π, *versus* area per molecule, A (Fig. 1). Surface pressure is defined as the difference between the surface tension at the air/water interface, σ_0, and the surface tension, σ, at the same interface in the presence of the investigated monolayer:

$$\pi = \sigma_0 - \sigma \tag{1}$$

The mole fractions of cholesterol (x_{CHO}) in the mixed monolayers varied from 0.1 to 0.9 (step value 0.1). It is evident that all compression isotherms are shifted towards left (smaller areas per molecule) with increasing x_{CHO} values, *i.e.* a condensing effect of cholesterol is manifested.

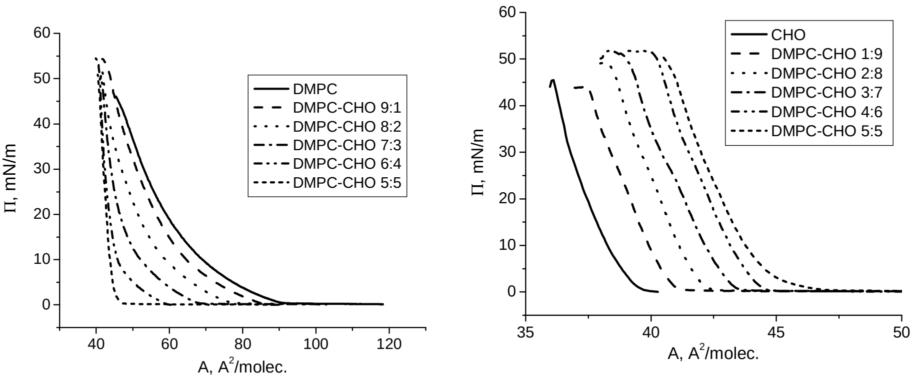

Figure 1. Representative compression isotherms for DMPC and DMPC-CHO mixed monolayers with $x_{CHO} \leq 0.5$ (a), and for CHO and DMPC-CHO mixed monolayers with $x_{CHO} \geq 0.5$ (b).

The differences in the collapse pressures (the highest lateral surface pressure for monolayer stability) for the various monolayers are also visible in these isotherms. While for the pure DMPC and CHO the values are the lowest (about 46 mN/m for DMPC, respectively 42 mN/m for CHO), the mixed monolayers present higher collapse pressures.

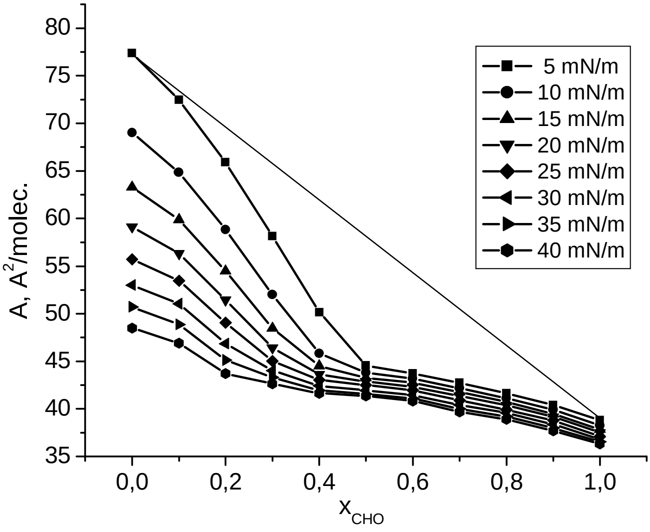

Figure 2. Mean molecular areas *vs.* cholesterol mole fractions in DMPC-CHO mixed monolayers at the surface pressures given in the inset.

A proof for the condensing effect of cholesterol in the mixed monolayers is given by the representation of mean areas per molecule, A, against the mixture composition, x_{CHO}, at constant values of the surface pressure, π. Such *isobars* are given in Fig. 2 for π-values from 5 up to 40 mN/m. This condensing effect, i.e. negative deviations from the mixing rule, represented by a straight line connecting the points for pure components (as the solid line given in Fig. 2 for π = 5 mN/m), is most pronounced for small values of the surface pressure, and it is maintained even with the highest lateral surface pressures.

This condensing effect of cholesterol, and therefore the higher packing density of mixed DMPC-CHO monolayers, can be ascribed to the attracting van der Waals forces and the hydrogen bondings between the phospholipids and cholesterol, stabilizing these mixed structures [13, 19-21] and inducing a chain ordering.

Isothermal compressibility of a monolayer is defined by:

$$C_s = -\frac{1}{A}\left(\frac{\partial A}{\partial \pi}\right)_T \tag{2}$$

Its reciprocal value, the surface compressibility modulus:

$C_s^{-1} = -A\left(\frac{\partial \pi}{\partial A}\right)_T$ (2a) the surface correspondent of the bulk modulus, $K = -V\left(\frac{\partial p}{\partial V}\right)_T$, is a measure of the interfacial elasticity and a characteristic for the variations in the physical state of the monolayers. The isothermal compressibility was calculated from the compression isotherms $\pi = f(A)_T$ in Fig. 1, by graphical derivation. Representations of surface pressures against C_s^{-1} values are given in Fig. 3.

In each case, the values of C_s^{-1} are roughly growing with increasing surface pressure, and reach a maximum for a surface pressure corresponding to the high packing in the monolayers before collapse. DMPC and mixed DMPC-CHO monolayers for $x_{CHO} \leq 0.2$ present the lowest and cholesterol (at least for high π-values) the highest C_s^{-1} values for the same surface pressure, while mixed monolayers show intermediate values. For cholesterol mole fractions above 0.5 the differences between mixed layers and pure cholesterol are diminished.

This surface compressibility modulus C_s^{-1}, is considered to be an indicator for the physical state of the monomolecular film [22]. When these values pass beyond 100 mN/m, the layer should attain the liquid-condensed (LC) state, whereas values above 250 mN/m suggest the presence of the solid state, implying a close packing of the hydrocarbon chains [6]. Applying this criterion, all the mixed DMPC-CHO monolayers can pass by compression in the LC state, and even in the solid state, for various compositions with a higher cholesterol content ($x_{CHO} \geq 0.4$).

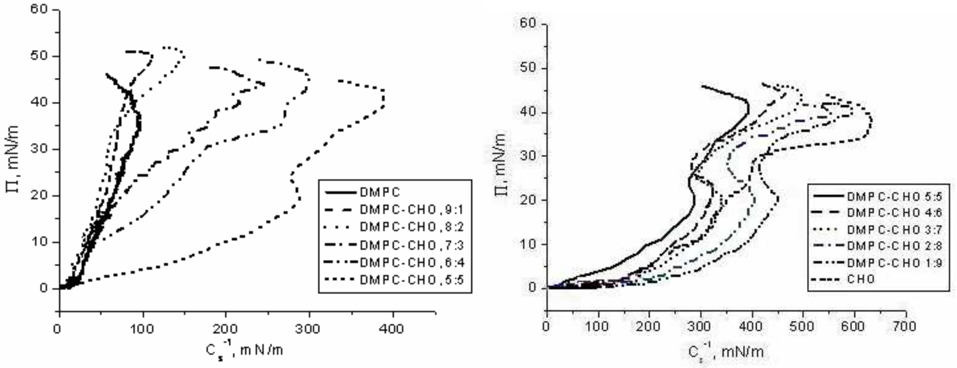

a. b.

Figure 3. Surface pressure *versus* reciprocal isothermal compressibility for DMPC and DMPC-CHO mixed monolayers with $x_{CHO} \leq 0.5$ (a), and for CHO and DMPC-CHO mixed monolayers with $x_{CHO} \geq 0.5$ (b).

A representation of the surface pressures at which film collapse occurs, as seen in the compressibility isotherms (Fig. 1), against the cholesterol content of the DMPC-CHO mixtures (Fig. 4) shows a maximum for cholesterol mole fractions between 0.4 and 0.5, thus the most stable monolayers are obtained for these compositions.

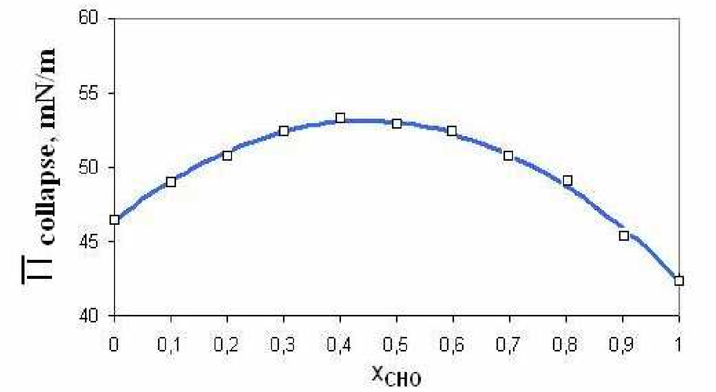

Figure 4. Surface pressures at film collapse *versus* cholesterol content in binary DMPC-CHO mixed monolayers.

AFM observations were used to complete the picture of DMPC, CHO and mixed DMPC-CHO layers near collapse pressure, transferred on glass surface. Representative AFM results are shown for pure DMPC film, (Fig. 5), pure cholesterol film (Fig. 6) and for one of the DMPC-CHO mixed monolayers, corresponding to a cholesterol mole fraction x_{CHO} =0.8 (Fig. 7).

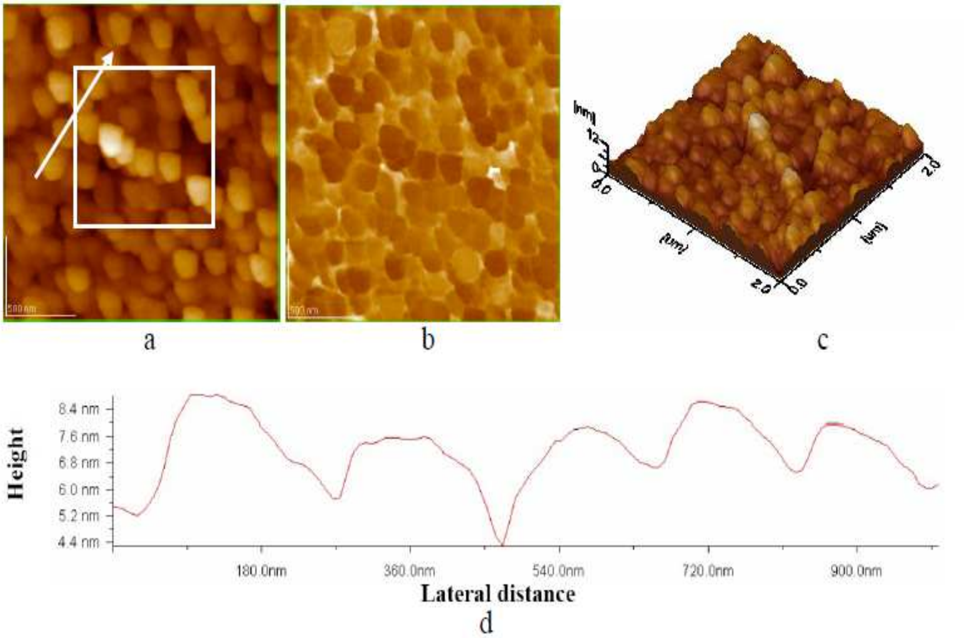

Figure 5. AFM images of DMPC film on optical polished glass near the collapse ($\pi_{collapse}$ = 46 mN/m). Scanned area 2 μm x 2 μm. a) 2D- topography; b) phase image; c) 3D-topography; d) profile of the cross-section along the arrow in panel a.

The 2D- and 3D-topography images (Fig. 5-7a and c) reveal nanostructures of high domains, up to 12 nm for DMPC (Fig. 5c) and the mixed layer (Fig. 7c) and to 10 nm for cholesterol (Fig. 6c). Most of these structures present an apparent height, as seen in the profiles of cross-sections, of about 8 or 9 nm for pure DMPC (Fig. 5 d) and the mixed film (Fig. 7d) and 5 – 6 nm for the cholesterol film (Fig. 6d). The phase (Fig. 5b, 6b) and the amplitude (Fig. 7b) images appear to be complementary to the topographic ones, showing the structural features of the monolayers. The size of the domains appears to be up to about 200 nm (Figs. 5d-7d).

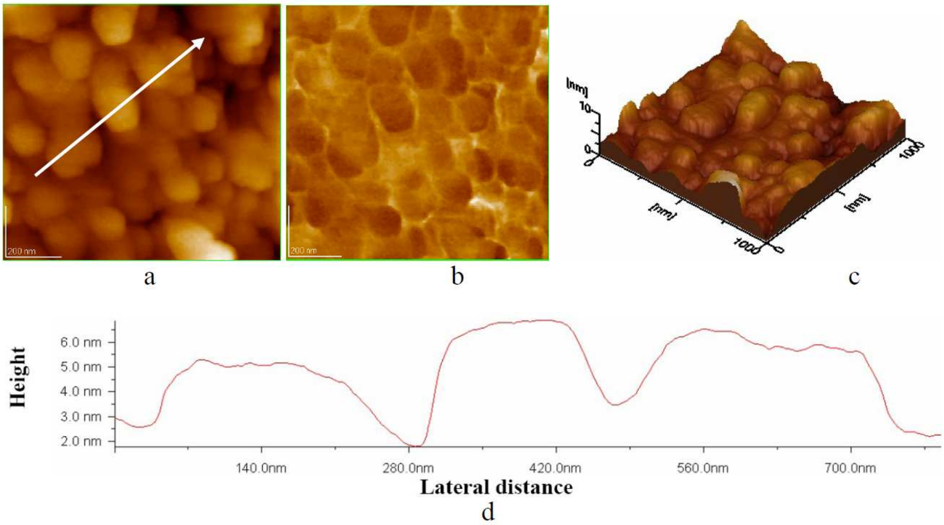

Figure 6. AFM images of cholesterol film on optical polished glass at collapse ($\pi_{collapse}$ = 42 mN/m). Scanned area 1 μm x 1 μm. a) 2D- topography; b) phase image; c) 3D-topography; d) profile of the cross-section along the arrow in panel a.

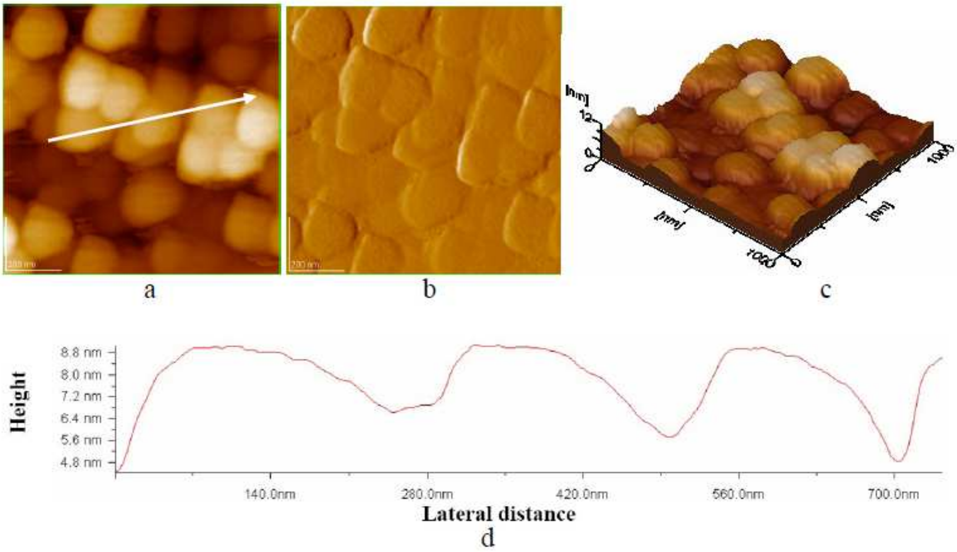

Figure 7. AFM images of a mixed DMPC-cholesterol film (x_{CHO} = 0.8) transferred on optical polished glass at $\pi_{collapse}$ = 50 mN/m. Scanned area 1 μm x 1 μm.
a) 2D- topography; b) amplitude image; c) 3D-topography;
d) profile of the cross-section along the arrow in panel a.

CONCLUSIONS

Cholesterol, DMPC and their mixtures containing the two biomolecules in ratios from 9:1 to 1:9 were studied as monolayers at the air/water interface and as Langmuir-Blodgett films transferred on solid glass support. These films are important as membrane models, and their investigation is a step towards the understanding of membrane structure and properties.

From the measured compression isotherms (surface pressure *vs*. molecular area) and isobars (molecular area *vs*. composition at constant surface pressure), the condensing effect of cholesterol in the mixed films with DMPC is clearly evidenced. It results from the chain ordering and the stabilization of the mixed structures, due to hydrogen bonds and van der Waals attractions between cholesterol and DMPC molecules, resulting in a higher packing density. The increased stability for DMPC-CHO mixed films at nearly equimolar ratio is also evidenced by regularities found in the collapse pressure of these films.

From the surface compressibility module of the monolayers, obtained by derivation of the compression isotherms, the physical states of the films (liquid-condensed state and solid state) could be assigned

AFM images of the films transferred on solid surface near their collapse pressure revealed the formation of characteristic nanostructured domains.

EXPERIMENTAL SECTION

1,2-Dimyristoyl-*sn*-glycero-3-phosphocholine (DMPC) and β-cholesterol (CHO) were purchased from Sigma (Saint Louis, USA) and used without further purification. Benzene (>99.8%) was a product of Lach-Ner (Czech Republic), hexane (>99%) and ethanol (>99.5%) were purchased from Merck (Germany). All organic solvents used were analytical grade reagents. Ultra pure water with a resistivity greater than 18 MΩcm, obtained from an Elga apparatus was used in all experiments. Its pH was 5.5 and its surface tension was superior to 71.8 mN/m at 25℃. All glas sware was cleaned with sulfochromic mixture and then abundantly rinsed with the distilled water. Optically polished glass was used as solid support in the deposition process, after cleaning with sulfochromic mixture followed by rinsing with deionized water.

Surface pressure vs. area per molecule isotherms were recorded using KSV LB Standard Trough (KSV Ltd., Finland) controlled by KSV-5000 software and equipped with two movable barriers, a Wilhelmy balance, and a dipper for monolayers transfer from air/water interface to solid support. A Teflon trough with effective area of 765 cm^2 was used in all experiments; the volume of the subphase was 1500 cm^3. Deionized highly purified water was used as the subphase. Before each measurement, the subphase surface was cleaned by sweeping and suction processes.

The spreading solutions used were made in benzene (CHO, ca. 1 mg/ml), ethanol/hexane mixture (2:98, v/v) for DMPC, and by mixing DMPC and CHO at different molar ratios (concentration of mixed solutions of about 1 μmol/ml). The organic solutions were spread with a Hamilton syringe. After spreading, the solution was left for 10 min for solvent evaporation. The compression of the monolayer was performed at a rate of 15 mm/min for CHO monolayer, 10 mm/min for DMPC monolayer and 15 mm/min for DMPC:CHO mixtures. All isotherms were recorded upon symmetric compression of the monolayer. For each monolayer composition, measurements were repeated at least three times.

AFM measurements were made on Langmuir-Blodgett (LB) films of DMPC in the absence and in the presence of CHO and on CHO pure films on optically polished glass supports. The vertical LB deposition method was used, at constant lateral surface pressures, near the collapse pressure of the individual monolayer. The measurements were conducted in tapping mode on the scanning probe microscope (AFM–JEOL 4210, Japan). The calibration of the AFM scanner was checked by imaging freshly cleaved highly oriented pyrolytic graphite (HOPG) and muscovite mica samples. Non-contact conical shaped tips of silicon nitride coated with aluminum were used. The tip was on a cantilever with a resonant frequency in the range of 200 - 300 kHz and with a spring constant of 17.5 N/m. We used low scan rates of 1 Hz and high scan rates in the range of 20-30 Hz to detect noise artefacts. The scan angle was also changed in different directions to observe real images from those corresponding to noise. AFM observations are repeated on different areas from 10 μm x 10 μm to 0.5 μm x 0.5 μm of the same LB film. The AFM images were obtained from at least three macroscopically separated areas on each LB film. All images were processed using the standard procedures for AFM. The widths and the thickness variations of the domains were estimated from AFM topographic images and cross-section profiles. AFM images consist of multiple scans displaced laterally from each other in y direction with 256 x 256 pixels. Low pass filtering was performed to remove the statistical noise without to loose the features of the sample. All AFM experiments were carried out under ambient laboratory conditions (about 20^{o}C) as previously reported [23-26].

ACKNOWLEDGMENTS

One of us (Roxana-Diana Paşca) has received financial support for this study from the *Babes-Bolyai University of Cluj-Napoca, Romania* (Programme No. 32/2009).

REFERENCES

1. W. R. Nes, *Lipids*, **1974**, *9*, 596.
2. J. Henriksen, A. C. Rowat, E. Brief, Y. W. Hsueh, J. L. Thewalt, M. J. Zuckermann, J. H. Ipsen, *Biophysical Journal,* **2006**, *90*, 1639.
3. J. Pencer, M. P. Nieh, T. A. Harroun, S. Krueger, C. Adams, J. Katsaras, *Biochimica Biophysica Acta*, **2005**, *1720*, 84.
4. J. Henriksen, J., A. C. Rowat, J. H. Ipsen, *European Biophysics Journal*, **2004**, *33*, 732.
5. M. D Ali, K. H. Cheng, J. Huang, *Proceedings of the Natural Academy of Sciences USA*, **2007**, *104*, 5372.
6. K. Sabatini, J.-P. Mattila, P. K. J. Kinnunen, *Biophysical Journal*, **2008**, *95*, 2340.
7. O. Albrecht, H. Gruler, E. Sackmann, *Journal of Colloid and Interface Sci*ence, **1981**, *79*, 319.
8. V. Vogel, D. Mobius, *Journal of Colloid and Interface Sci*ence, **1988**, *126*, 408.9. M. Tomoaia-Cotisel, Gh. Tomoaia, V. D. Pop, A. Mocanu, O. Cozar, N. Apetroaei, Gh. Popa, *Revue Roumaine de Chimie,* **2005***, 50*, 471.
10. L. Berthelot, V. Rosilio, M. L. Costa, S. Chierici, G. Albrecht, P. Boullanger, A. Baszkin, *Colloids and Surfaces B: Biointerfaces,* **1998**, *11***,** 239.
11. C. A. S. Andrade, N. S. Santos-Magalhães, C. P. de Melo, *Journal of Colloid and Interface Science*, **2006**, *298*, 145.
12. D. Matyszewska, R. Bilewicz, *Colloids and Surfaces A: Physicochemical and Engineering Aspects*, **2008**, *321*, 11.
13. P. Dynarowicz-Latka, K. Hac-Wydro, *Colloid Surfaces B: Biointerfaces*, **2004**, *37*, 21.
14. Y. Tagami, T. Narita, H. Ikigai, Y. Oishi, *Colloids and Surfaces A: Physicochemical and Engineering Aspects*, **2009**, *347*, 225.
15. B. Korchowiec, M. Paluch, Y. Corvis, E. Rogalska, *Chemistry and Physics of Lipids*, **2006**, *144*, 127.
16. Y. Su, Q. Li, L. Chen, Z. Yu, *Colloids and Surfaces A: Physicochemical and Engineering Aspects*, **2007**, *293*, 123.
17. Y. Tagami, H. Ikigai, Y. Oishi, *Colloids and Surfaces A: Physicochemical and Engineering Aspects*, **2006**, *284*, 475.
18. C. Yuan, L. J. Johnston, *Biophysical Journal*, **2001**, *81*, 1059.
19. Yeagle, P. L., *Biochimica et Biophysica Acta,* **1985**, *822*, 267.
20. E. E. Berring, K. Borrenpohl, S. J. Fliesler, A. Barnoski Serfis, *Chemistry and Physics of Lipids*, **2005**, *136*, 1.
21. K. Kim, C. Kim, Y. Byun, *Langmuir*, **2001**, *17*, 5066.
22. J. T. Davies, E. K. Rideal, “Interfacial Phenomena”, 2nd ed., Academic Press, New York, **1963**.
23. M. Tomoaia-Cotisel, A**.** Tomoaia-Cotisel, T. Yupsanis, G. Tomoaia, I. Balea, A. Mocanu, C. Racz, *Revue Roumaine de Chimie,* **2006***, 51*, 1181.
24. O. Horovitz, G. Tomoaia, A. Mocanu, T. Yupsanis, M. Tomoaia-Cotisel, *Gold Bulletin*, **2007**, *40*, 213.
25. M. Tomoaia-Cotisel, A. Mocanu, *Revista de Chimie (Bucharest),* **2008**, *59*, 1230.
26. A. Mocanu, I. Cernica, G. Tomoaia, L. D. Bobos, O. Horovitz, M. Tomoaia-Cotisel, *Colloids and Surfaces A: Physicochemical and Engineering Aspects*, **2009**, *338*, 93.

STUDIA UNIVERSITATIS BABEŞ-BOLYAI, CHEMIA, XLV, 2, TOM II, 2010

Dedicated to the memory of Prof. dr. Ioan Silaghi-Dumitrescu marking 60 years from his birth

STRUCTURE OF STARCH GRANULES REVEALED BY ATOMIC FORCE MICROSCOPY

MARIA TOMOAIA-COTISEL[a,*], NICOLAE CIOICA[b], CONSTANTIN COTA[b], CSABA RACZ[a], IOAN PETEAN[a], LIVIU DOREL BOBOS[a], AURORA MOCANU[a], OSSI HOROVITZ[a]

ABSTRACT. Atomic force microscopy (AFM) was used to reveal the micro and nanostructure of maize starch granules from Romanian cultivar. The size, shape and surface morphology of the native maize starch granules are shown by AFM observations. Numerous structures, protrusions (particles), pores or depressions and cracks were found on the surface of maize starch granules and they have a broad range of sizes. The occurrence of small spherical protrusions might be related with the highly branched amylopectin molecules in substantial agreement with the amylopectin blocklets model. The larger particles were also visualized, representing different associations of amylopectin and amylose and other granule surface components as previously discussed. The existence of rather smooth regions with low surface roughness and rougher zones on the starch granules is confirmed.

Keywords: *native maize starch, granule surface, supramolecular structuring, atomic force microscopy (AFM)*

INTRODUCTION

Currently, starch is widely used in its native form or after various modifications for plastics and food industry [1], as well as for pharmaceutical products [2, 3] and for orthopaedic implants [4]. The numerous applications of starch intensify the studies on starch granule structure due to the large variability of starch origins [1]. It is known that a differentiation in the starch granule structure and, consequently, in starch properties is related to the starch cultivar. The potential starch source in Romania might be the native maize starch, which is available in large quantities.

---

[a] *Babeş-Bolyai University of Cluj-Napoca, Faculty of Chemistry and Chemical Engineering, Department of Physical Chemistry, 11 Arany Janos Str., 400028 Cluj-Napoca, Romania;* * *mcotisel@chem.ubbcluj.ro*

[b] *INMA, 59 Al. Vaida-Voievod Str., 400436 Cluj-Napoca, Romania*

The surface morphology of granules is important for the characterization of the maize starch used as raw material for various applications, including the manufacturing of biodegradable plastics. In this respect, it is already understood that the starch processing involves many interfacial modifications and the rate of such changes is controlled mainly by the surface structure of granules. The data on the surface properties of Romanian maize starch granules is unavailable yet.

Starch granules are made of polysaccharides, consisting of D-glucose units, linked together into two different macromolecules, namely amylose and amylopectin [5]. Amylose contains an almost linear chain based on α-1,4 linked glucose residues. Its chain configuration is that of single helices. Amylopectin is a highly branched carbohydrate based on both α-1,4 and α-1,6 linkages [6-8]. Amylopectin has crystalline or amorphous structure and amylose is rather amorphous [9].

The amylose/amylopectin ratio in starch granules varies according to the source, the starch from most cereals containing about 20-30% amylose, but there are starches with up to 98% amylopectin, and also high amylose starch with 60-80% amylose [10]. The starch granules from different plants have different dimensions and various shapes, such as spherical, oval, disk, polygonal or rods [11, 12]. In the starch granule, amylose and amylopectin molecules seem to be structured in growth rings [9], while at the surface of the starch granule, a tightly associated amylose and amylopectin network is formed [13, 14]. Therefore, the size, shape and surface morphology of the starch granules are important data to be known for the different practical applications of starches [15-24].

Among the imaging techniques, the atomic force microscopy (AFM) provides an important tool for probing starch granule structure at molecular level. AFM studies have been performed on starch granules for starches from different botanical sources [18, 21, 22, 25-36]. However, the ultrastructure of the starch granules is not completely understood. The advantages of the AFM technique are related to the sample preparation, the ability to image under ambient air conditions, under almost normal structural conditions for the starch granules. The images are obtained as 2D- and 3D-topographies, phase and amplitude (error signals) images. In addition, the atomic force microscopy (AFM) can go to molecular or even atomic resolution (1-2 Å vertical resolution and less than 1 nm lateral resolution) [37-41].

In the present work we provide the micro- and nanostructure data by AFM imaging, such as size, shape and surface morphology, for native maize starch powder spread out in thin films or compacted into tablets.

RESULTS AND DISCUSSION

Size, shape and surface morphology of the starch granules

AFM images of the starch granule surface are obtained, in tapping mode of AFM operation, as two dimensional (2D) and three dimensional (3D) topographies, as amplitude (errors signal) images and phase images. The contrast in the AFM phase imaging makes possible the detection of variations in properties (such as: phase composition, stiffness, elasticity) of the granule surface (periphery).

A selection of AFM images for maize starch granules compacted into a tablet is given in Figures 1-3.

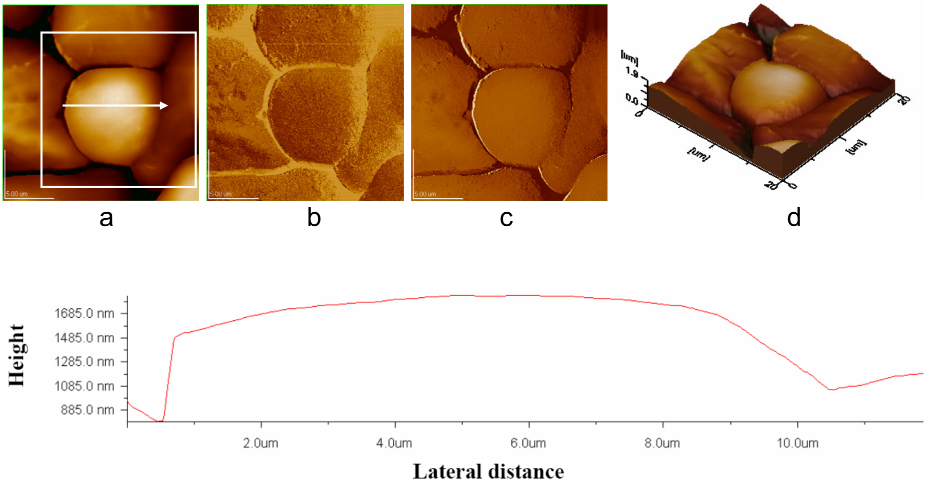

a b c d

e

Figure 1. AFM images of maize starch compacted as a tablet. Scanned area: 20 μm x 20 μm. a) 2D – topography; b) phase image; c) amplitude image; d) 3D-topography; e) profile of the cross-section along the arrow given in panel a.

Figure 1 shows a group of several starch granules with rather sharp granule contours. The granules of maize starch have mainly round and oval shapes (Figs 1 and 2). The central granule (see marked area) in Figure 1 is re-scanned in Figure 2, and it has a deformed spherical shape, with the diameter fluctuating between 9.0 μm and 9.5 μm. The height difference is between 1250 and 1300 nm (Figure 1e and 2e). Frequently, on the tablet surface, oval granules are found and their larger axis ranges from 5 to 16 μm.

By accurate imaging analysis, several depressions and pores of undefined oval shape are clearly observed in Figure 1 (a, b), particularly on the granule surface on the right of 2D-topography and phase images, and they are generally below 1 μm in size. The surface structures are detected on the profile (which is slightly undulated) of the cross-section (Figure 2e) along the arrow on the granule in Figure 2a.

Furthermore, the surface structures are clearly observed in the marked area, given in Figure 2a, at an enlargement corresponding to a re-scanning area of 1 μm x 1 μm, as shown in Figure 3.

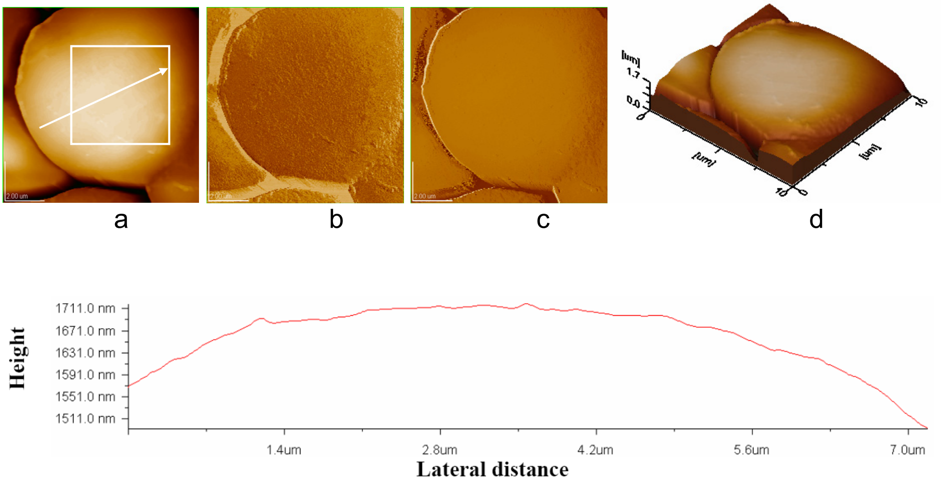

a b c d

e

Figure 2. AFM images of compacted maize starch powder (tablet). Scanned area: 10 μm x 10 μm. a) 2D – topography; b) phase image; c) amplitude image; d) 3D-topography; e) profile of the cross section along the arrow in panel a.

Figure 4-7 display the structure of outermost layer of maize starch powder spread out in thin film for several different magnifications (selected scanning areas), in order to prove the microstructure and the surface features of starch granule surface.

Figure 4 presents an oval shaped starch granule, which shows a rather regular contour (Figure 4a-c), with the long axis of about 5.6 μm (Figure 4d and the arrow in Figure 4a) and the difference in height of about 2000 nm (Figure 4d). Figure 5 shows a starch granule with irregular contour (Figure 5a-c), although it resembles to a rather oval shape (Figure 5d) with short axis of about 6 μm, estimated from the cross-section profile (Figure 5e) along the arrow given in Figure 5a. Its long axis, determined from Figure 5a, is about 8 μm. On the 3D-topography (Figure 5d) the structure of the granule surface is rather visible and it is significantly enhanced at higher magnifications, respectively at smaller scanned areas.

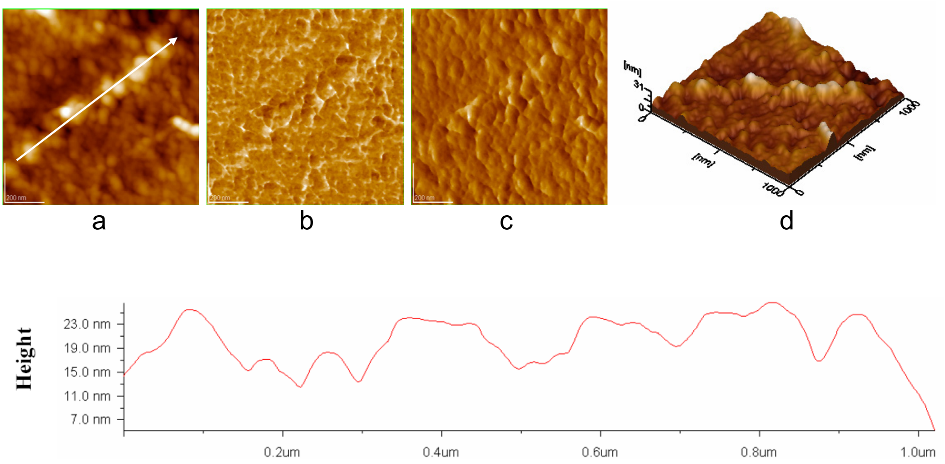

a b c d

e

Figure 3. AFM images of the compacted maize starch powder (tablet). Scanned area: 1 μm x 1 μm. a) 2D – topography; b) phase image; c) amplitude image; d) 3D-topography; e) profile of the cross section along the arrow in panel a.

For example, Figure 6 and 7 display clearly the nanostructure on the starch granule surface at two different areas scanned on the oval maize starch granule from Figure 4.

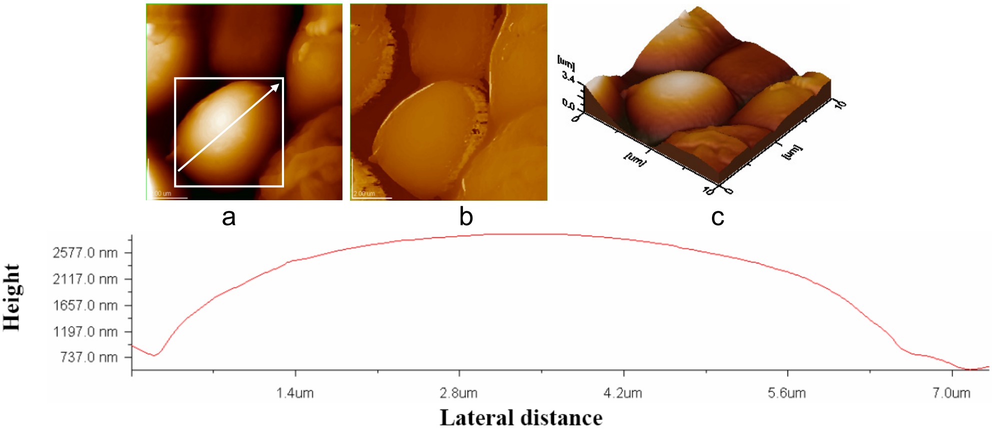

a b c

d

Figure 4. AFM images of the maize starch powder spread out in thin film. Scanned area: 10 μm x 10 μm. a) 2D – topography; b) amplitude image; c) 3D-topography; d) profile of the cross section along the arrow given in panel a.

From Figures 1, 2, 4 and 5, it is to be observed that almost all granules are well defined with rather sharp granule contours independently of sample preparation method. The granules of maize starch have mainly round and oval shapes, both in tablets and in thin films of powder spread out on adhesive tape. Occasionally, polygonal shapes of starch granules were also observed.

These data suggest that in the tablets obtained by compression of the maize starch powder, the starch granules are quite well packed and consequently, the granules show a rather good compactibility and compressibility. They also indicate a low surface fragility of granules surface in substantial agreement with the compaction behaviour reported on other starch samples [2, 3]. The compaction and the fragility behaviour of the starch powder is important in various applications such as in plastics production and for drug delivery systems. Undoubtedly, these observations might have implications in the formulation of poorly compactable drugs, starch powder being an important component [3] in such systems.

According to the AFM images, the granules of maize starch present a variety of forms, such as regular shapes from rather spherical (Figure 1 and 2) or elliptical and oval (Figure 4) to irregular oval form (Figure 5) or polygonal shape with rather smooth or rough surfaces with depressions or irregular holes of undefined shape. The surface roughness determined as root mean square (RMS) is given in Table 1.

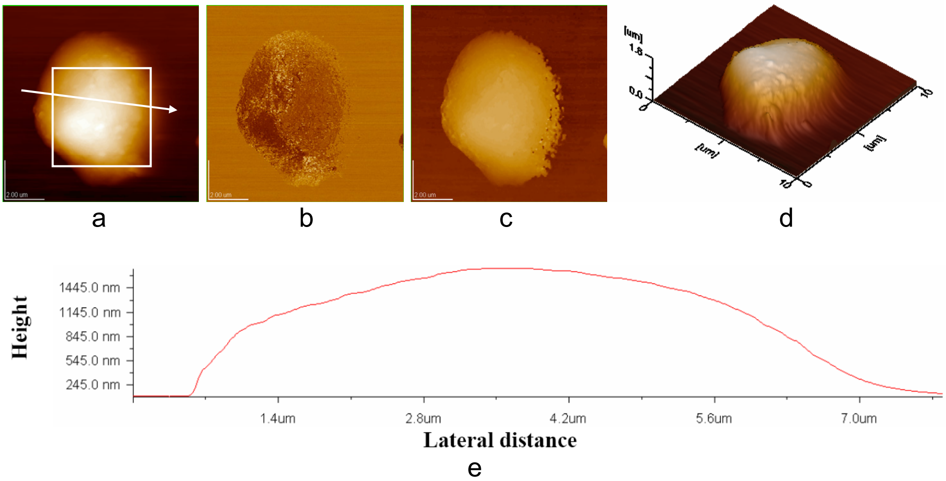

Figure 5. AFM images of the maize starch powder spread out in thin film. Scanned area: 10 μm x 10 μm. a) 2D – topography; b) phase image; c) amplitude image; d) 3D-topography; e) profile of the cross-section along the arrow in panel a.

Table 1. Surface roughness given as root mean square (RMS) for maize starch powders.

Figures	Scanned area, μm^2	RMS on tablet profile, nm	RMS on thin film profile, nm
Fig. 1	20 x 20	298	-
Fig. 2	10 x 10	55.3	-
Fig. 3	1 x 1	5.11	-
Fig. 4	10 x 10	-	568
Fig. 5	10 x 10	-	555
Fig. 6	2 x 2	-	12.4
Fig. 7	1 x 1	-	6.17

The granule size distribution is not deduced by AFM imaging, because a very large number of granules must be scanned for that purpose. The size distribution for the maize starch granules is obtained by scanning electron microscopy (SEM) measurements (unpublished results). The average size of the starch granules is about 9.3 μm with a standard deviation of 2.9 μm and with extreme values between 2 and 25 μm.

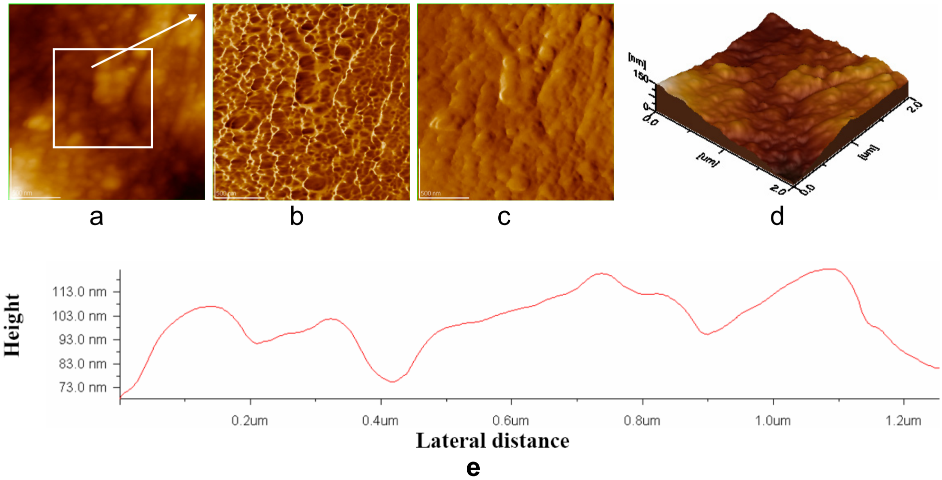

a b c d

e

Figure 6. AFM images of maize starch powder spread as a thin film. Scanned area: 2 μm x 2 μm. a) 2D – topography; b) phase image; c) amplitude image; d) 3D-topography; e) profile of the cross-section along the arrow in panel a.

Referring to the surface morphology, narrow pores or rather large depressions were observed at microstructural level on some parts of the surface of starch granules. These results suggest that structural differences exist even on the same granule surface, in good agreement with recently reported data on potato starch [42].

The fine structure of starch granule surface

Figure 3, 6 and 7 display numerous surface features of maize starch granules, which are rather pronounced for these magnifications.

By comparing the AFM images in Figure 3, given for the starch granules packed into a tablet, with the corresponding ones in Figure 6 and 7, for starch powder spread out in thin films, a certain morphological resemblance is clearly observed for the surfaces of maize starch granules. These data show that not only the microstructure of the starch granules is similar, but also the ultrastructure of the granule surface is comparable and practically independent of sample preparation method. This situation could reflect a strong interaction between the starch macromolecules, resulting in similar particle shapes at granule surface (periphery).

From the AFM images, 2D topographies (Figure 3a, 6a and 7a), and 3D topographies (Figure 3d, 6d and 7d), as well as phase images (Figure 3b, 6b and 7b) and amplitude images (Figure 3c, 6c and 7c), one can observe the surface structuration on the starch granules, primarily the presence of surface protrusions (small rounded and elongated nodules or particles).

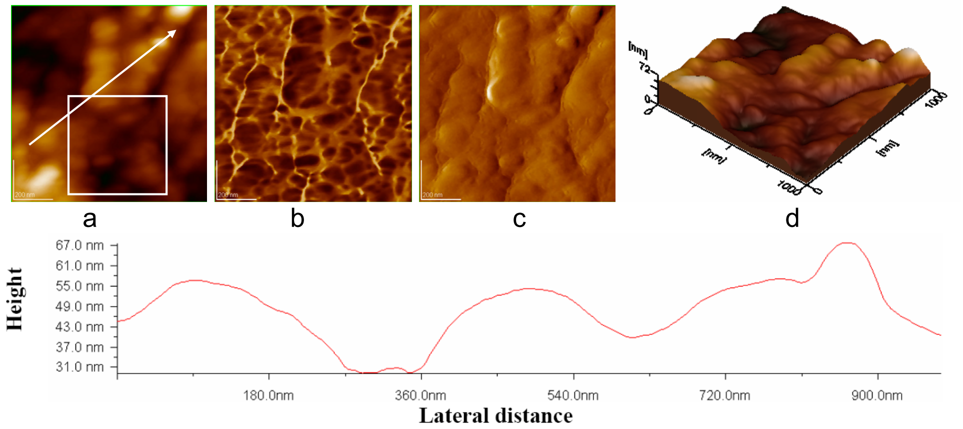

e

Figure 7. AFM images of the maize starch powder spread as a thin film. Scanned area: 1 μm x 1 μm. a) 2D – topography; b) phase image; c) amplitude image; d) 3D-topography; e) profile of the cross section along the arrow in panel a.

These particles are evidenced at small scanning areas, as given in Figure 3, 6 and 7 for the maize starch. In the profile of the cross-sections (Figure 3e, 6e and 7e) one can see the local nanostructure of the granule surface (see, arrows in Figure 3a, 6a and 7a) with nodules (nanoparticles) which protrude from the surface, generally between about 50 and 80 nm (Figure 3e and 7e) for the maize starch.

The apparent diameter of the smallest found features (about 30 nm) was comparable with the radius of curvature of the AFM probe tip (15-20 nm), so the images are expected to be subjected to tip convolution effects.

Anyway, the observed nanoparticles, named also protrusions, subparticles or nodules, are surface features and generally present rather round or elongated shapes on the granule surface of the maize starch granules. In addition, it is to be noted that particles in roughly the same range (about 20 to 50 nm size) were reported to be formed by precipitation with ethanol from suspensions of gelatinized potato starch [35]. They were also detected at the surface of wheat or oat starch granules [35].

The observed sizes are also in substantial agreement with the fine structure of granules of different types of starches found within the granule [27-29, 31] and on the surface [18, 22, 25, 33-35]. For instance, small particles of about 30 nm in diameter were also found in the internal structure of rice [27, 28], corn [29] and pea starches granules. On the granule surface of potato and wheat starches the fine particles more or less spherical of about 25 nm were also identified [18], which were observed both within and at the surface of starch granules degraded by alpha-amylase.

These nanoparticles on the granules surface could correspond to clusters built from amylopectin side chains bundled into blocklet structures [43], evidenced earlier both on the granule surface and in lamellar structures within the starch granule [44], in agreement with the proposed cluster model [18, 35]. They can be bundled further on into larger blocklets organized within the starch granule or on the surface of granule.

In other words, the small protrusions identified in this work, composed mainly of about 30 to 50 nm size nanoparticles might represent the ends of amylopectin side-chain clusters at the granule surface [18].

Therefore, our results support the blocklets model of the starch granule structure [43-45], independent of the starch botanical resources. According to the blocklets concept, the amylopectin forms nanoparticles on the granule surface of native maize starch. Furthermore, a complex surface network (arrangement) might be assembled among the different components bound on granule surface of the native maize starch.

Closer examination of the AFM images revealed a few quite large protrusions on granules surface of maize starch of roughly 120 nm in diameter placed above (Figure 3 and Figure 7) the flatter surface containing the 30 to 50 nm size nanostructures mentioned above.

On the other hand, the surface of the maize starch granules also possesses several larger protrusions of about 150 to 200 nm (low magnification, Figure 5).

Undoubtedly, the AFM images on the granules surface have demonstrated that the maize starch powder possesses substantially similar surface structures on different granules at nanostructural level for both tablet and thin films.

Even more, on the same granule surface, some zones are detected with a rather high roughness, and quite smooth zones with low roughness are also observed. The roughness, measured by the root mean square (RMS), is given in Table 1 for several selected scanned surfaces.

The surface roughness is apparently higher for the outermost layer of the thin film than for the corresponding value for the tablet surface (Table 1). This is a somehow expected situation due to the compressibility of the granules within the tablet.

There are exceptions, for very small scanned areas, when the roughness appears to be almost identical for both maize starch tablet and thin film (Table 1).

Due to the existence of various protrusions of different size, it appears rational to suggest that the amylopectin blocklets (the smallest identified particles) are probably enlarged either by their self assemblies and/or by their attachment to other granule surface components [46-48], such as amylose, granule proteins and phospholipids. Thus, the starch carbohydrate components will possibly build a highly complex network involving the proteins or lipids attached (or bound) to the starch granule surface. Such complex surface organisation supports the existence of a highly structured surface (periphery) of starch granules according to [49] and its role in maintaining the integrity of the starch granule. The effect of starch granule surface can be also evidenced in the starch gelatinization process, where chemical modifications of the granule surface take place.

CONCLUSIONS

We can conclude that the AFM technique is an appropriate tool for the observation of granules surface of the native maize starch. AFM allows a good visualization of the starch granules, revealing their shapes, surfaces morphology and sizes. The surface structures evidenced by AFM imaging, such as protruding nodules on the surface of the starch granules have various sizes, in a large range of values, from 30 nm to 80 nm. Frequently, fine particles were found to self assemble on the granule surface into rather straight arrangements forming rows (Figure 3 and 7).

The surface organization of the starch granule is probably consisting of blocklets as structural elements that have already been proposed for the association and clustering of amylopectin helices within the starch granule and on the granule surface. We suggest that the observed smallest fine particles might also correspond to the individual clusters of amylopectin in substantial agreement with the proposed cluster model and blocklets concept.

In future investigations we intend to deepen the understanding of the nanostructure of native maize starch with the aim to characterize and control the raw starch material, both native and in different processing stages, such as in gelatinization process, in manufacturing of thermoplastic starch products.

EXPERIMENTAL SECTION

A commercially available maize starch from Romanian cultivar was purchased from Nordic Invest, Cluj-Napoca, Romania. The humidity of the starch samples was about 12%, by the manufacturer analysis. The native maize starch powder was used as supplied.

AFM images were recorded using a AFM-JEOL 4210 (JEOL Ltd. Tokyo, Japan) operated in the tapping mode, thus allowing for the simultaneously topography, phase and amplitude images for each starch sample.

Starch samples were prepared by two methods, namely the starch powder was compacted into tablets or directly spread out in thin films on an adhesive tape. The starch tablets were prepared as follows: the starch powder (around 1g) is compressed in a hydraulic press in vacuum, without any binding agent. Starch powder was also spread on a double adhesive band, on which the starch granules are holding in place as a thin film. Then, each starch sample, tablet or thin film, was independently affixed to the AFM sample support. The outermost layer of starch tablet or of the thin film of starch granules was imaged in air with a scanner (30 μm x 30 μm maximum scan size) under normal air conditions, at room temperature (about 22 ^{o}C) and at atmospheric pressure.

All images were recorded in tapping mode using commercially available sharpened silicon nitride (Si_3N_4) probes (Mikromasch, Estonia). The conical shaped tips were on cantilevers with a resonant frequency in the range of 200 - 300 kHz and with a spring constant of 48 N/m.

Both a low scanning rate, 1 Hz, and a higher rate, in the range 2-6 Hz were used, in order to detect possible scanning artefacts or those resulting from the sample preparation method. The scanning angle was also modified on different directions, in order to distinguish between real images and those corresponding to artefacts. The AFM images consist of multiple scans displaced laterally from each other in y direction with 256 x 256 pixels. All AFM experiments were carried out under ambient laboratory temperature conditions as previously reported [37, 38].

AFM observations were repeated on different areas on the scanned surface (i.e. for different magnifications), resulting in scanned areas from 20 μm x 20 μm to 1 μm x 1 μm or scaled down even more (0.5 μm x 0.5 μm) for the same sample. The AFM images were obtained from at least six macroscopic zones separately identified on each sample. All the images were processed according to standard AFM proceeding, as described for example in [39-41].

In particular, on each sample of starch granules, AFM images were recorded at least at six macroscopically different locations on the surface, with each of the locations separated by at least 2 or 3 μm. All imaging data were analyzed using JEOL standard software.

ACKNOWLEDGMENTS

This research was financially supported by the project 31-039 from the 2nd National Program.

REFERENCES

1. J. Ubbink, A. Burbidge, R. Mezzenga, *Soft Matter*, **2008**, *4*, 1569.
2. C. K. Chang, F. A. Alvarez–Nunez, J. V. Rinella Jr., L.-E. Magnusson, K. Sueda, *AAPS PharmSciTech.*, **2008**, *9*, 597.
3. S. Edge, D. F. Steele, J. N. Staniforth, A. Chen, P. M. Woodcock, *Drug Development and Industrial Pharmacy*, **2002**, *28*, 989.
4. I.B. Leonor, A. Ito, K. Onuma, N. Kanzaki, R.L. Reis, *Biomaterials,* **2003,** *24***,** 579.
5. J. M. V. Blanshard, “Starch: Properties and Potential”, John Wiley and Sons, Brisbane, **1987**, p. 16-54.
6. H. F. Zobel, *Starch/Stärke*, **1988**, *40* (2), 44.
7. D. J. Gallant, B. Bouchet, A. Buleon, S. Perez, *European Journal of Clinical Nutrition*, **1992***, 46*, Suppl. 2, S3.
8. S. You, J. Jane, *Carbohydrate Polymers*, **2002**, *49* (3), 307.
9. J. Jane, *Journal of Applied Glycoscience*, **2006**, *53***,** 205.
10. N. Singh, J. Singh, L. Kaur, N. S. Sodhi, B. S. Gill, *Food Chemistry*, **2003**, *81***,** 219.
11. D. French, in “Starch: Chemistry and Technology”, R. L. Whistler, J. N. Bemiller, E. F. Paschall, Eds., Academic Press, London, **1984**, p. 183-247.
12. J. Jane, T. Kasemsuwan, S. Leas, H. Zobel, J. F. Robyt, *Starch/Stärke*, **1994**, *46* (4), 121.
13. J. Jane, J. J. Shen, *Carbohydrate Research*, **1993**, *247*, 279.
14. D. D. Pan, J. Jane, *Biomacromolecules*, **2000**, *1*, 126.
15. H. Fuwa, Y. Sugimoto, T. Takaya, Z. Nikuni, *Carbohydrate Research*, **1979**, *70*, 233.
16. M. R. Sandhya Rani, K. R. Bhattachrya, *Starch/Stärke*, **1995**, *47* (9), 334.
17. P. M. Baldwin, J. Adler, M. C. Davies, C. D. Melia, *Starch/Stärke*, **1994**, *46* (9), 341.
18. P.M. Baldwin, M. C. Davies, C. D. Melia, *International Journal of Bioogical Macromolecules*, **1997**, *21*, 103.
19. R. S. Policegoudra, S. M. Aradhya, *Food Hydrocolloids*, **2008**, *22*, 513.

20. S. Wang, J. L. Yu, O. Zhu, J. Yu, F. Jin, *Food Hydrocolloids*, **2009**, *23*, 426.
21. J. Szymonska, M. Targosz-Korecka, F. Krok, *Journal of Physics: Conference Series*, **2009**, *146*, 012027.
22. M. Sujka, J. Jamroz, *LWT – Food Science and Technology*, **2009**, *42*, 1219.
23. F. H. Cisneros, R. Zevillanos, L. Cisneros-Zevillanos, *Journal of Agricultural and Food Chemistry*, **2009**, *57*, 7363.
24. H. Yan, G. U. Zhengbiao, *Food Research. International*, **2010**, *43*, 767.
25. N. H. Thomson, M. J. Miles, S. G. Ring, P. R. Shewry, A. S. Tatham, *Journal of Vacuum Science and Technology B*, **1994**, *12*, 1565.
26. P. R. Shewry, M. J. Miles, N. H. Thomson, A. S. Tatham, *Cereal Chemistry*, **1997**, *74*, 193.
27. T. Ohtani, T. Yoshino, T. Ushiki, S. Hagiwara, T. Maekawa, *Journal of Electron Microscopy*, **2000**, *49,* 487.
28. T. Ohtani, T. Yoshino, S. Hagiwara, T. Maekawa, *Starch/Stärke*, **2000**, *52* (5), 150.
29. A. A. Baker, M. J. Miles, W. Herbert, *Carbohydrate Research*, **2001**, *330*, 249.
30. M. J. Ridout, A. P. Gunning, M. L. Parker, R. H. Wilson, V. J. Morris, *Carbohydrate Polymers*, **2002**, *50* (2), 123.
31. M. J. Ridout, M. L. Parker, C. L. Hedley, T. Y. Bogracheva, V. J. Morris, *Carbohydrate Research*, **2003**, *338*, 2135.
32. Z. Liu, C. Chen, Z. Ouvang, Y. Guo, J. Hu, M. Li, *Journal of Vacuum Science and Technology B*, **2001**, *19*, 111.
33. L. Juszczak, T. Fortuna, F. Krok, *Starch/Stärke*, **2003**, *55* (1), 1.
34. L. Juszczak, T. Fortuna, F. Krok, *Starch/Stärke*, **2003**, *55* (1), 8.
35. J. Szymonska, F. Krok, *International Journal of Biological Macromolecules*, **2003**, *33*, 1.
36. J. Cabálková, J. Přibyl, P. Skládal, P. Kulich, J. Chmelík, *Tree Physiology*, **2008**, *28*, 1593.
37. M. Tomoaia-Cotisel, in "Convergence of Micro-Nano-Biotechnologies" Vol. 9, Eds. M. Zaharescu, E. Burzo, L. Dumitru, I. Kleps, D. Dascalu, Romanian Acad. Press, Bucharest, **2006**, p. 147 - 161.
38. M. Tomoaia-Cotisel, A. Tomoaia-Cotisel, T. Yupsanis, G. Tomoaia, I. Balea, A. Mocanu, C. Racz, *Revue Roumaine de Chimie,* **2006***,* *51*, 1181.
39. O. Horovitz, G. Tomoaia, A. Mocanu, T. Yupsanis, M. Tomoaia-Cotisel, *Gold Bulletin*, **2007**, *40*, 213.
40. M. Tomoaia-Cotisel, A. Mocanu, *Revista de Chimie (Bucharest),* **2008**, *59*, 1230.
41. A. Mocanu, I. Cernica, G. Tomoaia, L. D. Bobos, O. Horovitz, M. Tomoaia-Cotisel, *Colloids and Surfaces, A*, **2009**, *338*, 93.
42. J. Huang, P. Zhang, Z. Chen, H. Li, *Carbohydrate Polymers*, **2010**, *80* (1), 215.
43. D. J. Gallant, B. Bouchet, P. M. Baldwin, *Carbohydrate Polymers*, **1997**, *32* (3-4), 177.
44. P. M. Baldwin, J. Adler, M. C. Davies, C. D. Melia, *Journal of Cereal Science*, **1998**, *27* (3), 255.

45. P. Laity, A. Cassidy, J. Skepper, B. Jones, R. Cameron, *European Journal of Pharmaceutics and Biopharmaceutics*, **2010**, *74*, 377.
46. P. L. Russell, B. M. Gough, P. Greenwell, A. Fowler, H. S. Munro, *Journal of Cereal Science*, **1987**, *5*, 83.
47. P. M. Baldwin, C. D. Melia, M. C. Davies, *Journal of Cereal Science*, *26***,** 329.
48. A. Rindlav-Westling, P. Gatenholm, *Biomacromolecules*, **2003**, *4*, 166.
49. J. Yu, P. R. Chang, X. Ma, X., *Carbohydrate Polymers,* **2010***, 79* (2), 296.

STUDIA UNIVERSITATIS BABEŞ-BOLYAI, CHEMIA, XLV, 2, TOM II, 2010

Dedicated to the memory of Prof. dr. Ioan Silaghi-Dumitrescu marking 60 years from his birth

SYNTHESIS AND SPECTROSCOPIC INVESTIGATIONS OF NEW UO_2^{2+}– POLYOXOMETALATE COMPLEXES

DAN RUSU[a], OANA BABAN[b], SIMINA DREVE[c], MIRCEA PUIA[d], MARIANA RUSU[b]

ABSTRACT. The $Na_{10}[(UO_2)_2(H_2O)_2X_2W_{20}O_{70}]\cdot nH_2O$ heteropolyoxo-metalates (Na_{10}1: X =Sb^{III}, n = 28; Na_{10}2: X =Bi^{III}, n = 34) were synthesized and investigated by chemical and thermal analysis, FT- IR, Raman, UV-Vis and fluorescence emission spectroscopies for determining subsequently the behavior of the encapsulated uranyl cations, their coordination by the tungstoantimonate(III) or tungstobismutate(III) fragments, and the corresponding pentagonal-bipyramidal local symmetry. Polyoxoanions $[(UO_2)_2(H_2O)_2X_2W_{20}O_{70}]^{10-}$ are structural similarly and consist from two β-B-$[XW_9O_{33}]^{9-}$ (X= Sb^{III}, Bi^{III}) framework which are linked by an equatorial belt of two $UO_2(H_2O)_2^{2+}$ units and two WO_2 groups.

Keywords: *Uranium (VI); Heteropolyoxotungstates; IR, Raman, UV, Vis and fluorescence emission spectroscopies.*

INTRODUCTION

The current research in polyoxometallate (POM) chemistry is characterized by the perception and the achievement of their applications in different areas, especially in the field of nanomaterials, catalysis, image reactive, as potential agents for nuclear waste sequestration and storage, magnetic chemistry and medicine [1]. At the same time, it must be pointed out that the polyoxometallate chemistry has a tradition in studying the formation and stability of heteropolyoxotungstates containing heteroatoms of lanthanides and actinides [2-15]. The structure of these polyoxotungstate species was first reported by Weakley [16], and it can be described as a 1:2 sandwich type structure of $Ln^{3+/4+}$ or An^{4+} ions with monolacunary polyoxoanions

---

[a] *Universitatea de Medicină şi Farmacie Iuliu Haţieganu, Facultatea de Farmacie, Str. E. Isac Nr. 13, RO-400023, Cluj-Napoca, Romania*

[b] *Universitatea Babeş-Bolyai, Facultatea de Chimie şi Inginerie Chimică, Str. M. Kogalniceanu Nr. 1, RO-400084 Cluj-Napoca, Romania, mrusu@chem.ubbcluj.ro*

[c] *Institutul Naţional pentru Izotopi şi Tehnologie Moleculară, Str. Donath Nr. 63, RO-400293 Cluj-Napoca, Romania*

[d] *Universitatea Babeş Bolyai, Facultatea de Fizică, Str. M. Kogalniceanu Nr. 1, RO-400084 Cluj-Napoca, Romania*

"ligands", such as $[Ln^{III}(PW_{11}O_{39})_2]^{11-}$, in which the metallic cations occupy a anti-phrysmatic coordinative position. Sometimes, although U^{IV} can be stabilized in these complexes, the chemistry of the aqueous solutions of the first actinides is dominated by trans-dioxin cations, from which the most familiar is UO_2^{2+}. Pope [17] reports the example of the heteropolyoxotungstate which incorporates the UO_2^{2+}, linear steric, as expected. Subsequently, other uranyl polyoxometallate complexes were reported. [18-27]

Since 1970 [28-30], a number of articles have been published regarding the $\{XW_{11}\}$, with ($X=Sb^{III}$, Bi^{III}), type of monolacunary polyoxocations and their complexes with a ratio of 1:1 with the di- and trivalent cations of transitional metals. Recently, these species have been revealed as dimmers on the basis of the structure determined on the Krebs salts $[Sb_2W_{22}O_{74}(OH)_2]^{12-}$, $[Sb_2W_{20}Fe^{III}{}_2O_{70}(H_2O)_6]^{8-}$, $[Sb_2W_{20}Co^{II}{}_2O_{70}(H_2O)_6]^{10-}$ and $[Bi_2W_{20}Fe^{III}{}_2O_{70}(H_2O)_6]^{6-}$ [31, 32]. The polyoxotungstate anion structure consists of two trilacunary groups $\{B\text{-}\beta\text{-}XW_9\}$, bonded by two additional tungsten atoms and other two additional tungsten centers with a weaker bond, which can be replaced with $M^{II/III}$ cations in the substituted polyoxoanions.

The Krebs $[X_2W_{22}O_{74}(OH))_2]^{12-}$ polyoxoanion type belongs to the clusters that incorporate different lacunary trivacante polyoxometallic fragments with the formula B-β $[XW_9O_{33}]^{9-}$ where X = Sb^{III}, Bi^{III}.

The aim of the present paper is to report the new natrium salts of the di-substituted Krebs tungstoantimonate and tungstobismutate $[(UO_2)_2(H_2O)_2X_2W_{20}O_{70}]^{10-}$, X = Sb^{III}, Bi^{III}. The 2:1 complexes corresponding to the formula $Na_{10}[(UO_2)_2(H_2O)_2X_2W_{20}O_{70}]$, X = Sb^{III}, Bi^{III} were obtained according to the following reaction:

$$2UO_2^{2+} + [X_2W_{22}O_{74}(OH)_2]^{12-} + 6H_2O \rightarrow [(UO_2)_2(H_2O)_4X_2W_{20}O_{70}]^{10-} + 2WO_4^{2-} + 6H^+ \quad (1)$$

In order to establish the behavior of UO_2^{2+} cations encapsulated in heteropolyoxometalates, the coordination pattern of the metallic ions to the Keggin fragments and the local symmetry around them, the new complexes were investigated by means of spectroscopic (FT-IR, Raman, UV, Vis and fluorescence emission) methods.

RESULTS AND DISCUSSIONS

Chemical and thermal analysis

The following abbreviations will be used: i) for the anions: **L₁** for $[[Sb_2W_{22}O_{74}(OH)_2]^{12-}$, **1** for $[(UO_2)_2(H_2O)_4Sb_2W_{20}O_{70}]^{10-}$, **L₂** for $[Bi_2W_{22}O_{74}(OH)_2]^{12-}$, **2** for $[(UO_2)_2(H_2O)_4Bi_2W_{20}O_{70}]^{10-}$ ii) for the salts: Na_{12}**L₁** for $Na_{12}[Sb_2W_{22}O_{74}(OH)_2]\cdot 42H_2O$, Na_{10}**1** for $Na_{10}[(UO_2)_2(H_2O)_4Sb_2W_{20}O_{70}]\cdot 28H_2O$, $Na_{12}[Bi_2W_{22}O_{74}(OH)_2]\cdot 44H_2O$, Na_{10}**2** for : $Na_{10}[(UO_2)_2(H_2O)_4Bi_2W_{20}O_{70}]\cdot 34H_2O$.

The chemical reaction of UO$_2^{2+}$ with $[X_2W_{22}O_{74}(OH)_2]^{12-}$ (X=Sb^{III}, Bi^{III}) in water can be described by eqn. (1). The isolation of the final products as sodium salt, and their recrystallization from hot water, resulted in relatively good yields of the Na$_{10}$**1** and Na$_{10}$**2.** The analytical data are presented in table 1.

Table 1. Analytical data of the Na$_{10}$**1** and Na$_{10}$**2** polyoxometalate complexes

Complex	Yield (g / %)	Colour	Found (calc.) (%)				
			Na	X	W	U	H_2O
Na$_{10}$**1**	4.15 / 65	Yellow-Orange	3,72 (3,60)	3.86 (3.81)	57.70 (57.57)	7.48 (7.45)	8.98 (9.02)
Na$_{10}$**2**	4.73 / 71	Yellow-Orange	3.54 (3.45)	6.28 (6.27)	55.60 (55.15)	7.18 (7.14)	10.22 (10.26)

Due to the fact that the $[X_2W_{22}O_{74}(OH)_2]^{12-}$ species -where X= Sb^{III}, Bi^{III} - were not stable in aqueous solutions, the reaction was led by adding solid sodium salt of the ligands to the $UO_2(NO_3)_2$ aqueous solution. The polyoxoanion complexes obtained were stable only in the presence of an excess of sodium ions. The complexes were crystallized, with a good yield, after a few days, from solution kept at 5 °C.

The suggested formula for $Na_{10}[(UO_2)_2(H_2O)_4Sb_2W_{20}O_{70}].28H_2O$ and $Na_{10}[(UO_2)_2(H_2O)_4Bi_2W_{20}O_{70}]\cdot 34H_2O$ complexes are consistent with results of the analyses of the final products (Table 1).

The thermo-gravimetric analysis shows that between 35-325 ^{0}C the mass loss was 1.3491 mg (8.98 %) and 1.5039 mg (10.22 %) for (Na$_{10}$**1**) and (Na$_{10}$**2**) complexes respectively. The water loss process took place in two successive phases: the first between 35-120 ^{0}C which corresponds to 28 (Na$_{10}$**1**) and 34 (Na$_{10}$**2**) crystallization water molecules respectively, and the second between 120-325 ^{0}C, corresponding to 4 coordinating water molecules for both complexes.

The DTA curves indicate two endothermic and two exothermic effects. The endothermic effects with a maximum temperature of ≈ 120 °C and ≈ 325 ^{0}C corresponds to the water loss processes. The exothermic effect with a maximum at ≈ 430 °C correspond to the crystallization process of the oxides from the mixture, and the exothermic effect with a maximum temperature at ≈ 500 °C corresponds to the phase transformation from the oxides structures in the mixture [33].

Vibrational spectra

FT – IR spectra

By comparing the FT-IR spectra of the uranyl complexes with those for the corresponding ligands and their shifts toward higher or lower frequencies, we obtained information regarding the UO$_2^{2+}$ ions coordination to the lacunary polyoxometallates units, the symmetry and the bond strength. The FT-IR spectra of the polyoxometallates generally exhibit contributions of the polyoxoanion frameworks. The characteristic IR vibration bands of Na_{10}**1** and Na_{10}**2** complexes, as compared to those of the Na_{12}**L_1** and Na_{12}**L_2** ligands, are shown in Table 2.

Table 2. Main vibration bands observed in the FT-IR spectra (cm^{-1})

Vibration	Na_{12}**L_1**	Na_{12}**L_2**	Na_{10}**1**	Na_{10}**2**
$\nu_{as}(W{=}O_t)$	939	948	940	948
$\nu_{as}(W–O_c–W)$	879	875	889 870	880 868
$W\text{-}O\text{-}UO_2^{2+}$			836	836
$\nu_{as}(W–O_e–W)$	798 762	790 735	775 720	795 720

In the 1000-700 cm^{-1} range, we observed characteristic bands, which we assigned to the asymmetric stretching vibrations of the bridges W-$O_{c,e}$-W, W-O_i and of the terminal bonds W=O_t.

All anti-symmetric frequency bands involving tungsten ions are shifted towards higher or lower frequencies (by 1 – 39 cm^{-1}) in the complex spectra, compared to the ligands.

The tiny shift of the $\nu_{as}(W{=}O_t)$ vibration indicates that terminal O_t atoms are not involved in the coordination of UO_2^{2+} ions.

The $v_{as}(W–O_c–W)$ vibration band of the tricentric W-O_c-W bond of the corner sharing WO_6 octahedra is split in both complexes, being shifted in the complexes spectra toward higher frequencies in comparison with the ligands. This is consistent with an increase in the anion cohesion, when the co-ordination of the uranyl ions in the polyoxometalates frameworks takes place.

The $v_{as}(W–O_e–W)$ vibration band of the tricentric W–O_e–W bond of the edge sharing WO_6 octahedra is split in both complexes, being shifted in the complexes spectra toward lower frequencies for Na_{10}**1** or higher for Na_{10}**2** in comparison with the ligands. This is consistent with a decrease or increase of the anions cohesion, when coordination of the uranyl ions in the polyoxometalates frameworks takes place.

The shift of $\nu_{as}(W–O_{c,e}–W)$ vibration bands is due to the uranyl ions coordination with the lacunary polyoxometalate ligands by O_c and O_e atoms.

In addition, the IR spectra of the uranyl polyoxometalate complexes exhibit at ~ 836 cm^{-1} a band which is assigned to the stretching vibrations of the $\nu_{as}(UO_2^{2+})$.

The $v_{as}(UO_2^{2+})$ bands are shifted in polyoxotungstate complexes to lower frequencies, in comparison with the corresponding band from the

$UO_2(NO_3)_2 \cdot 4H_2O$ (965 cm^{-1}) [34], because the polyoxometalate ligands form strong bonds with uranium by lowering the order of the U=O band and consistently lowering the ν_{as}(O=U=O) frequency.

Raman spectra

The Raman spectra of the complexes Na$_{10}$**1** and Na$_{10}$**2** (Figure 1) also show vibration bands which are characteristic to the polyoxometalate framework. The strongest bands occurring at 958 and 956 cm^{-1}, respectively, can be assigned to ν_s(W-O$_t$) vibrations. The less intense bands appearing in the 900-700 cm^{-1} range are assigned to the stretching of the W-O$_{c,e}$-W bridges, and the band appearing at 214 cm^{-1} is assigned to ν_s(W-O$_i$) vibration, where O$_i$ is an internal oxygen atom which links Sb or Bi and W atoms. In comparison to the related lacunary ligands Na$_{12}$**L$_1$** and Na$_{12}$**L$_2$,** a shift of these bands towards higher or lower energies is observed, indicating an increase in stability for the Na$_{12}$**L$_1$** and a decrease in stability for the Na$_{12}$**L$_2$** complexes of the polyoxoanion framework, upon coordination of the uranyl ions [35].

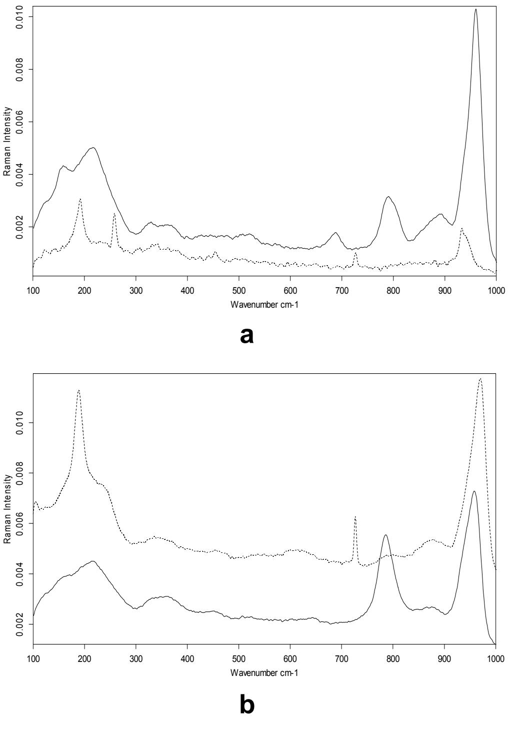

Figure 1. Raman spectra of the polyoxometalate complexes (solid linie) a) Na$_{10}$**1** and b) Na$_{10}$**2,** and of the related ligands (dotted linie) a) Na$_{12}$**L$_1$** and b) Na$_{12}$**L$_2$**.

Electronic spectra

UV-spectra

The complexes' spectra are similar to the ones of the ligands. Each spectrum presents two bands assigned to the $p_\pi \rightarrow d_\pi$ ligand-to-metal charge transfer transition in the W=O_t bonds and d_π–p_π–d_π electronic transitions between the energy levels of the W-$O_{c,e}$-W bonds (Table 3).

The higher energy band (ν_1), due to the d_π-p_π proper transitions from the W=O_t bonds, with an absorption maximum at ~ 210 nm, are insignificantly shifted in the complexes compared to the ligands, which can been associated with the lack of involvement of the terminal oxygen atoms in the coordination of the cations of uranyl.

The lower energy band (ν_2) corresponding to the d_π-p_π-d_π electronic transitions from the tri-centric W-$O_{c,e}$-W bonds, displays an expected absorption maximum in the range of 250-300 nm, for all polyoxotungstate complexes, shifted towards lower energies compared to the ligands, which is associated with the involvement of the oxygen atoms of these bonds in the coordination of the uranyl cations [36, 37].

Table 3. Charge transfer bands observed in the UV absorption spectra (cm^{-1}/nm)

Bands	Na_{12}**L_1**	Na_{12}**L_2**	Na_{10}**1**	Na_{10}**2**
ν_2 : $d_\pi \rightarrow p_\pi \rightarrow d_\pi$ (W–O_b–W)	39682/252	39525/253	39215/255 36200/276	39062/256 35840/279
ν_1 : $p_\pi \rightarrow d_\pi$ (W=O_t)	47169/212	47169/212	46728/214	46728/214

Visible-spectra

Visible spectra of the Na_{10}**1 and** Na_{10}**2** complexes are similar and present six bands. The transition assignments were made in accordance with [18], and were presented in Figure 2.

The visible electronic spectra of uranyl complexes exhibit two charge transfer bands at ~ 420 nm and ~430 nm respectively, which can be attributed to internal O=U=O transitions and four charge transfer bands at ~440, ~468, ~480 and ~500 nm which can be assigned to ligand – uranyl electronic transitions [17-21].

As resulting from the specialty literature, as well as from the present report, when it comes to the polyoxometalate-uranyl complexes, we observe a trend, namely that the U(VI) always adopts its favored seven-coordinate pentagonal-bipyramidal geommetry but with a certain degree of distortion, in order to accommodate the positions of the unsaturated oxygen donor atoms of the polyoxoanion [20,21].

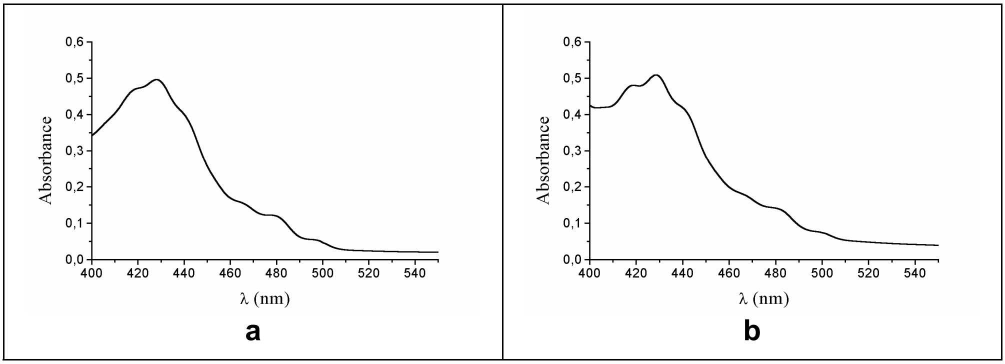

Figure 2. The electronic visible spectra of the polyoxometalate complexes: a) Na_{10}**1**; b) Na_{10}**2**.

Fluorescence emission spectra

The spectrofluorimetric analysis reveals a strong fluorescence emission in the range of 470–580 nm, corresponding to the excitation of the 300 nm band and a sharp emission at 824 nm for an excitation of the 550 nm band.

When comparing the values with some literature data, we can assume that the sharp emission band at 824 nm, presented in both uranyl systems, can be the fluorimetric signal of the uranyl ion in both systems [38-40].

The accuracy of the determinations and the shape of bands suggest that no important quenching phenomenon occurs, confirming the high purity of the Na_{10}**1**, and Na_{10}**2** complexes, respectively.

CONCLUSIONS

In this work, we have synthesized two new polyoxometalate complexes with uranyl ions of $[(UO_2)_2(H_2O)_4(X_2W_{20}O_{70})]^{10-}$, X = Sb^{III}, Bi^{III} type.

The UV and FT-IR spectra indicate the coordination of each uranyl ion to oxygen atoms from the corner-sharing and edge-sharing octahedra of the trilacunary Keggin anions.

Visible electronic spectra indicate the coordination of the uranyl cations in the $[(UO_2)_2(H_2O)_2(X_2W_{20}O_{70}]^{10-}$ complexes, too.

The fluorescence emission spectra reveal the presence of the uranyl ions in both studied compounds and suggest that no important quenching phenomenon occurs, confirming the high purity of Na_{10}**1** and Na_{10}**2** respectively.

According to our studies, we recommend for the uranyl polyoxometalate complexes a “sandwich” kind of structure, which consist of two B–β–XW_9O_{33} Keggin frameworks which are linked by two uranyl ions and two WO_2 fragments (Figure 3). Each uranium atom adopts the pentagonal- bi-pyramidal coordination, forming two equatorial bonds with the terminal oxygen atoms of one pair of two WO_6 octahedra bonded by common edges, which belong to one of the B–β–XW_9O_{33} fragments and a bond with the terminal oxygen of one of the WO_6 octahedra belonging to the other B–β–XW_9O_{33} fragment, the other two equatorial coordinating points of the uranyl cation being satisfied by two molecules of water.

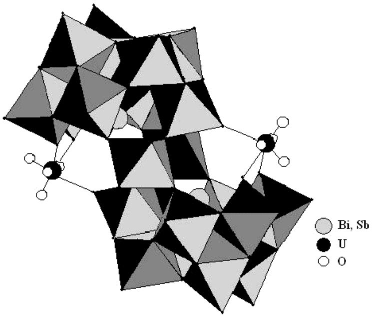

Figure 3. Proposed structure of the Na_{10}**1** and Na_{10}**2** polyoxometallate complexes.

EXPERIMENTAL SECTION

Materials

We have used reagent grade chemicals and all syntheses and studies were carried out in distilled water.

Both the sodium salt of the polyoxometallate ligand $Na_{12}[Sb_2W_{22}O_{74}(OH)_2]\cdot 42H_2O$ (Na_{12}**L₁**), and the sodium salt of the polyoxometalate ligand $Na_{12}[Bi_2W_{22}O_{74}(OH)_2]\cdot 44H_2O$ (Na_{12}**L₂**) were prepared as previously reported [31] and [32] respectively.

Synthesis of $Na_{10}[(UO_2)_2(H_2O)_4Sb_2W_{20}O_{70}]\cdot 28H_2O$ ($Na_{10}1$) and $Na_{10}[(UO_2)_2(H_2O)_4Bi_2W_{20}O_{70}]\cdot 34H_2O$ ($Na_{10}2$) complexes

To a solution of $UO_2(NO_3)_2\cdot 4H_2O$ (0.47 g, 2 mmol) in distilled water (50 ml) we added solid sodium salts of the ligand $Na_{12}[X_2W_{22}O_{74}(OH)_2]$ ($X=Sb^{III}$, Bi^{III}) (6.27 g Na_{12}**L₁** or 6.75 g Na_{12}**L₂**, respectively, 1 mmol). The slightly turbid yellow-orange final solution was strongly stirred at 70°C for 30 minutes, its pH was adjusted to the value of 4.5 with 1M HCl and filtered under suction. It was then cooled to room temperature and 10 g of NaCl was added. An orange-yellow precipitate appeared, which was recrystallized from hot water, having a pH value of 4.5. The orange translucent crystals of $Na_{10}[(UO_2)_2(H_2O)_4Sb_2W_{20}O_{70}]\cdot 28H_2O$ or $Na_{10}[(UO_2)_2(H_2O)_4Bi_2W_{20}O_{70}]\cdot 34H_2O$ respectively, were obtained within a few days from a solution kept at 5 °C. The yield was: 4.15 g (65%) and 4.73 g (71%), respectively.

Methods and instrumentation

We used inductively Coupled Plasma spectroscopy (I.C.P.) for the elemental analysis of uranium, antimonium, bismuth and tungsten and flamephotometry for sodium. The water content was thermogravimetrically determined, by means of a METTLER-TGA/SDTA 851^e device, with a balance sensibility of 1 mg, using a SOFT:STAR^e Software program. The working parameters are as follows: the working mass, m_{sample}=15.1280 mg for $Na_{10}[(UO_2)_2(H_2O)_4Sb_2W_{20}O_{70}]$ compound and m_{sample}=14.8256 mg for $Na_{10}[(UO_2)_2(H_2O)_4Bi_2W_{20}O_{70}]$ compound (temperature range, T=20-800 °C, the heating rate, dT/dt=10 °C, the balance sensibility, S=1 μg).

The FT-IR spectra were recorded with an Equinox 55 Bruker spectrophotometer on KBr pellets, in the 4000–400 cm^{-1} range. Raman spectra were recorded on solid powders, at room temperature, with a DILOR OMARS 89 Raman spectrophotometer. Electronic spectra were obtained in aqueous solutions within a range of λ =200-800 nm using a JASCO 530 spectrophotometer.

The fluorescence emission spectra were obtained using a ABLE& JASCO FP-6500 spectrofluorometer with 150W xenon lamp, solid sample sealed holder, with a PC acquisition system running on Microsoft Windows. The measurements were made by exposing the samples directly in the sealed solid holder, using an excitation degree of 300 nm and 550 nm respectively, at room temperature.

REFERENCES

1. M. T. Pope, A. Müller, *“Polyoxometalates. From Platonic Solids to Anti-Retroviral Activity”,* Kluwer Academic Publishers, Dordrecht, The Netherlands, **1994**, pp.1.
2. B.H. Myasoedov, *Sov. Radiochem.,* **1990**, *32,* 361.
3. Gh. Marcu, M. Rusu, A.V. Botar, *Rev. Roum. Chim.,* **1974**, *19*, 827.
4. Gh. Marcu, M. Rusu, *Rev. Roum. Chim.,* **1976**, *21,* 385.
5. Gh. Marcu, M. Rusu, *Rev. Roum. Chim.*, **1977**, *22*, 227.
6. Gh. Marcu, M. Rusu, L. Ochesel, *Rev. Roum. Chim.,* **1977**, *22,* 849.
7. M. Rusu, Gh. Marcu, E. Perte, *Rev. Roum. Chim.,* **1978**, *23*, 1403.
8. M. Rusu, Gh. Marcu, *Rev. Roum. Chim.*, **1979**, *24,* 351.
9. Gh. Marcu, M. Rusu, E. Perțe, *Rev. Roum. Chim.,* **1979**, *24,* 159.
10. Gh. Marcu, A. Botar, M. Rusu, *Rev. Roum. Chim.*, **1979**, *24*, 1465.
11. M. Rusu, A. Curticăpean, A. V. Botar, *Rev. Roum. Chim.*, **1995**, *41*, 687.
12. M. Rusu, D. Rusu, Gh. Marcu, *J. Radioanalyt. Nucl. Chem.,* **1999**, *242*, 119.

13. M. Rusu, D. Rusu, C. Roşu, A.R. Tomşa, Gh. Marcu, *J. Radioanalyt. Nucl. Chem.,* **1999**, *242*, 467.
14. M. Rusu, *J. Radioanalyt. Nucl. Chem.*, **2000**, *245*, 353.
15. M. Rusu, D. Rusu, C. Roşu, C. Crăciun, L. David, A.R.Tomşa, Gh. Marcu, *J. Radioanalyt. Nucl. Chem.,* **2000**, *245/2*, 363.
16. R.D. Peacock, T.J.R. Weakley, *J. Chem. Soc. A.*, **1971**, 1836.
17. K.C. Kim, M. T. Pope, *J. Am. Chem. Soc.,* **1999***, 121,* 8512.
18. K.C. Kim, M. T. Pope, *J. Chem. Soc. Dalton Trans.*, **2001**, 986.
19. C. Rosu, M. Rusu, C. Ciocan, *Rev. Chim. (Bucuresti),* **2002**, *53*, 57.
20. K. C. Kim, A.J. Gaunt, M. T. Pope, *Journal of Cluster Science,* **2002***, 13,* 423.
21. A.J. Gaunt, I. May, R. Copping, I. Bhatt, D. Collison, O.D. Fox, K.T. Holman, M.T. Pope, *J. Chem. Soc. Dalton Trans.*, **2003**, 3009.
22. C. Craciun, D. Rusu, L. Pop-Fanea, M. Hossu, M. Rusu, L. David, *Journal of Radioanal. and Nucl. Chem,* **2005**, *264(3*), 589.
23. R. Khoshnavazi, H. Eshtiagh-hossieni, M.H. Alizadeh, M.T. Pope, *Polyhedron*, **2006**, *25*, 1921.
24. R. Copping, I. May, D. Collison, C.J. Jones, C.A. Sharrad, M.J. Sarsfield, *Royal Society of Chemistry*, **2006**, 305.
25. R. Tan, X. Wang, F. Chai, Y. Ian, Z. Su, *Inorg. Chem. Commun*., **2006**, 1331.
26. R. Khoshnavazi, H. Eshtiagh-hossieni, M.H. Alizadeh, M.T. Pope, *Inorg. Chim. Acta*, **2007**, *360*, 686.
27. M.H. Alizadeh, M. Mohadeszadeh, *Journal of Clust. Sci.,* **2008**, *19(2)*, 435.
28. P. Souchay, M. Leray, G. Hervè, *C. R. Acad. Sci. Ser. C,* **1970**, *271*, 1337.
29. M. Michelon, P. Souchay, R. Massart, G. Hervè, *C. R. Acad. Sci., Ser. C*, **1971**, *273*, 1117.
30. M. Michelon, G. Hervè, *C. R. Acad. Sci., Ser. C,* **1972**, *273*, 209.
31. M. Bösing, I. Loose, H. Pohlmann, B. Krebs, *Chem. Eur. J*., **1997**, *3*, 1232.
32. I. Loose, E. Droste, M. Bosing, H. Pohlmann, M.H. Dickman, C. Rosu, M.T. Pope, B. Krebs, *Inorg. Chem*., **1999**, *38*, 2688.
33. M. Pospisil, *J. Thermal Analysis*, **1995**, *44*, 133.
34. W. M. Hosny, *Synth. React. Inorg. Met.-Org. Chem*., **1998**, *28*, 1029.
35. F. Rocchiccioli-Deltcheff, M. Fournier, R. Franck, R. Thouvenot, *Inorg. Chem.,* **1983**, *22*, 46.
36. G. M. Varga, E. Papaconstantinou, M.T. Pope, *Inorg. Chem.*, **1970**, *9,* 662.
37. H. So, M.T. Pope, *Inorg. Chem.*, **1972**, *11,* 1441.
38. S. Amayri, T. Arnold, T. Reich, H. Foerstendorf, G. Geipel, G. Bernhard and A. Massanek, *Environ. Sci. Technol.,* **2004**, *38*, 6032.
39. C. Jacopin, M. Sawicki, G. Plancque, D. Doizi, F. Taran, E. Ansoborlo, B. Amekraz C. Moulin, *Inorg. Chem.* **2003**, *42*, 5015.
40. X. Kong, Y. Ren, L. Long, R. Huang, L. Zheng, *Inorg. Chem. Comm.,* **2007**, 894.

STUDIA UNIVERSITATIS BABEŞ-BOLYAI, CHEMIA, XLV, 2, TOM II, 2010

Dedicated to the memory of Prof. dr. Ioan Silaghi-Dumitrescu marking 60 years from his birth

THE THERMODYNAMICS AND KINETICS OF SATURATED HYDROCARBON SEPARATION ON A DB-1 COLUMN

LÉNÁRD-ISTVÁN CSEPEI[a], CSABA BOLLA[b]

ABSTRACT. Results concerning the thermodynamics and kinetics of separation of some saturated hydrocarbons on a DB-1 non-polar capillary chromatographic column are presented. The effect of temperature on the retention time at constant carrier gas flow was studied in order to determine the adsorption enthalpy and adsorption entropy of the compounds on the poly-dimethyl-siloxane stationary phase. The dependence of the height equivalent to theoretical plate on the carrier gas linear velocities at constant temperature was also determined in order to have access to the optimal linear velocity, the longitudinal diffusion (B) and resistance to mass transfer (C) coefficients. These terms can be determined from the Golay equation. The linearization of the Golay equation is also presented.

Keywords: *gas chromatography, DB-1 capillary column, hydrocarbon isomer separation, adsorption enthalpy, adsorption entropy, Golay equation, longitudinal diffusion coefficient, resistance to mass transfer coefficient.*

INTRODUCTION

The efficiency of the gas chromatographic separation depends on many variables. These variables can be divided in two groups: design- and operational parameters. The design parameters are given by the construction of the chromatographic setup and include the following: the length, the diameter and the polarity of the chromatographic column, the stationary phase film thickness and the carrier gas viscosity. For the separation of a multi-component mixture using a chromatographic system with given design parameters one can vary the operational parameters, i.e the temperature of the column and the carrier gas flow rate. Both can be ramped with a desired rate [1-4].

---

[a] *Fritz Haber Institute der Max Planck Gesellschaft, Faradayweg 4-6, 14195 Berlin, Deutschland, cslenard@gmail.com*

[b] *Universitatea Babeş-Bolyai, Facultatea de Chimie şi Inginerie Chimică, Str. Kogălniceanu Nr. 1, RO-400084 Cluj-Napoca,Romania, csbolla@chem.ubbcluj.ro*

The separation of mixtures containing a few components can be made relatively easily by careful and consistent-with-reason variation of the operational parameters. However for the separation of a complex mixture the trial-and-error method might be very time consuming. Numerous examples of difficult-to-separate mixtures can be listed from various fields of chemistry:

- food control and research (separation of carbohydrates, fats, chiral flavor and aroma compounds) [5]
- pharmaceutical and toxicological analysis (screening for drugs and their metabolites in human blood) [6]
- forensic chemistry, analysis of controlled substances (drug profiling, the separation of derivatized amphetamines, opiates from impurities, adulterants and diluents) [7]
- environmental analysis (separation of polychlorinated biphenyls, heterocyclic amines, nitro-polyaromatic hydrocarbon isomers, tetra- and pentachloro-dibenzo-p-dioxin isomers, nitrogen and phosphorous containing pesticides [8], separation of PAHs and PCBs) [9]
- heterogeneous catalysis research (separation of alkane isomers formed in isomerisation/hydroisomerisation and catalytic cracking reactions [10-12], separation of alkane from olefin and water formed in oxidative dehydrogenation and partial oxidation reactions, separation of various partial oxidation products from different substrates) [13].

However a critical reader can identify a few shortcomings in some of the above mentioned literature. In most of the cases the authors report only the retention times, or the chromatogram is shown. The resolution is given very rarely. In several cases it is evident from the chromatograms that the peaks are partly overlapped [9-11]. The use of such a method for quantitative determinations lacks analytical rigor, especially when the authors claim the validation of a new chromatographic method for analytical purposes. It also can be noted that in most of the cases there is no description about the way how the chromatographic method was developed. Seemingly the temperature ramps, holding times and the carrier gas flow rate are set empirically/arbitrarily. In general, the optimization of the chromatographic method with respect to resolution and analysis time is seldom reported. In the following we present through three examples in more detail the above mentioned deficiencies.

Kim and Vane claimed the successful development of a chromatographic method for the simultaneous separation and identification of a mixture containing 40 PAH and PCB compounds [9]. The temperature program and carrier gas flow rate was given. The resolution was given only for the benzo[b]fluoranthene and benzo[k]fluoranthene peak-pair. These were found to be “80% resolved by 2 seconds”. However this is confusing, because the unit of the resolution is not percentage and seconds, but it is a dimensionless number. Some other peaks were characterized only qualitatively by shape and width. No comparison was given between the combined method developed by the authors and the existing method for the individual determination of PAHs and PCBs.

Claude et al. studied the hydro-isomerisation of n-C_{10}–n-C_{24} alkanes [10]. The products were analyzed by on-line gas-chromatography. The temperature program was the following: 10 ºC for 5 minutes than a ramp of 5 ºC/min to 120 ºC followed by the second ramp of 2 ºC/min to 200 ºC and finally the third ramp of 0,1 ºC/min up to 205 ºC. The mono- and multi-branched products eluted in two groups. Although the resolution is not given for the peak-pairs, from the chromatogram one can see that there are partly or totally overlapped peaks. The analysis time was 115-120 minutes, but apparently nothing elutes from the columns before 80 minutes. This means that only about 32% of the chromatogram contains information. The choice of the temperature program is strange because in gas chromatography the use of sub-ambient starting temperature is uncustomary for two reasons. The first reason is that after the completion of a measurement, the GC oven needs to be cooled down from 205 ºC to 10 ºC for the starting another analysis. The cooling is time consuming; therefore the sampling rate is lower than 1 injection/120 minutes. Moreover at that low starting temperature the long chain alkanes are condensing in the column inlet and possibly also in the injector port or valve system and vaporizing when the temperature becomes high enough.

Huybrechts et al. developed a high throughput reactor system for long-chain n-alkane hydroconversion combined with a fast analytical system [11]. They employed a multi-capillary column with poly-dimethylsiloxane stationary phase for the separation of the C_1-C_{10} products. The N_2 carrier gas flow rate was set to 67 ml/min. The temperature was ramped from 40 to 75 ºC by 15 ºC/min. The analysis time was only 3,2 minutes instead of 45 minutes for a conventional 50 m long capillary column. However the authors admitted that there were overlapped peaks, like 2,5-dimethyl-octane and 3,5-dimethyl-octane, 3,4-dimethyl-octane and 3-ethyl-4-methyl-heptane, 4-propyl-heptane and 4,5-dimethyl-octane, 4-ethyl-octane and 2,3-dimethyl-octane, 5-methyl-nonane and 4-methyl-nonane, 3-ethyl-octane and 3-methyl-nonane and 2-methyl-nonane, respectively. Because of the insufficient peak resolution the product selectivities are questionable. Apparently no attempt was undertaken to improve the resolution of peaks. Therefore it can be concluded that the analytical accuracy was sacrificed for fast data acquisition.

Whenever there is a need to separate a complex mixture it is recommended to develop and optimize the chromatographic method based on a rational way. For this purpose the knowledge of the thermodynamic and kinetic parameters of the separation is needed [1-4, 14, 15]. Possibly because of their apparent simplicity, computer programs and expert systems are becoming more and more extensively used for the method development. However these are based on a large number of retention time data determined under various conditions Thus, the method development is possible only for those compounds for which retention data already exists in the databases and libraries of these programs [4, 16]. Some gas chromatography companies claim that their software enables the user to develop a separation method from a single isothermal run.

The most important thermodynamic quantity of the separation is the adsorption enthalpy (heat of adsorption). This quantity gives information about the interaction between the adsorbent and adsorbate. Based on the strength of interaction the adsorption can be divided into three groups: physical, reversible chemical and irreversible chemical adsorption. The threshold value for the adsorption enthalpy between physical and chemical adsorption is 62,8 kJ/mol (or 15 kcal/mol) [2-4]. The adsorption entropy is connected to the loss of degrees of freedom upon adsorption of the molecules on the surface of the column material. Hence the adsorption entropy has a negative value [4]. From the rate theory one can determine the longitudinal diffusion coefficient and the resistance to mass transfer coefficient.

Besides the fact that all these quantities are indispensable for a rational development of the separation method, they are useful in understanding of the retention mechanism [1-4]. These information could also be explored in the Qualitative Structure Retention Relationship (QSRR) studies, i.e. the knowledge of thermodynamic and kinetic quantities gives a hint of which molecular variable (descriptor) has the greatest effect in the separation. Therefore this approach in QSRR would offer the possibility to reduce the number of variables in a rational way, to those which do have physical meaning in terms of the phenomena implied by the separation. It was already shown that a properly chosen equation involving 2-3 parameters among the physical variables (boiling point, molar refraction, molar volume, van der Waals volume, number of carbon atoms, dipole moment) and topological indices (connectivity index and general index of molecular complexity) gives a good correlation [17].

In this work we proposed to study the separation of some saturated hydrocarbons (n-hexane, 2-methyl-hexane, 3-methyl-hexane, 2,2-dimethyl-butane, 2,2-dimethyl-pentane, methyl-cyclopentane and cyclohexane) on a DB-1 capillary column. In the literature the Kováts retention indices of these compounds are available on DB-1 [18-21] and on various other capillary columns, determined mostly at 60ºC. A very good inter-laboratory reproducibility of the retention index on the same column can be observed. Moreover the intra-laboratory reproducibility of the Kováts retention index on three different columns, DB-1, squalene and SE-30 was also shown [21]. However, up to our best knowledge, the thermodynamic and kinetic parameters of the separation of these compounds on the poly-dimethyl-siloxane stationary phase are still missing. Therefore we aimed to determine these quantities. Since some of these hydrocarbons are the products of n-hexane isomerisation reaction, we also proposed to develop a separation method for a mixture of isomers.

RESULTS AND DISCUSSION

For the determination of the adsorption enthalpy and entropy of the analytes, isothermal chromatographic runs were performed in the temperature interval between 60 and 120ºC, at 2,0 ml/min constant carrier gas flow rate. The plot of retention time of the compounds at different temperatures is shown in Figure 1. The retention times seem to decrease exponentially with the temperature. The curves do not cross each other; therefore the elution order does not change in the studied temperature interval.

At the first glance it can be seen that the peaks are well resolved in the 60-90℃ interval. At higher temperature the difference of retention times of the adjacent peaks becomes closer to each other, suggesting the decrease of the resolution.

The elution order is the following: 2,2-dimethyl-butane; 2-methyl-pentane; 3-methyl-pentane; n-hexane; 2,2-dimethyl-pentane; methyl-cyclopentane; cyclohexane. This is in agreement with the literature. The Kováts retention indices corresponding to the compounds listed according to the elution order are the following: 538,0; 569,7; 584,4; 600; 625,7; 630,4; 664,2 [18-21]. The first four members of this elution order show that the retention time decreases with the branching of the carbon chain.

The retention factor (k) for each compound was calculated from the retention time (t_R) and gas holdup time (t_M), respectively, according to the equation (1). The gas holdup time was determined by measuring the retention time of air, which is neither retained nor separated to oxygen and nitrogen by the DB-1 column. The adjusted retention time ($t'_R=t_R-t_M$) is equal with the time the analyte spends on the stationary phase. Therefore the retention factor is the ratio between the times the analyte spends on the stationary phase and in the mobile phase, respectively.

The separation factor (α) has been calculated for the successively eluting peaks, according to the equation 2 and represented in function of temperature. The lower the separation factor, the more difficult to separate the peaks and vice versa. When two peaks are overlapped (partly or totally co-eluting), the separation factor becomes very close to or equal to 1.

$$k = \frac{t_R - t_M}{t_M} = \frac{t'_R}{t_M} \qquad (1)$$

$$\alpha = \frac{k_{i+1}}{k_i} = \frac{t'_{R,i+1}}{t'_{R,i}} \qquad (2)$$

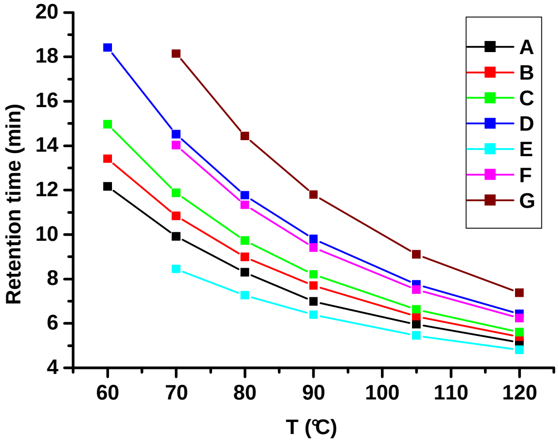

Figure 1. The effect of the temperature on the retention time of the analytes. A: 2-methyl-pentane, B: 3-methyl-pentane, C: n-hexane, D: methyl-cyclopentane, E: 2,2-dimethyl-butane, F: 2,2-dimethyl-pentane, G: cyclohexane.

It can be seen from Figure 2 (a) that the most difficult to separate peak-pair is methyl-cyclopentane and 2,2-dimethyl pentane. Surprisingly, the methyl-cyclopentane and cyclohexane peak-pair is the easiest to separate. The separation of the chain isomers of n-hexane is relatively easy. This separation is the most important from the point of view of n-hexane isomerisation reaction. For kinetic studies the reaction is carried out at low n-hexane conversion. In this case mostly 2-methyl-pentane and 3-methyl-pentane isomers are formed.

The resolution of the adjacent peaks has been calculated (equation 3). A resolution larger than 1,5 means baseline resolution of the adjacent peaks. The shapes of the resolution versus temperature curves are very similar to the retention factor versus temperature curves. Based on these figures it can be seen that an isothermal chromatographic method operating in the temperature interval between 80-105ºC is good with respect to the resolution of the peaks and the analysis time. The analysis time in case of an isothermal method at 80ºC would be roughly of 15 minutes. However the optimal method among the studied ones is the isothermal run at 105ºC. In this case the analysis time is reduced to about 10 minutes. The analysis time might be reduced further by developing a temperature programmed chromatographic method.

$$R_s = \frac{2 \cdot (t_{R,i+1} - t_{R,i})}{w_{i+1} + w_i} = \frac{2 \cdot (t'_{R,i+1} - t'_{R,i})}{w_{i+1} + w_i} \qquad (3)$$

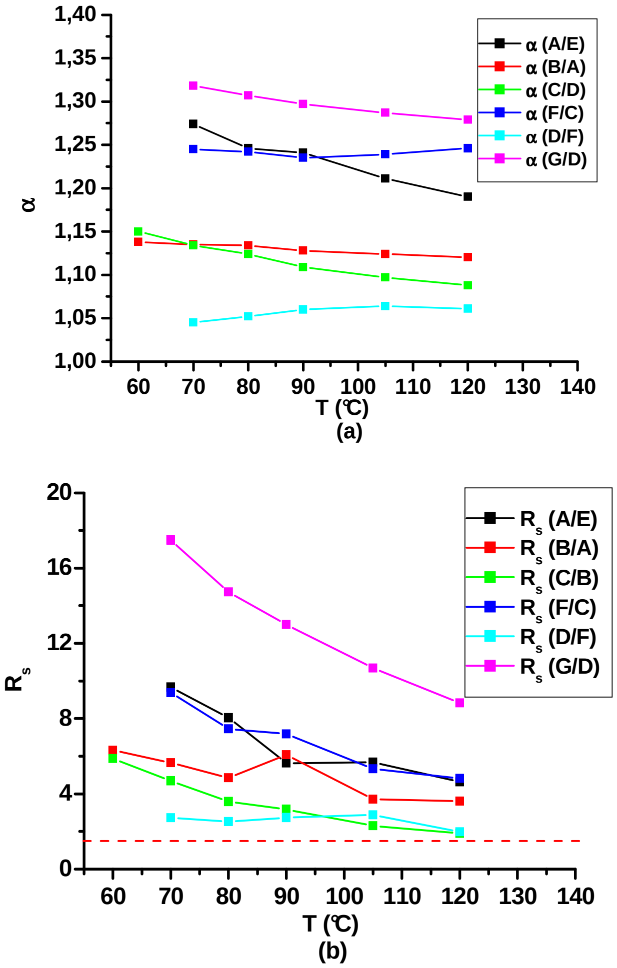

Figure 2. (a) The effect of the temperature on separation factor (α) of the successively eluting analytes. (b) The effect of the temperature on retention factor (R_S) of the successively eluting analytes. The dotted horizontal line at R_S=1,5 stands for the limit of baseline separation. The componds in both figures are: A: 2-methyl-pentane, B: 3-methyl-pentane, C: n-hexane, D: methyl-cyclopentane, E: 2,2-dimethyl-butane, F: 2,2-dimethyl-pentane, G: cyclohexane

The temperature programmed method can be developed experimentally, by trying different heating rates, starting- and end temperatures. The hold times at starting and end temperature can also be varied, but then the parameter space will be very large. Therefore a large number of experiments need to be done.

The other approach in method development is the modeling of the retention times under temperature programmed conditions. This is possible once the adsorption enthalpy and entropy is extracted from the isothermal runs [1-4, 14, 15].

For the determination of the thermodynamic quantities, the specific retention volume (V_g) was calculated (equation 4) at different column temperatures (T).

$$V_g = \frac{F_c \cdot j \cdot (t_R - t_M) \cdot 273}{m_{sp} \cdot T} \qquad (4)$$

For the calculation of V_g, the adjusted retention time was determined and normalized with the mass of the stationary phase (m_{sp}). The flow rate of the carrier gas (F_c) should be constant for the measurements at different temperatures (i.e. the GC was operated in constant flow mode). Because the inlet and outlet pressure (p_i and p_o, respectively) is different at different column temperatures, the pressure drop along the column also changes significantly with the variation of the temperature. Therefore the requirement for isothermal and isobaric operation mode is apparently infringed. To overcome this, the retention volume data should be corrected with the James-Martin correction factor (equation 5) [1-4].

$$j = \frac{3}{2} \cdot \frac{\left[\left(\frac{p_i}{p_o}\right)^2 - 1\right]}{\left[\left(\frac{p_i}{p_o}\right)^3 - 1\right]} \qquad (5)$$

We show here the simplification of the above equation for calculation of the James-Martin correction factor for large difference between the inlet and outlet pressure. When the relative pressure is higher than 6, the 2nd and 3rd power of the relative pressure is so high that the −1 term may be omitted from both the numerator and denominator of the above formula. Then it may be simplified further by canceling the power and the equation 6 will be equivalent with equation 5. The equivalence of these equations with the condition of $p_r>6$ is demonstrated by the Figure 3.

$$j = \frac{3}{2} \cdot \left(\frac{p_i}{p_o}\right)^{-1} \qquad (6)$$

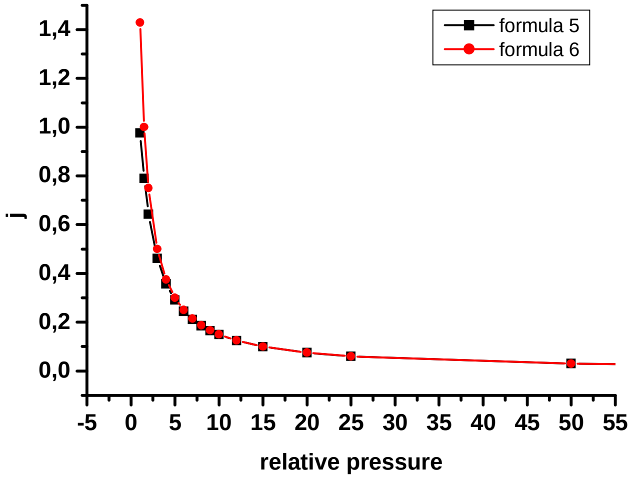

Figure 3. The James-Martin factor at different relative pressures.

Since the chromatographic experiments were done in a GC-MS setup, the end of the column is placed in the chamber of the mass spectrometer, where the pressure (p_o) is in the order of 10^{-8} bar. The inlet pressure (p_i) is slightly higher than the atmospheric pressure. Therefore the relative pressure (p_i/p_o) is in the order of 10^8. Because the above mentioned condition concerning the relative pressure is fulfilled, we used the simple equation (6) to calculate the James-Martin correction factor.

The logarithm of the specific retention volume was represented in function of the reciprocal temperature (Figure 4). The adsorption enthalpy was calculated from the slope of the straight line; while the adsorption entropy was calculated from the intercept, based on the equation (7) [1-4, 14]. The older literature [1] might be misleading with respect of the adsorption enthalpy. There the adsorption enthalpy is considered to be identical with the evaporation heat of the solute from a solution. However from the energetic point of view the adsorption-desorption equilibrium is not identical with the condensation-evaporation equilibrium.

The adsorption-desorption equilibrium involved by gas chromatography implies only adsorbate-adsorbent interactions at low adsorbate concentration (infinite dilution). In this case it is possible to determine the adsorption enthalpy of the adsorbate (analyte) on the adsorbent (stationary phase).

At higher adsorbate concentration the adsorbate-adsorbate interactions will have a contribution besides the adsorbate-adsorbent interaction. Therefore the apparent enthalpy will be a combination of the adsorption and condensation enthalpy.

$$\ln(V_g) = -\frac{\Delta H_{ads}}{R \cdot T} + \frac{\Delta S_{ads}}{R} \qquad (7)$$

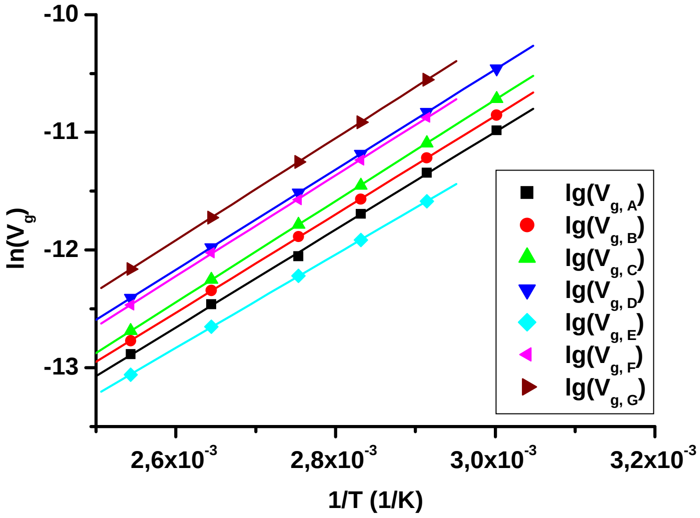

Figure 4. Plot of the logarithm of the specific retention volume (V_g) in function of the reciprocal temperature. A: 2-methyl-pentane, B: 3-methyl-pentane, C: n-hexane, D: methyl-cyclopentane, E: 2,2-dimethyl-butane, F: 2,2-dimethyl-pentane, G: cyclohexane.

In order to show that the thermodynamics of the adsorption and condensation is different, in the Table 1 we compiled the phase change thermodynamic quantities amongst the determined adsorption enthalpy and entropy. For comparison, we also determined the adsorption thermodynamic quantities for polar compounds like water, methanol and acetonitrile.

The magnitude of the adsorption enthalpy indicates physical adsorption of all the studied compounds on the stationary phase. The numerical values of adsorption enthalpy are close to each other regardless of the polarity of the analyte. This is not unexpected since the stationary phase is not polar. It can also be seen that the adsorption enthalpy of all the hydrocarbons are is 3 up to 4,5 kJ/mol more negative than the enthalpy of condensation. In case of the water and methanol the case was observed, however for the acetonitrile the adsorption enthalpy and condensation enthalpy are found to be equal within experimental errors.

The adsorption entropy determined from the Figure 3 has a significant negative value. This means that upon adsorption the degrees of freedom of the molecules are significantly reduced. The adsorption entropy of the hydrocarbons is almost the same. Compared to them the adsorption entropy of water, methanol and acetonitrile is more negative.

The condensation entropy is not readily available. However the vaporization entropy can be calculated based on the equation 8 [22]. The data needed for the calculation of the vaporization entropy are available. The enthalpy of vaporization is numerically equal to the absolute value of the condensation enthalpy (equation 9). Therefore the absolute value of the condensation entropy is equal with the vaporization entropy (equation 10). The values are close to 87-89 J/mol·K predicted by the Trouton's rule. However the water and methanol is a well known exception from the Trouton's rule due to hydrogen bonding.

It can be noted that the adsorption entropy is roughly 2,3 times more negative than the condensation entropy of the compounds. This also indicates that the thermodynamic parameters of adsorption and condensation are very different.

$$\Delta S_{vap} = \frac{\Delta H_{vap}}{T_{boil}} \qquad (8)$$

$$\Delta H_{vap} = -\Delta H_{con} \qquad (9)$$

$$\Delta S_{vap} = -\Delta S_{con} \qquad (10)$$

When the average linear velocity of the carrier gas is increased the retention times and peak widths are decreasing and vice versa. For the optimization of the average linear velocity (u), and the determination of the kinetic parameters the Golay equation was used [1-4]. The Golay equation is similar to the van Deemter equation which is applicable in case of the packed columns. However in the capillary columns there is no eddy diffusion, therefore the Golay equation does not contain the first term of the van Deemter equation.

The height equivalent of the plate theory (H) was determined at different carrier gas flow rates. On plot (5) one can see that the minimum of the curves correspond roughly to the optimal average linear velocity of 23 cm/s (or 0,8 ml/min carrier gas flow rate). However, if the resolution at higher carrier gas flow rate is satisfactory as it was shown above, one may apply higher flow rate to shorten the analysis time [3].

Table 1. The thermodynamic parameters of the adsorption of the componds on poly-dimethyl-siloxane stationary phase. ΔH_{ads} – adsorption enthalpy, ΔS_{ads} – adsorption entropy, ΔH_{con} – enthalpy of condensation [22, 23], T_{boil} – boiling point at atmospheric pressure [23], ΔS_{con}– the condensation entropy, ΔH_{con}-ΔH_{ads} – the absolute difference between the enthalpy of condensation and the adsorption enthalpy. A: 2-methyl-pentane, B: 3-methyl-pentane, C: n-hexane, D: methyl-cyclopentane, E: 2,2-dimethyl-butane, F: 2,2-dimethyl-pentane, G: cyclohexane, H: water, I: methanol, J: acetonitrile.

Compound	$-\Delta \tilde{H}_{ads}$ **(kJ/mol)**	$-\Delta \tilde{S}_{ads}$ **(J/molK)**	$-\Delta \tilde{H}_{con}$ **(kJ/mol)**	T_{boil} **(K)**	$-\Delta \tilde{S}_{con}$ **(J/molK)**	ΔH_{con}-ΔH_{ads} **(kJ/mol)**
A	34,5±0,4	214,1±2,7	30,0±0,1	334,0±0,1	89,9±0,3	4,5±0,4
B	34,8±0,1	213,7±0,5	30,3±0,1	336,4±0,4	90,1±2,7	4,5±0,9
C	35,8±0,1	215,6±0,3	31,1±0,9	341,9±0,3	91,0±0,3	4,7±0,1
D	36,6±0,8	212,3±0,2	31,7±0,1	345,0±0,2	91,9±0,3	3,7±0,1
E	33,0±0,1	211,6±0,6	27,8±0,1	322,9±0,1	86,1±0,3	5,2±0,1
F	35,6±0,2	213,3±1,3	32,5±0,1	352,3±0,3	92,3±0,3	3,1±0,2
G	36,0±0,1	211,9±0,4	33,0±2,0	353,9±0,2	93,2±5,7	3,0±2,0
H	34,7±0,8	237,2±4,9	40,7	373,2±0,4	109,1	-6,0
I	31,2±1,0	223,9±3,4	37,0±2,0	337,8±0,3	109,5±5,9	-5,8±2,2
J	33,6±0,2	219,2±1,4	33,3±0,3	354,8±0,4	93,9±0,9	0,2±0,4

For the determination of the longitudinal diffusion term (B) and resistance to mass transport term, one can perform a nonlinear fitting procedure according to the Golay equation 11.

$$H = \frac{B}{u} + C \cdot u \qquad (11)$$

Here we present the linearization of the Golay-equation. Both sides of the equation 11 were multiplied by the average linear velocity of the carrier gas (u). The resulted equation 12 is still nonlinear, but after performing $H \cdot u = Y$ and $u^2 = X$ variable changes, it can be transformed into the linear equation 13. Then the B and C parameters can be determined according to the conventional linear fitting procedure (Figure 6).

$$H \cdot u = B + C \cdot u^2 \qquad (12)$$

$$Y = B + C \cdot X \qquad (13)$$

The value of the longitudinal diffusion coefficient (B) is high and the resistance to mass transfer (A) is small. This is a known feature for a GC-MS system, because there is a very large pressure drop along the column [3,4]. The variation of B and C values with the structure of the compounds is difficult to interpret. However the numerical values of the longitudinal diffusion coefficient are statistically close to each other.

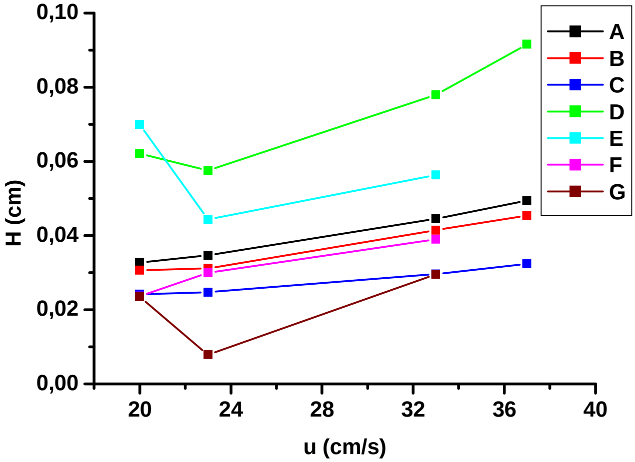

Figure 5. The effect of the carrier gas linear velocity on the height equivalent of the plate theory*.* A: 2-methyl-pentane, B: 3-methyl-pentane, C: n-hexane, D: methyl-cyclopentane, E: 2,2-dimethyl-butane, F: 2,2-dimethyl-pentane, G: cyclohexane.

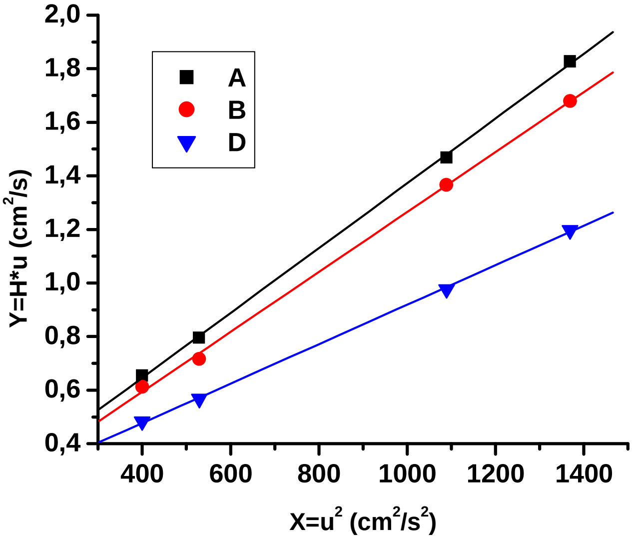

Figure 6*.* Fitting the linearized Golay equation. 2-methyl-pentane, B: 3-methyl-pentane, D: methyl-cyclopentane, the other compounds were omitted for clarity reasons.

Table 2. The longitudinal diffusion coefficient and resistance to mass transport of the compounds. (a) - because hexane was the solvent, and its peak was not symmetric (tailing) and much broader and compared to the other peaks, the data were omitted from this table.

Compound name	**B (cm^2/s)**	**C (s)**
2-methyl-pentane	1,62 ± 0,15	1,21 ± 0,02
3- methyl-pentane	1,46 ± 0,24	1,12 ± 0,03
n-hexane	(a)	(a)
methyl-ciklopentane	1,82 ± 0,11	0,74 ± 0,01
2,2-dimethyl-butane	1,41 ± 0,27	1,15 ± 0,06
2,2-dimethyl-pentane	1,73 ± 0,30	1,02 ± 0,04
ciklohexane	2,26 ± 0,35	0,99 ± 0,06

CONCLUSIONS

Jennings et al. pointed out in the preface of their textbook [3] that although chromatography is a very powerful analytical technique, many researchers are using it only as a means to an end and sometimes the better understanding of the chromatographic principles is lacking. However, due to the fact that it is such a powerful technique, even with little knowledge it is still possible to generate useful data. For the improvement of the data quality and quantity, the scientists who employ chromatography are encouraged for a more comprehensive understanding of their specific separation problem.

In this paper we proposed to follow these recommendations for the rational development of the separation method for some saturated hydrocarbons. In the first approach isothermal chromatographic runs were performed. An optimal chromatographic method was chosen with respect of resolution and analysis time. We also reported the thermodynamic and kinetic parameters of the separation process. These data will be used for the estimation of the retention times under temperature programmed conditions.

EXPERIMENTAL SECTION

The chromatographic measurements were performed on a GC-MS (Agilent 6890 GC coupled with Agilent 5975B MSD) setup. Two solutions have been prepared:

(a) 2-methyl-pentane and 3-methyl-pentane in n-hexane, and

(b) 2,2-dimethyl-butane, 2,2-dimethyl-pentane and cyclohexane in n-hexane as solvent. The concentration of all the compounds was approximately 1,0 vol%.

The sampling was performed via an automatic liquid sampler equipped with a 10 μl syringe. A volume of 1,0 μl solution has been injected in the liner heated up to 150℃. The split ratio was set to 1:15 for all the measurements. Helium was used for the split-flow.

DB-1 type non-polar column chromatographic column was used, which is suitable for general separation purposes. The length of the column was 60 m, the diameter was 320 μm, the thickness of the stationary phase was 5,0 μm. The stationary phase consists of 100% poly-dimethyl-siloxane. The characteristics of this stationary phase are the following: dispersion index=9, dipole index=0, acid-base index=0 [3]. Helium was used as carrier gas.

The first series of measurements consisted of isothermal runs at 60, 70, 80, 90, 105 and 120℃, and at constant carrier gas flow rate of 2,0 ml/min, respectively. In the second experiment series the carrier gas flow rate was set to 2,0; 1,6; 0,8 and 0,6 ml/min, respectively, while the column temperature was kept constant at 60℃. The average linear velocity of the carrier gas corresponding to the above flow rates were 37, 33, 23 and 20 cm/s, respectively. The variation of average linear velocities in a wider interval was not possible because of technical reasons. Flow rates lower than 0,6 ml/min could not be achieved because the pressure at the inlet of the column would be below the threshold level of 0,1 bar. However the upper limit of carrier gas flow rate of 2,0 ml/min was determined by the pumping capacity of the turbo-molecular pump of the MS detector.

REFERENCES

1. J. Tranchant, Principles and retention values, Isothermal-isobaric chromatography in J. Tranchant (ed.), Practical Manual of Gas Chromtography, Elsevier Publishing Company, Amsterdam, **1969**, 1.
2. H. Purnell, Gas Chromatography, Wiley, New York, **1962**, 75.
3. W. Jennings, E. Mittelfehldt, P. Stremple, Analytical Gas Chromatography, Academic Press, **1997**, 114.
4. R. L. Grob, E. F. Barry, Modern Practice of Gas Chromatography, Wiley, New York, **2004**, 615.
5. O. Fröhlich, G. Takeoka, K. H. Engel, Analysis of Food Ingredients, Chapter II. 73-171, in R. Wittkowsky, R. Matisek (eds.), Technomic Publishing Company Inc., **1990**, ISBN 1-56676-006-2.
6. M. E. Sharp, *J. Anal. Toxicol*, **1987**, *11*, 8.
7. M. D. Cole, The Analysis of Controlled Substances, Wiley, **2003**, ISBN 0-471-49252-1, 1.

8. T. Shibamoto (ed.), Chromatographic Analysis of Environmental and Food Toxicants, Marcel Dekker Inc., **1998**, ISBN 0-8247-0145-3, 1-93, 169.
9. A. Kim, Ch. Vane, Simultaneous Determination of PAHs and PCBs by GCMS Analysis, British Geological Survey, BGS Laboratory Technique Development, Internal Report IR/07/045, **2007**, free access under: http://nora.nerc.ac.uk/7569/1/IR07045.pdf
10. M. C. Claude, J. A. Martens, *J. Catal.*, **2000**, *190*, 39.
11. W. Huybrechts, J. Mijoin, P. A. Jacobs, J. A. Martens, *Appl. Catal. A: General*, **2003**, *243*, 1.
12. R. C. Striebich, Fast Gas Chromatography in J. Cazes (ed.) Encyclopedia of Chromatography, Marcel Dekker Inc., DOI 10.1081/E-Echr120004560, **2002**.
13. E. Yu. Yakovleva, O. V. Skrypnik, *J. Anal. Chem.,* **2008**, *63*, 5, 455.
14. R. P. W. Scott, Programmed Temperature Gas Chromatography, J. Cazes (ed.) Encyclopedia of Chromatography, Marcel Dekker Inc., DOI 10.1081/E-Echr120004560, **2002**.
15. V. Bartu, S. Wicar, *Anal. Chim. Acta*, **1983**, *150*, 245.
16. A. Braithwaite, F. J. Smith, Chromatographic Methods, 5th Edition, Kluwer Academic Publishers, **1999**, 417.
17. K. Héberger, *Anal. Chim. Acta*, **1989**, *223*, 161, and references therein.
18. E. Kováts, *Helv. Chim. Acta*, **1958**, *41*, 1915.
19. J. Krupčík, I. Skačáni, E. Benická, Pat Sandra, *Collect. Czech. Chem. Commun.,* **1994**, *59*, 2390.
20. A. J. Lubeck, D. L. Sutton, *J. Hi. Res. Chromatogr. and Chromatogr. Comm.*, **1983**, *6*, 328.
21. D. Estrel, M. Mohnke, F. Biermans, H. Rotzsche, *J. Hi. Resol. Chromatogr.*, **1995**, *18*, 403.
22. P. Atkins, J. de Paula, Atkins' Physical Chemistry, Oxford University Press, 8th Ed., **2006**, 87.
23. www.nist.webbook.org/chemistry

STUDIA UNIVERSITATIS BABEŞ-BOLYAI, CHEMIA, XLV, 2, TOM II, 2010

Dedicated to the memory of Prof. dr. Ioan Silaghi-Dumitrescu marking 60 years from his birth

THE STUDY OF POLYPHENOLS FROM *TRIFOLIUM PRATENSE* L. AND *MEDICAGO SATIVA* L. HYDROALCOHOLIC EXTRACTS BY HPLC-UV-MS

NELI-KINGA OLAH[a], DANIELA HANGANU[b],
LAURIAN VLASE[c], CODRUTA COBZAC[d]

ABSTRACT. The polyphenols are widespread compounds from plants having important pharmacological activities. *Trifolium pratense* L. and *Medicago sativa* L. are important cultivated medicinal plants mostly for their content in polyphenols and especially in isoflavons that are also polyphenolic compounds. The identification and quantitative determination of polyphenols from *Trifolium pratense* and *Medicago sativa* hydroalcoholic extracts was performed by a rapid HPLC-UV-MS methods by that can be identified a wide range of polyphenols. There were evaluated the native hydroalcoholic extracts and also the hydrolyzed extracts. There were found in *Trifolium pratense* hyperoside, isoquercitrine – glycosides having as aglykon quercetol, p-coumaric, ferulic, genistic and chlorogenic. In *Medicago sativa* were identified apigenine, p-coumaric, ferulic and genistic acids.

Keywords: *Trifolium pratense, Medicago sativa, polyphenols, HPLC-UV-MS*

INTRODUCTION

The polyphenols are important active compounds that are present in many plants. The flavonoids, including isoflavons, the polyphenyl carboxylic acids, the tannins, the coumarins take part from polyphenols family.

The polyphenols has important pharmacological properties, one of them being the antioxidant activity. They are important for maintain the health and also as therapeutic compounds in different diseases [1,2].

---

[a] *"Vasile Goldis" West University of Arad, Faculty of Pharmacy, Department of Pharmaceutical Industry, 1 Feleacului Street, 300041, Romania and SC PlantExtrakt SRL, 407059 Radaia, Jud. Cluj, Romania, olahdr@aol.com*

[b] *"Iuliu Hațieganu" University of Medicine and Pharmacy, Faculty of Pharmacy, Department of Pharmacognosy, Cluj-Napoca, 15 I. Creangă Street, Romania, handa_1964@yahoo.com*

[c] *"Iuliu Hațieganu" University of Medicine and Pharmacy, Faculty of Pharmacy, Department of Pharmaceutical Technology and Biopharmaceutics, Cluj-Napoca, 15 I.Creangă Street, Romania*

[d] *"Babes-Bolyai" University, Faculty of Chemistry and Chemical Engineering, Department of Analytical Chemistry, Arany Janos str. 11, Cluj-Napoca, Romania*

Trifolium pratense is a cultivated plant being known for its content in isoflavons as daidzein, genistein and formononetin, but contains also other polyphenols as flavonoids, coumarins and also other compounds like essential oil, cyanogenetic glycosides, etc. [2,3,4,5,6].

Medicago sativa is also a cultivated plant. It contains saponins, carotenoids, and polyphenols including isoflavons like genistein, daidzein and cumestans [2,3,7,8].

The total polyphenols can be evaluated by spectrophotometric methods using Folin-Ciocalteu [9] or Arrnow [10] reagent. The individual polyphenols can be identified and quantitatively determined just by chromatographic methods: TLC [11] and more exactly by HPLC coupled with UV-Vis spectrophotometric detector and mass-spectrometric detector [5,6,12,13,14,15,16,17].

This paper present the evaluation of polyphenolic profile from *Trifolium pratense* and *Medicago sativa* hydroalcoholic extracts using a HPLC-UV-MS method that provides the possibility of identification of a wide range of polyphenols.

RESULTS AND DISCUSSION

The table 1 presents the retention times found for 16 polyphenol standards respectively the equations for calibration curves obtained for each of 16 standards. In figure 1 can be seen the obtained chromatogram for the standards.

Table 1. The retention time and calibration curves equation for polyphenol standards

Peak no.	Name of standard	Retention time, min, r_t ± SD	Calibration curves equation A = peak area, c = concentration
1	Gentisic acid *	2.15± 0.07	A = -0,335 + 14,261c
3	Chlorogenic acid *	5.62± 0.05	A = -1,324 + 26,492c
5	p-coumaric acid	8.70± 0.08	A = -0,326 + 33,230c
6	Ferulic acid	12.20 ± 0.10	A = -1,017 + 39,558c
7	Sinapic acid	14.30 ± 0.10	A = -0,237 + 37,103c
8	Hyperoside	18.60 ± 0.12	A = 0,107 + 19,294c
9	Izoquercitrin	19.60 ± 0.10	A = -0,273 + 12,978c
10	Rutoside	20.20 ± 0.15	A = 0,227 + 13,473c
11	Myricetin	20.70 ± 0.06	A = 0,270 + 26,150c
12	Fisetin	22.60 ± 0.15	A = 0,292 + 17,190c
13	Quercitrin	23.00 ± 0.13	A = 0,048 + 10,698c
14	Quercetol	26.80 ± 0.15	A = -1,152 + 36,327c
15	Patuletine	28.70 ± 0.12	A = -0,430 + 31,450c
16	Luteolin	29.10 ± 0.19	A = -0,761 + 28,927c
17	Kaempferol	31.60 ± 0.17	A = -1,271 + 30,152c
18	Apigenin	33.10 ± 0.15	A = -0,909 + 20,403c

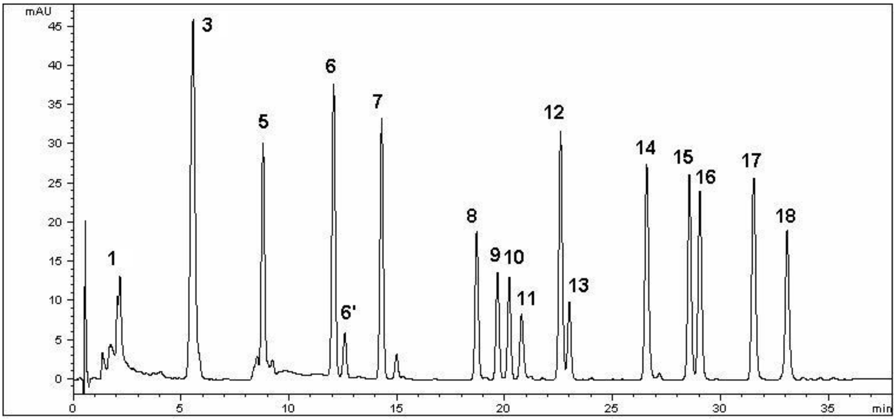

Figure 1. The chromatogram of polyphenol standards

In figures 2 and 3 can be seen the HPLC-UV chromatograms for the native hydroalcoholic and hydrolyzed *Trifolium pratense* extract. It can be identify in native extract the hyperoside and isoquercitrin from flavonoids group respectively in small amount, the free p-coumaric and ferulic acids. The identification of flavonoids was made based on comparison of retention time and MS spectra with those of the studied standards. These compounds can be also quantified by HPLC-UV. The small amount from p-coumaric and ferulic acids were identified based on them MS spectra. Because of small amount these compounds can not be exactly quantified by HPLC-UV.

The hyperoside and isoquercitrin free during the hydrolysis quercetol, they aglykon. These could be demonstrated by HPLC-UV-MS evaluation of hydrolyzed extract in that there were identified quercetin, p-coumaric, ferulic, chlorogenic and genistic acids. The higher amounts from p-coumaric and ferulic acids respectively the presence of other acids that can not be identified in the native extract, can be explained by the hydrolysis of the compounds in that they are naturally bounded. The quercetol, p-coumaric and ferulic acids were identified based on the comparison of retention times and MS spectra with those of the studied standards.

The chromatogram of native *Trifolium pratense* hydroalcoholic extract shows a main peak X at 21-22 minute that can not be identified as being one of the studied standards. The evaluation of MS spectra (figures 4 and 5) show that this compound has the molecular weight 448 (= 447 + 1 – the signal is for deprotonated molecule) and has a main fragment with molecular weight 286 (= 284 + 1 + 1 – the signal is for deprotonated fragment having a radical to a phenol position). The kaempferol and luteolin, both being flavonoid aglykons, has the molecular weight 286. This indicates that the unidentified can be glycosides of kaempferol or luteolin.

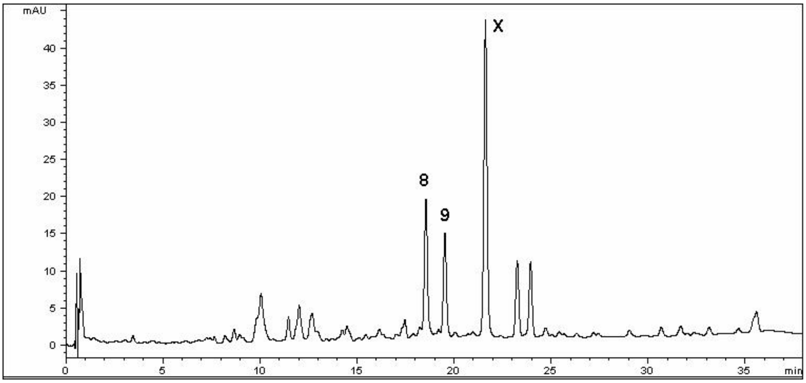

Figure 2. The chromatogram of native *Trifolium pratense* hydroalcoholic extracts

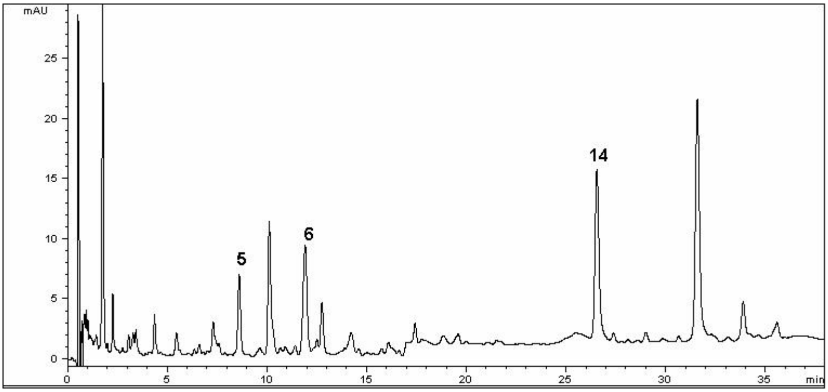

Figure 3. The chromatogram of hydrolyzed *Trifolium pratense* hydroalcoholic extracts

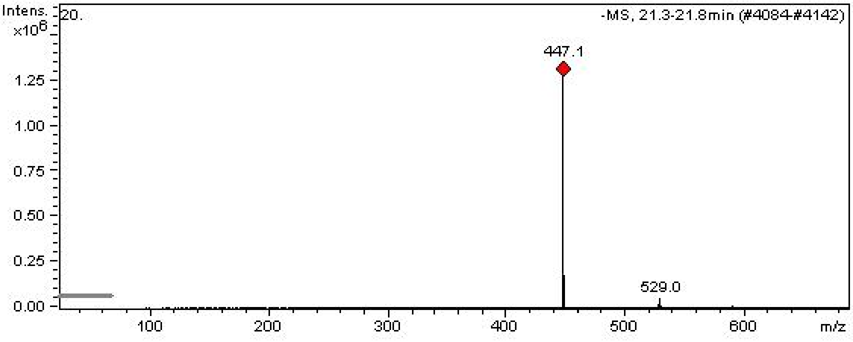

Figure 4. The MS spectra for compound X with molecular signal

In figures 6 and 7 can be observed the HPLC-UV chromatograms for native respectively hydrolyzed *Medicago sativa* hydroalcoholic extract. It can be identify in native extract the apigenin based on comparison of retention time and MS spectra with those of standard apigenin respectively the p-coumaric acid based on MS spectra. This result shows that the apigenin can be found in *Medicago sativa* also as free aglykon, in significant amount to be quantified. The p-coumaric acid is present in small amount as free acid in native extract.

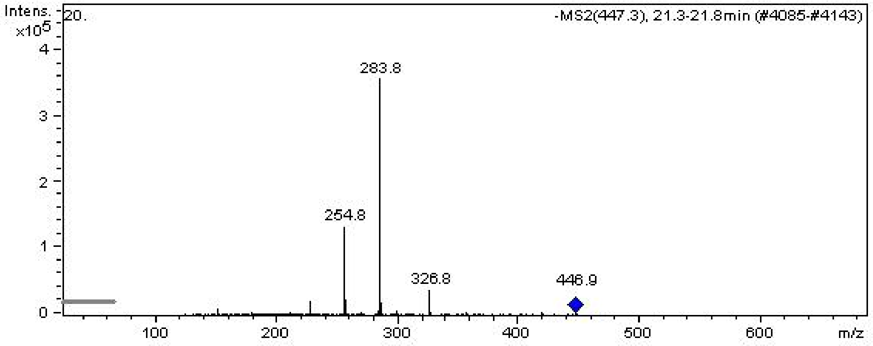

Figure 5. The MS spectra for compound X with fragmentation

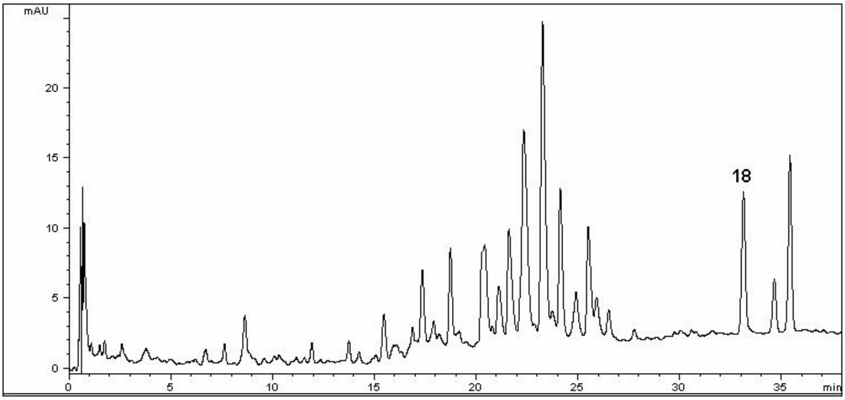

Figure 6. The chromatogram of native *Medicago sativa* hydroalcoholic extracts

The chromatograms show also a lot of significant compounds separated at 15-27 minute that can not be identified as being one of the studied standard compounds. After hydrolysis the chromatogram shows a lower level for apigenin and the unidentified compounds from 15-27 minutes. That indicated that also the unidentified compounds can be flavonoids, probably C-glycosides. The lower level of these compounds and of apigenin can be explained by the degradation of some flavonoidic compounds like apigenin in the hydrolysis condition.

In the hydrolyzed extract can be identified based on retention time and MS spectra in comparison with those of standards the following polyphenols: apigenin, ferulic and p-coumaric acids respectively based just on MS spectra the genistic acid. These results show that the polyphenolic acids are present in *Medicago sativa* mostly in bounded form. The apigenin, p-coumaric and ferulic acids can be quantified.

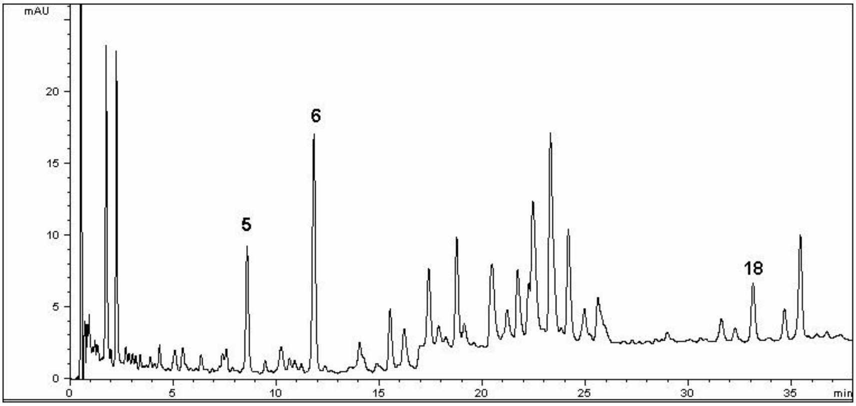

Figure 7. The chromatogram of hydrolyzed *Medicago sativa* hydroalcoholic extracts

In table 2 can be observed the retention times and MS spectra data of identified compounds that can be compared with those of the standards.

In table 3 are presented the results of quantitative determination on the identified compounds. It can be seen that the *Trifolium pratense* extract contains mostly flavonoids – hyperoside and isoquercitrin and smaller amount of bounded acids: p-coumaric acid and ferulic acid. The *Medicago sativa* extract contains apigenin in higher amount and in smaller amount bounded p-coumaric acid and ferulic acid.

The quercetol identified in this paper in the *Trifolium pratense* extract was found also by Booth in different commercial *Trifolium pratense* products. The result of quantitative determination for quercetol (5,581 μg/ml extract meaning 1,86 % reported to the dry plant) shows a higher value that found by Booth (1 %). Booth identified in *Trifolium pratense* also the kaempferol (0,07 %) and fisetin (0,02 %), in small amounts [4]. The kaempferol glycoside can not be certainly identified in the studied Romanian *Trifolium pratense*, neither the kaempferol in the hydrolyzed sample.

Table 2. The retention time and MS spectra data for identified compounds

Name of sample	Name of identified compound	Retention time, min, r_t	MS spectra data for identified compounds / standards
Trifolium pratense native extract	Hyperoside	18,6	463> 254.9, 270.9, 300.7
			463> 254.9, 270.9, 300.7
	Isoquercetin	19,6	463> 254.9, 270.9, 300.7, 342.8
			463> 254.9, 270.9, 300.7, 342.8
	p-coumaric acid	8,7	163> 118.7
			163> 118.7
	Ferulic acid	12,2	193.2> 133.7, 148.7, 177.6
			193.2> 133.7, 148.7, 177.6
Trifolium pratense hydrolyzed extract	Quercetol	26,8	301> 150.6, 178.6, 272.7
			301> 150.6, 178.6, 272.7
	p-coumaric acid	8,7	163> 118.7
			163> 118.7
	Ferulic acid	12,2	193.2> 133.7, 148.7, 177.6
			193.2> 133.7, 148.7, 177.6
	Chlorogenic acid	5,62	353.5>178.7, 190.7
			353.5>178.7, 190.7
	Genistic acid	2,15	153>108.7
			153>108.7
Medicago sativa native extract	Apigenin	33,1	269.2>148.6, 150.6, 224.7, 226.7
			269.2>148.6, 150.6, 224.7, 226.7
	p-coumaric acid	8,7	163> 118.7
			163> 118.7
Medicago sativa hydrolyzed extract	Apigenin	33,1	269.2>148.6, 150.6, 224.7, 226.7
			269.2>148.6, 150.6, 224.7, 226.7
	p-coumaric acid	8,7	163> 118.7
			163> 118.7
	Ferulic acid	12,2	193.2> 133.7, 148.7, 177.6
			193.2> 133.7, 148.7, 177.6
	Genistic acid	2,15	153>108.7
			153>108.7

Table 3. The results of quantitative determination of identified compounds

Sample	Compound	Concentration, □g/ml
Trifolium pratense native extract	Hyperoside	9,766
	Isoquercetin	11,206
Trifolium pratense hydrolyzed extract	Quercetol	5,581
	p-coumaric acid	1,900
	Ferulic acid	3,074
Medicago sativa native extract	Apigenin	11,206
Medicago sativa hydrolyzed extract	Apigenin	2,667
	p-coumaric acid	2,387
	Ferulic acid	4,424

The apigenin identified and quantified in the *Medicago sativa* extract was found in this plant by Stochmal also [8].

The results presented in this paper show that near isoflavons both plants contain also other flavonoids and polyphenolic acids. The polyphenolic acids (p-coumaric, genistic, chlorogenic and ferulic acids) from *Trifolium pratense* and *Medicago sativa* were studied in detail for first time in this paper.

CONCLUSIONS

Using the proposed HPLC method it can be separated a wide range of polyphenols from complex samples as the plant extracts. Using UV and MS detection can be identify also the compounds in small amounts due by the high sensitivity and more precise data that can be obtain with the MS detector.

In the studied plant extracts can be identified the main flavonoidic compounds and polyphenolic acids, both in free and bounded forms. Those existing in significant amounts could be also quantified by HPLC-UV. The present study confirm the presence of some flavonoids in both plants, compounds identified also by other researchers, but the detailed qualitative and quantitative study of polyphenolic acids in these plants is made for first time in this paper.

The identification and quantification of polyphenols from *Trifolium pratense* and *Medicago sativa* extracts is important for the study of therapeutically active compounds from these plants.

EXPERIMENTAL SECTION

There were used the aerial part of fresh plant from *Trifolium pratense* and *Medicago sativa*, both harvested from organic culture near Cluj, in 2008. The plants were botanical identified to PlantExtrakt, Radaia.

The hydroalcoholic extracts were obtained from fresh plant (70% moisture) using 90 % vol. ethanol (pharmaceutical grade) by cold maceration at room temperature, in 10 days. After 10 days of maceration by repetitive mixing the extracts were decanted and the plant residue was pressed. The extracts obtained from decantation and pressing were mixed and filtered. The fresh plant-extract ratio was 1:1 for both extracts.

The hydrolysis of extracts was made using 2N hydrochloric acid (Merck, Germany), 1 ml to 1 ml extract. The hydrolysis was performed at boiling temperature in 40 minutes.

There were used HPLC grade methanol (Merck, Germany) and analytical grade acetic acid (Merck, Germany) to perform the HPLC analysis. As standards were used genistic acid, chlorogenic acid, p-coumaric acid, ferulic acid, sinapic acid, hyperoside, isoquercitrin, rutoside, myricetin, fisetin, quercitrin, quercetol, patuletine, luteolin, kaempferol and apigenin purchased from Merck, Fluka, Sigma or LGC.

The experiment was carried out using an Agilent 1100 HPLC Series system (Agilent, USA) equipped with degasser, binary gradient pump, column thermostat, autosampler and UV detector. The HPLC system was coupled with an Agilent 1100 mass spectrometer (LC/MSD Ion Trap VL). For separation purpose, a reverse-phase analytical column was employed (Zorbax SB-C18 100 x 3.0 mm i.d., 3.5 µm particle); the working temperature was 48 °C. The detection of the compounds was performed on both UV and MS mode. The UV detector was set at 330 nm until 17.5 min, then at 370 nm. The MS system operated using an electrospray ion source in negative mode. The chromatographic data were processed using ChemStation and DataAnalysis software from Agilent, USA.

The mobile phase was a binary gradient prepared from methanol and solution of acetic acid 0.1% (v/v). The elution started with a linear gradient, beginning with 5% methanol and ending at 42% methanol, for 35 minutes; isocratic elution followed for the next 3 minutes with 42% methanol. The flow rate was 1 ml min^{-1} and the injection volume was 5 µl.

The MS signal was used only for qualitative analysis based on specific mass spectra of each compound. The MS spectra obtained from a standard solution of compounds were integrated in a mass spectra library. Later, the MS traces/spectra of the analysed samples were compared to spectra from library, which allows positive identification of compounds, based on spectral mach. The UV trace was used for quantification of identified compounds from MS detection. Using the chromatographic conditions described above, the polyphenols eluted in less than 35 minutes. The acids were identified by MRM mode and the other polyphenols by AUTO MS mode. The detection limits were calculated as minimal concentration producing a reproductive peak with a signal-to-noise ratio greater than three. Quantitative determinations were performed using an external standard method. Calibration curves in the 0.5–50 µg ml^{-1} range with good linearity (R2 > 0.999) for a five point plot were used to determine the concentration of polyphenols in plant samples.

REFERENCES

1. R. Hansel, O. Sticher, “Pharmakognosie. Phytopharmazie”, Springer Verlag, Berlin-Heidelberg-New York, **2004**, 735.
2. I. Ciulei, E. Grigorescu, U. Stanescu, „Plante medicinale. Fitochimie si fitoterapie“, Ed. Medicala, Bucuresti, **1993**, *729*, 677.
3. D. Heber, „PDR for Herbal Medicines“, IIIrd edition, Thomson, USA, *679*, 11.
4. N.L. Booth et al., *Journal of Complementary Medicine*, **2006**, *12 (2),* 133.

5. J. Polasek, E.F. Queiroz, K. Hostettmann, *Phytochem Anal.*, **2007**,*18(1),* 13.

6. Q. Wu, M. Wang, J.E. Simon, *J Chromatogr A.*, **2003**, *1016(2),* 195.

7. R.M. Feingold, *Archive of Intern Medicine*, **1990**, *159 (13),* 338.

8. A. Stochmal, S. Piacente, C. Pizza, F. De Riccardis, R. Leitz, W. Oleszek, *J. Agric. Food Chem.*, **2001**, *49 (2)*, 753.

9. *** Farmacopeea Romana, ed. X, Editura Medicala, Bucuresti, **1993**.

10. *** Farmacopeea Romana, ed. IX, Editura Medicala, Bucuresti, **1976**.

11. H. Wagner, S.Bladt, “Plant Drug Analysis”, Springer Verlag, Berlin-Heidelberg, **1996**.

12. S. Leucuta, L. Vlase, S. Gocan, L. Radu, C. Fodorea, *Journal of Liquid Chromatography & Related Technologies*, **2005**, *28 (19)*, 3109.

13. L. Bucur, L. Vlase, C. Fodorea, V. Istudor, *Revista de Chimie*, **2006**, *57 (2),* 189.

14. C.A. Dehelean, L. Vlase, C. Peev, D. Antal, C. Soica, *Revista de chimie*, **2006**, *57 (8),* 826.

15. G. Crisan, B. Kiss, L. Vlase, G. Balica, M. Tamas, *Chemistry of Natural Compounds*, **2009**, *45(6)*, 885.

16. M.J. Simirgiotis, G. Schmeda-Hirschmann, *J Chromatogr A.*, **2010**, *1217(4)*, 443.

17. P. Dugo, P. Donato, F. Cacciola, M.P. Germanò, A. Rapisarda, L. Mondello, *J. Sep. Sci.,* **2009**, *32(21),* 3627.

STUDIA UNIVERSITATIS BABEŞ-BOLYAI, CHEMIA, XLV, 2, TOM II, 2010

Dedicated to the memory of Prof. dr. Ioan Silaghi-Dumitrescu marking 60 years from his birth

KINETIC STUDIES OF SORPTION OF COPPER(II) IONS ONTO DIFFERENT CALCIUM-HYDROXYAPATIE MATERIALS

ERZSÉBET-SÁRA BOGYA[*], IOAN BÂLDEA, RÉKA BARABÁS,
ALEXANDRA CSAVDÁRI, GRAZIELLA TURDEAN,
VALENTINA-ROXANA DEJEU

ABSTRACT. A study on the removal of copper ions from aqueous solutions by synthetic hydroxyapatite and structurally modified apatite has been carried on under batch conditions. The influence of different sorption parameters, such as heat treatment of the material, particle size, initial metal ion concentration and temperature has been studied and discussed. Maximum adsorption capacity and efficiency were determined. The results showed that the removal efficiency of Cu(II) by hyrdoxyapatite containing silica (HAP-Si) could reach 99.7%, when the initial Cu(II) concentration was 5 mM. The mechanism of the sorption process was studied, by employing pseudo-first, pseudo-second-order kinetic models and intraparticle diffusion model. Activation energy for hydroxyapatite and $10\%_{wt}$ silica doped hydroxyapatite was obtained, considering pseudo-second-order kinetics model.

Keywords: *hydroxyapatite, modified hydroxyapatite, copper removal, kinetics, diffusion, activation energy*

INTRODUCTION

Hydroxyapatite (HAP) is a mineral, from the group of apatites, having the chemical formula $Ca_{10}(PO_4)_6(OH)_2$. Among the different calcium phosphates, hydroxyapatite is the most important bioceramic used in dentistry and orthopedic surgery [1-3]. One way to enhance the bioactive behavior of hydroxyapatite is to obtain substituted apatite, which resemble the chemical composition and structure of the mineral phase in bones. These ionic substitutions can affect the surface structure and charge of hydroxyapatite, which could have an influence on the material in biological environment. In this sense, an interesting way to improve the bioactivity of hydroxyapatite is the addition of silicon to the apatite structure, taking into account the influence

---

[*] *Babeş-Bolyai University, Faculty of Chemistry and Chemical Engineering, 11 Arany János Str., RO-400084 Cluj-Napoca, Romania, bogyaes@ubbcluj.ro*

of this element on the bioactivity of bioactive glasses and glass-ceramics [4,5]. In addition, several studies have revealed the considerable importance of silicon on bone formation and growth under *in vitro* and *in vivo* conditions [6].

Apatite can be used for remediation of soil and water from industrial and nuclear wastes due to their ability to retain a variety of ionic species, especially actinides and heavy metals [7,8]. The mechanisms of the metal cations retention are different and include: ion exchange, adsorption, dissolution/ precipitation, and formation of surface complexes [9].

The sorption of pollutants from aqueous solution plays an important role in wastewater treatment because it avoids the process of sludge elimination. Well-designed sorption processes have good efficiency and high quality of effluent after treatment. Sorption material can also be recycled. It is therefore understandable that the study of sorption kinetics in wastewater treatment is interesting as it provides insights into the reaction pathways and into the mechanism of sorption reactions. In addition, the kinetics allows the evaluation of the solute uptake rate which in turn controls the residence time of sorbate uptake at the solid–solution interface. Therefore, it is important to predict the rate at which pollutant is removed from aqueous solutions in order to design appropriate sorption treatment plants. To control the sorption kinetics, knowledge of the rate law describing the sorption system is required. The rate law is determined experimentally.

This paper aims to study the sorption of copper(II) ions onto structurally modified apatite, comparing it to normal hydroxyapatite, and establishing the best kinetic model and mechanism.

RESULTS AND DISCUSSION

As described by Sposito (1986) [10], sorption is the loss of a chemical species from an aqueous solution to a contiguous solid phase. Two of the principle mechanisms of sorption include adsorption, the two-dimensional accumulation of matter at the mineral-water interface; and precipitation, the three-dimensional growth of a solid phase. The study of the nature of copper sorption onto apatites represents the aim of this paper.

As mentioned in the experimental section, copper(II) sorption measurements were carried out with five types of material of two different particle sizes (> 90 μm and < 45 μm) and with calcined and non-calcined samples for each material at four different copper concentrations (10^{-4} M, 5×10^{-4} M, 10^{-3} M, 5×10^{-3} M).

For all non-calcined materials at the 10^{-3} M copper concentration, the sorption capacity was almost identical, meaning that the η (efficiency) was around 99.7 %, the difference between them consisting in the saturation time. For the calcined samples, the efficiency was about 60-70 % [11, 12].

The sorption efficiency is defined as $\eta = (c_0 - c_i)/c_0$; c_0 being the initial copper concentration, c_i the actual copper concentration at a specific time, and the sorption capacity given as $q_t = c_{adas} / m$; c_{ads} being the adsorbed amount of copper at a specific time in moles, and m the quantity of the material on which it was adsorbed in grams. The effect of the initial concentration of copper ions was also studied. Its efficiency was calculated for each material at four copper nitrate concentrations as presented in the legend of figure 1 (c_1 = 5 mM, c_2 = 1 mM, c_3 = 0.5 mM and c_4 = 0.1 mM).

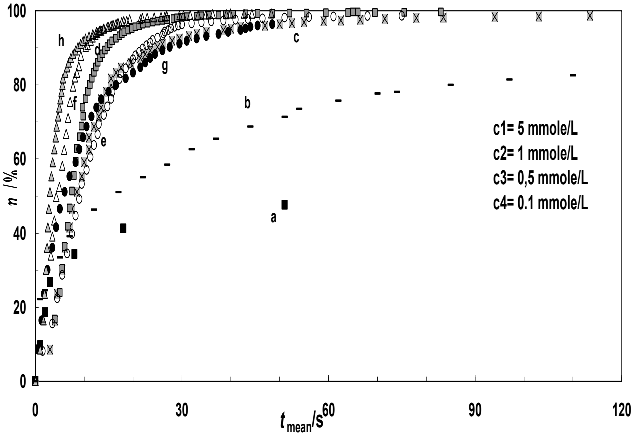

Figure 1. Sorption efficiency for different concentrations and materials as a function of time. of: ncHAP < 45 µm, c_1 (**a**); ncHAP-Si 10%$_{wt}$ Si < 45 µm, c_1 (**b**); ncHAP < 45 µm, c_2 (**c**); ncHAP-Si 10%$_{wt}$ Si < 45 µm, c_2 (**d**); ncHAP < 45 µm, c_3 (**e**); ncHAP-Si 10%$_{wt}$ Si < 45 µm, c_3 (**f**); ncHAP < 45 µm, c_4 (**g**); ncHAP-Si 10%$_{wt}$ < 45 µm, c_4 (**h**).

At the concentration of 5 mM the copper ions sorption efficiency for ncHAP was about 60%, comparable to HAP-Si with 10%$_{wt}$ silica that reaches the efficiency of above 99.6 %, and has the sorption capacity of 20.54 mg/g. cHAP does not sorbs copper ions at such high concentrations and HAP-Si 10%$_{wt}$ Si retains the amount of 50 %. At concentrations lower than 5 mM, sorption takes place at the 99.8 % efficiency for non-calcined materials, and also for calcined materials at concentrations equal or lower than 0.1 mM.

These results show that, for a rapid and complete sorption, the most suitable material is non-calcined silica hydroxyapatite with 10%$_{wt}$ of silica [11, 12].

The increase of temperature enhances the copper sorption for all the studied materials. At higher temperature the end time of the sorption for ncHAP-Si 10%$_{wt}$ silica >45 μm and 10^{-3} mol/L copper(II) concentration decreases below one minute.

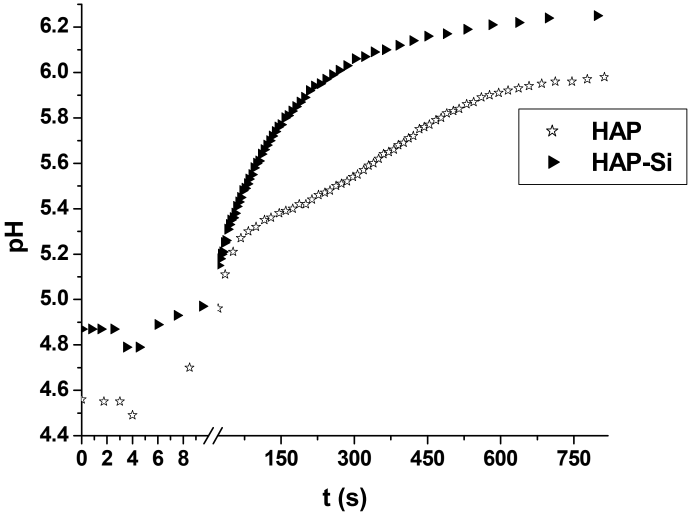

Figure 2. pH variation during the reaction of ncHAP and ncHAP-Si 10%$_{wt}$ Φ> 90 μm with copper ions ([Cu^{2+}]=10^{-3} mol/L)

Table 1. Initial and final pH in the case of copper nitrate reaction with apatites at 10^{-3} mol/L copper (II) concentration and T=293 K

Material	**pH$_i$**	**pH$_f$**
ncHAP >90 μm	5.16	5.75
ncHAP <45 μm	5.25	6.08
ncHAP-Si 5%$_{wt}$ Si >90 μm	5.2	6.08
ncHAP-Si 5%$_{wt}$ Si <45 μm	5.08	6.11
ncHAP-Si 5%+$_{wt}$ Si >90 μm	5.12	6.46
ncHAP-Si 5%+$_{wt}$ Si <45 μm	5.11	6.41
ncHAP-Si 10%$_{wt}$ Si >90 μm	5.19	6.75
ncHAP-Si 10%$_{wt}$ Si <45 μm	5.31	6.52
ncHAP-Si 15%$_{wt}$ Si >90 μm	5.11	5.91
ncHAP-Si 15%$_{wt}$ Si <45 μm	5.1	5.89

The pH of solution modifies between 4.7 and 6.2 (see figure 2), for 10^{-3} M Cu^{2+} concentration. Within the initial period of the process, it can be noticed a slight decrease of the pH in the case of materials with higher granulometry. This phenomenon can be caused by ionic exchange between the copper and protons on the superficial –OH sites. Later increase of pH values is due to the dissolution of the material in the acidic media and base hydrolysis. Table 1 compares the initial and final pH values for all the materials. The highest variation was observed at ncHAP-Si 10$_{\%wt}$ Si.

The release of calcium ions during copper(II) sorption was registered with a calcium selective electrode. It was observed that within a very short period calcium concentration increases due to the dissolution of the hydroxyapatite and then decreased significantly. After this initial stage, the calcium release is much slower then the copper sorption and therefore hydrogen ions should be released to maintain the balance of charge. This leads to the conclusion that copper-calcium ion exchange does not control the Cu^{2+} sorption.

Kinetic studies

In order to determine the rate constants, the two mostly used kinetic models in sorption processes, namely pseudo-first and pseudo-second order model, have been checked with our experimental data. Generally, the reaction rate is defined as the change of reactants or products per unit of time. In the case of first-order kinetics the reaction rate is represented as $r = k_1 c_A$, or in terms of sorption efficiency

$$\frac{d\eta}{dt} = k_1(1-\eta) \qquad (1.)$$

where, $\boldsymbol{k_1}$ is the first order rate coefficient (s^{-1}), $\boldsymbol{c_A}$ stands for the actual concentration of the reactant (mol/L), $\boldsymbol{\eta}$ the efficiency and $\boldsymbol{t}$ the time (s). The linear form, obtained by integration is

$$-\ln(1-\eta) = k_1 t \qquad (2.)$$

The data were treated based on the supposition that the process can be described by two consecutive first order steps. According to literature [13], the first step represents a rapid complexation on the specific sites of the HAP surface. The second step is attributed either to ion diffusion into the HA structure or to formation of hydroxyapatite containing this heavy metal instead of calcium. Based on this supposition equation (2.) has been plotted with the data for all the non-calcined materials (see figure 3). The slope of the linear part of the curve gives the first order rate constants for the two consecutive steps. The rate constant values and the regression coefficients are presented in table 2**.** The rate coefficients have higher values for the first step and at lower particle size. The higher calcium concentration of ncHAP-Si 5%+$_{wt}$ Si as compared to ncHAP-Si 5%$_{wt}$ Si does not influence positively the reaction rate. It indicates that the ionic exchange is not the rate determining step. The highest values of the apparent rate constants were calculated for ncHAP-Si 10%$_{wt}$ $\Phi<45$ μm, that is in concordance with the fastest reaction time.

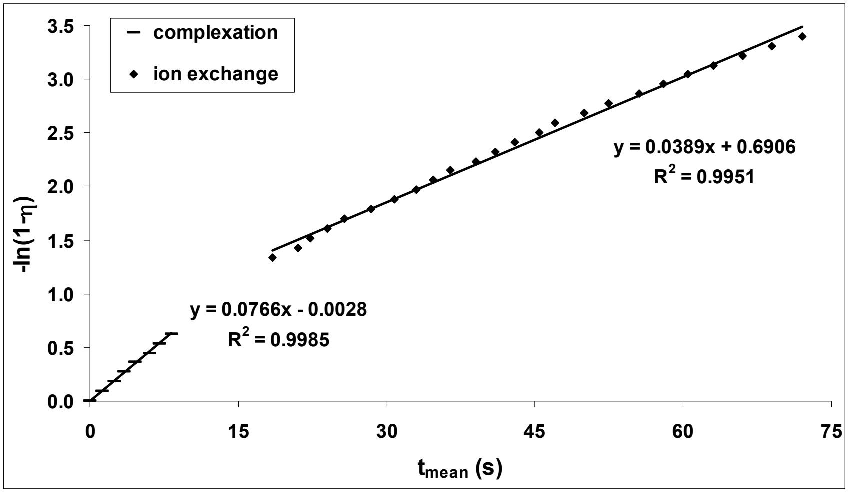

Figure 3. First order kinetics representation for ncHAP-Si 10 $\%_{wt}$ Si Φ,45 μm[Cu^{2+}]=1 mM. T=279 K

The pseudo-second order rate model, based on sorbent capacity [14], can be expressed as a differential equation:

$$\frac{dq_t}{dt}=k_2(q_e-q_t)^2 \tag{3.}$$

By integrating this within the same boundary conditions and rearranged, the following linear form is obtained:

$$\frac{1}{q_t}=\frac{1}{k_2q_e^2}+\frac{1}{q_e}t \tag{4}$$

Here $\boldsymbol{q_t}$ and $\boldsymbol{q_e}$ is amount of solute sorbed on the surface at a time $\boldsymbol{t}$ and at the equilibrium state. A plot of $\boldsymbol{t/q_t}$ versus $\boldsymbol{t}$ should give a straight line with a slope of $\boldsymbol{1/q_e}$ and the intercept of $\boldsymbol{1/k_2q_e^2}$ (see figure 4). Furthermore, the initial sorption rate $\boldsymbol{h}$ (mmol/g s), when $t\rightarrow0$, can also be calculated as follows: $\boldsymbol{h = k_2q_e^2}$ [15,16]. The experimental points lay on the unique straight line over a large period of time. As it can be seen in table 2 the amount of copper ions at equilibrium (mmol/g) is approximately constant for all the materials at the same initial copper (II) concentration. The correlation coefficients for the linear plots for the pseudo-second order rate law are better (>0.995) as compared to the values obtained with the first-order model. This suggests that the system does not obey first-order kinetics, but a pseudo-second order one. According Y. S. Ho and G. McKay [16] in systems described by pseudo-second order model the rate-limiting step may involve some strong interaction (valence forces) between sorbate species and active sites of adsorbent. This model provides the best correlation of the data.

Table 2. Comparison between experimental and calculated amounts of Cu(II) sorbed at equilibrium (q_e), sorption rate constants (k_1, k_1' and k_2) and corresponding regression coefficients (R^2), for pseudo-first and pseudo-second order kinetic models, at 293 K and $[Cu^{2+}]=10^{-3}$ M

pseudo-first order								**pseudo second order**					
Φ>90 μm				*Φ <45 μm*				*Φ>90 μm*			*Φ <45 μm*		
k_1	R^2	k_1'	R^2	k_1	R^2	k_1'	R^2	k_2	q_e	R^2	k_2	q_e	R^2
ncHAP													
0.051	0.997	0.011	0.996	0.118	0.987	0.06	0.995	0.249	0.21	1	1.634	0.206	1
ncHAP-Si $5\%_{wt}$ Si													
0.021	0.996	0.008	0.998	0.097	0.97	0.086	0.994	0.065	0.234	0.999	1.236	0.210	0.999
ncHAP-Si $5\%+_{wt}$ Si													
0.015	0.991	0.008	0.993	0.095	0.978	0.079	0.999	0.069	0.226	0.997	0.819	0.215	0.997
ncHAP-Si $10\%_{wt}$ Si													
0.069	0.99	0.024	0.995	0.071	0.94	0.096	0.985	0.470	0.213	1	1.425	0.218	0.995
ncHAP-Si $15\%_{wt}$ Si													
0.067	0.988	0.007	0.999	0.124	0.991	0.051	0.99	0.219	0.208	1	1.529	0.206	1

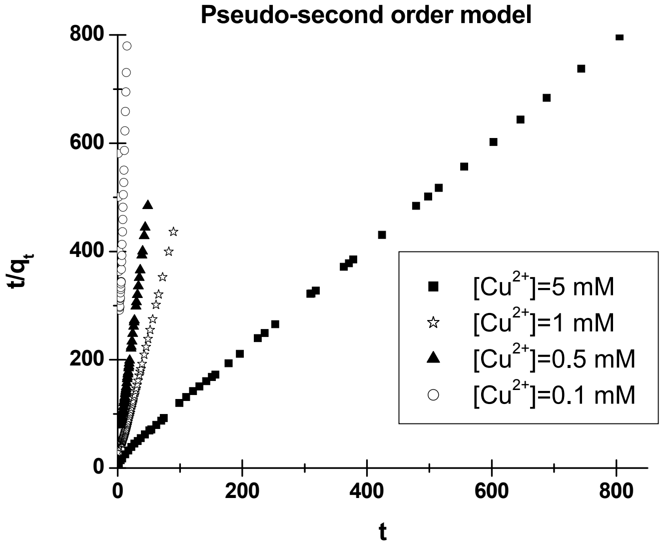

Figure 4. Pseudo-second order rate model for ncHAP-Si $10\%_{wt}$ <45 μm at different initial copper ion concentrations

By using the values of the second order rate constants determined at different temperatures (279, 293, 303, 313, 323 K), the experimental Arrhenius activation energy were obtained for two different concentration and material. The activation energy values are summarized in **Table 3.**

Table 3. Activation energy calculate by Arrhenius type linearization based on pseudo second order rate coefficient values for ncHAP and ncHAP-Si 10%$_{wt}$ Si

[Cu^{2+}] (M)		***10^{-3}***		***5 10^{-4}***	
Material	**Φ (μm)**	**Ea (kJ/mol)**	**R^2**	**Ea (kJ/mol)**	**R^2**
ncHAP	**>90**	35.82	0.972	30.57	0.986
	<45	20.33	0.981	57.46	0.987
ncHAP-Si 10%$_{wt}$ Si	**>90**	34.73	0.961	42.51	0.993
	<45	42.44	0.985	52.75	0.995

Their values are increased at higher granulometry and concentration, with the exception of ncHAP Φ>90 μm. The activation energies ranges within 20-60 kJ/mol, which indicates that the sorption of copper in not governed only by ion exchange mechanism. Based on literature data, energies between 8–16 kJ/mol are characteristic for the ion-exchange mechanisms [17].

Intraparticle diffusion

The mechanism of sorption is either film diffusion controlled or particle diffusion controlled. Before adsorption takes place, several diffusion processes known to affect the adsorption process takes place. The sorbate, will have to diffuse trough the bulk of the solution to the film surrounding the adsorbent and then into the micro pores and macro/ pores of the adsorbent. The first one is bulk diffusion resistance which of course is reduced if there is enough agitation to reduce the concentration gradient. The second is external mass transfer resistance and the third is intraparticle mass transfer resistance. When this last one is the rate limiting step, than sorption mechanism is controlled by intraparticle diffusion.

The model developed by Mackay and Poots [18] can be used to establish the mechanism of sorption.

$$q_t = K_{id} \cdot t^{1/2} + I \tag{5}$$

Where, $\boldsymbol{q_t}$ is the amount of copper ions sorbs at time ***t***. The slope of the linear part of the curve (i.e., $\boldsymbol{q_t}$ Vs $\boldsymbol{t^{0.5}}$) gives the initial rate of the sorption, controlled by intraparticle diffusion $\boldsymbol{K_{id}}$ (mg/g s$^{0.5}$). The extrapolation of the straight lines to the time axis gives intercepts ***I***, which are proportional to the boundary layer thickness. The kinetic constants and $\boldsymbol{R^2}$ values for the intraparticular diffusion model are shown on **Table 4.**

The values of the regression coefficients ($\boldsymbol{R^2}$) indicate that the model fits the experimental data quite well up to 55-70 % of the process, confirming the intraparticle diffusion in the sorption process. The boundary layer thickness is insignificant. Thus, the boundary layer acts as a viscous drag to the sorption [18].

Table 4. Kinetic constants and regression coefficients (R^2) for Mackay and Poots intraparticle diffusion equation and the efficiency value representative for the linear part of the curve for copper ion sorption on apatites

Material	K_{id}	I	R^2	η (%)
ncHAP Φ>90 μm	10^{-4}	$3\ 10^{-5}$	0.968	71
ncHAP-Si 5%$_{wt}$ Si Φ>90 μm	$6\ 10^{-5}$	$4\ 10^{-5}$	0.986	78
ncHAP-Si 10%$_{wt}$ Si Φ>90 μm	$2\ 10^{-4}$	$2\ 10^{-5}$	0.982	68
ncHAP-Si 15%$_{wt}$ Si Φ>90 μm	10^{-4}	10^{-4}	0.924	56

CONCLUSIONS

Hydroxyapatite modified with silica was synthesized by addition of sodium silicate to the reaction mixture. These materials were used in copper sorption experiments. The retaining capacity is influenced by calcination, silica content, particle size, initial copper concentration and temperature. Calcined materials show weak metal sorption properties and the silica containing materials have better sorption efficiency than unmodified hydroxyapatite. The 10%$_{wt}$ silica containing hydroxyapatite has the highest copper sorption efficiency. The pseudo-second order model, exhibiting the highest regression coefficients, describes better the sorption of copper onto all the materials. This model agrees with the assumption that the rate-limiting step is chemical sorption or chemisorption involving valence forces between sorbent and sorbate. The activation energies calculated with the pseudo-second order model, in the range of 20-60 kJ/mol also indicate the involvement of chemical interactions. Intrapaticle diffusion, irrespective of its mechanism, also plays an important role in this sorption process.

EXPERIMENTAL SECTION

Hydroxyapatite was prepared by the precipitation method described previously [11, 12], under continuous mechanical stirring. The used materials were: 0.5 mol/L solution of calcium nitrate, 0.3 mol/L solution of diammonium phosphate and 25 % ammonia solution (Merck, Germany). The diammonium phosphate and the ammonium solution were slowly added to the calcium nitrate solution. The reaction mixture pH was adjusted with ammonia to maintain in the range of 9 and 9.5, and the reaction temperature was kept at 20 °C by means of a FALC FA-90 thermostat. The reaction mixture was stirred by FALC mechanical stirrer for 20 hours. For the structurally modified hydroxyapatite, sodium silicate together with the diammonium phosphate and ammonia solution was added to the preparation mixture.

The reaction pH was also adjusted to a value between 9 and 9.5, the temperature was 20 °C and the reaction time was 8 h. Four types of silica-hydroxyapatite (HAP-Si) were prepared: with 5 %, 5 %+, 10 % and 15 mass % of silica. The HAP-Si with 5 %+ of silica content contained by 10 mass % more calcium compared to the other materials. After the reaction was accomplished, the precipitate was washed and filtered. The filtered material was dried for 24 hours at 105 °C. Thermal treatment of the samples was carried out at 1000 °C for one hour, in a Barnstead 47900 furnace.

The characteristics of the materials were established by Infra Red spectroscopy, scanning electron microscopy (SEM), X-ray and BET measurement. The results were presented previously [11, 12].

The prepared materials were employed in kinetic studies of Cu (II) ion retention. Copper nitrate solution was used, in the concentration range between 10^{-4} mol/L and 5 10^{-3} mol/L. A copper selective electrode (Tacussel PCU 2M) previously calibrated and a reference saturated K^+/KNO_3 electrode were used to monitor copper (II) concentration. A Digitronic DXP-2040 potentiometer was employed. The experiments were carried out in a double walled reactor, connected to a FALC FA-90 thermostat under continuous magnetic stirring, provided by a FALC FA-20 magnetic stirrer. Replicate runs were made and each time, values corresponding to the given potential were averaged.

The reagents were of analytical grade and twice-distilled water was used to prepare all solutions and suspensions. In order to reproduce conditions existing during the purification of waste water, no pH adjustment was made during the experiments. However, pH was monitored with a pH selective electrode during the experiments.

0.25 g sample and 50 mL of copper nitrate solution of different concentrations were used for each experiment. The decrease of electrode potential with time was measured and the data were recorded by a computer. The retained copper quantity, sorption efficiency, and capacity of the material were calculated using the Microsoft Excel and Origin 6.0 software. Analytical detection limit for Cu^{2+} was 5 μmol/L. The increase calcium ion concentration was registered with a calcium selective electrode. The detection limit was established at 5 10^{-7} mol/L.

REFERENCES

1. L. A. Landin, L. G. Danielsson, C Wattsgard, *Journal of Bone and Joint Surgery Br*, **1987**, *69-B*, 234.
2. J. Zhang, M. Maeda, N. Kotobuki, M. Hirose, H. Ohgushi, D. Jiang, M. Iwasa, *Materials Chemistry and Physics*, **2006**, *99*, 398.
3. V. P. Orlovskii, V. S. Komlev, S. M. Barinov, *Inorganic Materials,* **2002**, *38*, *10*, 973.
4. I. R. Gibson, S. M. Best, W. Bonfield, *Journal of Biomedical Materials Research*, **1999**, *44*, 422.
5. M. Vallet-Regi, D. Arcos, *Journal of Materials Chemistry,* **2005**, *15*, 1509.
6. F. Balas, J. Pérez-Pariente, M. Vallet-Regí, *Journal of Biomedical Materials Research Part A*, **2003**, *66A, 2*, 364.
7. W. Zheng, X.-m. Li, Q. Yang, G.-m. Zeng, X.-x. Shen, Y. Zhang, J.-j. Liu, *Journal of Hazardous Materials*, **2007**, *147, 1-2*, 534.
8. F. Fernane, M. O. Mecherri, P. Sharrock, M. Hadioui, H. Lounici, M. Fedoroff, *Materials Characterization*, **2008**, *59*, 554.
9. S. McGrellis, J.-N. Serafini, J. JeanJean, J.-L. Pastol, M. Fedoroff, *Separation and Purification Technology*, **2001**, *24*, 129.
10. S. K. Lower, P. A. Maurice, S. J. Traina, E. H. Carlson, *American Mineralogist*, **1998**, *83*, 147.
11. E. S. Bogya, R. Barabás, A. Csavdári, V. Dejeu, I. Baldea, *Chemical Papers*, **2009**, *63*, *5,* 568.
12. E. S. Bogya, R. Barabás, L. Bizo, V.R. Dejeu, *Proceedings of the 11th ECERS Conference, Polish Ceramic Society, Krakow*, **2009**, 1109-1113, ISBN: 978-83-60958-54-4.
13. A. Corami, S. Mignardi, V. Ferrini, *Journal of Hazardous Materials*, **2007**, *146*, *1-2,* 164.
14. I. Smiciklas, A. Onjia, S. Raicević, D. Janaćković, M. Mitrić, *Journal of Hazardous Materials*, **2008**, *152*, 876.
15. M. Fedoroff, G. Lefevre, M. Duc, S. Milonjic, C. Neskovic, *Materials Science Forum,* **2004**, *453-454*, 305.
16. Y.S. Ho, G. McKay, *Process Biochemistry*, **1999**, *34*, 451.
17. S. S. Dimovic, I. Plecas, M. Mitric, *Water Research*, **2006**, *40*, 2267.
18. J. C. Igwe, O. F. Mbonu, A. A. Abia, *Journal of Applied Science*, **2007**, *19*, 2840.

STUDIA UNIVERSITATIS BABEŞ-BOLYAI, CHEMIA, XLV, 2, TOM II, 2010

Dedicated to the memory of Prof. dr. Ioan Silaghi-Dumitrescu marking 60 years from his birth

THE VALUES OF BIOCHEMICAL INDICATORS IN PEOPLE WHO PRACTICE 'MAINTENANCE' AEROBICS

AURICA CREȚU[a], DENISA-IOANA CREȚU[b]

ABSTRACT. Physical effort affects by its stressful character the homeostatic level of the body, resulting in acceleration of biochemical reactions of aerobe and anaerobe nature. This article presents dynamics in the variation of some of the biochemical parameters of the blood in women who practice 'maintenance' aerobics.

Keywords: *effort, biochemical indicators, homeostasis*

INTRODUCTION

Biochemical parameters represent an area of investigation with various implications in terms of health control, quality of life as well as predisposition to certain pathological conditions arising from a labor that exceeds the effort capacity of the body. Studies conducted to date indicate that metabolic changes that occur during intense muscle activity largely depend on biochemical parameters and affect the efficiency of physical effort.

The aim of this study was to demonstrate that variations of certain biochemical indicators such as glucose, triglyceride levels, uric acid, magnesium and serum creatinine depend on the intensity of physical effort and they, in turn, act on the rate of achieving metabolic changes, disturbing the working capacity of the organism. The study of these parameters in women who have not practiced any sports before is of practical and public interest as more and more women turn to aerobics as a way to shape their body. When specific literature studies focus mainly on athletes or on items such as glucose and triglycerides, parameters like uric acid, magnesium and serum creatinine are vaguely raised. Therefore, our research intends to provide a complete, updated picture of the evolution of these five parameters in women aged 20-30 years old who practice aerobics.

---

[a] *Universitatea Babeş-Bolyai, Facultatea de Educație Fizică şi Sport, Extensia Bistrița, Str. Andrei Mureşanu Nr. 3-5, RO-420117 Bistrița, Romania, cretuaurica@yahoo.com*

[b] *Universitatea de Medicină şi Farmacie „Iuliu Hațieganu", Facultatea de Medicină, Str. Victor Babeş Nr. 8, RO-400012, Cluj-Napoca, denysa_crt@yahoo.com*

RESULTS AND DISCUSSION

The statistical tests applied revealed the results shown in Table 1.

Table 1. P values obtained after applying Student t Test

	January -April	April- July	January- July
Glucose (mg%)	**0,05**	**0,047**	**0,001**
Triglycerides (mg%)	0,08	0,42	0,07
Uric Acid (mg%)	0,17	0,28	0,34
Creatinine (mg%)	0,2	0,07	**0,03**
Magnesium (mg%)	0,19	**0,02**	0,07

* p ≤ 0.05-significant
** p ≥ 0.05-insignificant

Glucose values have significantly diminished in the interval January-April and January- July 2009, as seen in Figure 1. Diminished blood glucose values were significantly lower than the ones presented in the reference range (p = 0.001), in a gradual decrease.

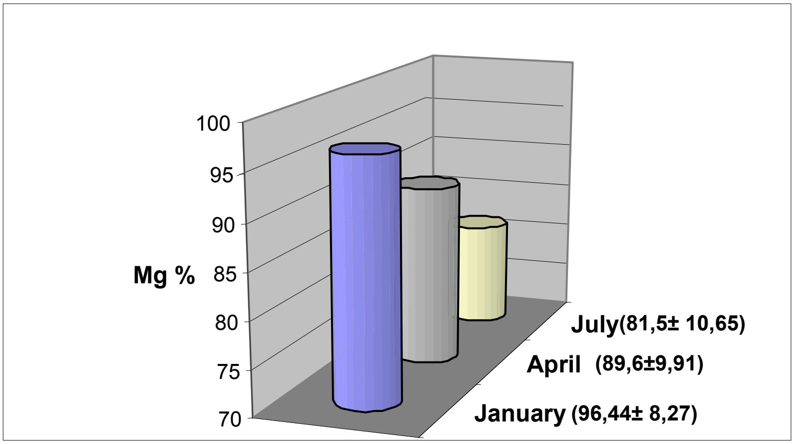

Figure 1. Glucose levels in January-July period (average± standard deviation)

In comparison with our study, similar results were obtained, but on obese, sedentary postmenopausal women who completed a 6-month (three times per week) program of aerobics.[1] Use of glucose during exercise and the amount of blood sugar metabolized per unit of insulin plasma as an indicator of insulin sensitivity increases only when weight loss is accompanied by exercise [1].

Although insignificant (statistically) changes were recorded, a decrease of triglycerides values suggests lipid mobilization after moderate physical exertion (Figure 2).

Studies performed on women aged between 30 and 50 after a single 60-minute aerobics session show an increase of free fatty acids during effort [2], as triglycerides stored in the fat tissue can be mobilized and sent in the form of free fatty acids used as an energy source and circulating lipids.

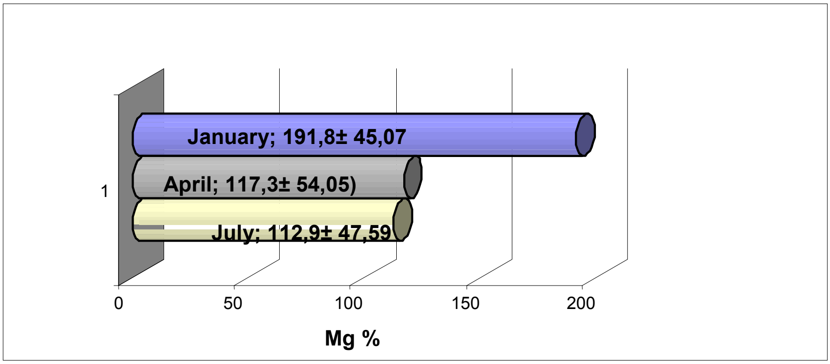

Figure 2. Mean values of triglycerides± standard deviation

Our study indicates that in the long-term effort uric acid presents an increase of the numerical values (Figure 3). Despite the fact that the variations had p>0,05, the mathematical increases of this indicator of free purines that were recorded are considered a sign of persistent metabolic fatigue or incomplete biochemical recovery.

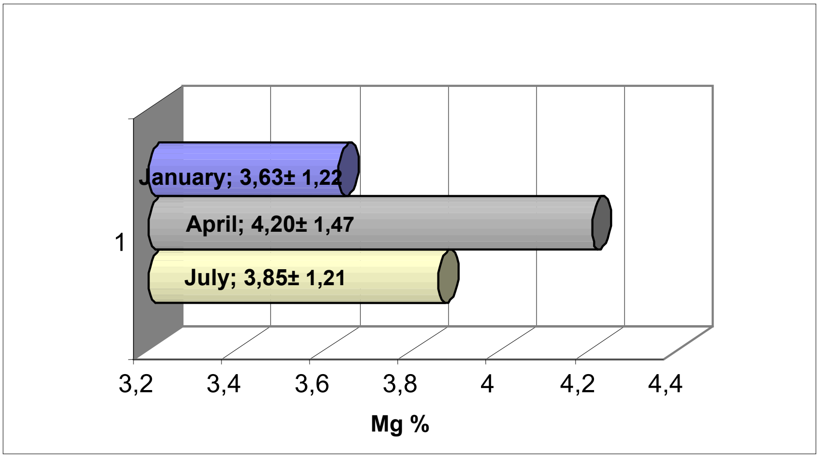

Figure 3. Uric acid-mean value changes (± standard deviation)

Specific literature contains limited knowledge concerning the evolution of uric acid during physical effort. Studies made on animals (horses subjected to a prolonged effort-endurance races) specify that uric acid can be used as a biochemical parameter in determining the metabolic activity during effort [3].

The hypomagnesaemia condition that was obtained in the first part of our study -January-April (although statistically insignificant) can be explained as a redistribution of magnesium in the body to accommodate the metabolic needs of our study participants-that were not prior engaged to any physical activity. However, a statistically significant numerical increase (p = 0.02) of magnesium in plasma in the April-July interval (after 6 months of prolonged effort, Figure 4), does not correlate with other findings concerning the conditions in which plasmatic Mg increases after physical exertion.

Magnesium is involved in many functions of the skeletal muscle. Other studies connect the inadequate intake of magnesium (in the form of pills or diet) with a deficiency status in athletes participating in sports requiring weight control. [4]

Specific literature explains hypomagnesaemia as stress caused by physical exercise or as the effect of lipolysis (since fatty acids are mobilized for muscle energy, lipolysis would cause a decrease in plasma Mg) whereas hypermagnesaemia occurs at athletes following short term high intensity exercise as the consequence of a decrease in plasma volume and a shift of cellular magnesium resulting from acidosis [5].

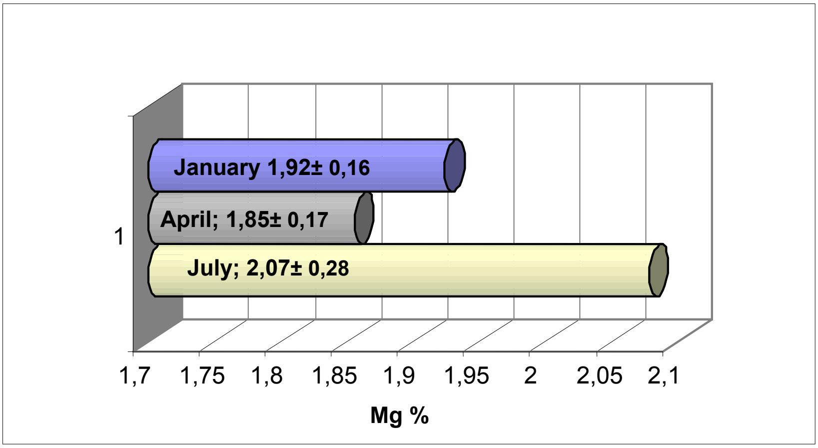

Figure 4. Changes of average values of magnesium (± standard deviation).

With regard to serum creatinine, this biochemical parameter increased significantly in July (p = 0.03) compared to the reference range-January (Figure 5).

In comparison with our study, other authors use the elevations of serum creatinine as an indicator of exertion-related muscle damage produced in healthy individuals that were subjected to a single session of 50 eccentric exercises.[6]

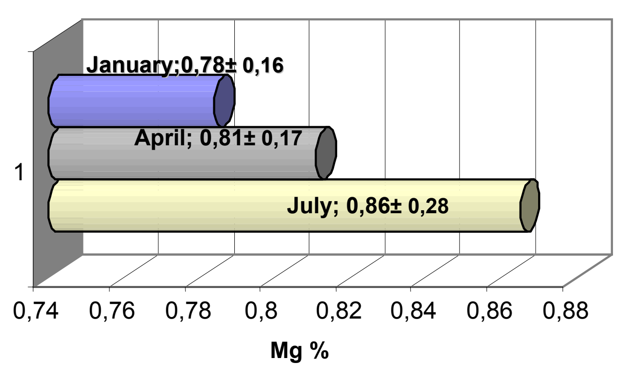

Figure 5. Serum creatinine changes during exercise and post-effort (mean values ± standard deviation)

CONCLUSIONS

1. The significant decrease of glucose parameters indicates that the physical strain was intense enough to mobilize blood sugar reserves. Furthermore, the fact that the values of this parameter have been progressively decreasing during the experiment point toward the fact that the participants had a balanced diet.

2. A decline of triglycerides levels, although statistically insignificant, reveals that the effects of physical exertion on the body in terms of weight loss facilitates fat mobilization and allows the energy deficit to rely less on a hypocaloric diet. On the other hand, exercises performed at moderate levels of intensity counteract undesirable lipid changes that occur with age.

3. The increase of uric acid and decrease of magnesium during the period January –April is a sign of incomplete metabolic recovery. However, reversing this report in the April-July interval, with the decline of uric acid and an increase of magnesium, point toward a better correlation between the effort capacity and the intensity of physical effort.

4. A continuous numerical increase of serum creatinine levels indicates a sustained muscular effort of the subjects.

5. Our data are gain added relevance compared to other studies from the fact that the determinations are made in three different points (January-April-July), focusing on the evolution on the biochemical parameters in time.

6. This study complements the existing data in literature concerning glucose, triglycerides, and adds new, innovating information on the changes of uric acid, magnesium and serum creatinine with reference to the increasingly segment of the population represented by women who practice aerobic workouts.

7. The practical applicability is more than obvious because progressively more women turn to aerobics as a method of maintenance. Therefore, the need of a personal, customized training program arises, that adjusts to the possibilities and necessities of each person in order to prevent internal imbalances such as our study showed.

EXPERIMENTAL SECTION

Our study refers to a group of 20 female subjects, aged 20-30 years, who have performed workouts with an aerobe character during January-July 2009. The exercises were carried out with a frequency of 3 sessions per week, 60 minutes each session. For the gradual accommodation of the body during exercise, the focus was on the slow adaptation of the subjects through the execution of movements that were destined to the selective influence of the locomotor's apparatus.

The determination of biochemical parameters in the collected blood was carried out at a specialized laboratory.

During the study, changes of the biochemical indicators were monitored in the following ranges:

- Baseline (control data/before the training program began) - January 2009;
- Second determination - after 2 months - beginning of April, 2009;
- Last investigation - July, 2009.

Statistical analysis

Data were analyzed using the Statistical Analysis Toolpak. To calculate batch variations Fisher test was used and for comparing data obtained from investigations T test: Two Sample Assuming Equal Variances and T-Test: Two Sample Assuming Unequal Variances were used. p <0.05 was considered significant. Correlation coefficients were calculated with the help of Correlation function-Data Analysis.

REFERENCES

1. A. S. Ryan, B. J. Nicklas, D. M. Berman, *Obesity (Silver Spring)*, **2006,** *14(6),*1064.
2. M. Charmas, B. H. Opaszowski, R. Charmas, D. Rózańska, E. Jówko, J. Sadowski, L. Dorofeyeva, *J. Strength. Cond. Res.*, **2009**, *23(3)*, 954.
3. F. Castejón, P. Trigo, A. Muñoz, C. Riber, *Equine Vet. J. Suppl.*, **2006**, *(36)*, 70.
4. F. H. Nielsen, H. C. Lukaski, *Magnes Res.*, **2006**, *19(3)*, 180.
5. Y. Rayssiguier, C. Y. Guezennec, J. Durlach, *Magnes Res.*, **1990**, *3(2)*, 93.
6. P. M. Clarkson, A. K. Kearns, P. Rouzier, R. Rubin, P. D. Thompson, *Med. Sci. Sports Exerc.*, **2006**, *38(4)*, 623.

STUDIA UNIVERSITATIS BABEŞ-BOLYAI, CHEMIA, XLV, 2, TOM II, 2010

Dedicated to the memory of Prof. dr. Ioan Silaghi-Dumitrescu marking 60 years from his birth

INTERMOLECULAR INTERACTIONS OF 1- AND 2-BROMOPROPANE WITH SOLVENT MIXTURES STUDIED BY INFRARED SPECTROSCOPY

RODICA GRECU[a], VIRGINIA COMAN[a]
AND ONUC COZAR[b]

ABSTRACT. The parameters of a vibrational band are sensitive to the environment created by solvents. The effects of the two solvent mixtures cyclohexane/tetrahydrofuran and carbon tetrachloride/acetonitrile on the frequency and half bandwidth of ν(C-Br) band of 1- and 2-bromopropane are investigated. The first mixture can be considered "ideal" and the frequency and half bandwidth of ν(C-Br) bands varies linearly on the mole fraction of the polar solvent. In the case of carbon tetrachloride/acetonitrile mixture, a process of "preferential solvation" with the maximum effect at 2 : 1 volume ratio was evidenced.

Keywords: *infrared spectroscopy, 1-bromopropane, 2-bromopropane, intermolecular interactions, solvent mixtures, preferential solvation index Z*

INTRODUCTION

Vibrational spectroscopy provides an effective mean of examining intermolecular interactions in non-aqueous solutions. The spectral band profile includes all information about the interactions of a normal vibrational mode with neighboring medium (first of all the static structural perturbations associated to the distribution of local configurations of the solvent).

The interaction of 2-bromopropane and *trans* and *gauche* conformational isomers of 1-bromopropane (named bromopropanes) with solvents is non-specific and is dominated by the dielectric properties of the solvents [1-3]. The Onsager reaction field [4] in which the solvent is represented by a continuum dielectric medium characterized by bulk dielectric constant ε was a suitable model to describe the interaction of bromopropanes with neat solvents.

---

[a] *Universitatea Babeş-Bolyai, Institutul de Cercetări în Chimie Raluca Ripan, Str. Fântânele 30, RO-400294 Cluj-Napoca, Romania, rodicagrecu2000@yahoo.com*

[b] *Universitatea Babeş-Bolyai, Facultatea de Fizică, Str. Kogălniceanu 1, RO-400084 Cluj-Napoca, Romania*

Reported in this paper are the effects of two solvent mixtures prepared from solvents of different polarities cyclohexane/tetrahydrofuran (CH/THF) and carbon tetrachloride/acetonitrile (CCl_4/CH_3CN) on the frequency and half bandwidth of ν(C-Br) band of 1- and 2-bromopropane.

RESULTS AND DISCUSSION

Dielectric properties of solvent mixtures

A mixture of two individual solvents is a medium that generally does not act additively according to its composition.

Theoretically, a binary solvent mixture is “ideal” when a parameter P_{mix} of the mixture is related with the parameters P_1 and P_2 of each solvent through the following relation:

$$P_{mix} = P_1x_1 + P_2x_2 \qquad (1)$$

where x_1, x_2 are the mole fractions of the components.

Practically, because of the molecular interaction forces the total volume of the mixture is inferior to the sum of the individual volumes and is difficult to find an ideal mixture.

The solvent mixtures used in this study have been cyclohexane/ tetrahydrofuran (CH/THF) and carbon tetrachloride/acetonitrile (CCl_4/ CH_3CN). Every mixture contains a nonpolar solvent (μ = 0) and a polar one. The dipolar moment of tetrafydrofurane is small (μ = 0.7 D) while the molecule of acetonitrile is a very polar one (μ = 3.5 D).

The mixture CH/THF is considered ideal. The values ε^{e}_{mix} of the dielectric constant experimentally determined for different solvent mixtures come near the values ε^{m}_{mix} calculated according to the relation (1) and vary linear with the mole fraction x_P of tetrahydrofuran.

Table 1. Values of the dielectric constants ε_{mix} for different solvent mixtures

Nonpolar/ polar solvent volume ratio	CH/THF mixture			CCl_4/CH_3CN mixture			
	x_P	ε^{m}_{mix}	ε^{v}_{mix}	x_P	ε^{m}_{mix}	ε^{v}_{mix}	ε^{e}_{mix}
1 : 0	0.000	2.024	2.024	0.000	2.234	2.234	2.234
30 : 1	0.042	2.255	2.200	0.058	4.233	3.337	3.004
20 : 1	0.062	2.365	2.282	0.084	5.129	3.854	3.381
10 : 1	0.116	2.662	2.524	0.155	7.576	5.370	4.502
5 : 1	0.208	3.167	2.936	0.269	11.505	7.955	6.617
2 : 1	0.397	4.206	3.854	0.479	18.743	13.711	11.797
1 : 1	0.568	5.145	4.822	0.648	24.568	19.467	17.576
1 : 2	0.725	6.008	5.684	0.786	29.324	25.188	23.727

Nonpolar/ polar solvent volume ratio	CH/THF mixture			CCl_4/CH_3CN mixture			
	x_P	ε^m_{mix}	ε^v_{mix}	x_P	ε^m_{mix}	ε^v_{mix}	ε^e_{mix}
1 : 3	0.798	6.409	6.146	0.846	31.392	28.080	26.896
0 : 1	1.000	7.520	7.520	1.000	36.700	36.700	36.710

ε^e_{mix}: dielectric constants experimentally determined for different solvent mixtures
ε^m_{mix}: dielectric constants of solvent mixtures calculated according to relation (1)
ε^v_{mix}: dielectric constants calculated according to relation (2)

For a CCl_4 / CH_3CN mixture, an important deviation from linearity in the dependence of ε^e_{mix} on the mole fraction x_P of acetonitrile was noticed. The experimental dielectric constants of this system are better approximated by the ε^v_{mix} values calculated according to the empirical relation (2):

$$\varepsilon^V_{mix} = \varepsilon_N V_N + \varepsilon_P V_P \tag{2}$$

where V is the volume fraction of solvents and the indexes N and P indicate the nonpolar and respectively the polar solvent from the mixture.

From the thermodynamic point of view the dielectric Onsager functions calculated [5] using different dielectric constants ε_{mix} are not suitable to describe the effects of a mixture of solvents even if this is considered ideal. The mixture composition or the non-homogeneity of the mixture in the vicinity of solute can modify even the dielectric constant of the individual solvents.

Frequency shift of ν(C–Br) infrared bands of bromopropanes

If the solute sample does not disturb the solvent structure, the maximum of the infrared absorption band should be shifted linearly with the mole fraction of the polar solvent from the mixture. This kind of variation was observed for the bromopropanes solved in the mixture CH/THF considered ideal (see Figure 1).

The dependence of the maximum of ν(C–Br) bands on the mole fraction of acetonitrile is non-linear under the effect of CCl_4/CH_3CN mixture (Figure 1). The effect is more pronounced at smaller concentrations, proving the importance of local effects of the medium in the proximity of the solute.

Generally, a non-linear dependence of the frequency of the absorption band on the mole fraction x_P is considered as a proof for a specific association solute-solvent, for example hydrogen bonding, but also as a result of a "dielectric enrichment" of the solvent shell around the dipolar solute molecule. If the mixture contains solvents having very different polarities, a process of "preferential solvation" occurs that disturbs their distribution into the electric field of a dipolar solute molecule. The composition of the solvent shell in the vicinity of solute could be different by the composition of the bulk mixture.

The process of "preferential solvation" in CCl_4/CH_3CN mixtures can be characterized by the index *Z* that expresses [6] the relation between the mole ratios $X = x_N/x_P$ and $Y = y_N/y_P$:

$$Y = X\,e^{-Z}$$

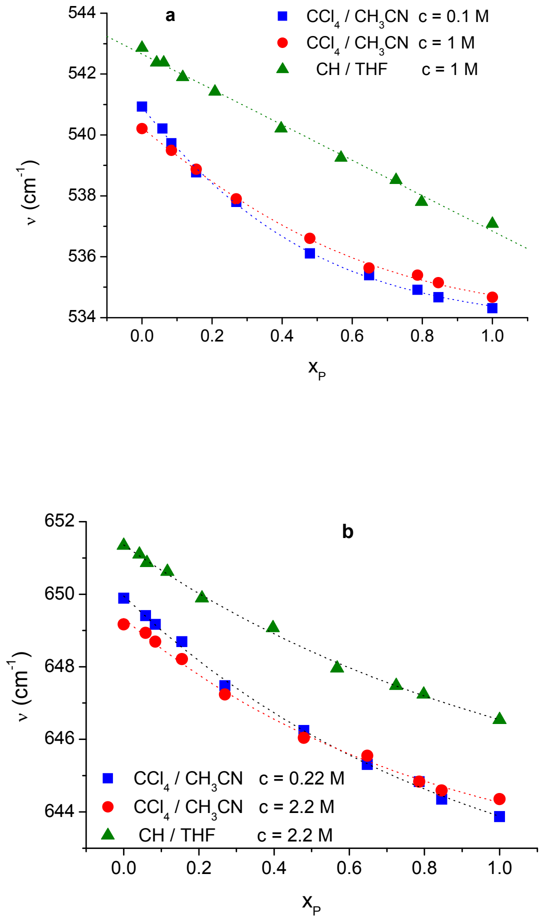

Figure 1. Dependence of ν(C-Br) frequency of (**a**) 2-bromopropane and (**b**) *trans* 1-bromopropane on the mole fraction of the polar solvent in CH/THF and CCl_4/CH_3CN mixtures (*c* is the molar concentration of the solute)

The mole fractions y_P of acetonitrile in the solvation shell of bromopropanes were calculated assuming a linear dependence of ν(C–Br) frequency on it. Because of small differences between the ν(C–Br) frequency values, the calculated index *Z* has an uncertainty of ±0.1.

Table 2. Mole fraction of polar solvent in the solvation shell y_P and index *Z* of "preferential solvation" of bromopropanes in CCl_4/CH_3CN mixtures (c= molar concentration of solutes)

x_P	y_P					
	2-bromopropane		*gauche* 1-bromopropane		*trans* 1-bromopropane	
	c=0.11M	c=1.00 M	c=0.22 M	c=2.20 M	c=0.22 M	c=2.20 M
0.058	0.149	0.120	0.125	0.097	0.106	0.090
0.084	0.208	0.169	0.176	0.138	0.150	0.129
0.155	0.344	0.289	0.300	0.243	0.260	0.228
0.269	0.512	0.450	0.461	0.392	0.414	0.372
0.479	0.724	0.671	0.691	0.617	0.639	0.597
0.648	0.840	0.804	0.811	0.763	0.780	0.748
0.786	0.913	0.891	0.895	0.866	0.876	0.856
0.846	0.940	0.924	0.927	0.906	0.913	0.898
1.000	1.000	1.000	1.000	1.000	1.000	1.000
Z	1.05	0.80	0.84	0.55	0.65	0.48

It can be noticed that *Z* value increases in the following order: *trans* 1-bromopropane < *gauche* 1-bromopropane < 2-bromopropane.

The decrease of solute concentration in CCl_4/ACN mixture determines also an increase of index *Z.* For all solutes, the difference $y_P – x_P$ has a maximum value for CCl_4 : CH_3CN volume ratio of 2 : 1 (x_P ~ 0.4). At this concentration the maximum half bandwidth was also evidenced.

Half bandwidth of ν(C-Br) infrared bands of bromopropanes

The changes observed in the parameter half bandwidth ($\Delta\nu_{1/2}$) of ν(C-Br) bands are related with the complexity of solvent medium in the vicinity of solute molecule, more exactly the part of molecule implied in the studied vibrational mode.

According to Yoshino [6] the greatest modification of the half bandwidth of an absorption band is expected for a value 0.5 of the mole fraction of the polar solvent from a solvent mixture if the difference between the solvation energy of the solute in the individual components of the mixture is zero.

The parameter $\Delta\nu_{1/2}$ of C-Br stretching band increases monotonously with the mole fraction of polar solvent from the bulk CH/THF mixture which is considered ideal (Figure 2).

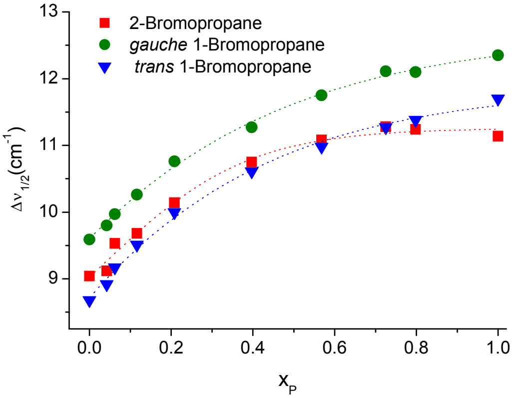

Figure 2. Dependence of the half bandwidth $\Delta\nu_{1/2}$ of ν(C-Br) band of 2-bromopropane (*c*=1.06 M) and 1-bromopropane (*c*=2.2 M) on the mole fraction x_P of tetrahydrofuran from the CH/THF mixtures

A different behaviour is noticed under the effect of CCl_4/CH_3CN mixture (Figure 3). A maximum half bandwidth for the mole fraction of acetonitrile ~0.4 is observed. This corresponds to a CCl_4 : CH_3CN volume ratio of 2 : 1 where, in the conditions of preferential solvation, the difference y_P-x_P is the greatest.

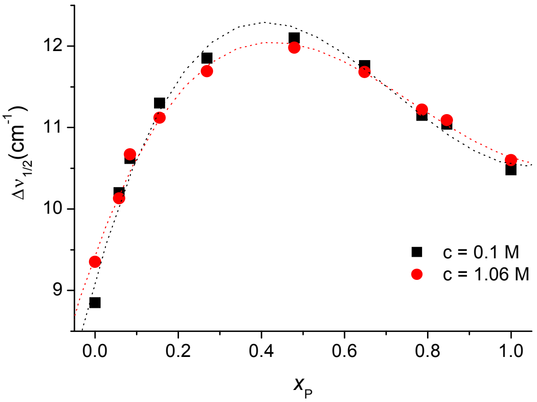

Figure 3. Dependence of the half bandwidth $\Delta\nu_{1/2}$ of 2-bromopropane ν(C-Br) band on the mole fraction x_P of acetonitrile from the CCl_4/CH_3CN mixtures (c is the molar concentration of solute)

In Figure 3 is presented the case of 2-bromopropane, but the graphs for the conformational isomers of 1-bromopropane are similar.

The maximum half bandwidth of ν(C-Br) band observed for values of mole fraction of acetonitrile smaller than 0.5 indicate a difference between the solvation energies of bromopropanes in the individual components of the CCl_4 / CH_3CN mixture

CONCLUSIONS

The solutes 2-bromopropane and 1-bromopropane do not disturb the “ideal” CH / THF solvent mixture.

The deviation from linear dependence of ν(C-Br) band frequency on mole fraction of acetonitrile observed under the effect of CCl_4/CH_3CN mixture is determined by the local “dielectric enrichment” of the solvation shell. The process of “preferential solvation” in this mixture can be characterized by the index *Z* which increases in the following order: *trans* 1-bromopropane < *gauche* 1-bromopropane < 2-bromopropane.

The maximum half bandwidth of ν(C-Br) band was observed for values of molar fraction of acetonitrile smaller than 0.5, indicating an increase of the difference between the solvation energy of bromopropanes in the individual components of the CCl_4/CH_3CN mixture. More exactly, the maximum broadening of ν(C-Br) band corresponds to the composition 2:1 of solvent mixture, for which the difference between mole fraction of acetonitrile in the bulk and in the vicinity of solute is the greatest.

EXPERIMENTAL SECTION

The analyzed spectra were collected using a JASCO 610 FTIR spectrometer, with a resolution of 0.5 cm^{-1} and sealed KBr cells of 0.012 and 0.062 cm path length. The spectra were obtained by subtracting the spectrum of pure solvent (multiplied with a proper factor which depends on the solute concentration) from that of the solution using the Spectra Analysis software of the spectrometer.

The frequency of ν(C-Br) vibrational mode of bromopropane compounds studied as neat liquids is 538.3 cm^{-1} for 2-bromopropane, 563.1 cm^{-1} for *gauche* isomer and 647.5 cm^{-1} for *trans* isomer of 1-bromopropane respectively.

The solvent mixtures used in this study, cyclohexane/ tetrahydrofuran (CH/THF) and carbon tetrachloride/acetonitrile (CCl_4/CH_3CN), were prepared from spectral grade solvents.

The solute concentrations were of 1.06 M for 2-bromopropane and 2.2 M for 1-bromopropane in both solvent mixtures and of 0.1 M and 0.22 M respectively, in CCl_4/CH_3CN solvent mixture.

The concentrations of 2-bromopropane were 0.1 M and 1.06 M and of 1-bromopropane were 0.22 M and 2.2 M in both solvent mixtures (CH/TH and CCl_4/CH_3CN).

ACKNOWLEDGMENTS

This paper is dedicated to the memory of Prof.dr Ioan Silaghi-Dumitrescu who provided scientific support in performing the *ab initio* calculations from the Ph.D. thesis by RG - „Spectre de absorbție la molecule poliatomice" (Absorption spectra of polyatomic molecules).

REFERENCES

1. R. Grecu, I. Bratu, O. Cozar, *Balkan Phys. Lett.*, **1997**, *5*, 231.
2. R. Grecu, A. Kun, I. Silaghi-Dumitrescu*, XXVI European Congress on Molecular Spectroscopy,* Villeneuve d'Ascq (France), 1-6 Sept. **2002***,* Book of Abstracts p.131.
3. R. Grecu, A. Kun, I. Silaghi-Dumitrescu, *J. Mol. Structure,* **2001***, 39,* 565.
4. L. Onsager, *J. Am. Chem. Soc.*, **1936**, *58*, 1486.
5. V. Bekárek, *Collect. Czech. Chem. Commun.,* **1989**, *54*, 3162.
6. S. P. Van, G. S. Hammond, *J. Am. Chem. Soc.*, **1978**, *100*, 3895.
7. T. Yoshino, *J. Chem. Phys.*, **1956**, *24*, 76.

STUDIA UNIVERSITATIS BABEŞ-BOLYAI, CHEMIA, XLV, 2, TOM II, 2010

Dedicated to the memory of Prof. dr. Ioan Silaghi-Dumitrescu marking 60 years from his birth

ADHESIVE INFLUENCE ON DOUBLE-LAP BONDED-JOINTS ASSEMBLIES

OVIDIU NEMES*

ABSTRACT. This work presents the influence of the adhesive on the double-lap joint assemblies. The adhesive characteristics and the influence on the stress distribution in double-lap adhesive bonded-joints assemblies' configuration are also presented.

Keywords: *structural adhesives, adhesive properties, double-lap adhesive assemblies*

INTRODUCTION

Adhesively bonded method distributes the stresses over the whole joining surface and removes the concentrations of stresses at the boundary of holes generated by bolting or riveting assemblies. Consequently, it is essential to know the stress distribution, which, because of its complexity, makes prediction of fractures difficult. To study the stress distribution it is very important to know the adhesive characteristics.

There are several models which try to define the stress distributions in double-lap [1 – 12]. Complex studies about various analytical models are compared by da Silva et al. [13].

Mortensen and Thomsen [14, 15] developed an approach for the analysis and design of various joints adhesively bonded. They took into account the influence of the interface effects between the adherends and they modelled the adhesive layer by assimilating it to a spring.

Diaz Diaz et al. [16] assumed in their classical double lap model that the adhesive thickness is small compared to that of the adherends and the stresses to be uniform through the adhesive thickness. The model can be considered as a stacking of Reisner-Mindlin plates and the equations based on this model were applied to the geometry of a symmetrical adhesively bonded joint. The model was validated by comparing the model results with those of a finite element calculation

---

[*] *Universitatea Tehnică din Cluj-Napoca, Facultatea de Ştiinţa şi Ingineria Materialelor, B-dul Muncii Nr. 103-105, RO-400641 Cluj-Napoca, Romania; ovidiu.nemes@sim.utcluj.ro*

Using a variational method and some simplifying assumptions, the author of this work developed and validated a new analytical model for a fast pre dimensioning of adhesive bonded assemblies [17-21]. The first stage consists in building a statically acceptable stress field, i.e. verifying the boundary conditions and the equilibrium equations. Then, the potential energy generated by such a stress field is calculated. In the third stage, the potential energy is minimized in order to determine the stress distributions. Finally, the analytical model proposed for double lap adhesive by bonded joints was validated using numerical and experimental methods.

In this paper, the adhesive influence on the stress distribution in double-lap adhesive bonded-joints assemblies' configuration was studied.

RESULTS AND DISCUSSION

A theoretical model of calculation of assemblies joined with adhesive, based on an energy method was developed by the author and coworkers [17-21]. After the determination of the cinematically acceptable field of stresses, according to the applied load, a variational calculus on the expression of elastic potential energy leads to the complete expression of the stress field in the whole assembly.

A first parametric analysis (geometrical and physicals parameters) is carried out on an assembly and makes it possible to deduce the optimal length and the thickness of the adhesive.

The performance of the adhesive bonded joints depends on the performance of the adhesive. The latest generations of adhesives, delivered in the form of film, make it possible to minimize the number of operations to make the join and greatly increase the mechanical resistance.

However, the design engineer must have at his disposal methods and/or reliable computer codes for predimensioning with known margins.

Using this energetical model, some analysis was carried out. The first step was to characterize the adhesive by tensile tests (plastic behavior of the adhesive was shows in experimental part).

Adhesive elastic modulus influence

The stresses in the adhesive are very important to predict the failure moment. For that it is primordial to have their distributions.

Figure 1 represents the influence of the elastic modulus of the adhesive on the shear stress distribution. The maximum peaks increase slightly when the elastic modulus increases.

Adhesive thickness influence

Another important parameter in double-lap adhesive bonded-joints assemblies' characterization is the thickness of the adhesive.

Figure 2 shows the influence of adhesive thickness on the adhesive shear stresses distribution. When the adhesive thickness increases, the maximum stresses in the adhesive decrease and the distribution tends to be uniform over the entire overlap length.

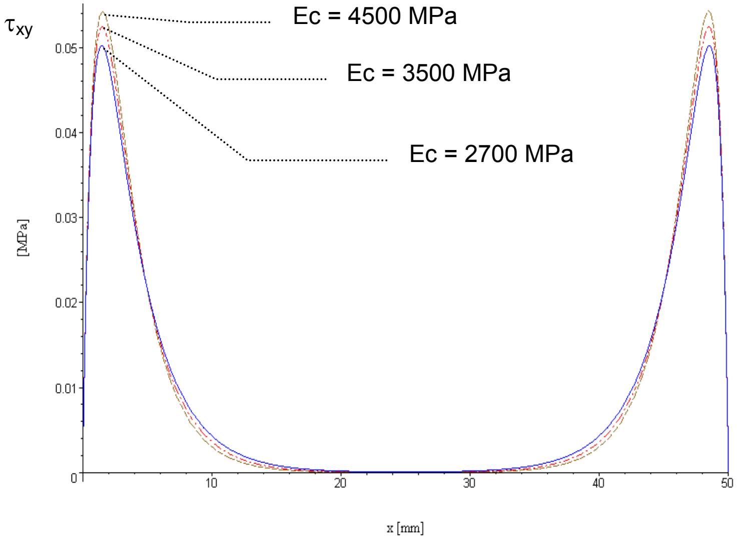

Figure 1. The influence of the elastic modulus of the adhesive on shear stress distribution in an AU 4G-AV 119-AU 4G assembly.

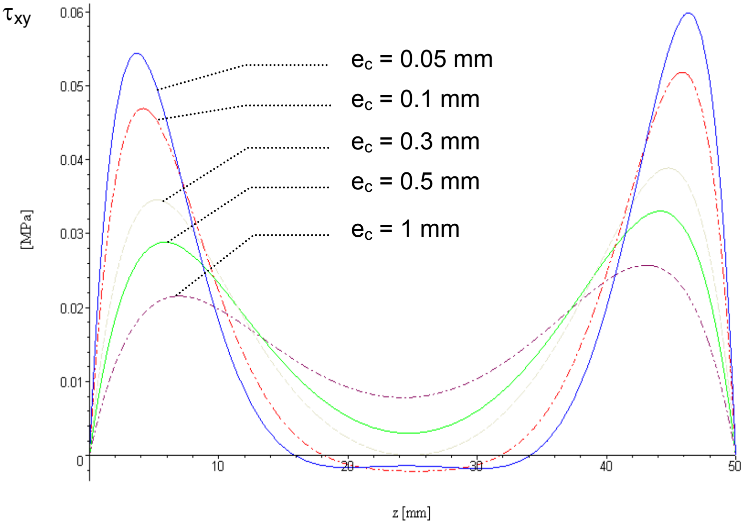

Figure 2. . The influence the of adhesive thickness on shear stress distribution in an AU 4G-AV 119-AU 4G assembly.

e_c = 0.05 mm, e_c = 0.1 mm, e_c = 0.3 mm, e_c = 0.5 mm, e_c = 1 mm

The analytical model underestimated the stresses in the adhesive, leading to an over-estimate of the forces at rupture. However, this model is reliable and allows fast analysis of this type of assembly.

EXPERIMENTAL PART

To obtain mechanical properties of the adhesive we have we carried out a plate with 10 layers of Redux adhesive film. The characteristics of the adhesive film, given by the manufacturer, are presented in table 1.

After the polymerization of the plate we cut out a piece with the following dimensions: 200x20x1.98 mm for tensile testing.

The tensile tests were carried out using an INSTRON 8862 system. The load is applied with imposed displacement at the speed of 0,5 mm/min. On certain tests we performed rises in cyclic loads (4 to 5 cycles).

The stress, displacement and deformations acquisition is carried out by a NICOLET-GOULD acquisition system.

The mechanical characteristics obtained by the tests are given in table 2. The double-lap adhesive bonded assembly has the following elements: two aluminium substrates AU 2024 T3 and a layer of epoxy adhesive AV 119 from Huntsman.

Table 1. Adhesive film technical data*.

HEXCEL COMPOSITES			Product Type:	Redux 312/5
Duxford			Batch No.:	054917A
Cambridge CB2 4QD,			Primes Type:	Redux 112
England			Batch No.:	V051196
	ADHESIVE TEST REPORT			
Specification IFS 201-216			Test No.:	17845
	Lap shear strength (MPa)			
	22 °C	80 °C		
	37.9	29.4		
	40.3	27.4		
	38.6	29.5		
	37.8	28.8		
	39.5			
Mean	38.8 MPa	28.8 MPa		
Min Ind.	37.8 MPa	27.4 MPa		
Requirements – Mean	35.0 MPa	28.0 MPa		
Min Ind.	32.0 MPa	25.0 MPa		

*Hexcel Composites

Figure 3 shows the plastic behavior of the adhesive.

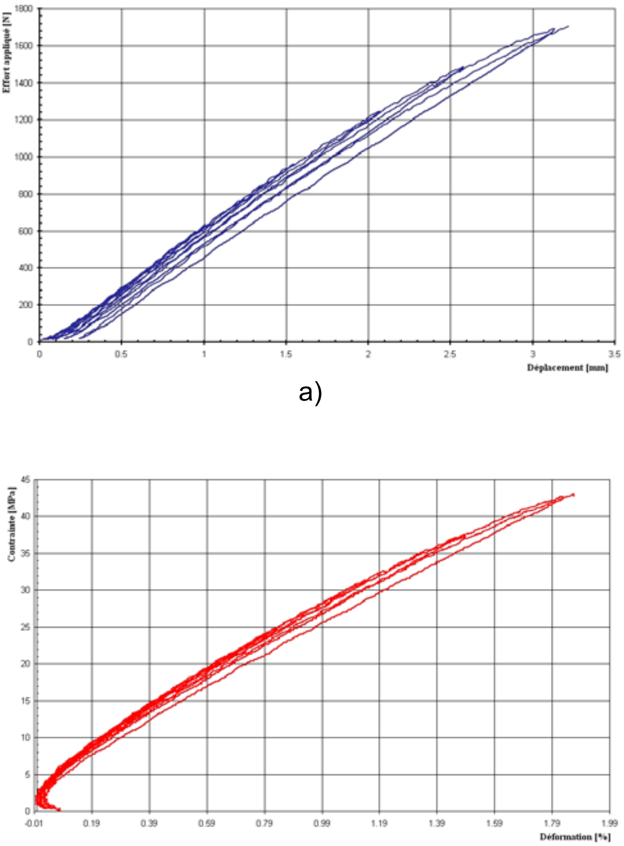

a)

b)

Figure 3. Adhesive tensile behaviour:
a) Applied load - displacement; b) Stress - deformation.

Table 2. Experimental results.

	$F_R^{(c)}$ [N]	$\sigma_{xx\,max}^{(c)}$ [MPa]	E_c [MPa]
1.	1730.47514	43.2618786	2014.07580
2.	2642.60815	44.7899687	2648.54446
3.	1708.61762	43.1469095	2750.00250

CONCLUSIONS

Based on presented case study, we can draw the following conclusions: the intensities of the peaks in the adhesive stress distribution are influenced by the elastic modulus of the adhesive. The maximum peaks increase slightly when the elastic modulus of the adhesive increase. As the adhesive thickness increases, the stresses in the adhesive decrease and the stress distribution is more uniform.

ACKNOWLEDGEMENT

The Ministry of Education and Research, Bucharest (ID-1100, PN II project) is thanked for the financial support of this work.

REFERENCES

1. O. Volkersen, Die Luftfahrtforschung, **1938**, 15, 41.
2. M. Goland, N.Y. Buffalo, E. Reissner, Journal of Applied Mechanics, **1944**, *66,* A17.
3. L.J. Hart-Smith, NASA-CR-112236, **1973**.
4. W.J. Renton, J.K. Vinson, Journal of Applied Mechanics, **1977**, 101.
5. I.U. Ojalvo, H.L. Eidinoff, AIAA Journal, **1978**, *16,* 204.
6. D.A. Bigwood, A.D. Crocombe, International Journal of Adhesion & Adhesives, **1989**, *9,* 229.
7. D.J. Allman, Journal of Mechanical Applied Mathematics, **1977**, *30,* 415.
8. O. Volkersen, Construction métallique, **1965**, *4,* 3.
9. Y. Gilibert, A. Rigolot, Mécanique des solides, **1979**, *288*, 287.
10. Y. Gilibert, A. Rigolot, Matériaux et Constructions, **1985**, *18*, 363.
11. Y. Gilibert, Matériaux et techniques, **1991**, 5.
12. L. Tong, International Journal of Solids Structures, **1994**, *31*, 2919.
13. L.F.M. da Silva, P.J.C. das Neves, R.D. Adams, J.K. Spelt, Int. J. Adhes. Adhes. **2009**, *29*, 319.
14. F. Mortensen, O.T. Thomsen, Composite Structures, **2002**, *56*, 165.
15. F. Mortensen, O.T. Thomsen, Composite Science and Technology, **2002**, *62*, 1011.
16. A. Diaz Diaz, R. Hadj-Ahmed, G. Foret, A. Ehrlacher, Int. J. Adhes. Adhes, **2009**, *29*, 67.
17. O. Nemes, F. Lachaud, A. Mojtabi, Int. J. Adhes. Adhes. **2006**, *26*, 474.
18. O. Nemes, Studia Universitatis Babes-Bolyai Chemia, **2007**, *52*, 175.
19. O. Nemes, F. Lachaud, A. Mojtabi, M. Borzan and St. Grigoras, Materials, Mater. Plast. **2008**, *45*, 390.
20. O. Nemes, F. Lachaud, J. Adhes. Sci. Technol. **2009**, *23* 1383.
21. O. Nemes, F. Lachaud, Int. J. Adhes. Adhes. **2010**, *30*, 288.